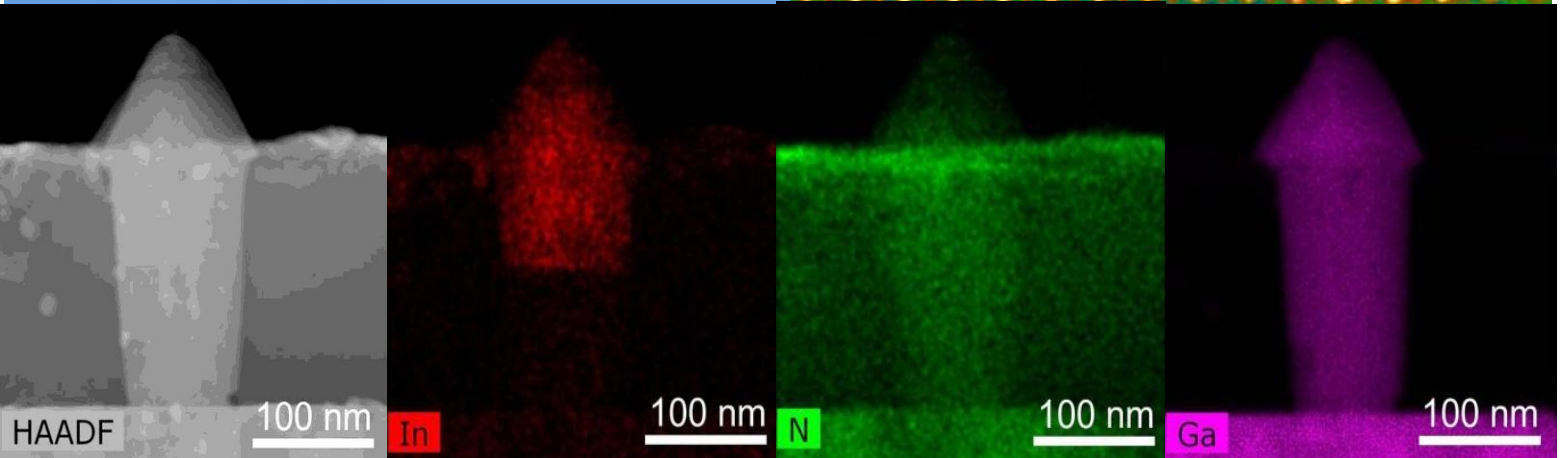
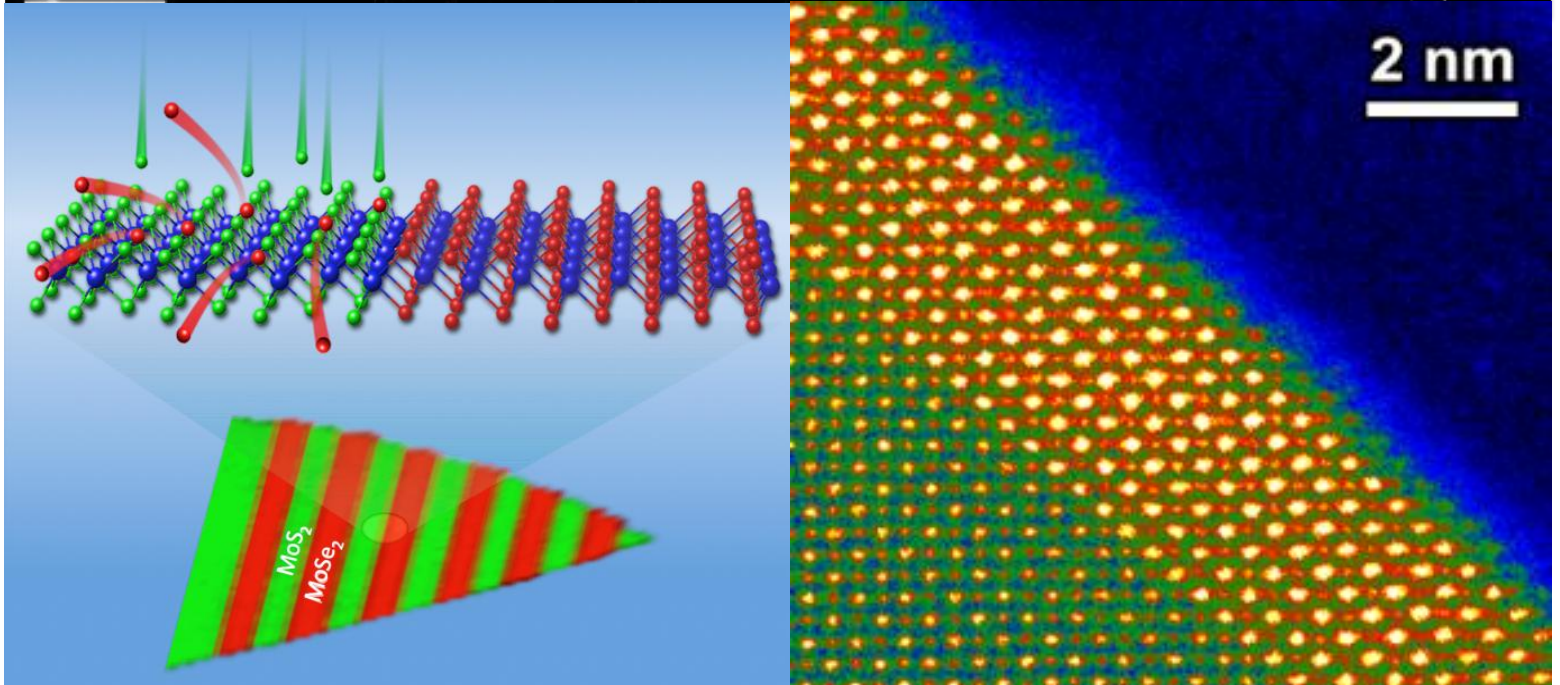
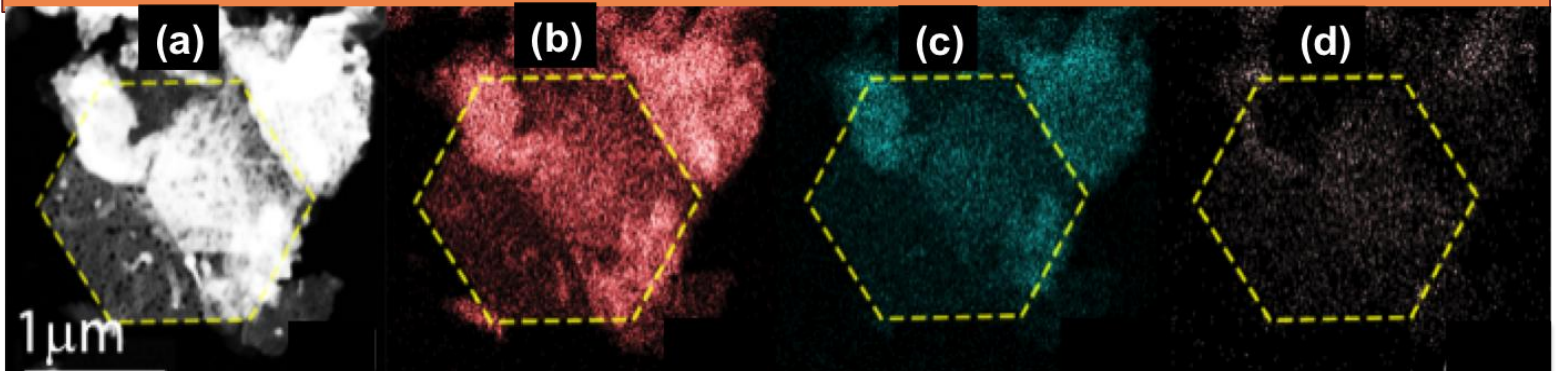


2015 Synthesis and Processing Science Principal Investigators' Meeting

*Hilton Washington DC North/Gaithersburg, Gaithersburg, MD
November 2-4, 2015*



U.S. DEPARTMENT OF
ENERGY

Office of
Science

Office of Basic Energy Sciences
Materials Sciences and Engineering Division

Top: Energy dispersive x-ray analysis showing the distribution of Cu, Ag and Se elements in the synthesized CuAgSe nano platelets obtained from Cu_{2-x}Se nano platelets through Ag⁺ ion exchange reaction at 300K: (a) original crystal, (b) Cu-K, (c) Se-K, (d) Ag-K. *Nanoscale* **7** (21), 9452 (2015). (Courtesy: P. Ferdinand Poudeu, University of Michigan)

Right Middle: Scanning transmission electron micrograph of a PNNL MBE-grown, all perovskite *pn* junction consisting of *p*-Sr_{0.12}La_{0.88}CrO₃ on *n*-SrTiO₃(001). *Adv. Mat.* **27**, 5191 (2015). (Courtesy: Scott Chambers, Pacific Northwest National Laboratory)

Left Middle: Arrays of semiconducting heterojunctions – the building blocks of ultrathin device electronics – were formed for the first time within a two-dimensional crystalline monolayer by lithographic patterning and pulsed laser deposition of sulfur. Sulfur atoms (green) replace selenium atoms (red) to convert MoSe₂ to MoS₂ in lithographically exposed regions (top) as shown by Raman spectroscopic mapping (bottom) of an actual MoSe₂/MoS₂ crystal. *Nature Commun.* **6**, 7749 (2015). (Courtesy: David Geohegan, Oak Ridge National Laboratory)

Bottom: From left to right, STEM image of a defect-free InGaN nanorod, and mapping images of element constituents in the InGaN nanorod. The colors of red, green, and purple represent In, N, and Ga respectively. *Nanotechnology* **25**, 225602 (2014). (Courtesy: Jung Han, Yale University)

This document was produced under contract number DE-AC05-06OR23100 between the U.S. Department of Energy and Oak Ridge Associated Universities.

The research grants and contracts described in this document are supported by the U.S. DOE Office of Science, Office of Basic Energy Sciences, Materials Sciences and Engineering Division.

Table of Contents

Foreword	vii
Program Description	xi
Agenda	xvii
Poster Sessions	xxiii
 Laboratory Projects' Abstracts	
<i>Anand Bhattacharya</i> , Argonne National Laboratory: Digital Synthesis: A Pathway to New Materials at Interfaces of Complex Oxides	3
<i>Ivan Božović</i> , Brookhaven National Laboratory: Atomic–Layer-by-Layer Molecular Beam Epitaxy Synthesis of Cuprate Superconductors.....	8
<i>Scott A. Chambers</i> , Pacific Northwest National Laboratory: Electronic, Magnetic, and Optical Properties of Doped Metal Oxide Epitaxial Films and Interfaces	13
<i>Amy J. Clarke</i> , Los Alamos National Laboratory: In-situ Monitoring of Dynamic Phenomena during Solidification.....	19
<i>Nancy J. Dudney</i> , Oak Ridge National Laboratory: Ion Transport and Structural Evolution of Solid Electrolytes.....	25
<i>David B. Geohegan</i> , Oak Ridge National Laboratory: Growth Mechanisms and Controlled Synthesis of Nanomaterials (ERKCS81): Nonequilibrium Synthesis of Ultrasmall Nanoparticles by Laser Vaporization as “Building Blocks” for Nanostructures and Thin Films	31
<i>Evgenii M. Levin</i> , Ames Laboratory: Novel Materials Processing and Preparation Methodologies Project: Thermoelectric Properties and NMR of Complex Materials	38
<i>Dongsheng Li</i> , Pacific Northwest National Laboratory: In Situ Investigations of Growth of Branched Crystal Structure	42
<i>Jun Liu</i> , Pacific Northwest National Laboratory: Molecularly Organized Nanostructural Materials.....	45
<i>Thomas A. Lograsso</i> , Ames Laboratory: Novel Materials Processing and Preparation Methodology Project: Single Crystal Growth of FeAs-based Superconductors	51

<i>Ralph E. Napolitano</i> , Ames Laboratory: Ordering in Glass-Forming Liquids: A Critical Component in the Dynamical Pathway.....	55
<i>Ralph E. Napolitano</i> , Ames Laboratory: Mechanisms of Crystallization in Glass-Forming Liquids: Interfaces, Diffusion, and Nucleation.....	60
<i>Ralph E. Napolitano</i> , Ames Laboratory: Metastable Phase Competition in Highly Undercooled Metallic Liquids and Glasses	65
<i>Cedomir Petrovic</i> , Brookhaven National Laboratory: Exploratory Materials Synthesis and Characterization	70
<i>Yevgeny Raitses</i> , Princeton Plasma Physics Laboratory: Fundamental Studies of Plasma-Based Synthesis of Nanomaterials: A Joint Challenge for Plasma and Materials Sciences.....	75
<i>Michael C. Tringides</i> , Ames Laboratory: Controlling Graphitic Substrates: Metal Intercalation, Li Barriers in Graphitic Battery Anodes and Graphene-Based Metamaterials	79
<i>Kai Xiao</i> , Oak Ridge National Laboratory: Growth Mechanisms and Controlled Synthesis of Nanomaterials (ERKCS81): Synthesis of Two-Dimensional Metal Chalcogenides by Laser Vaporization and CVD.....	85
<i>Mina Yoon</i> , Oak Ridge National Laboratory: Growth Mechanisms and Controlled Synthesis of Nanomaterials (ERKCS81): Modeling and Characterization of Ultrasmall Nanoparticles	92
University Grants' Abstracts	
<i>Michael S. Arnold</i> , University of Wisconsin–Madison: Direct Oriented Growth of Armchair Graphene Nanoribbons on Germanium	101
<i>Stacey F. Bent</i> , Stanford University: Studies of Surface Reaction and Nucleation Mechanisms in Atomic Layer Deposition	107
<i>Yves J. Chabal</i> , University of Texas at Dallas: Molecule-Sorbent Interactions in Metal Organic Framework Materials	112
<i>Eric Chason</i> , Brown University: A Unified Understanding of Residual Stress in Thin Films: Kinetic Model and Experiments	118
<i>I-Wei Chen</i> , University of Pennsylvania: Electric-Loading Enhanced Kinetics in Oxide Ceramics: Pore Migration, Sintering and Grain Growth	123
<i>Gabor Csathy</i> , Purdue University: Novel Sample Structures and Probing Techniques of Exotic States in the Second Landau Level	125

<i>John F. DiTusa</i> , Louisiana State University: Emergent Properties of Complex Transition Metal Compounds	129
<i>Mark D. Ediger</i> , University of Wisconsin–Madison: Stability, Structure, and Molecular Orientation in Organic Glasses Produced by Physical Vapor Deposition	133
<i>Chang-Beom Eom</i> , University of Wisconsin–Madison: Artificially Layered Superlattice of Pnictide by Design	137
<i>Andrei G. Fedorov</i> , Georgia Institute of Technology: Using Multi-Phase Energetic Precursor Jets to Enable New Modes of Focused Electron Beam Induced Processing (FEBIP)	141
<i>Kristen A. Fichthorn</i> , The Pennsylvania State University: Forces, Crystallization, and Assembly in Nanoparticle Suspensions	146
<i>Malancha Gupta</i> , University of Southern California: Understanding the Role of Viscosity and Deposition Rate during Vapor-Phase Free Radical Polymerization onto Liquid Surfaces	150
<i>Jung Han</i> , Yale University: Nanoscale Selective Growth and Microstructural Control of III-Nitride Growth	153
<i>A. John Hart</i> , Massachusetts Institute of Technology: Mesoscale Mechanochemistry of 2D Crystal Growth	159
<i>Hanchen Huang</i> , Northeastern University: Characteristic Length Scales of Growing Nanorods	164
<i>Himanshu Jain</i> , Lehigh University: Laser Fabrication of Single-Crystal Architecture in Glass: Control of Morphology	168
<i>Max G. Lagally</i> , University of Wisconsin–Madison: Synthesis and Processing Research in Group IV Nanomembranes	174
<i>Richard R. Lunt</i> , Michigan State University: Quasiepitaxial Growth of Organic Crystalline Thin-Films	181
<i>Lorenzo Mangolini</i> , University of California at Riverside: Non-equilibrium Effects in the Processing of Materials using Plasmas	185
<i>Zhiqiang Mao</i> , Tulane University: Novel Exotic Properties of Two-Dimensional Atomic Crystals of Layered Ternary Transition Metal Chalcogenides	189

<i>Theodore D. Moustakas</i> , Boston University: Growth of InGaN Quantum Dots by Liquid Phase Epitaxy (LPE) in an MBE Reactor	193
<i>Alexandra Navrotsky</i> , University of California at Davis: Thermochemistry of Oxides with Electrochemical and Energy Applications.....	197
<i>Ni Ni</i> , University of California at Los Angeles: Exploring Superconductivity at the Edge of Magnetic or Structural Instabilities	203
<i>George S. Nolas</i> , University of South Florida: A Fundamental Study of Inorganic Clathrates and Other Open-Framework Materials	207
<i>Eugene A. Olevsky</i> , San Diego State University: Fundamentals of Spark-Plasma Sintering: Materials Processing for Energy Applications	209
<i>Roberto Paiella</i> , Boston University: Plasmonic Metasurfaces for the Directional Control of Light Emission and Photodetection	215
<i>John H. Perepezko</i> , University of Wisconsin–Madison: New Oxide Materials for an Ultra High Temperature Environment	219
<i>Pierre F. Poudeu</i> , University of Michigan: Tailoring Charge Transport and Magnetism in Complex Half-Heusler/Full-Heusler Nanocomposites	223
<i>Bjoern Reinhard</i> , Boston University: New Optoplasmonic Materials for Next Generation Energy Systems	229
<i>Darrell G. Schlom</i> , Cornell University: Using Interfaces to Create Strongly Coupled Magnetic-Ferroelectrics	234
<i>Daniel P. Shoemaker</i> , University of Illinois at Urbana-Champaign: In Situ Thermodynamics and Kinetics of Mixed-Valence Inorganic Crystal Formation.....	244
<i>Theo Siegrist</i> , Florida State University: Discovery and Crystal Growth of New Oxide Phases from Metal Fluxes	248
<i>Jay A. Switzer</i> , Missouri University of Science and Technology: Electrodeposition of Water-Splitting Catalysts and Epitaxial Perovskite Films for Solar Energy Conversion	254
<i>Maria C. Tamargo</i> , The City College of New York: Enhanced Materials Based on Submonolayer Type-II Quantum Dots.....	259
<i>Peter W. Voorhees</i> , Northwestern University: The Dynamics of Complex Two-Phase Mixtures during Coarsening: From Dendritic to Bicontinuous Mixtures.....	265

<i>Xudong Wang</i> , University of Wisconsin–Madison: Synthesis of Three-Dimensional Nanowire Architecture with Enhanced Performance in Solar Energy Harvesting	269
<i>Boris I. Yakobson</i> , Rice University: Boron-Based Nanostructures, Stability, Functionality and Synthetic Routes	274
<i>Boris I. Yakobson</i> , Rice University: Mapping the Synthetic Routes for 2-Dimensional Materials	277
<i>Francisco Zaera</i> , University of California at Riverside: Atomic Layer Deposition (ALD) of Metal and Metal Oxide Films: A Surface Science Study	280
<i>Pengpeng Zhang</i> , Michigan State University: Utilizing Molecular Self-Assembly to Tailor Electrical Properties of Si Nanomembranes	285
<i>Guangwen Zhou</i> , State University of New York–Binghamton: In Situ Visualization and Theoretical Modeling of Early-Stage Oxidation of Metals and Alloys	290
<i>Joshua M. O. Zide</i> , University of Delaware: Growth and Properties of New Epitaxial Metal/Semiconductor Nanocomposites	294
Participant List	301
Author Index	305

FOREWORD

This abstract book comprises the scientific content of the 2015 Synthesis and Processing Science Principal Investigators' Meeting sponsored by the U.S. Department of Energy, Office of Science, Office of Basic Energy Sciences, Materials Sciences and Engineering (MSE) division. The meeting, held on November 2–4, 2015, at the Washington D.C. North/Gaithersburg Hilton, Gaithersburg, Maryland, is the fifth principal investigators' meeting on this topic and is one among a series of research theme-based principal investigators' meetings being held by the MSE division.

The purpose of this principal investigators' meeting is to bring together all of the researchers funded in the Synthesis and Processing Science core research activity so they can get a firsthand look at the broad range of materials science research that is being supported in this important research area. The meeting will serve as a forum for the discussion of new results and research highlights, thus fostering a greater awareness of significant new advances in the field and the research of others in the program. The confidential and collegial meeting environment is intended to provide unique opportunities to develop new collaborations among PIs, and new ideas. In addition, the meeting affords BES program managers an opportunity to assess the state of the entire program at one time on a periodic basis, in order to chart future directions and identify new programmatic needs.

This year's meeting focuses on four topics within the Synthesis and Processing Science portfolio: non-idealities in materials, systems far from equilibrium, computational materials modeling, and hierarchical material structures. In addition, a crosscutting fifth topic is on instrumentation for better synthesis. While this is one way of organizing and presenting the research within this broad portfolio, there are many other synergies that could be highlighted and will be considered at future meetings.

Let me take this opportunity to express my thanks to all the meeting attendees, for their active participation and sharing their ideas and new research results. Special thanks are given to the Meeting Chairs, P. Ferdinand Poudeu and Scott Chambers, for their dedicated efforts and invaluable assistance towards organizing this meeting. Finally, this meeting would not be possible without the logistical support from Teresa Crockett at DOE-MSE as well as Linda Severs at Oak Ridge Institute for Science and Education (ORISE).

Bonnie Gersten
Program Manager, Synthesis and Processing Science
Materials Sciences and Engineering Division
Office of Basic Energy Sciences
Office of Science
U.S. Department of Energy

Program Description

2015 DOE BES MSE Synthesis and Processing Science Principal Investigators' Meeting

The four topical sessions into which abstracts will be partitioned, and some crosscutting issues we want to explore, are:

- I. **Non-idealities in materials:** *Can we more deeply characterize and understand the non-idealities that inevitably occur during synthetic processes for model materials? How can we effectively utilize these defects to engineer useful structures, and thereby strengthen our ability to deal with the complexities of systems operating under more realistic conditions?*
- II. **Systems far from equilibrium:** *Can experiment and theory be bridged to construct accurate models of the evolution of materials away from equilibrium, and thus pave the way for new states of matter?*
- III. **Computational materials modeling - predicting synthesis and properties:** *What new opportunities do advances in computer science and technology offer for reaching the next level of rigor in materials modeling, predicting the properties of realistic materials, and revealing new pathways for experimental materials synthesis and processing?*
- IV. **Hierarchical material structures:** *How can advanced synthetic, characterization, and modeling tools be harnessed to enable the fabrication and understanding of artificially structured materials with hierarchical arrangements of matter and the attendant novel functionalities?*

Non-idealities in materials:

Materials design and computational materials modeling often start with the assumption of ideal composition (i.e., the targeted stoichiometry with no impurities) and perfect structure (all the atoms right where we want them and their sites are well defined). Following synthetic efforts, materials characterization is carried out at some level and functional properties are measured. The results are then often interpreted in terms of the idealized model. This approach is the most straightforward and least time consuming to pursue because defects are sometimes rather hard to detect, characterize, and model. However, this zeroth-order approach can be seriously misleading because, depending on the concentrations and relative influences of the defects that are present, the resulting structure-composition-property relationships may be at least partially, if not completely, incorrect. Some defects are the result of experimental design inadequacies and can be eliminated relatively easily. However, others are inevitable outcomes dictated by the laws of thermodynamics, particularly for more complex systems. Having the ability to detect, fundamentally understand, and predict non-idealities of all kinds would position investigators to harness these entities to advantage. As the astronomically large numbers of combinations of the more than 110 elements on the periodic chart are explored in the search for novel functionalities, having a robust strategy for detecting and dealing with non-idealities is essential.

Systems far from equilibrium:

The tendency of materials systems to move in the direction of thermodynamic equilibrium can sometimes alter system properties relative to what is sought in designing them. An example is an atomically abrupt epitaxial heterojunction between two dissimilar materials. If a heterojunction is given enough thermal energy to promote layer-by-layer epitaxial growth, entropic effects will often cause atoms at the solid/solid interfaces to diffuse across the junction, resulting in a mixed interfacial region. The properties of such a junction may or may not be what was hoped for. Accordingly, a grand challenge in materials science is to devise novel methods that harness such entropic effects. In many classes of materials, novel compositions, crystallographic orientations and morphologies can in principle be stabilized by synthesizing and/or processing under conditions far from equilibrium. However, there are significant gaps in our understanding of how and why systems far from equilibrium evolve as they do. Additionally, the influence of barriers which may trap the system in a non-equilibrium state is largely unknown. Modeling has the potential to fill in experimental knowledge gaps that defy our current suite of characterization tools. As a result, bridging theories across many length, time, and energy scales in order to elucidate organizing principles of systems away from equilibrium is a grand challenge.

Computational materials modeling - predicting synthesis and properties:

With the advent of massively parallel computers and the potential of exascale computing, materials modeling can be carried out with unprecedented levels of complexity and accuracy. Are these advances sufficient to turn computational modeling into a predictive synthesis tool? The new horizons include not only predicting the properties of complex material systems at equilibrium at levels of accuracy beyond DFT, but also understanding the dynamics of synthesis and phase transitions, both near to and far from equilibrium, and predicting those novel syntheses and processing pathways that would ultimately lead to new materials. Additionally, can one actually predict the structure of novel functional materials starting from a combination of elements in the desired chemical composition and stoichiometry or from the integration of elementary building blocks derived from simple crystal structures? What are challenges and opportunities for computational modeling from the perspective of practitioners?

Hierarchical material structures:

Learning to assemble hierarchical materials creates unique opportunities to explore the properties of matter at a fundamentally new level. Nanoscale crystallization from the vapor phase and in electrochemical cells, self-assembly of optoplasmonic molecules, focused electron beam induced deposition, and reactions within metal organic framework materials are some of the novel synthetic methods being explored to generate a variety of interesting and potentially useful materials structures that could impact several different technologies. At a fundamental level, our ability to design and control synthetic pathways determines final structural forms. Control of the synthesis process in turn depends in large part on the extent to which the hierarchical system of

interest can be characterized in real time. Likewise, the ability to rationally design useful synthetic pathways requires significant predictive power from modeling.

Informal discussions:

We will hold two informal evening discussions Monday and Tuesday before dinner with the goal of identifying grand challenges in materials modeling that might be achievable with new hardware and software resulting from the DOE Exascale Computing Initiative (<http://www.exascaleinitiative.org/>). The question is, what kinds of calculations would you like to see done if ~100x more computer horsepower was available for computational materials modeling? Each evening we will limit the scope of the discussion to the subject areas of the day (i.e., non-idealities in materials and systems far from equilibrium on Monday, and hierarchical material structures on Tuesday).

Our challenge this week:

This meeting brings together a diverse group of investigators with the potential to make significant progress in these four areas of importance to BES, and to stimulate the broader scientific community worldwide. Our goal for this meeting is to foster discussions and collaborations that will lead to advances in these arenas.

Agenda

Synthesis and Processing Science Principal Investigators' Meeting Agenda

Monday, November 2, 2015

7:00 – 8:00am *****Breakfast*****

8:00 – 8:15am *Introductory Remarks*
Meeting Chairs: Scott Chambers and Pierre Ferdinand P. Poudeu
Pacific Northwest National Laboratory / University of Michigan

Session 1 **Non-idealities in Materials**
Chair: **Ivan Bozovic**, Brookhaven National Laboratory

8:15 – 8:45am **Anand Bhattacharya**, Argonne National Laboratory
Magnetism at Interfaces of Complex Oxides: Challenges and Opportunities

8:45 – 9:15am **Scott Chambers**, Pacific Northwest National Laboratory
B-site Cation Disorder and Secondary Phase Formation in the MBE Growth of a
Ferromagnetic Double Perovskite – $\text{La}_2\text{MnNiO}_6$

9:15 – 9:45am **Darrell Schlom**, Cornell University
Point Defects—The Dirty Little Secret of Oxide Thin Films

9:45 – 10:15am *****Break*****

10:15 – 10:45am **Maria Tamargo**, City University of New York
Structural Properties of Sub-monolayer Type-II Quantum Dots: Measurement and Control of
Their Size and Density and Determination of Their Shape Anisotropy

Session 2 **Systems Far from Equilibrium**
Chair: **Michael Tringides**, Ames Laboratory

10:45 – 11:15am **David Geohegan**, Oak Ridge National Laboratory
Nonequilibrium Synthesis and Evolution of Building Blocks in Nanostructure Growth

11:15 – 11:45am **Yevgeny Raitses**, Princeton Plasma Physics Laboratory
Synergistic Roles of Plasma and Material Processes in Arc Synthesis of Nanomaterials

11:45 – 12:45pm *****Working Lunch / Poster Introductions*****

Session 3 **Division and Program Updates**

12:45 – 1:30pm **Linda Horton**, Director of Materials Science & Engineering
MSE Overview
Arvind Kini, Team Lead, Materials Discovery, Design and Synthesis
Program Updates
Bonnie Gersten, Program Manager, Synthesis and Processing Science
Program Updates

1:30 – 3:00pm **Poster Session I**

- Session 4** **Systems Far from Equilibrium (continued)**
Chair: **Michael Tringides**, Ames Laboratory
- 3:00 – 3:30pm **Guangwen Zhou**, SUNY– Binghamton
In Situ Atomic-Scale Imaging of the Oxidation of Metals and Alloys
- 3:30 – 4:00pm **Amy Clarke**, Los Alamos National Laboratory
Multi-scale Prediction and Control of Metal Alloy Solidification Dynamics
- 4:00 – 4:30pm **Ralph Napolitano**, Ames National Laboratory
Phase Selection in Highly Undercooled Metallic Liquids: Phases, Order, and Mechanisms in Al-Sm
- 4:30 – 4:45pm *****Break*****
- 4:45 – 5:15pm **Max Lagally** (BESAC member), University of Wisconsin-Madison
BESAC Report: “Challenges at the Frontiers of Matter and Energy: Transformative Opportunities for Discovery Science”
- 5:15 – 6:15pm Discussion Leaders: **James Davenport and Matthias Graf** (Program Managers for Theoretical Condensed Matter Physics, MSE)
Informal discussion – If the sky was the limit, what would we be modeling in the areas of non-idealities in materials and systems far from equilibrium?
- 6:15 – 7:15pm ***** Working Dinner / Meeting Discussions*****
- 7:15 – 8:45pm **Poster Session I (continued)**

Tuesday, November 3, 2015

- 7:00 – 8:00am *****Breakfast*****
- Session 5** **Hierarchical Material Structures**
Chair: **Jun Liu**, Pacific Northwest National Laboratory
- 8:00 – 8:30am **Xudong Wang**, University of Wisconsin
Development of Hierarchical 3D Nanowire Architectures by High-Temperature Derivatives of Atomic Layer Deposition
- 8:30 – 9:00am **Jay Switzer**, Missouri University of Science and Technology
Photoelectrochemical Water Oxidation on an Electrodeposited n-Si/SiO_x/Co/CoOOH Photoanode – A Close Look at the Catalyst
- 9:00 – 9:30am **Yves Chabal**, University of Texas, Dallas
Chemistry in Confined Environments: Water Reaction in MOF-74
- 9:30 – 10:00am *****Break*****
- 10:00 – 10:30am **Andrei Fedorov**, Georgia Tech
Using Multi-Phase Energetic Jets to Achieve Understanding of Precursor-Surface Interactions and Enable New Modes of Focused Electron Beam Induced Processing (FEBIP)

- 10:30 – 11:00am **P. Ferdinand Poudeu**, University of Michigan
Electron and Phonon Transport in Nanostructured Semiconductors
- 11:00 – 11:30am **Bjoern Reinhard**, Boston University
Directed Assembly of Optoplasmonic Hybrid Materials with Tunable Photonic-Plasmonic Properties
- 11:30 – 12:00pm **James De Yoreo**, Pacific Northwest National Laboratory
Workshop report on “Crystallization by Particle Attachment” held in December 2013 in Berkeley, California, sponsored by the Council on Geosciences of the U.S. Department of Energy, Office of Science, Office of Basic Energy Sciences
- 12:00 – 1:00pm *****Working Lunch / Poster Introductions*****
- 1:00 – 2:30pm **Poster Session II**
- Session 6** **Computational Materials Modeling**
Chair: **Mina Yoon**, Oak Ridge National Laboratory
- 2:30 – 3:00pm **Kristen Fichthorn**, Pennsylvania State University
How Structure-Directing Agents Control Nanocrystal Shape: PVP-Mediated Growth of Ag Nanocubes
- 3:00 – 3:30pm **Boris Yakobson**, Rice University
Modeling 2D materials, Steps from Explaining to Predicting
- 3:30 – 4:00pm **Hanchen Huang**, Northeastern University
From Atomistic Simulations to Closed-Form Theories of Nanorod Growth, and Beyond
- 4:00 – 4:30pm **Timo Thonhauser**, Wake Forest University
Modeling Van der Waals Interactions in Metal Organic Frameworks
- 4:30 – 4:45pm *****Break*****
- 4:45 – 5:15pm **Eugene Olevsky**, San Diego State University
Modeling of Field-Assisted Sintering: Predictive Materials Synthesis and Processing Optimization
- 5:15 – 6:15pm Discussion Leaders: **Peter Sushko and Kristen Fichthorn**
Pacific Northwest National Laboratory / Pennsylvania State University
Informal Discussion – *If the sky was the limit, what would we be modeling in the area of hierarchical material structures?*
- 6:15 – 7:15pm ***** Working Dinner / Meeting Discussions*****
- 7:15 – 8:45pm **Poster Session II (continued)**

Wednesday, November 4, 2015

7:30 – 8:30am ***Breakfast***

Session 7 **Instrumentation for Better Synthesis**
Chair: **Stacey Bent**, Stanford University

8:30 – 9:00am **Nancy Dudney**, Oak Ridge National Laboratory
Solid Electrolytes – Probing Synthesis and Interfaces with Neutrons and Electron
Microscopy

9:00 – 9:30am **John Di Tusa**, Louisiana State University
Techniques for Large Single-Crystal Growth of Transition Metal Compounds for Neutron
Scattering

9:30 – 10:00am **John Hart**, Massachusetts Institute of Technology
Force-Mediated Growth of Carbon Nanotubes

10:00 – 10:30am ***Break***

10:30 – 11:30am Summary of the State of the Art and Future Directions
Scott Chambers and Pierre Ferdinand P. Poudeu
Bonnie Gersten

11:30am **Meeting Adjourns**

Poster Sessions

Synthesis and Processing Principal Investigators' Meeting

POSTER SESSION I

Monday, November 2, 2015

1. *Digital Synthesis: A Pathway to New Materials at Interfaces of Complex Oxides*
Anand Bhattacharya, Argonne National Laboratory
2. *Using Interfaces to Create Strongly Coupled Magnetic-Ferroelectrics*
Darrell G. Schlom, Cornell University
3. *Atomic-layer-by-layer Molecular Beam Epitaxy Synthesis of Cuprate Superconductors*
Ivan Božović, Brookhaven National Laboratory
4. *Electronic, Magnetic, and Optical Properties of Doped Metal Oxide Epitaxial Films and Interfaces*
Scott A. Chambers, Pacific Northwest National Laboratory
5. *Growth and Properties of New Epitaxial Metal/Semiconductor Nanocomposites*
Joshua M. O. Zide, University of Delaware
6. *Novel Sample Structures and Probing Techniques of Exotic States in the Second Landau Level*
Gabor Csathy and Michael Manfra, Purdue University
7. *Nanoscale Selective Growth and Microstructural Control of III-Nitride Growth*
Jung Han, Yale University
8. *Enhanced Materials Based on Submonolayer Type-II Quantum Dots*
Maria C. Tamargo, The City College of New York
9. *Growth of InGaN Quantum Dots by Liquid Phase Epitaxy (LPE) in an MBE Reactor*
Theodore D. Moustakas, Boston University
10. *Plasmonic Metasurfaces for the Directional Control of Light Emission and Photodetection*
R. Paiella, Boston University
11. *A Unified Understanding of Residual Stress in Thin Films: Kinetic Model and Experiments*
Eric Chason, Brown University
12. *In-Situ Monitoring of Dynamic Phenomena during Solidification*
Amy J. Clarke, Los Alamos National Laboratory
13. *The Dynamics of Complex Two-Phase Mixtures During Coarsening:
From Dendritic to Bicontinuous Mixtures*
Peter W. Voorhees, Northwestern University
14. *Ordering in Glass-Forming Liquids: A Critical Component in the Dynamical Pathway*
R. E. Napolitano, Ames Laboratory
15. *Mechanisms of Crystallization in Glass-forming Liquids: Interfaces, Diffusion, and Nucleation*
R. E. Napolitano, Ames Laboratory
16. *Metastable Phase Competition in Highly Undercooled Metallic Liquids and Glasses*
M. J. Kramer, Ames Laboratory

17. *Growth Mechanisms and Controlled Synthesis of Nanomaterials (ERKCS81): Synthesis of Two-Dimensional Metal Chalcogenides by Laser Vaporization and CVD*
Kai Xiao, Oak Ridge National Laboratory
18. *Growth Mechanisms and Controlled Synthesis of Nanomaterials (ERKCS81): Nonequilibrium Synthesis of Ultrasmall Nanoparticles by Laser Vaporization as "Building Blocks" for Nanostructures and Thin Films*
David B. Geohegan, Oak Ridge National Laboratory
19. *Fundamental Studies of Plasma-Based Synthesis of Nanomaterials: A Joint Challenge for Plasma and Materials sciences*
Yevgeny Raitsev, Princeton Plasma Physics Laboratory
20. *Surface Structures Far-from-Equilibrium*
Michael C. Tringides, Ames Laboratory
21. *Direct Oriented Growth of Armchair Graphene Nanoribbons on Germanium*
Michael S. Arnold, University of Wisconsin-Madison
22. *Synthesis and Processing Research in Group IV Nanomembranes*
Max G. Lagally, University of Wisconsin-Madison
23. *Non-equilibrium Effects in the Processing of Materials using Plasmas*
Lorenzo Mangolini, University of California Riverside
24. *Understanding the Role of Viscosity and Deposition Rate during Vapor-Phase Free Radical Polymerization onto Liquid Surfaces*
Malancha Gupta, University of Southern California
25. *Stability, Structure, and Molecular Orientation in Organic Glasses Produced by Physical Vapor Deposition*
Mark D. Ediger, University of Wisconsin-Madison
26. *Quasiepitaxial Growth of Organic Crystalline Thin-Films*
Richard R. Lunt, Michigan State University
27. *Utilizing Molecular Self-Assembly to Tailor Electrical Properties of Si Nanomembranes*
Pengpeng Zhang, Michigan State University
28. *Atomic Layer Deposition (ALD) of Metal and Metal Oxide Films: A Surface Science Study*
Francisco Zaera, University of California
29. *Studies of Surface Reaction and Nucleation Mechanisms in Atomic Layer Deposition*
Stacey F. Bent, Stanford University
30. *Artificially Layered Superlattice of Pnictide by Design*
Chang-Beom Eom, University of Wisconsin-Madison
31. *Discovery and Crystal Growth of New Oxide Phases from Metal Fluxes*
Theo Siegrist, Florida State University

Synthesis and Processing Science Principal Investigators' Meeting

POSTER SESSION II Tuesday, November 3, 2015

1. *Characteristic Length Scales of Growing Nanorods
An Example of Basic Science Enabled Technology*
Hanchen Huang, Northeastern University
2. *Forces, Crystallization, and Assembly in Nanoparticle Suspensions*
Kristen A. Fichthorn, The Pennsylvania State University
3. *Growth Mechanisms and Controlled Synthesis of Nanomaterials (ERKCS81):
Modeling and Characterization of Ultrasmall Nanoparticles*
Mina Yoon, Oak Ridge National Laboratory
4. *Boron-Based Nanostructures, Stability, Functionality and Synthetic Routes*
Boris I. Yakobson, Rice University
5. *Mapping the Synthetic Routes for 2-Dimensional Materials*
Boris I. Yakobson, Rice University
6. *Fundamentals of Spark-Plasma Sintering: Materials Processing for Energy Applications*
Eugene A. Olevsky, San Diego State University
7. *Electric-Loading Enhanced Kinetics in Oxide Ceramics: Pore Migration, Sintering and Grain Growth*
I-Wei Chen, University of Pennsylvania
8. *Thermoelectric Properties and NMR of Complex Materials*
E. M. Levin, Ames Laboratory
9. *Emergent Properties of Complex Transition Metal Compounds*
John F. DiTusa, Louisiana State University
10. *Ion Transport and Structural Evolution of Solid Electrolytes*
Nancy Dudney, Oak Ridge National Laboratory
11. *In Situ Investigations of Growth of Branched Crystal Structure*
Dongsheng Li, Pacific Northwest National Laboratory
12. *In Situ Visualization and Theoretical Modeling of Early-Stage Oxidation
of Metals and Alloys*
Guangwen Zhou, State University of New York
13. *Mesoscale Mechanochemistry of 2D Crystal Growth*
A. John Hart, Massachusetts Institute of Technology
14. *New Oxide Materials for an Ultra High Temperature Environment*
John H. Perepezko, University of Wisconsin-Madison
15. *Exploring Superconductivity at the Edge of Magnetic or Structural Instabilities*
Ni Ni, University of California, Los Angeles

16. *Exploratory Materials Synthesis and Characterization*
Cedomir Petrovic, Brookhaven National Laboratory
17. *Single Crystal Growth of FeAs-based Superconductors*
Thomas A. Lograsso, Ames Laboratory
18. *In Situ Thermodynamics and Kinetics of Mixed-Valence Inorganic Crystal Formation*
Daniel P. Shoemaker, University of Illinois at Urbana-Champaign
19. *Novel Exotic Properties of Two-Dimensional Atomic Crystals of Layered Ternary Transition Metal Chalcogenides*
Zhiqiang Mao, Tulane University
20. *Laser Fabrication of Single-Crystal Architecture in Glass: Control of Morphology*
Himanshu Jain, Lehigh University
21. *A Fundamental Study of Inorganic Clathrates and Other Open-Framework Materials*
George S. Nolas, University of South Florida
22. *Tailoring Charge Transport and Magnetism in Complex Half-Heusler/Full-Heusler Nanocomposites*
Pierre Ferdinand Poudeu, University of Michigan
23. *Thermochemistry of Oxides with Electrochemical and Energy Applications*
Alexandra Navrotsky, University of California, Davis
24. *New Optoplasmonic Materials for Next Generation Energy Systems*
Bjoern Reinhard, Boston University
25. *Synthesis of Three-Dimensional Nanowire Architecture with Enhanced Performance in Solar Energy Harvesting*
Xudong Wang, University of Wisconsin-Madison
26. *Electrodeposition of Water-Splitting Catalysts and Epitaxial Perovskite Films for Solar Energy Conversion*
Jay A. Switzer, Missouri University of Science and Technology
27. *Molecularly Organized Nanostructural Materials*
Jun Liu, Pacific Northwest National Laboratory
28. *Using Multi-Phase Energetic Precursor Jets to Enable New Modes of Focused Electron Beam Induced Processing (FEBIP)*
Andrei G. Fedorov, Georgia Tech
29. *Molecule–Sor bent Interactions in Metal Organic Framework Materials*
Yves J. Chabal, University of Texas at Dallas

Laboratory Projects' Abstracts

Project Title: Digital Synthesis: A Pathway to New Materials at Interfaces of Complex Oxides

Principle Investigator: Anand Bhattacharya

Address: Materials Science Division, Bldg. 223, 9700 S. Cass Ave., Argonne National Laboratory, Argonne, IL 60657.

email: anand@anl.gov

Program Scope:

In our program, we seek to create, characterize and understand superlattices and heterostructures of complex oxides with novel electronic and magnetic states. We synthesize these materials using oxide molecular beam epitaxy (MBE). This allows us to tailor chemically precise interfaces with roughness comparable to or less than the length scales for interfacial charge transfer and exchange interactions.

The complex oxides host a very diverse range of collective states of condensed matter. The richness of observed phenomena in these materials, which have also presented some of the greatest challenges to our understanding, are due to their strongly interacting degrees of freedom. Surfaces and interfaces between complex oxides provide a unique environment where these degrees of freedom may ‘reconstruct’ and lead to new properties that are qualitatively different from those of their bulk constituents. More specifically, we seek to discover and explore states with novel responses to external electric fields, thermal gradients and magnetic fields. We explore novel magnetic structures that arise as a result of charge transfer, electronic states that arise as a result of strong spin-orbit coupling, multiferroic heterostructures and non-collinear interfacial magnetic structures. We seek to explore materials that are known to have interesting phases where the atoms have been ‘re-arranged’ in simple ways – for example by layering the cations in a manner such that the effects of disorder have been engineered away – to reveal new properties. We create these materials systems using ozone-assisted oxide MBE at Argonne, and characterize them using the major DOE facilities for neutron and photon scattering, and at the DOE Nanoscale Science Research Centers.

Recent Progress (since 2013):

1. Tailoring magnetic and electronic states via charge transfer at interfaces

In conventional semiconductors and metals, a mismatch between the chemical potential for charge carriers at an interface leads to charge transfer, interfacial electric fields and consequences such as band bending and Schottky barriers. In narrow band correlated insulators and metals derived from them, this charge transfer can have profound consequences. We investigated the interface between two very dissimilar perovskites, LaMnO_3 and LaNiO_3 . LaMnO_3 is an antiferromagnetic orbital-ordered Mott insulator and LaNiO_3 is a paramagnetic metal. In superlattices of $(\text{LaMnO}_3)_2/(\text{LaNiO}_3)_2$, we demonstrated that charge transfer at the interface leads to a metal-insulator transition and changes in the magnetic properties as n is varied (J. Hoffman et al., *Phys. Rev. B* 2013). The mechanism behind the metal insulator transition, which involves a transfer of spectral weight away from the Drude peak, was further elucidated in measurements of optical conductivity of these superlattices by our collaborators (P. Di Pietro et al., *Phys. Rev. Lett.* 2015). Charge transfer can also have a profound influence on properties of superlattices where both constituents are *metals*, due to the relatively large Thomas Fermi screening length in the $3d$ perovskite oxides. In superlattices of

$(\text{La}_{2/3}\text{Sr}_{1/3}\text{MnO}_3)_9/(\text{LaNiO}_3)_n$ where both constituent materials are metals, we used neutron scattering and x-ray absorption spectroscopy to show that interfacial charge transfer leads to a *non-collinear* magnetic structure. Our data are consistent with the development of a spin-spiral within the LaNiO_3 layers. (J. Hoffman et al., *arXiv:1411.4344*). Measurements of the angular dependence of Nernst effect combined with anisotropic magnetoresistance data confirm the non-collinear magnetic structure measured using neutron scattering on the same samples. We also have ongoing collaboration with Prof. Jian-Min Zuo’s group (UIUC) and with Dr. Albina Borisevich (ORNL) to understand how charge transfer might affect local electronic properties near these interfaces using transmission electron microscopy (STEM EELS).

2. Tailoring polarity in a two-dimensional nickelate with single atomic layer control

Many of the $3d$ transition metal oxides share a common structural MO_6 building unit—a central transition metal (TM) cation octahedrally coordinated with oxygen nearest neighbors. The electronic states in these materials can be modified by tailoring the M -O bonds, which typically

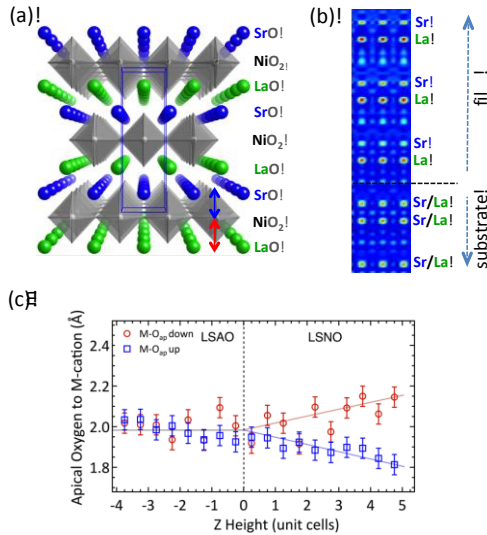


Fig. 1: (a) LaSrNiO_4 was grown as an artificially polar material by layering the cations as $\text{LaO}^{+1} + (\text{NiO}_2)^{-1} + \text{SrO}^0$, using MBE. (b) The cation layering is verified with x-ray phase retrieval techniques. (c) The Ni-O apical bonds (upper in blue, lower in red) distort to partially screen the electrostatic dipole imposed by the polar cation ordering.

include the application of epitaxial strain in thin films, or pressure and isovalent cation substitution in bulk samples. We have found a new route to tailor the M -O bonds without changes to the strain state or stoichiometry in two-dimensional perovskite nickelate ($n = 1$ in the Ruddlesden Popper (RP) series). We do this by tailoring the dipolar electrostatic interactions at the unit cell level in nominally non-polar LaSrNiO_4 via single atomic layer-by-layer synthesis using oxide-MBE. We can reconstruct the response of the crystal lattice to the induced polarity using an x-ray phase retrieval technique (COBRA). We find that the response of the O anions to the resulting local electric fields distorts the M -O bonds, being largest for the apical oxygens (O_{ap}). It also alters the Ni valence. This structural control strategy has broad implications for tailoring electronic properties in oxides that are sensitive to the M - O_{ap} bond geometry (B. B. Nelson-Cheeseman et al., *Adv. Funct. Mater.* 2014).

3. Spin Seebeck Effect in Paramagnets and Antiferromagnets

We have developed a new approach for generating spin currents in *patterned* magnetic heterostructures via the Spin Seebeck effect (SSE). By using a microscale on-chip local heater, we are able to generate a large thermal gradient confined to the chip surface *without* a large increase in the total sample temperature (S. Wu et al., *Appl. Phys. Lett.* 2014; *J. Appl. Phys.* 2015). This approach allows the study of the Spin Seebeck effect at very low temperatures (even less than 1K), as the total heat load from the patterned heater wire can be readily handled by standard cryostats. Using this approach, we discovered a large spin Seebeck effect in

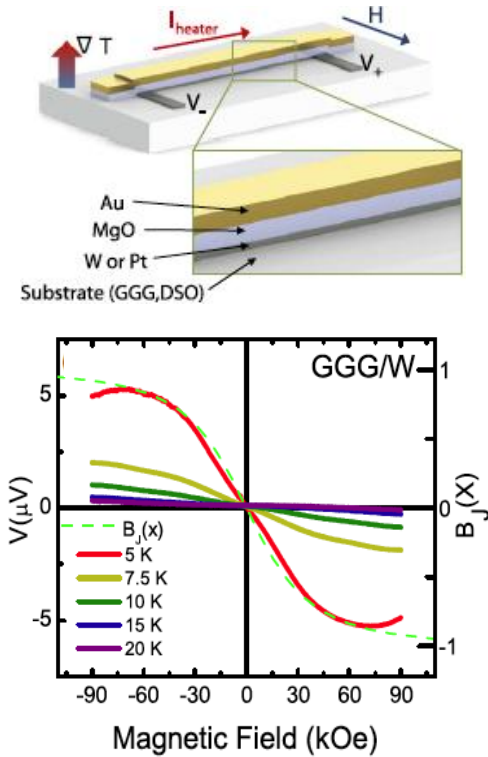


Fig. 2 Spin Seebeck effect measurement geometry (top panel). Spin current is detected via the inverse spin Hall effect (lower panel) for $\text{Gd}_3\text{Ga}_5\text{O}_{12}$, an insulating paramagnet. The green dotted line is the Brillouin function.

occur for a broad range of oxides, beyond the nickelate/manganite interfaces that we are currently exploring. A general understanding of what happens at such interfaces is lacking because the 3d transition metal oxides have narrow bands where the charge carriers are strongly correlated and the ideas of ‘band bending’ have to be considered in light of the dynamic nature of the bands, i.e. the sensitivity of the band structure to filling. More specific to our recent findings, we are interested in creating nanowires of LaNiO_3 and of $\text{La}_{2/3}\text{Sr}_{1/3}\text{MnO}_3/\text{LaNiO}_3$ bilayers where the spin-density wave like instabilities might manifest themselves, open gaps and create spatially modulated phases.

c) *Oxide MBE growth of 4d and 5d transition metal oxides:* We have set up a new oxide MBE system that will enable us to synthesize thin films and heterostructures of oxides incorporating 4d and 5d transition metals. The materials of interest include perovskite iridates, that have been the focus of much recent activity due to the interplay of spin-orbit coupling and Mott physics.³ The spin Seebeck effect measurement techniques developed in our program will be extended to the 4d and 5d transition metal pyrochlores, where a number of novel ground states are found,⁴ several of which may give rise to spin currents. Metallic 4d and 5d transition metal oxides may also be effective detectors of spin currents via the inverse spin Hall effect.

paramagnetic oxide insulators $\text{Gd}_3\text{Ga}_5\text{O}_{12}$ (GGG) and DyScO_3 (DSO), where the signal grows strongly in magnitude below $\sim 20\text{K}$. (S. Wu et al., *Phys. Rev. Lett.* 2015) and also in antiferromagnetic insulators (S. Wu et al., *arXiv:1509.00439*). GGG is a classical spin liquid at low temperatures ($<300\text{ mK}$), and we have carried out SSE experiments in this regime as well, where we now have a complete picture of how the SSE evolves in high magnetic fields ($\mu_B B \gg kT$) in a paramagnetic insulator. The techniques developed here can readily be extended to other geometrically frustrated spin systems.

Future Plans:

a) *Tailoring $M\text{-O}_{ap}$ bond lengths:* Motivated by our results in the past few years, we have plans to create and explore a number of materials systems using the synthesis approach that has been outlined earlier. In the cuprates, we will tailor the Cu-O_{apical} bond length¹ in a systematic way using dipoles and electrostatics and explore changes in properties including possible changes in T_c . In insulating single layer RP aluminates, there is a prediction² of a very large ($>200\%$) change in the optical bandgap in polar cation ordered analogs where the Al-O_{ap} bond length, which we plan to explore.

b) *Interfacial Charge Transfer in ‘Mott’ materials:* Fermi-level mismatch and charge transfer should

References

- ¹ "Band-structure trend in hole-doped cuprates and correlation with T_c max." Pavarini, E., et al. *Physical Review Letters* **87**, 047003 (2001).
- ² "Massive band gap variation in layered oxides through cation ordering", P. V. Balachandran and J. M. Rondinelli, *Nature Communications* **6**, 6191 (2015).
- ³ "Novel $J_{\text{eff}} = 1/2$ Mott state induced by relativistic spin-orbit coupling in Sr_2IrO_4 ." B. J. Kim et al. *Phys. Rev. Lett.* **101**, 076402 (2008).
- ⁴ "Magnetic pyrochlore oxides", J. S. Gardner, M. J. Gingras, & J. E. Greedan, *Reviews of Modern Physics* **82**, 53 (2010).

Publications (supported by Department of Energy, Basic Energy Sciences, since 2013):

- P1. "Near-nanoscale-resolved energy band structure of $\text{LaNiO}_3/\text{La}_{2/3}\text{Sr}_{1/3}\text{MnO}_3/\text{SrTiO}_3$ heterostructures and their interfaces." Thaddeus J. Asel, Hantian Gao, Tyler J. Heintz, Drew Adkins, Patrick M. Woodward, Jason Hoffman, Anand Bhattacharya, and Leonard J. Brillson. *J. Vac. Sci. Tech. B* **33**, 04E103 (2015).
- P2. "Spin Seebeck devices using local on-chip heating", S. M. Wu, F. Y. Fradin, J. Hoffman, A. Hoffmann, A. Bhattacharya, *J. Appl. Phys.* **117**, 17C509 (2015).
- P3. "Paramagnetic Spin Seebeck Effect", S. M. Wu, JE Pearson, A Bhattacharya, *Phys. Rev. Lett.* **114**, 186602 (2015).
- P4. "Spectral Weight Redistribution in $(\text{LaNiO}_3)_n/(\text{LaMnO}_3)_2$ superlattices from Optical Spectroscopy", P. Di Pietro, J. Hoffman, A. Bhattacharya, S. Lupi, A. Perucchi, *Phys. Rev. Lett.* **114**, 156801 (2015).
- P5. "Spin waves in micro-structured yttrium iron garnet nanometer-thick films", M. B. Jungfleisch, Wei Zhang, Wanjun Jiang, Houchen Chang, J. Sklenar, S.M. Wu, J. E. Pearson, A. Bhattacharya, J. B. Ketterson, Mingzhong Wu, A. Hoffmann, *J. Appl. Phys.* **117**, 17D128 (2015).
- P6. "Unambiguous separation of the inverse spin Hall and anomalous Nernst Effects within a ferromagnetic metal using the spin Seebeck effect" S.M. Wu, J. Hoffman, J.E. Pearson, A Bhattacharya, *Appl. Phys. Lett.* **105**, 092409 (2014).
- P7. "Polar cation ordering: A route to introducing > 10% bond strain into layered oxide films", Brittany B. Nelson-Cheeseman, Hua Zhou, Prasanna V. Balachandran, Gilberto Fabbris, Jason Hoffman, Daniel Haskel, James M. Rondinelli, Anand Bhattacharya, *Advanced Functional Materials* **24** (2014).
- P8. "Inductive crystal field control in layered metal oxides with correlated electrons", P. V. Balachandran, A. Cammarata, B. B. Nelson-Cheeseman, A. Bhattacharya and J. M. Rondinelli, *APL Materials* **2**, 076110 (2014).

- P9. "Dynamic layer rearrangement during growth of layered oxide films by molecular beam epitaxy", June Hyuk Lee, Guangfu Luo, I-Cheng Tung, Seo Chang, Zhenlin Luo, Milind Malshe, Milind Gadre, Anand Bhattacharya, Serge Nakhmanson, Jeffrey Eastman, Hawoong Hong, Julius Jellinek, Dane Morgan, Dillon Fong, and John Freeland, *Nature Materials* (2014).
- P10. "Correlating interfacial octahedral rotations with magnetism in $(\text{LaMnO}_{3+\delta})_N/(\text{SrTiO}_3)_N$ superlattices." Xiaofang Zhai, Long Cheng, Yang Liu, Christian M. Schlepütz, Shuai Dong, Hui Li, Xiaoqiang Zhang, Chu Shengqi, Zheng Lirong, Zhang Jing, Zhao Aidi, Hong Hawoong, Anand Bhattacharya, James N. Eckstein, Changgan Zeng, *Nature Communications* **5**, 4283 (2014).
- P11. "Oxygen-Vacancy-Induced Polar Behavior in $(\text{LaFeO}_3)_2/(\text{SrFeO}_3)$ Superlattices", Rohan Mishra, Young-Min Kim, Juan Salafranca, Seong Keun Kim, Seo Hyoung Chang, Anand Bhattacharya, Dillon D. Fong, Stephen J. Pennycook, Sokrates T. Pantelides, and Albina Y. Borisevich, *Nano Letters* **14**, 2694-2701 (2014).
- P12. "Magnetic Oxide Heterostructures", A. Bhattacharya and S.J. May, *Annual Review of Materials Research* **44**: 5.1 – 5.26 (2014).
- P13. "Charge transfer and interfacial magnetism in $(\text{LaNiO}_3)_n/(\text{LaMnO}_3)_2$ superlattices", J. Hoffman, I. C. Tung, B. Nelson-Cheeseman, M. Liu, J. Freeland, & A. Bhattacharya, *Phys. Rev B* **88**, 144411 (2013).
- P14. "Non-volatile ferroelastic switching of the Verwey transition and resistivity of epitaxial $\text{Fe}_3\text{O}_4/\text{PMN-PT}$ (011)", Ming Liu, J. Hoffman, J. Wang, J. Zhang, B. Nelson-Cheeseman, A. Bhattacharya, *Scientific Reports* **3**, Article No. 1876 (2013).

Atomic-layer-by-layer molecular beam epitaxy synthesis of cuprate superconductors

Ivan Božović, Anthony T. Bollinger and Jie Wu

Brookhaven National Laboratory, Upton NY 11973, USA

(i) Program scope

The mechanism of high-temperature superconductivity (HTS) is one of the most important problems in Condensed Matter Physics. Some basic facts - the dimensionality, the spin and the charge of free carriers, the nature of superconducting transition, the effective interaction that causes electron pairing - are still unclear. To attack these problems, we use atomic-layer-by-layer molecular beam epitaxy (ALL-MBE) to synthesize single crystal films of cuprates and other complex oxides, as well as heterostructures, multilayers and superlattices with atomically perfect interfaces, enabling novel experiments that were not possible so far.

The program impact is twofold. First, the group is the source of unique samples, including high-quality HTS films and multilayer heterostructures engineered down to a single atomic layer, that are enabling breakthrough research of few dozen groups at national laboratories and leading universities in US and abroad. Second, our own in-house experiments have also brought in several important results - discoveries of HTS interface superconductivity, Giant Proximity Effect, HTS in a single CuO_2 layer, and the (de)localization of electron pairs at the superconductor-insulator quantum phase transition. [1-15] We have shown that HTS films can be quite homogeneous, having a very uniform SC gap. Charge density waves and charge glass are observed in some samples, but none for optimal doping. Phase fluctuations drive the superconducting transition at every doping, but they fade out 10-15 K above T_c , so the pseudogap must have a different origin. *In-plane* charge excitations are strongly coupled to *out-of-plane* lattice vibrations. Superfluid can be confined to a single CuO_2 layer, with T_c equal to that in bulk samples. A large enhancement of T_c is seen in certain heterostructures. Pairs exist on both sides of the superconducting transition, be it induced thermally or by doping.

These and future experiments are hoped to provide clear-cut answers to at least some of the above questions, which could significantly impact research on HTS and more broadly on strongly-correlated materials.

(ii) Recent progress

In the last two years (FY 2014 and FY 2015) we have performed over 400 ALL-MBE synthesis experiments, most of which produced atomically smooth superconducting films. Every film was characterized by RHEED, $R(T)$ and/or $\chi(T)$ measurements and selected ones also by XRD and AFM. Many were patterned into micro- or nano-sized devices and were subject to detailed study of their physical properties and behavior. This resulted in a number of new observations, reported in 16 journal papers already published in FY 2014 and 2015, with 4 more papers completed and/or under review. The highlights are as follows.

Anomalous independence of interface superconductivity on carrier density [15]. The recent discovery of superconductivity at the interface of two non-superconducting materials has received much attention. In cuprate bilayers, T_c can be significantly enhanced compared to single-phase samples. [1] Several explanations have been proposed, invoking Sr inter-diffusion, accumulation and depletion of mobile charge carriers, elongation of the copper-to-apical-oxygen bond length, or a beneficial crosstalk between a material with a high pairing energy and another with a large phase stiffness. From each of these models, one would predict T_c to depend strongly on the carrier density in the constituent materials. We studied combinatorial libraries of $\text{La}_{2-x}\text{Sr}_x\text{CuO}_4$ - La_2CuO_4 bilayer samples - an unprecedentedly large set of over 800 different compositions, with the doping level x spanning a wide range ($0.15 < x < 0.47$) and the measured Hall coefficient varying by one order of magnitude. Nevertheless, across the entire sample set, T_c stayed essentially constant at about 40

K. [15] We inferred that doping up to the optimum level does not shift the chemical potential, unlike in ordinary Fermi liquids, thus posing a new challenge to theory of HTS in cuprates.

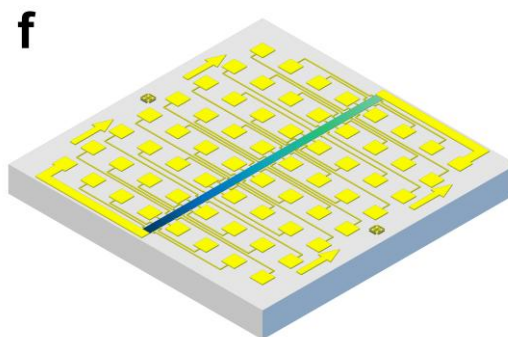
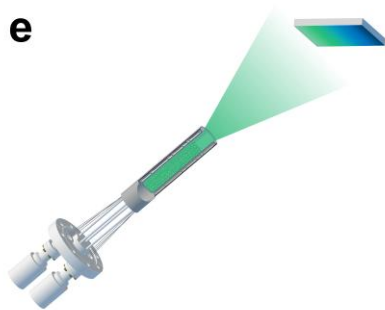
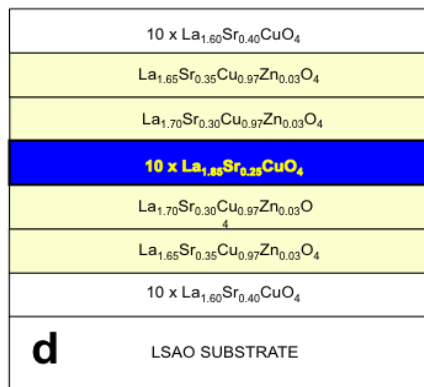
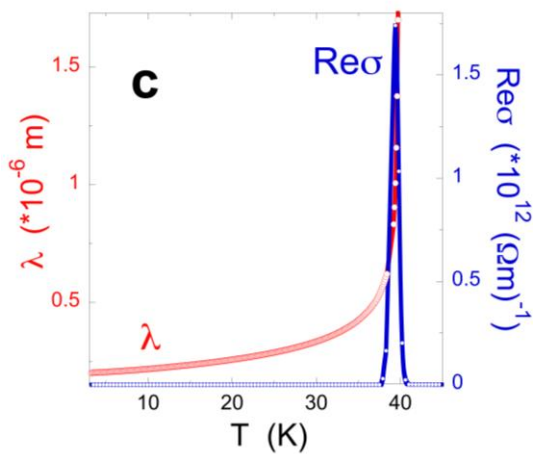
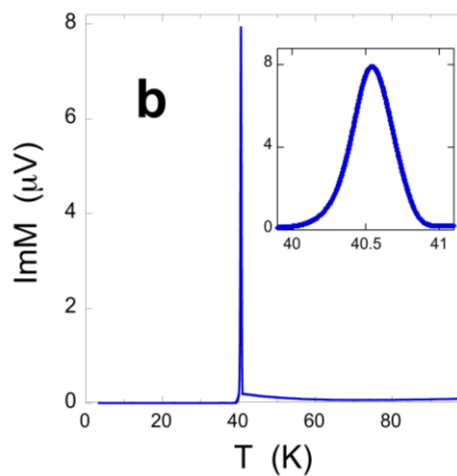
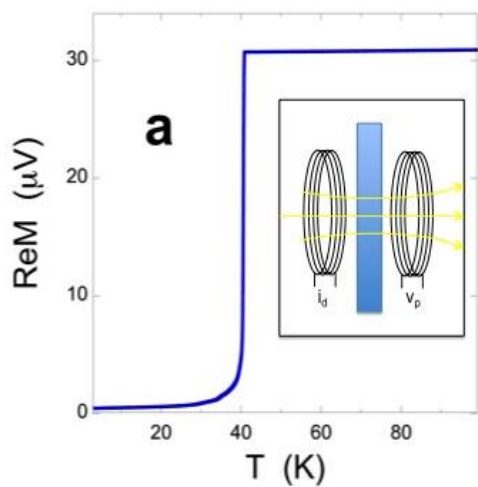


Figure 1 | **Synthesis and characterization techniques.** **a**, The real part of mutual inductance showing diamagnetic screening (the Meissner effect) when the film becomes superconducting. The schematic of the experiment is shown in the inset. The film is placed between a drive coil and a pickup coil. The sample holder is carved out of a single-crystal sapphire. The coils are set rigidly and the sample is spring-loaded, so that the geometry is fixed and reproducibility better than $\pm 0.1\%$. **b**, The imaginary part of mutual inductance shows that in this film, of $10 \times 10 \text{ mm}^2$ area, T_c is homogeneous to better than 0.1 K — there are no signs whatsoever of electronic inhomogeneity or phase separation. **c**, The penetration depth λ and the ac ($\nu = 40 \text{ KHz}$) conductivity derived from the complex impedance. **d**, A schematic of sample engineered for this study at the atomic-layer level. The active (superconducting) part of the film consists of a 5 unit cells (UC) thick layer of $\text{La}_{2-x}\text{Sr}_x\text{CuO}_4$. (One UC, 13.2 \AA thick, contains two CuO_2 planes.) It is protected by a 6 UC thick, metallic but non-superconducting $\text{La}_{1.55}\text{Sr}_{0.45}\text{CuO}_4$ buffer to isolate it from the substrate, and by another 6 UC thick $\text{La}_{1.55}\text{Sr}_{0.45}\text{CuO}_4$ overlayer to protect it from the atmosphere. In the two layers next to the interfaces, the Sr doping level is graded and 3% of Cu is substituted by Zn to quench interface superconductivity. **e**, The atomic sources are aimed at the substrate at a shallow angle, which results in a gradient in the deposition rate. **f**, The lithographic pattern used to fabricate linear combinatorial libraries for magneto-transport measurements. The central strip, 10 mm long and $300 \mu\text{m}$ wide, is divided into 32 segments, each $300 \mu\text{m}$ long, contacted from 64 gold pads. Longitudinal and Hall resistances can be measured at all pixels independently and simultaneously.

While cuprates superconductors exhibit many mysterious facets, but the ultimate question is why T_c is so high. The fundamental dichotomy is between the weak-pairing, Bardeen-Cooper-Schrieffer (BCS) scenario, and Bose-Einstein condensation (BEC) of strongly-bound pairs. It is hotly debated which of these pictures is appropriate for underdoped cuprates; on the other hand, it is commonly believed that on the overdoped side strongly-correlated fermion physics evolves smoothly into the conventional BCS behavior. To test this dogma, we have undertaken a comprehensive study that took ten years and encompassed several thousand of cuprate samples, probably without precedence in the history of Condensed matter physics. The large statistics enables us to identify clear trends and unravel intrinsic properties; this is essential when dealing with complex materials such as cuprates.

By atomic-layer engineering, we optimize the samples for the particular experiment. Using a continuous spread in composition we tune the doping level in steps of 0.01%. We have measured very accurately the key physical parameters (T_c , λ and ξ) of the superconducting state and established their precise dependence on doping, temperature, and external fields. We use high-throughput measurements on combinatorial libraries to study magneto-resistance and Hall effect in fields up to 90 T and measure accurately the coherence length ξ . We also measure the absolute value of penetration depth λ to the accuracy better than 1%. The synthesis and characterization techniques and typical data are illustrated in Fig. 1 below.

This wide-ranging study has been essentially completed and the results will be published soon. They bring in some great surprises, challenge the commonly held beliefs, rule out most theoretical models proposed so far, and point to an answer to our central question. In particular, the findings do not conform to BCS predictions anywhere in the phase diagram. Rather, evidence points to small, preformed pairs. This suggests that T_c is high because of strong pairing and unusual kinematics — in cuprates we may have the first example of a charged Bose gas and of *electronic* BEC. However, we emphasize that the simple BEC picture also fails at the overdoped side; unpaired fermionic charge carriers are also present, even as $T \rightarrow 0$, and their density increases with doping while the pair density decreases and eventually disappears.

(iii) Future plans

First, we plan to complete several major experiments aimed at addressing directly some of the remaining key questions about the mechanism of HTS in cuprates. These include a detailed study of scaling near the critical points, of superconducting fluctuations, interface superconductivity, proximi-

ty effects, and new phenomena in HTS nanostructures. We plan to expand the study to include few other HTS cuprate compounds.

Next, our ALL-MBE (“digital”) synthesis technique enables creation of novel artificial, metastable materials. New design opportunities emerge from rich interface physics, which includes massive atomic and electron reconstructions as well as various proximity effects arising from competition between different instabilities and order parameters. This presents a new direction in search for novel superconductors, which we intend to pursue.

(iv) References

1. A. Gozar et al., *Nature* 455, 782 (2008).
2. S. Smadici et al., *PRL* 102, 107004 (2009).
3. G. Logvenov et al., *Science* 326, 699 (2009).
4. V. Butko et al., *Adv. Mater.* 21, 1 (2009).
5. H. Zhou et al., *PNAS* 107, 8103 (2010).
6. A. Suter et al., *PRL* 106, 237003 (2011).
7. I. Sochnikov et al., *Nature Nanotech.* 5, 516 (2010).
8. E. Morenzoni et al., *Nature Comm.* 2, 272 (2011).
9. L. Bilbro et al., *Nature Physics* 7, 298 (2011).
10. A. Bollinger et al., *Nature* 472, 458 (2011).
11. M. Dean et al., *Nature Materials*, 11, 850 (2012).
12. D. Torchinsky et al., *Nature Materials*, 12, 387 (2013).
13. M. Dean et al., *Nature Materials* 12, 1019 (2013).
14. X. Shi et al., *Nature Materials*, 12, 47 (2013).
15. J. Wu et al., *Nature Materials*, 12, 877 (2013).

(v) DOE Sponsored Publications in the Last Two Years (10.01.2011 – 10.01.2013)

1. Publications intellectually led by this FWP

1. I. Bozovic and C. Ahn, “A new frontier for superconductivity”, *Nature Physics* 10, 892-895 (2014). (published December 2014)
2. G. Dubuis, X. He and I. Božović, “Ultra-thermal-stabilization of a closed cycle cryocooler”, *Rev. Sci. Instr.* 85, 103902 (2014). (October 2014)
3. N. E. Litombe, A. T. Bollinger, J. E. Hoffman and I. Božović, “La_{2-x}Sr_xCuO₄ Superconductor Nanowire Devices”, *Physica C* 506, 169-173 (2014). (15 November 2014)
4. S. Dietrich, W. Mayer, S. Vitkalov, A. Sergeev, A. T. Bollinger and I. Božović, “Frequency dispersion of nonlinear response in films of cuprate superconductors”, *Phys. Rev. B* 91, 060506 (R) (2015).
5. J. Wu and I. Božović, “Extremely fine tuning of doping enabled by combinatorial molecular-beam epitaxy”, *APL Materials* 3, 062401 (2015).
6. V. A. Gasparov and I. Božović, “Complex conductance of ultrathin La_{2-x}Sr_xCuO₄ films and heterostructures”, *Low-Temp. Phys.* (2015) in press.
7. V. A. Gasparov, X. He, G. Dubuis, D. Pavuna, N. D. Kushch, E. B. Yagubskii, J. A. Schlueter and I. Bozovic, “Magnetic field, frequency and temperature dependence of complex conductance of ultrathin La_{1.65}Sr_{0.45}CuO₄/La₂CuO₄ films and the organic superconductors □- (BEDT-TTF)₂Cu[N(CN)₂]Br”, *International Journal of Modern Physics B* (2015) in press.
8. G. Dubuis, X. He and I. Božović, “Ultra-thermal-stabilization of a closed cycle cryocooler”, *Rev. Sci. Instr.* 85, 103902 (2014).

9. J. Wu, O. Pelleg, G. Logvenov, A. T. Bollinger, Y. Sun, G. S. Boebinger, M. Vanević, Z. Radović and I. Božović, "Anomalous independence of interface superconductivity on carrier density", **Nature Materials** 12, 877-881 (2013). (published October 2013).

2) Collaborative publications (materials supplied and/or characterized by this FWP).

10. X. Leng, J. Pereiro, J. Strle, A. T. Bollinger and I. Božović, "Epitaxial growth of high quality WO_3 thin films", *APL Materials* 3, 096102 (2015).

11. X. Leng and I. Bozovic, "Controlling superconductivity in $\text{La}_{2-x}\text{Sr}_x\text{CuO}_{4+\delta}$ by ozone and vacuum annealing", *Journal of Superconductivity and Novel Magnetism* 28, 71-74 (2015).

12. F. Zheng, G. Logvenov, I. Bozovic, Y. Zhu and J. He, "Structural origin of enhanced critical temperature in ultrafine multilayers of cuprate superconducting films", *Phys. Rev. B* 89, 184509 (2014).

13. S. Smadici, G. Logvenov, I. Bozovic and P. Abbamonte, "Sequence of hole resonances in complex oxide heterostructures". *J. Phys. Cond. Mat.* 26, 155302 (2014).

14. P. D. C. King, H. I. Wei, Y. F. Nie, M. Uchida, C. Adamo, S. Zhu, X. He, I Bozovic, D. G. Schlom, and K. M. Shen, "Atomic-scale control of competing electronic phases in ultrathin LaNiO_3 ", **Nature Nanotechnology** 9, 443-447 (2014).

15. S. Smadici, J. C. T. Lee, G. Logvenov, I. Bozovic and P. Abbamonte, "Form factor dispersion at $\text{La M}_{5/2}$ edges and average density of resonant atoms", *J. Phys.: Condens. Matter* 26, 025303 (2014).

16. M. P. Dean, G. Dellea, R. S. Springell, F. Yakhou-Harris, K. Kummer, N. B. Brookes, X. Liu, Y.-J. Sun, J. Strle, T. Schmitt, L. Braicovich, G. Ghiringhelli, I. Bozovic and J. P. Hill, "Persistence of magnetic excitations in $\text{La}_{2-x}\text{Sr}_x\text{CuO}_4$ from the undoped insulator to the heavily overdoped non-superconducting metal", **Nature Materials** 12, 1019-23 (2013). (published October 2013).

Electronic, Magnetic, and Optical Properties of Doped Metal Oxide Epitaxial Films and Interfaces

S.A. Chambers, S.R. Spurgeon, P.V. Sushko, Y. Du, T.C. Droubay, T.C. Kaspar - PNNL

Program Scope

We explore fundamental phenomena related to electron-hole pair creation, propagation, and lifetime, collective defect interaction, and carrier spin polarization in complex oxide epitaxial films, heterojunctions and superlattices. Understanding these phenomena paves the way for effective and scientifically informed use of oxides in photovoltaics, photo- and thermo-electrochemical, and spintronic device technologies. We aim to discover the intricate relationships that exist between composition, structure and functional properties by using molecular beam epitaxy (MBE) in conjunction with a variety of characterization methods for determining composition, global and local structure and defect densities. Electronic, optical and magnetic properties are measured and interpreted in light of realistic, as opposed to idealized, models of the material system. Deep insight is gained by coupling experiment with classical and quantum mechanical modeling efforts. A key goal is an in-depth understanding of not only how defects influence properties, but also how defects can be harnessed and controlled for useful purposes. The specific scientific themes we investigate include: (i) tailoring electronic and optical properties through alloying, superlattice formation, and strain for the purpose of efficient visible light harvesting, (ii) exploring collective defect phenomena to generate novel and useful mesoscale structures, and, (iii) using ferromagnetic complex oxides for spin injection into non-magnetic semiconductors in simple spintronic devices.

Recent Progress

Electronic and optical properties of $\text{Sr}_x\text{La}_{1-x}\text{CrO}_3$ based heterostructures - We have investigated the functional properties of $\text{La}_{1-x}\text{Sr}_x\text{CrO}_3$ ($0 \leq x \leq 1$) (LSCO) epitaxial films deposited by MBE using x-ray diffraction (XRD), x-ray photoemission spectroscopy (XPS), Rutherford backscattering spectrometry (RBS), x-ray absorption spectroscopy (XAS), scanning transmission electron microscopy (STEM) and related spectroscopies, electrical transport, and *ab initio* modeling. LaCrO_3 is an antiferromagnetic insulator whereas SrCrO_3 is a metal.¹⁻³ Substituting Sr^{2+} for La^{3+} in LaCrO_3 effectively dopes holes into the top of valence band, leading to Cr^{4+} ($3d^2$) local electron configurations. Core-level and valence-band features monotonically shift to lower binding energy with increasing x , indicating downward movement of the Fermi level toward the valence band maximum.⁴ The material becomes a p -type semiconductor at lower doping levels and an insulator-to-metal transition is observed at $x \geq 0.65$, but only when the films are deposited with in-plane compression via lattice-mismatched heteroepitaxy. Valence band XPS reveals diminution of electronic state density at the Cr $3d t_{2g}$ -derived top of the valence band while O K-edge x-XAS shows the development of a new unoccupied state above the Fermi level as holes are doped into LaCrO_3 (Fig. 1a). The evolution of these bands with Sr concentration is accurately captured using density functional theory with a Hubbard U correction of 3.0 eV (DFT + U) (Fig. 1b). Resistivity data in the semiconducting regime ($x \leq 0.50$) do not fit perfectly well to either a polaron hopping or band conduction model, but are best interpreted in terms of a hybrid model. The activation energies are well reproduced by DFT + U .

Significantly, LSCO remains highly transparent even as it becomes p -type semiconducting for $0 < x \leq \sim 0.25$ (Fig. 2a). LSCO thus constitutes a new p -type TCO which shows competitive performance within a structure that can readily be integrated with other oxide electronic materials.⁵ Our LSCO films all exhibit positive Seebeck coefficients (S), confirming p -type conductivity. Fig. 2b shows that S decreases from 321 to 80 $\mu\text{V}/\text{K}$ from $x = 0.04$ to 0.5, while σ increases from 1.2 to 54 S/cm . The relationship between hole concentration (p) and S is not known for LSCO. However, p can be determined from S using a small-polaron hopping (SPH) model which is appropriate for materials with extremely low mobilities.⁶ We use the formula $S(c) = (k_B/e)\ln[2(1-c)/c]$ where k_B is Boltzmann's constant, e is the electronic charge, and c is the fraction of hopping sites occupied with holes. Hole creation by Sr doping at a La site thus corresponds to activation of an adjacent Cr site for hole hopping, i.e. $p(c) = cN_{\text{Cr}}$ where N_{Cr} is the Cr number density, $1.7 \times 10^{22}\text{cm}^{-3}$. Based on these formulae for $S(c)$ and $p(c)$, we determined the hole concentration to range from 7.9×10^{20} to $7.5 \times 10^{21}\text{cm}^{-3}$ with corresponding mobilities (from $\sigma = e\mu p$) of 0.009 to 0.04 cm^2/Vs for $x = 0.04$ to 0.5. The results are shown in Fig. 2c. Although the mobility is low, the carrier concentration can easily be made high (up to nearly 10^{22}cm^{-3}) by Sr substitution for La. Therefore, the conductivity can still be made high (up to $\sim 50\text{ S}/\text{cm}$). There are several device applications which would not be hampered by low mobility. These include rectifiers, photodetectors, solar cells and n -type junction field-effect transistors (n -JFET), all based on oxide pn junctions. In the n -JFET application, the high hole concentration in LSCO would cause the depletion zone to be in the n -type oxide with its significantly higher mobility, resulting in fast switching.

Fig. 2d shows optical transmittance for LSCO films on STO substrates in the visible and infrared regions. Transmittance was determined by averaging values at wavelengths of 420, 490, 560, 630 and 700 nm and includes the STO contribution. The spectrum for a 100 nm thick LCO film is indistinguishable from that of its substrate.

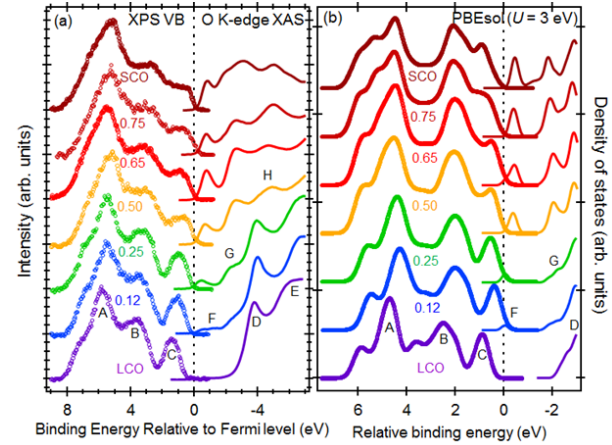


Fig. 1 (a) Valence band XPS and O K-edge XAS spectra for the $\text{La}_{1-x}\text{Sr}_x\text{CrO}_3$ film series; (b) analogous theoretical densities of states based on PBEsol + U ($U = 3\text{ eV}$).

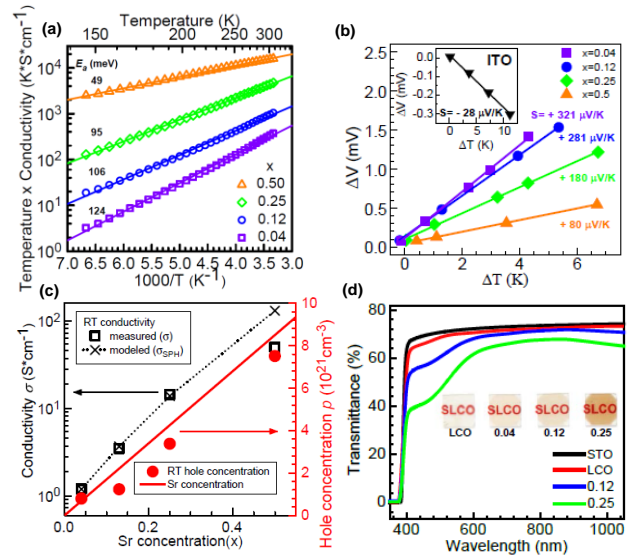


Fig. 2 (a) Temperature dependence of the conductivity. The $\text{La}_{0.50}\text{Sr}_{0.50}\text{CrO}_3$ film was deposited on LAO; all others were deposited on STO. (b) Seebeck coefficients (inset shows the same measurement for an ITO film, a n -type TCO). (c) Room-temperature conductivity and hole concentration vs. x . (d) Optical transmission and photographs of the LSCO films deposited on STO(001).

The LSCO films are less transparent because of absorption near 450 nm, resulting in slight brown coloration. In order to compare LSCO to other p -TCOs, we compute a figure of merit (FOM) originally suggested by Gordon⁷ and subsequently used by Arca *et al.*⁸ This FOM is the ratio of conductivity (σ) and optical absorption coefficient (α) with reflectance (R) neglected. In the $R = 0$ approximation, $\alpha \approx (1/d)\ln(1/T)$ and $FOM \approx -1/(R_s \ln T)$ (in units of $M\Omega^{-1}$), where T is the wavelength-averaged transmittance and R_s is the sheet resistance, which is in turn given by $1/\sigma d$ with d being the film thickness. Significantly, the use of R_s results in a cancellation of film thickness in the expression for FOM so that films of different thicknesses can be directly compared. A caveat is that the relatively weak dependence of transmittance on film thickness precludes quantitative comparison of films with vastly different thicknesses. We summarize the FOM values, and the data on which they are based, for our LSCO films as well as for other p -TCOs computed using the same formula in Fig. 3. Our highly crystalline LSCO epitaxial films show FOMs which are competitive with those of other d -orbital p -type TCOs. We note that the directly proportional dependence of FOM on inverse sheet resistance, and the inverse logarithmic dependence of FOM on T , result in very high FOM values for highly conductive samples, *even when the optical transparency is low*. For example, in the limit of $x = 1.0$, our SCO films are metallic and the conductivity is 750 S/cm. However, T drops to 0.29, and the resulting FOM for a 50 nm film is $3050 M\Omega^{-1}$. Similarly, the $Cu_xCr_{1-x}Mg_xO_2$ film reported in ref. 9 is doped sufficiently high that σ is 220 S/cm, but T is only 30% and F is $4600 M\Omega^{-1}$. It is thus important to look beyond the FOM and also consider σ , T and d when evaluating p -type TCOs.

Finally, we show in Fig. 4 recent results for a pn junction consisting of MBE-grown p - $La_{0.85}Sr_{0.15}CrO_3$ on 0.05 wt. % Nb-doped $SrTiO_3(001)$. Holes (electrons) generated by light absorption in the p - $La_{0.9}Sr_{0.1}CrO_3$ layer are expected to diffuse to the surface (bulk) based on the band alignment and built-in potentials determined by XPS and seen in

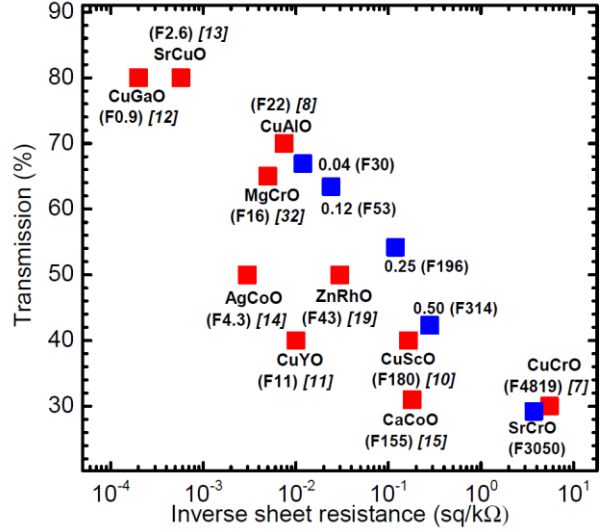


Fig. 3 Graphical representation of electrical resistance, optical transmission and figure of merit (FOM) for LSCO epitaxial films (blue squares) and other p -type TCOs (red squares). The numbers in parentheses marked with an F are the FOMs. The numbers in brackets are the citation numbers in ref. 5.

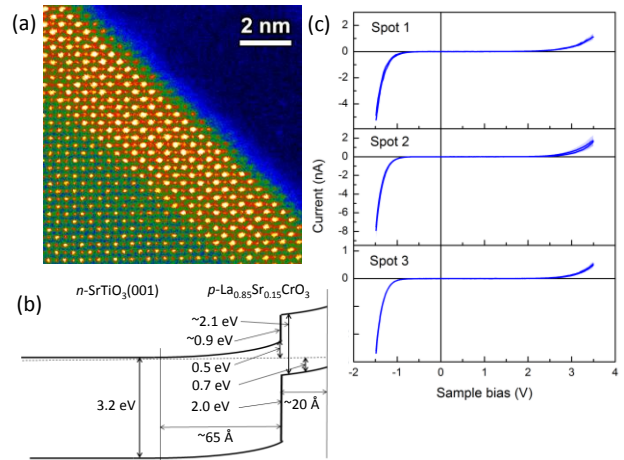


Fig. 4 (a) STEM-HAADF image of a p - $La_{0.85}Sr_{0.15}CrO_3/n$ - $SrTiO_3(001)$ heterojunction, (b) energy-level diagram extracted from XPS data, and, (c) conductive tip AFM IV curves measured in the dark for the heterojunction shown in (a). The sample bias was applied to the backside of the Nb-doped STO substrate.

Fig. 4b. The highly reproducible set of IV curves shown in Fig. 4c and obtained by conductive tip AFM reveals good rectifying behavior.

Future Plans

Moving forward, we are pursuing MBE-grown p - $\text{La}_{1-x}\text{Sr}_x\text{CrO}_3$ / n - $\text{SrTiO}_3(001)$ heterojunction fabrication along with IV measurements in the dark and under illumination. We are also working on the MBE-growth and properties of p - $\text{La}_{1-x}\text{Sr}_x\text{CrO}_3$ / n - $\text{Si}(001)$ with the goal of using the 1.1 eV band gap of Si to more effectively harvest visible light. There are formidable challenges associated with depositing epitaxial $\text{La}_{1-x}\text{Sr}_x\text{CrO}_3$ with Cr oxidized to a valence of $(3 + \delta)$ directly on Si(001) without also promoting SiO_2 formation.

We are also investigated MBE-grown epitaxial films of $\text{La}_2\text{MnNiO}_6$ (LMNO) on $\text{SrTiO}_3(001)$. We have found that despite the fact that Mn and Ni are present as $4+$ ($d^3 : t_{2g}^3 e_g^0$) and $2+$ ($d^8 : t_{2g}^6 e_g^2$) cations, respectively, and exhibit XMCD spectra indicating ferromagnetic coupling of Mn and Ni cations in the lattice, the volume-averaged moment per formula unit is considerably less than the expected $5 \mu_B$ per formula unit (f.u.), even after annealing in air. The highest moment recorded thus far after annealing is $\sim 4.5 \mu_B$ per f.u. RBS reveals that the volume-average stoichiometry is as targeted based on atom beam fluxes to within a few percent. Additionally, STEM images show that the as-grown films are nominally very well ordered. However, STEM-EDS reveals that there is considerable chemical disorder within the B-site sublattice (i.e. there is little long-range ordering of Mn and Ni cations) for as-deposited films. Air annealing results in substantial chemical ordering of Mn and Ni, accompanied by a sizeable increase in the magnetization as the ordered double perovskite forms. Nevertheless, the moment remains below $5 \mu_B$ per f.u. due to the formation of nanoscale NiO inclusions surrounded by Ni-doped LaMnO_3 . These phases were not detectable by STEM or EDS mapping. Atom probe tomography (APT) was needed to detect and characterize these inclusions. *Ab initio* modeling reveals that depletion of Ni from the mix of incoming atoms via formation of NiO inclusions results in Ni-doped LaMnO_3 which in equilibrium with LMNO. These results thus illustrate that unintended secondary phase formation can readily occur during the nucleation of complex oxide epitaxial films such as LMNO and that without adequate characterization, such phases can go completely undetected, yet can measurably alter functional properties.

References

- [1] P. V. Sushko, L. Qiao, M. Bowden, T. Varga, G. J. Exarhos, F. K. Urban III, D. Barton, S. A. Chambers, *Phys. Rev. Lett.* **110**, 077401 (2013).
- [2] K. H. L. Zhang, P. V. Sushko, R. Colby, Y. Du, M. E. Bowden, S. A. Chambers, *Nat. Comm.* **5**, 4669 (2014).
- [3] K. H. L. Zhang, Y. Du, P. V. Sushko, M. E. Bowden, V. Shutthanandan, L. Qiao, G. X. Cao, Z. Gai, S. Sallis, L. F. J. Piper, S. A. Chambers, *J. Phys.: Cond. Matter* **27**, 245605 (2015).
- [4] K. H. L. Zhang, Y. Du, P. V. Sushko, M. E. Bowden, V. Shutthanandan, S. Sallis, L. F. J. Piper, S. A. Chambers, *Phys. Rev. B* **91**, 155129 (2015).
- [5] K. H. L. Zhang, Y. Du, A. Papadogianni, O. Bierwagen, S. Sallis, L. F. J. Piper, M. E. Bowden, V. Shutthanandan, P. V. Sushko, S. A. Chambers, *Adv. Mater.*, in press (2015).
- [6] L. Farrell, K. Fleischer, D. Caffrey, D. Mullarkey, E. Norton, I. V. Shvets, *Phys. Rev. B* **91**, 125202 (2015).
- [7] R. G. Gordon, *Mater. Res. Soc. Bull.* **25**, 52 (2000).
- [8] E. Arca, K. Fleischer, I. V. Shvets, *Appl. Phys. Lett.* **99**, 111910 (2011).
- [9] R. Nagarajan, A. D. Draeseke, A. W. Sleight, J. Tate, *J. Appl. Phys.* **89**, 8022 (2001).

Publications

Scott A. Chambers, “*Probing perovskite interfaces and superlattices with x-ray photoemission spectroscopy*”, invited book chapter for *Hard X-ray Photoelectron Spectroscopy*, edit by J. Woicik, Springer, in press (2016).

Peng Xu, Timothy C. Droubay, Jong Seok Jeong, K. Andre Mkhoyan, Peter V. Sushko, Scott A. Chambers, Bharat Jalan, “*Quasi two-dimensional ultra-high carrier in a complex oxide broken-gap heterojunction*”, *Adv. Mater. Int.* in press (2015).

Kelvin Zhang, Yingge Du, Alexandra Papadogianni, Oliver Bierwagen, Shawn Sallis, Louis F.J. Piper, Mark E. Bowden, V. Shutthanandan, Peter V. Sushko, Scott A. Chambers, “*Perovskite Sr-doped LaCrO₃ as a new p-type transparent conducting oxide*”, *Adv. Mater.*, in press (2015).

Ryan B. Comes, Peng Xiu, Bharat Jalan, Scott A Chambers, “*Band alignment of epitaxial SrTiO₃ thin films with (LaAlO₃)_{0.3}-(Sr₂AlTaO₆)_{0.7}(001)*”, *Appl. Phys. Lett.* **107**, 131601 (2015).

Scott A. Chambers, Yingge Du, Meng Gu, Timothy C. Droubay, Steven P. Hepplestone, Peter V. Sushko, “*Dominance of interface chemistry over the bulk properties in determining the electronic structure of epitaxial metal/perovskite oxide heterojunctions*”, *Chem. Mater.* **27**, 4093 (2015).

Ryan B. Comes, Sergey Y. Smolin, Tiffany C. Kaspar, Ran Gao, Brent A. Apgar, Lane W. Martin, Mark E. Bowden, Jason B. Baxter, and Scott A. Chambers, “*Visible-light carrier generation in co-doped epitaxial titanate films*”, *Appl. Phys. Lett.* **106**, 092901 (2015).

J. Moghadam, K. Ahmadi-Majlan, X. Shen, T. Droubay, M. Bowden, M. Chrysler, D. Su, S. A. Chambers, and J. H. Ngai, “*Band-gap engineering at a semiconductor – crystalline oxide interface*”, *Adv. Mater. Int.*, **2**, 1400497 (2015).

J. J. Kas, F. D. Vila, J. J. Rehr, and S. A. Chambers, “*Real-time cumulant approach for charge transfer satellites in x-ray photoemission spectra*”, *Phys. Rev. B* **91**, 121112(R) (2015).

Guoqiang Li, Tamas Varga, Pengfei Yan, Zhiguo Wang, Chongmin Wang, Scott A. Chambers, Yingge Du, “*Crystallographic dependence of photocatalytic activity for WO₃ thin films prepared by molecular beam epitaxy*”, *Phys. Chem.-Chem. Phys.* **17**, 15073 (2015).

K.H.L. Zhang, Y. Du, P. V. Sushko, M. E. Bowden, V. Shutthanandan, S. Sallis, L.F.J. Piper, S.A. Chambers, “*Hole-induced insulator-to-metal transition in La_{1-x}Sr_xCrO₃ epitaxial films*”, *Phys. Rev.* **B 91**, 155129 (2015).

K.H.L. Zhang, Y. Du, P. V. Sushko, M. E. Bowden, V. Shutthanandan, L. Qiao, G. X. Cao, Z. Gai, S. Sallis, L.F.J. Piper, S.A. Chambers, “*Electronic and magnetic properties of epitaxial perovskite SrCrO₃(001)*”, *J. Phys: Cond. Mat.* **27**, 245605 (2015).

K.H.L Zhang, P.V. Sushko, R. Colby, M.E. Bowden, Y. Du, S.A. Chambers, “Reversible nano-structuring of SrCrO_{3-x} through oxidization and reduction at low temperatures”, *Nature Commun.* **5**, 4669 (2014).

Scott A. Chambers, “Stability at the Surface”, *Science* **346**, 1186 (2014).

Ryan B. Comes, Peter V. Sushko, Steve M. Heald, Robert J. Colby, Mark E. Bowden, and Scott A. Chambers, “*Band gap reduction and dopant interaction in epitaxial La,Cr co-doped SrTiO_3 thin films*”, *Chem. Mater.* **26**, 7073 (2014).

Yingge Du and Scott A. Chambers, “*Etalon-induced baseline drift and correction in atom flux sensors based on atomic absorption spectroscopy*”, *Appl. Phys. Lett.* **105**, 163113 (2014).

Yingge Du, Meng Gu, Tamas Varga, Chongmin Wang, Mark E. Bowden, and Scott A. Chambers, “*Facile WO_6 Octahedral Distortion and Tilting During WO_3 Heteroepitaxy on $\text{SrTiO}_3(001)$* ”, *ACS Appl. Mater. Int.* **6**, 143253 (2014).

Yingge Du, Timothy C. Droubay, Andrey V. Liyu, Guosheng Li, Scott A. Chambers, “Self-corrected sensors based on atomic absorption spectroscopy for atom flux measurements in molecular beam epitaxy”, *Appl. Phys. Lett.* **104**, 63110 (2014).

Y. Du, K. H. L. Zhang, Tamas Varga, and S. A. Chambers, “*RHEED beam-induced structural and property changes on MBE grown WO_3 thin films*”, *Appl. Phys. Lett.* **105**, 051604 (2014).

In-situ Monitoring of Dynamic Phenomena during Solidification

A.J. Clarke, D. Tournet, J.W. Gibbs, S.D. Imhoff, D.R. Coughlin,
J.C.E. Mertens, B.M. Patterson, and C.A. Yablinsky

Los Alamos National Laboratory
Materials Science and Technology Division
Materials Technology – Metallurgy (MST-6)
Los Alamos, NM 87545

Program Scope

Solidification of metal alloys is spatially and temporally multi-scale. We use real-time imaging to study metal alloy solidification dynamics and to inform, develop, and validate state-of-the-art computational models to achieve predictive capability. At the microscopic scale, we control thermal gradient (G) and solid-liquid interfacial velocity (V) during directional solidification to manipulate morphological and solutal evolution and experimentally determine the G - V combinations governing diffusion-

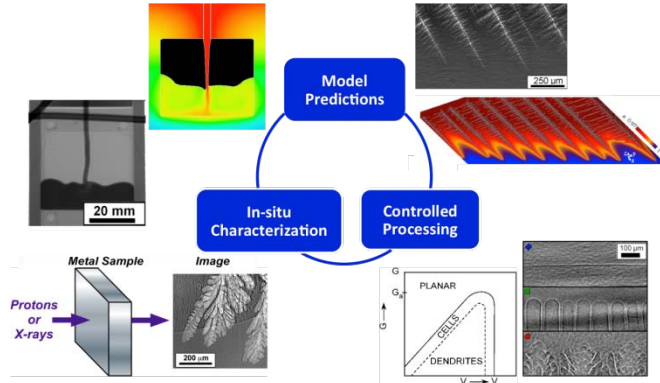


Figure 1. Multi-scale prediction and control of metal alloy solidification dynamics.

controlled growth transitions. We quantitatively compare our x-ray imaging of a dilute aluminum-copper alloy to three-dimensional (3D) phase-field (PF) simulations and successfully predict key microstructural characteristics, but only if solutal convection (identified by our experiments) is incorporated. At the mesoscopic scale, the evolution of dendritic arrays in aluminum-based alloys is compared to dendritic needle network (DNN) modeling. At the macroscopic scale, we use proton imaging to inform casting modeling and compare resulting structural and chemical variations with microstructural predictions. We also use dynamic transmission electron microscopy (DTEM) to study rapid solidification of nanocrystalline metal alloys films, relevant to additive manufacturing and welding. We are pursuing four-dimensional (4D) imaging (3D plus time) of hierarchical solidification structures and multi-scale experiments

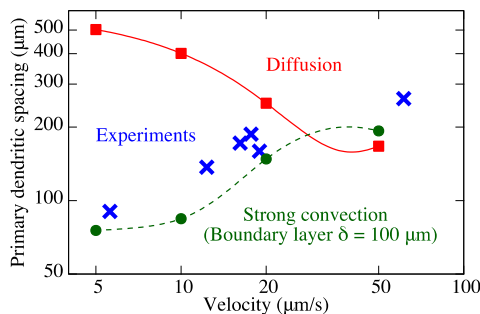


Figure 2. Results from x-ray imaging of controlled growth in an Al-Cu alloy during directional solidification and quantitative 3D PF simulations, highlighting the influence of liquid convection.

to support complementary solidification and micromechanical modeling. Experimental and computational visualization of solidification, coupled with controlled processing, will accelerate the synthesis and deployment of advanced materials with designed structures, properties, and performance.

Recent Progress

Experimentally, we use real-time (electron, x-ray, or proton) imaging to spatially and temporally study multi-scale solidification dynamics. We control G and V to explore microstructural selection mechanisms and identify growth regime transitions. For a dilute Al-Cu alloy, two major findings are: 1) the planar to cellular

regime transition occurs at a higher velocity ($\approx 3 \mu\text{m/s}$) than predicted by diffusional growth theory ($\approx 0.5 \mu\text{m}$) [1] and 2) the dependence of microstructural length scale significantly differs from classical diffusion theory and past experiments on transparent organic analogue materials. Close to the cell to dendrite transition, primary dendritic spacing increases instead of decreases with increasing interfacial velocity. As illustrated in Figure 2, this discrepancy is a manifestation of gravity-induced convection in the liquid, which we investigated with complementary 3D PF simulations. This example highlights the importance of real-time imaging in identifying the critical physics missing from models to achieve predictive capability.

X-ray imaging of a near-eutectic Al-16at.%Cu alloy during directional solidification also revealed convection in the liquid, resulting in stray Al-rich crystals trapped within lamellar eutectic (Al+Al₂Cu) solid [2]. Convection is clearly observed in Figure 3, where plumes of bismuth solute appear during tin-bismuth (Sn-Bi) alloy solidification parallel to gravity. In this study, the solidification conditions were varied to examine dendrite arm fragmentation [3], which may have a significant impact on the columnar-to-equiaxed transition – a crucial event that yields a change in grain morphology and size in castings. These experimental observations unambiguously highlight the importance of gravity-induced liquid flow, despite the constrained foil configuration intended to limit convection.

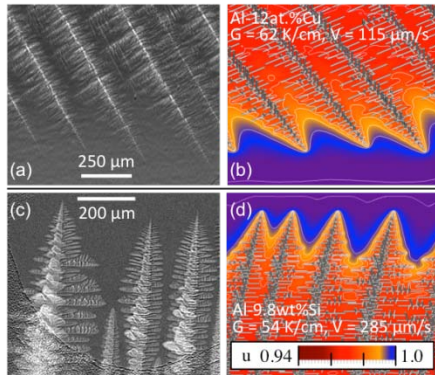


Figure 4. Directional solidification of (a,b) Al-Cu and (c,d) Al-Si alloys. (Left) X-ray images and (Right) 3D DNN model predictions at the same scale, showing normalized solute concentration u .

recently assessed the kinetics of liquid-liquid phase separation in an aluminum-indium (Al-In) alloy [6]. When a single liquid decomposes into two liquids with different compositions and densities (like oil and water), multiple growth mechanisms are possible, depending upon the environment and phase characteristics. Quantitative image

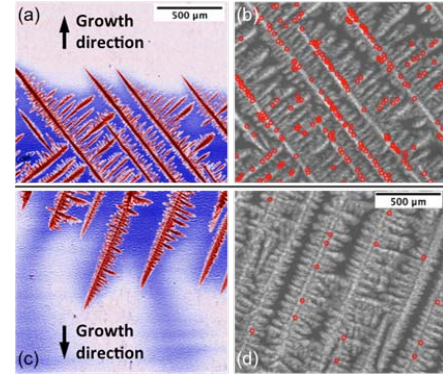


Figure 3. X-ray images of Sn-Bi alloy growth (a) anti-parallel and (c) parallel to gravity. Red and blue correspond to Sn- and Bi-rich regions, respectively. (b,d) Locations of fragmentation events (red circles).

While 3D PF is the method of choice for detailed solid-liquid interfacial modeling, larger length-scale simulations remain computationally challenging, if even feasible at all, for concentrated alloys that form complex, hierarchical dendritic networks of sharp branches during solidification. DNN modeling was developed for computationally efficient simulations of dendritic growth at the length-scale of solute transport in the liquid. The first comparisons of 3D DNN predictions with in-situ x-ray images of Al-based alloys are shown in Figure 4 [4,5]. For different metal alloys and solidification conditions, the model can predict microstructural characteristics like primary dendritic spacing critical to mechanical behavior.

Growth studies are not only limited to solidification. We

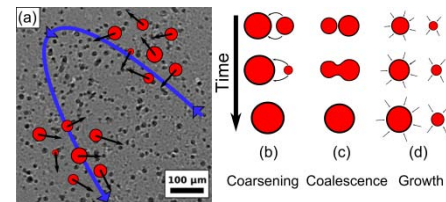


Figure 5. (a) An x-ray radiograph during liquid-liquid phase separation in Al₉₀In₁₀ and (b,c,d) diagrams highlighting growth mechanisms.

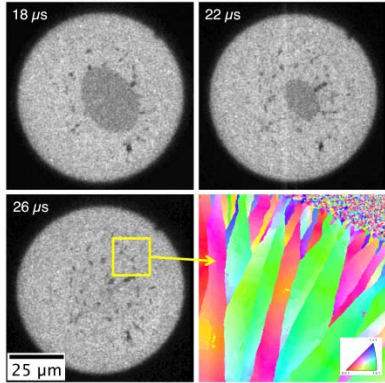


Figure 6. DTEM results of an Al-1%Si alloy showing the interface location over a few microseconds and the resulting crystallographic orientations of the grains.

kinetically-controlled solidification, which may provide the experimental data needed to bridge the limiting cases. At larger length scales, we use 800 MeV protons at LANL to watch casting mold filling and solidification (Figure 7). We also perform post-mortem structural, chemical, and mechanical characterization of these castings and use in-situ and ex-situ information to inform, develop, and validate multi-scale computational models. We also use high-energy micro-focused x-rays at LANL to image larger fields-of-view and higher density alloys (Figure 8) than afforded by synchrotron x-ray imaging, with improved spatial resolution over proton imaging.

To enable the creation of materials by design with tailored properties, we must understand the linkages between processing, structure, properties and performance. To this end, we are exploring micromechanical testing of Al-Cu alloy dendritic microstructures made during directional solidification experiments at Argonne National Laboratory's Advanced Photon Source (APS). 3D tomography of an example micromechanical specimen, tested at LANL while performing laboratory micro-computed tomography, is shown in Figure 9. Nano-indentations were performed on solidification microstructures to determine phase-specific mechanical properties. These early experimental results demonstrate the link from processing to mechanical behavior and are informing exploratory micromechanical modeling.

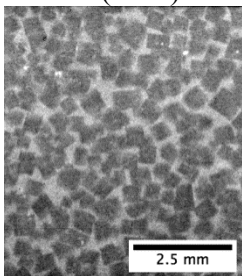


Figure 8. A high-energy micro-focus x-ray image of faceted Bi crystal growth in a Bi-Sn alloy, taken in the laboratory at LANL.

Future Plans

Several peer-reviewed journal articles are currently in preparation, including a two-part series summarizing our dilute Al-Cu alloy experimental and 3D PF modeling results, in collaboration with Prof. Alain Karma and Younggil Song at Northeastern University. Part 1 will summarize microstructural characteristics from our x-ray imaging compared to analytical expressions from solidification theory. Part 2 will present a quantitative comparison of

analysis was used to measure In-rich liquid droplet motion and population characteristics over time. We determined that droplet growth behaviors resemble well known steady-state coarsening laws, enhanced by concurrent growth due to supersaturation. Simplistic views of droplet motion are found to be insufficient until late in the reaction, due to a hydrodynamic instability caused by the large density difference between the dispersed and matrix liquid phases.

We are studying rapid solidification of nanocrystalline Al-Si alloy films using DTEM (Figure 6), in collaboration with Lawrence Livermore National Laboratory. Interfacial velocities (m/s) have been measured and we are performing post-mortem crystallographic analysis of these rapidly solidified microstructures. This work will extend our x-ray imaging of solidification in the diffusion-controlled regime to imaging of

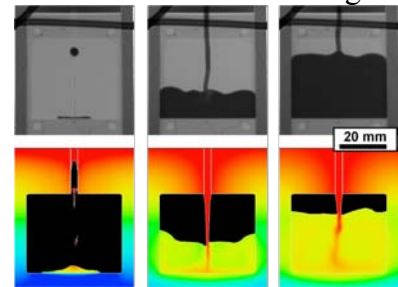


Figure 7. Proton radiography (pRad) images (top) and experimentally informed, continuum-scale simulation results (bottom) of a Sn-Bi alloy during casting mold filling.

selected experimental results with 3D PF simulations and discuss the role of solutal convection. We are also preparing an article on x-ray imaging of recrystallization and particle-assisted abnormal grain growth in a dilute Al-Cu alloy, in collaboration with Profs. Liz Holm and Tony Rollett at Carnegie Mellon University. An article comparing proton imaging of casting mold filling with continuum-scale modeling is also in preparation, in addition to several DTEM articles.

We will continue to analyze and interpret our multi-scale imaging of solidification dynamics and make comparisons to computational modeling and perform more x-ray and DTEM experiments. In November 2015, we will image grain boundaries (GBs) during directional solidification (see Figure 10) at APS to link GB dynamics and trajectories with material anisotropy and grain orientations, in collaboration with Prof. Alain Karma. Synergistic LANL Laboratory Directed Research and Development projects are also underway, including: 1) bridging length scales (from μm to m) in metal casting modeling; 2) adding convection into DNN for meso-scale simulations of realistic solidification conditions; 3) developing the hardware and software for 4D proton microscopy, which will also be applicable to 4D x-ray imaging of interest in this project; and 4) coupling of microstructural predictions from 3D DNN simulations to micromechanical modeling and comparisons with experimental results generated in this project.

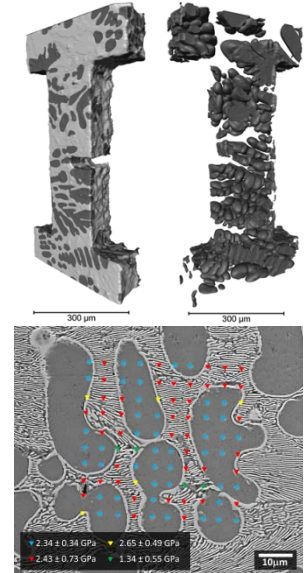


Figure 9. 3D tomography of a directionally solidified Al-Cu alloy micro-tensile specimen, with and without interdendritic eutectic structure and an SEM image showing nano-indentation locations.

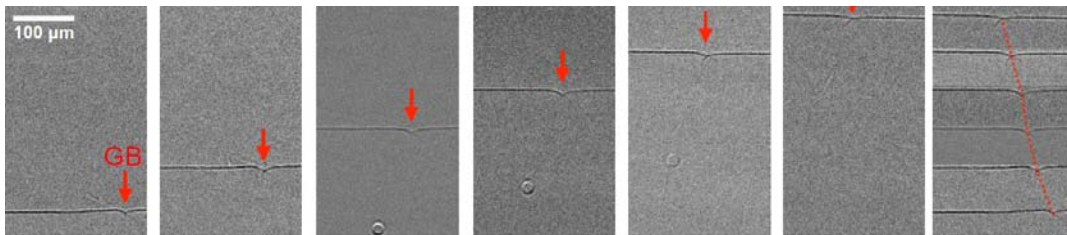


Figure 10. X-ray imaging of a “locked grain” below the onset of morphological instability during directional solidification of a dilute Al-Cu alloy.

References

- [1] W.W. Mullins, R.F. Sekerka. *Journal of Applied Physics* 1963, 34(2):323-329.
- [2] A.J. Clarke, D. Tourret, S.D. Imhoff, P.J. Gibbs, K. Fezzaa, J.C. Cooley, W.-K. Lee, A. Deriy, B.M. Patterson, P.A. Papin, K.D. Clarke, R.D. Field, and J.L. Smith. *Advanced Engineering Materials* 2015, 17(4):454-459.
- [3] J.W. Gibbs, D. Tourret, P.J. Gibbs, S.D. Imhoff, M.J. Gibbs, B.A. Walker, K. Fezzaa, and A.J. Clarke. *JOM* 2015, DOI: 10.1007/s11837-015-1646-7.
- [4] D. Tourret, A. Karma, A.J. Clarke, P.J. Gibbs, and S.D. Imhoff. *IOP Conference Series: Materials Science and Engineering* 2015, 84:012082.
- [5] D. Tourret, A.J. Clarke, S.D. Imhoff, P.J. Gibbs, J.W. Gibbs, and A. Karma. *JOM* 2015, 67(8):1776-1785.
- [6] S.D. Imhoff, P.J. Gibbs, M.R. Katz, T.J. Ott Jr., B.M. Patterson, W.-K. Lee, K. Fezzaa, J.C. Cooley, and A.J. Clarke. “Dynamic evolution of liquid-liquid phase separation during continuous cooling”, *Materials Chemistry and Physics* 2015, 153:93-1023.

DOE-funded publications (2 Year List)

1. A. Karma and D. Tourret. "Atomistic to continuum modeling of solidification microstructures", *Current Opinion in Solid State and Materials Science* 2015, DOI: 10.1016/j.cossms.2015.09.001.
2. C.L. Morris, E.N. Brown, C. Agee, T. Bernert, M.A.M. Bourke, M.W. Burkett, W.T. Buttler, D.D. Byler, C.F. Chen, A.J. Clarke, J.C. Cooley, P.J. Gibbs, S.D. Imhoff, R. Jones, K. Kwiatkowski, F.G. Mariam, F.E. Merrill, M.M. Murray, C.T. Olinger, D.M. Oro, P. Nedrow, A. Saunders, G. Terrones, F. Trouw, D. Tupa, W. Vogan, B. Winkler, Z. Wang, and M.B. Zellner. "New developments in proton radiography at the Los Alamos Neutron Science Center (LANSCE)", *Experimental Mechanics* 2015, accepted.
3. J.D. Roehling, A. Perron, J.-L. Fattebert, D.R. Coughlin, P.J. Gibbs, J.W. Gibbs, S.D. Imhoff, D. Tourret, J.K. Baldwin, A.J. Clarke, P.E.A. Turchi, and J.T. McKeown. "Imaging the rapid solidification of metallic alloys in the TEM", *Microscopy and Microanalysis* 2015, 21(S3):469-470, DOI: 10.1017/S1431927615003141.
4. J.W. Gibbs, D. Tourret, P.J. Gibbs, S.D. Imhoff, M.J. Gibbs, B.A. Walker, K. Fezzaa, and A.J. Clarke. "In situ x-ray observations of dendritic fragmentation during directional solidification of a Sn-Bi alloy", *JOM* 2015, DOI: 10.1007/s11837-015-1646-7.
5. A.J. Clarke, K. D. Clarke, R.J. McCabe, C.T. Necker, P.A. Papin, R.D. Field, A.M. Kelly, T.J. Tucker, R.T. Forsyth, P.O. Dickerson, J.C. Foley, H. Swenson, R.M. Aikin, and D.E. Dombrowski. "Microstructural evolution of a uranium-10 wt.% molybdenum alloy for nuclear reactor fuels", *Journal of Nuclear Materials* 2015, 465:784-792.
6. D. Tourret, A.J. Clarke, S.D. Imhoff, P.J. Gibbs, J.W. Gibbs, and A. Karma. "Three-dimensional multiscale modeling of dendritic spacing selection during Al-Si directional solidification", *JOM* 2015, 67(8):1776-1785.
7. D. Tourret, A. Karma, A.J. Clarke, P.J. Gibbs, and S.D. Imhoff. "Three-dimensional dendritic needle network model with application to Al-Cu directional solidification experiments", *Modeling of Casting, Welding and Advanced Solidification Processes (MCWASP XIV) IOP Conference Series: Materials Science and Engineering* 2015, 84:012082.
8. A.J. Clarke, D. Tourret, S.D. Imhoff, P.J. Gibbs, K. Fezzaa, J.C. Cooley, W.-K. Lee, A. Deriy, B.M. Patterson, P.A. Papin, K.D. Clarke, R.D. Field, and J.L. Smith. "X-ray imaging and controlled solidification of Al-Cu alloys toward creating microstructures by design", *Advanced Engineering Materials* 2015, 17(4):454-459.
9. S.D. Imhoff, P.J. Gibbs, M.R. Katz, T.J. Ott Jr., B.M. Patterson, W.-K. Lee, K. Fezzaa, J.C. Cooley, and A.J. Clarke. "Dynamic evolution of liquid-liquid phase separation during continuous cooling", *Materials Chemistry and Physics* 2015, 153:93-1023.

10. P.J. Gibbs, S.D. Imhoff, C.L. Morris, F.E. Merrill, C.H. Wilde, P. Nedrow, F.G. Mariam, K. Fezzaa, W.-K. Lee, and A.J. Clarke. "Multi-scale x-ray and proton imaging of metal solidification", *JOM* 2014, 66(8):1485-1492.
11. B.M. Patterson, K.C. Henderson, P.J. Gibbs, S.D. Imhoff, and A.J. Clarke. "Laboratory micro- and nano- scale x-ray tomographic investigation of Al-7at.%Cu solidification", *Materials Characterization* 2014, 95:18-26.
12. B.M. Patterson, K.C. Henderson, P.J. Gibbs, S.D. Imhoff, and A.J. Clarke. "Multi-scale imaging of Al-7at.% Cu eutectics using micro- and nano-scale x-ray computed tomography", *Microscopy and Microanalysis* 2014, 20(S3):780-781.
13. A.J. Clarke, S.D. Imhoff, P.J. Gibbs, J. C. Cooley, C. Morris, F.E. Merrill, B.J. Hollander, F. Mariam, T.J. Ott, M.R. Barker, T.J. Tucker, W.-K. Lee, K. Fezzaa, A. Deriy, B.M. Patterson, K.D. Clarke, J.D. Montalvo, R.D. Field, D.J. Thoma, J.L. Smith, and D.F. Teter. "Proton radiography peers into metal solidification", *Scientific Reports* 2013, 3:2020,
<http://www.nature.com/srep/2013/130619/srep02020/full/srep02020.html>
14. A.J. Clarke, S.D. Imhoff, J.C. Cooley, B.M. Patterson, W.-K. Lee, K. Fezzaa, A. Deriy, T.J. Tucker, M.R. Katz, P.J. Gibbs, K.D. Clarke, R.D. Field, D.J. Thoma, and D.F. Teter. "X-ray imaging of Al-7at.%Cu during melting and solidification", *Emerging Materials Research* 2013, 2(EMR2):90-98.

Ion Transport and Structural Evolution of Solid Electrolytes

Cheng Ma, Miaofang Chi, Yan Chen, Ke An, Juchuan Li^{††}, Chengdu Liang[†], and Nancy Dudney*

Center for Nanophase Materials Sciences, Spallation Neutron Source, and the Materials Science and Technology Divisions, Oak Ridge National Laboratory, Oak Ridge, TN 37831

[†] current - Ningde Amperex Technology Ltd, Fujian, China 352100

^{††}current Lawrence Berkeley National Laboratory, CA

Program Scope

Energy storage is essential for the harnessing of renewable energies that are intermittent. Solid electrolytes are expected to play an increasing role for energy storage devices as the need for safer, mechanically robust, and energy dense chemistries grows. Stabilizing the energy dense lithium metal anode is key for low-cost advanced battery chemistries such as Li-S and Li-air. The goal of this project is to provide a detailed, fundamental understanding of the role of chemistry, crystal structure, and microstructure on the key properties of solid electrolytes under the highly non-equilibrium conditions during operation of electrochemical energy storage (EES) systems. This goal will be achieved through three synergistically arranged aims: (1) Elucidation of the effect of atomic and meso-scale structures on ion transport in solids. (2) Understanding the influence of interfaces and interphases on the ion transport and electron transfer in EES systems. (3) Revealing the structural evolution and interface contact properties of SEIs and electrode-electrolyte interfaces in solid-state electrochemical cells.

The bulk and interface properties of the solid electrolytes are determined by rigorous control synthesis conditions, but the properties may further evolve due to chemical and electrochemical reactions. Understanding these complex processes requires in situ characterization during synthesis, interface fabrication and electrochemical operation. The program encompasses new materials and compositions, as well as known model materials formed via vapor, solid, and liquid synthesis routes. This includes highly conductive oxides, phosphates, and thiophosphates.

Recent Progress

Mesoscale domain structure creates ionic pathways. We have demonstrated that the mesoscopic length scale, despite being largely overlooked before, could be the key in correctly interpreting ionic transport within the material. For a particular crystalline electrolyte, there is often a rather wide variation among literature reports of the bulk conductivity which is likely attributable to subtle differences in the synthesis. In our investigation, a prototype Li-ion-conducting solid electrolyte, $\text{Li}_{0.33}\text{La}_{0.56}\text{TiO}_3$, has been studied and the results are summarized in Figure 1. Structural analysis at the mesoscopic scale by high resolution TEM revealed the

existence of highly localized 2D Li migration pathways in a seemingly disordered phase when annealed at 1350°C, LLTO1350. Such a mesoscopic framework insinuated that the number of

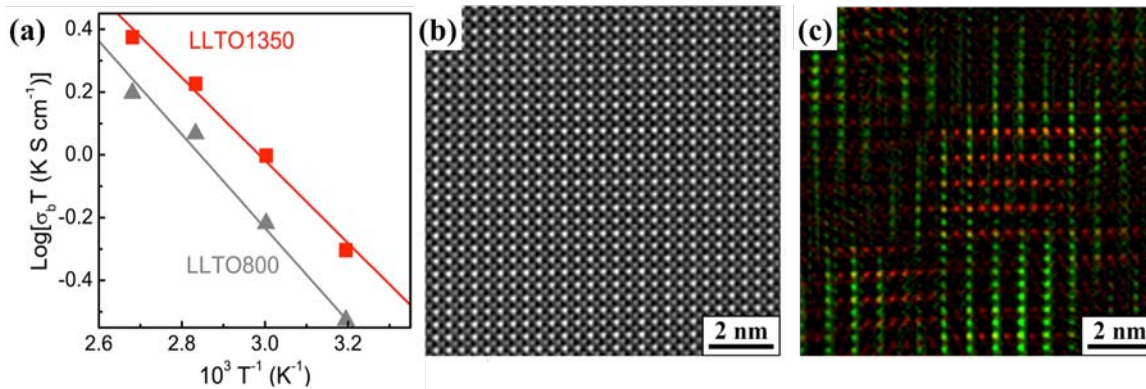


Figure 1 LLTO 1350 shows unexpected higher ionic conductivity compared to that of LLTO800 (a). HR-HAADT-STEM image of LLTO1350 indicates a random distribution of Li⁺, La³⁺ and vacancies at A-sites (b). Hidden meso-scale ordering structure was revealed in LLTO

facile Li percolation pathways, in sharp contrast to previous studies, was actually maximized by quenching from a high temperature. This mechanism allowed all the grains to effectively participate in the ionic transport and thus explains the puzzling high conductivity. By pointing out the critical role of mesoscopic structures in facile ionic transport, the insights obtained here not only allows for a more comprehensive understanding of ionic conduction, but may also lead to a new paradigm for designing high-performance ionic conducting materials.

Doping stabilizes the high ionic conductivity phase. The synthesis mechanism of doped $\text{Li}_7\text{La}_3\text{Zr}_2\text{O}_{12}$ garnets (LLZO), one of the most promising oxide Li ion electrolytes, has been explored by in-situ neutron diffraction. It is well known that stabilizing the cubic phase and realizing the maximum ionic conductivity are sensitive to the site occupation and concentration of cation dopants. Our neutron diffraction recorded during high temperature synthesis, reveals details of the formation of the cubic and tetragonal phases. As shown in Figure 2, $\text{La}_2\text{Zr}_2\text{O}_7$ and Li_2ZrO_3 are revealed as intermediate phases in the synthesis process. The off-stoichiometry due to the evaporation of Li_2CO_3 may cause the residual of those intermediate phases in the as-

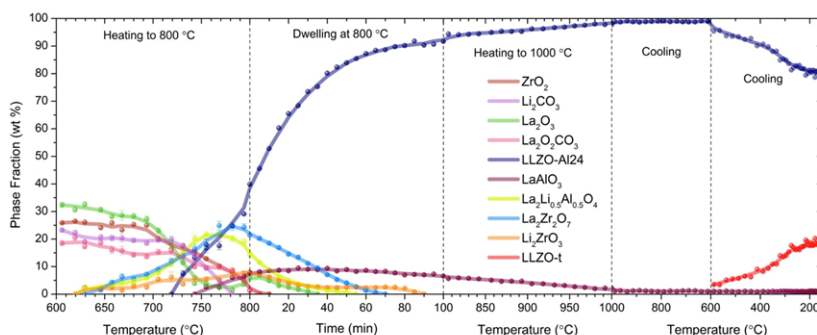


Figure 2 Fraction of the cubic and tetragonal phases of Al-doped LLZO in situ by ND during synthesis.

synthesized garnet bulk. Dopants inhibits the fast first order phase transition at ~ 630 °C, however, a small amount of tetragonal phase tends to form in the doped garnets through a diffusion process. Based on the in-situ observations, guidelines on suppressing the formation of those low-conductive phases have been provided to achieve improved electrolytic performance in garnets via the synthesis optimization.

Tuning the solid solution optimizes the ionic conductivity. A newly synthesized family of crystalline electrolytes, $\text{Li}_{3+x}\text{Ge}_x\text{As}_{1-x}\text{S}_4$ ($0 < x < 0.5$) has a dramatically enhanced conductivity due to the aliovalent substitution of Ge for As. As shown in Figure 3, the activation energy for the most conductive composition is only 0.17 eV, which was one of the lowest activation energies among the lithium-ion conductors. Poor chemical compatibility with metallic Li however, requires addition of a surface passivation layer. For this, $3\text{LiBH}_4 \cdot \text{LiI}$ deposited from solution, produced excellent lithium cycleability and a low interface resistance. Using the two electrolytes in tandem provides a wide electrochemical window up to 5 V versus the Li anode. Further experiments, such as those described below, are needed to understand the gradients in electrochemical potential across the stacked electrolytes.

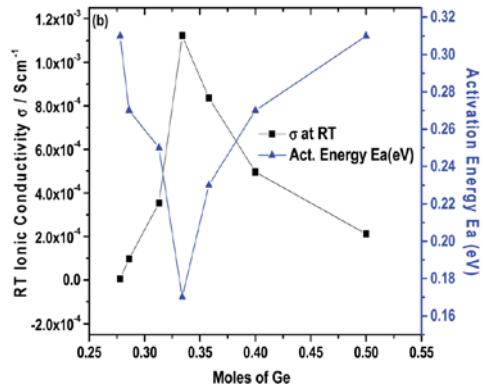


Figure 3 Ionic conductivity and activation energy at room temperature as a function of the Ge:As mole ratio.

In situ microscopy reveals interface reaction with Li metal. Very few solid electrolytes are stable with lithium metal; doped $\text{Li}_7\text{La}_3\text{Zr}_2\text{O}_{12}$ is believed to be one which is stable, although the interface is often highly resistive. In this work, we are investigating exactly how the interface evolves when first contacted with Li. TEM methods were used to unambiguously characterize the interaction between LLZO and Li metal; the LLZO-Li contact was made *in-situ* within the TEM, as shown in Figure 4, thereby providing a direct comparison of the same region of solid electrolytes before and after the formation of SE/Li interfaces. In addition, the creation of artifacts associated with sample preparation and handling can be prevented. We observe that the interface exhibited a structure and chemistry

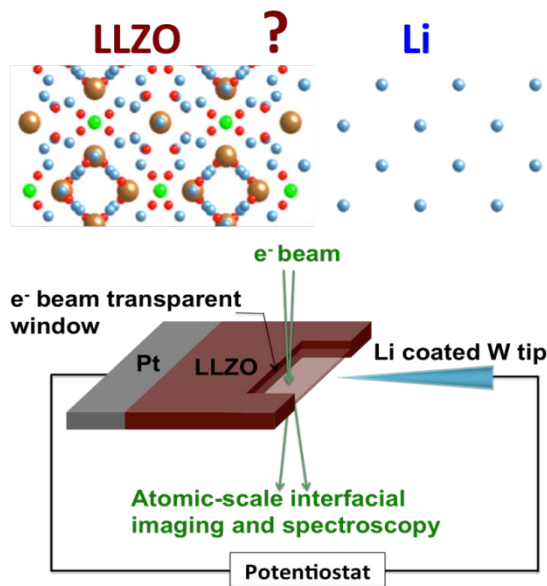
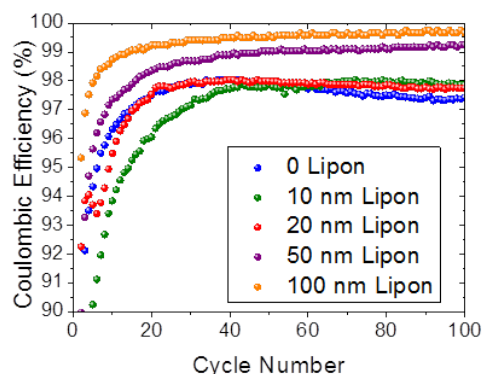


Figure 4 The TEM set-up for *in situ* investigation of solid electrolytes-metallic lithium interfaces is schematically shown.

distinct from that of bulk LLZO. Moving forward, these observations will be correlated with the measured interfacial ionic conductivity to provide new insight regarding the microscopic origin of the LLZO/Li interfacial behavior. This is an important step in realizing durable cycling of high-capacity Li metal anodes.

Artificial interface layers promote interface stability. Incorporation of a thin solid electrolyte film at an electrode interface, such as for Li metal electrodes, may act as a passivation layer. But because the passivation is not understood, the synthesis of such layers is largely trial and error. By constructing model interfaces and conducting detailed charge transfer studies, we have determined how a thin glass electrolyte film, known as Lipon, acts to passivate the interface of Li_xSi with a liquid electrolyte. Figure 5 shows that a minimum Lipon thickness of 50 nm is needed to stabilize the interface and approach 100% cycling efficiency; this critical thickness may be associated with electronic leakage current through the ultra-thin Lipon.



Further studies, where the Li counter electrode is replaced with a 3-volt cathode, are being used to probe the contact potential and potential gradient across the thin solid electrolyte.

Figure 5 Cycling efficiency for Lipon coated Si anode as a function of the Lipon thickness

Future Plans

As shown by these examples, there is still much to learn about how precise control of the synthesis refines the crystalline phase and lattice structure to promote facile ion conduction. We will continue to investigate sulfide and oxide solid electrolytes, particularly the meso-scale features which are being revealed for the first time. Studies of the interfaces formed of solid electrolytes contacting lithium and other reversible electrodes will fill a critical knowledge gap. Facile ion transport across such interfaces is critical to practical solid state devices. Future work will aim to integrate our neutron, electron microscopy and electrochemical capabilities to reveal the intrinsic interface stability, ion transport paths, and the role of reaction or barrier layers. This research tackles the grand challenges for advanced electric energy storage via the discoveries of new functional materials that enable affordable and safe storage of electricity in large scale.

Publications supported by BES in the Last Two Years

1. E. Rangasamy, J.C. Li, G. Sahu, J. Keum,; N. J. Dudney, C.D. Liang, “Pushing the Theoretical Limit of Li-CF_x Batteries: a Tale of Bi-functional Electrolyte,” *Journal of the American Chemical Society*, **136**, 6874–6877 (2014).
2. G. Sahu, Z. Lin, J. Li, Z. Liu, N.J. Dudney, C.D. Liang, “Air-Stable, High-Conduction Solid Electrolytes of Arsenic-Substituted Li₄SnS₄,” *Energy & Environmental Science*, **7**, 1053-1058 (2014).
3. G. Sahu, E. Rangasamy, J.C. Li, Y. Chen, K. An, N. J. Dudney, and C.D. Liang, “A High-Conduction Ge Substituted Li₃AsS₄ Solid Electrolyte with Exceptional Low Activation Energy,” *Journal of Materials Chemistry A*, **2**, 10396-10403 (2014).
4. E. Rangasamy, G. Sahu, J. Keum, A. Rondinone, N. J. Dudney, C. D. Liang, “A High Conducting Oxide - Sulfide Composite Lithium Superionic Conductor,” *Journal of Materials Chemistry A*, 4111-4116 (2014).
5. C. Ma, K. Chen, C.D. Liang, C.W. Nan, R. Ishikawa, K. More and M.F. Chi, “Atomic-Scale Origin of the Large Grain-Boundary Resistance in Perovskite Li-ion-Conducting Solid Electrolytes,” *Energy & Environmental Science*, **7**, 1638-1642 (2014).
6. J.C. Li, N. J. Dudney, J. Nanda, C.D. Liang, “Artificial SEI to Address the Electrochemical Degradation of Silicon Electrodes,” *ACS Applied Materials & Interfaces*, **6**, 10083-10088 (2014).
7. Y. Chen, L. Yang, F. Ren, K. An, “Visualizing the Structural Evolution of LSM/xYSZ Composite Cathodes for SOFC by *in-situ* Neutron Diffraction,” *Scientific Reports*, **4**, 5179 (2014).
8. C. Ma, E. Rangasamy, C.D. Liang, J. Sakamoto, K. More, M. Chi, “Excellent Stability of a Lithium-Ion-Conducting Solid Electrolyte upon Reversible Li⁺/H⁺ Exchange in Aqueous Solutions,” *Angewandte Chemie-International Edition*, **54**, 129-133 (2015). Distinguished by cover highlight and as hot paper.
9. Z. Lin, C.D. Liang, “Lithium-Sulfur Batteries: from Liquid to Solid Cells,” *Journal of Materials Chemistry A*, **3**, 936 (2015).
10. Yan Wu, Cheng Ma, Jihui Yang, Zicheng Li, Lawrence F. Allard, Chengdu Liang, and Miaofang Chi; “Probing the Initiation of Voltage Decay in Li-Rich Layered Cathode Materials at Atomic Scale” *Journal of Materials Chemistry A* 2015, **3**, 5385 – 5391
11. E. Rangasamy, Z. Liu, M. Gobet, K. Oilar, S. Greenbaum, W. Zhou, H Wu, and C.D. Liang*; “An Iodide-based Li₇P₂S₈I superionic conductor” *Journal of the American Chemical Society* 2015, **137**, 1384-1387
12. Zhan Lin and Chengdu Liang, “Lithium-Sulfur Batteries: from Liquid to Solid Cells” *Journal of Materials Chemistry A*, 2015, **3**, 936-958. (invited)
13. Juchuan Li ,* Cheng Ma , Miaofang Chi , Chengdu Liang , and Nancy J. Dudney* Solid Electrolyte: the Key for High-Voltage Lithium Batteries *Adv. Energy Mater.* **5**, 1401408 (2015)
14. Nancy Dudney and Juchuan Li, “Wire it right – utilizing all the energy in a Battery” *Science*, **347**, 6218 (2015), Invited perspective.
15. H. D. Liu, C.R. Fell, K. An, L. Cai, Y.S. Meng, “In-situ neutron diffraction study of the xLi₂MnO₃·(1-x)LiMO₂ (x=0, 0.5; M = Ni, Mn, Co) layered oxide compounds during electrochemical cycling,” *J. Power Sources*, **240**, 772 (2013).

16. A. K. Naskar, Z. Bi, Y. Li, S. K. Akato, D. Saha, M. Chi, C. A. Bridges and M. P. Paranthaman, "Tailored recovery of carbons from waste tires for enhanced performance as anodes in lithium-ion batteries," *RSC Adv.* **4**, 38213-38221 (2014).
17. D. Santhanagopalan, D. Qian, T. McGilvray, Z. Wang, F. Wang, F. Camino, J. Graetz, N.J. Dudney, Y. S. Meng, "Interface Limited Lithium Transport in Solid-State Batteries," *The Journal of Physical Chemistry Letters*, **5** (2), 298-303 (2014).
18. S. Wang, Y. Chen, S. Fang, L. Zhang, M. Tang, K. An, K. S. Brinkman, F. Chen, "Novel Chemically Stable $\text{Ba}_3\text{Ca}_{1.18}\text{Nb}_{1.82-x}\text{Y}_x\text{O}_{9-\delta}$ Proton Conductor: Improved Proton Conductivity through Tailored Cation Ordering," *Chem. Mater.* **26** (6), 2021-2029 (2014).
19. M. Gobet, S. G. Greenbaum, G. Sahu, C.D. Liang, "Structural Evolution and Li Dynamics in Nanophase Li_3PS_4 by Solid-State and Pulsed-Field Gradient NMR," *Chemistry of Materials*, 3558–3564 (2014).
20. Y. Wu, C. Ma, J. H. Yang, Z. C. Li, L. F. Allard, C. D. Liang, M. F. Chi*, "Probing the initiation of voltage decay in Li-rich layered cathode materials at the atomic scale," *Journal of Materials Chemistry A* **3**(10), 5385-5391 (2015). PTS#52487
21. Raymond R. Unocic, Loïc Baggetto, Gabriel M. Veith, Jeffery A. Aguiar, Kinga A. Unocic, Robert L. Sacci, Nancy J. Dudney and Karren L. More "Probing battery chemistry with liquid cell electron energy loss spectroscopy", *Chem. Commun.*, 2015, Advance Article DOI: 10.1039/C5CC07180A, Accepted 15 Sep 2015.

Growth Mechanisms and Controlled Synthesis of Nanomaterials (ERKCS81): Nonequilibrium Synthesis of Ultrasmall Nanoparticles by Laser Vaporization as “Building Blocks” for Nanostructures and Thin Films

David B. Geohegan,¹ Alex Puretzky,¹ Gyula Eres,² Mina Yoon,¹ Kai Xiao,¹
Gerd Duscher,^{2,3} Christopher M. Rouleau,¹ Masoud Mahjouri-Samani,¹
Mengkun Tian,³ Kai Wang,¹ Bing Huang,¹ and Xufan Li¹

¹Center for Nanophase Materials Sciences and ²Materials Science and Technology Division,
Oak Ridge National Laboratory, Oak Ridge, TN 37831

³Dept. of Materials Science and Engineering, Univ. of Tennessee, Knoxville, 37996

Program Scope

The overarching goal of the research program is to understand the link between the growth mechanisms and the resulting structure of nanoscale materials. The emphasis is on the development of real-time methods to induce and probe chemical and physical transformations away from thermodynamic equilibrium, in order to controllably synthesize nanomaterials with enhanced properties resulting from metastable structures. The approach relies on correlating the real-time diagnostic measurements with predictive theoretical methods and post-growth characterization by imaging, spectroscopy, and atomic-resolution analytical electron microscopy, to develop a framework for the deterministic synthesis of nanomaterials with desired properties.

Specific aims of the program are:

- (1) To reveal the kinetic pathways by which “building blocks” are involved in the growth of nanostructures through the development of real-time measurement approaches and modeling.
- (2) To understand the special role of nonequilibrium growth environments in capturing metastable phases and structures with novel nanoscale properties through the development of new synthesis and processing approaches incorporating in situ diagnostics.
- (3) To understand the atomistic interactions governing the design and synthesis of nanostructures with specific configurations and functionalities through predictive theory and associated experiments.

Recent Progress

One of the great challenges in understanding the synthesis of nanostructures is to identify the key precursors and reaction pathways leading to different hierarchical assemblies and determinable phases. We employ time-resolved in situ spectroscopic and imaging diagnostics to characterize the vapor phase growth environment as well as to measure the kinetics of nanostructure nucleation, growth, and termination. However, identifying the key precursors, and fundamental “building blocks”,

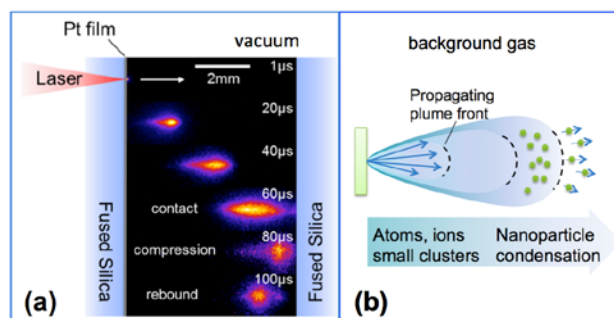


Figure 1. (a) Gated images of hot Pt nanoparticles generated by pulsed fs-laser vaporization were captured by intensified CCD-array imaging to understand their propagation in vacuum (shown) and their slowing dynamics in background gases (not shown here). (b) The model developed from this study permitted the understanding of how nanoparticles generated in ns-PLD by condensation within a propagating atomic/molecular laser plume can penetrate background gases significantly beyond the normal plume range, to deposit nearly pure fluxes of ultrasmall nanoparticles for the assembly of new architectures.

that we hypothesize govern the evolution of interfaces during nanostructure nucleation and growth is typically extremely difficult.

Recently we have investigated the nonequilibrium growth conditions and tunability of the laser vaporization process to produce nearly-pure fluxes of ultrasmall nanoparticles (UNPs) with diameters ~ 3 nm. These UNPs were then deposited by pulsed laser deposition (PLD) and investigated as well-defined “building blocks” for the assembly of both two-dimensional (2D) metal chalcogenide nanosheets, and metal oxide (principally TiO_2) nanostructures. This phenomena of nanoparticle formation is regarded as a complicating factor for the formation of smooth epitaxial films in PLD, however we are exploiting the formation of UNPs as a method of stoichiometric transfer of transformable, metastable “building blocks” for synthesis of a variety of nanostructures.

As shown in Figure 1(a), to understand how nanoparticles propagate in background gases we used gated, intensified CCD-array imaging of very unique, pure nanoparticle clouds produced by femtosecond-laser through-thin-film-ablation of nm’s-thin films. The narrow velocity distribution of the hot Pt nanoparticles ejected directly from the surface could be characterized by the images, and provided a unique opportunity to understand how nanoparticles propagate in background gases. In associated experiments, using a second time-delayed laser pulse and imaging the Rayleigh scattered light from the nanoparticles, the slowing and stopping of ~ 160 nm Pt nanoparticles in different Ar pressures was directly measured and found to occur in accordance with an Epstein drag model (e.g., stopping in 25 Torr Ar at a distance of 10 mm within 200 μs). These measurements allowed the development of model predictions for nanoparticle slowing in background gases, and along with it a new discovery for plume propagation in PLD (as illustrated in Figure 1(b)). Ultrasmall nanoparticles that form by condensation in the slowing atomic and molecular plume were predicted to propagate significant distances (e.g., 7.5 cm at 0.1 Torr), well beyond the typical plume range of atoms and molecules, thereby explaining the formation of architectures consisting of pure nanoparticles in our experiments. This ability to form plumes of pure nanoparticles permitted the exploration of UNPs as “building blocks” for nanostructure growth in our experiments.

Two-dimensional metal chalcogenides – from nanosheets to large single crystals

Recently we demonstrated the first direct PLD of functional metal chalcogenide nanosheet networks by laser vaporizing a pure GaSe crystalline target in background Ar. Plume propagation was characterized by *in situ* ICCD-imaging. High (1 Torr) Ar background gas pressures were found to be crucial for the stoichiometric growth of GaSe nanosheet networks. As shown in Figure 2(a), we discovered that the “building blocks” responsible for the stoichiometric transfer of material from target to substrate were amorphous

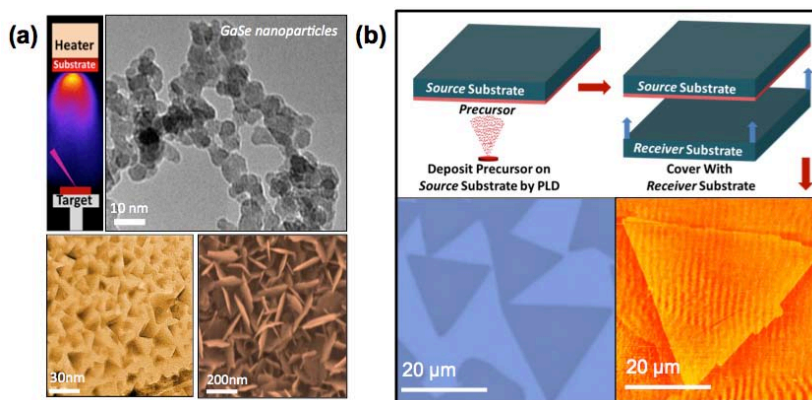


Figure 2. (a) Ultrasmall nanoparticles of amorphous GaSe produced by laser vaporization of a GaSe target can be collected at room temperature or deposited in nanoparticle architectures. When deposited at 500-750°C, they serve as “building blocks” to grow few-layer GaSe nanosheet networks in lateral or vertical orientations, with size and orientation determined by growth conditions. (b) Patterns of these amorphous nanoparticles (GaSe or MoSe_2) can be deposited, and transferred by thermal annealing to a nearby receiver substrate for the growth of large mono- to few-layer GaSe or MoSe_2 single crystals.

GaSe UNPs. UNPs of other metal dichalcogenides, such as MoSe₂, provided similar results with the layer number of the nanosheets controllable by the number of laser pulses. The nanosheets were found to have excellent crystallinity, and the networks exhibited high photoresponsivity. As shown in Figure 2(b), to understand the conversion process, amorphous UNPs of both materials were deposited on quartz substrates in different patterns, then covered with a receiver substrate to form a confined vapor transport growth (VTG) reactor, and thermally annealed in background Ar gas. Large monolayer crystalline domains (~ 100 μm lateral sizes) of GaSe and MoSe₂ were found to grow on the cooler receiver substrate, or continuous monolayer films if desired, with the coverage and layer number controllable by the “digital” nature of the PLD process. This novel PLD-VTG synthesis and processing method offers a unique approach for the controlled growth of large-area, metal chalcogenides with a desired number of layers in patterned growth locations for optoelectronics and energy related applications. Time-resolved, in situ diagnostics of the growth kinetics for both processes are in progress.

Hierarchical Assembly of Crystalline Nanostructures from UNP “Building Blocks” – Black TiO₂

Similarly, using ‘amorphous’ ultrasmall nanoparticle (UNP) “building blocks” deposited by PLD, the formation of metal oxide mesoscale nanoparticle architectures, nanorods, and nanosheets with interesting metastable phases has been recently discovered. As shown in Figure 3 (top panel), ~ 3 nm TiO₂ UNPs deposited by PLD in 30-100 mTorr O₂ can be accomplished at room temperature to result in nearly pure hierarchical assemblies of nanoparticle networks. These architectures can be post-annealed to crystallize into hyperbranched, mesoporous architectures that have been used as catalyst supports and functional electrodes for dye sensitized solar cells and photocatalytic water splitting. However, the particles can also serve as ‘building blocks’ to dynamically incorporate/evolve into novel crystal phases and structures on heated substrates such as TiO₂(B), cubic TiO₂, or ‘black TiO₂’ depending on the kinetics and thermodynamics. A variety of nanostructures such as crystalline nanorods, crystalline 2D nanosheets, or crystalline films can be obtained. Understanding how the phases of nanoparticle assemblies evolve from UNPs deposited at different temperatures requires an understanding of phase evolution in individual nanoparticles and at nanoparticle interfaces, which we are investigating with controlled synthesis experiments, state-of-the-art electron microscopy, and modeling.

Recently, in controlled annealing of TiO₂ amorphous UNPs, we discovered a new form of “black” TiO₂ that demonstrates that the synthesis pathways have a critical influence on the formation of properties and

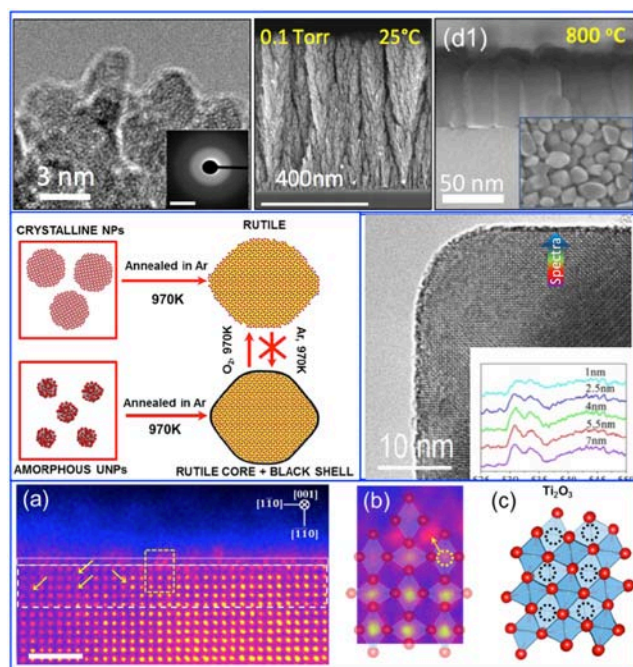


Figure 3. (top) Ultrasmall nanoparticles of amorphous TiO₂ produced by laser vaporization and collected at 25°C form hierarchical nanoparticle architectures. When deposited at 800°C, however, anatase nanorods are formed. (middle) Controlled experiments annealing amorphous UNPs collected at RT form larger nanoparticles of a new form of “black TiO₂”. EELS spectra reveal the emergence of a stable Ti₂O₃ phase responsible for the black color as visualized (bottom) with ultrahigh resolution Z-STEM and associated modeling of defect evolution.

functionality. Black and other forms of reduced TiO_2 are interesting because of the band gap reduction that is associated with the color change that occurs when UNPs synthesized by pulsed laser vaporization are annealed in a highly reducing atmosphere. The dramatic bandgap reduction to ~ 1.8 eV is key to increased absorption of visible light that leads to higher efficiency of TiO_2 in various photoelectrocatalytic processes. Characterization by atomic-resolution TEM imaging in Fig. 3 shows that although the as-synthesized UNPs are clearly identifiable by their shape, Selected Area Electron Diffraction (SAED) reveals that they lack coordinated crystalline order. After annealing in Ar the films of such particles turn black and particles of varying size, crystallinity, and phase can be clearly identified. Figure 3 (middle) illustrates that amorphous UNPs sinter and evolve a structure with a quite different phase evolution than that obtained by annealing crystalline nanoparticles. Depth profiling using highly spatially-resolved Electron Energy Loss Spectroscopy (EELS), Nano Beam Electron Diffraction (NBED), and atomic resolution TEM were performed on a representative rutile particle of 15 nm size illustrates the range of possible product states of the various reaction pathways. The O-K edge EELS shows that the particles evolve from a rutile phase at their core, with the peaks broadening as the 1-2 nm surface layer is approached. The switching of the intensity ratios of the two main EELS peaks near the surface layer uniquely identifies the formation of Ti_2O_3 . As the oxygen deficiency increases during crystallization from the center of the ultrasmall particle, the phase changes from pure rutile, to defective rutile, and finally the oxygen deficiency becomes so severe that a transformation into Ti_2O_3 occurs. These measurements show that the present black TiO_2 is actually a core-shell rutile- Ti_2O_3 structure. The similarity in the EELS of very small particles and the surface layer identifies the disordered 1-2 nm near surface region as a viable model for the structure of very small particles. This is an important conclusion because it paves the way for using theory and computational modeling to treat the formation of TiO_2 UNPs from a finite number of atoms that can be correlated directly with atomic scale resolution measurements.

Future Plans

The evolution of ultrasmall nanoparticle “building blocks” into 2D layered crystals or 3D nanostructures, illustrated here through experiments, provides a unique opportunity to link atomic-resolution electron microscopic characterization with new modeling approaches to realistically describe the evolution of interfaces and phases. Through the use of monochromated EELS to characterize band structure and band gaps of individual nanoparticles to the use of nanobeam electron diffraction to investigate the origins of sub-nanometer structure within individual ‘amorphous’ nanoparticles, our project is advancing electron microscopy as a tool to understand nanostructure evolution in concert with new modeling approaches. Linking these descriptors within the framework of computer simulation is a goal of the project. UNPs are large, yet computationally-tractable systems. Our ambitious plans to understand their evolution through this combined microscopy/modeling approach are described in a separate abstract, where progress on the identification of structural evolution within 3D TiO_2 UNPs has already been made, and the evolution of 2D phase and structure is also described.

For the vapor transport growth of two-dimensional materials, where varieties of precursor “building blocks” have not yet been well-defined in the literature, we are studying both typical growth conditions within CVD reactors and plan to characterize the growth environment using gas-phase laser spectroscopy. Through the introduction of tunable fluxes of reactants provided by pulsed laser vaporization plumes in background gases, we plan to controllably investigate the effects of altering the flux of materials from atomic and molecular units, to cluster and particulates. In addition to the need to develop growth models that accurately describe the type and mobility of precursor species on substrates, a great variety of fundamental questions exists for the growth of 2D materials,

including the role of the substrate, the evolution of edge states, causes for compositional variations and defects. As we have done with graphene and nanotubes in the past, we are planning to “watch” 2D crystals grow using time-resolved imaging and laser spectroscopy. Microscope-based laser spectroscopy of the photoluminescence, Raman scattering, absorption, and other informative nonlinear effects have been developed and are routinely used to post-characterize 2D crystals. Our plans involve *in situ* use of these techniques during 2D crystal growth within microreactor environments to understand and control defects, doping, edge structure, and layer stacking. Progress and plans in these areas are described more fully in a separate abstract.

DoE Sponsored Publications in the Last Two Years

1. S. R. Wagner, B. Huang, C. Park, J. Feng, M. Yoon, and P. Zhang, “Growth of Metal Phthalocyanine on Deactivated Semiconducting Surfaces Steered by Selective Orbital Coupling”, *Phys. Rev. Lett.* **115**, 096101 (2015).
2. B. Huang, H. Zhuang, M. Yoon, B. G. Sumpter, and S.-H. Wei, “Highly stable two-dimensional silicon phosphides: Different stoichiometries and exotic electronic properties”, *Phys. Rev. B* **91**, 121401 (R) (2015).
3. M. Tian, M. Mahjouri-Samani, G. Eres, R. Sachan, M. Yoon, M. F Chisholm, K. Wang, A. A Puzetky, C. M Rouleau, D. B Geohegan, G. Duscher “Structure and Formation Mechanism of Black TiO₂ Nanoparticles”, *ACS Nano* **ASAP** Sep 22, 2015.
4. M. Tian, M. Mahjouri-Samani, G. Eres, R. Sachan, M. F Chisholm, K. Wang, A. A Puzetky, C.M Rouleau, M.Yoon, D. B Geohegan, G. Duscher, “Phase Determination of Black TiO₂ Nanoparticles”, *Microscopy and Microanalysis* **21** (S3), 815 (2015).
5. X. Li, L. Basile, B. Huang, C. Ma, J. Lee, I. V Vlassioug, A. A Puzetky, M.-W. Lin, M. Yoon, M. Chi, J. C Idrobo, C. M Rouleau, B. G Sumpter, D. B Geohegan, K. Xiao, “Van der Waals Epitaxial Growth of Two-Dimensional Single-Crystalline GaSe Domains on Graphene”, *ACS Nano* **9**(8), 8078 (2015).
6. M. Mahjouri-Samani, M-W. Lin, K.Wang, A. R Lupini, J. Lee, L. Basile, A. Boulesbaa, C. M Rouleau, A. A Puzetky, I.N. Ivanov, K.Xiao, M. Yoon, D. B Geohegan, “Patterned arrays of Lateral Heterojunctions Within Monolayer Two-Dimensional Semiconductors”, *Nat. Comm.* **6**, 7749 (2015).
7. A. Puzetky, L. Liang, X. Li, K. Xiao, K. Wang, M. Mahjouri-Samani, L. Basile, J. C. Idrobo, B. G. Sumpter, V. Meunier, and D. B. Geohegan “Low-Frequency Raman Fingerprints of Two-Dimensional Metal Dichalcogenide Layer Stacking Configurations”, *ACS Nano* **9**(6) 6333 (2015).
8. X. Li, L. A. Basile, M. Yoon, C. Ma, A. Puzetky, J. Lee, J. Idrobo, M. Chi, C. Rouleau, D. B. Geohegan, and K. Xiao, “Revealing the preferred interlayer orientations and stackings of two-dimensional bilayer gallium selenide crystals”, *Angew. Chemie Int. Ed.* **54**(9) 2712 (2015).
9. B. Huang, H.L. Zhuang, M. Yoon, B. G. Sumpter, “Highly stable two-dimensional silicon phosphides: different stoichiometries and exotic electronic properties”, *Phys. Rev. B* **91**, 121401 (R) (2015).
10. M. H. Lahiani, J. Chen, F. Irin, A. A Puzetky, M. J Green, M. V. Khodakovskaya, “Interaction of carbon nanohorns with plants: Uptake and biological effects”, *Carbon*, **81**, 807 (2015).

11. C. M. Rouleau, A. A. Puzetzky, and D. B. Geohegan “Slowing of femtosecond laser-generated nanoparticles in a background gas”, *Appl. Phys. Lett.* **105**(21), 213108 (2014).
12. K. L. Grosse, V. E. Dorgan, D. Estrada, J. D. Wood, I. Vlassiuk, G. Eres, J. W. Lyding, W. P. King, and E. Pop “Direct observation of resistive heating at graphene wrinkles and grain boundaries”, *Appl. Phys. Lett.* **105**, (14) 143109 (2014).
13. M. Mahjouri-Samani, M. Tian, K. Wang, A. Boulesbaa, C. M. Rouleau, A.A. Puzetzky, M. A. McGuire, B. R. Srijanto, K. Xiao, G. Eres, G. Duscher, and D. B. Geohegan “Digital Transfer Growth of Patterned 2D Metal Chalcogenides by Confined Nanoparticle Evaporation” *ACS Nano* **8**(11), 11567 (2014).
14. A.A. Puzetzky, I. A. Merkulov, C. M. Rouleau, G. Eres and D. B. Geohegan “Revealing the surface and bulk regimes of isothermal graphene nucleation and growth on Ni with in situ kinetic measurements and modeling” *Carbon* **79**, 256 (2014).
15. M. Mahjouri- Samani, R. Gresback, M. Tian, K. Wang, A. A. Puzetzky, C. M. Rouleau, G. Eres, I. N. Ivanov, K. Xiao and M. A. McGuire, "Pulsed Laser Deposition of Photoresponsive Two- Dimensional GaSe Nanosheet Networks" *Adv. Funct. Mat.* **24**, 6365 (2014).
16. C. M. Rouleau, C.-Y. Shih, L. V. Zhigilei, A. A. Puzetzky, and D. B. Geohegan, “Nanoparticle generation and transport resulting from femtosecond laser ablation of ultrathin metal films: Time-resolved measurements and molecular dynamics simulations” *Appl. Phys. Lett.* **104**, 193106 (2014).
17. G. Eres, M. Regmi, C. M. Rouleau, J. Chen, I. N. Ivanov, A. A. Puzetzky, and D. B. Geohegan, “Cooperative Island Growth of Large Area Single-Crystal Graphene by Chemical Vapor Deposition on Cu “ *ACS Nano* **8**(6), 5657 (2014).
18. X. Li, M. Lin, A. A. Puzetzky, J. C. Idrobo, C. Ma, M. Chi, M. Yoon, C. M. Rouleau, I. I. Kravchenko, D. B. Geohegan, and K. Xiao, “Controlled Vapor Phase Growth of Single Crystalline, Two-Dimensional GaSe Crystals with High Photoresponse”, *Scientific Reports* **4**, 5497 (2014).
19. B.Huang, H-X. Deng, H.Lee, M. Yoon, B. G. Sumpter, F. Liu, S. C. Smith, and S.-H. Wei, "Exceptional Optoelectronic Properties of Hydrogenated Bilayer Silicene", *Phys. Rev. X* **4**, 021029 (2014).
20. T. Callcott, H. H. Weitering and N. Mannella “Origins of electronic band gap reduction in Cr/N codoped TiO₂” *Phys. Rev. Lett.* **112**, 036404 (2014).
21. A. A. Puzetzky, D. B. Geohegan, S. Pannala, C. M. Rouleau, “Exploring growth kinetics of carbon nanotube arrays by in situ optical diagnostics and modeling” *SPIE LASE*, 8969 896904 (2014).
22. C. M. Rouleau, M. Tian, A. A. Puzetzky, M. Mahjouri-Samani, G. Duscher, D. B. Geohegan, “Catalytic nanoparticles for carbon nanotube growth synthesized by through thin film femtosecond laser ablation,” *SPIE LASE* **8969**, 896907 (2014).
23. L. Oakes, A. Westover, M. Mahjouri-Samani, S. Chatterjee, A. Puzetzky, C. M Rouleau, D. B Geohegan, C. L Pint, “Uniform, Homogenous Coatings of Carbon Nanohorns on Arbitrary Substrates from Common Solvents” *ACS Appl. Mater. Interfaces* **5**, 13153–13160 (2013).
24. D. B Geohegan, A. A Puzetzky, M. Yoon, G. Eres, C. Rouleau, K.Xiao, J. Jackson, J.Readle,

M. Regmi, N. Thonnard, G. Duscher, M. Chisholm, K. More, “Laser Interactions for the Synthesis and In Situ Diagnostics of Nanomaterials” Ch. 7 in *Lasers in Materials Science*, pp: 143-173. Springer Series in Materials Science **191**, Springer International Publishing, Switzerland 2014.

25. C.Parks Cheney, P. Vilmercati, E. W. Martin, M. Chiodi, L. Gavioli, M. Regmi, G. Eres, T. A. Callcott, H. H. Weiering and N. Mannella “Origins of electronic band gap reduction in Cr/N codoped TiO₂“, *Phys. Rev. Lett.* **112**, 036404 (2014).

FWP: Novel Materials Processing and Preparation Methodologies
Project: Thermoelectric Properties and NMR of Complex Materials

E.M. Levin,^{1,2} Q. Xing,¹ and T.A. Lograsso^{1,3}

¹ – Division of Materials Sciences and Engineering, US DOE Ames Laboratory,
² – Department of Physics and Astronomy, ³ – Department of Materials Sciences
and Engineering, Iowa State University, Ames, IA 50011

Project Scope

The objectives of the Novel Materials Processing and Preparation Methodologies FWP are to quantify and control processing-structure-property relationships: the science of how chemistry, structural state and phase assemblage determine the properties of highly functional materials, manipulate and design materials functionality, and test theoretical predictions about properties of materials including thermoelectric. These materials enable to convert thermal energy to electrical utilizing the Seebeck effect and attract great attention for a long time. However, there are indications that a fundamental understanding of the Seebeck effect is still lacking. Our goal is to establish correlations between the (i) Seebeck coefficient, and (ii) composition, synthesis, crystal structure, carrier concentration, effective mass and scattering, using complex tellurides as model systems. PI E.M. Levin, who conducted research in the area of thermoelectric materials during last several years, joined Novel Materials Processing and Preparation Methodologies FWP since 2014. An advantage for FWP is that he brought an expertise in the area of energy-related materials and their characterization, while an advantage to him is that expertise of FWP in synthesis of high quality materials should be used for better understanding of fundamental properties of various materials.

Recent Progress

During last two years we have studied complex tellurides and silicides by X-ray diffraction at various temperatures, microstructure using electron scanning microscopy, composition by energy dispersive spectroscopy, Seebeck coefficient, electrical resistivity, and thermal conductivity, and ¹²⁵Te and ²⁹Si nuclear magnetic resonance (NMR) measurements [1b-8b].

Mg₂Si-based materials are well-known thermoelectric materials attracting attention for several years [1a-4a]. We studied Mg₂Si-Si alloys to understand possible combination of various properties of multiphase materials attributed to each phase [5b]. The directionally solidified alloy of Mg₄₅Si₅₅ shows the eutectic Mg₂Si-Si structure with Mg₂Si matrix and discontinuous Si network (Fig. 1).

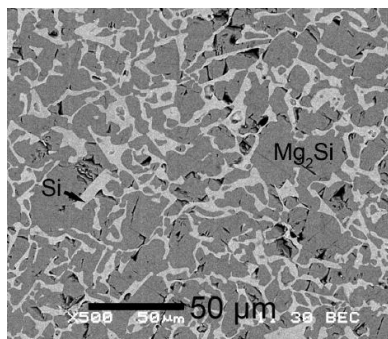


Fig. 1. Backscattered electron image of solidified Mg₄₅Si₅₅ alloy from the transverse view near the top edge.

Fig. 2 shows ^{29}Si NMR spectra of $\text{Mg}_{45}\text{Si}_{55}$ with two peaks, at -177 ppm and -80 ppm. Based on literature data, these peaks can be attributed to Mg_2Si [5a] and Si [6a] phases, respectively. The ratio of the intensities of these peaks reflects the relative amount of Mg_2Si and Si phases. Note that Cu addition to Mg_2Si -Si does not change the solidification of the alloy [5b].

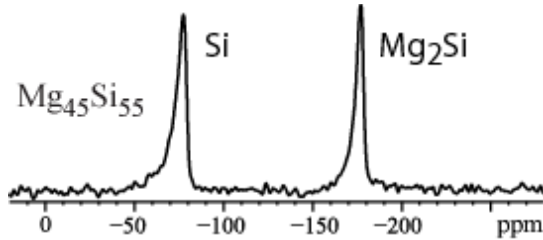


Fig. 2. ^{29}Si NMR spectra of $\text{Mg}_{45}\text{Si}_{55}$; the left peak should be attributed to the pure Si, while the right peak to Si in Mg_2Si .

^{29}Si NMR spin-lattice relaxation time, T_1 , measurements enable to derive the distribution of the carrier concentration in Mg_2Si -Si alloys. T_1 is determined by hyperfine coupling between the nuclear spin and free (mobile) charge carriers, and its value depends on the carrier concentration. Depending on the sample and heat treatment, T_1 for the Mg_2Si and Si phases shows two components, short and long, varying in a range between 12 and 300 s. Using calibration data for ^{29}Si NMR, the carrier concentration was estimated, which varies from $\sim 7 \times 10^{18}$ to $\sim 9 \times 10^{19} \text{ cm}^{-3}$.

Measurements of the Seebeck coefficient, electrical resistivity, and thermal conductivity show that electronic transport in Mg_2Si -Si alloys is mostly determined by the Si phase, while the thermal transport is limited by the Mg_2Si phase. By utilizing all characterization tools, we show that various experimental methods can be used as complementary methods to better understand the individual and combined properties of multiphase alloys [5b].

Interesting results were obtained for complex GeTe-based materials. GeTe alloyed with Ag and Sb form $\text{Ag}_x\text{Sb}_x\text{Ge}_{50-2x}\text{Te}_{50}$ alloys, well-known high-efficiency TAGS. We studied the effects of separate replacement of Ge in GeTe by Ag or Sb ($\text{Ag}_x\text{Ge}_{50-x}\text{Te}_{50}$ and $\text{Sb}_x\text{Ge}_{50-x}\text{Te}_{50}$ alloys) [7b]. Our data (Fig. 3, at the top) show that Ag reduces the Seebeck coefficient, while Sb increases it. Within common model for metals and semiconductors [7a], $S \sim m^*/n^{2/3}$, where m^* is carrier effective mass and n is the carrier concentration; if m^* is constant, S mostly depends on the carrier concentration. The carrier concentration in tellurides can be obtained from ^{125}Te NMR spin-lattice relaxation measurements [2b].

^{125}Te NMR spectra for GeTe-based alloys are shown on Fig. 3 (at the right). The NMR signal for GeTe is observed at +160 ppm. Replacement of Ge by Ag shifts the signal to more positive values. In contrast, replacement of Ge by Sb shifts the signal to more negative values. Such changes can be attributed to the changes in the Knight shift, which depends on T_1 and, therefore, on the carrier concentration. ^{125}Te NMR spin-lattice relaxation measurements confirm that Ag reduces T_1 , while Sb increases it, i.e. Ag increases the carrier concentration while Sb reduces it.

Comparison of the data for GeTe, $\text{Ag}_x\text{Ge}_{50-x}\text{Te}_{50}$, $\text{Sb}_x\text{Ge}_{50-x}\text{Te}_{50}$, and $\text{Ag}_2\text{Sb}_2\text{Ge}_{46}\text{Te}_{50}$ allow us to confirm theoretical prediction [8a] that Ag and Sb in GeTe ($\text{Ag}_x\text{Ge}_x\text{Ge}_{50-2x}\text{Te}_{50}$ materials or TAGS) form atomic pairs. The existence of such pairs can explain high efficiency of TAGS materials.

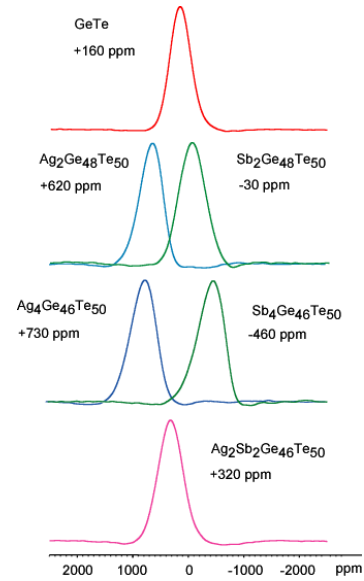
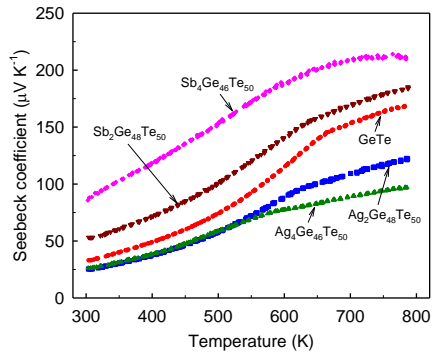


Fig. 3. Temperature dependencies of the Seebeck coefficient (at the top) and ^{125}Te NMR spectra (at the right) of GeTe, $\text{Ag}_x\text{Ge}_{50-x}\text{Te}_{50}$, and $\text{Sb}_x\text{Ge}_{50-x}\text{Te}_{50}$. ^{125}Te NMR spectra for $\text{Ag}_2\text{Sb}_2\text{Ge}_{46}\text{Te}_{50}$ are shown for comparison.

Earlier we found that doping of TAGS-85 ($\text{Ag}_{6.5}\text{Sb}_{6.5}\text{Ge}_{37}\text{Te}_{50}$) with 1 at.% rare earth Dy significantly enhances the Seebeck coefficient and thermoelectric efficiency [9a]. To better understand the effects of rare earths on crystal structure and thermoelectric properties of GeTe-based materials, we have synthesized and studied $\text{Ge}_{49}\text{Te}_{50}\text{R}_1$ alloys with $\text{R} = \text{La}, \text{Pr}, \text{Gd}, \text{Dy},$ and Yb , i.e. rare earth elements with different atomic size and localized magnetic moment [8b]. We found that rare earth atoms can produce strong effect on some parameters. GeTe has low-temperature rhombohedral and high-temperature cubic structure, and rhombohedral-to-cubic transformation may affect its thermoelectric properties. The transition can be seen via evaluation of two Bragg peaks, (024) and (220) (Fig. 4). The temperature when GeTe becomes mostly cubic, T_{cubic} , is ~ 660 K, while replacement of Ge by 1 at.% La increases T_{cubic} up to ~ 700 K.

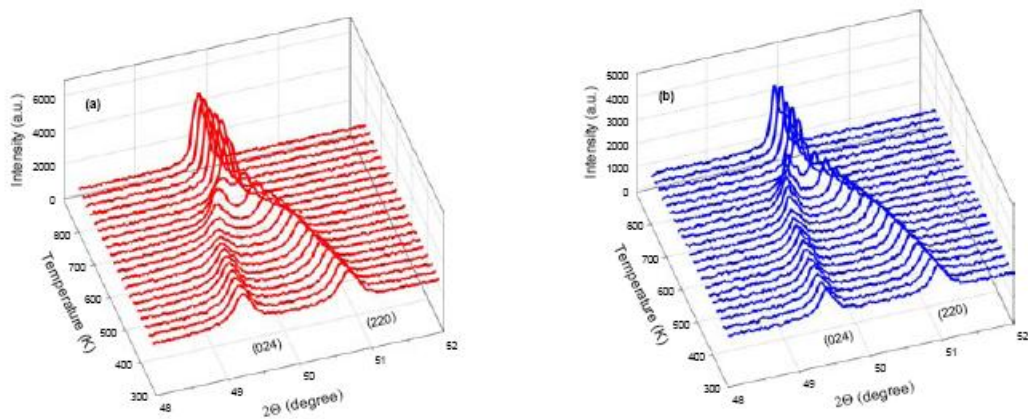


Fig. 4. XRD patterns showing (024) and (220) peaks for (a) GeTe and (b) $\text{Ge}_{49}\text{Te}_{50}\text{La}_1$; replacement of Ge by 1 at.% La increases the temperature of rhombohedral-to-cubic transition.

We also have found that alloying of GeTe with Gd and Dy (atoms with large magnetic moments) results in significant magnetic contribution to the Seebeck coefficient. In general, a comprehensive study of GeTe-based materials allowed us to establish important correlations and significantly increase our understanding of thermoelectric materials.

Future Plans

- ◆ Synthesize several series of GeTe-based materials where Ge is replaced by various elements and conduct a comprehensive study using common and advanced (^{125}Te NMR) methods.
- ◆ Establish structure–property correlations for complex GeTe-based materials, to understand a role of rhombohedral-to-cubic transformation on the Seebeck coefficient and other related properties.
- ◆ Test our hypothesis: (i) [Ag+Sb] in $\text{Ag}_x\text{Sb}_x\text{Ge}_{50-2x}\text{Te}_{50}$ (TAGS materials) form atomic pairs, (ii) atomic pairs affect the carrier effective mass and density of electron states near the Fermi level, (iii) these pairs result in high efficiency of TAGS materials.
- ◆ ^{125}Te NMR in complex tellurides still needs to be better understood. The emphasis is to continue to develop algorithms for use of NMR spectroscopy to obtain useful information from spin-lattice relaxation measurements, signal width, Knight and chemical shifts for complex tellurides.

References

- [1a] M. Akasaka *et al.* *J. Appl. Phys.* **104**, 013703 (2008).
- [2a] S. Fiameni *et al.* *Solid State Chem.* **193**, 142 (2012).
- [3a] D. Cederkrantz *et al.* *J. Appl. Phys.* **111** 023701 (2012).
- [4a] T. Yi *et al.* *J. Mater. Chem.* **22**, 24805 (2012).
- [5a] E. Ratai *et al.* *J. Phys. Chem. B* **107**, 12573 (2003).
- [6a] F. Dogan *et al.* *J. Electrochem. Soc.* **160**, A312 (2013).
- [7a] G.J. Snyder and E. S. Toberer. *Nature Mater.* **7**, 105 (2008).
- [8a] K. Hoang *et al.* *Phys. Rev. B* **81**, 115106 (2010).
- [9a] E.M. Levin *et al.* *Advanced Funct. Mater.* **22**, 2766 (2012).

Our Recent Publications

- [1b] E.M. Levin, M.F. Besser, and R. Hanus. *J. Appl. Phys.* **114**, 083713 (2013).
- [2b] E.M. Levin, J.P. Heremans, M.G. Kanatzidis, and K. Schmidt-Rohr. *Phys. Rev. B* **88**, 115211 (2013).
- [3b] E.M. Levin, R. Hanus, M. Hanson, W.E. Straszheim, and K. Schmidt-Rohr. *Physica Status Solidi A* **210**, 2628 (2013).
- [4b] E.M. Levin, M.J. Kramer, and K. Schmidt-Rohr. *J. Phys. and Chem. Solids* **75**, 1269 (2014).
- [5b] E.M. Levin, R. Hanus, J. Cui, Q. Xing, T. Riedemann, T.A. Lograsso, and K. Schmidt-Rohr. *Materials Chemistry and Physics*, **158**, 1 (2015).
- [6b] E.M. Levin, J. Cui, and K. Schmidt-Rohr. Under review, *Solid State NMR* (2015).
- [7b] E.M. Levin. Under review, *Phys. Rev. B* (2015).
- [8b] E.M. Levin *et al.* In preparation.

In situ investigations of growth of branched crystal structure

Dongsheng Li, Pacific Northwest National Laboratory, Richland, WA 99354, USA

Program Scope

The objective of this project is to develop an understanding of the formation mechanisms that determine nanocrystal size and morphology to enable the design of highly branched nanowires with tailored physical and chemical properties. Here I will develop a predictive understanding for two important categories of non-classical processes of branched nanowire formation: (1) particle-based growth (i.e. TiO₂ branched nanowire growth[1], Figure 1A, particularly oriented attachment (OA), and (2) competition between classical and non-classical mechanisms, specifically screw dislocation-driven trunk growth and vapor-liquid-solid (DD-VLS) branch nucleation (i.e. PbS branched nanowire growth[2], Figure 1B).

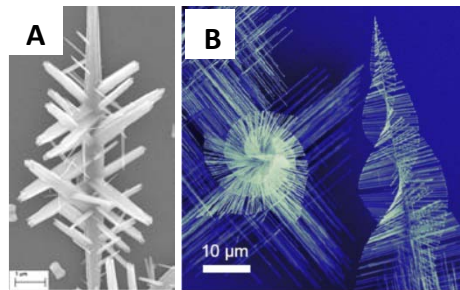


Figure 1. SEM images of branched TiO₂ nanostructures¹; B: PbS “pine-tree” nanowires²;

Development of a predictive understanding of those processes requires data on the dynamics of nanocrystal formation as it happens — rather than just information about the nanocrystals after they are formed. This work will employ *in situ* transmission electron microscopy and atomic force microscopy, which provide direct observation of atomic structure under actual conditions of the synthesis process, to investigate the movement and assembly of the precursors that are key elements in the synthesis of nanowires. This phenomenon will be correlated with the surface charge of the precursors, as well as the orientation-dependent forces between them. Finally, the role of competition between classical and non-classical mechanisms will be determined.

Recent Progress

Our previous *in situ* TEM investigation in iron oxide system shows that, in the iron oxide system, primary particles interact with one another through translational and rotational diffusion until a near-perfect lattice match is obtained either with true crystallographic alignment or across a twin plane[3]. Oriented attachment then occurs through a sudden jump-to-contact. Analysis of the acceleration during attachment indicates it is driven by electrostatic attraction. Ex-situ TEM analysis shows that the TiO₂ nanowire branching occurs through attachment of anatase nanoparticles to rutile wires on a specific crystallographic plane for which the anatase-to-rutile transformation leads to creation of a (101) twin plane.

Our hypothesis is that attachment is due to reduction of surface energy and the driving forces that bring the particles together are a mix dipole-dipole interactions, van der Waals forces, and Coulombic interactions. Therefore they can be controlled via pH, ionic strength (IS), and ionic speciation.

In our preliminary investigation, we first study particle mediated growth system. We will employ the AFM-based DFS approach to directly measure the forces, which drives OA events, between crystal facets to determine the absolute free energy of binding directly comparable to in situ TEM result. We investigate the orientation-dependent forces between nanoparticles.

In my preliminary experiments, I have successfully fabricated crystallographically oriented face-specific AFM “tips” (Figure 2A and B) and measured forces between (001) planes of ZnO, TiO₂, and mica. Initial DFS measurements of the forces between (001) crystal basal planes of mica, (001) planes of and (001) planes of ZnO show that the forces have strong relationship to pH, IS, and crystal orientation as shown in Figure 3A and B.

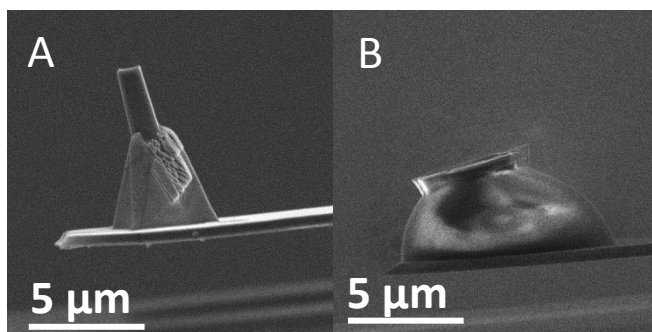


Figure 2. Customized crystallographic TiO₂ crystal (101) and mica (001) as AFM tips

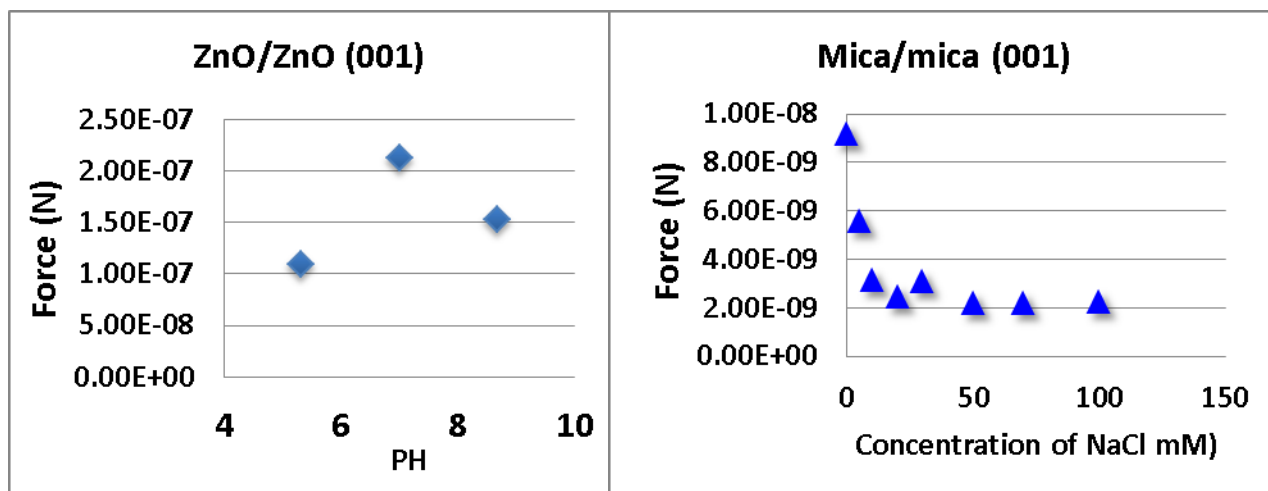


Figure 3. DFS measurements of the forces between (001) crystal basal planes of ZnO, (001) planes of mica, showing strong relationship between forces and pH and IS of solutions.

Future Plans

Our future plan involves (1) investigation of TiO₂ branched nanostructures formation via OA and extraction of the kinetic parameters that control them via in situ TEM, DFS/AFM and

zeta potential; (2) investigation of PbS pine tree formation via DD-VLS and the thermodynamic and kinetic factors via in situ TEM; (3) study of electron beam effects study carried out throughout the in situ TEM experiments

References

- [1] D. Li, F. Soberanis, J. Fu, W. Hou, J. Wu, and D. Kisailus, "Growth mechanism of highly branched titanium dioxide nanowires via oriented attachment," *Crystal Growth & Design*, vol. 13, pp. 422-428, Feb 2013.
- [2] M. J. Bierman, Y. K. A. Lau, A. V. Kvit, A. L. Schmitt, and S. Jin, "Dislocation-driven nanowire growth and Eshelby twist," *Science*, vol. 320, pp. 1060-1063, May 2008.
- [3] D. Li, M. H. Nielsen, J. R. I. Lee, C. Frandsen, J. F. Banfield, and J. J. De Yoreo, "Direction-specific interactions control crystal growth by oriented attachment," *Science*, vol. 336, pp. 1014-1018, 25 May 2012.

Publications

N/A (Project just started Aug, 2015)

Molecularly Organized Nanostructural Materials

Jun Liu, Maria Sushko, James J. De Yoreo, Praveen Thallapally

Pacific Northwest National Laboratory

Richland, WA 99352

Program Scope

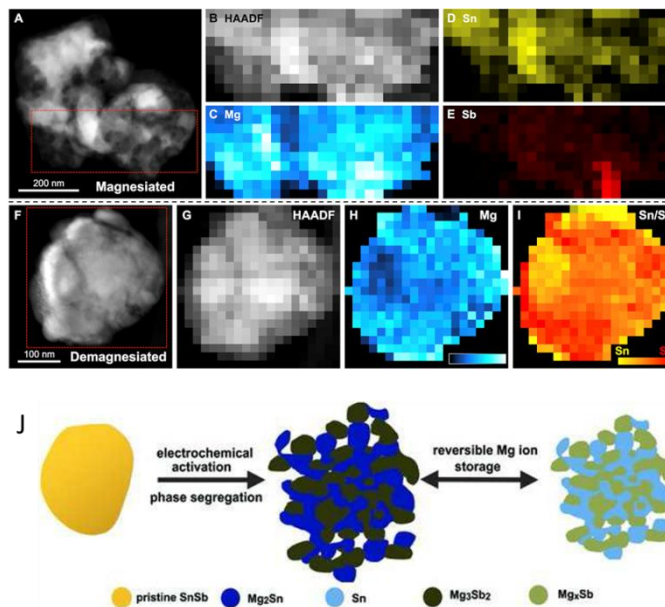
The goal of this project is to develop innovative approaches employing molecularly directed interfacial reactions to control crystallization and self-assembly of functional nanocomposites for energy storage and other applications. The central challenge is to develop principles to predict the synthesis of hierarchical materials with structural ordering across scales from atomic to nanoscale and beyond. This project will focus on interfacially controlled nucleation in synthesizing carbon-metal-metal oxide nanocomposite materials. The knowledge gained will be extended to understand and control self-assembly of materials with both atomic and longer length-scale ordering, and furthermore, to develop principles for synthesizing hierarchical structures through multi-generation nucleation processes. State-of-the-art transmission electron microscopy (TEM), atomic force microscopy (AFM), nuclear magnetic resonance (NMR), and extensive molecular and mesoscale computer modeling will be used to elucidate fundamental mechanisms of interfacial binding, nucleation and self-assembly.

Recent Progress

Graphene templated synthesis approaches for nanosized energy storage materials: We have demonstrated that specific carbon surfaces can function as molecular template to control nucleation using functionalized graphene sheets as model materials. One example is Chevrel phase $M_xMo_6T_8$ (M =metal, T =S, Se, or Te) for reversible multivalent ions intercalation with and without the presence of nucleation directing substrates (Chem Mat, 2014). Graphene sheets direct the nucleation and growth of particles and were critical for obtaining nanoscale particles. The synthesized nanocubes were tested as the active materials for multivalent Mg ions and Zn ions storage and were found to have substantially improved intercalation kinetics and higher reversible capacity. Graphene template synthesis was also used for preparing SnSb anode materials for Mg ion batteries (Adv. Mat., 2015). The SnSb alloy particles were synthesized on graphene substrate using $SnCl_2$ and $SbCl_3$ as precursors and a combination of solvothermal reaction and hydrogen reduction processes. We revealed that the pristine alloy SnSb particles experienced particle breakdown and phase segregation to Sn-rich and Sb-rich phases upon insertion of Mg ions. Both experimental analysis and density functional theory simulations suggest that the Sn-rich phase is particularly active and provides most of the capacity whereas

the Sb-rich phase is not as active. The interface between these two Sb-rich and Sn-rich phases is found to play a key role in promoting the formation and stabilization of the cubic Sn phase that is favorable for fast and reversible Mg insertion.

Figure 1. STEM characterization of Mo_6S_8 and the reaction mechanism. Magnesiated A–E) and demagnesiated F–I) electrodes. (A,F) Overview of the particle prior. (B,G) Simultaneous HAADF detector intensity map and EDS elemental intensity maps for Mg (C,H), Sn (D,I, yellow), and Sb (E,I, red). The EDS maps for Sn and Sb have been overlaid in (I) to highlight the correspondence between the phase segregated domains with regions of high or low Mg content in (H). The Mg elemental maps are displayed in cyan-hot, where black/dark blue is low Mg intensity and light blue/white is high Mg intensity. J. Schematic illustration of the electrochemical reaction mechanism of SnSb particles with Mg ions. Pristine SnSb particle experiences breakdown and phase segregation during electrochemical activation, and reversible Mg ion storage for activated SnSb alloys.

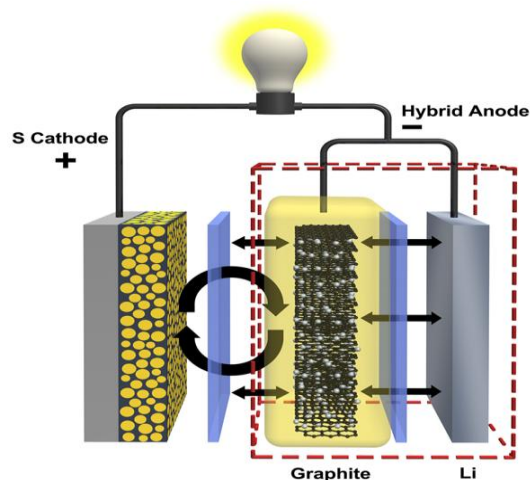


The role of high surface carbon was further studied in carbon- V_2O_5 composites for energy storage and the materials transformation mechanism during charge-discharge (to be submitted). The high surface area carbon was synthesized using resorcinol and formaldehyde as precursors (RFC), and the composite material was synthesized using the ambient hydrolysis deposition method with controlled loading and calcination of vanadium oxytriisopropoxide to V_2O_5 . We found that the crystalline phase transition of V_2O_5 was substantially hindered by the interfacial interactions between carbon surface and V_2O_5 clusters, which helps retaining the high surface area of the composite at $\sim 600 \text{ m}^2/\text{g}$ and the highly dispersed state of the V_2O_5 . We found that the composite material with highly dispersed V_2O_5 showed high capacity exceeds 300 mAh/g and fast charge transfer kinetics, and has potential as the cathode for Mg batteries. We identified that the Mg ions storage mechanism is through molecular reactions with the highly dispersed V_2O_5 and is surface controlled, and shows pseudocapacitive behavior.

Carbon Surface for Manipulating Electrochemical Reactions: In addition to controlling nucleation, carbon surfaces can modulate electrochemical reactions (Nature Comm, 2014). This concept is demonstrated in Li-S batteries. Lithium-sulfur batteries have high theoretical energy density and potentially low cost, but significant challenges such as severe capacity degradation prevent its widespread adoption. We conducted a fundamentally new design using electrically connected graphite and lithium metal as a hybrid anode to control undesirable surface reactions on lithium. The lithiated graphite placed in front of the lithium metal functions as an artificial self-regulated solid electrolyte interface layer to actively control the electrochemical reactions

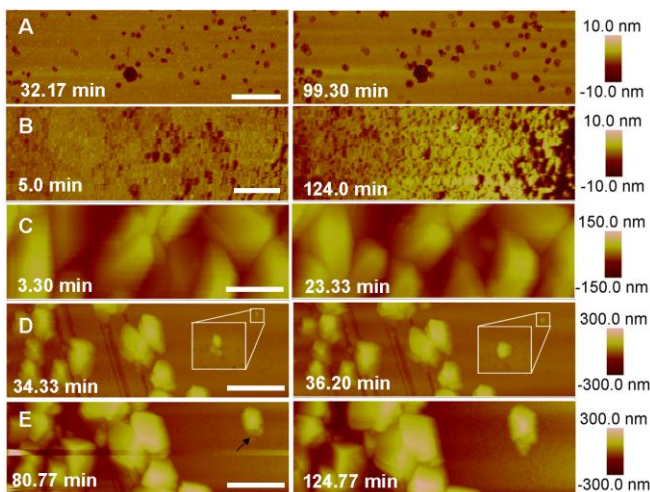
and minimize the deleterious side reactions, which significantly improves performance. Li-S battery incorporating this hybrid anode delivers a capacity of more than 800 mAh g⁻¹ for 400 cycles at a high rate of 1737 mA g⁻¹, corresponding to only 11% capacity fade and a Coulombic efficiency above 99%. This simple hybrid concept may also provide new lessons for protecting metal anodes in other energy storage devices.

Figure 2. Schematic of the hybrid anode design to manipulate the surface reactions on Li-S batteries. In the intrinsic cell design, the anode is made of Li metal connected with graphite. Lithiated graphite in the integrated anode multifunctions as an artificial, self-regulating SEI film on Li surface to dynamically “pump” Li⁺ ions. In addition the lithiated graphite works as a physical barrier to modulate the polysulfides concentration gradient in the cell, transferring the sulfur “contamination” issue from Li metal to the graphite side.



Fundamental study of nucleation: Hierarchical porous materials with crystalline structure are one of the most important families of complex functional material. The molecular assembly mechanism of the framework in these materials on which the structure and morphology control is based remains largely unknown. In-situ atomic force microscopy (AFM) provides the one of most direct way to answer these mechanism questions by observing nucleation and growth of metal organic frameworks (MOFs) in real time. Herein we study the nucleation and growth process of a MOF, zeolitic imidazolate framework ZIF-8 by using ZnO (001) face as the substrate and 2-methyl-imidazole as the linker. The nucleation of ZIF-8 occurs through the dissolution of ZnO and complex of released Zn²⁺ with the linker. The slow rate of ZnO dissolution together with continuous flux of linker solution makes possible to control the driving force for ZIF nucleation. The nucleation process at different concentrations of linker is studied, at the lowest concentration of 5 mM, no nucleation of ZIF is observed at 60 °C, at highest concentration of 500 mM, the nucleation of ZIF too fast to be monitor in AFM time scale (~3 min). At the concentration of 25 mM, 50 mM and 75 mM at 60 °C, the detailed nucleation and growth process of ZIF-8 is studied. The nucleation is highly selective on different sites. That is, the nucleation of crystallites has preference on the pre-formed step edges rather than terraces on ZnO (001) faces. The smallest observed nuclei have size up to 12.5 nm, these nuclei will merge together to form larger crystal with size of 41.0 nm and the growth rate of 1.20 nm/min. The secondary nucleation happens both at the surface and edge of ZIF-8 crystal after 34 min, the secondary nucleation at edge are more preferential than that on the surface. Our study enables direct identification of the fundamental units during the nucleation and growth stage of ZIF-8 on different crystal faces. These findings will be applicable to numerous nanoporous materials and support efforts to synthesize and design new frameworks with controlled properties. This study opens the door for quantitatively describing the fundamental nucleation phenomena is complex energy materials.

Figure 3. The in-situ AFM images of nucleation and growth process of ZIF-8 on ZnO (001) face. A) dissolution of ZnO (001) face in water. B) ZnO (001) face in the condition of 5 mM 2-methyl-imidazole and 60°C; C) ZnO (001) face in the condition of 500 mM 2-methyl-imidazole and 60°C; D) ZnO (001) face in the condition of 25 mM 2-methyl-imidazole and 60°C, the newly formed ZIF-8 nuclei merge into a larger crystal; E) the secondary nucleation of ZIF-8 on the edge and surface of ZIF-8. Scale bars: A) 1 μm ; B) and C) 400 nm; D) and E) 2 μm .



Future Plans

1. Fundamental understanding of nucleation on well-defined nanostructured carbon substrates. This task will focus on nucleation in a range of energy relevant materials, revealing the nature of the nucleation sites, elucidating early stages of nucleation including the molecular events and phase evolution leading to the final stable structure. The materials systems will consist of metals (Pt, Au, Ni, Cu) and metal oxides (NiO, CuO, MnOx, VOx) nucleated on well-defined carbon structures including carbon nanotubes, graphene, or carbon fibers, as well as well-defined, oriented metal oxides such as ZnO and TiO₂.
2. Interface controlled template-directed self-assembly and nanocrystal nucleation. This task will explore the interdependent processes of surfactant self-assembly and nanoparticle nucleation at interfaces to form ordered structures with both atomic and mesoscale ordering. Specifically, we will investigate self-assembly of anionic and cationic surfactants and block copolymers coupled with nucleation of metal oxides (SiO₂, TiO₂, ZrO₂) on graphene and carbon nanotube substrates.
3. Higher order structures. This task will explore and apply principles of interfacially controlled nucleation to create complex higher order structures through multiple generations of nucleation events using ZnO as the canonical materials system.

Publications

1. Darkins R., Sushko M. L., Liu J., and Duffy D. M. (2015) The effect of surface topography on the micellisation of hexadecyltrimethylammonium chloride at the silicon-aqueous interface. *Journal of Physics-Condensed Matter* 27, (5) Article # 054008. 10.1088/0953-8984/27/5/054008
2. Banerjee D., Liu J., and Thallapally P. K. (2015) Separation of C2 hydrocarbons by porous materials: Metal organic frameworks as platform. *Comments on Inorganic Chemistry* 35, (1) 18-38. 10.1080/02603594.2014.976704
3. Liu J. (2014) Charging graphene for energy. *Nature Nanotechnology* 9, (10) 739-741. 10.1038/nnano.2014.233
4. Cheng Y. W., Parent L. R., Shao Y. Y., Wang C. M., Sprenkle V. L., Li G. S., and Liu J. (2014) Facile synthesis of Chevrel phase nanocubes and their applications for multivalent energy storage. *Chemistry of Materials* 26, (17) 4904-4907. 10.1021/cm502306c
5. Cheng Y. W., Shao Y. Y., Zhang J. G., Sprenkle V. L., Liu J., and Li G. S. (2014) High performance batteries based on hybrid magnesium and lithium chemistry. *Chemical Communications* 50, (68) 9644-9646. 10.1039/c4cc03620d
6. Darkins R., Sushko M. L., Liu J., and Duffy D. M. (2014) Stress in titania nanoparticles: an atomistic study. *Physical Chemistry Chemical Physics* 16, (20) 9441-9447. 10.1039/C3CP54357A
7. Liu J., Lu P. J., Liang S., Liu J., Wang W., Lei M., Tang S., and Yang Q. (2015) Ultrathin Li3VO4 nanoribbon/graphene sandwich-like nanostructures with ultrahigh lithium ion storage properties. *Nano Energy* 12, 709-724. 10.1016/j.nanoen.2014.12.019
8. Cheng Y. W., Liu T. B., Shao Y. Y., Engelhard M. H., Liu J., and Li G. S. (2014) Electrochemically stable cathode current collectors for rechargeable magnesium batteries. *Journal of Materials Chemistry A* 2, (8) 2473-2477. 10.1039/c3ta15113a
9. Herbert S. A., Janiak A., Thallapally P. K., Atwood J. L., and Barbour L. J. (2014) Diffusion of vaporous guests into a seemingly non-porous organic crystal. *Chemical Communications* 50, (98) 15509-15512. 10.1039/c4cc07366e
10. Cheng, YW; Liu, TB; Shao, YY; Engelhard, MH; Liu, J; Li, GS (2014) Electrochemically stable cathode current collectors for rechargeable magnesium batteries, *JOURNAL OF MATERIALS CHEMISTRY*, Volume: 2, Issue 8, 2473-2477, DOI: 10.1039/c3ta15113a, Published: 2014
11. Ji, LW; Gu, M; Shao, Y; Li, XL; Engelhard, M; Arey, B; Wang, W; Nie, ZM; Xiao, J; Wang, CM; Zhang, JG and Liu, J. (2014) Controlling SEI Formation on SnSb-Porous Carbon Nanofibers for Improved Na Ion storage, *Advanced Materials*. DOI: 10.1002/adma.201304962.
12. Huang, C; Xiao, J; Shao, YY; Zheng, JM; Bennett, WD; Lu, DP; Laxmikant, SV; Engelhard, M; Ji, LW; Zhang, J; Liu, J (2014) Manipulating surface reactions in lithium-sulphur batteries using hybrid anode structures," *NATURE COMMUNICATIONS* Volume: 5, DOI: 10.1038/ncomms4015.

13. Shao, YY; Gu, M; Li, XL; Nie, ZM; Zuo, PJ; Li, GS; Liu, TB; Xiao, J; Cheng, YW; Wang, CM ; Liu, J (2014) Highly Reversible Mg Insertion in Nanostructured Bi for Mg Ion Batteries, NANO LETTERS , Volume: 14 , Issue: 1, Pages: 255-260, DOI: 10.1021/nl403874y.
14. Nie, ZM; Zhou, XY; Zhang, QF; Cao, GZ; Liu, J (2013) Aggregated TiO₂-Based Nanotubes for Dye Sensitized Solar Cells, "SCIENCE OF ADVANCED MATERIALS, Volume: 5, Issue: 11, Pages: 1750-1755, DOI: 10.1166/sam.2013.1622.
15. Shao, YY; Xiao, J; Wang, W; Engelhard, M; Chen, XL; Nie, ZM; Gu, M; Saraf, LV; Exarhos, G; Zhang, JG; Liu, J "Surface-Driven Sodium Ion Energy Storage in Nanocellular Carbon Foams, NANO LETTERS, Volume: 13, Issue: 8, Pages: 3909-3914, DOI: 10.1021/nl401995a.
16. Lei, CH; Chen, BW; Li, XL; Qi, W; Liu, J, "Non-destructively shattered mesoporous silica for protein drug delivery (2013) MICROPOROUS AND MESOPOROUS MATERIALS, Volume: 175, Pages: 157-160, DOI: 10.1016/j.micromeso.2013.03.022.
17. Chen, BW; Qi, W; Li, XL; Lei, CH; Liu, J (2013) Heated Proteins are Still Active in a Functionalized Nanoporous Support Chen, BW, SMALL, Volume: 9, Issue: 13, Pages: 2228-2232, DOI: 10.1002/sml.201202409
18. Moon, GH; Shin, Y; Choi, D; Arey, BW; Exarhos, GJ; Wang, C; Choi, W; Liu, J (2013) Catalytic templating approaches for three-dimensional hollow carbon/graphene oxide nano-architectures, NANOSCALE, Volume: 5, Issue: 14 , Pages: 6291-6296 , DOI: 10.1039/c3nr01387a.

FWP: Novel Materials Processing and Preparation Methodology
Project: Single Crystal Growth of FeAs-based Superconductors

Yong Liu, Qingfeng Xing, and Thomas A. Lograsso

Ames Laboratory, Ames, IA 50011

Program Scope

The *Novel Materials Preparation and Processing Methodologies* (Novel Materials) FWP is a synthesis-oriented research effort engaged in maintaining and enhancing the synthesis capabilities of the laboratory. We develop advanced processing techniques for the reproducible growth of high quality novel materials in polycrystalline and single crystalline forms. We perform detailed investigations on materials systems whose functionality is highly sensitive to synthesis pathways (e.g., thermoelectrics) to provide scientific understanding of the synthesis-structure-property relationship in newly discovered materials and in materials systems that are difficult to process due to reactivity, volatility, and toxicity (Fe-As superconductors).

The objectives of the Novel Materials FWP are to:

- Develop unique capabilities and processing knowledge in the bulk preparation, purification, and fabrication of inorganic metals, alloys, and compounds;
- Advance our Nation's ability to synthesize and characterize high purity, high quality materials, primarily in single crystal form, but also as metastable forms, such as ribbons, powders, or films;
- Quantify and control processing-structure-property relationships: the science of how chemistry, structural state, and phase assemblage determine the properties of highly functional materials;
- Manipulate and design functionality, and test theoretical predictions about new materials.

In pursuing the objectives of Novel Materials, the FWP focuses its efforts on energy-relevant materials where reproducible synthesis is challenging and the materials properties are particularly sensitive to synthesis pathways.

Recent Progress

$K_xFe_{2-y}Se_2$ superconductors are characteristic of phase separation feature. However, the nature of phase separation is not well understood. We have demonstrated that the superconducting phase is the remnant of high temperature phase after iron vacancy order-disorder transition. The

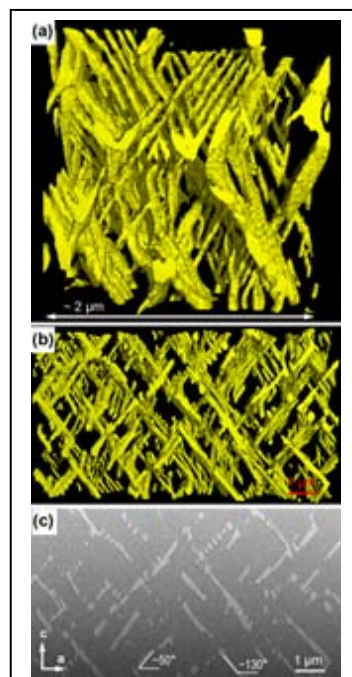


Figure 1. (a) and (b) Reconstructed 3D morphology of the stripe phase in the pseudo-single-crystal $K_xFe_{2-y}Se_2$. (c) A raw image of (0 1 0) plane used for 3D reconstruction of the volume shown in (b).

superconducting phase should not form without iron vacancy order-disorder transition. By focused ion beam-scanning electron microscopy (FIB-SEM), we further revealed that the superconducting phase forms a contiguous 3D architecture composed of parallelepipeds that have a coherent orientation relationship with the majority phase. Our results provide a reasonable explanation for the highly divergent results in the previous report on the processing techniques and stoichiometry in the starting materials [1-2].

Less work has been done in overdoped $\text{Ba}_{1-x}\text{K}_x\text{Fe}_2\text{As}_2$ single crystals because it is difficult to grow high-quality single crystals with sharp superconducting transitions. We have developed an inverted temperature gradient method to grow large and high-quality BaK122 single crystals [3]. see Figure 2. The top zone is set as the cold zone, such that nucleation initiates at the liquid surface layer upon cooling. Furthermore, the surface layer saturates because of the loss of K and As by evaporation, which produces “evaporation growth” on top of the melt. Because BaK122 single crystals start to crystallize from the liquid melt surface, the likelihood of trapped flux or impurities is reduced compared to growth inside the bulk of the liquid. We harvested large crystals with in-plane size up to $18 \times 10 \text{ mm}^2$.

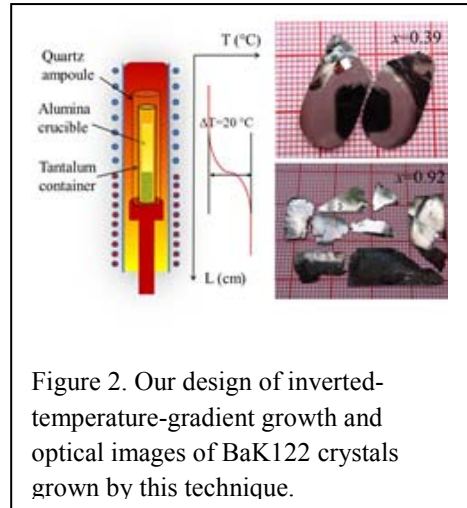


Figure 2. Our design of inverted-temperature-gradient growth and optical images of BaK122 crystals grown by this technique.

We have grown single crystals of bcc Fe-Ga-Zn for the first time, with up to 4.6 at. % Zn, using a 15 Bar Bridgman furnace to overcome the high vapor pressure of Zn and obtain homogeneous crystals [4]. The magnetostriction and elastic constants were measured and found to increase only slightly over those of the binary alloys, significantly short of the theoretically predicted value for a composition of $\text{Fe}_{87.5}\text{Ga}_{6.25}\text{Zn}_{6.25}$. Comparing the $-b_1$ values for Fe-Ga (see Figure 3), the Fe-Ga-Zn data are only 2% higher at the lowest e/a value and increase to 6% higher at the highest e/a value. Our work has definitively shown that while trends in magnetoelasticity can be predicted, the magnitude of enhancement is not accurately calculated and this discrepancy between theoretical and experimental findings is believed to stem from the inability to simulate the random distribution of Zn and Ga throughout the bcc iron lattice.

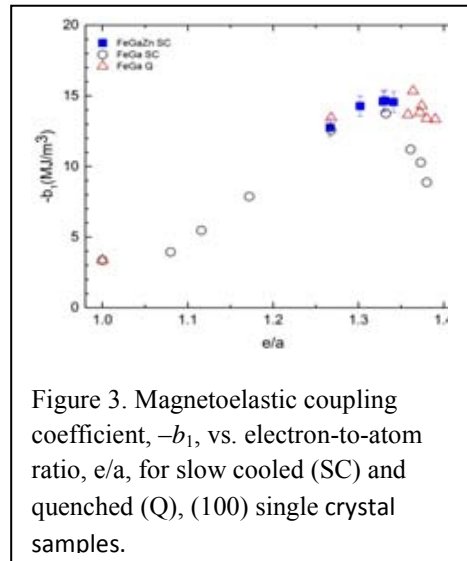


Figure 3. Magnetoelastic coupling coefficient, $-b_1$, vs. electron-to-atom ratio, e/a , for slow cooled (SC) and quenched (Q), (100) single crystal samples.

Future Plans

LnOFeAs and AeFFeAs systems have identical crystal structures. However, AeFFeAs compounds have two building blocks, i.e., AeF and FeAs layers, instead of the LnO layers in

LnOFeAs compounds. CaFeAsF_{1-x} crystals with maximum dimensions of approximately $2 \times 0.5 \times 0.0045 \text{ mm}^3$ were obtained from mixtures of Fe powder with CaAs and FeF_2 in the stoichiometric ratio [9]. However, superconductivity was not observed in the crystals. We propose that alternate flux materials could be Ca, Ba, CaAs, BaAs, BaF_2 , CaF_2 and FeF_2 .

We propose that some layered perovskite-related titanates, niobates and tantalates can act as potential substrates for thin film growth of iron pnictide and high T_c cuprate superconductors [10]. We will focus on $A_n B_n O_{3n+2}$, $A' A_{k-1} B_k O_{3k+1}$, and hexagonal $A_m B_{m-1} O_{3m}$, where A represents alkaline earth metals or rare earth metals, and B represents transition metals. Due to the very close structural relationship with cubic perovskite ABO_3 , single crystals of these materials may even replace SrTiO_3 , LaAlO_3 , and MgO , commonly used as substrates for growth of those novel materials. We will use optical floating zone furnace techniques to grow single crystals.

We will synthesize several series of GeTe- and PbTe-based materials where Ge or Pb, respectively, is replaced by Ag, Sb, Bi, Sn, and other elements, and conduct a comprehensive study using common methods, XRD (300-800 K), SEM and EDS (both at 300 K), the Seebeck coefficient, electrical resistivity, thermal conductivity (300-800 K), Hall effect (1.8-380 K) and ^{125}Te NMR (250-380 K). While common methods appear to be well established, understanding the physics of thermoelectric materials with these methods always requires state-of-the-art analysis. For example, SEM imaging might be perceived as “run-of-the-mill” work, but correct interpretation of SEM results demands careful signal differentiation by varying the incident beam energy and using the advanced capabilities of a high performance instrument. Furthermore, ^{125}Te NMR in complex tellurides still needs to be better understood. The emphasis is to continue to develop algorithms for use of NMR spectroscopy to obtain useful information from spin-lattice relaxation time, signal width, Knight and chemical shifts, and chemical shift anisotropy for complex tellurides and other materials.

References

1. Z. Wang, Y. Cai, Z. W. Wang, C. Ma, Z. Chen, H. X. Yang, H. F. Tian, and J. Q. Li, *Phys. Rev. B* **91**, 064513 (2015).
2. C.-H. Wang, T.-K. Chen, C.-C. Chang, C.-H. Hsu, Y.-C. Lee, M.-J. Wang, P. M. Wu, M.-K. Wu, arXiv:1502.01116.
3. Y. Liu, M. A. Tanatar, W. E. Straszheim, B. Jensen, K. W. Dennis, R. W. McCallum, V. G. Kogan, R. Prozorov, and T. A. Lograsso, *Phys. Rev. B* **89**, 134504 (2014).
4. T. A. Lograsso, N. J. Jones, D. L. Schlagel, Ga. Petculescu, M. Wun-Fogle, J. B. Restorff, A. E. Clark, and K. B. Hathaway, *J. Appl. Phys.*, **117**, 17E701 (2015).
5. E.M. Levin, B.A. Cook, J.L. Harringa, and S.L. Bud'ko, R. Venkatasubramanian, and K. Schmidt-Rohr, *Adv. Funct. Mater.* **21**, 441, (2011).
6. E.M. Levin, S.L. Bud'ko, and K. Schmidt-Rohr. *Adv. Funct. Mater.* **22**, 2766 (2012).
7. E.M. Levin, M.J. Kramer, and K. Schmidt-Rohr. *J. Phys. Chem. Solids* **75**, 1269 (2014).
8. E.M. Levin, M.F. Besser, and R. Hanus. *J. Appl. Phys.* **114**, 083713 (2013).

9. J. Tao, S. Li, X. Zhu, H. Yang, H. Wen, *Science China Physics, Mechanics and Astronomy* **57**, 632 (2014).
10. F. Lichtenberg, A. Herrnberger, and K. Wiedenmann, *Progress in Solid State Chemistry* **36**, 253 (2008).

Publications

1. T. A. Lograsso, N. J. Jones, D. L. Schlagel, G. Petculescu, M. Wun-Fogle, J. B. Restorff, A. E. Clark, and K. B. Hathaway, *Journal of Applied Physics*, **117**, 17e701 (2015).
2. R. L. Hadimani, Y. Melikhov, D. L. Schlagel, T. A. Lograsso, K. W. Dennis, R. W. McCallum, and D. C. Jiles, *Journal of Applied Physics*, **117**, 17d106 (2015).
3. N. J. Jones, G. Petculescu, M. Wun-Fogle, J. B. Restorff, A. E. Clark, K. B. Hathaway, D. Schlagel, and T. A. Lograsso, *Journal of Applied Physics*, **117**, 17a913 (2015).
4. J. S. Kim, G. R. Stewart, Y. Liu, and T. A. Lograsso, *Physical Review B*, **91**, 214506 (2015).
5. E. M. Levin, R. Hanus, J. Cui, Q. Xing, T. Riedemann, T. A. Lograsso, and K. Schmidt-Rohr, *Materials Chemistry and Physics*, **158**, 1-9 (2015).
6. S. Francoual, J. Strempler, J. Warren, Y. Liu, A. Skaugen, S. Poli, J. Blume, F. Wolff-Fabris, P. C. Canfield and T. Lograsso, *J. Synchrotron Rad.* **22**, 1207 (2015).
7. Yong Liu and Thomas A. Lograsso, *Phys. Rev. B* **90**, 224508 (2014).
8. Y. Liu, M. A. Tanatar, W. E. Straszheim, B. Jensen, K. W. Dennis, R. W. McCallum, V. G. Kogan, R. Prozorov, and T. A. Lograsso, *Physical Review B*, **89**, 134504 (2014).
9. H. Kim, M. A. Tanatar, Yong Liu, Zachary Cole Sims, Chenglin Zhang, Pengcheng Dai, T. A. Lograsso, and R. Prozorov, *Physical Review B*, **89**, 174519 (2014).
10. F.S. Elkin, I.P. Zibrov, A.P. Novikov, S.S. Khasanov, V.A. Sidorov, A.E. Petrova, T.A. Lograsso, J.D. Thompson, and S.M. Stishov, *Solid State Communications*, **181**, 41 (2014).
11. V. Fournée, E. Gaudry, J. Ledieu, M.C. de Weerd, D.M. Wu, and T. Lograsso, *ACS Nano*, **8**, 3646 (2014).
12. P. Lazpita, J.M. Barandiaran, V.A. Chernenko, B.V. Garcia, E.D. Tajada, T. Lograsso, and D.L. Schlagel, *Journal of Alloys and Compounds*, **594**, 171 (2014).
13. A. Provino, P. Manfrinetti, K. A. Gschneidner, Jr., S. K. Dhar, D. L. Schlagel, T. A. Lograsso, G. Miller, S. Thimmaiah, A. M. Russell, A. Becker, Ya. Mudryk, *Acta Materialia*, **73**, 27 (2014).
14. Q. Zhang, M. Ramazanoglu, S. Chi, Y. Liu, T. A. Lograsso, and D. Vaknin, *Physical Review B*, **89**, 224416 (2014).
15. V. Taufour, N. Foroozani, J. Lim, M. A. Tanatar, U. Kaluarachchi, S. K. Kim, Y. Liu, T. A. Lograsso, V. G. Kogan, R. Prozorov, S. L. Budko, J. S. Schilling, P. C. Canfield, *Physical Review B*, **89**, 220509 (2014).
16. Halyna Hodovanets, Yong Liu, Anton Jesche, Sheng Ran, Eun Deok Mun, Thomas A. Lograsso, Sergey L. Bud'ko, and Paul C. Canfield, *Phys. Rev. B* **89**, 224517 (2014).

Ordering in glass-forming liquids: A critical component in the dynamical pathway

K.M. Ho^c, C.Z. Wang^{a,c}, R. T. Ott^a, R. E. Napolitano^{a,b}, M. J. Kramer^{a,b}

^aMaterials Science and Engineering Division, Ames Labs DOE

^bDepartment of Materials Science and Engineering, Iowa State University

^cDepartment of Physics, Iowa State University

^dChemistry Department, Iowa State University

Program Scope

The unique feature surrounding transformation kinetics in glass-forming systems is the development of non-crystalline forms of short-range order (SRO) and medium-range order (MRO), and these can play a substantial role in the determining the transformation pathways. In this task area, we aim to understand the development of such order along with the fundamental connections to the thermodynamic forces and mechanisms that ultimately dictate the dynamical pathways involving crystallization and/or glass formation. Experiments (1, 2) and computer simulations (3, 4) have revealed SRO and MRO in glass-forming alloys, and we explore these effects in the selected model systems of Cu-Zr and Al-Sm. Fig. 1 shows a molecular dynamics prediction of the influence of cooling rate on the extent and character of regions of icosahedral order in a Cu_{64.5}-Zr_{35.5} alloy, as revealed by a cluster alignment analysis method (5-7). The principal objective is to build comprehensive self-consistent descriptions of the relevant forms of ordering, the critical connections to measurable thermo-kinetic properties, and the dependence on composition, temperature, and thermal history. Here, we summarize recent progress, challenges, and future directions.

Recent Progress

Recent advancements in this task area include both computational and experimental efforts to characterize short- and medium-range order (MRO) as a function of temperature and cooling rate. The challenge here is that cooling rates accessible by molecular dynamics are several orders of magnitude greater than those attainable in experiments (Fig. 1), and we are working to close this gap from both ends. Experimentally, we are employing container-less levitation processing, laser processing, and sputtering deposition access higher (but controllable) cooling rates experimentally. Computationally, we have extended the range of our molecular dynamics simulations to mimic cooling rates several orders of magnitude lower than previously possible, yielding structures that more closely resemble experimentally obtained systems. Using the cluster alignment analysis we reported previously(8), we have examined the cooling rate dependence of medium-range order in this regime for Cu_{64.5}Zr_{35.5}, and we have quantified the aggregate character of this order in comparison with experiment. For this same alloy, we have clearly correlated dynamic heterogeneity to the structural heterogeneity by examining atomic diffusion paths relative to regions of short- and medium-range order. In addition, we have made

experimental measurements of heat capacity for undercooled liquids of $\text{Cu}_{64.5}\text{Zr}_{35.5}$, $\text{Cu}_{50}\text{Zr}_{50}$, $\text{Al}_{90}\text{Sm}_{10}$, $\text{Al}_{90}\text{Tb}_{10}$, and $\text{Al}_{80}\text{Sm}_{20}$. These efforts are described briefly below.

An accurate description of atomic structures in undercooled liquids and glasses is vital to study the phase competition and selection using molecular dynamics (MD) simulations. Conventional MD simulations utilize ultrahigh cooling rates of 10^9 - 10^{13} K/s. As a result, the

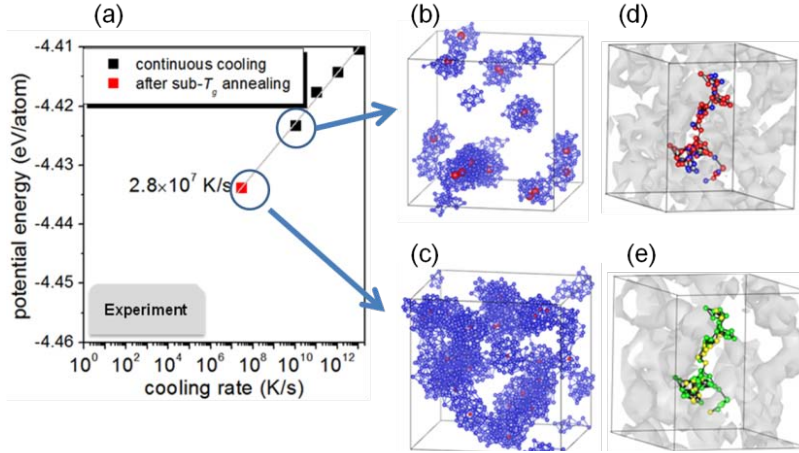


Figure 1 (a) The potential energy of the models as a function of cooling rate, by applying the $sub-T_g$ annealing the cooling rate can be effectively reduced to 2.8×10^7 K/s. The BMRO in the models prepared using the cooling rate of 1.0×10^{10} (b) and 2.8×10^7 K/s (c), respectively. Red and blue atoms are centers and coordinated atoms of BMRO, respectively. A typical diffusion trajectory during the $sub-T_g$ annealing approach is shown in (d) and (e), respectively. In (d), the gray isosurface is the ISRO network, the diffusing atom is shown in red when it is outside ISRO. In (e), the gray isosurface is the BMRO network, the diffusing atom is shown in green when it is outside BMRO.

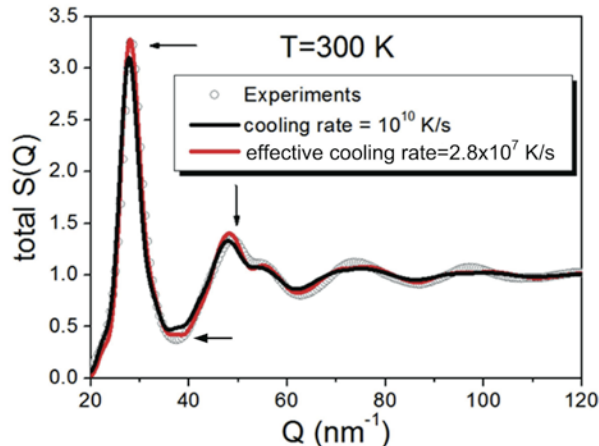


Fig. 2. Comparison of MD structures with experimental measurements (cooling rate $\sim 10^6$ K/s), showing advantage of $sub-T_g$ annealing.

obtained atomic structures can differ substantially from the real structures. We have carried out the $sub-T_g$ annealing approach to reduce the cooling rates, where the model was isothermally annealed close to the glass transition temperature for several microseconds in MD simulations. For $\text{Cu}_{64.5}\text{Zr}_{35.5}$ metallic glasses, a cooling rate of 2.8×10^7 K/s can be reached after $sub-T_g$ annealing at 700 K for $2.2 \mu\text{s}$, which is by far the lowest cooling rate achieved for this alloy using MD simulations. As a comparison it will take 30 times longer for

conventional MD simulations to reach the same cooling rate. The icosahedral short-range order (ISRO) and the Bergman-type medium-range order (BMRO) are significantly enhanced in the slowly cooled model. The enhanced ordering is found to have substantial impact on the dynamics most of the atomic jumps performed by the diffusing atoms are outside ISRO and BMRO. It indicates that the structural heterogeneity is closely related with dynamical heterogeneity. ISRO and BMRO form the solid-like backbone, whereas diffusion is confined to the liquid-like regions where such ordering is depleted in Cu-Zr metallic glasses.

Direct experimental measurements that correlate with the extent and nature of structural order in the system are critical to building a self-consistent comprehensive description of the thermo-kinetic landscape upon which to base prediction of transformation dynamics. One such connection lies in the structure factor, measurable by X-ray diffraction, as we have discussed (Fig. 2). Another quantity that can be used for direct comparison is the heat capacity, which reflects the structural state. However, this quantity is difficult to measure in undercooled liquids because of their unstable and transient nature. To address this issue, we have developed an integral heat (Q) method for differential scanning calorimetry (DSC) {Wang, 2014 #637}, where we use the time-dependent nature of the crystallization transition to yield various transition temperatures by varying the heating (or cooling) rate within a range that does not result in a change in the reaction products. By measuring the total integrated heat of transition, we have measured enthalpy with temperature, relative to the product crystalline phase for $\text{Cu}_{50}\text{Zr}_{50}$ and $\text{Cu}_{64.5}\text{Zr}_{35.5}$.

Future Plans

A key focus of our future work is to develop suitable order parameters that effectively describe *the evolution of SRO and MRO under different undercooling rates*. Such order parameters can be directly used in advanced sampling techniques to further accelerate the kinetics in MD simulations, such as template-assistant MD (TAMD) and metadynamics. In the TAMD approach, extra forces are applied on each atom to steer the system to align the local order with a selected template, which is expected to drive the system quickly toward the basin representing the template. In metadynamics, history-dependent bias potentials are added on the fly to the underlying free energy landscape of the system, helping the system jump out of the current metabasin and explore nearby basins. Preliminary results with TAMD show that the effective cooling rate can already be reduced to 6.5×10^6 K/s. Currently, we have successfully constructed the free energy surface of pure metals including Cu and Al, and some typical Lennard-Jones systems, using conventional Steinhardt Q4 and Q6 parameters, and order parameters derived from cluster-alignment studies. We intend to extend such studies to multicomponent systems.

In addition, the order parameters are expected to describe the structural transitioning from amorphous to crystalline phases during crystallization. Then, one can use such parameters to study nucleation in supercooled liquids with metadynamics. One can also express various thermodynamic and kinetic quantities that govern the phase transformation in terms of such order parameters. Thus, accurate description and parameterization of both the extent and character of ordering is the critical link between atomistic behavior, transformation mechanisms, and the analytical descriptions of the thermo-kinetic landscape that are critical to prediction and realization of phase selection in highly driven systems and meso-scale modeling of the associated structures. Meso-scale approaches, such as phase-field simulation will be applied to investigate phase morphologies and competitive crystallization structures, guided mainly by experimental observation but using parameters obtained largely from atomistic modeling.

We will continue to extend our experimental access to higher cooling rates using levitation, laser, and deposition processing, providing access to a broader transformation space and closing the gap with between experiments and molecular dynamics. In addition, we will use levitation (drop calorimetry) and DSC methods (9) to perform heat capacity measurements for Al-Sm and Cu-Zr alloys, over a range of compositions and temperatures.

References

1. A. Hirata *et al.*, Direct observation of local atomic order in a metallic glass. *Nat Mater* **10**, 28-33 (2011).
2. A. C. Y. Liu *et al.*, Systematic Mapping of Icosahedral Short-Range Order in a Melt-Spun Zr₃₆Cu₆₄ Metallic Glass. *Physical Review Letters* **110**, 205505 (2013).
3. Y. Q. Cheng, E. Ma, Atomic-level structure and structure-property relationship in metallic glasses. *Progress in Materials Science* **56**, 379-473 (2011).
4. D. B. Miracle, A structural model for metallic glasses. *Nature materials* **3**, 697-702 (2004).
5. F. Zhang *et al.*, Effects of sub-T_g annealing on Cu_{64.5}Zr_{35.5} glasses: A molecular dynamics study. *Appl Phys Lett* **104**, 061905-061905 (2014).
6. Y. Zhang *et al.*, Cooling rates dependence of medium-range order development in Cu_{64.5}Zr_{35.5} metallic glass. *Phys Rev B* **91**, (2015).
7. Y. Zhang *et al.*, Strong correlations of dynamical and structural heterogeneities with localized soft modes in a Cu-Zr metallic glass. *Applied Physics Letters* **105**, 151910 (2014).
8. X. W. Fang, C. Z. Wang, Y. X. Yao, Z. J. Ding, K. M. Ho, Atomistic cluster alignment method for local order mining in liquids and glasses. *Phys Rev B* **82**, 184204 (2010).
9. T. Wang, T. E. Cullinan, R. E. Napolitano, A new method for measuring the thermodynamic properties of undercooled liquid and amorphous Cu-Zr alloys. *Acta Mater* **62**, 188-196 (2014).

Publications

1. X. W. Fang, L. Huang, C. Z. Wang, K. M. Ho, and Z. J. Ding, "Structure of $\text{Cu}_{64.5}\text{Zr}_{35.5}$ Metallic Glass by Reverse Monte Carlo Simulations," *Journal of Applied Physics*, **115**, 053522 (2014). [10.1063/1.4865164](https://doi.org/10.1063/1.4865164)
2. M. J. Kramer, M. I. Mendeleev, and M. Asta, "Structure of Liquid Al and $\text{Al}_{67}\text{Mg}_{33}$ Alloy: Comparison between Experiment and Simulation," *Philosophical Magazine*, **94**, 1876-1892 (2014). [10.1080/14786435.2014.886786](https://doi.org/10.1080/14786435.2014.886786)
3. F. Zhang, M. I. Mendeleev, Y. Zhang, C. Z. Wang, M. J. Kramer, and K. M. Ho, "Effects of Sub- T_g Annealing on $\text{Cu}_{64.5}\text{Zr}_{35.5}$ Glasses: A Molecular Dynamics Study," *Applied Physics Letters*, **104**, 061905 (2014). [10.1063/1.4864652](https://doi.org/10.1063/1.4864652)
4. T. Wang, T. E. Cullinan, and R. E. Napolitano, "A New Method for Measuring the Thermodynamic Properties of Undercooled Liquid and Amorphous Cu-Zr Alloys," *Acta Materialia*, **62**, 188-196 (2014). [10.1016/j.actamat.2013.09.047](https://doi.org/10.1016/j.actamat.2013.09.047)
5. Y. Zhang, C. Z. Wang, F. Zhang, M. I. Mendeleev, M. J. Kramer, and K. M. Ho, "Strong Correlations of Dynamical and Structural Heterogeneities with Localized Soft Modes in a Cu-Zr Metallic Glass," *Applied Physics Letters*, **105**, 151910 (2014). [dx.doi.org/10.1063/1.4898779](https://doi.org/10.1063/1.4898779)
6. S. R. Wilson and M. I. Mendeleev, "Dependence of Solid-liquid Interface Free Energy on Liquid Structure," *Modelling and Simulation in Materials Science and Engineering*, **22**, 065004 (2014).
7. F. S. Ke, G. Q. Yue, B. Shen, F. Dong, S. Y. Wang, Y. X. Zheng, L. Y. Chen, C. Z. Wang, and K. M. Ho, "Bergman-type Medium-Range Order in Rapid Quenched $\text{Ag}_{0.74}\text{Ge}_{0.26}$ Eutectic Alloy Studied by *ab initio* Molecular Dynamics Simulation," *Acta Materialia*, **80**, 498-504 (2014). [10.1016/j.actamat.2014.06.049](https://doi.org/10.1016/j.actamat.2014.06.049)
8. Y. Zhang, M. I. Mendeleev, C. Z. Wang, R. Ott, F. Zhang, M. F. Besser, K. M. Ho, and M. J. Kramer, "Impact of Deformation on the Atomic Structures and Dynamics of a Cu-Zr Metallic Glass: A Molecular Dynamics Study," *Physical Review B*, **90**, 174101 (2014). [0.1103/PhysRevB.90.174101](https://doi.org/10.1103/PhysRevB.90.174101)
9. F. Zhang, M. Ji, X. W. Fang, Y. Sun, C. Z. Wang, M. I. Mendeleev, M. J. Kramer, R. E. Napolitano, and K. M. Ho, "Composition-dependent Stability of the Medium-range Order Responsible for Metallic Glass Formation," *Acta Materialia*, **81**, 337-344 (2014). [10.1016/j.actamat.2014.08.041](https://doi.org/10.1016/j.actamat.2014.08.041)
10. Y. Zhang, C.Z. Wang, M.I. Mendeleev, F. Zhang, M.J. Kramer, K. M. Ho, "Diffusion in a Cu-Zr metallic glass studied by microsecond-scale molecular dynamics simulations". *Phys Rev B* **91**, (2015).
11. Y. Zhang, F. Zhang, C.Z. Wang, M.I. Mendeleev, M.J. Kramer, K. M. Ho, "Cooling rates dependence of medium-range order development in $\text{Cu}_{64.5}\text{Zr}_{35.5}$ metallic glass". *Phys Rev B* **91**, (2015).

Mechanisms of crystallization in glass-forming liquids: interfaces, diffusion, and nucleation

M.I. Mendeleev^c, K.M. Ho^c, R. T. Ott^a, C.Z. Wang^{a,c}, R. E. Napolitano^{a,c}, M. J. Kramer^{a,b}

^aMaterials Science and Engineering Division, Ames Labs DOE

^bDepartment of Materials Science and Engineering, Iowa State University

^cDepartment of Physics, Iowa State University

^dChemistry Department, Iowa State University

Program Scope

This program area is aimed at understanding the principal structures and mechanisms that govern crystallization in glass-forming systems. The large departure from equilibrium (i.e. undercooling) attainable in a glass forming system gives rise to a competitive crystallization scenario involving multiple highly driven phases. In this case, kinetic mechanisms related to interface structures, local order, and atomic mobility may govern the phase selection. In this subtask, we focus on these mechanisms of crystallization and their influence on transition dynamics. Efforts include experimental and computational methods to measure specific properties such as interfacial free energy, interface mobility, and diffusivity, and to examine the mechanisms and multi-scale nucleation and growth phenomena associated with crystallization.

Recent Progress

Molecular dynamics (MD) simulation can considerably contribute toward an enhanced understanding of the relation between the SLI free energy and bulk material properties. First, significant progress has been achieved in the development of methods to determine γ from MD simulation (1-3). Second, it has been recognized that the interatomic potentials employed in classical MD simulation may be regarded as an additional “knob” that computational scientists may twist to sample a much larger set of materials than are observed in nature. In this study, starting from realistic semi-empirical potentials for Al and Na we developed sets of new potentials to explore the effect of liquid structure and latent heat on the SLI free energy. Next the SLI free energy was determined from MD simulation and the obtained data were compared with the Ewing relation (4) which takes the form, $\gamma = C'_T \rho_s^{2/3} T_m \Delta S_m + C_O \rho_s^{2/3} T_m S_O$, where ΔH_m is the latent heat of melting, ρ_s is the atomic density in the bulk solid phase and S_O is the liquid excess entropy. The first term is the well

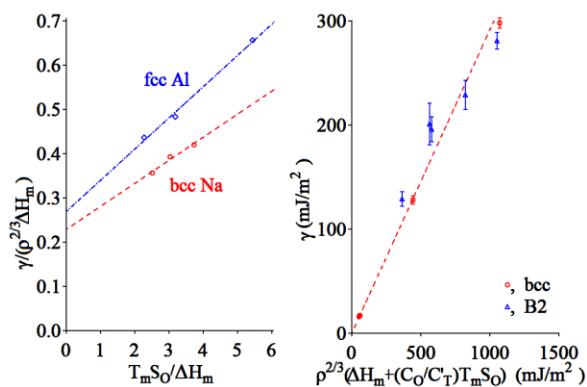
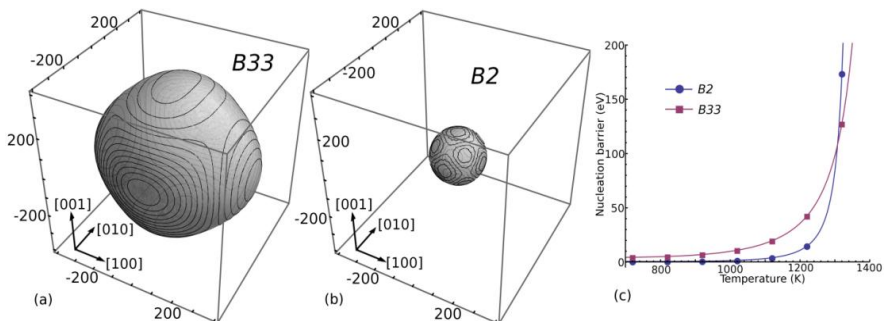


Figure 1. Comparison between the Ewing relation and the MD data.

known Turnbull relation. The second term is related to the liquid structure, and our results (Fig. 1) have shown that this term is important, indicating that liquid structure must be accounted for in the interfacial free energy. Figure 1 also shows that the Ewing relation obtained from the bcc dataset also provides a reasonable description of the B2 data and therefore, can be used to predict the SLI free energy based on just easily accessible bulk material properties.

High-energy X-ray diffraction (XRD) measurements of undercooled, electrostatically levitated $\text{Ni}_{50}\text{Zr}_{50}$ liquid droplets revealed that the solidification pathway proceeded through the nucleation and growth of the metastable B2 phase, which persisted for several seconds before the appearance of the stable B33 phase (5). To explain the obtained results we determined the solid-liquid interface (SLI) free energies and the bulk driving forces for solidification for both competing phases from molecular dynamics (MD) simulation (see Fig. 3). For all temperatures approximately 100 K below the B2 melting temperature, the B2 nucleation barrier is always less than that for B33. Hence, our MD simulations suggest that the undercooled liquid is significantly more stable with respect to B33 than B2 for undercoolings comparable to the experimentally observed values. We will continue developing this approach to predict the phase transformation pathways when a glass is prepared from liquid (including glass formation itself).

Figure 2. (a) and (b) show SLI free energies (in mJ/m^2) of the B33 and B2 phases as a function of the interface inclination \mathbf{n} in the crystal reference frame. (c), The nucleation barrier ΔG^* for these phases.



The structure and related phenomenology of solid-liquid interface (SLI) have been subjects of interest for decades (6-8). It is well known that the solid phase can induce layering in the liquid phase close to the interface along the direction perpendicular to the interface. However, ordering in the lateral direction and its effect on phase selection and growth kinetics is less understood. Using atomic mobility as a criterion to distinguish solid-like and liquid-like regions, we explore the phenomenology in the vicinity of a moving SLI. As an example, Fig. 3a shows a SLI between the $\text{Al}_{120}\text{Sm}_{22}$ “big cube” phase (BCP) at $t = t_0$. The atomic density along the perpendicular direction is given in Fig. 3b, where one clearly sees the induced layering on the liquid side for both SLIs. In our MD simulations, the BCP phase readily grows with a fairly fast growth rate of $\sim 0.15 \text{ \AA}/\text{ns}$. Such a high interface mobility is clearly reflected in the lateral plane ordering shown in Fig. 3c, the contour plot of the atomic density of the first layer on the liquid side (indicated by the arrow in Fig. 3b) at two instants - shortly before and after the interface moves to its current (t_0) position. At $t_0 - \Delta t$, some crystalline order that matches the BCP phase already emerges. At $t_0 + \Delta t$, although the interface has barely moved, the ordering in the liquid layer is strongly enhanced. Such rapid enhancement of crystalline order greatly facilitates continuous growth of the BCP phase.

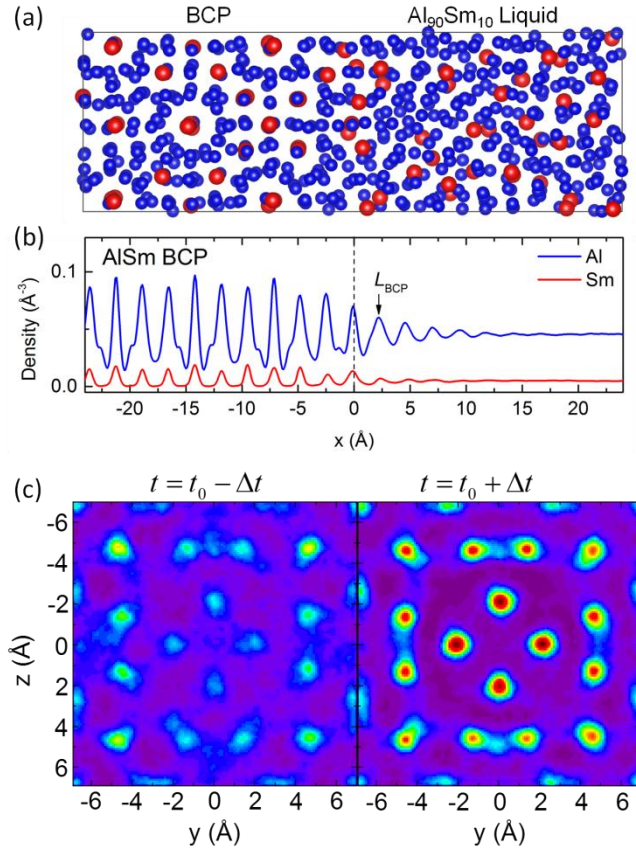


Figure 3 (a) A snapshot of the BCP/liquid interface at $t = t_0$. (b) The density profile along the perpendicular direction for Al and Sm atoms. The dashed line indicates the interface position determined based on atomic mobility. The arrow indicated the first layer in the liquid phase. (c) The contour plot of the atomic density at $t_0 - \Delta t$ and $t_0 + \Delta t$ ($\Delta t = 1.2$ ns).

thermodynamic database (11) to predict specific diffusivities and compares well with reported experimental data for 0.6 at.% and 5.6 at.% Sm in Al-Sm alloys (10, 12).

Future Plans

Future work will include using a suite of synthesis and processing techniques to systematically investigate phase selection response and to help direct our computational and analytical modeling efforts. Our goal is to extend our experimental observations of crystallization kinetics across all temperatures from the melting temperature (or liquidus) to below the glass transition temperature for the Al-Sm system. Methods will include levitation melting with free cooling, isothermal holding, splat cooling, and triggered growth; laser-trace melting/freezing; and magnetron sputter deposition.

MD simulations will be used to determine SLI free energies for stoichiometric compounds that compete to nucleate in the Al-Sm and Ni-Cu-Zr systems, investigate how the SLI free energy depends on temperature and interface curvature under conditions when

Controlling transformation pathways in glass-forming liquids requires a comprehensive description of diffusivity, including the composition and temperature dependence of the associated kinetic arrest. In the computational study reported here (9), we examine atomic diffusion in Al-Sm liquids using ab initio molecular dynamics (AIMD) and determine the diffusivities of Al and Sm for selected alloy compositions. Through assessment of our AIMD result, we construct a general formulation for Al-Sm liquid, involving a diffusion mobility database that includes composition and temperature dependence. A Volmer-Fulcher-Tammann (VFT) equation is adopted for describing the non-Arrhenius behavior observed in the undercooled liquid, associated with enhanced local ordering. The composition dependence of diffusivity is found to be quite strong, even for the Al-rich region, contrary to the sole previous report (10) on this binary system. The model is used in combination with the available

nucleation in fact occurs, investigate the role of point defects in nucleation and interface properties, study the relationship between physical properties and nucleation rates.

We will perform capillary tube liquid diffusion couple experiments to measure diffusivity in Al-Sm and Cu-Zr liquids. We will employ container-less processing techniques (electrostatic and electromagnetic levitation) to attain high degrees of liquid state undercooling for Al-Sm, Al-Tb, and Ni-Zr alloys. Controlled cooling of bulk droplets and triggered nucleation will be implemented to probe select domains of temperature and composition.

We also plan to extend the study of the interfacial ordering to other SLIs involved in the rich phase transformations of the Al-Sm system. This information, together with thermodynamic and kinetic analysis, will be used to evaluate the dominant factors that govern the phase selection in this prototypical system. In addition, our preliminary results of classical MD simulations indicate that an FCC Al seed can trigger the nucleation of a hexagonal phase. This provides an opportunity to study the mechanisms for heterogeneous nucleation.

References

1. M. Asta *et al.*, Solidification microstructures and solid-state parallels: Recent developments, future directions. *Acta Mater* **57**, 941-971 (2009).
2. J. J. Hoyt, M. Asta, A. Karma, Atomistic and continuum modeling of dendritic solidification. *Materials Science & Engineering R-Reports* **41**, 121-163 (2003).
3. B. B. Laird, R. L. Davidchack, Direct calculation of the crystal-melt interfacial free energy via molecular dynamics computer simulation. *Journal of Physical Chemistry B* **109**, 17802-17812 (2005).
4. R. H. Ewing, Free energy of crystal-melt interface from radial distribution function. *Journal of Crystal Growth* **11**, 221-& (1971).
5. D. G. Quirinale *et al.*, Appearance of metastable B2 phase during solidification of Ni50Zr50 alloy: electrostatic levitation and molecular dynamics simulation studies. *Journal of physics. Cond. matter : an Inst. of Phys. journal* **27**, 085004-085004 (2015).
6. W. D. Kaplan, Y. Kauffmann, Structural Order in Liquids Induced by Interfaces with Crystals. *Annual Review of Materials Research* **36**, 1-48 (2006).
7. A. L. Greer, Liquid metals: Supercool order. *Nature materials* **5**, 13-14 (2006).
8. M. Guerdane, H. Teichler, B. Nestler, Local Atomic Order in the Melt and Solid-Liquid Interface Effect on the Growth Kinetics in a Metallic Alloy Model. *Phys. Rev. Lett.* **110**, (2013).
9. T. Wang *et al.*, A computational study of diffusion in a glass-forming metallic liquid. *Sci Rep-Uk* **5**, (2015).
10. N. Wang, Y. E. Kalay, R. Trivedi, Eutectic-to-metallic glass transition in the Al-Sm system. *Acta Mater* **59**, 6604-6619 (2011).
11. S. H. Zhou, R. E. Napolitano, Modeling of thermodynamic properties and phase equilibria for the Al-Sm binary system. *Metall Mater Trans A* **39A**, 502-512 (2008).
12. N. Wang, R. Trivedi, Temperature-dependent Diffusion Coefficient in the fragile glass forming system of Al-Sm. *Unpublished work*, (2014).

Publications

1. S.R. Wilson, K.G.S.H. Gunawardana and M.I. Mendeleev, *Solid-liquid interface free energies of pure bcc metals and B2 phases*, J. Chem. Phys. **142**, 134705 (2015).
2. D.G. Quirinale, G.E. Rustan, S.R. Wilson, M.J. Kramer, A.I. Goldman and M.I. Mendeleev, *Appearance of metastable B2 phase during solidification of Ni₅₀Zr₅₀ alloy: electrostatic levitation and molecular dynamics simulation studies*, J. Phys.: Condens. Matter **27**, 085004 (2015).
3. S. R. Wilson and M. I. Mendeleev, "Dependence of Solid-liquid Interface Free Energy on Liquid Structure," *Modelling and Simulation in Materials Science and Engineering*, **22**, 065004 (2014).
4. S. R. Wilson and M. I. Mendeleev, "Anisotropy of the Solid-liquid Interface Properties of the Ni-Zr B33 Phase from Molecular Dynamics Simulation," *Philosophical Magazine*, **95**, 224-241 (2015). 10.1080/14786435.2014.995742
5. T. Cullinan, I. Kalay, Y. E. Kalay, M. Kramer, and R. Napolitano, "Kinetics and Mechanisms of Isothermal Devitrification in Amorphous Cu₅₀Zr₅₀," *Metallurgical and Materials Transactions A*, **46**, 600-613 (2015). 10.1007/s11661-014-2661-y
6. K. G. S. H. Gunawardana, S. R. Wilson, M. I. Mendeleev, and X. Song, "Theoretical Calculation of the Melting Curve of Cu-Zr Alloys," *Physical Review E*, **90**, 052403(2014). 10.1103/PhysRevE.90.052403
7. T. Wang, F. Zhang, L. Yang, X.W. Fang, S.H. Zhou, M.J. Kramer, C.Z. Wang, K.M. Ho, R.E. Napolitano, "A computational study of diffusion in a glass-forming metallic liquid". *Sci Rep-Uk* **5**, (2015).
8. Y. Zhang, C.Z. Wang, M.I. Mendeleev, F. Zhang, M.J. Kramer, K. M. Ho, "Diffusion in a Cu-Zr metallic glass studied by microsecond-scale molecular dynamics simulations". *Phys Rev B* **91**, (2015).

Metastable phase competition in highly undercooled metallic liquids and glasses

M. J. Kramer^{a,b}, R. E. Napolitano^{a,b}, M.I. Mendeleev^a, K.M. Ho^c,
R. T. Ott^a, X.Y. Song^{a,d}, C.Z. Wang^{a,c}

^aMaterials Science and Engineering Division, Ames Labs DOE

^bDepartment of Materials Science and Engineering, Iowa State University

^cDepartment of Physics, Iowa State University

^dChemistry Department, Iowa State University

Program Scope

Increasing technological demand for materials with new or enhanced functionality calls for expanding the set of accessible structures and chemistries. The methods of materials genomics enable the efficient identification of stable materials that may possess desirable properties, but metastable, multiphase, and defect-enabled states are excluded from such searches, and predictions of stability or even metastability do not themselves provide a path to realization. Glass-forming metals offer a rich landscape of non-equilibrium states, both crystalline and non-crystalline, and far-from-equilibrium avenues to access them. This point is illustrated in Fig. 1, showing the extraordinary wealth of intermediate metastable structures that may appear during devitrification of an $\text{Al}_{90}\text{Sm}_{10}$ alloy. To understand phase selection dynamics in this motivating example and other similar scenarios, this task area aims to identify critical energetic and mechanistic links between thermodynamic quantities, interfacial structures, and the kinetics of transformation events that control phase competition in highly driven systems.

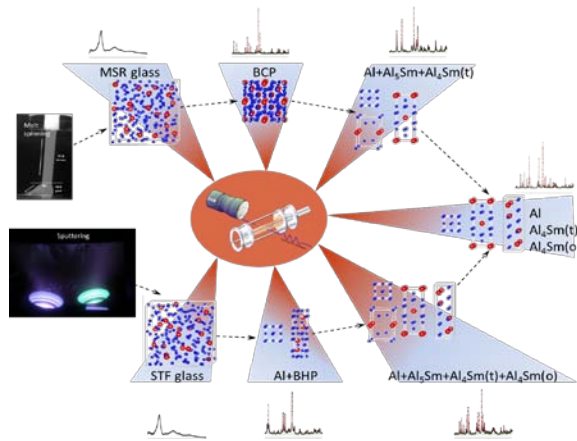


Fig.1. A schematic illustration of two distinct crystallization scenarios in Al-Sm, realized by heating an amorphous melt spun ribbon (MSR) and sputtered thin film (STF), yielding $\text{Al}_{120}\text{Sm}_{22}$ and $\text{Al}_{20}\text{Sm}_4$ complex phases, respectively.

To meet this challenge, we combine synthesis techniques, X-ray diffraction (XRD), thermal analysis, electron microscopy, ab initio calculations, molecular dynamics (MD) simulations, and adaptive genetic algorithms (ADA) in an integrated scheme for materials discovery.

Recent Progress

For the Al-Sm system, the amorphous phases realized in melt spun ribbons (MSR) and magnetron sputtered thin films (STF) exhibit very similar structural order, as measured by their pair distribution functions (PDFs), yet these two structures devitrify following vastly different pathways (Fig. 1). When quenched from the liquid, the glass exhibits a polymorphic

transformation that results in the “big cubic phase” (BCP) a cubic $\text{Al}_{120}\text{Sm}_{22}$ phase with a lattice parameter of 13.904 \AA , space group $I m \bar{3} m$ (No. 229) exhibiting 6 unique Wyckoff positions (1). The glass formed by sputtering develops pronounced compositional inhomogeneities before the formation of fcc Al and a “big hexagonal phase” (BHP), a hexagonal $\text{Al}_{20}\text{Sm}_4$ phase with space group No.182 ($P6_322$) and with 5 Wyckoff positions (2). In both cases, the initial devitrifying transition consumes the entire sample, after which the resulting crystalline phases are observed to further transform, following strikingly different pathways. Both pathways

eventually converge toward the same phase composition (although the end states exhibit significantly different microstructures).

The first challenge in understanding the dynamics exhibited in this benchmark experiment is to solve for the complex unknown structures realized through these far-from-equilibrium processes. The approach we have developed (1, 2) effectively integrates: (i) lattice and space group information from high-resolution XRD; (ii) AGA analysis for structure determination (3); (iii) cluster alignment analysis (4) to reveal the underlying order; (iv) MD simulations for crystal growth; and (iv) Rietveld analysis to capture the defect distribution. Once the phases are identified and well described, we look for keys in the local structural that may be linked to the phase selection behavior. For example, we use our previously developed cluster alignment analysis to reveal the dominant local cluster motifs in the glass and identify particular motifs present in both the non-crystalline precursor and the metastable crystalline phases that initially form. We also use MD simulations to investigate the plausibility of the implied crystal growth scenario and compare the MD growth product with the experimental diffraction data, where site occupancies and defect structures are relevant or even critical.

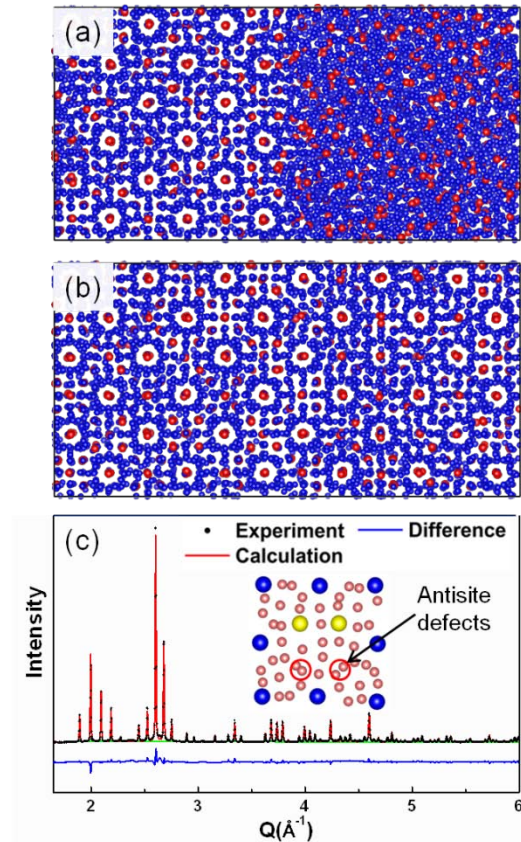


Figure 2 (a). A cubic $\text{Al}_{160}\text{Sm}_{11}$ seed is put in contact with undercooled $\text{Al}_{90}\text{Sm}_{10}$ liquid at $T = 800 \text{ K}$. (b). The liquid phase is fully grown into a defected cubic phase with the same composition in $\sim 260 \text{ ns}$. (c) The XRD pattern of the as-grown phase shows excellent agreement with that of the experiments. Red circles in the inset of (c) show the antisite defects revealed in the MD simulations.

Devitrification of glassy alloys is an ideal system with which to model systems far-from-equilibrium. These systems can form complicated metastable structures often precipitate instead of simpler, more stable compounds which, as in this example are dependent on the material’s synthesis. Navigating the phase selection process requires understating of the initial state of the disordered alloy and kinetically accessible states through the energy landscape. This in turn

requires knowledge of the structure of the unknown compounds which do form. This also requires the ability to predict other metastable phases which may compete. This is where the AGA is a critical tool since it provides a means of not only solving the structures of the unknown but observed compounds, but aids in determining the energy of competing structures. However, feedback with experimental data is crucial since the DFT can not easily address vacancies or antisite defects associated with partial occupancy of Wyckoff positions. Figure 2 illustrates how we determine the big cube phase that precipitates during the initial crystallization of melt-spun $\text{Al}_{90}\text{Sm}_{10}$ alloys. In Figure 2a, a parent big cube phase with the composition $\text{Al}_{60}\text{Sm}_{11}$ identified in AGA search is put in contact with undercooled $\text{Al}_{90}\text{Sm}_{10}$ liquid at $T = 800$ K. Figure 2b shows that the liquid is fully crystallized in about 260 ns. Containing multiple vacancies and antisite defects, the as-grown structure has a composition that matches the initial liquid phase. With no need for fitting occupancies or atomic positions, the XRD pattern of the as-grown structure shows excellent agreement with experiment (Figure 2c), indicating that the grown structure correctly captures the nature of the defects of the big cube phase. The same procedure is also applied to solve a big hex structure during the devitrification of $\text{Al}_{90}\text{Sm}_{10}$ alloys prepared by magnetron sputtering.(2)

Future Plans

We will continue to implement the AGA to solve unknown crystalline phases observed in our *in situ* diffraction experiments. In addition to predicting unknown crystal structures, AGA plays an important role in developing classical potentials. Due to significant spatial and temporal constraints of *ab initio* calculations, utilizing semi-empirical potentials still is necessary to fully describe the thermodynamic and kinetic properties of undercooled liquids and glasses. Based on our previous experience with Cu-Zr and Al-Sm systems, it is usually not sufficient to include only experimentally observed compounds in the potential development procedure. The AGA method readily identifies a series of metastable phases with relatively low formation energy. Although many of these phases are not observed experimentally, they provide useful information regarding packing motifs and bonding characters of the system. Inclusion of these extra phases has dramatically improved the reliability of potentials. Once all phases are described, the phase selection in the supercooled liquid can be studied by a combination of interrupted DSC, TEM, XRD and *in situ* SAXS and WAXS. The *in situ* SAXS/WAXS experiments are particularly powerful for studying phase selection because SAXS probes the nano-scale topological/chemical rearrangements that precede devitrification while WAXS provides a direct measure of the crystal structures of nucleating phases.

We will consider the dynamics of both crystalline and non-crystalline phases that compete at high undercooling and give rise to complex transformation sequences involving multiple transient structures. First, we will compute the thermodynamic stability of specific crystalline phases using *ab initio* calculations and by using (quantum mechanics) corrected MD potentials in a statistical perturbation theory. These calculations provide important baseline information about ground state energies upon which to build a more complete thermodynamic

description that accounts for entropy/temperature effects and additional thermodynamic features that complicate phase formation under realistic conditions. Second, we will utilize MD simulations to assess the role of solutes and packing effects at nonzero temperatures, providing the means to observe (through simulation) many realistic features of transformations. Third, we will employ a CALPHAD-style solution-based thermodynamic approach (5-7) for comprehensive thermodynamic modeling of the relevant multi-component multiphase systems and scenarios that govern transformations over broad composition and temperature ranges. Building on our prior treatment of driving forces for non-equilibrium solidification, these thermodynamic models will be used, along with diffusivity and interfacial properties (from experiments and MD simulations), to construct a self-consistent thermo-kinetic landscape that will enable analytical prediction and realization of phases and structures.

References

1. Z. Ye *et al.*, Unconventional phase selection in high-driven systems: A complex metastable structure prevails over simple stable phases. *arXiv preprint arXiv:1502.00023*, (2015).
2. Z. Ye *et al.*, Discovery of a metastable Al₂₀Sm₄ phase. *Appl Phys Lett* **106**, 1903-1903 (2015).
3. S. Q. Wu *et al.*, An adaptive genetic algorithm for crystal structure prediction. *Journal of Physics: Condensed Matter* **26**, 35402-35402 (2014).
4. X. W. Fang, C. Z. Wang, Y. X. Yao, Z. J. Ding, K. M. Ho, Atomistic cluster alignment method for local order mining in liquids and glasses. *Phys Rev B* **82**, 184204 (2010).
5. S. H. Zhou, Y. Wang, L. Q. Chen, Z. K. Liu, R. E. Napolitano, Solution-based thermodynamic modeling of the Ni-Al-Mo system using first-principles calculations. *Calphad* **46**, 124-133 (2014).
6. S. H. Zhou, R. E. Napolitano, Phase stability for the Cu-Zr system: First-principles, experiments and solution-based modeling. *Acta Mater* **58**, 2186-2196 (2010).
7. S. H. Zhou, Y. Wang, L. Q. Chen, Z. K. Liu, R. E. Napolitano, Solution-based thermodynamic modeling of the Ni-Ta and Ni-Mo-Ta systems using first-principle calculations. *Calphad* **33**, 631-641 (2009).

Publications

1. X. W. Fang, L. Huang, C. Z. Wang, K. M. Ho, and Z. J. Ding, "Structure of $\text{Cu}_{64.5}\text{Zr}_{35.5}$ Metallic Glass by Reverse Monte Carlo Simulations," *Journal of Applied Physics*, **115**, 053522 (2014). 10.1063/1.4865164
2. F. Zhang, I. McBrearty, R. T. Ott, E. Park, M. I. Mendeleev, M. J. Kramer, C. Z. Wang, and K. M. Ho, "Discovery of a Meta-Stable Al-Sm Phase with Unknown Stoichiometry Using a Genetic Algorithm," *Scripta Materialia*, **81**, 32-35 (2014). 10.1016/j.scriptamat.2014.02.019
3. F. Zhang, M. I. Mendeleev, Y. Zhang, C. Z. Wang, M. J. Kramer, and K. M. Ho, "Effects of Sub- T_g Annealing on $\text{Cu}_{64.5}\text{Zr}_{35.5}$ Glasses: A Molecular Dynamics Study," *Applied Physics Letters*, **104**, 061905 (2014). 10.1063/1.4864652
4. Y. Zhang, C. Z. Wang, F. Zhang, M. I. Mendeleev, M. J. Kramer, and K. M. Ho, "Strong Correlations of Dynamical and Structural Heterogeneities with Localized Soft Modes in a Cu-Zr Metallic Glass," *Applied Physics Letters*, **105**, 151910 (2014). dx.doi.org/10.1063/1.4898779
5. F. Zhang, M. Ji, X. W. Fang, Y. Sun, C. Z. Wang, M. I. Mendeleev, M. J. Kramer, R. E. Napolitano, and K. M. Ho, "Composition-dependent Stability of the Medium-range Order Responsible for Metallic Glass Formation," *Acta Materialia*, **81**, 337-344 (2014). 10.1016/j.actamat.2014.08.041
6. T. Cullinan, I. Kalay, Y. E. Kalay, M. Kramer, and R. Napolitano, "Kinetics and Mechanisms of Isothermal Devitrification in Amorphous $\text{Cu}_{50}\text{Zr}_{50}$," *Metallurgical and Materials Transactions A*, **46**, 600-613 (2015). 10.1007/s11661-014-2661-y
7. K. G. S. H. Gunawardana, S. R. Wilson, M. I. Mendeleev, and X. Song, "Theoretical Calculation of the Melting Curve of Cu-Zr Alloys," *Physical Review E*, **90**, 052403(2014). 10.1103/PhysRevE.90.052403
8. K. G. S. H. Gunawardana and X. Song, "Free Energy Calculations of Crystalline Hard Sphere Complexes Using Density Functional Theory," *Journal of Physical Chemistry B* (2014). 10.1021/jp5090907
9. T. Wang, F. Zhang, L. Yang, X.W. Fang, S.H. Zhou, M.J. Kramer, C.Z. Wang, K.M. Ho, R.E. Napolitano, "A computational study of diffusion in a glass-forming metallic liquid". *Sci Rep-Uk* **5**, (2015).
10. Z. Ye, F. Zhang, Y. Sun, M.I. Mendeleev, R.T. Ott, E. Park, M.F. Besser, M.J. Kramer, Z. Ding, C.Z. Wang, K.M. Ho "Discovery of a metastable $\text{Al}_{20}\text{Sm}_4$ phase." *Applied Physics Letters* **106**(10), (2015).
11. Y. Zhang, C.Z. Wang, M.I. Mendeleev, F. Zhang, M.J. Kramer, K. M. Ho, "Diffusion in a Cu-Zr metallic glass studied by microsecond-scale molecular dynamics simulations". *Phys Rev B* **91**, (2015).
12. Y. Zhang, F. Zhang, C.Z. Wang, M.I. Mendeleev, M.J. Kramer, K. M. Ho, "Cooling rates dependence of medium-range order development in $\text{Cu}_{64.5}\text{Zr}_{35.5}$ metallic glass". *Phys Rev B* **91**, (2015).

Exploratory Materials Synthesis and Characterization

Cedomir Petrovic and Hyejin Ryu (Stony Brook student up to September 2014)

Condensed Matter Physics and Materials Science, Brookhaven National Laboratory

Program Scope

We concentrate on exploratory synthesis and characterization of the new model materials of current interest in condensed matter physics. In addition, we often focus on advanced synthesis of known materials in order to enable important physical and structural investigations. We put strong effort in the discovery of new phenomena associated with correlated behavior of electrons in energy related materials. Most often materials are synthesized in the single crystal form since many observables of interest are tensor quantities and since this allows for the investigation of physical properties that are free of grain boundary influences. We use range of techniques suitable for exploratory materials synthesis and crystal growth: conventional arc melting and powder metallurgical techniques, solution methods, high temperature intermetallic, oxide, sulfide or salt fluxes, chemical vapor transport and deposition. Automated physical and structural characterization is the essential component of the lab. In order to optimize synthesis parameters, it is necessary to characterize structural and physical properties of materials. Quite often the same methods are used to investigate crystal structure, transport, thermodynamic and magnetic properties, sometimes at the extreme conditions. We perform high magnetic fields and low temperature measurements at NHMFL Tallahassee and HZDR Dresden. We also use EXAFS beamlines at NSLS and we are constantly engaged in the buildup of our synthesis and characterization capabilities. We currently pursue several research directions: Dirac and topological materials, quantum criticality and metal – insulator transitions. Our work enhances materials space available to BNL and other research groups. This program includes training of the next generation of scientists. Students from neighboring universities (Brown, Columbia, Johns Hopkins, Stony Brook) were being educated in materials physics, arts and crafts of crystal growth, materials synthesis and characterization.

Recent Progress

Advances in synthesis/crystal growth. High temperature metallic solutions are the method of choice for synthesis of many important correlated electron systems such as heavy fermions or iron based superconductors. Volatile and/or hazardous ingredients require the use of fume hoods. In order to be able to synthesize such materials in large size for neutron scattering, we have custom designed and installed two box furnaces with tall chambers that can accept large crucibles. Together with a centrifuge used for filtration, such system enables risk-free synthesis of large sample volumes. Furthermore, we have custom designed and installed a multi-zone



Fig. 1: Rotating gradient furnace in vertical position.

gradient furnace (Fig. 1) that has ability to rotate. In the horizontal position it will be used for vapor transport crystal growth in large volumes whereas in the vertical position it will be used to suppress evaporation in synthesis of samples with volatile ingredients such as chalcogenides.

Exploratory synthesis and characterization of novel materials. Highlights in FY13-15:

a) Large transverse magnetoresistance ($1.33 \cdot 10^5$ % in 2 K and 9 T field, and $4.33 \cdot 10^6$ % in 0.4 K and 32 T field, without saturation) and field-induced metal-semiconductor transition in NbSb₂ single crystal (Pub 1; Fig. 2). The sign reversal of the Hall resistivity and Seebeck coefficient in the field, plus the electronic structure reveal the coexistence of a small number of holes with high mobility and a large number of electrons with low mobility in distinct volumes of the electron and hole pockets. The large effect is attributed to the change of the Fermi surface in magnetic field in addition to large magnetoresistance expected for high mobility metals.

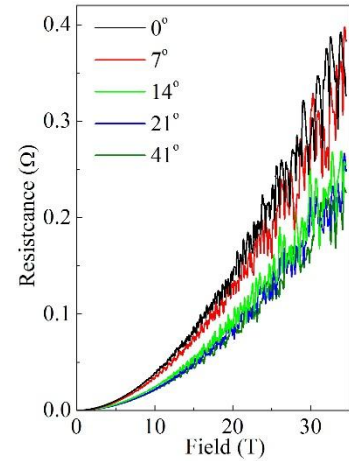


Fig. 2: Typical SdH oscillation of NbSb₂ in 0.42 K with magnetic field up to 32 Tesla at NHMFL.

b) Large thermoelectric power *S* due to electronic correlations in RuSe₂ (Pub. 2 – the first scientific publication of NSLS2). RuSe₂ is a semiconductor that crystallizes in a cubic pyrite unit cell similar to FeSb₂, material with highest known thermoelectric power factor. Pyrites and marcasites (e.g. FeSb₂) both feature distorted octahedral coordination of Ru/Fe in the local structure. The Seebeck coefficient of RuSe₂ exceeds -200 μ V/K around 730 K (Fig. 3). Ir substitution results in the suppression of the resistivity and the Seebeck coefficient, suggesting the removal of the peaks in density of states near the

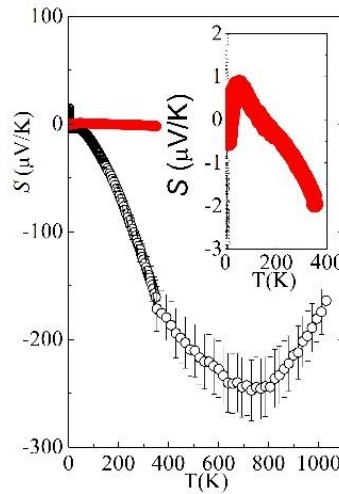


Fig. 3: *S* of (Ru_{1-x}Ir_x)Se₂; *x* = 0 (black) and 0.1 (red).

Fermi level and the importance of the electronic correlations in enhanced thermoelectricity. However, corner-sharing octahedra impede electric conductivity in RuSe₂ (Fig. 4).

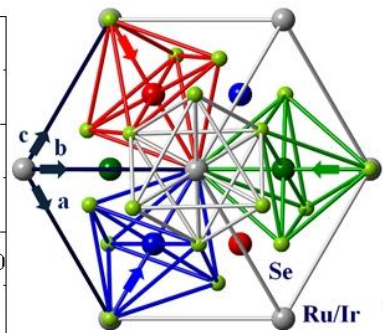


Fig. 4: Pyrite-type crystal structure along (111). The RuSe₆ octahedra share corners in the pyrite unit cell as opposed to orthorhombic marcasite edge-sharing FeSb₆ octahedra. This inhibits the overlap of *d_{xy}* bands and quasi 1D conductivity.

Advanced materials synthesis and crystal growth. We have enabled several important

STM, neutron and low temperature transport studies in the past two years. These include:

a) Direct verification that heavy fermion superconductivity stems from magnetically mediated Cooper pairing (Pub. 3). STM measurements on high quality single crystals of CeCoIn₅ elucidated the heavy-fermion band structure using quasiparticle interference imaging and

revealed quantitatively the momentum space structure of the f -electron magnetic interactions. Then, by solving the superconducting gap equations on the two heavy-fermion bands with these magnetic interactions as mediators of the Cooper pairing, a series of quantitative predictions were derived that are in agreement with the measured characteristics of CeCoIn₅.

b) In the cleanest samples of Ce_{1-x}R_xCoIn₅ (R = rare earth) the London penetration depth was consistent with the existence of line nodes in the superconducting gap. Substitutions of Ce with La, Nd, and Yb lead to similar monotonic suppressions of T_c. While La and Nd substitution leads to a dirty nodal superconductor response, Yb substitution suggests a change from nodal to nodeless superconductivity. This happens in the same doping range where changes of the Fermi-surface topology were reported, implying that the nodal structure and Fermi-surface topology are closely linked (Pub. 4).

c) Synthesis of large crystals of heavy fermion superconductor CeRhIn₅ enabled inelastic neutron scattering studies (Pub. 5). Preliminary results showed the breakdown of the single-quasiparticle description of the spin excitations in a helical itinerant heavy fermion magnet.

Future Plans

In the next period we will pursue several crosscutting directions. These include:

Dirac materials. In contrast to graphene and topological insulators, Dirac fermions in bulk Dirac materials¹ coexist with metallic states derived from other electronic bands at the Fermi level. Hence, due to electronic complexity, bulk crystals can be used to observe Dirac fermions in the environment of for example correlated quasiparticles, magnetic or superconducting orders. There are number of energy relevant materials where Dirac states have been observed, e.g. BaFe₂As₂ with spin density wave (parent compound of Fe-based high-T_c superconductors) or high performance thermoelectrics.²⁻³ In particular Weyl semimetals⁴ have recently raised considerable interest due to the monopole defects (sources and sinks) of Berry curvature – Weyl points in Brillouin zone. Since new bulk materials are necessary for large-scale power generation⁵ we will focus on exploratory synthesis of new bulk Dirac and Weyl materials in order to examine exotic quasiparticles, magnetic states, correlations and in particular thermoelectric⁶ properties. Furthermore, single layers of most such materials are likely to be produced by exfoliation (similar to graphene) due to 2D anisotropy and the interlayer binding energy which is similar to graphite.⁷

Quantum criticality. Complexity of copper oxide materials implies that progress might be made by comparison with other exotic superconductors where competing interactions and phenomena - including recently observed charge fluctuations - can be observed at simpler or tunable settings. Examples include magnetic heavy fermion metals or charge density wave superconductors near putative charge quantum critical point (QCP). High quality single crystals of heavy fermion metals synthesized in our group enabled the Bogoliubov quasiparticle interference imaging of heavy fermion band structure and insight into dynamic susceptibility by inelastic neutron scattering (e.g. Pubs. 3,5) . Having exposed magnetic mechanism of heavy

fermion Cooper pairing, we will extend studies to heavy fermion systems with magnetic order. Similarly, some low dimensional chalcogenide materials or organic superconductors host features similar to putative charge QCP.⁸⁻⁹ We will search for new materials in this class and explore disorder effects.

Heavy fermion-like states and metal-insulator transitions in d- electron metals. We will explore materials with quasiparticle mass enhancement in narrow bands, similar to classical *4f*-based compounds. Crystal structure types and materials include mixed anion oxychalcogenides; if the anions are from the different row of the Mendeleev chart, different size and ionic polarization may lead to layered structure due to ordered occupancy of different crystallographic sites.¹⁰

References

1. T.O. Wehling, A.M. Black-Schaffer and A.V. Balatsky, “Dirac Materials”, *Advances in Physics* 63, 1 (2014).
2. P. Richard, K. Nakayama, T. Sato, M. Neupane, Y.-M. Xu, J. H. Bowen, G. F. Chen, J. L. Luo, N. L. Wang, X. Dai, Z. Fang, H. Ding, and T. Takahashi “Observation of Dirac Cone Electronic Dispersion in BaFe_2As_2 ”, *Phys. Rev. Lett.* 104, 137001 (2010).
3. Haijun Zhang, Chao-Xing Liu, Xiao-Liang Qi, Xi Dai, Zhong Fang and Shou-Cheng Zhang, “Topological insulators in Bi_2Se_3 , Bi_2Te_3 and Sb_2Te_3 with a single Dirac cone on the surface”, *Nature Physics* 5, 438 (2009).
4. Andrei Bernevig “It has been a Weyl coming”, *Nature Physics* 11, 699 (2015).
5. Joseph P. Heremans, Mildred S. Dresselhaus, Lon E. Bell and Donald T. Morelli, “When thermoelectrics reached the nanoscale”, *Nature Nanotechnology* 8, 471 (2013).
6. Yong Xu, Zhongxue Gan, and Shou-Cheng Zhang, “Enhanced Thermoelectric Performance and Anomalous Seebeck Effects in Topological Insulators”, *Phys. Rev. Lett.* 112, 226801 (2014).
7. Hongming Weng, Xi Dai, and Zhong Fang, “Transition-Metal Pentatelluride ZrTe_5 and HfTe_5 : A Paradigm for Large-Gap Quantum Spin Hall Insulators”, *Phys. Rev. X* 4, 011002 (2014).
8. H. Barath, M. Kim, J. F. Karpus, S. L. Cooper, P. Abbamonte, E. Fradkin, E. Morosan, and R. J. Cava, “Quantum and Classical Mode Softening Near the Charge-Density-Wave–Superconductor Transition of Cu_xTiSe_2 ”, *Phys. Rev. Lett.* 100, 106402 (2008).
9. Y. I. Joe, X. M. Chen, P. Ghaemi, K. D. Finkelstein, G. A. de la Peña, Y. Gan, J. C. T. Lee, S. Yuan, J. Geck, G. J. MacDougall, T. C. Chiang, S. L. Cooper, E. Fradkin and P. Abbamonte, “Emergence of charge density wave domain walls above the superconducting dome in 1T-TiSe_2 ”, *Nature Physics* 10, 421 (2014).
10. Simon J. Clarke, Paul Adamson, Sebastian J. C. Herkelrath, Oliver J. Rutt, Dinah R. Parker, Michael J. Pitcher, and Catherine F. Smura, “Structures, Physical Properties, and Chemistry of Layered Oxychalcogenides and Oxypnictides”, *Inorganic Chemistry* 47, 8473 (2008).

Publications (Selected out of 30 total published and 18 supported by this FWP since 09/2013; full list at: <http://www.bnl.gov/cmpmsd/emsc/pubs.asp>)

1. Kefeng Wang, D. Graf, Lijun Li, Limin Wang and C. Petrovic “Anisotropic giant magnetoresistance in NbSb₂”, *Scientific Reports* 4, 7328 (2014).
2. Kefeng Wang, Aifeng Wang, A. Tomic, Limin Wang, A. M. Milinda Abeykoon, E. Dooryhee, S. J. L. Billinge and C. Petrovic “Enhanced thermoelectric power and electronic correlations in RuSe₂”, *Applied Physics Letters – Materials* 3, 041513 (2015).
3. J. S. Van Dyke, F. Masee, M. P. Allan, J. C. Seamus Davis, C. Petrovic and D. Morr “Direct evidence for a magnetic f-electron-mediated Cooper pairing mechanism of heavy-fermion superconductivity in CeCoIn₅”, *Proc. Natl. Acad. Sci. U. S. A.* 32, 11663 (2014).
4. Hyunsoo Kim, M. A. Tanatar, R. Flint, C. Petrovic, Rongwei Hu, B. D. White, I. K. Lum, M. B. Maple and R. Prozorov “Nodal to Nodeless Superconducting Energy-Gap Structure Change Concomitant with Fermi-Surface Reconstruction in the Heavy-Fermion Compound CeCoIn₅”, *Physical Review Letters* 114, 027003 (2015).
5. C. Stock, J. A. Rodriguez-Rivera, K. Schmalzl, E. E. Rodriguez, A. Stunault, and C. Petrovic “Single to Multiquasiparticle Excitations in the Itinerant Helical Magnet CeRhIn₅”, *Phys. Rev. Lett.* 114, 247005 (2015).

Fundamental Studies of Plasma-Based Synthesis of Nanomaterials: A Joint Challenge for Plasma and Materials sciences

Yevgeny Raitses¹, Igor Kaganovich¹, Brent Stratton¹, Mikhail Shneider², Roberto Car³, Bruce Koel⁴, Predrag Krstic⁵, Michael Keidar⁶, and Mohan Sankaran⁷

¹Princeton Plasma Physics Laboratory, ²Department of Mechanical & Aerospace Engineering, ³Department of Chemistry, ⁴Department of Chemical & Biological Engineering, Princeton University, Princeton, NJ 08543

⁵Theoretik LLC, New York, NY, ⁶Department of Mechanical & Aerospace Engineering, The George Washington University, Washington DC, 20052, ⁷Department of Chemical & Biomolecular Engineering, Case Western Reserve University, Cleveland, OH 44106

Program Scope

The main goal of this project is to develop an understanding of the synergy of plasma and nanoscale material processes in carbon, boron nitride (BN), and hybrid B-C-N nanostructure synthesis, including but not limited to, fullerenes, nanotubes and nanofibers. The research program focuses on the integration of three areas:

- 1) Characterization of the plasma properties relevant to the synthesis processes;
- 2) Development and utilization of unique in-situ diagnostics of nanoparticles and nanostructures in the plasma and gas phase;
- 3) Development and validation of state-of-the-art nanomaterial simulation codes and relevant plasma models, which serves as a basis for integrated multiscale modeling of nanomaterial synthesis processes.

This research strongly emphasizes characterization of equilibrium and non-equilibrium plasmas at atmospheric pressure as well as synthesized nanomaterials. The focus is on the fundamental and interdisciplinary science associated with the synthesis of nanoparticles and nanostructures by atmospheric pressure arc discharges. We utilize a helium DC arc discharge with a vaporized anode at atmospheric pressure, or anodic arc, which has been successfully applied to the synthesis of a broad class of nanomaterials, including carbon nanoparticles and nanostructures and metal nanoparticles. The proposed research includes comprehensive experimental and theoretical studies of three major steps for arc synthesis of the above nanostructures: evaporation of anode materials; formation of atomic species and clusters; nucleation and growth of nanoparticles and nanostructures.

Our integrated approach for characterization of synthesis processes is: i) spatial and temporal measurements of plasma properties provide an input for modeling of atomistic processes; ii) modeling results of formation of nanoparticles and nanostructures are validated by in-situ diagnostics of nanoparticles and nanostructures synthesized in plasma; iii), synthesized

nanomaterials are extracted from the plasma during the arc and collected after the synthesis process. The extracted and collected materials are then characterized by ex-situ material evaluation to validate in-situ measurements and provide an additional input for modeling.

Recent Progress

The first year of the project has been devoted to comprehensive characterization of the carbon arc discharge as the source of nanoparticles, development of advanced *in-situ* diagnostics, and the selection of appropriate numerical tools for studies of synthesis processes in plasmas.

Ablation and Deposition Processes in Arc Discharge for Nanosynthesis Ablation of the anode electrode in the arc provides a feedstock of atoms and molecules for nanomaterial synthesis. Controlling of the ablation is important for overall control of the synthesis processes, including nucleation and growth of nanoparticles and nanostructures. Therefore, a considerable effort was made to study what arc parameters determine the ablation process. Experimental studies revealed that the nanosynthesis arc can operate in two different ablation/deposition regimes depending on the anode diameter (Figure 1) [1,2].

One regime is characterized by the enhanced ablation rate, which is favorable for high yield synthesis of nanomaterials, because the yield of nanomaterials is determined by ablation rate. The second regime has a small and approximately constant ablation rate. Our recent studies demonstrated that the difference between these two regimes is determined by thin layers of space charge near the electrodes. These layers, so-called anode sheath and cathode sheaths, determine the amount of particles and heat fluxes to the electrodes. In the enhanced ablation regime, the electron heat flux to the anode is much higher than in the low ablation regime. A detailed theoretical description

of the ablation process was developed and successfully explained experimental observations. The model includes coupled processes of ablation, deposition, latent heat released during the deposition, and thermionic emission from surfaces.

An important implication of these results is that for stable operation of the DC arc discharge, the cathode deposit must be conductive and therefore, for synthesis of non-conductive nanomaterials, the arc method needs to be modified to include, for example, forced convection of the flow in order to remove the non-conductive deposit or to use an AC arc discharge or electrodeless plasma, which would be less affected by the deposit than a DC arc. Moreover, the proposed physical mechanisms responsible for two ablation modes of the consumed anode can be relevant to other arc synthesis methods, including synthesis of metal nanoparticles.

Development of advanced in-situ laser diagnostics of nanoparticles and related theoretical studies We have developed a variety of diagnostic tools for characterization of

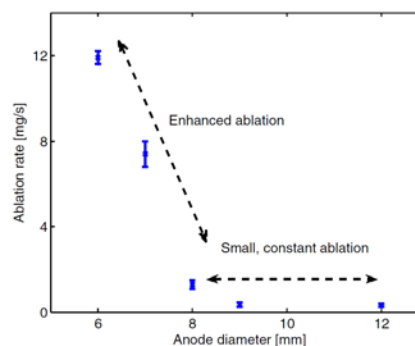


Figure 1. Two main ablation modes of the arc discharge for synthesis of carbon nanotubes.

plasma properties and in situ measurements of nanoparticles and nanostructures. These diagnostics include optical emission spectroscopy (OES), Coherent Rayleigh-Brillouin Scattering (CRBS), Laser Induced Fluorescence (LIF), Laser-Induced Incandescence (LII), as well as specially designed probe system for electrostatic extraction of nanoparticles.

The LIF will be a key diagnostic for measurement of precursor species to nanoparticle formation in the arc plasma, including carbon and boron atoms and ions, C_2 , C_3 , and metallic atoms and ions. An LIF diagnostic has been constructed and is being tested prior to initial measurements in the arc plasma.

The CRBS will be used to detect nanoparticles of less than 50 nm in the plasma. By exploiting the strong interaction between particles polarizability with intense laser fields, the CRBS will allow characterization of the type, size, density, and temperature of nanoparticles at various locations in the discharge. Unlike spontaneous Rayleigh-Brillouin Scattering and Mie scattering, CRBS relies on the creation of periodic gratings within a medium (plasma or gas) and provide much higher sensitivity and measurement resolution. According to modeling of expected CRBS signals, this diagnostic will have high sensitivity and should be capable of detecting spherical nanoparticles at concentrations as low as 0.005%. Higher sensitivity is expected for nanotubes. Assembly of the CRBS setup was completed and satisfactory performance was demonstrated by obtaining a single laser shot CRBS spectrum in air. A capability to measure well-characterized nanoparticles to test the system is being implemented.

As a part of the CRBS development, we conducted a comprehensive study of the dynamic polarizability of carbon nanotubes and fullerenes. The intensity of the CRBS signal in a gas with suspended nanoparticles is proportional to the polarizability of the nanoparticles. Thus it is important to know the anisotropy of the polarizability tensor of the nanotubes and non-spherical fullerenes, and we have calculated the frequency-dependent electric polarizability and the photoabsorption spectra of carbon nanomaterials of different shapes and sizes in the frequency domain from static to the ultraviolet region of the spectrum. These linear response theory calculations have been based on time-dependent density functional theory (TDDFT) using the efficient Liouville-Lanczos approach implemented in the open source Quantum ESPRESSO (QE) package. The results demonstrate that CRBS will distinguish these structures through rotation of the polarization (Figure 2).

Another diagnostic system developed for in situ detecting of nanoparticles in plasma is LII. The LII is capable to detect nanoparticles of larger than 10 nm using the incandescence signal after short-pulse laser heating. The LII was applied for detecting of nanoparticles in gas without plasma.

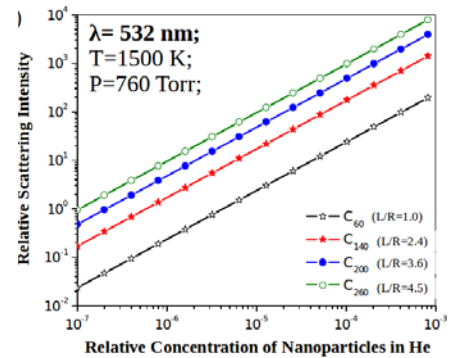


Figure 2. Spontaneous Rayleigh scattering of nanoparticles computed from the TDDFT polarizability: The relative Rayleigh scattering intensity predicted for CRBS detection of different carbon nanoparticles with different aspect ratios.

Based on results of these experiments, we proposed and implemented improvements to the LII model for the determination of nanoparticles sizes. These improvements include heat transfer effects for complex nanostructures such as multi-walled nanotubes and also self-consistent description of charging effects with and without the presence of plasma. An important implication of these studies is that a large buildup of positive charge induced by thermionic electron emission due to irradiation by laser and/or plasma may induce disintegration of agglomerated nanoparticles and nanotube bundles when the electrostatic Coulomb repulsion force between nanoparticles is stronger than the van der Waals bond energies.

Future Plans

The project will follow the following main steps: 1) Comprehensive characterization of plasma arc environments (electron temperature and density, densities and temperatures of ionic, atomic and molecular species) for nanosynthesis of carbon, B-C-N and boron nitride nanotubes using OES, LIF and probe diagnostics; 2) Application of advanced in situ laser diagnostics including CRBS and LII, for detecting of nanoparticles in the plasma; 3) Advanced atomistic simulations of nucleation and growth of nanoparticles and nanostructures taking into account plasma effects such as heating and charging; 4) Development of reduced models for arc plasma growth of carbon and boron nitride nanotubes.

References

- [1] A. J. Fetterman, Y. Raitses, M. Keidar, “Enhanced ablation of small anodes in a carbon nanotube arc plasma”, *Carbon* 46, 1322 (2008).
- [2] J. Ng and Y. Raitses, “Role of the cathode deposit in the carbon arc for the synthesis of nanomaterials”, *Carbon* 77, 80 (2014).

Publications

1. J. Ng and Y. Raitses, “Self-organisation processes in the carbon arc for nanosynthesis”, *J. Appl. Phys.* 117, 063303 (2015).
2. V. Nemchinskiy and Y. Raitses, “Atmospheric pressure arc discharge with ablating graphite anode” *J. Phys. D: Appl. Phys.* 48, 245202 (2015).
3. J. M. Mitrani and M. N. Shneider, “Time-resolved laser-induced incandescence from multiwalled carbon nanotubes in air”, *Appl. Phys. Lett.* 106, 043102 (2015)
4. X. Fang, J. Donahue, A. Shashurin and M. Keidar “Plasma-based graphene functionalization in glow discharge” *Graphene* 4, 1 (2015).
5. M. N. Shneider, “Carbon nanoparticles in the radiation field of the stationary arc discharge”, *Phys. Plasmas* 22, 073303 (2015).
6. A. Shashurin, M. Keidar “Synthesis of 2D materials in arc plasmas” *J. Phys. D: Appl. Phys.* 48, 314007 (2015).
7. S. Ghosh et al., “Atmospheric-pressure dielectric barrier discharge with capillary injection for gas-phase nanoparticle synthesis”, *J. Phys. D: Appl. Phys.* 48, 314003 (2015).

Controlling graphitic substrates : metal intercalation, Li barriers in graphitic battery anodes and graphene-based metamaterials.

K.M. Ho^{1,2}, M.Hupal¹, P. A. Thiel^{1,3}, M.C.Tringides^{1,2} and C. Z. Wang¹

¹ Ames Laboratory, ² Department of Physics-ISU, ³ Department of Chemistry-ISU
Ames IA 50011

I. Program Scope

The goals of this FWP are the controlled growth of nanostructured materials and their use to solve important technological problems. Novel properties emerge as the nanostructure dimensions are reduced, when compared to bulk materials, because boundary atoms have enhanced reactivity, and electron confinement plays a bigger role in defining the nanostructure properties. Utilizing our previous expertise, we plan to grow and use tunable metal nanostructures in three new directions, related to graphitic applications[1-3]. (i) Studying metal growth on graphene/graphite to modify graphene properties by intercalation.(ii) Measuring the controlling barriers for Li adatoms on graphene/graphite (adsorption, diffusion, and adatom-adatom interaction) to optimize Li storage in Li ion batteries (LIBs). (iii) Using our extensive expertise in preparing high quality graphene to apply it for Terahertz and Metamaterials applications, because of carrier tunability and reduced energy loss in graphene when compared to metals.

II. Previous work

Extensive work [4] to understand the metal/graphitic interaction (i.e. on graphene and graphite) has been carried out because this interaction is key to optimize metal contacts and high quality spin filters in graphene devices. In almost all cases studied, it was found experimentally and confirmed theoretically

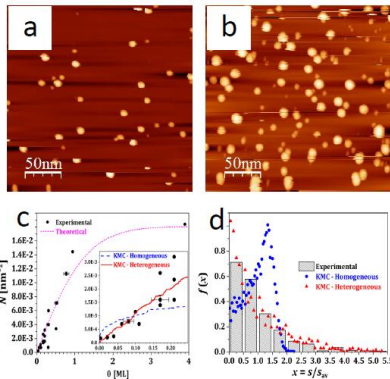


Fig. 1. (a) and (b) STM images of Cu clusters on HOPG terraces. (c) (d) The coverage dependence and island size distributions indicate heterogeneous nucleation. Image size 250 x 250 nm².

that metal adsorption on graphene was 3-d, because the adsorption energy of a metal atom on graphene is smaller than the metal cohesive energy[4]. A standard method to study the grown morphology is to measure the nucleated island density n as a function of growth parameters (temperature T , flux rate F and coverage θ). From these measurements the diffusion and adsorption barriers are extracted. For graphene uses it is important to prepare low resistance metal contacts, so it is necessary to find ways to grow metals in 2-d (layer-by-layer).

It was also found that in some cases the standard scaling theory of nucleation for metals is not applicable, and long range repulsive interactions become increasingly important with deposited coverage. The role of even a small fraction of charged ions in the incident metal atom beam was shown to dramatically modify the nucleation during growth of Cu on graphite, as seen in fig.1 [5]. High island densities are observed which are incompatible with DFT calculations of the Cu diffusion barrier on graphite, found to be very low ($\sim 20\text{meV}$). An alternative explanation is deposition-mediated heterogeneous nucleation (due to the small fraction of Cu ions) was validated.

The important role van der Waals forces play in graphene stability and their role in metal/graphitic interactions was also clarified. Despite extensive work over many years in the literature related to metal growth on graphite, inconsistencies exist. We have critically reviewed the body of work [6], to be used as a guide by the whole community.

Graphene based spintronic devices require understanding the growth of magnetic metals like rare earth metals. The majority of the grown islands have triangular instead of hexagonal shapes, expected for hcp(0001) bulk Dy crystals[7]. By analyzing the island shape distribution and stacking sequence, it was deduced that the Dy islands have fcc(111) structure.

Using DFT, it was shown that QSE can induce oscillatory electrostatic potential because of workfunction differences in different terraces, parts of a Pb crystalline mesa grown over stepped Si(111). The electric field generated because of the electrostatic potential variation with terrace height, guides the positively charged Mg adatoms to terraces of low workfunction, thus resulting in a modulation of the adsorbed coverage with terrace height, as seen experimentally[8].

Recently Eu on graphene experiments indicate that metal intercalation is a very effective method for controlling island nucleation, because of spatial variation of doping, due to the intercalation[9]. A key question is mass transport, i.e., how atoms uniformly deposited on the surface populate only the pristine areas. Using DFT calculations, we show that due to the spatial variations of the doping an alternating lateral electric field (similar to the workfunction variation due to QSE discussed earlier) which guides adatoms from intercalated to pristine areas.

Classically, the onset of nucleation is defined in terms of a critical cluster of the condensed phase that forms from the gradual aggregation of randomly diffusing adatoms. Experiments in Pb/Si(111) at low temperature have discovered a dramatically different type of nucleation, with perfect crystalline islands emerging “explosively” out of the compressed wetting layer[10]. The unexpectedly high island growth rates and the directional correlations in the growth of neighboring islands suggest that nucleation is a result of the highly coherent motion of the wetting layer over mesoscopic distances.

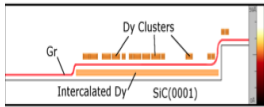
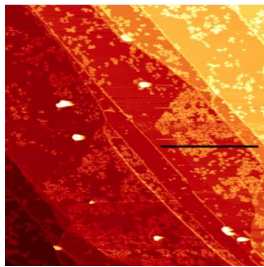


Fig.2 The 500 x 500 nm² growth of Dy on graphene/SiC (top). Higher nucleation is observed in the intercalated areas, as indicated in the schematic (bottom).

III. Future Plans

Based on the previous extensive expertise we have gained on the metal/graphitic interaction, we plan to pursue three new future directions.

IIIa. Controlling graphene properties by metal intercalation Surface-tailored intercalation of metals in layered compounds offers a versatile way to modify the surface properties of these materials. It has the potential to form 2-d metal layers that are chemically and mechanically protected, spatially localized, and functionally tailored. The combination of intercalated surface islands plus the modified overlayer could be useful in magnetic storage devices, micro- and nano-mechanical systems, and plasmonics In this FWP , we will focus on determining the basic factors that control surface intercalation of transition metals (TMs) and rare earths (REs), and on manipulating their chemical, spatial, and interfacial characteristics. Fig.2 shows how Dy nucleation is preferred on

intercalated (after heating to high temperature) than pristine graphene areas.

For layered carbon, there are essentially two classes of intercalation systems. One class is based on bulk compounds of graphite, which are well-known and diverse; in these the intercalant occupies the galleries between carbon sheets [11]. The other is based on supported graphene [12], where the intercalant is at or near the graphene-support interface. Many of the basic issues surrounding surface intercalation of TMs and REs, in both classes, have received little or no attention. These include the driving force, mechanism, and kinetics of intercalation; the spatial density and distribution of the intercalant; and the way in which intercalation changes surface properties of the graphene layer(s) on top. These basic issues will be investigated in the proposed work, simultaneously and synergistically with the exploration of practical methods for achieving patterned surfaces at the nanoscale to microscale. Graphene intercalation has been used mainly for doping, but the amount and distribution of intercalant atoms has not been studied systematically.

Intercalation involves complex diffusion processes along and between layers, and the stable states depend sensitively upon van der Waals interactions. The microscopic mechanisms and dynamics of these processes are not well understood. Several mechanisms for spontaneous surface intercalation under supported graphene have been considered in the literature, with varying levels of justification: diffusion from edges of graphene flakes toward the interior [13,14]; penetration at nanoscale features such as

domain boundaries or nanoscale cracks [13]; intercalation through localized or point-like defects [9,13]. Overall, the details of the intercalation pathways are still under much debate.

Compared with surface intercalation beneath supported graphene, there has been almost no exploration of surface intercalation on graphitic substrates. Moreover, the kinetics of surface intercalation, with associated diffusion pathways and diffusion barriers of metal atoms within the interstitial gallery, have not been probed. We will perform experiments and theoretical calculations to elucidate the details of intercalation and diffusion pathways and kinetics.

III.b Measuring key atomistic Li barriers in graphene/graphite for optimal LIB operation. Inhomogeneity and disorder are intentionally introduced in LIBs to enhance charge capacity (i.e. increase number of binding sites) but their detrimental role in slowing Li diffusion and reducing recycling capacity is not fully characterized. The interplay between effects related to tuning these barriers is critical in determining battery performance[15-17]. We plan to measure/calculate these key barriers on benchmark graphitic surfaces and use them as reference parameters to be compared with the corresponding barriers in real LIBs. The comparison of benchmark to real barriers will clarify the range over which real barriers can be mutually tuned for optimal battery performance.

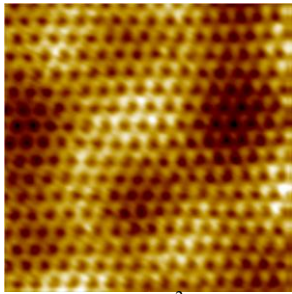


Fig. 3 3.7x3.7nm² showing the graphene lattice with the 6√3 periodicity (bright blobs).

Very limited work exists in the literature related to Li growth on graphitic surfaces and few theoretical estimates of the adsorption and diffusion energy barriers based on DFT have been carried out [16]. Since these barriers are the important ones controlling the Li storage and recycling in LIBs we will study adsorption, nucleation, and diffusion of Li on graphitic substrates over a wide range of sub-monolayer coverages. Very low coverage (~0.01ML) experiments will be used to measure the single adatom diffusion barrier E_d and the adatom dipole interaction ΔE from the spatial distribution of the Li adatoms. Independently, in other experiments, we will measure the nucleated island densities as a function of growth parameters (temperature and flux rate). Using the scaling theory of nucleation[18], E_d and cohesive energy E_c will be extracted to be compared with the results obtained from the adatom distributions. We will use our expertise in measuring chemical diffusion $D(\theta)$

as a function of coverage using the STM-based current fluctuation method because the Li recycling involves diffusion in the presence of other Li adatoms. We will employ temperature programmed desorption (TPD) to measure desorption of Li from graphite and determine the adsorption energy E_a . In TPD, the rate of desorption (proportional to pressure) is measured as a function of temperature. The current theoretical estimates for the relevant barriers are adsorption energy $E_a=1.08\text{eV}$, the diffusion energy $E_d=0.32\text{eV}$ and no estimate of the Li-Li interaction. Our experimental measurements will be compared to these preliminary estimates.

Besides the submonolayer coverage experiments we will look at the multi-layer growth for Li to verify if it is 3-d, similar to the growth mode for the other metals studied by us [4]. Earlier LEED work has shown Li non-crystalline cluster formation on top of graphite, and upon heating to 200 °C, diffusion into the bulk. On the other hand, ARPES studies of graphene grown on SiC have shown room temperature Li intercalation, from changes in the graphene electronic band structure. The transfer of Li into the bulk is the crucial process controlling the Li amount that can be stored. Our experiments will image the grown Li multilayer morphology, determine the temperatures where the Li 3-d clusters become crystalline, determine the onset of Li diffusion into the bulk as a function of Li deposited amount and temperature, and identify possible differences between multilayer Li growth on graphene versus graphite.

III.c Growth of High Quality Epitaxial Graphene for Metamaterials To prepare well-characterized epitaxial graphene (EG) grown on SiC of the highest quality (fig.3) and to use it for plasmonics and MM applications [19]. The FWP has extensive experience in preparing large domains of defect-free EG of uniform thickness (single, bilayer, intercalated graphene). Besides the advantage of plasmon confinement within a single atomic layer, graphene is less lossy than metals and its carrier density can be easily tuned, either by gating or by doping. This tunability offers many different ways to control the EM response and establishes graphene as a promising material for Terahertz (THz) applications.

In addition, a new approach is planned to isolate graphene from substrate excitations (that can shorten plasmon lifetime) ,i.e., by intercalating randomly distributed gas adatoms between graphene and the substrate [20]. Gas adatoms will be also used to decouple the different layers in stacked graphene (i.e. a universally sought structure because it will increase conductance without compromising the single layer graphene advantages). Intercalation offers another possibility to confirm an outstanding prediction that stacked and decoupled graphene layers can be used to tune plasmonic resonances over a wider frequency range and with much higher dynamic range for the resonance amplitude. The accurate knowledge of the graphene conductivity will be used to design and fabricate patterned graphene samples with improved MM properties for the frequency range of interest.

We plan to use this expertise in collaboration with the MM FWP to prepare well characterized samples with enhanced performance for plasmomics and THz applications. The design and modeling of novel MM structures requires an accurate knowledge of the graphene conductivity $\sigma(\omega)$. Conflicting values exist in the literature for the model parameters, the Drude weight α and the collision frequency γ . Partially this is due to the low quality of the graphene samples but our ability to grow defect-free graphene and to introduce disorder in controlled ways will measure how plasmon lifetimes depend on disorder and clarify the contradictory results.

References

- 1 K. S. Novoselov *et al.* *Science* 306,666 (2004).
2. C. Berger *et al.* *J. Phys. Chem. B*, 108, 19912 (2004)
3. A. H. Neto *et al* *Rev. Mod. Phys.* 81, 109 (2009).
4. X. Liu *et al* *Crystals* 3(1), 79-111 (2013)
5. D. Appy, *et al* *Progress in Surface Science* 89 219 (2014)
6. D. Appy *et al*, *Phys. Rev. B* 90 195406 (2014)
- 7 M T Hershberger *et al*, *J. Phys.: Cond. Mat.* 25 225005 (2013)
- 8 X. Liu *et al* *Phys. Rev. B* 89 041401(2014)
9. S. Schumacher *et al*, *Nano Letters* **13** (2013)
10. M. T. Hershberger *et al* *Phys. Rev. Lett.* 113 236101 (2014)
11. M. S. Dresselhaus *Adv. Physics* **51** (2002).
12. M. Batzill, " *Surf. Sci. Rep.* **67** (2012).
13. M. Petrovic *et al*, *Nature Communications* **4** (2013).
14. J. Baringhaus *et al*, *Applied Physics Letters* **104** (2014)
- 15 S. Goriparti *et al* , *Journal of Power Sources* 257 421 (2010)
- 16 R. Raccichini *et al*, *et al.* *Nat. Mat.* 14 271 (2014)
- 17 N. A. Kaskhedikar and J. Maier *Adv. Mater.*, 21 2664 (2009)
- 18 J. W. Evans *et al.* *Surf. Sci. Reports* 61 1 (2006)
- 19 M. Hupalo *et al* *Phys. Rev. B* 80 041401 (2009)
- 20 C. Riedl *et al*, *Phys. . Rev. Lett.* 103, 246804 (2009)

Publications from Previous Support (FY 2013-2015)

1. Z. Chromcova, M. C. Tringides, and Z. Chvoj, "Nucleation on a Stepped Surface with an Ehrlich-Schwobel Barrier," *Journal of Physics-Condensed Matter*, **25**, 265003 (2013). 10.1088/0953-8984/25/26/265003
2. M. T. Hershberger, M. Hupalo, P. A. Thiel, and M. C. Tringides, "Growth of Fcc(111) Dy Multi-Height Islands on 6H-SiC(0001) Graphene," *Journal of Physics-Condensed Matter*, **25**, 225005 (2013). 10.1088/0953-8984/25/22/225005
3. X. J. Liu, C. Z. Wang, M. Hupalo, K. M. Ho, and M. C. Tringides, "Metals on Graphene: Interactions, Growth Morphology, and Thermal Stability," *Crystals*, **3**, 7(2013).<http://dx.doi.org/10.3390/cryst3010079>

4. G. P. Zhang, X. J. Liu, C. Z. Wang, Y. X. Yao, J. Zhang, and K. M. Ho, "Electronic and Spin Transport Properties of Graphene Nanoribbon Mediated by Metal Adatoms: A Study by the QUAMBO-NEGF Approach," *Journal of Physics-Condensed Matter*, **25**, 105302 (2013). [10.1088/0953-8984/25/10/105302](https://doi.org/10.1088/0953-8984/25/10/105302)
5. S. Q. Wu, C. Z. Wang, Z. Z. Zhu, K. M. Ho, "Understanding the Role of Silicon Oxide Shell in Oxide-Assisted SiNWs Growth," *Materials Chemistry and Physics*, **148**, 1145-1148 (2014). [10.1016/j.matchemphys.2014.09.036](https://doi.org/10.1016/j.matchemphys.2014.09.036)
6. K. L. Man, M. C. Tringides, M. M. T. Loy, and M. S. Altman, "Superdiffusive Motion of the Pb Wetting Layer on the Si(111) Surface," *Physical Review Letters*, **110**, 036104 (2013)
7. W. J. Lee, J. G. Chang, A. C. Yang, Y. T. Wang, W. S. Su, C. Z. Wang, and K. M. Ho, "Influence of Oriented Topological Defects on the Mechanical Properties of Carbon Nanotube Heterojunctions," *Journal of Applied Physics*, **114**, 144306 (2013). [10.1063/1.4824539](https://doi.org/10.1063/1.4824539)
8. N. Liu, Z. Q. Zheng, Y. X. Yao, G. P. Zhang, N. Lu, P. J. Li, C. Z. Wang, and K. M. Ho, "Fine Band Gap Modulation Effects of a GNRs by an Organic Functional Group: A First-Principles Study," *Journal of Physics D: Applied Physics*, **46**, 235101 (2013). [10.1088/0022-3727/46/23/235101](https://doi.org/10.1088/0022-3727/46/23/235101)
9. G. P. Zhang, X. Liu, C. Z. Wang, Y. X. Yao, J. Zhang, and K. M. Ho, "Electronic and Spin Transport Properties of Grapheme Nanoribbon Mediated by Metal Adatoms: A Study by the QUAMBO-NEGF Approach," *Journal of Physics Condensed Matter*, **25**, 105302 (2013). [10.1088/0953-8984/25/10/105302](https://doi.org/10.1088/0953-8984/25/10/105302)
10. N. Liu, N. Lu, Y. X. Yao, G. P. Zhang, C. Z. Wang, and K. M. Ho "Cross-sectional Aspect Ratio Modulated Electronic Properties in Si/Ge Core/Shell Nanowires," *Journal of Physics D: Applied Physics*, **46**, 135302 (2013). [10.1088/0022-3727/46/13/135302](https://doi.org/10.1088/0022-3727/46/13/135302)
11. G. D. Lee, E. Yoon, N. M. Hwang, C. Z. Wang, and K. M. Ho, "Formation and Development of Dislocation in Graphene," *Applied Physics Letters*, **102**, 021603 (2013). [10.1063/1.4775671](https://doi.org/10.1063/1.4775671)
12. D. Appy, H. P. Lei, C. Z. Wang, M. C. Tringides, D.J. Liu, J. W. Evans, and P.A. Thiel, "Transition Metals on the (0001) Surface of Graphite: Fundamental Aspects of Adsorption, Diffusion, and Morphology," *Progress in Surface Science*, **89**, 219-238, (2014). [10.1016/j.progsurf.2014.08.001](https://doi.org/10.1016/j.progsurf.2014.08.001)
13. D. Appy, H. P. Lei, Y. Han, C.Z Wang, M. C. Tringides, D. Shao, E. J. Kwolek, J. W. Evans, and P. A. Thiel, "Determining Whether Metals Nucleate Homogeneously on Graphite: A Case Study with Copper," *Physical Review B*, **90**, 195406 (2014). [10.1103/PhysRevB.90.195406](https://doi.org/10.1103/PhysRevB.90.195406) november
14. X. Liu, C-Z Wang, H-Q Lin, M. Hupalo, P. A. Thiel, K-M Ho, and M. C. Tringides, "Structures and Magnetic Properties of Fe Clusters on Graphene," *Physical Review B*, **90**, 155444 (2014). [10.1103/PhysRevB.90.155444](https://doi.org/10.1103/PhysRevB.90.155444) october
15. C. D. Yuen, G. J. Miller, H. P. Lei, C. Z. Wang, and P. A. Thiel, "Structure of the Clean Gd₅Ge₄(010) Surface," *Journal of Physics-Condensed Matter*, **25**, 485002 (2013). [10.1088/0953-8984/25/48/485002](https://doi.org/10.1088/0953-8984/25/48/485002)
16. A. V. Matetskiy, L. V. Bondarenko, D. V. Gruznev, A. V. Zotov, A. A. Saranin, and M. C. Tringides, "Structural Transformations in Pb/Si(111) Phases Induced by C₆₀ Adsorption," *Journal of Physics-Condensed Matter*, **25**, 100503 (2013). [10.1088/0953-8984/25/39/395006](https://doi.org/10.1088/0953-8984/25/39/395006)

17. X. J. Liu, C. Z. Wang, M. Hupalo, H. Q. Lin, K. M. Ho, and M. C. Tringides, "Quantum Confinement Induced Oscillatory Electric Field on a Stepped Pb(111) Film and Its Influence on Surface Reactivity," *Physical Review B*, **89**, 041401 (2014). 10.1103/PhysRevB.89.041401
18. H. P. Lei, C. Z. Wang, Y. X. Yao, Y. G. Wang, M. Hupalo, D. McDougall, M. Tringides, and K. M. Ho, "Strain Effect on the Adsorption, Diffusion, and Molecular Dissociation of Hydrogen on Mg (0001) Surface," *Journal of Chemical Physics*, **139**, 224702 (2013). 10.1063/1.4839595
19. M. T. Hershberger, M. Hupalo, P. A. Thiel, C. Z. Wang, K. M. Ho, and M. C. Tringides, "Nonclassical Explosive Nucleation in Pb/Si(111) at Low Temperatures," *Physical Review Letters*, **113**, 236101 (2014). 10.1103/PhysRevLett.113.236101 3 December 2014
20. X. Liu, C-Z Wang, H-Q Lin, and K-M Ho, "Magnetic Moment Enhancement for Mn₇ Cluster on Graphene," *Journal of Physical Chemistry C*, **118**, 19123-19128 (2014). 10.1021/jp504329c
21. C. Brun, T. Cren, V. Cherkez, F. Debontridder, S. Pons, D. Fokin, M. C. Tringides, S. Bozhko, L. B. Ioffe, B. L. Altshuler, and D. Roditchev, "Remarkable Effects of Disorder on Superconductivity of Single Atomic Layers of Lead on Silicon," *Nature Physics*, **10**, 444-450 (2014). 10.1038/nphys2937
22. F. Zhang, B. C. Wood, Y. Wang, C-Z Wang, K-M Ho, and M-Y Chou, "Ultrafast Bulk Diffusion of AlH_x in High-Entropy Dehydrogenation Intermediates of NaAlH₄," *Journal of Physical Chemistry C*, **118**, 18356-18361 (2014). 10.1021/jp504550m
23. X. Liu, Y. Han, J. W. Evans, A. K. Engstfeld, R. J. Behm, M. C. Tringides, M. Hupalo, H. Q. Lin, Li Huang, K.M. Ho, D. Appy, P. A. Thiel, and C. Z. Wang "Growth Morphology and Properties of Metals on Graphene" *Progr. Surf. Sci.* **90** 397 (2015)
24. "A combined STM and SPA-LEED study of the "explosive" nucleation and collective diffusion in Pb/Si(111)" H. Hattab, M. Hupalo, M. T. Hershberger, M. Horn von Hoegen, M.C. Tringides *Surf. Sci.* (in press)

Growth Mechanisms and Controlled Synthesis of Nanomaterials (ERKCS81): Synthesis of Two-Dimensional Metal Chalcogenides by Laser Vaporization and CVD

**Kai Xiao,¹ Masoud Mahjouri-Samani,¹ Xufan Li,¹ Kai Wang,¹ Alex Puretzky,¹
Mina Yoon,¹ Mengkun Tian,³ Gerd Duscher,^{2,3} Christopher M. Rouleau,¹
Gyula Eres,² Bing Huang,¹ and David B. Geohegan¹**

¹Center for Nanophase Materials Sciences and ²Materials Science and Technology Division,
Oak Ridge National Laboratory, Oak Ridge, TN 37831

³Dept. of Materials Science and Engineering, Univ. of Tennessee, Knoxville, 37996

Program Scope

The overarching goal of the research program is to understand the link between the growth mechanisms and the resulting structure of nanoscale materials. The emphasis is on the development of real-time methods to induce and probe chemical and physical transformations away from thermodynamic equilibrium, in order to controllably synthesize nanomaterials with enhanced properties resulting from metastable structures. The approach relies on correlating the real-time diagnostic measurements with predictive theoretical methods and post-growth characterization by imaging, spectroscopy, and atomic-resolution analytical electron microscopy, to develop a framework for the deterministic synthesis of nanomaterials with desired properties.

Specific aims of the program are:

- (1) To reveal the kinetic pathways by which “building blocks” are involved in the growth of nanostructures through the development of real-time measurement approaches and modeling.
- (2) To understand the special role of nonequilibrium growth environments in capturing metastable phases and structures with novel nanoscale properties through the development of new synthesis and processing approaches incorporating in situ diagnostics.
- (3) To understand the atomistic interactions governing the design and synthesis of nanostructures with specific configurations and functionalities through predictive theory and associated experiments.

Recent Progress

Layered materials, grown as monolayers or few-layered two-dimensional (2D) crystals, are emerging as novel new materials for optoelectronic applications. 2D nanosheets of transition metal dichalcogenides (TMDs, with the stoichiometry MX_2 with metals such as Mo, W, Ti, Zr, etc. and $\text{X}=\text{S}, \text{Se}, \text{Te}$) and their heterostructures offer an exciting new platform for potential applications of these materials in optoelectronics and nanophotonics as well as exquisitely well-described interfaces for combined experimental and theoretical studies. The fundamental optoelectronic properties of 2D nanosheet heterostructures originate from the sensitive interplay between van der Waals (vdW), charge transfer (CT), and orbital hybridization (OH) interactions at atomic-scale interfaces. These same vdW/CT/OH interactions also govern the synthesis of these materials, determining how strongly atomic, molecular, and cluster “building blocks” interact with the substrate (either epitaxy or vdW-epitaxy) and each other.

Recently we have employed both chemical vapor deposition (CVD) and pulsed laser deposition (PLD) to explore the nucleation and growth processes of a variety of 2D crystals (e.g., GaSe, MoSe_2 ,

WS₂, WSe₂, etc.) and their heterostructures (both lateral and vertical) on various substrates. Understanding the mechanisms by which 2D nanomaterials grow on different substrates is essential in order to synthesize these nanomaterials with well-defined numbers of layers, large crystalline domains, and ordered stacking required by many potential applications. Synthesis of 2D nanomaterials, e.g., metal chalcogenide nanosheets, have common challenges that include: 1) controlling nucleation density, domain orientation, and number of layers, 2) rapid growth over large areas, and 3) growth of large crystalline grains. To address these challenges development of *in situ* diagnostic approaches for controlling and understanding growth mechanisms of these materials are required. Here, we discuss our specific results on 2D metal chalcogenides growth by CVD on SiO₂ substrates and graphene, which demonstrates that the interlayer coupling including charge transfer is responsible for the preferred orientations observed among the bilayer crystals and heterostructures. In addition, we show how the digital delivery of precise amount of sulfur atoms by PLD with super-thermal kinetic energies were used to control sulfurization (doping) for either alloying or total conversion of MoSe₂ to MoS₂ to form lateral heterojunctions.

Van der Waals epitaxial growth of 2D crystals by a chemical vapor deposition method

vdW heteroepitaxial growth of 2D crystals is attracting more and more interest because self-assembly processes during growth should result in reproducible, energetically-preferred interlayer orientations, more seamless stacking, and clean, sharp interfaces. Although the interactions with the substrate in van der Waals type epitaxial growth are much weaker than in standard epitaxy, such interactions can still have a strong influence on the growth and properties of 2D materials. Here we investigate the CVD synthesis of layered 2D metal chalcogenide (GaSe, MoSe₂) nanosheets on various substrates to characterize the growth environment and understand the preferred orientations of 2D atomic layers on substrate by vdW epitaxy. The size, density, shape, thickness, and uniformity of the 2D GaSe crystals on SiO₂ were shown to be controllable by growth duration, growth region, growth temperature, and argon carrier gas flow rate. The argon carrier gas flow rate was found to play an important role in controlling the thickness of the resulting crystals. At low carrier flow rate, uniform, large (up to ~60 μm in lateral size), single-crystalline, triangular monolayer GaSe crystals were grown on SiO₂ substrates, with the layer number controlled by diffusion through the boundary layer.¹ However, at higher carrier flow rates, monolayer GaSe growth changed reproducibly to bilayer GaSe crystals (0° or 60° interlayer rotations) in a “layer-plus-island” mode.² Theoretical analysis reveals that the preferred orientations among the bilayer GaSe crystals were determined by the energies of the interlayer coupling. In order to explore the atomistic effect of substrates on the vdW epitaxial growth of 2D crystals, GaSe atomic layers were grown on transferred CVD-grown graphene

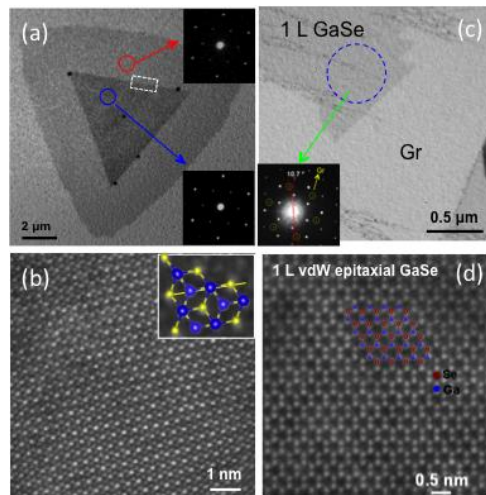


Figure 1 Revealing the atomic resolution structure of bilayer GaSe crystals and GaSe monolayer on graphene by growth directly on TEM grids. BF-TEM images of (a) bilayer GaSe crystals with AB stacking pattern and (b) GaSe on graphene with 10.9° lattice rotation. Insets are SAED patterns from the area indicated by solid circles. Corresponding ADF-STEM images of (c) the bilayer and (d) heterostructure. Insets are magnified images and intensity profiles along the solid lines.

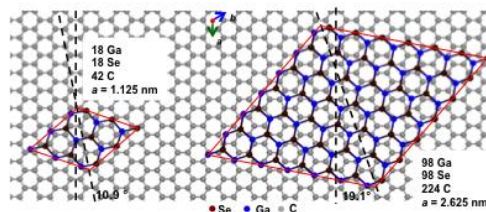


Figure 2 Schematic illustrations of vdW heterostructure unit cells (supercells) constructed by 1L GaSe epitaxy on 1L graphene with interlayer lattice rotations of 10.9° and 19.1°, respectively.

(Gr).³ GaSe crystals are found to nucleate predominantly on random wrinkles or grain boundaries of graphene, share a preferred lattice orientation with underlying graphene, and grow into large (tens of microns) irregularly-shaped, single-crystalline domains. The domains grow with triangular edges that eventually merge into large single crystals. Electron diffraction revealed that the GaSe domains are predominantly oriented with a 10.9° interlayer rotation with the underlying graphene (Fig. 1c). Theoretical investigations of the interlayer energetics reveal that this interlayer rotation is the most energetically preferred vdW heterostructure (Fig. 2) with the smallest supercell (a non-intuitive orientation that minimizes interlattice atomic mismatch). In addition, strong charge transfer in these GaSe/Gr vdW heterostructures is predicted, which agrees with the observed enhancement in the Raman E^2_{1g} band of monolayer GaSe and highly-quenched photoluminescence compared to GaSe/SiO₂. This result reveals that the charge transfer of 2D crystals and other chemical/physical interactions with the substrate such as the electronic properties of substrates (e.g., metal, insulator, semiconductor) govern the growth processes.

To provide atomistic understanding of 2D material growth, and especially how monolayers and bilayers of 2D metal chalcogenides nucleate and grow, we developed synthesis methods for vapor phase growth directly on Transmission Electron Microscopy (TEM) grid substrates. Various 2D metal chalcogenides, including GaSe, MoSe₂, MoS₂, WS₂, and WSe₂ single crystal islands were grown on SiO₂/Si, graphene, and SiO₂ membrane substrates. On membranes of SiO₂ or transferred graphene on grids, atomic-resolution Annular Dark Field Scanning Transmission Electron Microscopy (ADF-STEM) and Bright Field TEM (BF-TEM) was used to reveal the structure of single-crystal monolayer¹, atomic stacking in bilayer GaSe crystals² and GaSe/Gr heterostructure³ (Fig. 1). We revealed the edge structures of the crystals, and learned that interlayer stacking controlled the bilayer crystal structure and the orientation of epilayers, which consequently determines the crystal's optoelectronic properties. Our theoretical analysis has shown that the interlayer coupling is highly correlated to the local crystal symmetry, which is responsible for the preferred orientations observed among the bilayer crystals and heterostructures.

Isoelectronic doping of 2D transition metal dichalcogenide crystals for heterostructures

Doping is one of the essential technologies needed in various applications of 2D materials. Isoelectronic doping (substitutional or alloy) has the effect of mitigating the effects of deep traps, unintentional impurities, and dislocations in 2D materials. Isoelectronic doping introduces trapping potentials in the lattice due to the difference of electronegativities between host and impurities to tune the bandgap of 2D crystals. However, stable and highly-efficient doping techniques still remain a challenge. Pulsed laser deposition has long been renowned for its ability to transfer stoichiometry from targets to substrates, for its digital delivery of precise quantity of reactants, and for the inherent kinetic energy in the process to enable non-equilibrium growth conditions. In recent work, we demonstrated that PLD conditions tailored to deliver stoichiometric UNPs of ‘amorphous’ GaSe

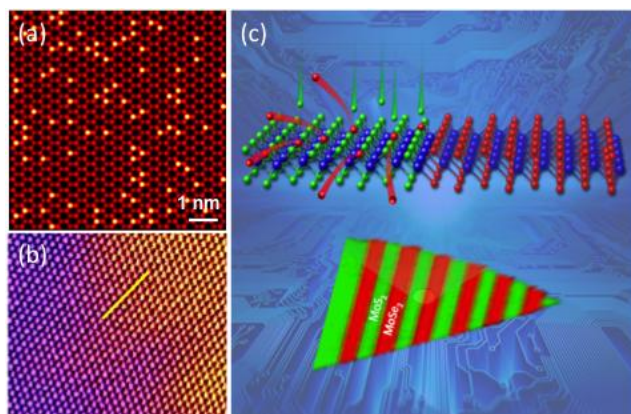


Figure 3 Atomic resolution ADF-STEM image of (a) W-doped MoSe₂ (b) the junction between MoS₂ on the left, and MoSe₂ on the right obtained by converting monolayer MoSe₂ using S atoms deposited by PLD. (c) Complex, scalable arrays of semiconductor heterojunctions—promising building blocks for future electronics—were formed within a 2D monolayer of MoSe₂ by converting lithographically exposed regions to MoS₂.

or MoSe₂ to hot substrates could directly synthesize metal chalcogenide (GaSe, MoSe₂) nanosheets.^{5,6} In addition, we explored pulsed laser vaporization as a nonequilibrium method to effect substitutional doping and conversion of existing 2D crystals.

We have recently demonstrated the isoelectronic doping of 2D crystals of MoSe₂ using PLD-generated laser plumes (of sulfur in vacuum) and by CVD methods (using tungsten from WO₃). The sulfur incorporation efficiency is related to the kinetic energy of the arriving sulfur species. Through the digital delivery of a precise amount of sulfur atoms with super thermal kinetic energies during the doping process, the controlled sulfurization for either alloying or total conversion of MoSe₂ to MoS₂ were achieved. Using well-developed and scalable photolithography processes, a variety of patterns exposed to the sulfur plume produced predefined arrays of lateral MoS₂/MoSe₂ heterojunctions within a single monolayer in a single processing step. Figure 3 shows an atomic-resolution ADF-STEM image of the W-doped MoSe₂ and the junction between the converted (left, MoS₂) region and a lithographically-protected (right, MoSe₂) region of the original 2D crystal. PLD therefore provides a controllable and efficient way to explore doping kinetics through the digital delivery of precise quantities of the dopant.

In summary, 1) we employed graphene as a template for suppressing other metastable orientations during nucleation for large area single crystal GaSe growth by vdW epitaxy. Our experimental and theoretical analysis have shown that the interlayer coupling is highly correlated to the local crystal symmetry, which is responsible for the preferred orientations observed among the bilayer crystals and heterostructures. 2) Pulsed laser evaporation doping of 2D materials provided a controllable and efficient way to explore the doping dynamics through the digital delivery of precise quantities of the dopant. Understanding the mechanisms by which 2D crystals grows on different substrates or by doping is essential in order to synthesize 2D crystals with tuned bandgaps, the well-defined numbers of layers and ordered stacking required by many potential applications.

Future Plans

We have demonstrated 2D materials were controlled synthesized from the vapor transport process by using CVD and PLD, however, the detailed growth mechanisms have not yet been well understood. We propose to use in situ, time-resolved diagnostics of both the growth environment and the crystal growth to understand the kinetic pathways and reactive intermediates for 2D TMD nucleation and growth. For example, our preliminary results show the shapes of 2D crystal are determined by difference in the growth rates for zigzag and armchair edges. We are exploring a novel growth-etch-regrowth method for 2D GaSe crystals combined with in situ Raman scattering, time-resolved reflectivity, and direct optical and TEM imaging to reveal nucleation and growth kinetics. With real-time control, we will be able to stop and restart growth under different processing conditions to assess and adjust etching rates, understand how the competition between etching and growth processes shape the evolution of crystal edges for a comparison with classical theories (e.g., kinetic Wulff construction vs. Ehrlich-Schwoebel step barrier growth mechanism). As for the exploring the doping mechanism, we will use imaging and ion probes to measure the kinetic energy of the sulfur plume, and with discrete laser pulse-by-pulse delivery of sulfur to understand the kinetics and flux-dependence of the MoSe₂ to MoS₂ conversion process using in situ Raman spectroscopy, OAS and PL to characterize the crystal structure vibrational modes and band gap evolution vs. pulse number and time. With these in situ capabilities we propose to isolate metastable states with intermediate band gaps in the MoSe_{2-x}S_x system for examination by ADF-STEM and associated atomistic modeling of the conversion process.

References

1. X. Li, M. Lin, A. A. Puretzky, J. C. Idrobo, C. Ma, M. Chi, M. Yoon, C. M. Rouleau, I. I. Kravchenko, D. B. Geohegan,

- and K. Xiao, “Controlled Vapor Phase Growth of Single Crystalline, Two-Dimensional GaSe Crystals with High Photoresponse”, *Scientific Reports* **4**, 5497 (2014).
2. X. Li, L. Basile, B. Huang, C. Ma, J. Lee, I. V Vlassiouk, A. A Puzetzy, M.-W. Lin, M. Yoon, M. Chi, J. C Idrobo, C. M Rouleau, B. G Sumpter, D. B Geohegan, K. Xiao, “Van der Waals Epitaxial Growth of Two-Dimensional Single-Crystalline GaSe Domains on Graphene”, *ACS Nano* **9**(8), 8078 (2015).
 3. X. Li, L. A. Basile, M. Yoon, C. Ma, A. Puzetzy, J. Lee, J. Idrobo, M. Chi, C. Rouleau, D. B. Geohegan, and K. Xiao, “Revealing the preferred interlayer orientations and stackings of two-dimensional bilayer gallium selenide crystals”, *Angew. Chemie Int. Ed.* **54**(9) 2712 (2015).
 4. M. Mahjouri-Samani, M-W. Lin, K.Wang, A. R Lupini, J. Lee, L. Basile, A.Boulesbaa, C. M Rouleau, A. A Puzetzy, I.N. Ivanov, K.Xiao, M. Yoon, D. B Geohegan, “Patterned arrays of Lateral Heterojunctions Within Monolayer Two-Dimensional Semiconductors”, *Nat. Comm.* **6**, 7749 (2015).
 5. M. Mahjouri-Samani, M. Tian, K. Wang, A. Boulesbaa, C. M. Rouleau, A.A. Puzetzy, M. A. McGuire, B. R. Srijanto, K. Xiao, G. Eres, G. Duscher, and D. B. Geohegan “Digital Transfer Growth of Patterned 2D Metal Chalcogenides by Confined Nanoparticle Evaporation” *ACS Nano* **8**(11), 11567 (2014).
 6. M. Mahjouri-Samani, R. Gresback, M. Tian, K. Wang, A. A. Puzetzy, C. M. Rouleau, G. Eres, I. N. Ivanov, K. Xiao and M. A. McGuire, D. B. Geohegan "Pulsed Laser Deposition of Photoresponsive Two-Dimensional GaSe Nanosheet Networks" *Adv. Funct. Mat.* **24**, 6365 (2014).

DoE Sponsored Publications in the Last Two Years

1. S. R. Wagner, B. Huang, C. Park, J. Feng, M. Yoon, and P. Zhang, “Growth of Metal Phthalocyanine on Deactivated Semiconducting Surfaces Steered by Selective Orbital Coupling”, *Phys. Rev. Lett.* **115**, 096101 (2015).
2. B. Huang, H. Zhuang, M. Yoon, B. G. Sumpter, and S.-H. Wei, “Highly stable two-dimensional silicon phosphides: Different stoichiometries and exotic electronic properties”, *Phys. Rev. B* **91**, 121401 (R) (2015).
3. M. Tian, M. Mahjouri-Samani, G. Eres, R. Sachan, M. Yoon, M. F Chisholm, K. Wang, A. A Puzetzy, C. M Rouleau, D. B Geohegan, G. Duscher “Structure and Formation Mechanism of Black TiO₂ Nanoparticles”, *ACS Nano* **ASAP** Sep 22, 2015.
4. M. Tian, M. Mahjouri-Samani, G. Eres, R. Sachan, M. F Chisholm, K. Wang, A. A Puzetzy, C.M Rouleau, M.Yoon, D. B Geohegan, G. Duscher, “Phase Determination of Black TiO₂ Nanoparticles”, *Microscopy and Microanalysis* **21** (S3), 815 (2015).
5. X. Li, L. Basile, B. Huang, C. Ma, J. Lee, I. V Vlassiouk, A. A Puzetzy, M.-W. Lin, M. Yoon, M. Chi, J. C Idrobo, C. M Rouleau, B. G Sumpter, D. B Geohegan, K. Xiao, “Van der Waals Epitaxial Growth of Two-Dimensional Single-Crystalline GaSe Domains on Graphene”, *ACS Nano* **9**(8), 8078 (2015).
6. M. Mahjouri-Samani, M-W. Lin, K.Wang, A. R Lupini, J. Lee, L. Basile, A.Boulesbaa, C. M Rouleau, A. A Puzetzy, I.N. Ivanov, K.Xiao, M. Yoon, D. B Geohegan, “Patterned arrays of Lateral Heterojunctions Within Monolayer Two-Dimensional Semiconductors”, *Nat. Comm.* **6**, 7749 (2015).
7. A. Puzetzy, L. Liang, X. Li, K. Xiao, K. Wang, M. Mahjouri-Samani, L. Basile, J. C. Idrobo, B. G. Sumpter, V. Meunier, and D. B. Geohegan “Low-Frequency Raman Fingerprints of Two-Dimensional Metal Dichalcogenide Layer Stacking Configurations”, *ACS Nano* **9**(6) 6333 (2015)
8. X. Li, L. A. Basile, M. Yoon, C. Ma, A. Puzetzy, J. Lee, J. Idrobo, M. Chi, C. Rouleau, D. B. Geohegan, and K. Xiao, “Revealing the preferred interlayer orientations and stackings of two-dimensional bilayer gallium selenide crystals”,

- Angew. Chemie Int. Ed.* **54**(9) 2712 (2015).
9. B. Huang, H.L. Zhuang, M. Yoon, B. G. Sumpter, “Highly stable two-dimensional silicon phosphides: different stoichiometries and exotic electronic properties”, *Phys. Rev. B* **91**, 121401 (R) (2015).
 10. M. H. Lahiani, J. Chen, F. Irin, A. A Puzetzky, M. J Green, M. V. Khodakovskaya, “Interaction of carbon nanohorns with plants: Uptake and biological effects”, *Carbon*, **81**, 807 (2015).
 11. C. M. Rouleau, A. A. Puzetzky, and D. B. Geohegan “Slowing of femtosecond laser-generated nanoparticles in a background gas”, *Appl. Phys. Lett.* **105**(21), 213108 (2014).
 12. K. L. Grosse, V. E. Dorgan, D. Estrada, J. D. Wood, I. Vlassiouk, G. Eres, J. W. Lyding, W. P. King, and E. Pop “Direct observation of resistive heating at graphene wrinkles and grain boundaries”, *Appl. Phys. Lett.* **105**, (14) 143109 (2014).
 13. M. Mahjouri-Samani, M. Tian, K. Wang, A. Boulesbaa, C. M. Rouleau, A.A. Puzetzky, M. A. McGuire, B. R. Srijanto, K. Xiao, G. Eres, G. Duscher, and D. B. Geohegan “Digital Transfer Growth of Patterned 2D Metal Chalcogenides by Confined Nanoparticle Evaporation” *ACS Nano* **8**(11), 11567 (2014).
 14. A.A. Puzetzky, I. A. Merkulov, C. M. Rouleau, G. Eres and D. B. Geohegan “Revealing the surface and bulk regimes of isothermal graphene nucleation and growth on Ni with in situ kinetic measurements and modeling” *Carbon* **79**, 256 (2014).
 15. M. Mahjouri- Samani, R. Gresback, M. Tian, K. Wang, A. A. Puzetzky, C. M. Rouleau, G. Eres, I. N. Ivanov, K. Xiao and M. A. McGuire, "Pulsed Laser Deposition of Photoresponsive Two- Dimensional GaSe Nanosheet Networks" *Adv. Funct. Mat.* **24**, 6365 (2014).
 16. C. M. Rouleau, C.-Y. Shih, L. V. Zhigilei, A. A. Puzetzky, and D. B. Geohegan, “Nanoparticle generation and transport resulting from femtosecond laser ablation of ultrathin metal films: Time-resolved measurements and molecular dynamics simulations” *Appl. Phys. Lett.* **104**, 193106 (2014).
 17. G. Eres, M. Regmi, C. M. Rouleau, J. Chen, I. N. Ivanov, A. A. Puzetzky, and D. B. Geohegan, “Cooperative Island Growth of Large Area Single-Crystal Graphene by Chemical Vapor Deposition on Cu “ *ACS Nano* **8**(6), 5657 (2014).
 18. X. Li, M. Lin, A. A. Puzetzky, J. C. Idrobo, C. Ma, M. Chi, M. Yoon, C. M. Rouleau, I. I. Kravchenko, D. B. Geohegan, and K. Xiao, “Controlled Vapor Phase Growth of Single Crystalline, Two-Dimensional GaSe Crystals with High Photoresponse”, *Scientific Reports* **4**, 5497 (2014).
 19. B.Huang, H-X. Deng, H.Lee, M. Yoon, B. G. Sumpter, F. Liu, S. C. Smith, and S.-H. Wei, "Exceptional Optoelectronic Properties of Hydrogenated Bilayer Silicene", *Phys. Rev. X* **4**, 021029 (2014).
 20. T. Callcott, H. H. Weiering and N. Mannella “Origins of electronic band gap reduction in Cr/N codoped TiO₂” *Phys. Rev. Lett.* **112**, 036404 (2014).
 21. A. A. Puzetzky, D. B. Geohegan, S. Pannala, C. M. Rouleau, “Exploring growth kinetics of carbon nanotube arrays by in situ optical diagnostics and modeling” *SPIE LASE*, 8969 896904 (2014).

22. C. M. Rouleau, M. Tian, A. A. Puretzky, M. Mahjouri-Samani, G. Duscher, D. B. Geohegan, “Catalytic nanoparticles for carbon nanotube growth synthesized by through thin film femtosecond laser ablation,” *SPIE LASE* **8969**, 896907 (2014).
23. L. Oakes, A. Westover, M. Mahjouri-Samani, S. Chatterjee, A. Puretzky, C. M Rouleau, D. B Geohegan, C. L Pint, “Uniform, Homogenous Coatings of Carbon Nanohorns on Arbitrary Substrates from Common Solvents” *ACS Appl. Mater. Interfaces* **5**, 13153–13160 (2013).
24. D. B Geohegan, A. A Puretzky, M. Yoon, G. Eres, C. Rouleau, K.Xiao, J. Jackson, J.Readle, M. Regmi, N. Thonnard, G. Duscher, M. Chisholm, K. More, “Laser Interactions for the Synthesis and In Situ Diagnostics of Nanomaterials” Ch. 7 in *Lasers in Materials Science*, pp: 143-173. Springer Series in Materials Science **191**, Springer International Publishing, Switzerland 2014.
25. C.Parks Cheney, P. Vilmercati, E. W. Martin, M. Chiodi, L. Gavioli, M. Regmi, G. Eres, T. A. Callcott, H. H. Weitering and N. Mannella “Origins of electronic band gap reduction in Cr/N codoped TiO₂ “, *Phys. Rev. Lett.* **112**, 036404 (2014).

Growth Mechanisms and Controlled Synthesis of Nanomaterials (ERKCS81): Modeling and Characterization of Ultrasmall Nanoparticles

**Mina Yoon,¹ Mengkun Tian,³ Gyula Eres,² Gerd Duscher,^{2,3} Alex Puretzy,¹
Masoud Mahjouri-Samani,¹ Kai Wang,¹ Kai Xiao,¹ Christopher M. Rouleau,¹
Bing Huang,¹ Xufan Li¹ and David B. Geohegan¹**

**¹Center for Nanophase Materials Sciences and ²Materials Science and Technology Division,
Oak Ridge National Laboratory, Oak Ridge, TN 37831 and
the ³Dept. of Materials Science and Engineering, Univ. of Tennessee, Knoxville, 37996**

Program Scope

The overarching goal of the research program is to understand the link between the growth mechanisms and the resulting structure of nanoscale materials. The emphasis is on the development of real-time methods to induce and probe chemical and physical transformations away from thermodynamic equilibrium, in order to controllably synthesize nanomaterials with enhanced properties resulting from metastable structures. The approach relies on correlating the real-time diagnostic measurements with predictive theoretical methods and post-growth characterization by imaging, spectroscopy, and atomic-resolution analytical electron microscopy, to develop a framework for the deterministic synthesis of nanomaterials with desired properties.

Specific aims of the program are: (1) To reveal the kinetic pathways by which “building blocks” are involved in the growth of nanostructures through the development of real-time measurement approaches and modeling, (2) To understand the special role of nonequilibrium growth environments in capturing metastable phases and structures with novel nanoscale properties through the development of new synthesis and processing approaches incorporating in situ diagnostics, and (3) To understand the atomistic interactions governing the design and synthesis of nanostructures with specific configurations and functionalities through predictive theory and associated experiments. Theoretical methods are used to understand fundamental mechanisms of synthesis in order to guide the formation of nanostructures tailored to enhance energy storage, catalysis, thermal management, and photovoltaics in support of DOE's energy mission.

Recent Progress

Understanding atomistic interactions governing the synthesis of nanostructures with specific configurations and functionality: titanium oxide nanoparticle “building blocks” and “black TiO₂”

Ultrasmall (~ 3 nm diameter) nanoparticles of TiO₂ were formed by pulsed laser vaporization of TiO₂ targets in oxygen and used as “building blocks” as they annealed under different conditions to transform into different crystalline phases and structures.¹ The example of “black” TiO₂ demonstrates that the synthesis pathways have a critical influence on the formation of properties and functionality. Black and other forms of reduced TiO₂ are interesting because of the band gap reduction that is associated with the color change that occurs when ultrasmall nanoparticles (UNPs) synthesized by pulsed laser vaporization are annealed in a highly reducing atmosphere. Characterization by atomic-resolution TEM imaging shows that although the as synthesized UNPs are clearly identifiable by their shape, Selected Area Electron Diffraction (SAED) reveals that they lack coordinated crystalline order.

However, recently we have examined *single* as-synthesized UNPs with sub-nm spatial resolution employing Nano Beam Electron Diffraction (NBED) and electron energy loss spectroscopy (EELS). As shown in Figure 1, regions of the nanoparticle exhibit diffraction spots indicating that the amorphous TiO_2 nanoparticle already has TiO_6 octahedra, but randomly ordered. These measurements within a single, computationally-tractable nanoparticle, give an opportunity to develop an understanding of the evolution of crystalline order and energetics within a single, metastable UNP “building block” as it is annealed to acquire an energetically-preferred crystalline phase. Understanding of phase transformations on the single-nanoparticle level is an essential first step toward a model for the assembly of UNP building blocks to larger nanostructures. NBED and EELS appear to be excellent “descriptors” to correlate experiment and modeling.

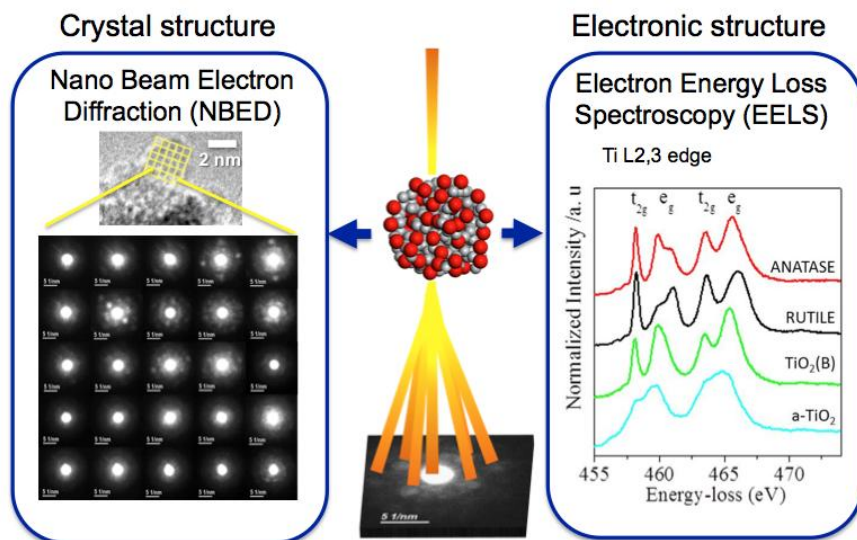


Figure 1. Sub-nm spatial resolution electron diffraction and EELS reveal regions of crystalline order within a single 3 nm TiO_2 ‘amorphous’ nanoparticle. Such measurements provide “descriptors” for crystal structure and electronic structure that can be calculated and compared with theoretical simulations of possible atomic configurations within a single UNP “building block”.

Development of Hybrid Optimization Algorithm for the Identification of Ti_nO_{2n} Nanoparticle Systems

We are developing a hybrid optimization algorithm to theoretically explore atomic structure configurations of TiO_2 nanostructures.² Our ultimate goal is to theoretically simulate experimentally synthesized ultrasmall nanoparticles, and to identify the structural characteristics and energy landscape

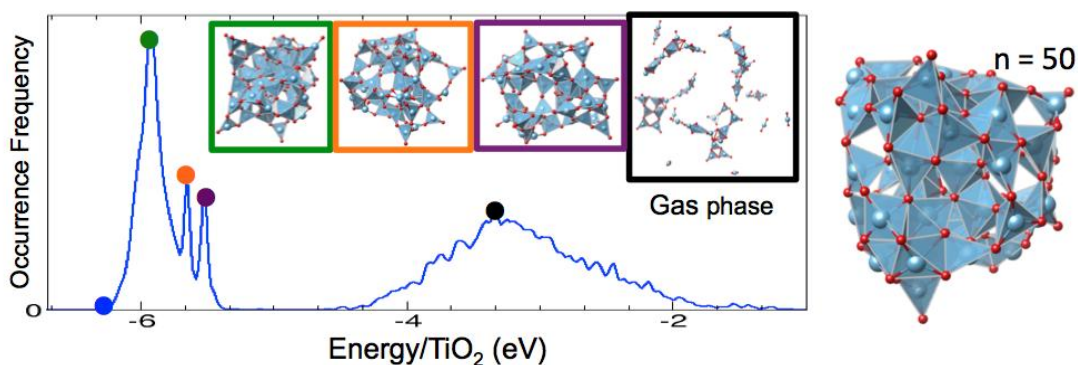


Figure 2. Energy distribution of identified $(\text{TiO}_2)_{50}$ particles using the hybrid optimization algorithm. Spatial distributions of representing structures at the peak locations are shown in the inset. The right panel highlights the polygonal units of a nanoparticle.

of plausible UNP $(\text{TiO}_2)_n$ clusters ($n=1-1000$). Much of the literature on identification of (meta)stable Ti_nO_{2n} nanoparticles using evolutionary optimization algorithms utilizes Genetic Algorithm, which typically requires discretizing the search space, or simulated annealing, which does not utilize a population-based search. The use of newer, more powerful evolutionary algorithms remains to be explored. Furthermore, the effectiveness of optimization algorithms is often gauged by their ability to identify the global minimum energy structure, or their ability to reproduce an empirically observed structure with some frequency. Such assessments validate an algorithm's performance against its stated goal, but inhibit the comparison of algorithms developed to meet different goals.

Our proposed hybrid algorithm includes a modified differential evolution algorithm, and a permutation operator to perform global optimization on a set of randomly generated structures. This set is then refined using a Broyden-Fletcher-Goldfarb-Shanno Quasi-Newton algorithm, which calculates the gradient of the potential energy based on the well-established force field potential [3] for the system, with respect to atom positions only. We confirmed consistency with numerical results found in the literature for stable clusters ($n < 20$). The smallest structures are either metastable (kinetically accessible) or near the global minimum. This scheme defines effectiveness as the ability of an algorithm to produce a set of structures whose energy distribution follows the regression as the number of Ti_nO_{2n} increases without specifying an exact distribution to allow for flexibility between approaches.

Figure 2, as an example, presents the distributions of $(\text{TiO}_2)_{50}$ structures in the energy space, obtained from our approach. Two main peaks in the distribution plot represent condensed phase and gas phase at the low energy and high energy, respectively. The results indicate that our stochastic approach mimics the synthesis experimental conditions, such that those two physical phases are identified without imposing any constraints during the global optimization search. Further analysis discovers a strong correlation between the density of polygonal units and the structural stabilities, that is, as the polyhedral

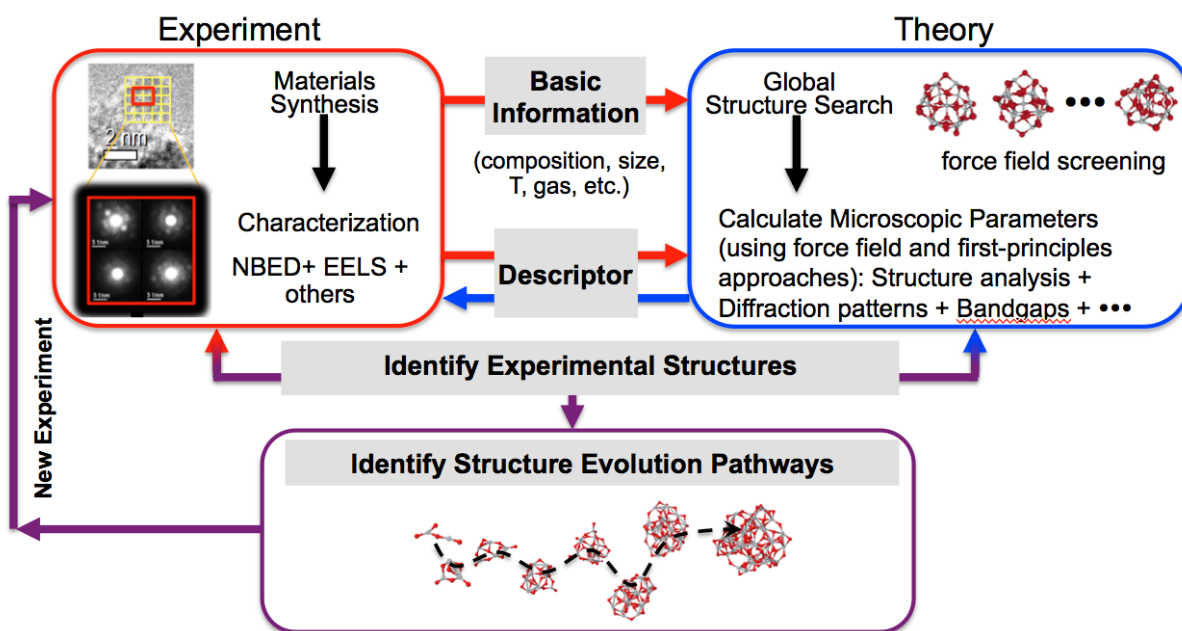


Figure 3. – Illustration of a theory-experiment combined scheme proposed in this project. Theoretical approach combines the development of global structure search, force field, and first-principles approaches. Experimental techniques are materials synthesis using various techniques and materials characterization using NBED and EELS, etc. The goal of this approach is to identify experimentally synthesized UNPs, and to identify their structure evolution pathways, by implementing unique theoretical approaches. [unpublished]

unit density gets higher, the structural stability increases. The right panel of Fig.2 illustrates the location of the polyhedral units of one of the found structure. We further identified a set of global or metastable configurations of Ti_nO_{2n} up to ~ 100 , where the energy of the nanoparticles approach to that of bulk value as the system size increases. Combining first-principles theory we analyzed electronic properties of some of the obtained structures, which will be experimentally verified.

Figure 3 summarizes our current and future approaches that combine atomistic theory and synthesis and characterization experiment. Based on the basic information from experiment, such as composition and sizes, we have constructed theoretical model/tool to efficiently explore configuration space of UNPs. We expect the calculations to predict statistics for the occurrence frequency of the particles with different energetic stabilities. We have already performed some analysis of a large distribution of UNPs, where their total energies are described using relatively affordable force field approach. Our analysis approaches include basic structural and electronic properties, where more accurate and computationally much more expensive, quantum mechanical description is necessary. In the course of the quantum mechanical analysis, we will have a feedback loop with experiment that analyze electronic and structural properties of UNPs using characterization tools such as EELS and NBEDs. Eventually the theory-experiment loop will continue in identifying structure evolution pathways and suggesting new experiments to refine the theoretical modeling.

Future Plans

Ultrasmall nanoparticles (UNPs) show very unique features and they can be used as building blocks for synthesis of other nanoscale materials. Therefore, identifying and understanding their structures, phases, and interactions are central to control synthesis of nanowires, nanoparticle assemblies, thin films, and 2D nanosheets from the UNPs. To address this challenge, our theoretical approach to explore a configuration space of molecules by combining efficient total energy calculations and computational optimizer algorithm will be further developed and applied to the UNPs building blocks. Once those intermediates or nanoclusters are identified for a given experimental condition, detailed analysis of their structural and electronic properties will be performed using state-of-the-art first-principles approaches, where theoretical results will be compared with experimental data such as HRTEM, XRD, EELS. Then, we will move forward to model processes of doping of UNPs and process of forming larger nanostructures through melting and sintering UNPs at high temperatures.

References

1. M. Tian, M. Mahjouri-Samani, G. Eres, R. Sachan, M. Yoon, M. F Chisholm, K. Wang, A. A Puretzky, C. M Rouleau, D. B Geohegan, G. Duscher "Structure and Formation Mechanism of Black TiO_2 Nanoparticles", *ACS Nano* **ASAP** Sep 22, 2015.
2. E. Inclan, D. Geohegan, and M. Yoon (to be submitted).
3. M. Matsui and M. Akaogi, *Mol. Simul.* 6, 239 (1991).

DoE Sponsored Publications in the Last Two Years

1. S. R. Wagner, B. Huang, C. Park, J. Feng, M. Yoon, and P. Zhang, "Growth of Metal Phthalocyanine on Deactivated Semiconducting Surfaces Steered by Selective Orbital Coupling", *Phys. Rev. Lett.* **115**, 096101 (2015).
2. B. Huang, H. Zhuang, M. Yoon, B. G. Sumpter, and S.-H. Wei, "Highly stable two-dimensional silicon phosphides: Different stoichiometries and exotic electronic properties", *Phys. Rev. B* **91**, 121401 (R) (2015).
3. M. Tian, M. Mahjouri-Samani, G. Eres, R. Sachan, M. Yoon, M. F Chisholm, K. Wang, A. A Puzetzky, C. M Rouleau, D. B Geohegan, G. Duscher "Structure and Formation Mechanism of Black TiO₂ Nanoparticles", *ACS Nano* **ASAP** Sep 22, 2015.
4. M. Tian, M. Mahjouri-Samani, G. Eres, R. Sachan, M. F Chisholm, K. Wang, A. A Puzetzky, C.M Rouleau, M.Yoon, D. B Geohegan, G. Duscher, "Phase Determination of Black TiO₂ Nanoparticles", *Microscopy and Microanalysis* **21** (S3), 815 (2015).
5. X. Li, L. Basile, B. Huang, C. Ma, J. Lee, I. V Vlassiuk, A. A Puzetzky, M.-W. Lin, M. Yoon, M. Chi, J. C Idrobo, C. M Rouleau, B. G Sumpter, D. B Geohegan, K. Xiao, "Van der Waals Epitaxial Growth of Two-Dimensional Single-Crystalline GaSe Domains on Graphene", *ACS Nano* **9**(8), 8078 (2015).
6. M. Mahjouri-Samani, M.-W. Lin, K. Wang, A. R Lupini, J. Lee, L. Basile, A. Boulesbaa, C. M Rouleau, A. A Puzetzky, I.N. Ivanov, K. Xiao, M. Yoon, D. B Geohegan, "Patterned arrays of Lateral Heterojunctions Within Monolayer Two-Dimensional Semiconductors", *Nat. Comm.* **6**, 7749 (2015).
7. A. Puzetzky, L. Liang, X. Li, K. Xiao, K. Wang, M. Mahjouri-Samani, L. Basile, J. C. Idrobo, B. G. Sumpter, V. Meunier, and D. B. Geohegan "Low-Frequency Raman Fingerprints of Two-Dimensional Metal Dichalcogenide Layer Stacking Configurations", *ACS Nano* **9**(6) 6333 (2015).
8. X. Li, L. A. Basile, M. Yoon, C. Ma, A. Puzetzky, J. Lee, J. Idrobo, M. Chi, C. Rouleau, D. B. Geohegan, and K. Xiao, "Revealing the preferred interlayer orientations and stackings of two-dimensional bilayer gallium selenide crystals", *Angew. Chemie Int. Ed.* **54**(9) 2712 (2015).
9. B. Huang, H.L. Zhuang, M. Yoon, B. G. Sumpter, "Highly stable two-dimensional silicon phosphides: different stoichiometries and exotic electronic properties", *Phys. Rev. B* **91**, 121401 (R) (2015).
10. M. H. Lahiani, J. Chen, F. Irin, A. A Puzetzky, M. J Green, M. V. Khodakovskaya, "Interaction of carbon nanohorns with plants: Uptake and biological effects", *Carbon*, **81**, 807 (2015).
11. C. M. Rouleau, A. A. Puzetzky, and D. B. Geohegan "Slowing of femtosecond laser-generated nanoparticles in a background gas", *Appl. Phys. Lett.* **105**(21), 213108 (2014).
12. K. L. Grosse, V. E. Dorgan, D. Estrada, J. D. Wood, I. Vlassiuk, G. Eres, J. W. Lyding, W. P. King, and E. Pop "Direct observation of resistive heating at graphene wrinkles and grain boundaries", *Appl. Phys. Lett.* **105**, (14) 143109 (2014).
13. M. Mahjouri-Samani, M. Tian, K. Wang, A. Boulesbaa, C. M. Rouleau, A.A. Puzetzky, M. A. McGuire, B. R. Srijanto, K. Xiao, G. Eres, G. Duscher, and D. B. Geohegan "Digital Transfer

- Growth of Patterned 2D Metal Chalcogenides by Confined Nanoparticle Evaporation” *ACS Nano* **8**(11), 11567 (2014).
14. A.A. Puztzky, I. A. Merkulov, C. M. Rouleau, G. Eres and D. B. Geohegan “Revealing the surface and bulk regimes of isothermal graphene nucleation and growth on Ni with in situ kinetic measurements and modeling” *Carbon* **79**, 256 (2014).
 15. M. Mahjouri-Samani, R. Gresback, M. Tian, K. Wang, A. A. Puztzky, C. M. Rouleau, G. Eres, I. N. Ivanov, K. Xiao and M. A. McGuire, "Pulsed Laser Deposition of Photoresponsive Two-Dimensional GaSe Nanosheet Networks" *Adv. Funct. Mat.* **24**, 6365 (2014).
 16. C. M. Rouleau, C.-Y. Shih, L. V. Zhigilei, A. A. Puztzky, and D. B. Geohegan, “Nanoparticle generation and transport resulting from femtosecond laser ablation of ultrathin metal films: Time-resolved measurements and molecular dynamics simulations” *Appl. Phys. Lett.* **104**, 193106 (2014).
 17. G. Eres, M. Regmi, C. M. Rouleau, J. Chen, I. N. Ivanov, A. A. Puztzky, and D. B. Geohegan, “Cooperative Island Growth of Large Area Single-Crystal Graphene by Chemical Vapor Deposition on Cu “ *ACS Nano* **8**(6), 5657 (2014).
 18. X. Li, M. Lin, A. A. Puztzky, J. C. Idrobo, C. Ma, M. Chi, M. Yoon, C. M. Rouleau, I. I. Kravchenko, D. B. Geohegan, and K. Xiao, “Controlled Vapor Phase Growth of Single Crystalline, Two-Dimensional GaSe Crystals with High Photoresponse”, *Scientific Reports* **4**, 5497 (2014).
 19. B.Huang, H-X. Deng, H.Lee, M. Yoon, B. G. Sumpter, F. Liu, S. C. Smith, and S.-H. Wei, "Exceptional Optoelectronic Properties of Hydrogenated Bilayer Silicene", *Phys. Rev. X* **4**, 021029 (2014).
 20. T. Callcott, H. H. Weitering and N. Mannella “Origins of electronic band gap reduction in Cr/N codoped TiO₂” *Phys. Rev. Lett.* **112**, 036404 (2014).
 21. A. A. Puztzky, D. B. Geohegan, S. Pannala, C. M. Rouleau, “Exploring growth kinetics of carbon nanotube arrays by in situ optical diagnostics and modeling” *SPIE LASE*, **8969** 896904 (2014).
 22. C. M. Rouleau, M. Tian, A. A. Puztzky, M. Mahjouri-Samani, G. Duscher, D. B. Geohegan, “Catalytic nanoparticles for carbon nanotube growth synthesized by through thin film femtosecond laser ablation,” *SPIE LASE* **8969**, 896907 (2014).
 23. L. Oakes, A. Westover, M. Mahjouri-Samani, S. Chatterjee, A. Puztzky, C. M. Rouleau, D. B. Geohegan, C. L. Pint, “Uniform, Homogenous Coatings of Carbon Nanohorns on Arbitrary Substrates from Common Solvents” *ACS Appl. Mater. Interfaces* **5**, 13153–13160 (2013).
 24. D. B. Geohegan, A. A. Puztzky, M. Yoon, G. Eres, C. Rouleau, K. Xiao, J. Jackson, J. Readle, M. Regmi, N. Thonnard, G. Duscher, M. Chisholm, K. More, “Laser Interactions for the Synthesis and In Situ Diagnostics of Nanomaterials” Ch. 7 in *Lasers in Materials Science*, pp: 143-173. Springer Series in Materials Science **191**, Springer International Publishing, Switzerland 2014.
 25. C. Parks Cheney, P. Vilmercati, E. W. Martin, M. Chiodi, L. Gavioli, M. Regmi, G. Eres, T. A. Callcott, H. H. Weitering and N. Mannella “Origins of electronic band gap reduction in Cr/N codoped TiO₂ “, *Phys. Rev. Lett.* **112**, 036404 (2014).

University Grants' Abstracts

Direct Oriented Growth of Armchair Graphene Nanoribbons on Germanium

Michael S. Arnold, Materials Science and Engineering, University of Wisconsin-Madison

Program Scope

The overarching objective of the present grant is to learn how to synthesize both monolayered and multilayered nanostructured graphene materials without highly detrimental etch-induced disorder and with exceptional properties – from the bottom-up via chemical vapor deposition (CVD). The proposed research is being carried out in 4 thrusts:

- A. Understanding the growth of unpatterned graphene on metal surfaces via CVD;
- B. Constricting the growth of monolayered graphene on the nanoscale from the bottom-up;
- C. Templating nanostructured multi-layered graphene and graphite from the bottom-up; and,
- D. Exploiting metal surfaces to catalyze the repair of the defective edges of nanostructured graphene.

Recent Progress

Progress in two areas will be highlighted.

1. Breakthrough in substrate-driven template-less graphene nanoribbon synthesis.

We have discovered an exciting, unexpected, powerful new route for synthesizing graphene nanoribbons. The synthesis overcomes roadblocks that have plagued the nanoribbon field and is performed on a Ge(001) surface.[1]

Overview: Graphene can be transformed from a semimetal into a semiconductor if it is confined into nanoribbons narrower than 10 nm with controlled crystallographic orientation and well-defined armchair edges. However, the scalable synthesis of nanoribbons with this precision directly on insulating or semiconducting substrates has not been possible. We have realized the bottom-up synthesis of graphene nanoribbons on Ge(001) via CVD. The nanoribbons are self-aligning, are self-defining with predominantly smooth armchair edges, and have tunable width to < 10 nm and aspect ratio to > 60.

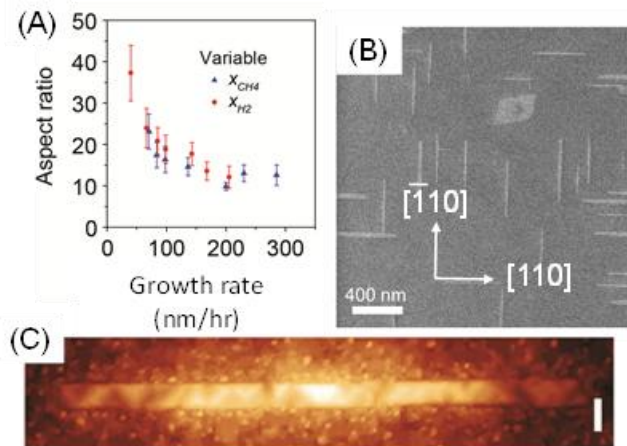


Fig. 1. Graphene nanoribbon CVD on Ge(001). (A) Crystal aspect ratio diverges as growth rate slows. (B) Ribbons self-align along crystallographic directions of Ge. (C) STM image of 10 nm wide nanoribbon on Ge. The features on the Ge surface are oxidation features arising from transfer from CVD to STM chambers in ambient.[1]

We have learned how to drive graphene crystal growth on Ge(001) with a giant anisotropy. At a vanishingly small growth rate, at high hydrogen partial pressure, and by using CH₄ as a precursor, graphene crystals evolve anisotropically, resulting in nanoribbons with high aspect ratio and smooth, straight edges. We find that the one-dimensional nature of growth is insensitive to the bulk Ge dopant concentration ($N_{Sb} < 1.5 \times 10^{18} \text{ cm}^{-3}$), Ge surface treatment prior to synthesis (OH, H, and Cl functionalization), and annealing time before growth. Nanoribbons are not observed on Ge(110) nor Ge(111) under any growth condition.

Low-energy electron microscopy (LEEM) and diffraction (LEED), in collaboration with the group of Richard Martel at the University of Montreal, have been used to determine the orientation of the graphene lattice with respect to the underlying Ge and with respect to the ribbon edges (Fig. 2A-D). The overlaid LEED patterns in Fig. 2A taken at 121 eV and 135 eV establish the Ge[110] and $[\bar{1}10]$ directions. The LEED pattern in Fig. 2B obtained at 67 eV shows that the graphene lattice primarily exists within two families of crystallographic orientations, denoted by the orange and purple hexagons. Both of these families of ribbons have edges that are macroscopically aligned with the armchair direction of graphene. This edge orientation is unique in that graphene crystals grown on Cu and Ni typically have edges that are aligned along the zigzag direction of graphene. Within each family, there are two unique graphene orientations that are rotated $2.9 \pm 0.4^\circ$ ($\sim 3^\circ$) relative to the Ge<110> directions, as indicated by the diffraction spots belonging to the orange family that are circled in red and blue in Fig. 2B. These nanoribbon orientations are depicted in Fig. 2D. Dark-field imaging in Fig. 2C indicates that some of the ribbons are single-crystalline, corresponding to either the $+3^\circ$ or -3° graphene orientation, whereas others are bi-crystalline, in which the crystal lattice of one half of the ribbon is rotated by $2 \times 3^\circ = 6^\circ$ with respect to the other half. This data indicates that the nanoribbons nucleate in their center and then grow in opposite directions along their length.

Ultra-high vacuum STM, in collaboration with the group of Nathan Guisinger at Argonne National Laboratory, has been used to substantiate the LEED data and to determine the atomic nature of the graphene nanoribbon edges on Ge(001). Using topographic data alone, we can set

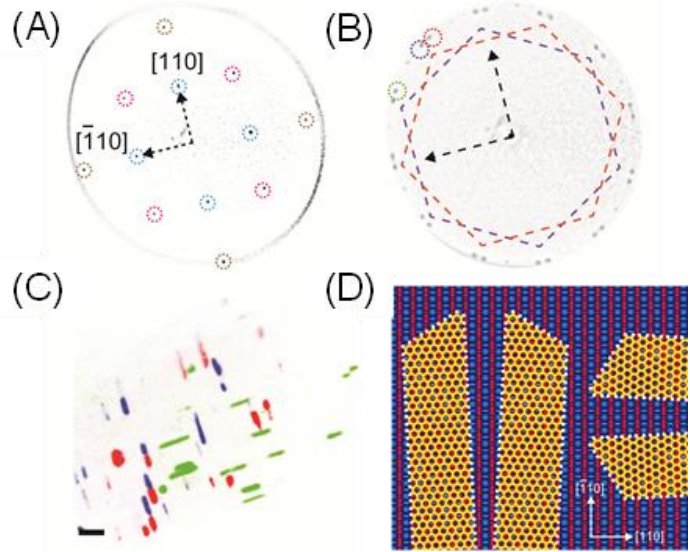


Fig. 2. Graphene nanoribbon CVD on Ge(001). (A-D) LEEM characterization of graphene nanoribbons on Ge(001). (A) Overlaid LEED patterns showing the {01} (cyan), {02} (brown), and {11} (magenta) diffracted beams from the unreconstructed Ge(001) surface. (B) LEED pattern obtained showing the purple and orange families of graphene orientations rotated by 30° and the splitting of the spots by 6° within each family. Arrows indicate the Ge<110> directions as shown in A. (C) Superposition of dark-field images of graphene nanoribbons on Ge(001) in which green, blue, and red channels of the image originate from the {01} graphene diffraction spots circled with the same color in B. Scale bar is 1 μm. (D), Schematic depicting the four nanoribbon orientations that are detected.[1]

an upper limit on the edge roughness. For example, the representative 40 nm ribbon segment in Fig. 1 has roughness of < 0.5 nm (two lattice constants of graphene). However, we can learn more about the edge structure from quantum interference patterns caused by inter-valley backscattering (not shown) of charge carriers at the ribbon edges. The presence of coherent interference patterns at edges combined with the small line edge roughness indicates that the edges consist primarily of smooth armchair segments.

Interestingly, the Ge surface selectively forms hill-and-valley structures below the nanoribbons and below continuous graphene films (not shown). The facet angle is shallow for thin ribbons and becomes steeper, as the ribbons grow wider and eventually merge to form a continuous graphene film, with an angle of about 8° , consistent with the Ge(107) facet.

This breakthrough is important because the synthesis of nanoribbons with armchair edges, the definition of ribbons with width < 10 nm, and the direct integration of nanoribbons onto insulating or semiconducting platforms have been difficult. Our direct, self-defining growth offers precise control over the ribbon structure beyond the fidelity of top-down lithography and yields a relatively pristine nanoribbon/substrate interface. The ribbons are self-aligning, and ribbons with $w < 10$ nm can still be hundreds of nanometers in length, opening the door for exploration of dense nanoribbon arrays as logic, photonic, and sensing components in integrated circuits. Improved control over the ribbon placement will enhance the viability of these applications. These results are also technologically important because they enable a scalable, high throughput pathway for integrating nanoribbons directly on conventional semiconductor wafer platforms that are compatible with planar processing, like Ge wafers and potentially epitaxial Ge films on Si or GaAs wafers.

2. Catalytic zigzag nanoribbon edge repair

We have pioneered a method to repair the disordered edges of graphene nanostructures (that have been lithographically patterned from the top-down) and convert them into relatively smooth zigzag edges via annealing on a Cu substrate.

Overview: Top-down subtractive lithography has previously been used to pattern graphene nanostructures which lack ideal properties due to (i) limited resolution and (ii) disordered edges. We have invented a method to convert such disordered edges into relatively smooth zigzag edges via annealing on a Cu substrate at ~ 950 °C (Fig. 3).[2] The Cu catalyzes the re-arrangement of graphene edge atoms to energetically favorable sites, inducing zigzag edge faceting. We exploit processes that are inherent to graphene CVD on Cu substrates to drive the edge repair, in particular, the fact that both growing and etching graphene domains show preference to the zigzag edge due to favorable energetics or kinetics.

Some of the foundations for achieving this nanoribbon edge repair have already been presented during previous Synthesis and Processing meetings. We first demonstrated proof of principle catalytic edge repair for graphene nanoribbons patterned on the surface of Cu foils. However, due to the polycrystalline nature of the foils, the process was not robust or repeatable and thus it was difficult to conduct a comprehensive study of the phenomenon.

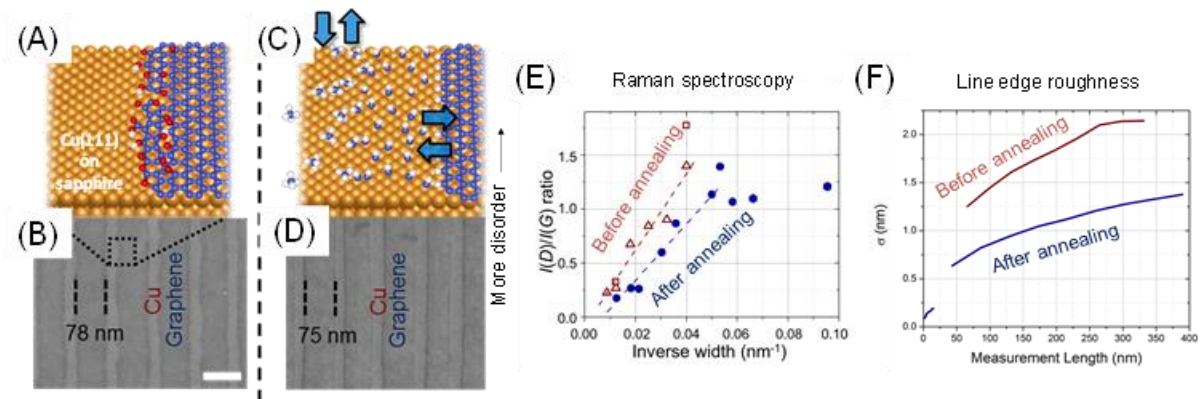


Fig. 3. Catalytic edge repair. Schematic (top) and SEM (bottom) of GNRs (A,B) after top-down patterning, and (C,D) after edge-annealing (SEM same magnification, scale bar = 100 nm). (E) Raman defect ratio $I(D)/I(G)$ vs. (nanoribbon width) $^{-1}$ for edge-annealed (blue) versus top-down patterned (red) graphene nanostructures. (F) Line edge roughness before and after annealing.[2]

Since then, we have demonstrated improved repeatability by conducting the experiments on Cu(111) thin films on sapphire rather than foils. Moreover, we have advanced our understanding of the etching and growth reaction mechanisms and intermediates during graphene CVD and during catalytic edge repair during which growth and etching reactions are balanced.[3] We have now combined these advances and conducted a complete study of nanoribbon edge repair.

In our complete study[2], we have shown that the dimensions of graphene nanostructures can be increased, decreased, or held constant (Fig. 3A-D) during annealing by tuning the relative balance between growth and etching, described by a fundamental growth rate equation. To demonstrate the flexibility of the method, we lithographically patterned graphene nanoribbons with zigzag or armchair orientations, or alternatively perforated graphene with circular holes, and then annealed these nanostructures to realize zigzag edge termination in each case, with nanostructure feature size tailored from 8 to 80 nm. The annealed nanostructures have smoother zigzag edges (~40% reduction in 1σ line edge roughness, Fig. 3E), and Raman spectroscopy confirms that they have lower edge disorder than top-down patterned samples (Fig. 3F). We expect these results, combined with next generation state-of-the-art lithography, will enable the wafer scale patterning of narrow graphene nanostructures with smooth zigzag edges, suitable for many applications.

Future Plans

We will focus on fundamental studies of the nucleation and growth of graphene and graphene nanoribbons on Ge. The goal will be to fundamentally understand the synthesis so that we can better control it.

References

1. Arnold MS et al., NATURE COMMUNICATIONS, 6, 8006 (2015).
2. Arnold MS et al., SOLID STATE COMMUNICATIONS, In Press (2015).
3. Arnold MS et al., JOURNAL OF MATERIALS CHEMISTRY C, 2, (14) pp 744-755 (2014).

Complete list of publications resulting from work supported by this grant over the previous two years (2013-2015)

1. **Jacobberger RJ, Arnold MS**, [*Graphene Growth Dynamics on Epitaxial Copper Thin Films*](#), CHEMISTRY OF MATERIALS, 25 (6), pp 871–877 (2013)
2. **Wu M-Y, Arnold MS**, [*Design Length Scales for Carbon Nanotube Photoabsorber Based Photovoltaic Materials*](#), JOURNAL OF APPLIED PHYSICS, 113, 204504 (2013)
3. **Safron NS, Arnold MS**, [*Experimentally-Determined Intermediate Hydrocarbon Species Model of Atmospheric-Pressure Chemical Vapor Deposition of Graphene on Cu*](#), JOURNAL OF MATERIALS CHEMISTRY C, 2, (14) pp 744-755 (2014)
4. Johnson PS, Huang C, Kim M, **Safron NS, Arnold MS**, Wong BM, Gopalan P, Himpsel FJ, [*Orientation of a Monolayer of Dipolar Molecules on Graphene from X-ray Absorption Spectroscopy*](#), LANGMUIR, DOI: 10.1021/la500183b (2014)
5. **Xu F, Wu M-Y, Safron NS, Singha Roy S, Jacobberger RM, Bindl DJ**, Seo J-H, Chang T-H, Ma Z, **Arnold MS**, [*Highly Stretchable Carbon Nanotube Transistors with Ion Gel Gate Dielectrics*](#) NANO LETTERS, 4 (2), pp 682–686 (2014)
6. Huang C, Kim M, Wong B, **Safron NS, Arnold MS**; Gopalan P, [*Raman Enhancement of a Dipolar Molecule on Graphene*](#), JOURNAL OF PHYSICAL CHEMISTRY C, 118 (4), pp 2077–2084 (2014)
7. **Brady G, Jacobberger R, Singha Roy S, Wall M, Arnold M**, [*Raman Imaging as a Tool for Characterizing Carbon Nanomaterials*](#), AMERICAN LABORATORY, (2014)
8. **Yumin Y, Bindl DJ, Jacobberger RM, Wu M-Y, Singha Roy S, Arnold MS**, [*Semiconducting Carbon Nanotube Aerogel Bulk Heterojunction Solar Cells*](#), SMALL, (2014)
9. Grechko M, **Ye Y**, Mehlenbacher R, McDonough T, **Wu M-Y, Jacobberger R, Arnold M**, Zanni, M, [*Diffusion Assisted Photoexcitation Transfer in Coupled Semiconducting Carbon Nanotube Thin Films*](#), ACS NANO, (2014)
10. **Brady G, Jacobberger R, Singha Roy S, Wall M, Arnold M**, [*Raman Imaging as a Tool for Characterizing Carbon Nanomaterials*](#), AMERICAN LABORATORY, (2014)
11. **Safron NS**, Choi JW, Kim M, **Shin N**, Gopalan P, **Arnold MS**, [*Zigzag faceting and width refinement of graphene nanoribbons and nanoporations via catalyzed edge-annealing on Cu\(111\)*](#), SOLID STATE COMMUNICATIONS, In Press (2015)
12. **Jacobberger RM**, Kiraly B, Fortin-Deschenes M, Levesque PL, McElhinny KM, **Brady GJ**, Rojas Delgado R, **Singha Roy S**, Mannix A, Lagally MG, Evans PG, Desjardins P, Martel R, Hersam MC, Guisinger NP, **Arnold MS**, [*Direct Oriented Growth of Armchair Graphene Nanoribbons on Germanium*](#), NATURE COMMUNICATIONS, 6, 8006 (2015)

13. **Jacobberger RM**, Machhi R, Wroblewski J, Taylor B, Gillian-Daniel AL, **Arnold MS**, [*Simple Graphene Synthesis via Chemical Vapor Deposition*](#), JOURNAL OF CHEMICAL EDUCATION, 10.1021/acs.jchemed.5b00126 (2015)
14. **Jacobberger RM**, Levesque P, Xu F, Wu M-Y, Choubak S, Desjardins P, Martel R, **Arnold MS**, [*Tailoring the Growth Rate and Surface Facet for Synthesis of High-Quality Continuous Graphene Films from CH₄ at 750 °C via Chemical Vapor Deposition*](#), JOURNAL OF PHYSICAL CHEMISTRY C, 119 (21), pp 11516-11523 (2015)
15. **Wu M-Y, Zhao J, Xu F**, Chang T-H, **Jacobberger RM**, Ma Z, **Arnold MS**, [*Highly Stretchable Carbon Nanotube Transistors Enabled by Buckled Ion Gel Gate Dielectrics*](#), APPLIED PHYSICS LETTERS, 107, 053301 (2015)
16. Kiraly B, **Jacobberger RM**, Mannix A, Campbell G, Bedzyk M, **Arnold MS**, Hersam MC, Guisinger NP, SUBMITTED (2015).

Studies of Surface Reaction and Nucleation Mechanisms in Atomic Layer Deposition

Stacey F. Bent
sbent@stanford.edu
Department of Chemical Engineering
Stanford University, Stanford, CA 94305

Program Scope

The overarching goal of this program is to understand the fundamental mechanisms of nucleation and growth in atomic layer deposition (ALD). ALD, a method for depositing thin films of numerous semiconducting, insulating and metallic materials using an alternating series of self-limiting reactions between gas phase precursors and the substrate, is proving to be an enabling technique for creating the innovative nanostructured materials needed for future applications, including those in solar energy and photoelectrocatalysis. Despite its growing technological importance, a fundamental, molecular-level understanding of most ALD processes is still lacking.

This project applies both experimental and theoretical methods to uncover surface reaction and nucleation mechanisms active during ALD. A combination of *in situ*, *in vacuo*, and *ex situ* X-ray photoelectron spectroscopy, infrared spectroscopy, synchrotron radiation photoelectron spectroscopy, and synchrotron radiation X-ray diffraction (XRD) and X-ray scattering studies are employed, together with complementary theory and modeling. We provide new mechanistic insights in representative ALD systems: those of metals (e.g. Pt, Ru) as well as those of binary and ternary metal oxides. The work aims to provide the scientific foundation required for the ultimate design and synthesis of new materials for applications in energy, electronics, and catalysis.

Recent Progress

Our results over the past two years have introduced several new insights into the mechanisms of nucleation and growth in both metal and metal oxide ALD, as described below. We also completed the construction of various instruments for performing *in situ* measurements (XRD, X-ray scattering, XPS, and IR) and have expanded our toolbox of *ex situ* techniques and analyses of ALD processes as well.

Understanding and Controlling Metal Nucleation by ALD

Over the past year, we continued fundamental studies aimed at understanding the processes of nucleation and growth during metal ALD. Our work explored several directions: nucleation of Pt on graphene substrates, the effect of more reactive counter-reactants on Pt ALD, and the nature of epitaxial Pt deposition on single crystal SrTiO₃.

Expanding upon our earlier studies of Pt ALD on highly ordered pyrolytic graphite (HOPG), we investigated the role of the substrate on Pt nucleation by studying ALD on graphene. We demonstrated the selective deposition of metal at the line defects of graphene, notably grain boundaries, by ALD, as confirmed by electron microscopy (Figure 1).

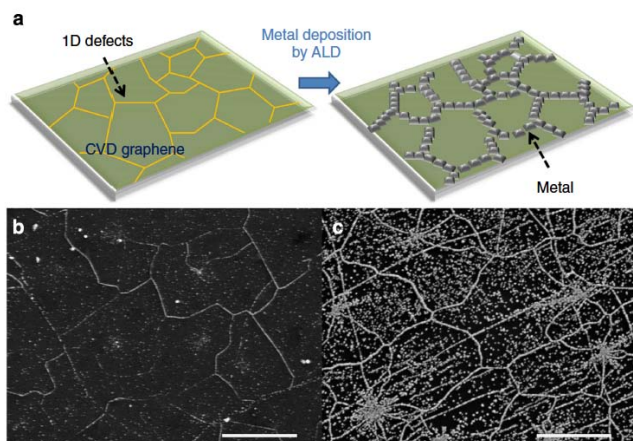


Figure 1. Selective Pt growth by ALD on one-dimensional defect sites of polycrystalline CVD graphene. (a) Schematic; (b) and (c) SEM images of CVD graphene on a glass substrate after 500 ALD cycles and 1000 ALD cycles of Pt deposition, respectively.

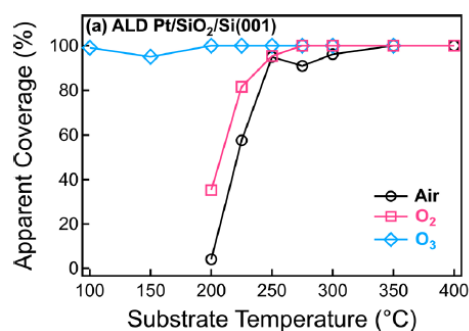


Figure 2. Apparent coverage measured by SEM versus substrate temperature of 400 cycles of Pt ALD using three counter reactants. ALD with O₃ can occur at temperatures as low as 100°C.

We showed that Pt is deposited predominantly on graphene's grain boundaries, folds and cracks due to the enhanced chemical reactivity of these line defects. The Pt-decorated graphene samples were then tested for hydrogen gas sensing at room temperature, in collaboration with the group of Prof. Zhenan Bao. The results show that selective functionalization of graphene defect sites, together with the nanowire morphology of the deposited Pt, yields improvements in sensing applications.

To understand if nucleation difficulties could be mitigated by more reactive counter reactants, we probed the effect of ozone on nucleation and growth during Pt ALD. Looking first at growth on SiO₂, we showed that O₃ leads to a higher growth rate than that using either air or O₂ counter reactants, and also enables ALD at lower deposition temperatures (as low as 100 °C, see Figure 2). Interestingly, Pt ALD using air on an O₃-pretreated surface showed almost the same growth rate as Pt ALD using O₃. The data indicate that O₃ strongly affects the surface species toward fast nucleation of Pt.

We also showed that ozone has a strong effect on Pt nucleation on graphite. As we have reported previously, ALD Pt using O₂ is selectively deposited on the intrinsic step edges because the step edge sites are much more active for Pt nucleation than the basal planes. In contrast to O₂, a continuous Pt film is obtained on the HOPG surface when O₃ is used (Figure 3). Pretreatment of the graphite by O₃ prior to Pt ALD using an O₂ reactant shows a similar, continuous Pt film morphology to that obtained from the full O₃-based ALD process. Our analysis revealed that O₃ etches the graphite surface and generates pits containing additional step edges, resulting in an increase of Pt nucleation. The nucleation of Pt is less active at lower deposition temperatures because the generation of additional step edges is dependent on temperature. This Pt ALD process using a reactive O₃ reactant can be an effective route to fabricate uniform and continuous Pt films on 3D carbon substrates.

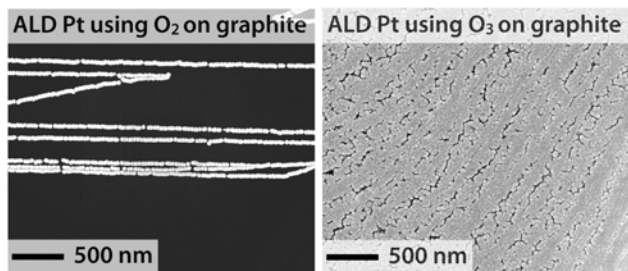


Figure 3. SEM images following 400 cycles of Pt ALD on graphite using O_2 compared with that using O_3 .

We also examined the epitaxial growth of Pt deposited by atomic layer deposition on single crystal $SrTiO_3$ substrates, as characterized using 2D grazing incidence x-ray diffraction (GIXRD) at SSRL. The orientation of the Pt thin film was determined by combining a series of GIXRD images to generate a Pt(111) pole figure. For $SrTiO_3$ [001] substrates, epitaxial growth was observed along with randomly oriented growth. For $SrTiO_3$ [101] substrates,

epitaxial growth and Pt [111] oriented fiber texture were observed. Six peaks within the Pt [111] fiber texture ring are present indicating preferential alignment with the substrate to minimize the energy at the Pt / $SrTiO_3$ interface.

Mechanistic Studies of Ternary Metal Oxide ALD

With the rapid expansion of potential applications of ALD materials, there is increasing interest in ALD processes that go beyond the deposition of binary materials to allow for the synthesis of alloyed, doped, ternary, or quaternary materials. However, for ALD of such materials, typically achieved by combining multiple binary ALD processes, it is often difficult to correlate the material properties and growth characteristics with the process parameters due to a limited understanding of the underlying surface chemistry.

We investigated growth of zinc tin oxide (ZTO) as a model system for ALD of ternary materials. ZTO films were deposited by alternating growth of tin oxide (SnO_x) and zinc oxide (ZnO) with tetrakis(dimethylamino)tin and diethylzinc precursors and water counter reactant. We showed that the growth rate of ZTO is strongly reduced as compared to the growth rates of the binaries, especially at low bilayer periods and low tin cycle fractions. By combining DFT calculations and *in situ* quadrupole mass spectrometry (QMS), we showed that the ZnO growth rate is reduced when SnO_x layers are inserted, with a significant reduction in surface reaction site density during even a single SnO_x cycle. DFT results suggest one possible explanation for the decrease in growth rate: it may be a consequence of the four exchangeable ligands of the TDMASn precursor used in SnO_x growth compared to the two ligands of the DEZn precursor used in the ZnO cycles. Another possible explanation is ligand poisoning. By gas-phase Fourier transform infrared (FTIR) spectroscopy, the dimethylamine product of the SnO_x ALD process is observed not only during SnO_x ALD but also when depositing ZnO after SnO_x , indicating incomplete removal of the ligands of the tin precursor from the surface. These remaining ligands may poison the surface against further reaction, and thereby contribute to the observed nucleation delay for ZnO ALD during the deposition of ZTO. The correlation between precursor molecular structure and materials growth that we established for the ZTO system will likely apply to other ALD processes where precursors follow ligand-exchange surface chemistries as well.

Another important question in ternary metal oxide ALD is how well mixed the constituents are in the film. The extremely surface sensitive technique of low energy ion scattering (LEIS) was applied to the ZTO ALD model system to address this question. At the low temperatures used for

deposition (150°C) there is little evidence for atomic scale mixing even with the smallest possible bilayer period, and instead a morphology with small ZnO inclusions in a SnO_x matrix is deduced. Post-annealing of such laminates above 400 °C however produces a stable surface phase, likely the inverted spinel of zinc stannate, Zn₂SnO₄, with a 30% increased density. Further annealing to 800 °C results in films containing crystalline Zn₂SnO₄, or multilayered films of crystalline ZnO, Zn₂SnO₄ and SnO₂ phases, depending on the bilayer period.

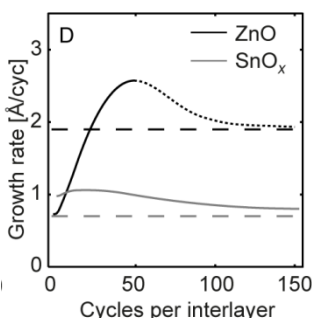


Figure 4. Instantaneous growth rates extracted from ellipsometry. Steady state binary growth rates indicated by dashed horizontal lines.

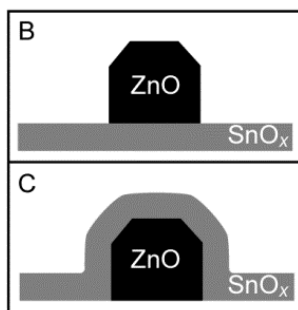


Figure 5. Illustration of suggested island type growth mode of ZnO on SnO_x, and layer-by-layer type growth of SnO_x on ZnO.

The instantaneous growth rates of ZnO on SnO_x and SnO_x on ZnO were measured as a function of number of cycles past the interface. Mechanistically, the behavior in Figure 4 may be understood as a consequence of a limited number of nucleation sites found on the SnO_x surface, which initially suppresses the growth rate of the ZnO.

Eventually the surface area of the growing ZnO islands surpasses that of a corresponding planar growth surface, temporarily leading to a higher growth rate compared to steady state. As the islands coalesce into a film after additional interlayer cycles, the steady state growth rate will be approached. The latter is illustrated by the drawn, dotted part of the curve in Figure 4. Interestingly, the initial SnO_x growth exceeds the steady state growth rate observed for thicker films. We conclude that ZnO initially nucleates more slowly by island type growth on SnO_x than on ZnO, and conversely that SnO_x grows faster on ZnO than on SnO_x by layer-by-layer type growth (see illustration in Figure 5), due to varying densities of hydroxylated surface sites available on these surfaces and surface poisoning by persisting tin precursor ligands.

Future Plans

We will seek a deeper understanding of ALD mechanisms in metal, metal oxide, and metal sulfide systems. We plan to extend our studies of ALD on different substrates, including those of 2D materials such as MoS₂ or WS₂. The results from these studies are intended to help us to discover strategies for enhancing the nucleation of ALD on technologically-important surfaces for production of uniform ultra-thin films, which remains a key challenge in the field. We will also continue to build our program on mechanistic studies of alloyed, doped, ternary, and quaternary metal oxide ALD, which have many interesting materials properties as well as many unanswered questions as to their nucleation, growth and degree of intermixing. We will also explore a new research direction: the synthesis of 2D materials via ALD. 2D materials such as MoS₂ are currently of great interest due to their important electronic properties as well as catalytic activity, and synthesizing thin film coatings of these 2D materials opens many interesting possibilities. However, there is almost nothing known about the mechanism of film formation, and we will perform studies to elucidate the steps by which both in-basal-plane and out-of-plane bonds form and propagate.

DoE Sponsored Publications in the Last Two Years

1. “Thin film characterization of zinc tin oxide deposited by thermal atomic layer deposition,” M. N. Mullings, C. Hägglund, J. T. Tanskanen, Y. Yee, S. Geyer, and S. F. Bent, *Thin Solid Films*, **556** (2014) 186–194
2. “Correlating growth characteristics in atomic layer deposition with precursor molecular structure: the case of zinc tin oxide,” J. T. Tanskanen, C. Hägglund, and S. F. Bent, *Chem. Mat.* **556** (2014) 186-194, [dx.doi.org/10.1021/cm403913r](https://doi.org/10.1021/cm403913r).
3. “Atomic layer deposition of metal at graphene line defects,” K. Kim[†], H. B. R. Lee[†], R. W. Johnson, J. T. Tanskanen, N. Liu, M. G. Kim, C. Pang, C. Ahn, S. F. Bent, and Z. Bao, *Nature Commun.*, **5**:4781 (2014), [10.1038/ncomms5781](https://doi.org/10.1038/ncomms5781).
4. “Effect of O₃ on growth of Pt by atomic layer deposition,” H. B. R. Lee, K. L. Pickrahn, and S. F. Bent, *J. Phys. Chem. C*, **118** (2014) 12325–12332, [dx.doi.org/10.1021/jp502596n](https://doi.org/10.1021/jp502596n).
5. “Structural evolution of platinum thin films grown by atomic layer deposition,” S. M. Geyer, R. Methaapanon, R. W. Johnson, S. Brennan, M. F. Toney, B. M. Clemens, and S. F. Bent *J. Appl. Phys.*, **116** (2014) 064905, [dx.doi.org/10.1063/1.4892104](https://doi.org/10.1063/1.4892104).
6. “An atomic layer deposition chamber for in situ X-ray diffraction and scattering analysis,” S. M. Geyer, R. Methaapanon, R. W. Johnson, D. G. Van Campen, A. Metha, and S. F. Bent, *Rev. Sci. Instrum.*, **85** (2014) 055116, <http://dx.doi.org/10.1063/1.4876484>.
7. “A brief review of atomic layer deposition: from fundamentals to applications,” R. W. Johnson, A. Hultqvist, and S. F. Bent, *Materials Today*, Invited Review Article, **17** (2014) 236-246, [dx.doi.org/10.1016/j.mattod.2014.04.026](https://doi.org/10.1016/j.mattod.2014.04.026).
8. “Formation of continuous Pt films on the graphite surface by atomic layer deposition with reactive O₃,” H. B. R. Lee and S. F. Bent, *Chem. Mat.* (2015) doi: [10.1021/acs.chemmater.5b03076](https://doi.org/10.1021/acs.chemmater.5b03076)
9. “Epitaxial atomic layer deposition of platinum on strontium titanate characterized by grazing incidence x-ray diffraction,” S. M. Geyer, R. W. Johnson, A. Mehta, and S. F. Bent, submitted.
10. “Thermal adsorption-enhanced atomic layer etching of Si₃N₄,” W. H. Kim, D. Sung, S. Oh, J. Woo, S. Lim, H. Lee and S. F. Bent, submitted.
11. Growth, intermixing and surface phase formation for zinc tin oxide thin film laminates produced by atomic layer deposition, C. Hägglund, T. Grehl, J. T. Tanskanen, Y. Yee, M. N. Mullings, A. J.M. Mackus, C. MacIsaac, B. M. Clemens, H. H. Brongersma, and S. F. Bent, to be submitted.

Molecule–Sorbent Interactions in Metal Organic Framework Materials

Kui Tan, Erika Fuentes, **Y. J. Chabal**, University of Texas at Dallas
Debasis Banerjee, Benjamin J. Deibert, Hao Wang, **Jing Li**, Rutgers University
Pieremanuele Canepa, Sebastian Zuluaga, **Timo Thonhauser**, Wake Forest University

Program Scope

The aim of this program is to develop a fundamental understanding of the interaction of guest molecules such as H₂, CO₂, N₂, and CH₄ in porous metal organic framework (MOF) materials, using a combination of novel synthesis, *ab initio* modeling, and characterization. In particular, we combine high-pressure/low-temperature *in-situ* infrared (IR) absorption and Raman measurements with gas adsorption-desorption experiments and calculations based on density functional theory, to study molecular interactions in different MOF materials. One of the goals is to provide insight concerning the role of unsaturated metal centers in enhancing molecular uptake, selective adsorption, and diffusion. The short-term impact of the proposed work is the control and understanding of common MOF systems, making it possible to determine the theoretical loading limits and stability of a specific class of materials. The long-term impacts are the development of 1) theoretical and experimental methods to gain a fundamental understanding of molecular interactions within MOFs, and 2) new guidelines to synthesize microporous MOFs with tailored molecular binding, selectivity, and other targeted functionalities.

Recent Progress

a) *Structural, elastic, thermal, and electronic responses of small-molecule-loaded metal-organic framework materials [1]* –

We have combined infrared spectroscopy, nano-indentation measurements, and *ab initio* simulations to study the evolution of structural, elastic, thermal, and electronic responses of the metal organic framework MOF-74-Zn when loaded with H₂, CO₂, CH₄, and H₂O. We find that the molecular adsorption in this MOF triggers remarkable responses in all of these properties of the host material, with specific signatures for each of the guest molecules. With this comprehensive study we are able to clarify and correlate the underlying mechanisms regulating these responses with changes of the physical and chemical environment. Our findings suggest that metal organic framework materials in general, and MOF-74-Zn in particular, can be very promising materials for novel transducers and sensor applications, including highly selective small-molecule detection in gas mixtures. This work was featured on the cover page of J. Mater. Chem. A – see Figure 1.

b) *Water reaction mechanism in metal organic frameworks with coordinatively unsaturated metal ions: MOF-74 [2,3]* – Water dissociation represents one of the most important reactions in catalysis. However, its mechanism on most oxide surfaces is not well understood due to the experimental challenges of preparing surface structures and characterizing reaction pathways. We proposed the metal organic framework MOF-74 as an ideal model system to study water reactions. Combining *in situ* IR spectroscopy and *ab initio* calculations, we explored the MOF-

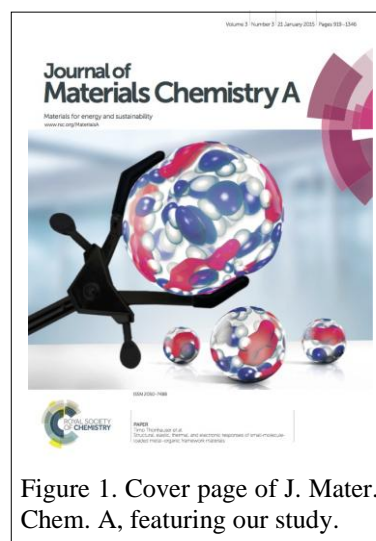


Figure 1. Cover page of J. Mater. Chem. A, featuring our study.

74/water interaction as a function of vapor pressure and temperature. We showed that, while adsorption is reversible below the water condensation pressure at room temperature, a reaction takes place at ~ 150 °C even at low water vapor pressures. This important finding is unambiguously demonstrated by a sharp absorption band that appears at 970 cm^{-1} when D_2O is introduced above 150 °C, which we attribute to an O–D bending vibration on the phenolate linker

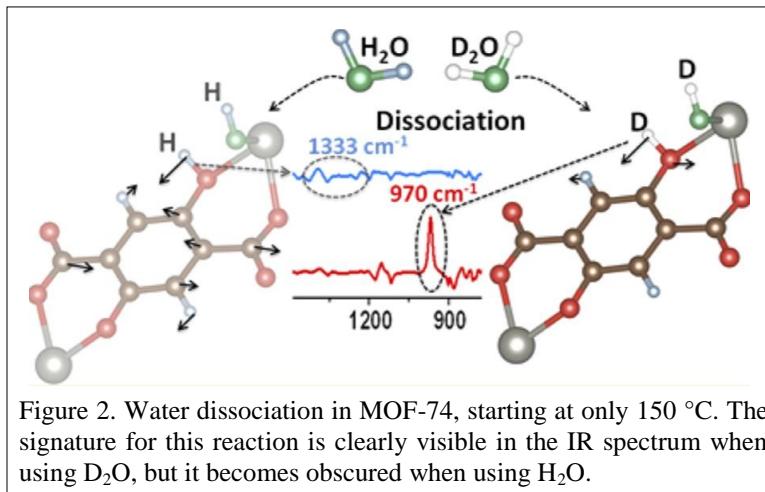


Figure 2. Water dissociation in MOF-74, starting at only 150 °C. The signature for this reaction is clearly visible in the IR spectrum when using D_2O , but it becomes obscured when using H_2O .

(see **Error! Reference source not found.**). Although H_2O undergoes a similar dissociation reaction, the corresponding O–H mode is too strongly coupled to MOF vibrations to detect. *Ab initio* calculations could identify the O–D mode at 970 cm^{-1} and derived a pathway and kinetic barrier for the reaction: the D (H) atom is transferred to the oxygen of the linker phenolate group, producing the notable O–D absorption band at 970 cm^{-1} , while the OD (or OH) binds to the open metal sites. This novel mechanism for water dissociation adds to the understanding of molecular water interaction with cation-exposed surfaces to enable development of more efficient catalysts for water dissociation.

c) Competitive co-adsorption of CO_2 with H_2O , NH_3 , SO_2 , NO , NO_2 , N_2 , O_2 , and CH_4 in M-MOF-74 ($M = \text{Mg}$, Co , Ni): the role of hydrogen bonding [4] – By examining the competitive co-adsorption of several small molecules in M-MOF-74 ($M = \text{Mg}$, Co , Ni) with *in-situ* infrared spectroscopy and *ab initio* simulations, we find that the binding energy at the most favorable (metal) site is not a sufficient indicator for prediction of molecular adsorption and stability in MOFs. Instead, the occupation of the open metal sites is governed by kinetics, whereby the interaction of the guest molecules with the MOF organic linkers controls the reaction barrier for molecular exchange. Specifically, the displacement of CO_2 adsorbed at the metal center by other molecules such as H_2O , NH_3 , SO_2 , NO , NO_2 , N_2 , O_2 , and CH_4 is mainly observed for H_2O and NH_3 , even though SO_2 , NO , and NO_2 have higher binding energies than CO_2 and H_2O . *Ab initio* simulations evaluated the barriers for the $\text{H}_2\text{O} \rightarrow \text{CO}_2$ and $\text{SO}_2 \rightarrow \text{CO}_2$ exchange to be 13 and 20 kJ/mol, respectively, explaining the slow exchange of CO_2 by SO_2 , compared to water. Furthermore, the calculations revealed that the kinetic barrier for this exchange is determined by the specifics of the interaction of the second guest molecule (e.g., H_2O or SO_2) with the MOF ligands. Similar considerations apply to the other molecules, accounting for much easier CO_2 exchange with NH_3 than with NO , NO_2 , CH_4 , O_2 , and N_2 molecules. In this work, critical parameters such as kinetic barrier and exchange pathway were unveiled and provided insight into the mechanism of competitive co-adsorption, underscoring the need of combined studies to uncover the atomistic interactions influencing co-adsorption of small molecules in MOFs.

d) The first case of commensurate adsorption of atomic gas in a microporous MOF which exhibits the highest selectivity of xenon over other noble gases [5] – In industry, cryogenic rectification for separating xenon from other noble gases such as krypton and argon is an energy and capital intensive process. We showed that a microporous metal-organic framework (MOF), namely $\text{Co}_3(\text{HCOO})_6$ is capable of effective capture and separation of xenon from other noble

gases. Henry's constant, isosteric heats of adsorption (Q_{st}), and IAST selectivity were calculated based on single component sorption isotherms. With the highest Q_{st} reported to date, $\text{Co}_3(\text{HCOO})_6$ demonstrates high adsorption capacity for xenon and highest IAST selectivity for Xe-Kr among all MOFs investigated so far. To mimic real world conditions, breakthrough experiments were conducted on Xe-Kr binary mixtures at room temperature and 1 atmosphere. The results were consistent with the calculated data. Our gas adsorption measurements and molecular simulation study also revealed that xenon could be adsorbed, representing the first example of commensurate adsorption of atomic gases near ambient conditions.

e) *Distinct reversible colorimetric and fluorescent low pH response on a water-stable zirconium-porphyrin metal-organic framework* [6] – We synthesized a water-stable zirconium-porphyrin MOF (PCN-222) and investigated its reversible colorimetric and fluorescent “turn-off-turn-on” pH response. The tcpp ligand in the mesoporous framework is the main reason for the very sensitive optical signal. The colorimetric response was achieved under acidic conditions starting at $\text{pH} = \sim 3$ and persisted under concentrated acidic conditions. The sensitive optical response properties of the soluble porphyrin-derivative molecular species could be realized in an easily accessible and stable, solid-state single-phase bulk material and without the formation of aggregates. Additionally, we showed that the material has the advantage of full reversibility and reusability that outperforms its molecular analogues and is highly suitable to act as both a luminescent as well as colorimetric solid-state sensor for the low pH values covering a relatively wide pH range. To the best of our knowledge, this is the first report of a colorimetric MOF pH sensor. This work was featured on the front cover of Chem. Comm.

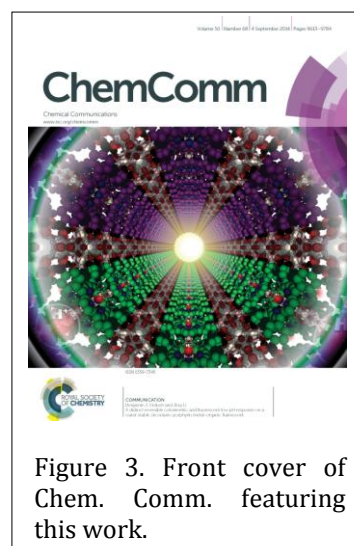


Figure 3. Front cover of Chem. Comm. featuring this work.

f) *Porous luminescent MOFs for explosive sensing* [7,8] – We designed, synthesized, and structurally characterized a group of luminescent metal-organic frameworks (LMOFs) with closely related structures. Engineering one of the ligand with different functional groups led to distinct porosity and luminescent properties of these compounds, which drastically affected their sensing performances. The effective detection of high explosive RDX with extremely low vapor pressure was achieved by an indirect route via fast and highly sensitive sensing of a ketone vapor that inevitably co-exists in the explosive product. IR spectroscopic and guest sorption studies show that LMOF-121 interacts more strongly with acetone than with cyclic ketones as a result of size compatibility. On the other hand, LMOF-202 adsorbs other ketones more strongly than LMOF-121. The effects of electron and energy transfer processes on both fluorescence enhancement (by ketones) and quenching (by DNT) were elucidated for LMOF-202, by comparing to LMOF-121 with similar porosity but different electronic structure. Tuning the porosity and electronic properties specifically towards a detection target could significantly improve sensitivity and selectivity. Such a strategy can be very helpful in designing highly efficient sensory materials.

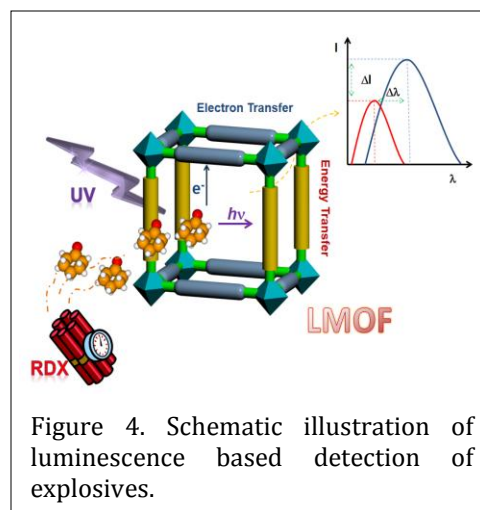


Figure 4. Schematic illustration of luminescence based detection of explosives.

References

- [1] P. Canepa, K. Tan, Y. Du, H. Lu, Y. J. Chabal, and T. Thonhauser, *Structural, elastic, thermal, and electronic responses of small-molecule-loaded metal-organic framework materials*, *J. Mater. Chem. A* **3**, 986 (2015).
- [2] K. Tan, N. Nijem, Y. Gao, S. Zuluaga, J. Li, T. Thonhauser, and Y. J. Chabal, *Water interactions in metal organic frameworks*, *Cryst. Eng. Comm.* **17**, 247 (2015).
- [3] K. Tan, S. Zuluaga, Q. Gong, P. Canepa, H. Wang, J. Li, Y.J. Chabal, and T. Thonhauser, *Water reaction mechanism in metal organic frameworks with coordinatively unsaturated metal ions: MOF-74*, *Chem. Mater.* **26**, 6886 (2014).
- [4] K. Tan, S. Zuluaga, Q. Gong, Y. Gao, N. Nijem, J. Li, T. Thonhauser, and Y. J Chabal, *Competitive coadsorption of CO₂ with H₂O, NH₃, SO₂, NO, NO₂, N₂, O₂, and CH₄ in M-MOF-74 (M = Mg, Co, Ni): The role of hydrogen bonding*, *Chem. Mater.* **27**, 2203 (2015).
- [5] H. Wang, K. X. Yao, Z. J. Zhang, J. Jagiello, Q. H. Gong, Y. Han, and J. Li, *The first example of commensurate adsorption of atomic gas in a MOF and effective separation of xenon from other noble gases*, *Chem. Sci.* **5**, 620 (2014).
- [6] B. J. Deibert and J. Li, *Distinct reversible colorimetric and fluorescent low pH response on a water-stable zirconium-porphyrin metal-organic framework*, *Chem. Comm.* **50**, 9636 (2014).
- [7] Z. C. Hu, K. Tan, W. P. Lustig, H. Wang, Y. G. Zhao, C. Zheng, D. Banerjee, Q. H. Gong, T. J. Emge, Y. J. Chabal, and J. Li, *Effective sensing of RDX via instant and selective detection of ketone vapors*, *Chem. Sci.* **5**, 4873 (2014).
- [8] D. Banerjee, Z. C. Hu, and J. Li, *Luminescent metal-organic frameworks as explosive sensors*, *Dalton. Transac.* **43**, 10668 (2014), invited perspective article.

Future Plans

Our studies have shown that there are three fundamental roadblocks to the development of MOFs for novel applications: synthesis methods, ability to incorporate species post processing (mass transport), and charge transfer mechanisms between host and guest; we plan to tackle all three issues. For synthesis, we will focus on a systematic approach using pre-formed metal precursors (clusters) and tailored ligands with targeted functionalities instead of using simple metal salts. This novel approach will be supported by *ab initio* calculations and spectroscopic studies to provide direct guidance on synthesis optimization. Second, we will explore the diffusion of a variety of species in MOFs, from small gas phase molecules to ions in solution. This will involve *ab initio* molecular dynamics simulations and transition-state searches, which will identify the “bottlenecks” to diffusion and thus provide guidelines for the synthesis of novel MOFs with better diffusion properties. Furthermore, we will carry out an in-depth study to investigate the effect of guest molecules on MOFs via changes in optical behavior such as luminescence signal changes. We also plan to incorporate catalytic activity by incorporating molecular catalysts within the MOF, guided in the best choices for active metal and ligands by *ab initio* simulations. Finally, we will examine the interaction of molecular species with the MOF host to understand the mechanism of charge transfer from or into the framework. These phenomena have a strong impact on properties such as luminescence, photo-reactions, and photocatalysis.

DOE Sponsored Publications in the Last Two Years (9/2013 – 9/2015)

1. H. H. Wu, C. G. Thibault, H. Wang, K. A. Cychosz, M. Thommes, and J. Li, *Effect of temperature on hydrogen and carbon dioxide adsorption hysteresis in an ultramicroporous MOF*, Micopor. Mesopor. Mat. **219**, 186 (2016), online 9/15.
2. T. Thonhauser, S. Zuluaga, C. A. Arter, K. Berland, E. Schröder, and P. Hyldgaard, *Spin signature of nonlocal correlation binding in metal-organic frameworks*, Phys. Rev. Lett. **115**, 136402 (2015).
3. B. J. Deibert, J. M. Zhang, P. F. Smith, K. W. Chapman, S. Rangan, D. Banerjee, K. Tan, H. Wang, N. Pasquale, F. Chen, K. B. Lee, G. C. Dismukes, Y. J. Chabal, and J. Li, *Highly active 'polytype-birnessite' MnO_x water oxidation catalyst formed in-situ from Mn^{II}₄O₄ MOF precursor: Structural investigation of an amorphous catalyst*, Chem. Eur. J. **21**, 13218 (2015).
4. K. Tan, S. Zuluaga, Y. Gao, Q. Gong, N. Nijem, J. Li, T. Thonhauser, and Y. J. Chabal, *Competitive co-adsorption of CO₂ with H₂O, NH₃, SO₂, NO, NO₂, N₂, O₂, CH₄ in M-MOF-74 (M = Mg, Co, Ni): The role of hydrogen bonding*, Chem. Mater. **27**, 2203 (2015).
5. P. Canepa, K. Tan, Y. J. Du, H. B. Lu, Y. J. Chabal, and T. Thonhauser, *Structural, elastic, thermal, and electronic responses of small-molecule-loaded metal-organic framework materials*, J. Mater. Chem. **3**, 986 (2015), selected as "HOT" article for 2015.
6. S. Zuluaga, L.-H. Liu, N. Shafiq, S. M. Rupich, J.-F. Veyan, Y. J. Chabal, and T. Thonhauser, *Structural band-gap tuning in g-C₃N₄*, Phys. Chem. Chem. Phys. **17**, 957 (2015).
7. K. Tan, N. Nijem, Y. Gao, S. Zuluaga, J. Li, T. Thonhauser, and Y. J. Chabal, *Water interaction in metal organic framework*, Cryst. Eng. Comm. **17**, 247 (2015).
8. D. Banerjee, H. Wang, B. J. Deibert, and J. Li, *Alkaline earth metal based metal-organic frameworks: Synthesis, properties, and applications*, in The Chemistry of Metal-Organic Frameworks, Edited by Stefan Kaskel (Wiley-VCH, 2015).
9. Z. Hu, K. Tan, H. Wang, Y. Zhao, C. Zheng, D. Banerjee, Q. Gong, T. J. Emge, Y. J. Chabal, and J. Li, *Effective sensing of RDX via instant and selective detection of ketone vapors*, Chem. Sci. **5**, 4873 (2014).
10. H. Wang, K. X. Yao, J. J. Zhang, J. Jagiello, Q. H. Gong, Y. Han, and J. Li, *The first example of commensurate adsorption of atomic gas in a MOF and effective separation of xenon from other noble gases*, Chem. Sci. **5**, 620 (2014).
11. B. J. Deibert and J. Li, *Distinct reversible colorimetric and fluorescent low pH response on a water-stable zirconium-porphyrin metal-organic framework*, Chem. Comm. **50**, 9636 (2014).
12. D. Banerjee, Z. C. Hu, and J. Li, *Luminescent metal-organic frameworks as explosive sensors*, Dalton Trans. **43**, 10668 (2014), invited perspective, top 20 most accessed Dalton Transactions articles in 2014.
13. Z. C. Hu, B. J. Deibert, and J. Li, *Luminescent metal-organic frameworks for chemical sensing and explosive detection*, Chem. Soc. Rev. **43**, 5815 (2014), invited review.

14. K. Tan, S. Zuluaga, Q. Gong, J. Li, T. Thonhauser, and Y. J. Chabal, *Water reaction mechanism in metal organic frameworks with coordinatively unsaturated metal ions: MOF-74*, Chem. Mater. **26**, 6886 (2014).
15. N. Nijem and Y. J. Chabal, *Adsorbate interactions in metal organic frameworks studied by vibrational spectroscopy*, Comments on Inorg. Chem. **34**, 78 (2014), invited review.
16. S. Zuluaga, P. Canepa, K. Tan, Y. J. Chabal, and T. Thonhauser, *Study of van der Waals bonding and interactions in metal organic framework materials*, J. Phys.: Cond. Matter **26**, 133002 (2014).
17. K. Tan, P. Canepa, Q. Gong, J. Liu, D. H. Johnson, A. Dyevoich, P. Thallapally, T. Thonhauser, J. Li, and Y. J. Chabal, *Mechanism of preferential adsorption of SO₂ into two microporous paddle wheel frameworks M(bdc)(ted)_{0.5}*, Chem. Mater. **25**, 4653 (2013).
18. P. Canepa, C. A. Arter, E. M. Conwill, D. H. Johnson, B. A. Shoemaker, K. Z. Soliman, and T. Thonhauser, *High-throughput screening of small-molecule adsorption in MOF*, J. Mater. Chem. A **1**, 13597 (2013).

A unified understanding of residual stress in thin films: kinetic model and experiments

Eric Chason, Brown University, School of Engineering

Program Scope

Controlling residual stress is critical for enhancing performance and reliability in thin films. Yet despite much study, the connection between the film growth process and the resulting stress is not well understood. The goal of the work in this program is to develop a comprehensive framework that can quantitatively explain and predict the residual stress in terms of the underlying kinetic processes and microstructural parameters.

Wafer curvature is used to measure the stress evolution in real time for different processing conditions and microstructure. To interpret these data, we have developed a model that relates the stress to the underlying physical processes. In this abstract we report on advances in several different topical areas: 1) the use of patterned films to understand stress vs. thickness; 2) the competing effects of grain growth and growth rate on stress evolution and 3) extension of the model to interpret measurements of sputter-deposited films.

Recent progress

Model for stress: The work is centered around a model we have developed that predicts the stress evolution during thin film growth (described more fully in [1]). The model focuses on the stress-generating processes that occur at the top of the grain boundary as the film grows (i.e., at the triple junction shown schematically in figure 1). Tensile stress (σ_T) is generated by the attractive force between adjacent grains as they merge to form new segments of grain boundary [2]. Compressive stress (σ_C) is generated by the insertion of atoms into the grain boundary, driven by the non-equilibrium growth conditions that raise the chemical potential on the surface. Balancing these kinetic processes produces a rate equation for the stress in each layer (indexed by i) as the film grows:

$$\sigma_i = \sigma_C + (\sigma_T - \sigma_C) \cdot \exp\left(\frac{-\beta D}{L} \frac{dh_{gb}}{dt}\right) \quad (1)$$

where D is an effective diffusivity, L is the grain size and β is a kinetic parameter. The rate at which the grain boundary grows (dh_{gb}/dt) determines the relative balance between the stress-generating processes.

Understanding stress vs thickness by using patterned films: In many films, the stress

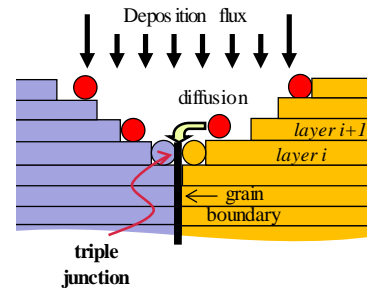


Figure 1. Schematic of film around triple junction for model of stress evolution.

changes from tensile to compressive as the thickness increases, which has been a long-standing puzzle. We can explain this with our growth model by considering how dh_{gb}/dt changes as the microstructure evolves during growth. At the initial point of coalescence, the grain boundary grows very rapidly because of the steep contact angle between the coalescing grains. As the film becomes thicker, however, the velocity of the grain boundary decreases asymptotically to the average rate (R). The dependence of eq. 1 on dh_{gb}/dt shows how this makes the stress less tensile/more compressive with increasing thickness.

Although this explains why the stress changes, it is difficult to compare quantitatively with typical experiments where the grain shape is not known. To address this, we have grown films on lithographically-patterned substrates so that we can control the film morphology. We use electrodeposition so that the islands grow with a constant radial growth rate. For a 2-d array, the islands grow in the form of hemispheres while for a 1-d array they grow in the form of half-cylinders. SEM images of each type of surface morphology are shown in figure 2.

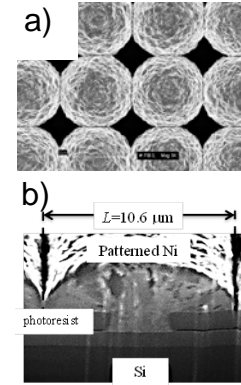


Figure 2. SEM image of Ni islands in a) 2-d and b) 1-d arrays.

These morphologies allow us to calculate the stress-thickness evolution for comparison with the experiments. For the 2-d patterned films, we have shown that the model agrees with the data for multiple growth rates using the same model parameters [3]. More recently we have measured the stress evolution in 1-d arrays with different spacings [4]. Measurements of the stress-thickness for a 1-d pattern spacing of $5.3 \mu\text{m}$ are shown in figure 3 for multiple growth rates from $0.32 - 5.27 \text{ nm/s}$. The calculations from the model (solid lines) agree very well with the data, capturing the dependence on the growth rate. All the calculations shown in the figure were done with a single set of values for the model parameters (σ_T , σ_C and βD); the only difference between them is the growth rate.

To understand the dependence on the length scale, similar measurements were done on patterned films with different spacings, L . The data for were fit to the model using the same values of σ_C and βD but allowing σ_T to be different for each spacing (based on the Hoffman model [2]). A plot of the steady-state stress vs. growth rate for each value of L is shown in figure 3b (the solid line is the fit to the model). The values of the parameter σ_T from the fitting agree with $L^{-1/2}$ as predicted by the model.

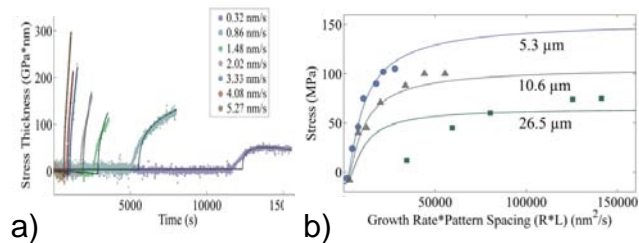


Figure 3. a) Stress-thickness vs. time for 1-d island array with spacing of $5.3 \mu\text{m}$. b) Steady-state stress for 1-d arrays with different spacings. Solid lines are fit to model.

Dependence of steady-state stress on growth rate and grain size: In earlier work, we have shown that the dependence of the steady-state stress on the growth rate in electrodeposited Ni is well-explained by the model. However, in many films that grain

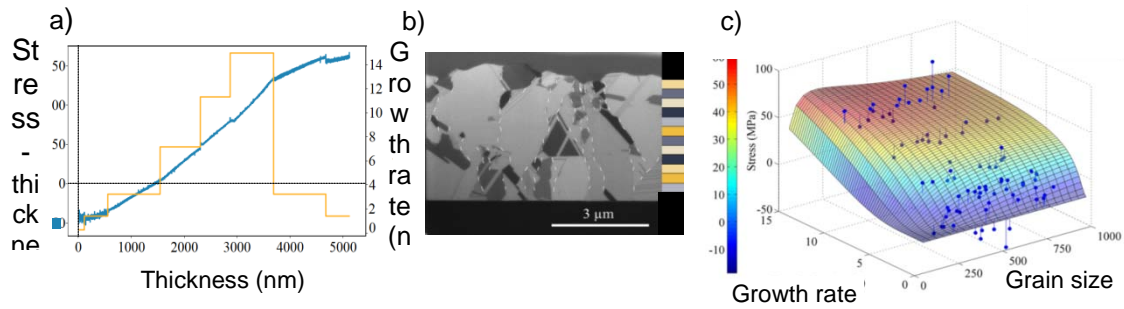


Figure 4. a) Measurements of stress-thickness vs thickness at different growth rates (shown by yellow lines) for electrodeposited Cu. b) FIB cross-section used to determine grain size at different thicknesses. c) Stress vs. growth rate and grain size.

size changes as the thickness increases which can modify the stress. If the grain size changes throughout the thickness of the film (referred to as zone II growth [5]), this can lead to an additional stress due to densification of the film. In other systems, the grain size changes primarily at the surface (zone T) or not at all (zone I).

Our recent studies have focused on understanding the combined effects of grain size and growth rate on the stress evolution. In the first series of experiments, we have studied electrodeposited Cu that grows with a zone T microstructure. Measurements were performed at different growth rates as shown in figure 4a. After growth, the film was cross-sectioned in order to determine the grain size corresponding to each period of growth at different rates (figure 4b). From these measurements we are able to plot the simultaneous dependence of the steady-state stress on the growth rate and grain size. For comparison with the model, we calculate the stress over this range of parameters using eq. 1 and setting dh_{gb}/dt equal to the average growth rate (appropriate for the steady-state regime). The colored surface corresponds to the calculated values from the model using only 3 parameters to fit the entire set of data. The shape of the surface shows the simultaneous growth rate and grain size dependence of the steady-state predicted by the model, consistent with the measurements.

More recently, we have extended this to include films that grow in zone II through a collaboration with Prof. Carl Thompson at MIT. Measurements by Yu and Thompson [6] show that the stress during UHV evaporation of Ni films does not reach a steady-state because of grain growth in the film. Importantly, they also measured the grain size as a function of thickness and show that it depends linearly on the thickness. We have performed preliminary analysis of these data in which we include the tensile stress due to grain growth in the film. We have found that the grain size dependence in our model coupled with tensile stress due to grain growth is able to explain the measured stress evolution as a function of temperature and growth rate.

Extension of model to include effects of energetic particles (sputter deposition): Recent measurements by Abadias' group [7] have quantified the stress during sputter deposition of Mo films at different growth rates and pressures (shown in figure 5). The effect of the energetic particles leads to different behavior (i.e., more compressive/less tensile stress with higher growth rates) than for non-energetic growth. We extended our model to include effects of energetic particles at the grain boundaries and in the bulk of the film.

Preliminary results suggest that the model (shown by solid lines) is able to explain both the growth rate and pressure dependence. It also explained measurements of stress vs. grain size (not shown).

Future Plans

In the future we will continue efforts to validate and improve the model in order to build a comprehensive understanding of stress in thin films. The results will hopefully establish this model as a paradigm for understanding residual stress that can be used to predict stress under different conditions and guide optimization of growth parameters.

Experiments will be performed in a number of materials and deposition systems (evaporation, electrodeposition, sputter deposition, ion-assisted growth) to develop a common framework that can include all the different effects of the processing conditions. Analysis of this experimental work will enable us to build up a database of parameters for different materials that can be compared with other experiments to explore their physical basis. For instance, measurements of stress at different temperatures will let us determine the activation energy for the diffusivity that can be compared with other studies of grain boundary and surface diffusion. Similarly, the tensile stress parameters can be compared with surface/interfacial energies for validation of the Hoffman model. We will also perform a systematic study of adding energetic effects to growth effects by measuring the same material (e.g., Cu) during evaporation, evaporation with ion bombardment (ion-assisted growth) and sputter deposition. Modeling efforts (e.g., molecular dynamics (MD), finite element analysis, kinetic Monte Carlo (KMC), etc.) will be done in collaboration with others to test the mechanisms included in the model.

In the longer term, we plan to extend the model to study the growth of alloys. The equations for the stress will be modified to include the effects of two mobile species. Preliminary studies suggest that the results will be similar in form to eq. 1 but with more complex parameters depending on the different species. This suggests interesting possibilities such as the introduction of a small concentration of a highly mobile species to enhance compressive stress in the film. An experimental program to study stress in alloy films will guide the model development and test the results.

References

1. E. Chason, *Thin Solid Films* 526, 1 (2012).
2. R. W. Hoffman, *Thin Solid Films* 34, 185 (1976).
3. E. Chason, J.W. Shin, C. -H. Chen, A. Engwall, C. Miller, S.J. Hearne, L.B. Freund, *J. Appl. Phys.* 115, 123519 (2014)
4. E. Chason, A.M. Engwall, C.M. Miller, C. -H. Chen, A. Bhandari, S.K. Soni, S.J. Hearne, L.B. Freund, B.W. Sheldon, *Scripta Mat.* 97, (2015) 33
5. J.A. Thornton, *J Vac. Sci. & Tech.* 12, (1975) 830
6. H.Z. Yu, C.V. Thompson, *Acta Materialia* 67 (2014) 189.
7. A. Fillon, G. Abadias, A. Michel, C. Jaouen, *Thin Solid Films* 519, (2010) 1655.

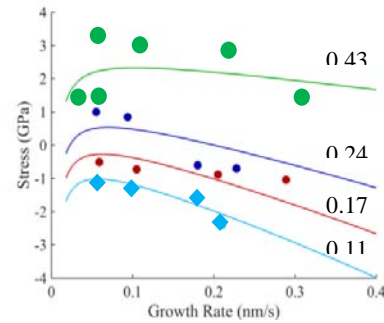


Figure 5. Measurements of steady-state stress vs. growth rate and pressure for Mo deposited by sputtering .

DoE Sponsored Publications in the Last Two Years

1. E. Chason, A. Engwal, F. Pei, M. Lafouresse, U. Bertocci, G. Stafford, D. N. Buckley, J. A. Murphy, C. Lenihan, “Understanding residual stress in electrodeposited Cu thin films”, *J. Electrochemical Soc.* 160, D3285 (2013).
2. E. Chason, J.W. Shin, C. –H. Chen, A. Engwall, C. Miller, S.J. Hearne, L.B. Freund, “Growth of patterned island arrays to identify origins of thin film stress,” *J. Appl. Phys.* 115, 123519 (2014)
3. E. Chason, A.M. Engwall, C.M. Miller, C. –H. Chen, A. Bhandari, S.K. Soni, S.J. Hearne, L.B. Freund, B.W. Sheldon, “Stress evolution during growth of 1-d island arrays: kinetics and length scaling,” *Scripta Mat.* 97, (2015) 33
4. Yohei Ishii, Charbel S. Madi, Michael J. Aziz and Eric Chason, “Stress evolution in Si during low energy ion bombardment,” *J. Mater. Res.* 29, 2942 (2014).
5. Eric Chason, Alison M. Engwall, “Relating residual stress to thin film growth processes via a kinetic model and real-time experiments”, *Thin Solid Films* (2015) in press, available online.

Electric-Loading Enhanced Kinetics in Oxide Ceramics: Pore Migration, Sintering and Grain Growth

I-Wei Chen, University of Pennsylvania

Program Scope

Understanding the thermodynamics and kinetics of new microstructure-relevant phenomena triggered or assisted by electric loading in oxide ceramics, especially those of zirconia and structurally related oxide.

Recent Progress

Electric field has significant effects on microstructure evolution (e.g. sintering, grain growth, etc.) of ceramics due to Joule heating, off-diagonal coupling of kinetics and non-equilibrium defect chemistry. Recent progresses from this project include:

I. Under constant environment heating rate and applied voltage, an electric field must lead to thermal runaway in any materials with a negative temperature coefficient of resistivity [1] and, for partially dense ceramics, flash sintering. We have obtained an analytic solution to the thermal runaway problem [2-3], which correctly predicts the runaway temperatures in excellent agreement with the on-set temperatures of more than a dozen flash-sintering studies. The analysis revealed a strong correlation with the resistivity class of the material, thus adding to its predictive power.

II. In fast-ion conductors which includes fast-ion wind and slow counter-ion diffusion, their coupling via short-circuit paths can be made possible by an electric field/current [4]. Such coupling can then completely destabilize the otherwise extraordinarily stable microstructure of these ceramics at unexpectedly low temperatures. Examples so far observed in zirconia include migration of pores (hence sintering) [4-6], gas bubbles [5-6], and space-filling particles (e.g., alumina and silica.) Other couplings of the above kind may conceivably exist in other material classes, thus causing their microstructure instability.

III. In kinetics-limited cases, an electric field may exacerbate the mismatch between a large energy flux and slow interface kinetics, creating non-equilibrium conditions allowing huge defect supersaturation. For example, in zirconia (both 8YSZ in the cubic form and 3YSZ in the tetragonal form) there is now reliable experimental [7] and theoretical evidence that reduced cations rendered by an electric field/current/potential enjoy much faster kinetics. In this way, sintering and grain growth are locally enhanced as an indirect result of electric field.

IV. Since the electric field/current imposed in experiments is often very large, ample opportunities exist for Rayleigh-type instabilities to arise leading to localization of

field/current/energy. Examples of this kind have been seen in 3YSZ, leading to dendrite-like grains with a huge (~100) aspect ratio.

Future Plans

We will collect detailed statistics of particle migration and dendrite-like grains to allow microstructure modeling. Bicrystal experiments on pore and particle migration will be conducted to isolate the effect of grain boundaries and crystallography. Defect calculations based on empirical potentials and first-principles will be performed to understand the kinetics under equilibrium and supersaturated conditions. Experiments under conditions that simulate electrically-induced supersaturation will be designed to provide additional tests of these ideas.

References

[1] J. Park and I-W. Chen, "In Situ Thermometry Measuring Temperature Flashes Exceeding 1700°C in 8 mol% Y₂O₃-Stabilized Zirconia under Constant-Voltage Heating," *J. Am. Ceram. Soc.*, **96** [3], 697-700 (2013).

[2] Y-H. Dong and I-W. Chen, "Predicting the Onset of Flash Sintering," *J. Am. Ceram. Soc.*, **98** [8], 2333-2335 (2015).

[3] Y-H. Dong and I-W. Chen, "Onset Criterion for Flash Sintering," *J. Am. Ceram. Soc.*, DOI: 10.1111/jace.13866 (2015).

[4] I-W. Chen, S-W. Kim, J. Li, S-J. L. Kang and F. Huang, "Ionmigration of Neutral Phases in Ionic Conductors," *Adv. Energy Mater.* **2**, 1383-1389 (2012).

[5] S-W. Kim, S-J. L. Kang and I-W. Chen, "Ionmigration of Pores and Gas Bubbles in Ytria-Stabilized Cubic Zirconia," *J. Am. Ceram. Soc.*, **96** [4], 1090-1098 (2013).

[6] S-W. Kim, S-J. L. Kang and I-W. Chen, "Electro-Sintering of Ytria-Stabilized Cubic Zirconia," *J. Am. Ceram. Soc.*, **96** [5] 1398-1406 (2013).

[7] S-W. Kim, S-G. Kim, J-I. Jung, S-J. L. Kang and I-W. Chen, "Enhanced Grain Boundary Mobility in Ytria-Stabilized Cubic Zirconia Under an Electric Current," *J. Am. Ceram. Soc.*, **94** [12], 4231-4238 (2011).

Publications

Y-H. Dong and I-W. Chen, "Predicting the Onset of Flash Sintering," *J. Am. Ceram. Soc.*, **98** [8], 2333-2335 (2015).

Y-H. Dong and I-W. Chen, "Onset Criterion for Flash Sintering," *J. Am. Ceram. Soc.*, DOI: 10.1111/jace.13866 (2015).

Novel sample structures and probing techniques of exotic states in the second Landau level

Principal Investigators: Gabor Csathy and Michael Manfra

Institution: Purdue University

Address: 525 Northwestern Ave., West Lafayette, IN 47907

E-mail of PIs: gcsathy@purdue.edu, mmanfra@purdue.edu

Program Scope

The two-dimensional electron gas hosts a wealth of unusual phases arising from the interplay of reduced dimensionality and strong electron-electron interactions. Recently it was suggested that this system may support unusual ground states which harbor exotic particles with special topological properties. Specifically, the ground states are thought to have Abelian and non-Abelian properties of various kinds [a]. The most interesting states form in the region of the phase space commonly referred to as the second Landau level.

Examples of such unusual ground states in the second Landau level are the fractional quantum Hall states at the quantum numbers $5/2$ and $12/5$. These ground states are not only of fundamental interest as they may manifest behavior not seen in any other physical system, but also may find technological utility in fault-tolerant schemes for quantum computation [b]. These exotic states are, however, fragile and hence they develop only under special conditions.

Two-dimensional electron gases are realized in a large variety of semiconductor hosts. GaAs/AlGaAs plays an important role among these semiconductors and the low temperature mean free path is the longest. Because of the very long mean free path, conditions are favorable for the development of a large number of exotic ground states, including several states believed to be non-Abelian.

At Purdue University we have developed a synergistic experimental program based on systematic growth and ultra-low temperature measurement of high quality GaAs/AlGaAs crystals tailored to answering outstanding questions concerning the collective behavior of the correlated electronic ground states of the two-dimensional electron gas. Our primary focus is the study of the fractional quantum Hall states and exotic electronic solids of the second Landau level, i.e. corresponding to Landau level filling factors $2 \leq \nu \leq 4$. The goal of our program is to use state-of-the-art growth and incisive experimental measurement techniques to generate new insight into the nature of the exotic correlated states of the second Landau level.

Recent Progress

This project builds on the ongoing collaboration of the PIs and unique experimental capabilities developed at Purdue University. **Manfra** operates state-of-the art MBE growth producing wafers with record high mobility. **Csathy** has an ultra-low temperature instrument capable of producing one of the lowest electron temperatures of 5 mK.

Advances in material growth In the past year we have made several advances in material quality and improved our understanding of the relationship between disorder-induced scattering, ever-present density inhomogeneity, and low temperature transport characteristics in the second Landau level. Improvements made to our MBE system and materials preparation techniques resulted in a dramatic improvement in low temperature mobility. We produced samples with

mobility in excess of $35 \times 10^6 \text{ cm}^2/\text{Vs}$ - a 75% improvement over our first growth campaign. Importantly, we discovered that the purity of gallium source material is the primary limiting factor in the achievement of ultra-high mobility. As shown in the Fig. 1 below, in-situ purification of gallium resulted in discrete jumps in mobility.

While mobility is one metric of film quality we have also made progress in our understanding of what parameters control the strength of the fragile states in the second Landau level. In collaborative work with the Folk group at Univ. of British Columbia we demonstrated

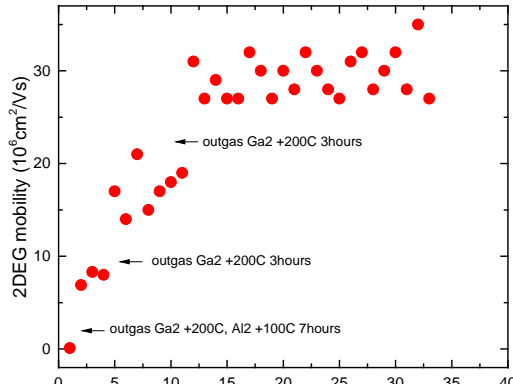


Figure 1: Mobility as a function of growth number and outgassing of gallium source.

the careful study of low temperature illumination and thermal annealing can increase the excitation gap at $\nu=5/2$ ($\Delta_{5/2}$) to 0.6K [11]. While $\Delta_{5/2}$ increases by a factor of 3 in these illumination experiments, mobility changes minimally, indicating that the disorder that controls the strength of the gap is not the same that sets mobility. We have initiated experiments to determine what metrics of two-dimensional electron gas quality measured during sample screening at $T=0.3\text{K}$ correlate best with low temperature ($T=10\text{mK}$) behavior in the second Landau level. In addition to mobility we also measure quantum scattering time and the resistivity at $\nu=5/2$ at $T=0.3\text{K}$. We find interesting behavior where the resistivity at $5/2$ saturates to a minimum value of approximately $40\Omega/\text{sq}$. even as the mobility continues to improve during the growth campaign (see Fig. 2). Our initial data indicate that the value of $5/2$ resistivity at $T=0.3\text{K}$ correlates inversely with the strength of the $\nu=5/2$ gap and is a better indicator of transport in the second Landau level at low temperatures than mobility.

Studies of the effects of heterostructure design We have also studied the impact of heterostructure design on the transport properties in the second Landau level in samples with an in-situ back gate [2]. In this work we demonstrated the placement of AlAs/GaAs superlattice between the back gate and the 2DEG has enormous impact on reducing the gate-to-2DEG leakage current. Reduction of gate leakage is extremely important in devices designed to explore states in the second Landau level. In this work we demonstrated that leakage current as low as a few 10s of picoamps can result in heating detrimental to observation of fragile correlated states in the second Landau level. Properly designed heterostructures allowed us to produce devices that could be tuned from full depletion up to an electron density of $3.35 \times 10^{11} \text{ cm}^{-2}$, where we observed $\Delta_{5/2}=625\text{mK}$, the highest value to be reported to date. These devices form a novel platform where the properties of the second Landau can be explored as a function of the electron density.

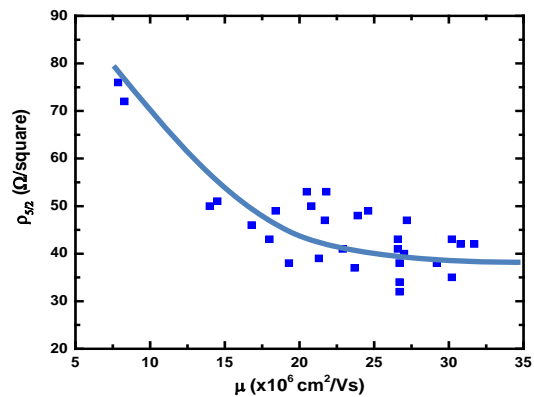


Figure 2: Resistivity at $5/2$ filling at $T=0.3\text{K}$ as a function of mobility.

Alloy disorder and the even denominator fractional states Unraveling the impact of disorder is an important endeavor in contemporary condensed matter physics. Disorder is well understood in the single particle regime, but remains under scrutiny in novel systems such as topological insulators and atomic condensates. In contrast, understanding disorder in correlated electron

systems, often referred to as many-body localization, continues to pose serious challenges. The Molecular Beam Epitaxy technique allows not only the growth of very low disorder 2DEGs, but also enables controlled introduction of minute amounts of disorder into the 2DEG. Such specially tailor samples with one kind of disorder, called alloy disorder, were recently grown by Manfra [4] and studied at low temperatures in Csathy's laboratory [3]. As reported in a recent Physical Review Letters, a very surprising lowering of the mobility threshold for the even denominator 5/2 fractional state has been observed. Indeed, in high quality samples the 5/2 state has not been observed below the mobility of $7 \times 10^6 \text{ cm}^2/\text{Vs}$. In contrast, Csathy and his students found a mobility threshold in alloy samples of only $1.8 \times 10^6 \text{ cm}^2/\text{Vs}$. The lowering of the mobility threshold is currently not yet understood. However, these results are expected to stimulate theoretical research on disorder effects and provide input for the design of future, improved sample structures.

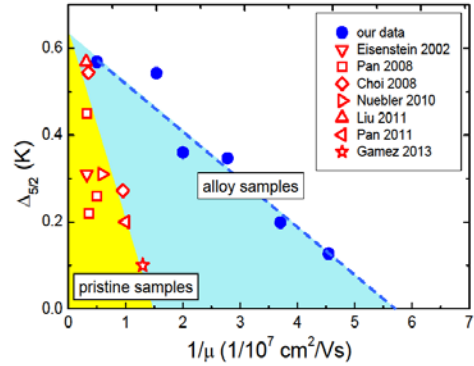


Figure 3: The gap at 5/2 filling as a function of mobility for pristine and alloy samples.

Tuning the exotic states with hydrostatic pressure One current focus of Csathy's research is the development of novel, incisive techniques probing the two-dimensional electron gas. Historically the most popular measurement technique used in investigations of this system is electronic transport. However, over the last decade or so it became increasingly clear that the probing of the new topologically ordered states requires more sophisticated techniques. Measurement of these systems at high hydrostatic pressures is one such technique currently being implemented by Csathy. The commercial pressure cell used is seen in the figure in the right. At pressures of the order of 10,000 atmospheres one can tune many relevant quantities which are expected to impact numerous ground states. We have recently discovered a novel transition from a fractional quantum Hall state to an electronic stripe phase [1].

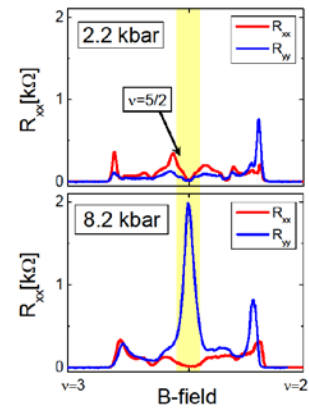


Figure 4: The application of hydrostatic pressure induces an unexpected phase transition.

Collaborative efforts Under this program, **Manfra** has grown high quality materials used by several researchers, many of whom are DOE supported: Piczuk at Columbia, Zudov at Univ. Minnesota, Kono at Rice, and Engel at the National High Magnetic Field Lab in Tallahassee [5-13]. **Csathy** is using the ultra-low temperature capability in his lab to work with two other DOE supported colleagues: Du at Rice [14] and Rokhinson at Purdue.

Future Plans We will continue our effort in studying disorder effects by expanding the energy gap measurements for other types of well-controlled disorder, such as charged disorder. We expect that disorder-specific information will guide us in further improvements of the growth process and may lead to new insight of the behavior of these systems. Encouraged by our recent results, we will continue to study pressure effects in the GaAs system. Specifically, we will investigate the spin polarization effects in the exotic ground states. We have recently started an effort to study the evolution of the interesting ground state with the width of the quantum well they reside in. Such investigations involve a coordinated effort between growth and ultra-low temperature measurement and are part of our long term effort aimed at exploring unconventional collective behavior in low-dimensional systems.

References

- a) A. Stern, “Non-Abelian States of Matter”, *Nature (London)* **464**, 187 (2010).
- b) C. Nayak, S. Simon, A. Stern, M. Freedman, and S. Das Sarma, “Non-Abelian Anyons and Topological Quantum Computing”, *Review of Modern Physics.* **80**, 1083 (2008)

Publications acknowledging DOE BES support since 2013

1. N. Samkharadze, K.A. Schreiber, G.C. Gardner, M.J. Manfra, E. Fradkin, and G.A. Csathy, “Observation of a transition from a topologically ordered to a spontaneously broken symmetry phase”, in press with *Nature Physics* (2015)
2. J.D. Watson, G.A. Csathy, and M.J. Manfra, “Impact of heterostructure design on transport properties in the second Landau level in in-situ back-gated two-dimensional electron gases”, *Physical Review Applied* **3**, 064004 (2015)
3. N. Deng, G.C. Gardner, S. Mondal, E. Kleinbaum, M.J. Manfra, and G.A. Csathy, “Anomalous Robustness of the $\nu=5/2$ Fractional Quantum Hall state in the Presence of Alloy Disorder”, *Physical Review Letters* **112**, 116804 (2014)
4. G.C. Gardner, J.D. Watson, S. Mondal, N. Deng, G.A. Csathy, and M.J. Manfra, “Growth and electrical characterization of $\text{Al}_{0.24}\text{Ga}_{0.76}\text{As}/\text{Al}_x\text{Ga}_{1-x}\text{As}/\text{Al}_{0.24}\text{Ga}_{0.76}\text{As}$ modulation-doped quantum wells with extremely low x ”, *Applied Physics Letters* **102**, 252103 (2013)
5. Q. Shi, P.D. Martin, A.T. Hatke, M.A. Zudov, J.D. Watson, G.C. Gardner, M.J. Manfra, L.N. Pfeiffer, and K.W. West, “Shubnikov–de Haas oscillations in a two-dimensional electron gas under subterahertz radiation”, *Physical Review B* **92**, 081405 (2015)
6. Z. Wan, A. Kazakov, M.J. Manfra, L.N. Pfeiffer, K.W. West, and L.P. Rokhinson, “Induced superconductivity in high-mobility two-dimensional electron gas in gallium arsenide heterostructures”, *Nature Communications* **6**, 7426 (2015)
7. M.J. Manfra, “Molecular Beam Epitaxy of Ultra-High-Quality AlGaAs/ GaAs Heterostructures: Enabling Physics in Low-Dimensional Electronic Systems”, *Annu. Rev. Condens. Matter Phys.* **5**, 347 (2014)
8. Q. Zhang, T. Arikawa, E. Kato, J.L. Reno, W. Pan, J.D. Watson, M.J. Manfra, M.A. Zudov, M. Tokman, M. Erukhimova, A. Belyanin, and J. Kono, “Superradiant Decay of Cyclotron Resonance of Two-Dimensional Electron Gases”, *Physical Review Letters* **113**, 047601 (2014)
9. N.J. Goble, J.D. Watson, M.J. Manfra, and X.P.A. Gao, “Impact of short-range scattering on the metallic transport of strongly correlated two-dimensional holes in GaAs quantum wells”, *Physical Review B* **90**, 035310 (2014)
10. S. Chakraborty,1 A. T. Hatke,1 L. W. Engel,1 J. D. Watson,2,3 and M. J. Manfra, “Multiphoton processes at cyclotron resonance subharmonics in a two-dimensional electron system under dc and microwave excitation”, *Physical Review B* **90**, 195437 (2014)
11. M. Samani, A.V. Rossokhaty, E. Sajadi, S. Luscher, J. A. Folk, J. D. Watson, G.C. Gardner, and M.J. Manfra, “Low-temperature illumination and annealing of ultrahigh quality quantum wells”, *Physical Review B* **90**, 121405 (2014)
12. A.T. Hatke, M. A. Zudov, J. D. Watson, M. J. Manfra, L. N. Pfeiffer, and K. W. West, “Effective mass from microwave photoresistance measurements in GaAs/AlGaAs quantum wells”, *Journal of Physics: Conference Series* **456**, 012040 (2013)
13. A.T. Hatke, M.A. Zudov, J.D. Watson, and M.J. Manfra, L.N. Pfeiffer, and K.W. West, “Evidence of Effective Mass Reduction in GaAs/AlGaAs Quantum Wells”, *Physical Review Letters* **B 87**, 161307 (2013)
14. Tingxin Li, Pengjie Wang, Hailong Fu, Lingjie Du, Kate Schreiber, Xiaoyang Mu, Xiaoxue Liu, Gerard Sullivan, G.A Csathy, Xi Lin, and Rui-Rui Du, “Observation of Helical Luttinger-Liquid in InAs-GaSb Quantum Spin Hall Edges”, in press with *Physical Review Letters*

Emergent properties of complex transition metal compounds.

J. F. DiTusa¹ (ditusa@phys.lsu.edu), R. Jin¹, Z. Mao², J.D. Zhang¹, W. A. Shelton³, E. W. Plummer¹, and D. P. Young¹

¹Department of Physics & Astronomy, Louisiana State University, Baton Rouge, LA 70803

²Department of Physics & Engineering Physics, Tulane University, New Orleans, LA 70118

³Department of Chemical Engineering, Louisiana State University, Baton Rouge, LA 70803

Program Scope

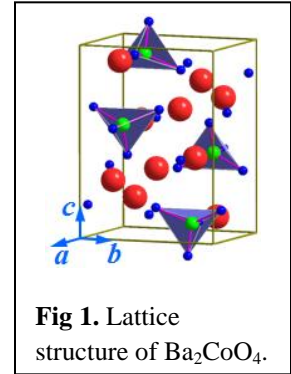
LaCNS, a DOE EPSCoR program, aims to build a major neutron scattering infrastructure capable of treating both soft and hard materials. The objectives of this initiative include the discovery of the role of coupling of degrees of freedom that determine the emergent properties of complex materials, the training of students and postdocs in synthesis and neutron scattering techniques, and the building of new scientific communities who will become the next generation of neutron users with a specific target of increasing the base of users of the Spallation Neutron Source and the High Flux Isotope Reactor in the USA.

The main scientific focus of this program is to understand the role of coupling between the important degrees of freedom in complex materials and its impact on the structure/property relationship, and to explore how this information can be applied in the guided-design of materials with desired properties. For hard materials, our goal is to tune dominant couplings that impact the magnetic, electronic, and phonon properties of complex transition metal compounds to enhance a critical property in order to derive new functionality. Since neutron characterization often requires the availability of large high quality single crystals, a major thrust in this research program focuses on their synthesis. Students and postdocs are being trained in a variety of synthesis techniques, including, solid-state reactions, arc melting, chemical vapor transport, metallic flux growth, RF induction melting, Bridgman, Czochralski, high pressure/high temperature growth, and optical floating zone. In addition to supporting the mission of the LaCNS, our single crystal growth activities strengthen the United States' presence in the global synthesis community, which has weakened over the last few decades.

Recent Progress

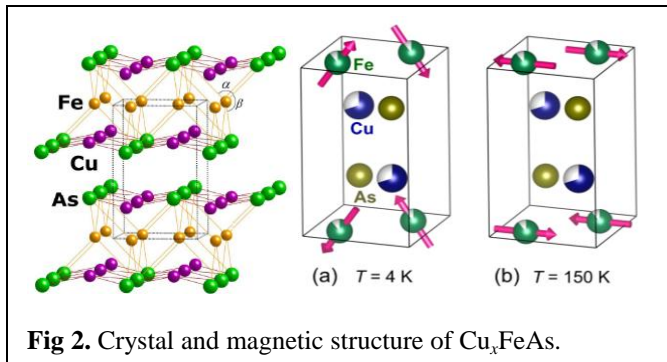
The materials systems under investigation in the LaCNS hard matter program include transition metal oxides such as Sr_2RuO_4 (Sr214) and $\text{Sr}_3\text{Ru}_2\text{O}_7$ (Sr327) which have been of continuing interest because of the competing magnetic states and their connection to *p*-wave superconductivity. Here we focus on Ru-site substitutions which tend to modify the lattice and nucleate magnetically ordered phases. The evolution of the spin-lattice coupling with chemical substitution is investigated using various techniques including neutron scattering. The growth of large single crystals with high purity is essential. The floating-zone technique is ideal for ruthenates, since the process does not require a crucible and the starting materials are well mixed

in the liquid state. However, due to the high melting temperature and the volatile nature of Ru metal, the growth of either single-layered or double-layered ruthenates requires precise control over the starting composition, atmosphere, and growth rate. Recently we have discovered that Fe substitution for Ru in Sr214 leads to a commensurate antiferromagnetic (AFM) ordering which is distinct from Mn or Ti substitutions which lead to an incommensurate AFM state or from Co doping resulting in a ferromagnetic (FM) ground state¹. This magnetic order is accompanied by charge localization suggesting a strong coupling between the charge and magnetic degrees of freedom. Similarly, we have synthesized large single crystals of $\text{Sr}_3(\text{Ru}_{1-x}\text{Mn}_x)_2\text{O}_7$ for exploring charge-spin-lattice couplings. Mn doping tends to reduce the structural distortion and at the same time enhances AFM interactions resulting in an unusual quasi-2D AFM order². Of particular interest is the non-standard temperature dependence of the AFM order parameter and the spin dynamics. Using neutron scattering, we find, for the first time in the Sr327 system, an energy gap for spin wave excitations for $x=0.16$ demonstrating a Mn induced anisotropy.



Despite the separation between CoO_4 tetrahedra in the lattice structure of Ba_2CoO_4 (Fig. 1), it is AFM below 25 K. Large single crystals have been grown using the floating-zone technique. With the application of an O_2 atmosphere during the growth, stoichiometric Ba_2CoO_4 can be obtained, implying that Co is in its highest oxidation state. Using neutron scattering, we identified a spin gap due to the single-ion anisotropy of Co^{4+} [3]. Moreover, there is clear dispersion along the a -axis but not along the c -axis, indicating low-dimensional magnetism.

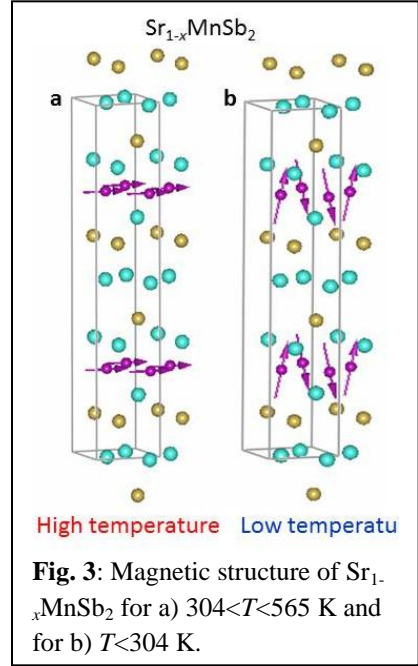
We also have a strong synthesis effort in designing materials with unconventional but highly desirable properties. Currently, we are investigating several materials that are relatives to the Fe-based superconducting systems. Using the flux method, we have successfully grown single crystals of Cu_xFeAs , which is isostructural (Fig. 2) to superconducting LiFeAs ⁴. Here we find that uniaxial pressure does not induce magnetic correlations as expected. Although Cu_xFeAs is isostructural to LiFeAs (Fig. 3)⁴, it is not superconducting. Instead our neutron scattering experiments revealed a collinear G-type AFM order below 220 K. This state evolves into a canted AFM state below 142 K explaining the weak FM behavior observed below 60 K. The G-



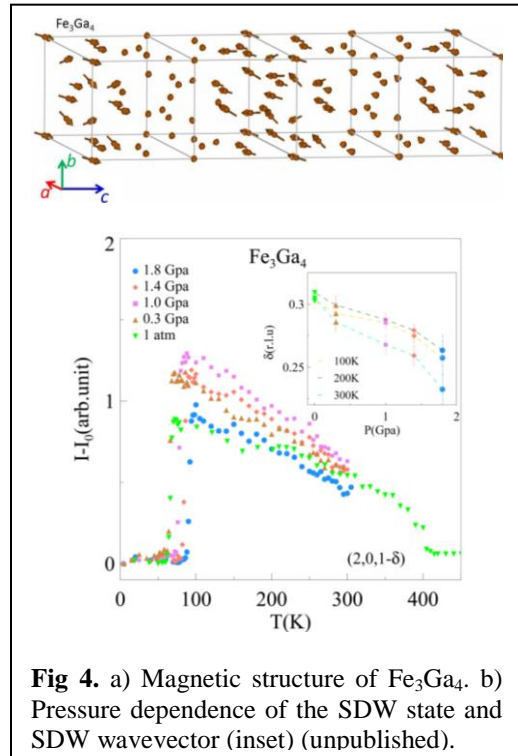
type AFM order of Cu_xFeAs bears striking similarity to the high- T_c cuprates, thus directly bridging the Fe-based and Cu-based unconventional super-conducting systems. Other related materials that we are exploring include newly discovered BaMn_2Sb_2 which is isostructural to BaFe_2As_2 , a member of the 122 family of superconductors⁵. Large single crystals of

BaFe₂As₂ and Ba(Mn_{1-x}Fe_x)₂Sb₂ were grown to explore the magnetic, charge carrier, thermodynamic, and structural properties. Recently, Liu et al. have synthesized a new topological semimetal, Sr_{1-x}MnSb₂ that is likely the first FM Weyl semimetal⁶. The Weyl semimetal state refers to a Dirac semimetal that lacks either time-reversal or space inversion symmetry so that each Dirac point with chiral symmetry splits into two Weyl points. Here we have characterized the magnetic ordering of this interesting system finding two magnetically ordered structures at high and low temperatures (Fig. 3).

Using Bridgman and optical floating zone techniques, we have synthesized large single crystals of Fe₃Ga₄[7]. Our neutron scattering data indicate that an incommensurate spin density wave (SDW) ordering competes with a FM ground state such that there is a reentrance of the FM state above 300 K. In addition, we have explored the sensitivity of the SDW ordering to physical pressure (Fig. 4).



The B20 crystal structure is interesting because it is chiral, allowing spin-orbit coupling to play a key role in electronic and magnetic properties. A large number of binary silicides and germanides form in this crystal structure which is responsible for both helimagnetism and the formation of Skyrmion lattice phases that are ubiquitous in this family of materials⁸. In an initial series of polycrystalline samples, we have discovered that chemical substitution series between the non-magnetic small gap insulator RuGe (B20) and the diamagnetic metal CoGe, Ru_{1-x}Co_xGe, yields magnetic metals for a wide range of x. Large single crystals of this series were grown by the Bridgman technique and will allow us to map out the magnetic phase diagram.



Future Plans

Our future plans involve both the continued study of these materials, as well as to identify new materials for investigation, with a focus on the use of neutrons to probe the elastic and inelastic properties. The goal is to connect the results of neutron scattering experiments to their novel emergent properties. The growth of high quality single crystals will continue to be an indispensable component to our research program.

References

- ¹M. Braden *et al.* *Phys. Rev. Lett.* **88**, 197002 (2002); J. E. Ortmann *et al.* *Nat. Sci. Rep.* **3**, 2950 (2013).
- ²D. Mesa *et al.*, *Phys. Rev. B* **85**, 180410 (2012).
- ³R. Jin *et al.* *Phys. Rev. B* **73**, 174404 (2006).
- ⁴B. Qian *et al.* *Phys. Rev. B* **91**, 014504 (2015).
- ⁵B. Saparov and A. S. Sefat, *J. Sol. St. Chem.* **204**, 32-39 (2013).
- ⁶J. Liu *et al.* *arxiv.org/pdf/1507.07978* (2015).
- ⁷J. H. Mendez *et al.* *Phys. Rev. B* **91**, 144409 (2015).
- ⁸S. Muhlbauer *et al.* *Science* **323**, 915-919 (2009).

Publications

Qian, B., Hu, J., Liu, J., Han, Z., Zhang, P., Guo, L., Jiang, X., Zou, T., Zhu, M., Dela Cruz, C. R., Ke, X. and Z.Q. Mao. "Weak ferromagnetism of $\text{Cu}_x\text{Fe}_{1+y}\text{As}$ and its evolution with Co doping." *Phys. Rev. B* **91**, 014504 (2015).

Wang, H., Lou, W., Luo, J., Wei, J., Liu, Y., Ortmann, J. E. and Z. Q. Mao, "Enhanced superconductivity at the interface of W/Sr₂RuO₄ point contact." *Phys. Rev. B* **91**, 184514 (2015).

Dzamukova, M.R., Lvov, Y.M., Fakhrullin, R.F., "Enzyme-activated intracellular drug delivery with tubule clay nanoformulation." *Scientific Reports (Nature Publ)* **5**, 10560 (2015).

Y. Lvov, R. Fakhrullin, L. Zhang, , "Halloysite Clay Nanotubes for Loading and Sustained Release of Functional Compounds", *Adv. Mater.* accepted (2015).

Xuan, S.; Lee, C. -H.; Chen, C.; Doyle, A. B.; Zhang, Y.; Li, G.; John, V. T.; Hayes, D.; Zhang, D. Design, Synthesis and Characterization of Polypeptoid Thermogels and Investigation of Stem Cell and Protein Encapsulation. *J. Am. Chem. Soc.*, submitted (2015).

Bhaskaran-Nair, K., Kowalski, K., Moreno, J., Jarrell, M. and Shelton, W.A., "Equation of motion coupled cluster methods for electron attachment and ionization potential in polyacenes," *Journal of Physical Chemistry A*, submitted (2015).

Bhaskaran-Nair, K., Kowalski, K., Valiev, M., Wang, X. and Shelton, W.A., "Coupled cluster characterization of the ionization potentials and electron affinities of GFP chromophores," *Physical Chemistry Chemical Physics*, submitted (2015).

Nesterov: Youm, S. G., Hwang, E., Chavez, C. A., Li, X., Chatterjee, S., Lusker, K. L., Lu L., Strzalka, J., Ankner, J. F., Losovyj, Y., Garno, J. C. and Nesterov, E. E. "Polythiophene Thin Films by Surface-Confined Polymerization," *Journal of the American Chemical Society*, submitted (2015).

Stability, Structure, and Molecular Orientation in Organic Glasses Produced by Physical Vapor Deposition

D.M. Walters, A. Gujral, J. Jang, S.S. Dalal, and M.D. Ediger
Department of Chemistry
University of Wisconsin-Madison, Madison, WI 53706

Program Scope

Organic glasses with high density, low enthalpy, and remarkably high kinetic stability can be prepared by physical vapor deposition (PVD).¹ We are investigating the extent to which high kinetic stability and tailored anisotropy can coexist in the same material. These experiments build upon the recent development of a high-throughput temperature-gradient methodology to efficiently prepare and characterize organic glasses. Using materials applicable to organic electronics, we are working to further our fundamental understanding of the vapor-deposited glasses and the amorphous state by pursuing the following objectives: 1) Utilize grazing-incidence and wide-angle x-ray scattering, and optical absorption and emission, to characterize vapor-deposited glasses. 2) Find and understand general trends in the properties of glasses prepared by depositing single and multiple component systems. We seek to identify the range of anisotropic amorphous structures that can be produced by PVD and develop the mechanistic understanding needed to predict the anisotropy produced by specific deposition conditions. 3) Build upon recent work showing that PVD can produce “stable glasses” with unprecedented thermal stability by investigating the extent to which stable glass packing can also increase photochemical stability and resistance to crystallization.

Recent Progress

Anisotropic Molecular Orientation. We have applied our high-throughput sample preparation protocol, developed with DOE support, to characterize glasses used in organic electronics.² Figure 1 illustrates our protocol schematically. During vapor deposition, two copper fingers are heated or cooled to induce a temperature gradient across a bridging substrate. After deposition, different spots on the substrate are measured to characterize glasses prepared at many substrate temperatures on a single sample. Our approach provides a highly efficient method to investigate the impact of substrate temperature on glass properties, which we have previously shown to be a controlling factor in model glassformers.^{3,4}

Using our upgraded spectroscopic ellipsometer, we can detect dichroism

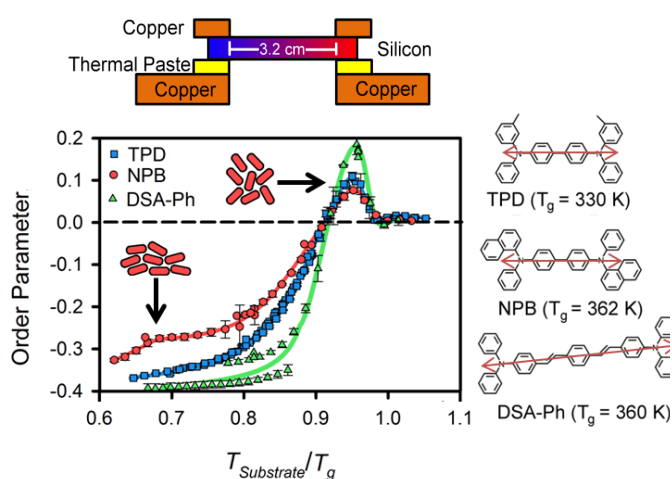


Figure 1. Top: A diagram of the temperature gradient sample holder. Bottom: Orientational order parameter for three linear molecules as a function of substrate temperature during vapor deposition, as determined by spectroscopic ellipsometry.

and quantify molecular orientation. By measuring the dichroism of a strong transition dipole along the long axis of the linear molecules, we are sensitive to the average orientation of the entire molecule. The orientation is quantified by calculating an orientational order parameter where vertically aligned molecules have an order parameter value of 1, horizontally aligned molecules have a value of -0.5, and randomly arranged molecules have a value of zero.

Figure 1 shows the trend in molecular orientation for three linear molecules used in organic electronics. At high substrate temperatures, ordinary glasses are prepared and molecules are isotropic. At slightly lower substrate temperatures, molecules show a slight tendency for vertical orientation, while at low substrate temperatures molecules show a strong tendency for horizontal orientation. This result demonstrates that a wide range of molecular orientations are accessible for a single molecule. Furthermore, all three linear molecules have the same trend in molecular orientation when the substrate temperature is scaled relative to their glass transition temperature, T_g . This suggests that orientation depends primarily on substrate temperature rather than the aspect ratio of the molecule. Simulations by collaborators Lyubimov and de Pablo suggest the orientation depends on the mobility of the surface and the structure of the surface of the equilibrium supercooled liquid.^{2,5} Additionally, we found that these organic electronic materials form highly stable glasses with similar trends in density and kinetic stability as previously observed in model glassformers.²

We have extended our studies of molecular orientation to two component systems by measuring the molecular orientation of DSA-Ph, a light emitter which can be highly anisotropic (Figure 1), in Alq_3 , an isotropic host. This design mimics active layers in OLEDs, where a light emitter is dispersed in a host matrix to reduce concentration quenching. Remarkably, we observe the same trend in the molecular orientation of DSA-Ph in neat films and multicomponent films (Figures 1 and 2), with the features shifted to higher temperatures with increasing volume fraction of Alq_3 (Figure 2). These data collapse when scaled by the T_g of the mixture, suggesting that the mobility of the material is the dominant factor in determining molecular orientation of an emitter in an isotropic host.

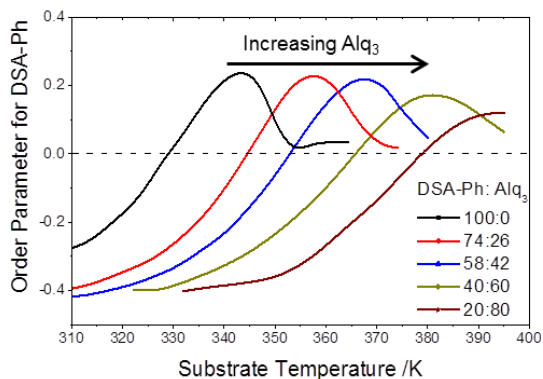


Figure 2. Orientational order parameter of DSA-Ph in films with different volume fraction of Alq_3 .

Anisotropic Molecular Packing. Previously, we have used X-ray scattering to investigate structural anisotropy in vapor deposited glasses.⁶ To extend this work, we have applied our high-throughput sample preparation technique (described above) to X-ray studies of anisotropic molecular packing in vapor-deposited glasses used in organic electronics. We have been awarded synchrotron beam time at the Stanford Synchrotron Radiation Lightsource (SSRL) to further our investigations.

We have characterized molecular packing in vapor deposited glasses of TPD using X-ray facilities on-campus and at SSRL.⁷ Figure 3 shows representative scattering patterns obtained from grazing incidence X-ray scattering (GIWAXS) measurements from SSRL for two TPD glasses prepared with different substrate temperatures. Variation in the scattering intensity indicates changes in the anisotropic molecular packing of the different glasses.

X-ray scattering measurements reveal that the molecular packing in TPD glasses varies from face-on to edge-on tendencies as a function of substrate temperature.⁷ These results, in conjunction with the orientation order parameter measured by ellipsometry (Figure 1), give us a more complete picture of the structure of TPD glasses. As is illustrated schematically in Figure 3, at low substrate temperatures molecules are preferentially horizontally orientated with face-on packing. When $T_{\text{substrate}} = 315$ K, molecules are preferentially vertically orientated and are packed edge-on with respect of the substrate.

We have also made GIWAXS measurements on vapor-deposited glasses of DSA-Ph, another system of interest in organic electronics with tunable molecular orientation (Figure 1). Preliminary results suggest that DSA-Ph glasses show the same trends in molecular packing with substrate temperature as TPD, but are even more ordered.

Thermal stability. We have measured the thermal stability of vapor-deposited glasses of TPD, a hole transport material used in organic electronics, and discovered the transformation mechanism for these thin films.⁸ When heated above T_g , we found that vapor-deposited glasses of TPD transform to a liquid via constant velocity propagating fronts, as is illustrated in Figure 4. Transformation fronts have previously been observed for model stable glass formers^{9,10} but are unprecedented in systems used for organic electronics. By combining a new, high-throughput annealing procedure with our previously developed high-throughput sample preparation, we systematically measured the effect of substrate temperature and annealing temperature on the thermal stability of the TPD glasses. This extended data range allowed us to deconvolute the effect of the mobility of the liquid and the structure of the glass, and we found that they are independent factors in controlling the thermal stability of TPD films. As shown in Figure 4, TPD films have similar front velocities and substrate temperature dependence as model glassformers, such as indomethacin (IMC), suggesting universal transformation behavior in stable, vapor-deposited glasses. These results may aid in designing active layers in organic electronics with increased thermal stability.

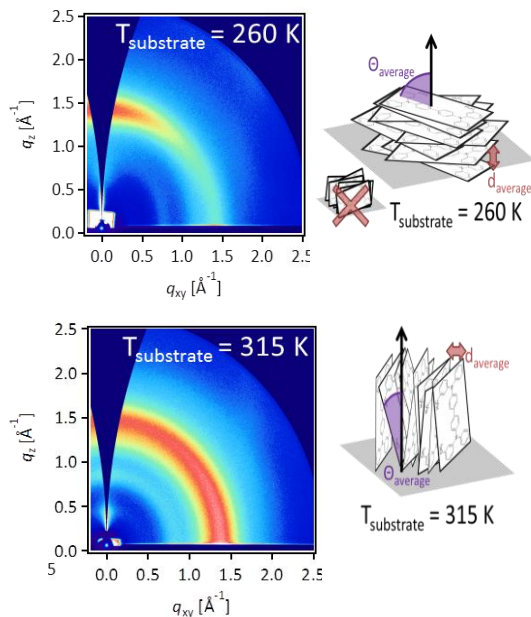


Figure 3. GIWAXS data and schematics illustrating the anisotropic molecular packing for TPD glasses prepared at two substrate temperatures. Schematics exaggerate the order in the films.

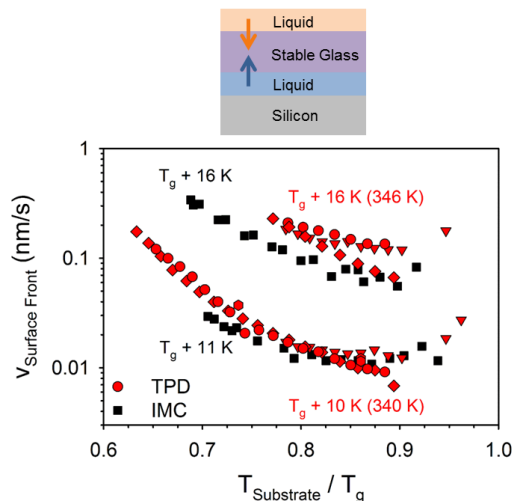


Figure 4. Top: Illustration of a stable glass transforming to a liquid via propagating fronts. Bottom: Free surface initiated front velocity of TPD and IMC glasses deposited at a range of substrate temperatures at several annealing temperatures, measured by ellipsometry.

Future Plans

For the next two years, we have the following priorities: 1) Characterize the molecular orientation and packing in vapor-deposited glasses of disc-shaped and nearly-spherical molecules to investigate the influence of molecular shape on anisotropy. 2) Using our granted SSRL beam time, characterize three molecules with GIWAXS and WAXS to further probe for structure-property relationships. 3) Study the molecular orientation of two component films with an anisotropic host material to investigate how the orientation of the host may influence that of the dopant. 4) Develop fluorescence measurements to characterize the molecular orientation of phosphorescent emitters at very low (~3%) concentrations in host materials.

References:

- (1) Swallen, S. F.; Kearns, K. L.; Mapes, M. K.; Kim, Y. S.; McMahon, R. J.; Ediger, M. D.; Wu, T.; Yu, L.; Satija, S. *Science* **2007**, *315*, 353–356.
- (2) Dalal, S. S.; Walters, D. M.; Lyubimov, I.; de Pablo, J. J.; Ediger, M. D. *Proc. Natl. Acad. Sci.* **2015**, *112*, 4227–4232.
- (3) Kearns, K. L.; Swallen, S. F.; Ediger, M. D.; Wu, T.; Yu, L. *J. Chem. Phys.* **2007**, *127*, 154702.
- (4) Dalal, S. S.; Fakhraai, Z.; Ediger, M. D. *J. Phys. Chem. B* **2013**, *117*, 15415–15425.
- (5) Lyubimov, I.; Antony, L.; Walters, D. M.; Rodney, D.; Ediger, M. D.; de Pablo, J. J. *J. Chem. Phys.* **2015**, *143*, 094502.
- (6) Dawson, K. J.; Zhu, L.; Yu, L.; Ediger, M. D. *J. Phys. Chem. B* **2011**, *115*, 455–463.
- (7) Gujral, A.; O'Hara, K. a.; Toney, M. F.; Chabinyk, M. L.; Ediger, M. D. *Chem. Mater.* **2015**, *27*, 3341–3348.
- (8) Walters, D. M.; Richert, R.; Ediger, M. D. *J. Chem. Phys.* **2015**, *142*, 134504.
- (9) Swallen, S. F.; Traynor, K.; McMahon, R. J.; Ediger, M. D. *Phys. Rev. Lett.* **2009**, *102*, 065503.
- (10) Dalal, S. S.; Ediger, M. D. *J. Phys. Chem. B* **2015**, *119*, 3875–3882.

DOE-Sponsored Research Publications (last 2 years):

- (1) Dalal, S. S.; Fakhraai, Z.; Ediger, M. D. *J. Phys. Chem. B* **2013**, *117*, 15415–15425.
- (2) Dalal, S. S.; Ediger, M. D. *J. Phys. Chem. B* **2015**, *119*, 3875–3882.
- (3) Dalal, S. S.; Walters, D. M.; Lyubimov, I.; de Pablo, J. J.; Ediger, M. D. *Proc. Natl. Acad. Sci.* **2015**, *112*, 4227–4232.
- (4) Walters, D. M.; Richert, R.; Ediger, M. D. *J. Chem. Phys.* **2015**, *142*, 134504.
- (5) Gujral, A.; O'Hara, K. a.; Toney, M. F.; Chabinyk, M. L.; Ediger, M. D. *Chem. Mater.* **2015**, *27*, 3341–3348.
- (6) Lyubimov, I.; Antony, L.; Walters, D. M.; Rodney, D.; Ediger, M. D.; de Pablo, J. J. *J. Chem. Phys.* **2015**, *143*, 094502.

Program Title: Artificially Layered Superlattice of Pnictide by Design

Principle Investigator: Chang-Beom Eom

Mailing Address: Room 2166 ECB, 1550 Engineering Drive, University of Wisconsin-Madison,
Madison, WI 53706

E-mail: eom@engr.wisc.edu

Program Scope

The goals of the program are to grow artificially engineered superlattices of pnictide materials by atomic layer-controlled growth, and to understand how structure property-relationships interact with the novel superconductivity in the pnictides so as to develop new understanding, applications, and devices. The critical scientific issues we will address include growth mechanisms, interaction between superconductivity and magnetism, interfacial superconductivity and physics of flux pinning in pnictide thin film heterostructures. We expect that this goal will also enable an understanding of the fundamental heteroepitaxial growth of intermetallic systems on oxide surfaces and role of interfacial layers in a sufficiently general way that can be applied broadly to many different material systems.

The discovery of superconductivity with transition temperatures of 20K-50K in iron-based materials has initiated a flurry of activity to understand and apply these novel materials. The superconducting mechanism, the structural transitions, the magnetic behavior above and below T_c , the doping dependence, and the critical current and flux-pinning behavior have all been recognized as critical to progress toward understanding the pnictides. A fundamental key to both basic understanding and applications is the growth and control of high-quality epitaxial thin films and superlattices with atomic layer control. The ability to control the orientation, the strain state, defect and pinning site incorporation, the surface and interfaces, and the layering at the atomic scale, are crucial in the study and manipulation of superconducting properties.

An important characteristic of the Co-doped BaFe_2As_2 (Ba-122) material is the relatively low values of doping required to produce superconductivity. This leads to homogeneous films, and similar lattice constants between differently doped films, and great potential for epitaxial superlattices. The 122 materials share the fundamental iron-containing planes that are believed to be responsible for superconductivity, and they potentially all share the same basic mechanism of superconductivity, with a leading candidate being s^+ pairing between electron and hole pockets at the zone center and boundary. All share the five Fe $3d$ -orbitals important in the electronic structure, leading to a richness that has great potential for manipulation. In addition, the likely coexistence of magnetism and superconductivity for low-doping, and the nearby structural transitions in the intermediate-doping region, offer great flexibility in the design of new superlattices of, for instance, doped 122 and perovskite oxides, 122 layers of different doping levels, and doped 122 layers with the semi-metallic undoped parent compound.

We are guided to the main goals by our understanding developed over the last three years in relating pnictide structural and superconducting properties. The new film growth methods used in this project enables us to not only resolve these uncertainties, but also to design and synthesize new pnictide atomic layered structures that explore the limits of this material's superconducting properties. The **thrusts** of our project are:

- (1) *Atomic-layer-controlled growth of artificially engineered superlattice synthesis*
- (2) *Designing interfacial superconductivity at pnictide and FeSe interfaces.*
- (3) *Investigation of interaction between superconductivity and magnetism by proximity effect*
- (4) *Understanding and control of flux-pinning mechanisms*
- (5) *Study of growth mechanisms of heteroepitaxial superlattices and artificial pinning centers*

Recent Progress

1. Atomic-layer-controlled growth of $\text{Ba}(\text{Fe}_{1-x}\text{Co}_x)_2\text{As}_2$ films

BACKGROUND

The discovery of superconductivity with transition temperatures of 20K-50K in iron-based materials has initiated a flurry of activity to understand and apply these novel materials. The superconducting mechanism, the structural transitions, the magnetic behavior above and below T_c , the doping dependence, and the critical current and flux-pinning behavior have all been recognized as critical to progress toward understanding the pnictides. A fundamental key to both basic understanding and applications is the growth and control of high-quality epitaxial thin films and superlattices with atomic layer control. The ability to control the orientation, the strain state, defect and pinning site incorporation, the surface and interfaces, and the layering at the atomic scale, are crucial in the study and manipulation of superconducting properties.

DISCUSSION and FINDINGS

We have studied the influence of perovskite substrate surface termination on the properties of superconducting pnictide thin films to understand the thermodynamic equilibrium between at pnictide thin film/oxide interfaces. To explain the dependence on substrate surface termination, we proposed the schematic growth model of Co-doped BaFe_2As_2 described in Fig. 1. Due to the different crystal structures, the interface with SrO terminated substrate will have high interfacial energy with the film, and need additional stabilization through surface reconstruction. However, Ba layer as the 1st layer on top of TiO_2 surface maintains the perovskite stacking of SrTiO_3 . We find in this case that the unit cell of BaFe_2As_2 grows epitaxially after reaching interfacial equilibrium. In contrast, it is relatively hard to reach phase stability at the interface between Ba122 and SrO surface because arsenic is volatile as a starting layer. Fe and Co elements may interdiffuse/intermix with Ti at the surface of SrTiO_3 to move toward thermodynamic stability. We have grown Co-doped pnictide thin films on SrTiO_3 (001) substrates with the controlled termination states. As-received SrTiO_3 substrates have the mixed termination states of both TiO_2 and SrO, whereas the single TiO_2 termination can be attained by chemical etching treatments using buffered hydrofluoric (BHF) acid etchant.

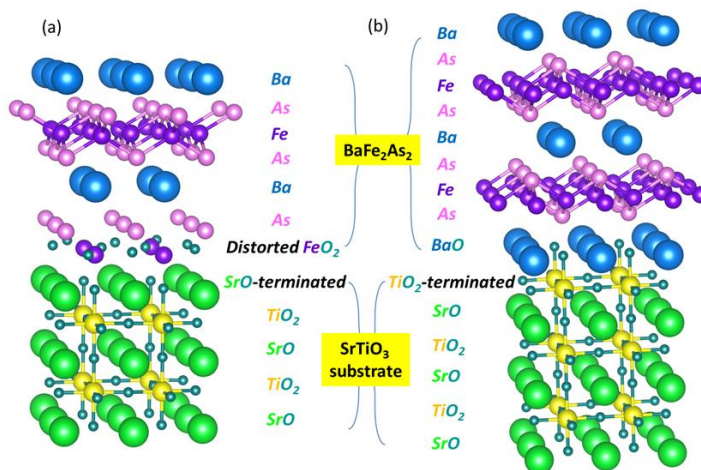


Figure 1. Schematic model of BaFe_2As_2 thin film on (a) TiO_2 and (b) SrO-terminated SrTiO_3 .

Scanning transmission electron microscopy

(STEM) measurements show that the interfacial layer depends on the surface termination of SrTiO_3 substrates. In TiO_2 -terminated regions, a Ba layer was imaged as the first interfacial layer, whereas a FeAs layer was shown on SrO-terminated regions as shown in Fig. 2. Note that one unit-cell of BaFe_2As_2 is consisted of the stacking structures of Ba-AsFeAs-Ba-AsFeAs-Ba. Therefore, clear and abrupt interface for epitaxial BaFe_2As_2 film growth can be apparently found on TiO_2 -terminated SrTiO_3 with less diffusion. On the other hand, there is more diffusion with broader interface on SrO surface termination. We have also found that superconducting transition temperature (T_c) for Ba122 on TiO_2 -terminated SrTiO_3 is significant higher than mixed surface terminated SrTiO_3 . In particular, the difference in T_c is

much more pronounced in ultrathin films because atomically sharp interface can be formed and chemical diffusion is also suppressed with less reaction layer.

Importance of findings both from experimental and theoretical perspectives:

Based on theoretical calculations and STEM imaging at the Ba122/SrTiO₃ interfaces with the surfaces termination control, we have confirmed that non-perovskite Ba-122 films shows atomically sharp and well-defined interfaces with TiO₂-terminated STO perovskites. This interface engineering is not only

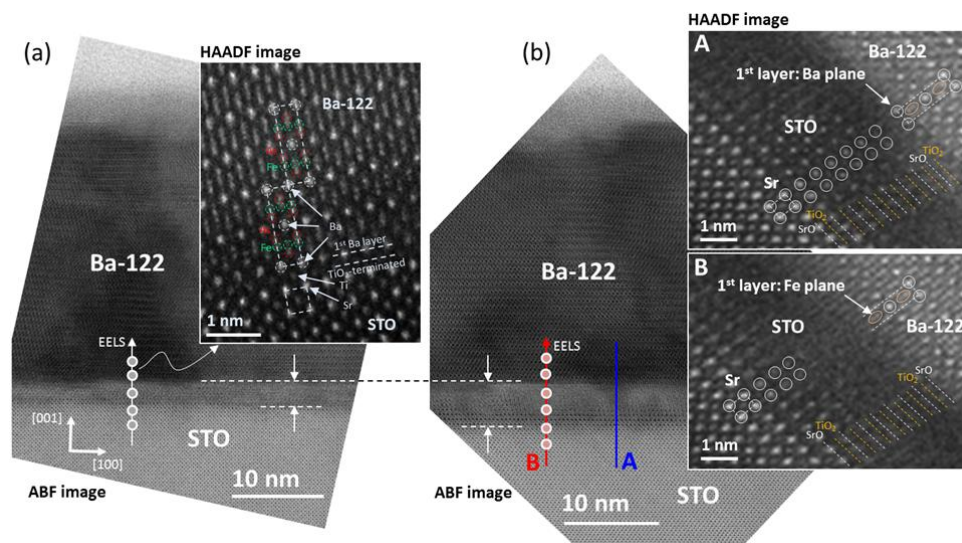


FIG. 2. High resolution STEM ABF and HAADF images for 24 nm thick Ba-122 films on (a) TiO₂-terminated STO by BHF etching and (b) mixed surface termination of as-received STO. There is a clear interface with Ba layer as a 1st layer on top of TiO₂ terminated STO, whereas SrO surface termination has blurred interface with more diffusion.

improve performance and new functionalities of Fe-based superconducting thin films with engineered interface of various perovskite oxide substrates.

Future Plans

(1) Superconductivity and magnetism at atomically abrupt Pnictide interfaces

The interaction between magnetism and superconductivity is central to the physics of pnictide superconductors, as well as other modern superconductors with potential applications. We have demonstrated that epitaxial heterostructures with sharp interfaces can be made between the optimally-doped material Ba(Fe,Co)₂As₂ and other doping levels, as well as insulators such as SrTiO₃, and metallic ferromagnets such as Ni, Co, and Fe. We will compare two different Normal Metal (N) / Superconductor (S) configurations, using the same superconducting layer and changing the N layer properties to determine the interfacial interaction of superconductivity and magnetism. The SC material will be fixed at optimal doping Ba(Fe_{0.92}Co_{0.08})₂As₂ (x=0.08), with maximum T_c (see Fig. 3, the phase diagram for Ba-122 with Co doping). In the first N_u (undoped normal metal) /S (superconductor) interface, the normal metal (N_u) will be undoped BaFe₂As₂ in which the AFM-SDW correlations dominate. In the second N_o (overdoped normal metal) /S (superconductor) interface, the normal metal (N_o) will be heavily doped Ba122 (x=0.20), a paramagnetic metal with no AFM ordering and no SC transition. In Fig. 3 the blue, purple and red arrows represent, respectively, the low doping, optimally doping and over-doping Ba-122 compounds, whose relative interaction we propose to study. Any weakening or enhancement of superconductivity in these systems (i.e., seen as a decrease or increase of T_c) will provide a straightforward demonstration of the competitive nature or coexistence of the two long-range orders. The comparison between the two heterostructures will also determine if magnetism has an important role as mediator in the interaction that drives superconductivity in pnictides.

limited to STO substrates, but can also be used to explore the STO buffer layer on various perovskite substrates with different lattice parameters and artificially layered superlattices. We believe that deliberately strained STO template layer with TiO₂ surface termination can also open many possibilities for fundamental research for strain engineering in monolayer FeSe. It can be tailored to

(2) Designing interfacial superconductivity at FeSe interfaces

We plan to grow FeSe monolayers on different ferroelectric surfaces in collaboration with Lian Li's group at UW-Milwaukee, exploiting our group's long history in the preparation of strained ferroelectric films. The motivation here is the suggestion that screening by ferroelectric (FE) phonons may be responsible for the greatly enhanced T_c in monolayer FeSe grown on SrTiO₃ (STO). Such FE phonons in STO are relevant at temperatures below ~100K when the dielectric constant becomes quite large, but are present already at higher temperatures in other FE materials such as BaTiO₃.

Alternative ferroelectric surfaces will be explored starting with biaxially strained epitaxial thin films of Ti- surface terminated BaTiO₃ on rare-earth scandate ($REScO_3$) substrates with different lattice parameters. These new substrates include seven different $REScO_3$ compositions with lattice constants that vary in 0.01 Å increments. High quality single crystal BaTiO₃ thin films are necessary, as bulk single-crystal substrates of BTO crack easily under thermal cycling due to the phase transitions. The strain state and remnant polarization of the strained BaTiO₃ thin film prior to FeSe monolayer deposition can be controlled by using substrates with different lattice mismatch, keeping the FE film thickness less than the critical one for relaxation. Such film strain will change the frequency of the zero-point FE phonon mode, the mode suggested as responsible for the dielectric screening, offering a new parameter to control the dielectric screening of the FeSe film. In addition, the final surface termination of these FE films (i.e., AO or BO₂, or mixed) can be controlled by *in situ* RHEED before the FeSe monolayer films are grown, offering an additional degree of freedom as compared to single-crystal substrates. We also plan to study the electronic band structures of monolayer FeSe on strained SrTiO₃ template using our ARPES system. We are currently setting up an ARPES system integrated with *in situ* laser MBE thin film growth system.

References (which acknowledge DOE support)

1. "Gate-tunable superconducting weak link behavior in top-gated LaAlO₃-SrTiO₃", V.V. Bal, M.M. Mehta, S. Ryu, H. Lee, C.M. Folkman, C.B. Eom, V. Chandrasekhar, *Appl. Phys. Letts.*, **106**, 212601, (2015)
2. "Epitaxial CrN Thin Films with High Thermoelectric Figure of Merit", C.X. Quintela, J.P. Podkaminer, M.N. Luckyanova, T.R. Paudel, E.L. Thies, D.A. Hillsberry, D.A. Tenne, E.Y. Tsymbal, G. Chen, C.B. Eom, and F. Rivadulla, *Adv. Mat.*, **27**, 3032, (2015)
3. "Atomic and electronic structures of superconducting BaFe₂As₂/SrTiO₃ superlattices" P. Gao, Y. Zhang, S. Y. Zhang, S. Lee, J. Weiss, J. R. Jokisaari, E. E. Hellstrom, D. C. Larbalestier, C. B. Eom, and X. Q. Pan, *Phys. Rev B.*, **B91**, 104525 (2015)
4. "Development of very high J_c in Ba(Fe_{1-x}Co_x)₂As₂ thin films grown on CaF₂", C. Tarantini, F. Kametani, S. Lee, J. Jiang, J. D. Weiss, J. Jaroszynski, E. E. Hellstrom, C. B. Eom and D. C. Larbalestier, *Scientific Report*, **4** : 7305 (2014)
5. "Electrodynamics of superconducting pnictide superlattices", A. Perucchi, F. Capitani, P. Di Pietro, S. Lupi, S. Lee, J.H. Kang, J. Jiang, J.D. Weiss, E.E. Hellstrom, C.B. Eom, P. Dore, *Appl. Phys. Letts.*, **104**, 222601 (2014)
6. "Epitaxial Al₂O₃ capacitors for low microwave loss superconducting quantum circuits" K.-H. Cho, U. Patel, J. Podkaminer, Y. Gao, C. M. Folkman, C. W. Bark, S. Lee, Y. Zhang, X. Q. Pan, R. McDermott and C. B. Eom, *APL Materials*. **1**, 042115 (2013)
7. "Transmittance and reflectance measurements at terahertz frequencies on a superconducting BaFe_{1.84}Co_{0.16}As₂ ultrathin film: an analysis of the optical gaps in the Co-doped BaFe₂As₂ pnictide" A. Perucchi, L. Baldassarre, B. Joseph, S. Lupi, S. Lee, C.B. Eom, J. Jiang, J.D. Weiss, E.E. Hellstrom, P. Dore, *European Physical Journal B*, **86**, 274 (2013)

Other References

8. "Electron Pairing Without Superconductivity", Guanglei Cheng, Michelle Tomczyk, Shicheng Lu, Josh Veazey, Mengchen Huang, Patrick Irvin, Sangwoo Ryu, Hyungwoo Lee, Chang-Beom Eom, C. Stephen Hellberg, Jeremy Levy, *Nature*, **521**, 196, (2015)

Using Multi-Phase Energetic Precursor Jets to Enable New Modes of Focused Electron Beam Induced Processing (FEBIP)

Andrei G. Fedorov, G. W. Woodruff School of Mechanical Engineering, Georgia Tech

Program Scope

Current program focuses on developing new capabilities and establishing the fundamental understanding of using energized gas and liquid phase jet precursor delivery for FEBIP, including:

Gas Jet Molecular Modeling and Simulations: We are developing a novel approach based on dynamic adaptation of number of simulated particles in a computational cell, or Adaptive Direct Simulation Monte Carlo (Adaptive-DSMC), which has a range of applicability and validity across the entire range of flow regimes realized in Gas-Jet-Assisted FEBIP. First set of comprehensive gas-jet simulations under relevant experimental conditions have been performed, which demonstrated – for the first time - the impact of supersonic jet focusing on localization of molecular flux on the substrate, and confirmed via complimentary experiments on PMMA (contaminant) ablative removal (“cleaning”) and high purity tungsten nanostructure growth from an organometallic $W(CO)_6$ precursor with minimal entrapment of C/CO ligands.

Energized Gas Jet Assisted Electron Beam Etching (FEBIE) of Graphene: We demonstrated that use of a microjet enabling supersonic delivery of heated oxygen yields a substantial improvement in the Focused Electron Beam Induced Etch (FEBIE) rate and parasitic carbon contamination removal, which provide a path to overcome intrinsic challenges of using FEBIE as a “direct write” tool for nanoscale patterning of graphene electronic devices.

Dynamic Modulation Graphene Electronic Properties Using FEBID Carbon Doping: We discovered a new phenomenon of controllable carbon doping of graphene, which allows tuning of local electronic properties of a graphene conduction channel using focused electron beam induced deposition (FEBID). An “n-p-n” junction on graphene conduction channel is formed near the source and drain metal contacts by partial carbon deposition of the FEBID carbon atoms, which are physisorbed and weakly bound to graphene and diffuse towards the middle of graphene conduction channel due to their surface chemical potential gradient, resulting in negative shift of Dirac voltage. In combination with using energetic inert gas jets for locally tuning the FEBID carbon dopant distribution and transport properties, these findings establish a new route to resist-free, “direct-write” functional patterning of graphene-based electronic devices with potential for on-demand re-configurability.

Electrospray-assisted Focused Electron Beam Induced Deposition (ES-FEBID) from Liquid Phase Precursors: We invented and experimentally demonstrated a fundamentally new approach to FEBID using liquid phase precursors delivered using the jet/droplet electrospray process into a vacuum environment of deposition chamber. Not only this process dramatically expands the range of precursors available for FEBID, but also allows for dynamically controlled formation of a large in extent, stable thin liquid film enriched with the precursor on the surface of deposition substrate, which allows for scalable formation of nanostructures over large surface areas.

Recent Progress

Adaptive DSMC for Gas-Jet Simulation: New Technique Development and Validation. Gas jet interactions with the substrate surface are foundational to FEBIP. Therefore, complimentary gas-jet simulations and experiments have been performed to spatially and quantitatively characterize the substrate properties due to impingement from a supersonic gas-jet. The Adaptive-DSMC unique capability is to transcend several orders of magnitude variation in the molecular mean free path upon gas jet introduction from the external supply reservoir to the vacuum environment of the deposition chamber, ultimately predicting the spatially resolved molecular flux and impingement energy on the surface. The strategy behind the adaptive algorithm is to use the “cell factor” – the ratio between simulation particles

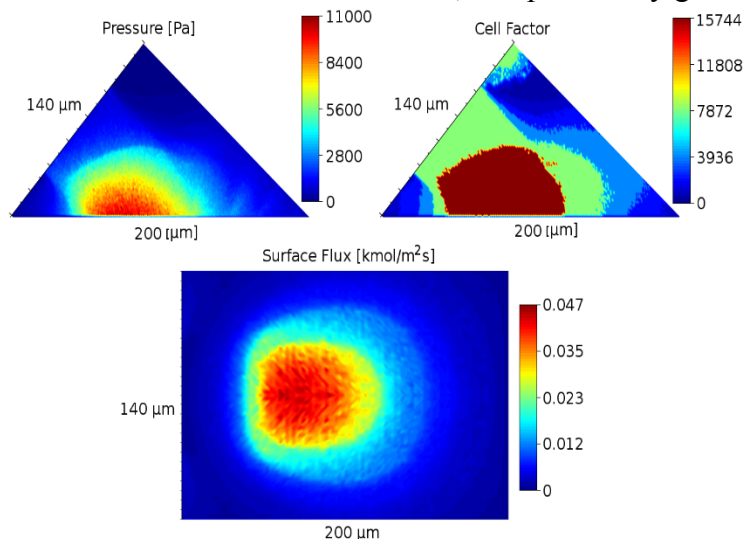


Fig. 1 (Clockwise): Adaptive DSMC simulation of Ar gas-jet emanating from a 75 μm ID nozzle onto an evacuated substrate tilted at 45°. The magnitude of the cell factor defines the isolines bounding different flow regimes (continuous, transitional, rarefied) within computational domain. The ultimate result is prediction of the magnitude and distribution of the molecular flux on substrate.

and physical particles – to vary from one computational cell to the next. This allows each cell to hold a computationally practical number of particles for each regime and the same molecular physics to be applied to each regime. The Adaptive-DSMC has been applied to simulate experimental conditions typically used in our Gas-Jet FEBID with results shown in Figure 1, which are in excellent agreement with experiments.

Supersonic Gas Jet Assisted Electron Beam Etching of Graphene. Along with a focused electron beam induced deposition (FEBID) technique, focused electron beam induced etching (FEBIE) also provides a superior lithographic capability to controllably manipulate material structure and properties. Especially, it is very promising when applied to 2D monolayer materials, such as graphene, whose electronic properties can be changed from semi-metallic to semiconducting by nanoscale modification of its geometry to nanoribbons. We investigated the utility of energized (heated) oxygen micro-jets for accomplishing high resolution FEBIE with minimal parasitic carbon deposition and fast etching time. Using

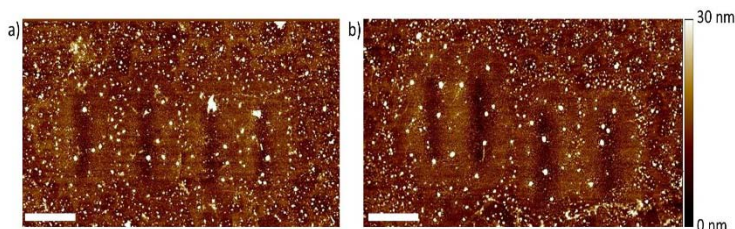


Fig. 2: Line etching of graphene with different flow rates of oxygen micro-jets, 3 sccm, 5 sccm, 7 sccm and 10 sccm (from the left to the right), at two different jet temperatures: a) room temperature (24 °C) and b) heated to 100 °C. Scale bar: 4 μm .

10 μm ID injection nozzle we first optimized the electron irradiation zone in order to determine the best location surrounding the center of an oxygen jet impact area for FEBIE. At a fixed nozzle position and oxygen jet conditions (10 sccm & $T_{\text{jet}} \sim 24^\circ\text{C}$), graphene etching was successful at all locations within $\pm 20 \mu\text{m}$ from the center point of the jet impact area with the point of direct jet line-of-sight to be most optimal for etching. Using electron beam current $\sim 250 \text{ pA}$, energy $\sim 10 \text{ kV}$, and dose $\sim 2 \times 10^{19} \text{ e}^-/\text{cm}^2$, line etching was performed with oxygen flow rates from 3 sccm to 10 sccm at two distinct gas-jet temperatures, 24°C vs. 100°C . Fig. 2 shows AFM images after FEBIE. At both gas jet temperatures, increasing flow rates from 3 sccm to 5 sccm improved the etching outcome and reduced the thickness of ‘halo’ deposits. Further increase of oxygen flow rates degrades etching quality due to increased chamber pressure, promoting e-beam scattering. Compared to the etching result with room-temperature oxygen jets, heating jets to 100°C led to improved etching (Fig. 2b). Specifically, with 5 sccm oxygen micro-jets, etching depth was measured $\sim 4 \text{ nm}$ for the heated vs $\sim 3 \text{ nm}$ for the unheated jets. This indicates that thermally energized, oxygen micro-jets can overcome many challenges (poor resolution, long etching time and parasitic carbon deposition) of FEBIE.

Dynamic Modulation of Graphene Electronic Properties Using FEBID Carbon Doping.

Controllable carbon doping using FEBID was demonstrated to modulate electronic properties of graphene (Fig. 3), both the local formation and evolution of the p-n junction and long-term stabilized modification of its doping state. Initially, CVD graphene in electronic devices is p-doped by PMMA residues from the graphene transfer process and lithography steps. Upon electron beam treatment with a low electron dose $\sim 1 \times 10^{18} \text{ e}^-/\text{cm}^2$, locally concentrated FEBID carbon is deposited near the graphene-metal junction, where the primary electron beam strikes, which establishes an “n-p-n” junction on the graphene channel. At room temperature, the weakly interacting FEBID carbon atoms diffuse towards the middle of the graphene channel due to their surface concentration gradient and rearrange their structure reducing the level of initial graphene p-type doping. When a high electron dose $\sim 1 \times 10^{19} \text{ e}^-/\text{cm}^2$ treatment is used, FEBID carbon film is deposited on the graphene channel uniformly throughout with sufficiently high surface density, which completely reverses doping state of the graphene channel from p-type to n-type. When combined with oxygen-jet FEBIE, these experiments not only highlight a unique capability for tuning the graphene’s electronic properties *via* controlled carbon FEBID doping, but also suggests a new possibility of using energized gas jets for local control of doping state by selective carbon removal.

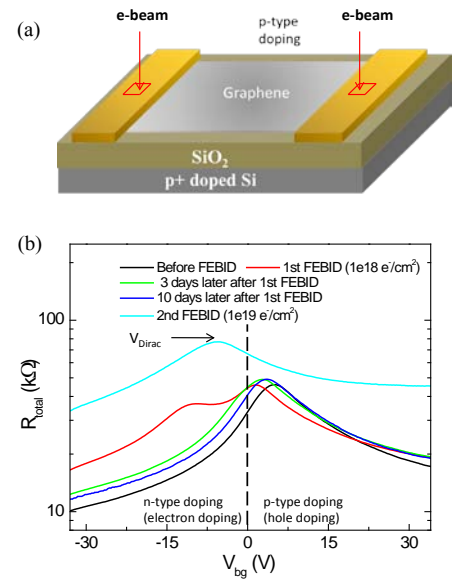


Fig. 3. (a) Schematic of FEBID treatment of graphene device channel via irradiation of metal contacts. (b) Change of the electric transfer characteristic (R_{tot} vs. V_{bg}) upon FEBID of carbon, showing dynamic control of doping state of the graphene channel.

Electrospray (ES)-Jet-Assisted FEBID from Liquid Phase Precursors. Exploratory work has been conducted to investigate the use of liquid-phase ionic precursors delivered via nanoelectrospray (nanoES)-driven jets coupled with FEBID to form deposits upon e-beam mediated electrochemical reduction of precursor. The process of nanoES-FEBID is described in Figure 4. A pre-filled pulled glass capillary is mounted in the SEM chamber and the tip is brought near to the substrate. A high-voltage power supply is used to apply a positive bias to the capillary, relative to grounded substrate, to deliver liquid precursor via the electrohydrodynamic Taylor cone-jet. Thin liquid pool is achieved by initiating spray and adjusting the potential and the tip/substrate gap until a liquid pool of desired width is observed. Upon exposure to the electron beam at 25 keV and 13.4 nA, silver and carbon nanopillar deposits have been rapidly grown at the rate exceeding by 4 orders of magnitude the current state-of-the-art for gas-phase FEBID.

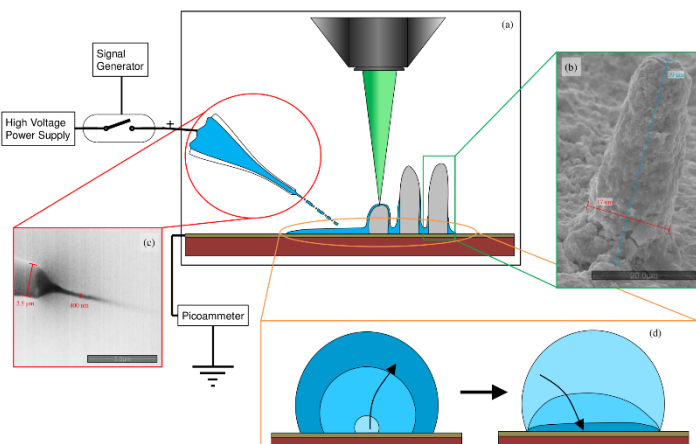


Fig. 4: (a) Schematic of ES-Jet-FEBID. A pulled glass capillary emitting nanoelectrospray sustains a pool of liquid that supplies precursor to the deposition site. Deposits grow from the deposition site, forming pillars if the beam is held in-place. (b) A silver pillar, 17 μm base width and 39 μm height, deposited from silver nitrate precursor. (c) SEM image of nanoES Taylor cone-jet from a 2.5 μm outer diameter tip. (d) Thin liquid film is achieved by forming a droplet of desired width, then reducing the spray voltage until a sufficient thinning occurs via solvent evaporation.

Future Plans

Energetic Gas Jet FEBID & Simulations. Two key parameters of the energetic gas jet - the molecular flux on the substrate and internal energy of precursor molecules due to gas heating at the nozzle - will be experimentally correlated with and tuned to affect the key deposition parameters, such as substrate temperature and the precursor sticking coefficient. In concert with these experiments, adaptive-DSMC modeling will be performed to be able to relate the experimentally measured macroscopic properties to fundamental molecular properties of the precursor species, substrate material and jet flow regime. Ultimately, this basic understanding will provide a foundation for in silico optimal design of energetic gas-jet assisted FEBIP process.

Energized Gas Jet FEBIE of 2D Materials. Fundamental limits will be assessed to provide a complete map of FEBIE outcomes (etch rate, spatial resolution, and extent of parasitic carbon deposition around etched domains) as function of experimental conditions for etchant delivery by the gas jet for graphene and other emerging 2D electronic materials (MoS_2 , hBN, etc). Adaptive DSMS simulations will be used to aid in interpretation of experimental observations, which will ultimately enhance our first-principles understanding of micro-jet assisted FEBIE.

ES-Jet-Assisted FEBID from Liquid Phase Precursors. The focus is on gaining fundamental understanding of physico-chemical mechanisms underlying liquid phase FEBID through probing interactions between primary, secondary and solvated electrons with electrified precursor liquids.

Publications

1. Kim, S., Russell, M., Henry, M., Kim, S., Naik, R., Voevodin, A. A., Jang, S., Tsukruk, V. V. and Fedorov, A. G., “Dynamic modulation of electronic properties of graphene by localized carbon doping using focused electron beam induced deposition”, *Nanoscale*, **7**, 14946-14952 (2015).
2. Kim S., Kulkarni D. D., Davis, R., Kim, S. S., Naik, R. R., Voevodin, A. A., Jang, S., Tsukruk, V. V. and Fedorov A. G., “Controlling Physicochemical State of Carbon on Graphene Using Focused Electron Beam Induced Deposition (FEBID)”, *ACS Nano* **8** (7), 6805-6813 (2014).
3. Fedorov, A., Kim, S, Henry, M., Kulkarni, D., Tsukruk, V. V., “Focused electron beam induced processing (FEBIP) for emerging applications in carbon nanoelectronics”, *Appl. Phys. A – Mat. Sci. & Proc.*, **invited**, **117**, pp. 1659-1674 (2014).
4. Kim, S., Henry, M. and Fedorov, A. G., “High resolution patterning of graphene using focused electron beam induced etching (FEBIE) with an assist of energetic oxygen microjet”, *Appl. Phys. Lett.*, in review (2015).
5. Fisher, J., Kottke, P. A., Kim, S. and Fedorov, A. G., “Rapid electron beam writing of topologically complex 3D nanostructures using liquid phase precursor”, *Nano Lett.*, in review (2015).
6. Kim, S, Russell, M., Kulkarni, D., Henry, M., Kim, S., Naik, R., Voevodin, A. A., Jang, S., Tsukruk, V. V. and Fedorov, A., Activating “invisible” glue: using electron beam for enhancement of interfacial properties of graphene-metal contact, *ACS Nano*, in review (2015).

Forces, Crystallization, and Assembly in Nanoparticle Suspensions

K. A. Fichthorn (PI) and R. M. Rioux (Co-PI)
Department of Chemical Engineering
The Pennsylvania State University
University Park, PA, 16802

Program Scope

In the past decade, an astounding variety of intricate nanostructures, having at least one dimension of 100 nm or less, have been synthesized via solution-phase techniques. These nanostructures will benefit numerous applications in energy technology. It has been emphasized that the sizes, shapes, phases, and assembly or dispersion of the nanoparticles can significantly impact their performance. A deep, fundamental understanding of the phenomena that promote shape-selective growth and assembly in these syntheses would enable tight control of nanostructure morphologies in next-generation techniques and allow for the synthesis of more elaborate nanostructures. In many systems, structure-directing agents (SDAs) are used. These agents can range from small monomer molecules to high-molecular-weight polymers. Although there is a great deal of experimental evidence indicating that SDAs can play a pivotal role in selectively producing various nanostructures, their exact role remains elusive.

In this work, complementary theoretical and experimental methods are used to quantify the binding of SDAs to coinage-metal surfaces and to resolve mechanisms of shape-selective growth. On the theoretical side, first-principles, dispersion-corrected, density-functional theory (DFT) and classical molecular dynamics (MD) simulations are employed to quantify binding energies, as well as mechanisms by which solution-phase growth occurs. Two experimental platforms – isothermal titration calorimetry and *in-situ*, liquid-phase, high resolution transmission electron microscopy – are being developed and used to quantify SDA binding energies to various nanostructures and provide a real-time, *in-situ* view of nanostructure growth.

Recent Progress

Our recent theoretical work is inspired by an experimental study of Xia *et al.* [1], who probed the growth of cubic Ag nanocrystal seeds in ethylene glycol (EG) solvent using polyvinylpyrrolidone (PVP). PVP is a well-known SDA for promoting {100}-faceted Ag nanocrystals and this capability has been attributed to preferential binding of PVP to Ag(100) [2]. They found that {100}-faceted seed cubes continue to grow as cubes, if the concentration of PVP is sufficiently high. Below a critical PVP concentration, the cubic seeds evolve into cuboctahedra and

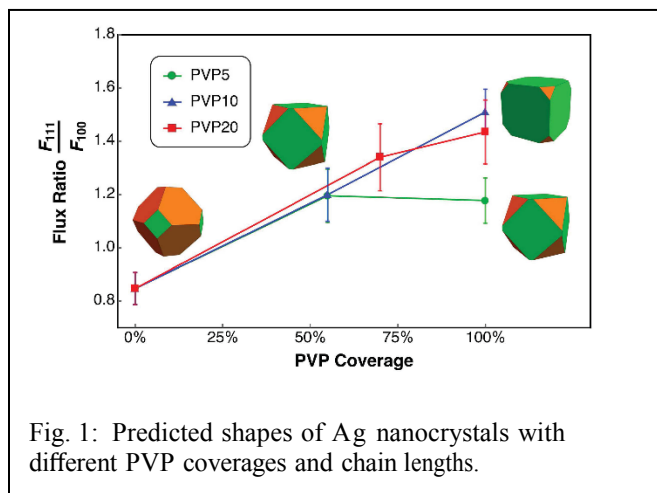


Fig. 1: Predicted shapes of Ag nanocrystals with different PVP coverages and chain lengths.

{111}-faceted octahedra. These relatively large nanostructures (40-100 nm size range) are likely controlled by kinetics and the kinetic Wulff construction can be used to predict shape evolution.

We used MD simulations and theory to probe the octahedron-to-cube transition seen experimentally by Xia *et al.* [1]. Our MD simulations are based on an empirical potential that we fit to our results from dispersion-corrected DFT [3-5]. Using MD, we calculated potentials of mean force to obtain the free-energy profiles for Ag atoms to approach PVP-covered surfaces in EG solution. We also quantified the mean-first passage time for solution-phase Ag atoms to reach Ag(100) and Ag(111) facets. We find that PVP induces kinetic Ag nanocrystal shapes by regulating the relative Ag fluxes to these facets. Strong PVP binding to Ag(100) leads to a larger Ag flux to Ag(111) and cubic nanostructures through two mechanisms: enhanced Ag trapping by more extended PVP films on Ag(111) and a reduced free-energy barrier for Ag to cross lower-density films on Ag(111). Figure 1 shows our predicted shapes for Ag nanocrystals with different PVP coverages and chain lengths. These are consistent with experiment.

Our recent experimental progress has concentrated on three primary aspects: (i) synthesis of phase-pure, high yielding Ag cube and octahedron syntheses; (ii) development of a robust ITC method for evaluating the thermodynamic parameters for PVP binding through displacement titration of thiols; (iii) influence of small PVP-like molecules on the growth of Ag cubes. Additional topics being investigated but not discussed here include the synthesis of PVP “dimers” with varying alkyl spacers and the quantification of PVP on Ag nanoparticle (cubes and octahedron) by gel permeation chromatography, which will be used to quantify how many ligands are displaced.

High yielding synthesis of cubes [6] and octahedra [7] were achieved with minor modification of published protocols (**Figure 2A and B**). These particles were filtered to produce monodisperse Ag particle populations, followed by numerous washing to remove excess and weakly bound PVP from the surface. We have previously demonstrated that thiol adsorption on coinage metal nanoparticle surfaces provides strong sigmoidal signals the ITC due the strength of the Au-S bond [8]. Since a colloidal nanoparticle surface is never free of adsorbate, we developed a displacement titration method using thiol to quantify the thermodynamics of PVP binding by the following equation,

$$K_{app} = \frac{K_{high}}{1 + K_{low}[L_{low}]}$$

where K_{app} is the measured apparent affinity, K_{high} is the affinity of thiol for

Ag, K_{low} and L_{low} represent the affinity of PVP for Ag and the concentration of low-affinity ligand in the calorimeter cell [9]. **Figure 2C** demonstrates the adsorption of thiol to a minimally PVP-covered surface without PVP addition to the calorimeter. On basis of two additional experiments, the form of K_{app} with $[L_{low}]$ will follow the trend shown in **Figure 2D**. K_{high} and K_{low} are expected to be extracted by fitting the equation to various K_{app} evaluated by the single

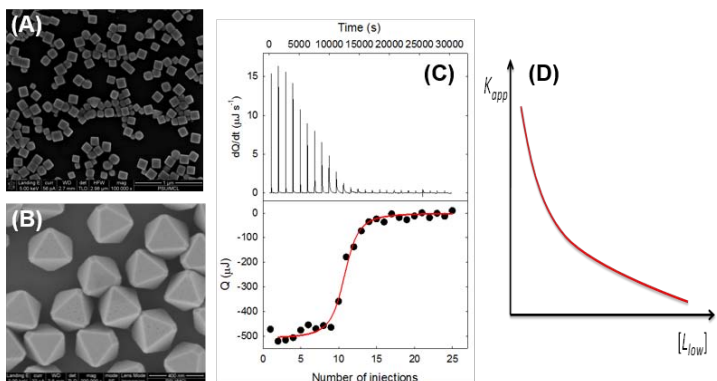


Figure 2. (A-B) SEM micrograph of Ag cubes and octahedral, respectively. (C) titration of 2.86 mM 3-mercaptopropionic acid to PVP-covered Ag cube (0.22 mM of surface Ag atom) (D) proposed relationship between K_{app} and concentration of low affinity ligand.

independent binding depending on $[L_{low}]$. We believe these displacement titration calorimetric measurements using thiols as a probe is the best experimental approach to measuring reliable thermodynamic binding parameters of PVP to Ag, and these K_{low} values can be compared with values determined by Fichthorn.

While it has been demonstrated that low molecular weight PVP (< 10 K) is unable to promote the formation of Ag cubes, we investigated the influence of small molecule PVP-like analogs on the synthesis of Ag cubes. These small molecule analogs are similar to those studied using DFT by the Fichthorn group [5]. **Figure 3** demonstrates that the smallest PVP analog (2-pyrrolidone (2P)) has the greatest influence on the yield of cubic particles. This is a particularly interesting result because it demonstrates that the number of contacts per PVP chain is critical for shape control and upon the addition of a molecule like 2P that is small enough to access the growing Ag surface and is able to displace some PVP chain surface interactions which reduces shape control. This effect is 2P concentration dependent (data not shown). The lack of influence of the presence of 1-(ethyl/octyl/dodecyl)-2-pyrrolidone is associated with the steric effect associated with the alkyl backbone which doesn't enable access to the surface and therefore has limited influence on particle growth.

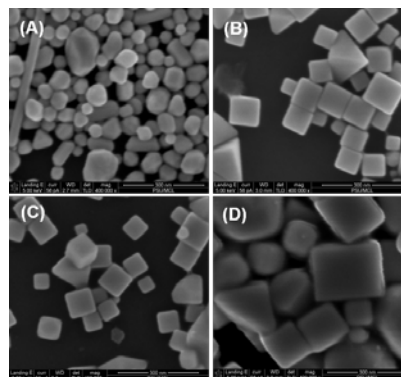


Figure 3. SEM micrographs of Ag particles synthesized by the polyol method with 147 mM PVP (55K) and 1147 mM of (A) 2-pyrrolidone; (B) 1-ethyl-2-pyrrolidone; (C) 1-octyl-2-pyrrolidone; and (D) 1-dodecyl-2-pyrrolidone.

Future Plans

A number of activities are planned for the upcoming year that are already underway. A major effort is centered around using our recently developed force field to describe aspects of PVP-mediated nanocrystal growth: calculating solid-liquid interfacial free energies to predict thermodynamic Wulff shapes of Ag nanocrystals, examining the kinetics of restructuring of small Ag nanocrystals to understand how nanocrystal shape depends on nanocrystal size, investigating the nucleation mechanisms of Ag nanocrystals, and following up on Rioux's experimental results. Rioux will continue to develop the displacement titration method for octahedron particles detailed in Figure 2, as well as quantify the coverage of PVP on Ag cubes and octahedron. Another ongoing effort focuses on characterizing the binding of self-assembled hexadecylamine layers to Cu(100) and Cu(111) to understand the workings of this small-molecule SDA.

References

1. X. Xia, J. Zeng, L.-K. Oetjen, and Y. Xia, "Quantitative analysis of the role played by poly(vinylpyrrolidone) in seed-mediated growth of Ag nanocrystals" *J. Am. Chem. Soc.* **134**, 1793-1801 (2012).
2. Y. Xia, Y. Xiong, B. Lim, and S. E. Skrabalak, "Shape-controlled synthesis of metal nanocrystals: simple chemistry meets complex physics?" *Angew. Chem. Int. Edit.* **48**, 60-103 (2009).

3. Y. Zhou, W. A. Saidi, and K. A. Fichthorn, "A force field for describing the PVP-mediated solution-phase synthesis of shape-selective Ag nanocrystals", *J. Phys. Chem. C* **118**, 3366-3374 (2014).
4. W. A. Saidi, H. Feng, and K. A. Fichthorn, "The binding of PVP to Ag surfaces: Insight into a structure-directing agent from dispersion-corrected density-functional theory," *J. Phys. Chem. C* **117**, 1163-1171 (2013).
5. W. Al-Saidi, H. Feng, and K. A. Fichthorn, "Adsorption of polyvinylpyrrolidone on Ag surfaces: Insight into a structure-directing agent", *Nano Letters* **12**, 997-1001 (2012).
6. S. H. Im, Y. T. Lee, B. Wiley, Y. Xia, "Large-scale synthesis of silver nanocubes: The role of HCl in promoting cube perfection and monodispersity", *Angew. Chem. Int. Ed.* **44**, 2154-2157 (2005).
7. A. Tao, P. Sinsersuksakul, P. Yang, "Polyhedral silver nanocrystals with distinct scattering signatures", *Angew. Chem. Int. Ed.* **45**, 4597-4601.
8. V. Ravi, J. M. Binz, R. M. Rioux, "Thermodynamic Profiles at the Solvated Inorganic-Organic Interface: The Case of Gold-Thiolate Monolayer" *Nano Lett.* **13**, 4442-4448 (2013).
9. D. D. Hu, M. R. Eftink, "Thermodynamic Studies of the Interactions of TRP Aporepressor with Tryptophan Analogs", *Biophys. Chem.* **49**, 233-239 (1994)

Publications

1. K. A. Fichthorn, "Molecular Phenomena in Colloidal Nanostructure Synthesis", *Molecular Simulation* **40**, 134-140 (2014).
2. B. D. Smith, K. A. Fichthorn, D. J. Kirby, L. M. Quimby, D. A. Triplett, P. González, D. Hernández, and C. D. Keating, "van der Waals Forces Drive Orientation of Two-Component Metallic Nanowires within Smectic Arrays: Experiment and Simulation", *ACS Nano* **8**, 657-670 (2014).
3. Y. Zhou, W. Al-Saidi, and K. A. Fichthorn, "A force field for describing the PVP-mediated solution-phase synthesis of shape-selective Ag nanocrystals", *J. Phys. Chem. C* **118**, 3366-3374 (2014).
4. M. Raju, A. C. T. van Duin, and K. A. Fichthorn, "Mechanisms of Oriented Attachment of TiO₂ Nanocrystals in Vacuum and Humid Environments: Reactive Molecular Dynamics", *Nano Lett.* **14**, 1836-1842 (2014).
5. K. A. Fichthorn, "Atomic-Scale Theory and Simulations for Colloidal Metal Nanocrystal Growth", *J. Chem. Eng. Data* **59**, 3113-3119 (2014).
6. Y. Zhou and K. A. Fichthorn, "Internal Stress-Induced Orthorhombic Phase in Fivefold-Twinned Noble-Metal Nanowires", *J. Phys. Chem. C* **118**, 18746-18755 (2014).
7. K. A. Fichthorn, "Atomic-Scale Aspects of Oriented Attachment", *Chem. Eng. Science* **121**, 10-15 (2015).
8. S.-H. Liu, W. A. Saidi, Y. Zhou, and K. A. Fichthorn, "Synthesis of {111}-faceted Au Nanocrystals Mediated by Polyvinylpyrrolidone: Insights from Density-Functional Theory and Molecular Dynamics", *J. Phys. Chem. C* **119**, 11982-11990 (2015).
9. X. Qi, T. Balankura, and K. A. Fichthorn, "How structure-directing agents control nanocrystal shape: PVP-mediated growth of Ag nanocubes" (Submitted to *Nano Lett.*)
10. V. Ravi, J. M. Binz, R. M. Rioux, "Thermodynamic Profiles at the Solvated Inorganic-Organic Interface: The Case of Gold-Thiolate Monolayer" *Nano Lett.* **13**, 4442-4448 (2013).
11. R. M. Rioux and J. W. Chang, Provisional Patent Application Serial No.62/108,381. ISOTHERMAL TITRATION CALORIMETRY METHODS FOR EVALUATION OF THERMODYNAMIC BINDING PROPERTIES (filed January 27, 2015).

Understanding the Role of Viscosity and Deposition Rate during Vapor-Phase Free Radical Polymerization onto Liquid Surfaces

Malancha Gupta, University of Southern California

Program Scope

Our goal is to uncover the mechanisms associated with polymer nucleation, particle growth, and film formation at the vapor/liquid interface during initiated chemical vapor deposition (iCVD) onto liquid surfaces. The iCVD process is a solventless free radical polymerization technique that is traditionally used to deposit thin polymer coatings onto solid substrates from acrylate and acrylamide precursors.^{1,2,3} In the iCVD process, monomer and initiator molecules are flowed into a vacuum chamber where the initiator molecules are broken into free radicals by a heated filament array. The initiating radicals and monomer molecules diffuse to the surface of the cooled substrate and polymerization occurs via a free radical mechanism. We have recently shown that liquids with negligible vapor pressures such as ionic liquids (ILs) and silicone oils can be used as substrates in the iCVD process (Figure 1).^{4,5,6,7} The liquid surface provides new initial conditions for growth due to the mobility of the polymers on liquid surfaces. Our goal is to uncover the molecular mechanisms that govern polymer nucleation and growth at the vapor/liquid interface by systematically studying how different parameters such as liquid viscosity and polymer deposition rate affect the structure and size of the films and particles.

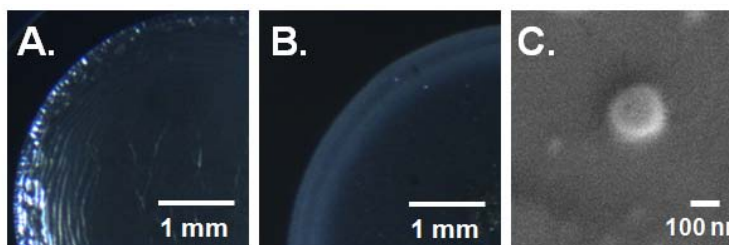


Figure 1. (A) Deposition of fluoropolymer results in a polymer film on silicone oil, (B) whereas deposition of poly(4-vinylpyridine) results in distinct polymer particles. (C) SEM image confirms deposition of distinct particles.

Recent Progress

During this research period, we focused on the polymerization of cross-linked polymers. We had previously found that linear polymers form films or particles on liquid surfaces.⁸ The morphology depends on the surface tension interactions between the polymers and the liquid surfaces, which can be quantified by a spreading coefficient. Systems with positive spreading coefficients form films and systems with negative spreading coefficients form particles. For the past year, we studied the deposition of cross-linked polymers at liquid surfaces since cross-linked polymers have less mobility than linear chains and therefore the dynamics will be different. Our results were interesting. We found that although the spreading coefficients of these cross-linked systems predict the formation of particles, we instead observe the formation of microstructured films. These microstructured films are unique only to cross-linked systems.

We systematically studied the deposition of the cross-linked polymer, poly(ethylene glycol diacrylate) (PEGDA), onto a range of silicone oils with varying viscosities. We used scanning electron microscopy to examine the microstructured films and we found that the films contained micron-sized coral-like microstructures that were comprised of spherical aggregates. We examined the chemical composition of the films by Fourier transform infrared spectroscopy and we found that the microstructured films are composed of homopolymer PEGDA.

We examined the growth on 5, 100, 500, and 5000 cSt silicone oil. Our data showed that the microstructured films grow by simultaneous polymer aggregation at the liquid surface and wetting of the liquid on the growing aggregates. Atomic force measurements and SEM images showed that the microstructures decreased in size with increasing liquid viscosity. This decrease in the feature size is due to slower rates of polymer diffusion resulting in less aggregation on the liquid surface. This also leads to less void space between the microstructures and therefore a decrease in the thickness of the microstructured films with increasing liquid viscosity. The films formed on the high viscosity (5000 cSt) silicone oil were smooth due to very slow diffusion of the polymer at the liquid surface. (Figure 2)

Increasing the liquid viscosity decreases the diffusion rate of the polymer on the liquid surface, but also decreases the wetting rate of the liquid on the polymer. We therefore studied the effect of the polymer deposition rate in order to determine which effect dominates the growth mechanism of the films. Increasing the polymer deposition rate increases the molecular weights of the nucleated chains which diffuse slower on the liquid surface. We examined the growth on 5, 100, 500, and 5000 cSt silicone oil. At every viscosity, increasing the deposition rate decreased the roughness of the film and decreased the total film thickness. Since the wetting rate of the liquid on the polymer is constant at the same liquid viscosity, the changes in the film morphology on the same viscosity liquid with increasing deposition rate demonstrates that the growth of the microstructured films is dominated by the diffusion and aggregation of polymer at the liquid surface.

In addition to PEGDA films, we also created cross-linked copolymer films by depositing 2-hydroxyethyl methacrylate (HEMA) cross-linked with EGDA (P(HEMA-co-EGDA)) and 1-vinyl-2-pyrrolidone (VP) cross-linked with EGDA (P(VP-co-EGDA)). The copolymer films also contain microstructures.

Future Plans

Our future goal is to study the deposition of non-cross-linked polymers onto liquids. The deposition of non-cross-linked polymers leads to the formation of nanoparticles. We plan to study the parameters that affect the nucleation and growth of these particles. We will systematically study the particle size and polydispersity as a function of the viscosity of the liquid and the deposition rate. Our data will be compared to the data for cross-linked systems in order to understand how polymer diffusion is affected in our system.

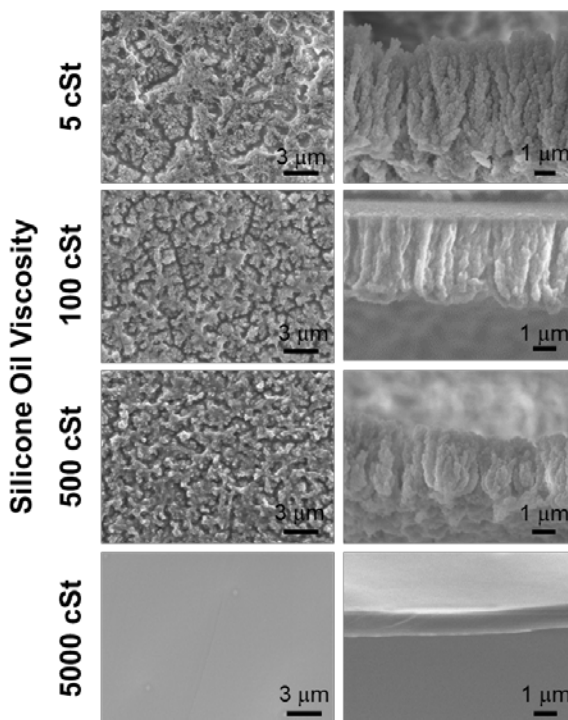


Figure 2. SEM images of the bottomsides and cross-sections of PEGDA films removed from the silicone oil as a function of viscosity.

References

1. "Initiated Chemical Vapor Deposition (iCVD) of Poly(alkyl acrylates): An Experimental Study." K. K. S. Lau, K. K. Gleason, *Macromolecules*, 2006, 39, 3688-3694.
2. "Initiated Chemical Vapor Deposition of Linear and Cross-linked Poly(2-hydroxyethyl methacrylate) for Use as Thin-Film Hydrogels." K. Chan, K. K. Gleason, *Langmuir*, 2005, 21, 8930-8939.
3. "Initiated Chemical Vapor Deposition of Poly(1*H*,1*H*,2*H*,2*H*-perfluorodecyl acrylate) Thin Films." M. Gupta, K. K. Gleason, *Langmuir*, 2006, 22, 10047-10052.
4. "Vapor-Phase Polymerization in the Presence of an Ionic Liquid." P. D. Haller, R. J. Frank-Finney, M. Gupta, *Macromolecules*, 2011, 44, 2653-2659.
5. "Encapsulation of Ionic Liquids within Polymer Shells via Vapor Phase Deposition." L. C. Bradley, M. Gupta, *Langmuir*, 2012, 28, 10276-10280.
6. "Formation of Heterogeneous Polymer Films via Simultaneous or Sequential Depositions of Soluble and Insoluble Monomers into Ionic Liquids." L. C. Bradley, M. Gupta, *Langmuir*, 2013, 29, 10448-10454.
7. "Ultrathin Free-Standing Polymer Films Deposited onto Patterned Ionic Liquids and Silicone Oil." R. J. Frank-Finney, P. D. Haller, M. Gupta, *Macromolecules*, 2012, 45, 165-170.
8. "Effect of Surface Tension, Viscosity, and Process Conditions on Polymer Morphology Deposited at the Liquid–Vapor Interface," P.D. Haller, L.C. Bradley, M. Gupta, *Langmuir*, 2013, 29, 11640-11645.

Publications

"Microstructured Films Formed on Liquid Substrates via Initiated Chemical Vapor Deposition of Cross-Linked Polymers," L. C. Bradley, M. Gupta, *Langmuir*, 2015, 31, 7999.

Nanoscale Selective Growth and Microstructural Control of III-nitride Growth

Ge Yuan, Jie Song, and Jung Han

Department of Electrical Engineering
Yale University, New Haven CT, 06520

Program Scope

Selective area growth (SAG), a technique using lithography to mask and expose portions of surface to direct vapor-phase precursors to crystallize on specific surface sites, has become a powerful and versatile method to reduce the dislocation density in heteroepitaxy.¹⁻³ A reduction of dislocation density by a factor of 10 to 100 in SAG has been accomplished by dislocation blocking and bending.^{4,5} With the advance in lithography, the concept of SAG has also been applied to nanoscale. In the nanoscale SAG, aspect ratio trapping (ART),⁶⁻⁸ the use of growth channels or constructs that have a high aspect ratio and small cross-section (compared to the motion of dislocations) to trap the dislocations, has been developed. An example of using ART to prepare dislocation-free, fully relaxed InGaN nanorods is shown in Figure 1(b) based on our previous DOE EBS project.⁹

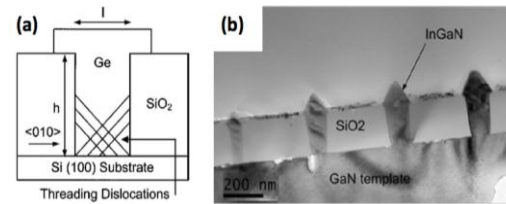


Figure 1 (a) A schematic drawing illustrating the concept of dislocation existing growth region from geometry-based trapping.⁸ (b) a cross-sectional TEM showing nanoscale SAG of dislocation-free InGaN.⁹

However, other than the dislocation reduction mechanism mentioned above, several fundamental questions related to synthesis science in the nanoscale SAG need to be addressed.

(1) How does nanoscale constriction in one direction impact the microstructure evolution in the other orthogonal directions? In the vertical epitaxial direction, the nano-trenches would act like a "roller press" that plays an active role in "forcing out" defects in heavily-mismatched growth in the vertical growth direction. Yet there is little knowledge regarding the coalescence dynamics along the lateral direction over micrometer scale. (2) How does the presence of nanoscale geometric boundaries affect the crystallographic orientation in selective area epitaxy? Is it possible to influence if not direct the crystallographic orientation by the geometric shape of the nano-trenches?

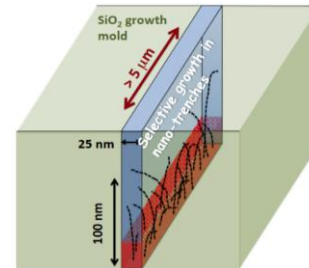


Figure 2. A schematic drawing of selective growth in a nano-trench

Within the scope of this project, we propose to investigate the fundamental dynamics of vertical and longitudinal growth evolution in the nano-trenches. Further, the possibility to guide and direct crystal orientation with amorphous dielectric nano-trenches, in a way similar to graphoepitaxy,¹⁰ will be explored. We believe that SAG in a nano-trench would be a perfect test ground to understand the role of layer-dielectric interaction. InN, of which recent study has shown superior transport properties in defect free nanowires,¹¹

is chosen as a case study to demonstrate the efficacy and unveil the science in nanoscale SAG.

Recent Progress

A. Evolution selection growth

We have recently demonstrated single crystal GaN growth on amorphous $\text{SiO}_2/\text{Si}(100)$ template.¹² For a material to transform from amorphous to single crystalline, it requires effective reduction of degree of freedom (DOF) in atomic/grain alignment from 3 (the three Euler angles) to 0. We succeeded in doing so by combining conventional micron-size SAG with a phenomenon called “evolutionary selection” (ES)¹³ in material deposition. In our lab, we prepared special growth tunnels described in Figure 3. We sputtered AlN on $\text{SiO}_2/\text{Si}(100)$ substrates which exhibits a textured microstructure (preferred AlN (0001) orientation; this process helped to reduce the DOF from 3 to 1, leaving the in-plane rotation as the remaining DOF. Using polycrystalline AlN as both a structural mold and growth seed, we

fabricated micron-size SiO_2 tunnel structures that allow for selective area lateral growth with confinement in both horizontal and vertical directions. During the SAG process, GaN grains grow out of the sidewall of the textured AlN films and undergo a 2nd evolutionary selection. After the selection, the DOF is reduced to 0 and GaN becomes single crystalline within a few micrometers. In this demonstration, the horizontal ES growth by SAG was used for facilitate the reduction of DOF from 1 to 0. A synchrotron micro-focused XRD was exploited to study the evolutionary selection grown GaN on SiO_2 .¹⁴ Theoretical modeling of the 3-dimensional confined SAG within a tunnel was carried out.¹⁵ The gas flow regimes and mass transport through laterally and vertically confined masks were analyzed. The full understanding and control of the ES growth technique is expected to enable a scalable and effective method for integration of device quality semiconductor crystals with non-crystalline substrates, and further apply the use of channel confined masks to achieve other desirable growth configurations. The knowledge of evolutionary growth can enlighten us to pursue further in the nano-scale SAG regime. We believe that using nano-trenches, it will be possible to carry out orientation selection with grain alignment directed by nano-walls to reduce the degree of freedom in crystal orientation.

B. Nanoscale selective area growth (SAG) of InGaN nanorods

GaN-based light emitting diodes (LEDs) have attracted intense focus for many years due to the prospect of solid-state lighting. The internal quantum efficiency of planar

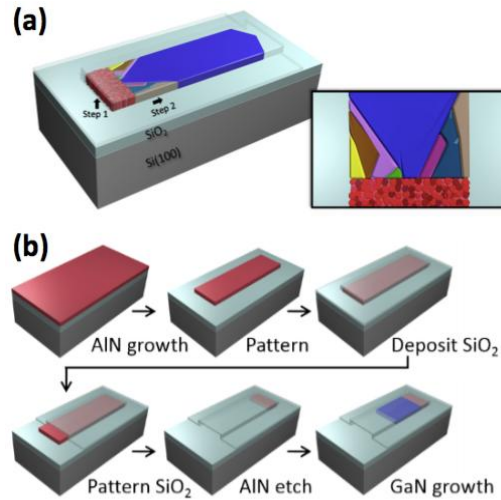


Figure 3 (a) Illustration of the concept of ES growth from a textured thin film (red layer) to produce single-crystal layer (blue region), (b) the processing sequence to carry out SAG ES growth.¹²

GaN-based LEDs drops precipitously towards longer wavelengths as the In composition increases, a phenomenon known as the “green gap”. In our lab, we addressed the intellectual impasse of creating device quality, high indium content InGaN by a combination of interference lithography (IL) to create nanoscale features with a special pulsed flow modulation technique to enhance the surface diffusion during selective area growth of InGaN.⁹ We prepared InGaN nanorods as a nano-template for growing higher In composition InGaN nano-LEDs. We studied the mechanism for improving the selectivity of InGaN nanorods during selective area growth. The selectivity was improved by enhancing the diffusion length of Ga precursor on SiO₂ with the temporal pulsing of the TEGa source during growth. With optimization of the growth conditions, we obtained InGaN nanorods with different In compositions. Images of the InGaN nanorods are shown here. Dislocations are eliminated at the nanorods/template interface. The height of dislocation-free InGaN nanorods greatly exceeds (by at least ten times) the critical thickness encountered in conventional heteroepitaxy. Photoluminescence from the InGaN nanorods can be tuned continuously from near ultraviolet (400 nm) to green (~500 nm). Such a breakthrough provides pathway for InGaN nanorods to be used as templates for growing higher In composition light emitting diodes. Our experience in the nano-scale SAG, the lithography techniques, the nano-scale material, optical, and electrical characterization tools will enable us to explore and understand the fundamental science in the microstructure evolution and crystal orientation selection in the nano-SAG.

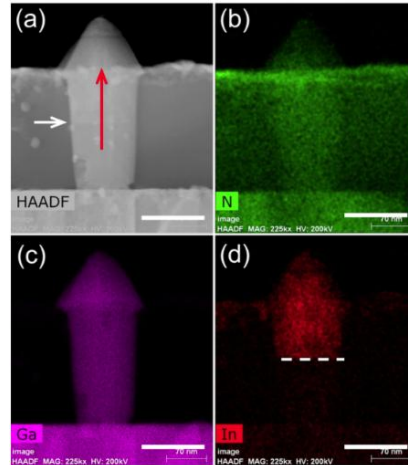


Figure 4 Demonstration of InGaN nanorods by nano-scale SAG. (a) STEM HAADF of an InGaN nanorod, (c) – (d) The EDXS mapping results of N, Ga, and In, respectively. The InGaN nanorod shows a sharp interface with the GaN nano-buffer.⁹

C. Selective area growth (SAG) of InN

Our group has performed a comprehensive study of InN SAG and lateral growth over micron-size openings on MOCVD GaN. The challenge in the (selective) growth of InN is related to the comparable strength in the In-N covalent bond and the In-In metallic bond. Perfect selectivity and a record lateral overgrowth have been obtained (Figure 5 (a)). The window for successful SAG was delineated and plotted as the green region in Figure 5 (b).

At a temperature above roughly 650°C, significant desorption of InN takes place and the surface is populated with In droplets. Below approximately 570°C the pyrolysis of NH₃ in MOCVD becomes insufficient and we started to observe either In droplets or a loss of

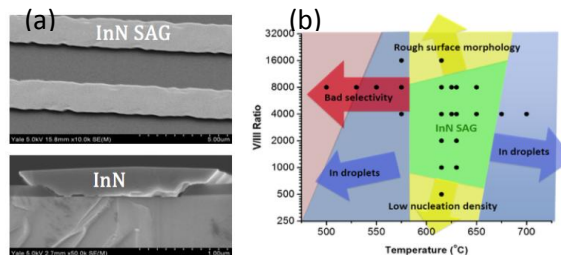


Figure 5 (a) Upper, an inclined SEM image of InN SAG-ELO stripes showing perfect selectivity; lower, a cross-sectional image of InN laterally overgrown on GaN. (b) A phase diagram of InN SAG as a function of temperature and V/III ratio.

selectivity (red region). Within the right temperature range, one needs to control the V/III ratio such that In adatoms will have sufficient diffusivity and there is enough supersaturation for nucleation. Our study of InN growth is summarized in Figure 5 (b); We also note that our study of the microscale SAG serves only as a rough map for selectivity and uniform nucleation; the rather narrow window identified in summary plot does not provide enough flexibility in controlling the microstructural evolution. It is revealed in the x-ray diffraction rocking curves of InN prepared by micro-scale SAG has a FWHM of almost 2° . Our preliminary data, as well as those reported by other groups using planar epitaxy, strongly suggest the need to carry out InN SAG using nano-trenches to obtain defect-free samples. Both the geometric effect with small openings, a high-aspect-ratio, and enhanced nanowall interactions, will facilitate a surface-mediated, nanoscale “roller-pressing” of the defective and dispersive InN nuclei to achieve micrometer scale dislocation reduction. Our expertise in the conventional micron-size SAG, particularly in InN SAG will serve general guidelines in carrying out the InN nano-scale selective area growth.

Future Plans

We plan to develop nanolithography technology for patterning high aspect ratio SiO_2 nano-trenches on Si(100), GaN, and textured AlN templates using e-beam lithography and reactive ion dry etching. Selective area growth of InN on the nano-patterned samples will be studied. InN grown in nano-trenches will be characterized using TEM, STM, SEM, EBSD, and micro X-ray diffraction. The effect of geometry confinement, growth condition on microstructural evolution and crystal orientation will be investigated.

References

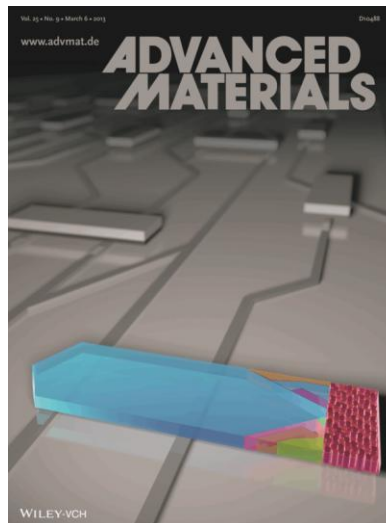
1. F. W. Tausch, Jr., and A. G. Lapierre III, “A Novel Crystal Growth Phenomenon: Single Crystal GaAs Overgrowth onto Silicon Dioxide”, *J. Electrochem. Soc.* 112, 706 (1965)
2. M. Michelitsch, “Epitaxial Growth of GaAs Through Cracks in SiO_2 Masks”, *J. Electrochem. Soc.* 112 747 (1965)
3. P. Gibart, “Metal Organic Vapor Phase Epitaxy of GaN and Lateral Overgrowth”, *Rep. Prog. Phys.* 67, 667 (2004)
4. P. Vennéguès, “Defect Reduction Methods for III-Nitride Heteroepitaxial Films Grown Along Nonpolar and Semipolar Orientations”, *Semicond. Sci. Technol.* 27, 024004 (2012)
5. T. S. Zheleva, O. Nam, M. D. Bremser, and R. F. Davis, “Dislocation Density Reduction via Lateral Epitaxy in Selectively Grown GaN Structures”, *Appl. Phys. Lett.* 71, 2472 (1997)
6. E. A. Fitzgerald, Y. H. Xie, D. Brasen, M. L. Green, J. Michel, P. E. Freeland, and B. E. Weir “Elimination of Dislocations in Heteroepitaxial MBE and RTCVD $\text{Ge}_x\text{Si}_{1-x}$ Grown on Patterned Si Substrates”, *J. Electron. Mater.* 19, 949 (1990)

7. J. S. Park, J. Bai, M. Curtin, B. Adekore, M. Carroll, and A. Lochtefeld, "Defect reduction of Selective Ge Epitaxy in Trenches on Si (001) Substrates Using Aspect Ratio Trapping", *Appl. Phys. Lett.* 90, 052113 (2007)
8. T. A. Langdo, C. W. Leitz, M. T. Currie, E. A. Fitzgerald, A. Lochtefeld, and D. A. Antoniadis, "High Quality Ge on Si by Epitaxial Necking", *Appl. Phys. Lett.* 76, 3700 (2000)
9. J. Song, B. Leung, Y. Zhang, and J. Han, "Growth, Structural and Optical Properties of Ternary InGaN Nanorods Prepared by Selective-Area Metalorganic Chemical Vapor deposition", *Nanotechnology* 25, 225602 (2014)
10. M.W. Geis, D.C. Flanders, and Henry I. Smith, "Crystallographic Orientation of Silicon on an Amorphous Substrate Using An Artificial Surface-Relief Grating and Laser Crystallization", *Appl. Phys. Lett.* 35, 71 (1979)
11. S. Zhao, O. Salehzadeh, S. Alagha, K. L. Kavanagh, S. P. Watkins, and Z. Mi, "Probing the Electrical Transport Properties of Intrinsic InN Nanowires", *Appl. Phys. Lett.* 102, 073102 (2013)
12. B. Leung, J. Song, Y. Zhang, and J. Han, "Evolutionary Selection Growth: Towards Template-Insensitive Preparation of Single-Crystal Layers", *Advanced Materials* 25, 1285 (2013).
13. A. van der Drift, "Evolutionary Selection, A Principle Governing Growth Orientation in Vapour-Deposited Layers," *Philips Res. Rep.*, 22, 267 (1967).
14. V. Kachkanov, B. Leung, J. Song, Y. Zhang, M.-C. Tsai, G. Yuan, J. Han and K. P. O'Donnell, "Structural Dynamics of GaN Microcrystals in Evolutionary Selection Selective Area Growth probed by X-ray Microdiffraction", *Scientific Reports*, 4, 4651 (2014)
15. B. Leung, M.-C. Tsai, J. Song, Y. Zhang, K. Xiong, G. Yuan, M. E. Coltrin, and J. Han, "Analysis of Channel Confined Selective Area Growth in Evolutionary Growth of GaN on SiO₂", *J. Crystal Growth* 426, 95 (2015)

DoE Sponsored Publications in the Last 2 Years

1. J. Song, D. Chen, B. Leung, Y. Zhang and J. Han "Single Crystalline GaN Tiles Grown on Si (111) Substrates by Confined Lateral Guided Growth to Eliminate Wafer Bowing", *Adv. Mater. Interfaces* 2015, 2, 1500014
2. B. Leung, M.-C. Tsai, J. Song, Y. Zhang, K. Xiong, G. Yuan, M. E. Coltrin, and J. Han, "Analysis of Channel Confined Selective Area Growth in Evolutionary Growth of GaN on SiO₂", *J. Crystal Growth* 426, 95 (2015)
3. V. Kachkanov, B. Leung, J. Song, Y. Zhang, M.-C. Tsai, G. Yuan, J. Han and K. P. O'Donnell, "Structural Dynamics of GaN Microcrystals in Evolutionary Selection Selective Area Growth probed by X-ray Microdiffraction", *Scientific Reports*, 4, 4651 (2014)
4. J. Song, B. Leung, Y. Zhang, and J. Han, "Growth, Structural and Optical Properties of Ternary InGaN Nanorods Prepared by Selective-Area Metalorganic Chemical Vapor deposition", *Nanotechnology* 25, 225602 (2014)
5. B. Leung, et al., "Using the evolutionary selection principle in selective area growth to achieve single-crystalline GaN on SiO₂", *Int. J. Hi. Spe. Ele. Syst.* 23, 1450003 (2014)

6. G. Yuan, S. H. Park, B. Leung, and J. Han, “New Directions in GaN Material Research: Thinner and Smaller”, Proc. SPIE 8986, Gallium Nitride Materials and Devices IX, 89860C (2014)
7. B. Leung, et al., “Using the evolutionary selection principle in selective area growth to achieve single-crystalline GaN on SiO₂”, Int. J. Hi. Spe. Ele. Syst. **23**, 1450003 (2014)
8. Leung, J. Song, Y. Zhang, and J. Han, “Evolutionary Selection Growth: Towards Template-Insensitive Preparation of Single-Crystal Layers”, Advanced Materials **25**, 1285 (2013). [Featured on cover page]



Mesoscale Mechanochemistry of 2D Crystal Growth

PI: A. John Hart, Massachusetts Institute of Technology

1. Program Scope

The goal of this program is to investigate the influence of mechanical forces on the nucleation and growth of carbon nanostructures, with specific focus on graphene as a model system for 2D crystal growth. In our original DOE BES program, we developed techniques and instrumentation to study the influence of forces on carbon nanotube (CNT) growth, and since the beginning of the renewal program (September 2014) we are seeking to study how to manipulate the graphene growth process by application of localized or global forces to the thin film interface (e.g., Ni-graphene-SiO₂). In the past year, we have made two main accomplishments: first, we have nearly completed our work on CNT growth which enabled further refinements to our force-controlled system to begin the new project, and is enabling an integrated understanding of the mesoscale mechanical coupling that influences aligned CNT growth. Therefore, in this abstract, we present work we continued on CNTs while refining our CVD system, and our new work which so far has focused on the design and fabrication of an electrostatic tool for in situ manipulation of graphene growth.

2. Recent Progress

2.1 *In situ* mechanical manipulation of growing carbon nanotubes (CNTs)

From our previous work, we have revealed that mechanical forces exerted on CNTs as they grow can have a significant impact on the characteristics of vertically aligned CNT forests. To better understand and control the effects of external forces, we have designed and built a custom chemical vapor deposition (CVD) reaction chamber (Fig 1). This system (the ‘mechanochamber’) can apply a constant force to a CNT forest as it grows inside the chamber while measuring the forest height, using a pushing probe connected in series to a load cell, optical encoder, and voice coil actuator. The system was used to apply static compressive forces throughout growths, ranging from 0.1 to 10g (~1.2 to ~125 kN/m² pressure for the 1 mm diameter pillar forest geometry).

Plots of the forest height vs. time is shown in Fig. 1.B Numerical differentiation of these curves reveals the growth kinetics; Fig 1.C shows the maximum growth rate for each of the applied loads. It was found that even small increases in applied compressive load results in a

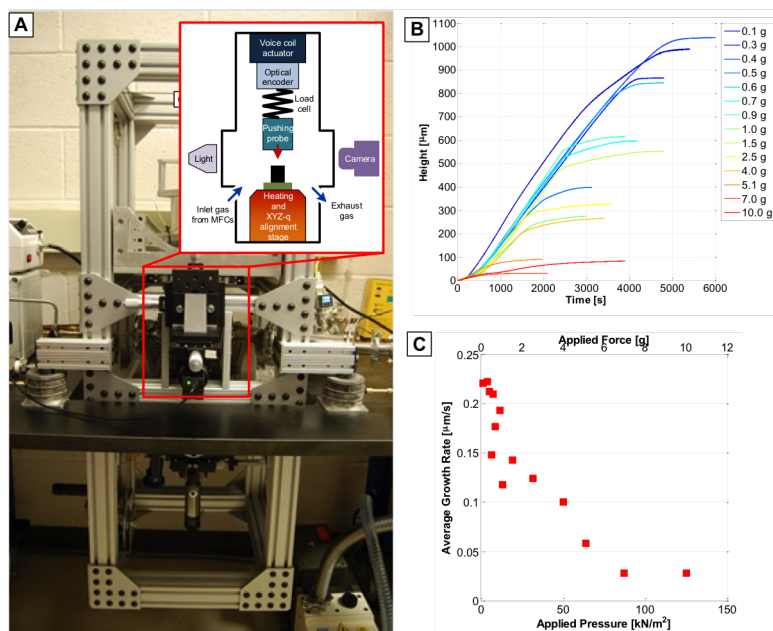


Figure 1. (A) Photograph of the custom-built reaction chamber for *in situ* mechanical force application during CVD, with an inset schematic of the critical components. (B) Plot of CNT forest heights throughout the growths for different static compressive loads, and (C) the corresponding average growth rates.

measurable decrease in the growth rate and hastens the onset of growth termination.

Three regimes of force-controlled CNT growth behavior were identified. Low forces (0.1 - 0.6 g) resulted in typical growth and termination behavior. However, the forests grown under moderate forces (0.7 – 4 g) buckled during growth. Even greater forces (5 – 10 g) prevented the CNTs from self-organizing into a forest. These regimes are identified by the growth

(height) kinetics curves for the collective forest (**Fig. 2.A**), showing a long period of growth at a high rate followed by rapid termination for low forces (blue), a buckle denoted by a sudden drop in the growth rate followed by growth at a lower rate for moderate forces (green), and immediate decay of a small growth rate for high forces (red). These findings are supported by SEM images of the pillars (**Fig. 2.B-D**), and also by *ex-situ* characterization of the forests by small-angle X-ray scattering (SAXS). Analysis of the scattering data allows the determination of an orientation parameter ranging in value from 1 (vertically aligned) to -0.5 (horizontally aligned), with a value of 0 indicating no directionality. Results for samples from the three regimes (**Fig. 2.E**) show that there may be a slight decrease in vertical alignment of the CNTs between the low and moderate applied forces, but at high force there is a complete loss of vertical alignment and actually a slight horizontal orientation of the CNTs [1]. In addition, we have begun to perform experiments with time-varying forces to investigate the ability of a growing forest to respond to changes in forces, and how the growth rate, morphology, and termination are affected.

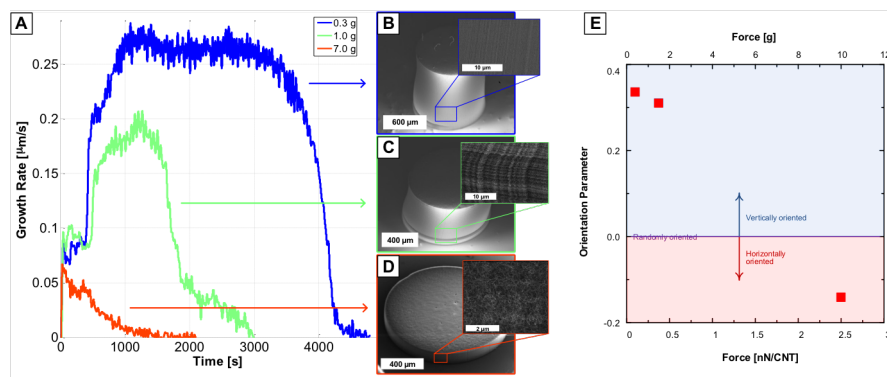


Figure 2. (A) Growth kinetics for an experiment performed in each regime: low (blue), moderate (green) and high (orange) applied force. (B-D) SEM images of CNT forests grown in each regime, with insets of higher magnification to show the tortuosity of individual CNTs. (E) Orientation parameters for samples from each regime as obtained by analysis of small-angle X-ray scattering intensity maps.

2.2 Simulations of growth of mechanically coupled CNTs

Insights on how mesoscale coupling influences CNT growth is enabled by modeling of CNT-CNT interactions along with the dynamic growth process. This work is built on a model that was developed in our group to investigate the strength of CNT yarns that are put in tension [2]. This model creates a three-dimensional representation of CNTs (**Fig. 3.A,B**), determines which CNTs are close enough such that they are within range of van der Waals attractive forces and a contact between them is created, determines the deformation due to van der Waals forces of the CNT cross-section as two CNTs come into contact, finds the strength of the contacts, and adds a growth segment to the bottom of the CNTs proportional in size to their growth rates. Then the geometry of the CNTs in the form of nodes connected by bar elements and contacts in the form of spring elements (**Fig. 3.C**) are used by ANSYS finite element software to displace to the CNTs to simulate growth and determine the resulting stresses. The force measured at the base of each CNT for a simulation of two CNTs of different diameters coming into contact is plotted vs. the mean CNT height in **Fig. 3.D**, with maps of force throughout each CNT at various steps throughout the simulation (**Fig. 3.E**). The smaller CNT is assumed to grow slower than the larger CNT, resulting in the creation of tensile force (red) throughout the smaller CNT and compressive

force (blue) throughout the larger CNT once the CNTs come into contact. These simulations show that the mechanical coupling of CNTs of differing growth rates results in dynamic force development and morphological evolution.

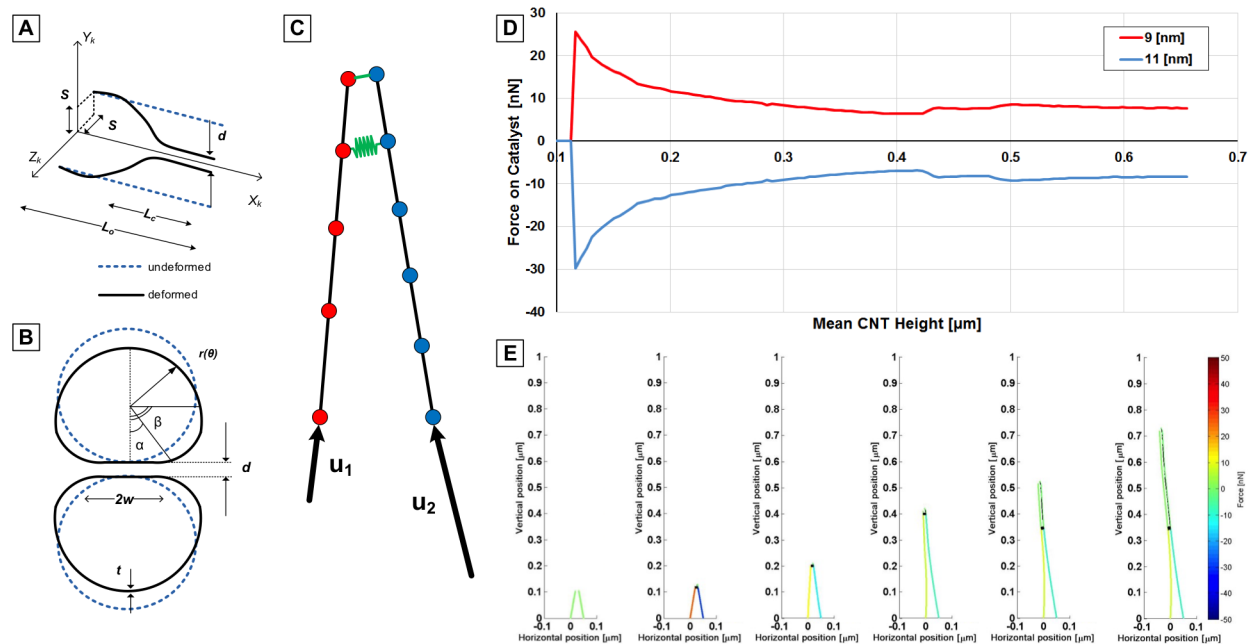


Figure 3 (A) Geometric representation of two CNTs coming into contact and (B) the resulting deformed cross sections of the CNTs used as a model. (C) Finite element geometry of two CNTs growing at different rates. (D) Force at the base of each CNT throughout a simulation and (E) force distribution across the CNTs at selected steps of the simulation.

2.3 An electroadhesive tool for in situ mechanical manipulation of graphene

To enable in situ mechanical manipulation of graphene using the mechanically controlled CVD system, we have designed and fabricated an electroadhesive tool that has the capability to control its adhesion force by varying external voltage (**Fig. 4.A**). In addition, the tool is compatible with the harsh growth conditions inside the CVD furnace (i.e. high temperature, reactive gas flow, etc), so it can also be used for in-situ measurement of adhesion force between graphene layers.

The device comprises of conductive electrodes embedded in an insulating layer, such as polymer and ceramic (**Fig. 4.B**). By applying alternative positive and negative charges to adjacent electrodes, electric fields set up opposite charges on the surface of the counterpart material in contact and cause electrostatic attraction between the tool and the counterpart surface [3-5]. The electroadhesion force per area is a function of the square of the applied voltage. Thus, for a preselected tool design, the adhesion force can be controlled by the applied V , within the limits imposed by electrical breakdown. A prototype electroadhesive tool has been fabricated on a Si/SiO₂ substrate by conventional lithographic microfabrication methods, involving deposition of TiN in an interdigitated pattern using lift-off process to create the conductive electrodes, and SiO₂ insulating layer deposited on top by CVD (**Fig. 4.C,D**). The estimated electroadhesion force of the prototyped tool vs. applied voltage is shown in **Figure 4.E**. Initial experiments using this tool to manipulate graphene on substrates with controlled surface chemistry and roughness are being performed.

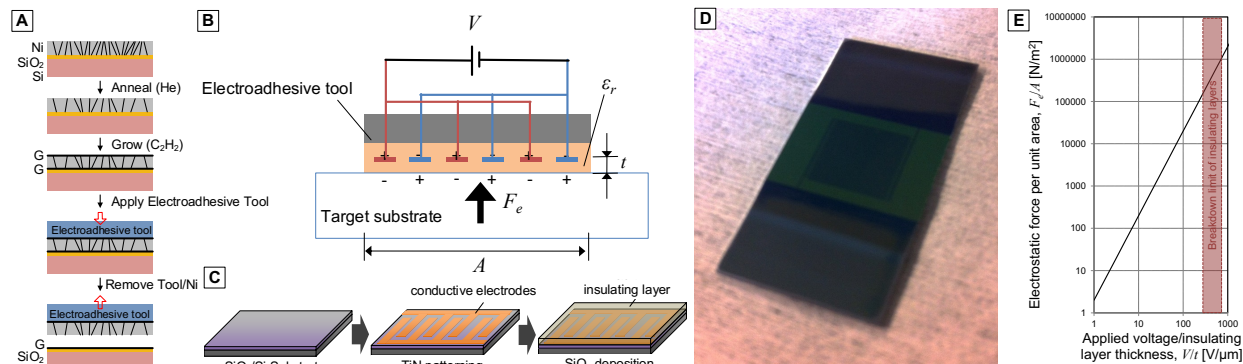


Figure 4 Schematics showing

(A) the stages of interfacial graphene growth and metal film delamination, (B) the electrostatic force generated by electroadhesive tool for in-situ film delamination, and (C) the tool fabrication procedure. (D) Photograph of prototyped electroadhesive tool having TiN as conductive electrodes and SiO₂ as insulating layer, and (E) plot of estimated electrostatic force of the prototype according to the applied voltage.

3. Future Plans

We plan to complete the study of force-modulated growth of CNT forests with additional time-varying compressive force experiments to test the capability of a forest growth to recover from growing under load and to determine the limits of force a growing forest can withstand. This will be combined with additional dynamic modeling, of the coupled forces between CNT pairs and ensembles, to understand how the time-varying forces influence the rate and quality of CNT growth. Combined with insights from TEM experiments that we are also preparing for publication, we will conclude this aspect of the DOE-funded work.

We will then utilize these understandings and the capabilities of our custom equipment to investigate the effects of force on graphene and other 2D material growth. First, we will aim to develop a better understanding of the nucleation and growth of 2D materials by CVD, using graphene as a model example, using *in situ* Raman spectroscopy and optical microscopy techniques. We then hope to investigate the role of mechanical stresses on the growth process, and how they affect diffusion of the reacting species, microstructural evolution of the catalyst film, nucleation and growth energetics, and adhesion energies between the 2D material and the substrate. Our custom CVD chamber with its micromanipulator can also be used in conjunction with the electroadhesion tool we developed in order to investigate the effects of out-of-plane forces on 2D material growth, and to perform *in situ* measurements of adhesion forces

4. References

1. Bedewy, M., et al., *Collective Mechanism for the Evolution and Self-Termination of Vertically Aligned Carbon Nanotube Growth*. Journal of Physical Chemistry C, 2009. 113(48): p. 20576-20582.
2. Rao, A., S. Tawfick, M. Bedewy, and A.J. Hart, *Morphology-driven mechanics and strength limits of carbon nanotube yarns*. In review.
3. Prahlad, H., Pelrine, R., Stanford, S., Marlow, J. and Kornbluh, R., *Electroadhesive robots -- wall climbing robots enabled by a novel, robust, and electrically controllable adhesion technology*, IEEE International Conference on Robotics and Automation, May 19-23, 2008, Pasadena, CA, USA.
4. Krahn, J. and Menon, C. *Electro-dry-Adhesion*, Langmuir, vol. 28, pp. 5438-5443, 2012.
5. Ruffatto III, D., Shah, J. and Spenko, M., *Increasing the adhesion force of electrostatic adhesives using optimized electrode geometry and a novel manufacturing process*, Journal of

Electrostatics, 2014, 72, pp.147-155.

5. Publications (Past 2 years)

1. M. Bedewy, B. Farmer, and A. J. Hart. Synergetic Chemical Coupling Controls the Uniformity of Carbon Nanotube Microstructure Growth. *ACS Nano*, 8(6):5799–5812, 2014. <http://dx.doi.org/10.1021/nn500698z>.
2. A. Ya'akobovitz, A.J. Hart. Enhanced Surface Capacitance of Cylindrical Micropillar Arrays. *Sensors and Actuators A: Physical*, 219:32–37, 2014. <http://dx.doi.org/10.1016/j.sna.2014.08.004>
3. A. Ya'akobovitz, M. Bedewy, A. J. Hart. Electrostatic Capacitance and Faraday cage behavior of carbon nanotube forests. *Applied Physics Letters* 106, 053106, 2015. <http://dx.doi.org/10.1063/1.4907609>.
4. A. Ya'akobovitz, M. Bedewy, A. Rao, A.J. Hart. Strain Relaxation and Resonance of Carbon Nanotube Forests Under Electrostatic Loading. *Carbon*, 96, 250-258, 2015. <http://dx.doi.org/10.1016/j.carbon.2015.09.038>.
5. J. Li, M. Bedewy, E. Polsen, S. Tawfick, A. Orbaek, A. J. Hart. Highly Repeatable Synthesis of Aligned Carbon Nanotubes by Dynamic Decoupling of Catalyst Annealing and CVD Growth. *In preparation*.
6. M. Bedewy, V. Balakrishnan, E. Meshot, D. Zakharov, E. Stach, A. J. Hart. Real-Time Dynamics of Carbon Nanotube Nucleation and Crowding. *In preparation*.
7. N. Dee, M. Bedewy, A. J. Hart. Force-Modulated Growth of Carbon Nanotubes. *In preparation*.

Characteristic Length Scales of Growing Nanorods *an example of basic science enabled technology*

PI: Hanchen Huang, Northeastern University, Boston, MA

Program Scope

Through a combination of analytical formulations, atomistic computer simulations, and physical vapor deposition experiments, the objectives of research are: (1) identification / discovery of the multiple characteristic length scales of growing nanorods, (2) establishment of interdependence of these characteristic length scales and their dependence on growth conditions, and (3) science-based growth of nanorods through the discovery of length scales and gained knowledge of these dependences and important through knowledge integration.

Recent Progress

This report focuses on three relatively more important advancements, leaving out others.

The first category of accomplishment is the development of a theoretical framework of nanorod growth, consisting of two closed-form theories of characteristic length scales [1,2], as shown in Figure 1.

One characteristic length scale is the smallest diameter of metallic nanorods:

$$L_{\min} \approx \left[\left(\frac{10}{\alpha^2} \right) \ln(n/2) \left(\nu_{3D} / F_e \right) \right]^{1/5} \quad \text{Here,}$$

L_{\min} represents the smallest diameter; n is the number of stacked layers that make up the height of the nanorod, which is on the order 1000; α is a geometrical factor where $\alpha = \pi / 4$ for circular cross-sections and $\alpha = 1$ for square across-sections; ν_{3D} is the diffusion jump rate of adatoms over multiple-layer surface steps; and F_e is the effective deposition rate. This length scale is a new concept, and the closed-form enables clear insight on how it depends on processing conditions and materials properties.

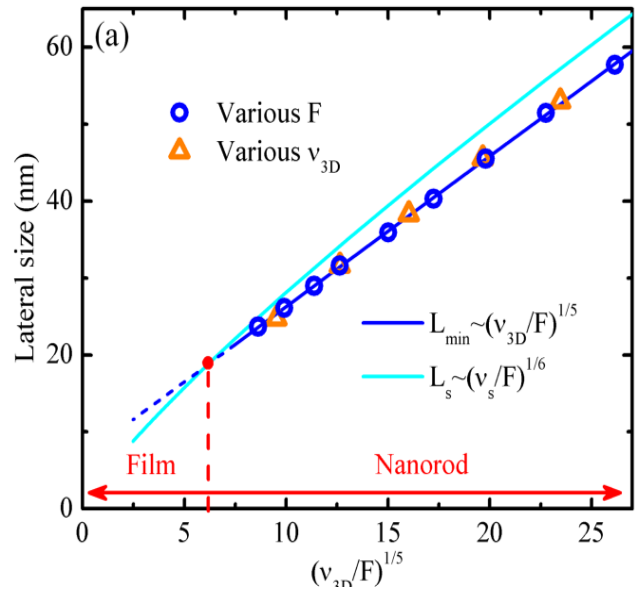


Figure 1: Length scales L_{\min} & L_s vs diffusion $(\nu_{3D}/F_e)^{1/5}$

The other characteristic length scale is intrinsic separation of metallic nanorods:

$$L_s = 1.9 \left(\frac{12 \nu}{7\pi F} \right)^{1/6} \quad \text{Here, } L_s \text{ represents the separation of metallic nanorods; } \nu \text{ is the diffusion}$$

jump rate of adatoms over multiple-layer surface steps; and F is the deposition rate. This length

scale is an old concept, but a closed-form never existed. Similarly to the first theory, this also enables clear insight on how it depends on processing conditions and materials properties.

As one demonstration of the impacts of the closed form theories, Figure 1 reveals the phase domains of growth – in the form of either “film” at ultra low diffusion or “nanorod” above a threshold amount of diffusion. This revelation is counterintuitive. In fact, merely one year before these theories were ready, this group published a set of experimental results with the word “anomaly” in the title [3]. Normally, as diffusion is reduced, nanorods of smaller diameter will result. Instead, our own experiments showed that nanorods of smaller diameter did not result but continuous film resulted. This experimental observation was an anomaly according to the understanding at the time. With the two closed forms theories, as shown in Figure 1, this “anomaly” now is predicted and should be considered “normal”!

The second category of accomplishment is the experimental realization of the smallest well-separated metallic nanorods [1].

In nano materials research, being able to grow smaller structures can mean advancement. However, claiming the growth of the smallest structure can easily cause an uproar.

Luckily, for us the smallest diameter of nanorods is predicted by a closed-form theory. Further, the other closed-form theory also reveals how the separation of nanorods varies. Guided by the theoretical framework, we have successfully achieved the smallest well-separated metallic nanorods. Figure 2 shows that the smallest Cu nanorods are on the order of 25 nm in diameter; this number becomes about 7 nm for Au.

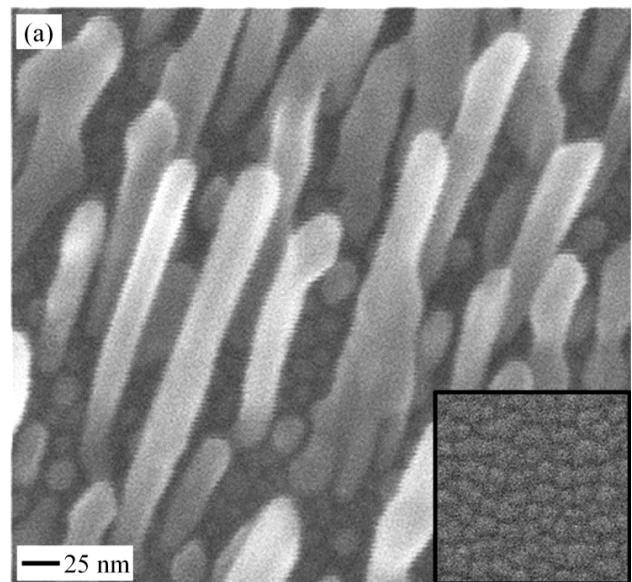


Figure 2: SEM image of Cu nanorods

The third category of accomplishment is in the form of a patented technology – metallic glue in ambient [4,5].

Taking advantage of the “smallest” and “well-separated” nature of the metallic nanorods, as shown in Figure 2, we now have proposed and achieved metallic glue in ambient – at room temperature, in air, and under small pressure of a few megapascals. To glue two solids, we coat each with metallic nanorods and push the two solids together with nanorods facing each other. The well-separated nature allows nanorods to easily interpenetrate, and the small dimension promotes fast surface diffusion. As a result, the two sets of nanorods sinter to form continuous metallic glue. Such metallic glues have many advantages. For example, their leak resistance (to

air or moisture) is at least 1000X better than that of polymer glue, so their use in organic solar cells would meet the US DoE standard of leak resistance. As another example, because the metallic glue forms at room temperature, they can take the place of solder for printed-circuit-board connections in integrated circuits with minimal thermal budget.

This technology development is an example of how BES research can lead to technologies that are directly relevant to DoE missions.

Future Plans

A major effort will be in the generalization of the nanorod growth theory. So far, we have formulated the smallest diameter of nanorod. On the other extreme, there are characteristic length scales of epitaxial thin film growth – such as the dimension of mounds according to the wedding cake model. In the extreme of growing the smallest metallic nanorods, multiple-layer surface steps dominate; in the extreme of epitaxial thin film growth, monolayer surface steps dominate. In between the two extremes, monolayer and multiple-layer surface steps both affect the growth, and the dynamics of conversion between monolayer and multiple-layer surface steps will be the key in the generalized theory of growth, which applies for both nanorod growth and thin film growth.

Like in the past, we will continue to design nanorods in parallel with the theoretical development and will continue to use the combination of analytical formulations, atomistic computer simulations, and physical vapor deposition experiments in our studies.

References

1. X. B. Niu, S. P. Stagon, Hanchen Huang*, J. K. Baldwin, and A. Misra, “Smallest Metallic Nanorods Using Physical Vapor Deposition”, **Physical Review Letters** *110*, 136102 (2013).
2. L. G. Zhou and Hanchen Huang*, “Critical Separation of Nuclei During Physical Vapor Deposition”, **Applied Physics Letters** *100*, 141605 (2012).
3. S. P. Stagon, Hanchen Huang*, J. K. Baldwin, and Amit Misra, “Anomaly of Film Porosity Dependence on Deposition Rate”, **Applied Physics Letters** *100*, 61601 (2012).
4. S. P. Stagon and Hanchen Huang*, “Airtight Metallic Sealing at Room Temperature under Small Mechanical Pressure”, **Scientific Reports** *3*, 3066 (2013).
5. Stephen P. Stagon and Hanchen Huang, “Low Pressure Low Temperature Nanorods Bonding and Sealing”, **PCT/US 2014/043139**.

Publications

1. S. P. Stagon, P. R. Elliot, and Hanchen Huang*, “Metallic Glue in Ambient Environment”, **Advanced Materials & Processes** invited (2015).
2. P. R. Elliott, S. P. Stagon, and Hanchen Huang*, “Control of Separation and Diameter of Ag Nanorods through Self-organized Seeds”, **Scientific Reports** (2015) accepted.
3. P. M. Favi, M. M. Valencia, P. R. Elliott, A. Restrepo, M. Gao, Hanchen Huang, J. J. Pavon and T. J. Webster, “Shape and Surface Chemistry Effects on the Cytotoxicity and Cellular Uptake of Metallic Nanorods and Nanospheres”, **Journal of Biomedical Materials Research Part A** (2015) DOI: 10.1002/jbm.a.35518.
4. P. R. Elliott, S. P. Stagon, Hanchen Huang*, D. Furrer, S. Burlatsky, and T. Filburn, “Combined Hydrophobicity and Mechanical Durability Through Surface Nanoengineering”, **Scientific Reports** 5, 9260 (2015).
5. L. Bachenheimer, P. R. Elliott, S. P. Stagon, and Hanchen Huang*, “Enhanced Thermal Stability of Ag Nanorods through Capping”, **Applied Physics Letters** 105, 213104 (2014).
6. S. P. Stagon and Hanchen Huang*, “Controllable Growth of Aluminum Nanorods using Physical Vapor Deposition”, **Nanoscale Research Letters** 9, 400 (2014).
7. Xiangcheng Sun, Stephen Stagon, Hanchen Huang, Jun Chen and Yu Lei, “Functionalized Aligned Silver Nanorod Arrays for Glucose Sensing through Surface Enhanced Raman Scattering”, **RSC Advances** 4, 23382-23388 (2014).
8. Guangming Cheng, Tzu-Hsuan Chang, Qingquan Qin, Hanchen Huang and Yong Zhu, “Mechanical Properties of Silicon Carbide Nanowires: Effect of Size-dependent Defect Density”, **Nano Letters** 14, 754-758 (2014).
9. S. P. Stagon and Hanchen Huang*, “Airtight Metallic Sealing at Room Temperature under Small Mechanical Pressure”, **Scientific Reports** 3, 3066 (2013).
10. X. B. Niu, S. P. Stagon, Hanchen Huang*, J. K. Baldwin, and A. Misra, “Smallest Metallic Nanorods Using Physical Vapor Deposition”, **Physical Review Letters** 110, 136102 (2013).
11. S. P. Stagon and Hanchen Huang*, “Synthesis and Applications of Small Metallic Nanorods from Solution and Physical Vapor Deposition”, **Nanotechnology Reviews** 2, 259-267 (2013).
12. L. G. Zhou and Hanchen Huang*, “Response Embedded Atom Method of Interatomic Potentials”, **Physical Review B** 87, 45431 (2013).
13. L. G. Zhou and Hanchen Huang*, “Controversy over Elastic Constants Based on Interatomic Potentials”, **Journal of Engineering Materials and Technology – ASME Transaction** 135, 11010 (2013).

Laser fabrication of single-crystal architecture in glass: control of morphology

PI: Himanshu Jain. Co-PI: Volkmar Dierolf

Lehigh University, Bethlehem, PA USA

Program Scope

Numerous energy devices and technologies rely on the availability of suitable single crystals of complex compositions in appropriate form. The conventional thermal processes for fabricating single crystals from the melt are not suitable for many important multi-component systems because either the material decomposes before melting, or undesired phases form by incongruent solidification of the melt. We are addressing this generic challenge of material fabrication by attempting to grow a single crystal architecture by heating glass to peak crystallization temperature with a suitable laser without melting. The project focuses on developing an understanding of the laser-crystallization process that will allow the control of size, geometry and orientation of the laser-written single crystal, specifically enabling the fabrication of a bend in the single-crystal line and then a 2D planar single crystal, without altering the orientation of the lattice.

Our approach is based on two hypotheses: (i) The key element for the desired control of the crystal growth is the *dynamic temperature profile which determines rate-controlling local diffusivities and interfacial reaction kinetics*. (ii) A laser can help realize complex heating profiles that are not possible with any other technique. Consequently, we are determining the heat profile and the dependence of growth on local (anisotropic) temperature gradient. With this information appropriate dynamic temperature profile are being established, which would yield specified crystal geometry (shape and size) in a given glass. High resolution spatial light modulator technology, which has become readily available only recently, is to be used to shape precisely and vary dynamically essentially arbitrary beam profiles. The initial crystal growth experiments are to be performed on IR transmitting Sb-Se, Ge-Se and Sb-S/Se-I chalcogenide systems comprised of active crystal phases that have unusual combination of superior piezoelectric, photoelectric, pyroelectric and pyro-optic properties. These systems allow a systematic variation of network dimensionality, hence growth anisotropy. Successful understanding of single crystal growth process in these compositions would help establish its broad applicability to various other glass forming systems.

Recent Progress

Fabrication of single crystal architecture in glass requires slow nucleation and rapid crystal growth rates such that once a nucleus is formed only one single crystal grows. Unlike classical glass-ceramic process, laser heating largely precludes nucleation except in the immediate vicinity of localized heated zone. Even then, unlike for the case of usual crystal growth from the melt or solution, these requirements become particularly challenging for the case of glass → single-crystal transformation where formation of multiple crystals is thermodynamically feasible.

1. All solid-state single crystal growth: At first, crystal dots were formed on surface of Sb_2S_3 glass by a 639 nm CW laser. Fig. 1 shows an image sequence of the nucleation and growth of the Sb_2S_3 single crystal on the surface of glass of the same chemical composition. The growth of Sb_2S_3 crystal after a few seconds is very fast ($\sim 10\text{-}15 \mu\text{m/s}$). Electron backscattered diffraction (EBSD) mapping shows that only one nucleus was introduced that grows at the glass surface (Fig. 1(b-e)). The nucleus which appears at the glass surface grows very rapidly and does not give chance for other nuclei to form and grow. Furthermore, the nucleation of Sb_2S_3 crystals on stoichiometric glass is significantly faster than on $16\text{SbI}_3\text{-}84\text{Sb}_2\text{S}_3$ glass, confirming that glass composition can be manipulated for avoiding the formation of multiple nuclei and thereby enhancing the chance of single crystal fabrication.

The results demonstrate for the first time the possibility of growing single crystal from glass exclusively by solid-state transformation. There are two independent key observations, which prove that the glass \rightarrow single crystal transformation occurs entirely in the solid state. First, scratches that were present on the glass surface before laser irradiation (most clearly in the region of the lines – see arrows in Fig. 2(a)) persist through the crystallization process, indicating that the nucleation

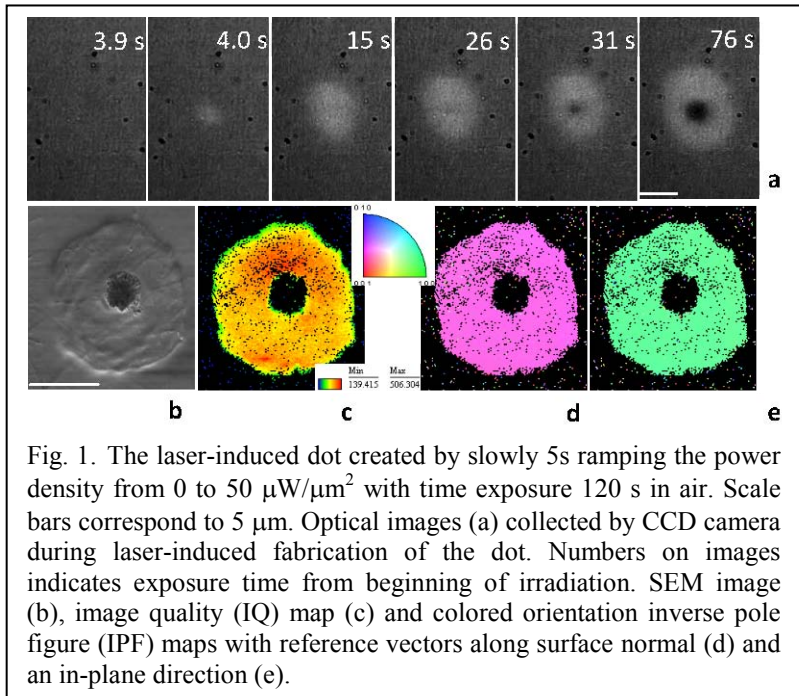


Fig. 1. The laser-induced dot created by slowly 5s ramping the power density from 0 to $50 \mu\text{W}/\mu\text{m}^2$ with time exposure 120 s in air. Scale bars correspond to $5 \mu\text{m}$. Optical images (a) collected by CCD camera during laser-induced fabrication of the dot. Numbers on images indicates exposure time from beginning of irradiation. SEM image (b), image quality (IQ) map (c) and colored orientation inverse pole figure (IPF) maps with reference vectors along surface normal (d) and an in-plane direction (e).

and growth processes occur without forming a melt that would have altered the surface morphology. Second, the in situ observation of the crystal growth process demonstrates that the crystallization occurs at the leading, not the trailing edge of the laser beam. This mode of crystal growth provides a proof-of-concept for fabricating single crystals of complex materials that melt incongruently, decompose or undergo phase transformation during heating to melt temperature.

2. Crystal growth with rotatory lattice orientation: EBSD mapping indicates that the laser-crystallized line starting from a single dot is essentially a single crystal. However, a more careful analysis revealed gradual, but continuous rotation of the lattice about a direction parallel to glass surface but normal to laser scanning direction, e.g. for Sb_2S_3 glass the crystal rotates by $\sim 50^\circ$ over a length of $100 \mu\text{m}$. Fig. 2 shows maps for three orthogonal EBSD reference directions of such a crystal line. There is no change in the orientation of lattice perpendicular to laser scanning direction (TD, Fig. 2, d), but a gradual change of color (orientation) from the start to the end of the line for the other two orthogonal directions (Fig. 2b, c).

The X-ray microdiffraction at Lawrence Berkeley National Laboratory (LBNL) probed the orientation of crystal up to 100 μm deep. Laue images, obtained from line, comprise of split reflex spots with rod-like intensity distribution, similar to the reflections observed for plastically deformed pure metal single crystals. The laser-grown Sb_2S_3 single crystal appears as if it is “plastically deformed”, with unpaired dislocations and small-angle tilt boundaries. The growing crystal accommodates its structural mismatch with glass matrix by introducing such dislocations, which might even organize to form tilt dislocation walls, but that remains to be determined. These dislocations cause rotation along the direction of growth, which coincides with the laser scanning direction.

3. Growth of 2D single crystal layer: To fabricate 2D single crystal, first a single crystal line was formed for use as the initial nucleation site for subsequent single crystal lines formed by rastering the laser beam perpendicular to this line. A 2D single-crystal pattern was obtained by ‘stitching’ successive lines. A successful example of this methodology is shown in Fig. 3 where each line was 50 μm long (horizontal in the figure) and shifted by 10 μm from the preceding line in the vertical direction. As above, the colored crystal orientation deviation (COD) map of the 2D pattern

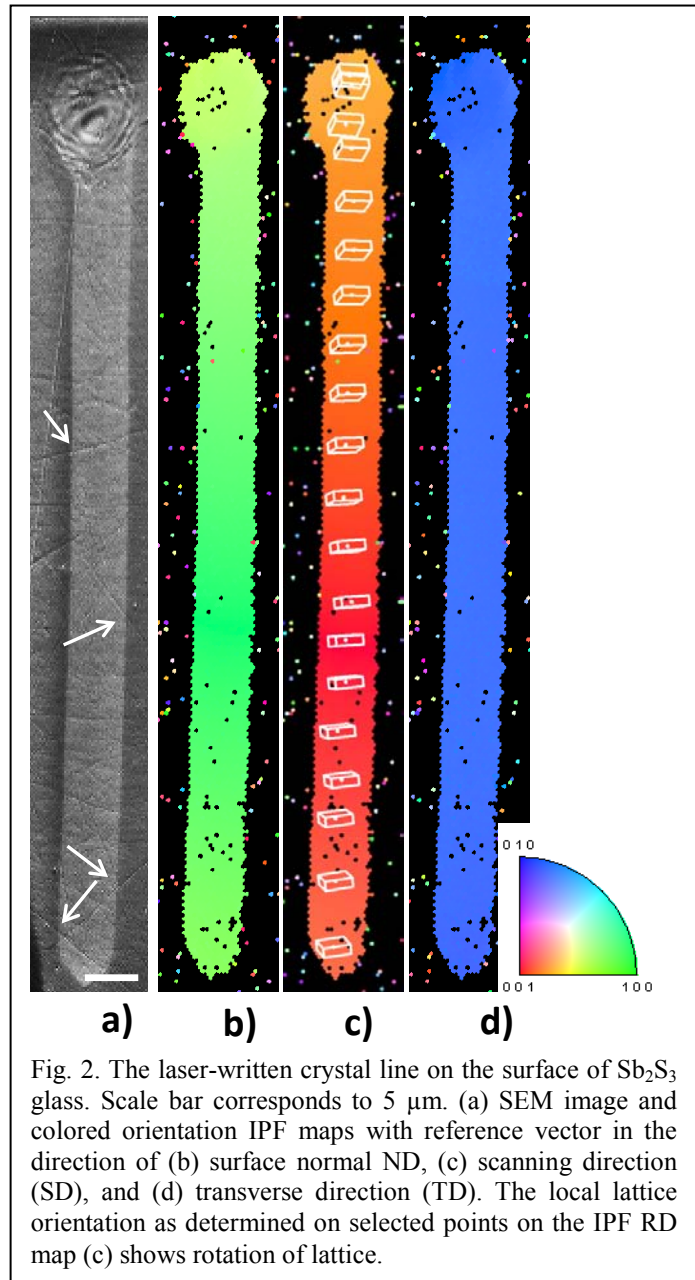


Fig. 2. The laser-written crystal line on the surface of Sb_2S_3 glass. Scale bar corresponds to 5 μm . (a) SEM image and colored orientation IPF maps with reference vector in the direction of (b) surface normal ND, (c) scanning direction (SD), and (d) transverse direction (TD). The local lattice orientation as determined on selected points on the IPF RD map (c) shows rotation of lattice.

shows gradual but small color change only between the lines in vertical direction ($<0.1^\circ/\mu\text{m}$); there is virtually no rotation along the lines (horizontal direction in the figure).

In conclusion, we: (1) demonstrated for the first time the feasibility of all-solid-state single crystal growth from glass; (2) discovered a gradual rotation of lattice laser-written single-crystals to accommodate density mismatch by incorporating unpaired dislocations in the structure; and (3) demonstrated the fabrication of 2D single crystal architecture as well as bent single-crystal lines.

Future Plans

1. Correlation between laser beam profile and single crystal growth. The main focus of the project in the next period will be on establishing the impact of laser beam profile, hence the local temperature profile, on the nucleation and growth of single crystal. The usual Gaussian intensity profile of the laser beam from a diode has already proven to be problematic for single crystal growth. For example, the high intensity in the center of typical beams causes evaporation while the crystal grows at the periphery, as in Fig.1. To overcome such problems and develop a general understanding of the role of beam profile in laser

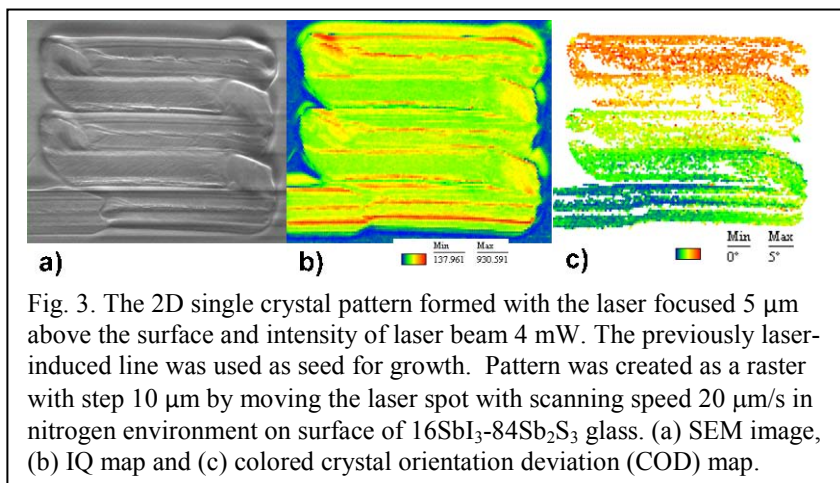


Fig. 3. The 2D single crystal pattern formed with the laser focused 5 μm above the surface and intensity of laser beam 4 mW. The previously laser-induced line was used as seed for growth. Pattern was created as a raster with step 10 μm by moving the laser spot with scanning speed 20 $\mu\text{m}/\text{s}$ in nitrogen environment on surface of 16SbI₃-84Sb₂S₃ glass. (a) SEM image, (b) IQ map and (c) colored crystal orientation deviation (COD) map.

crystallization, we will manipulate beam profile with a spatial light modulator (SLM) to create desired intensity patterns on the sample. We have observed that often the laser-induced crystal nuclei of Sb₂S₃ exhibit preferred orientation when formed in glass matrix. We propose to investigate and establish correlation between the beam profile and crystal orientation systematically, by controlling the intensity and shape of laser beam during nucleation using SLM.

2. Characterization and control of lattice rotation during crystal growth. As noted above, the lattice of single crystal line formed on the surface of glass undergoes gradual rotation to accommodate the density mismatch between the glass and crystal. However, the magnitude of this rotation ($^{\circ}/\mu\text{m}$) varies significantly with the orientation of crystal line relative to laser scanning direction. In fact, for some specific direction this rotation may not occur at all. We will continue investigating the mechanism of oriented nucleation and ‘rotating’ growth of Sb₂S₃ crystals, by characterizing the nature of interface between the crystalline and the surrounding glass phases, difference in their short-range order as well as stress and dislocation distribution generated by density/structure mismatch. Potentially useful techniques for our purpose are: X-ray fluorescence imaging and EXAFS spectroscopy as well as X-ray microdiffraction, which will be performed with the required sub-100nm spatial resolution at National Synchrotron Light Source II, Brookhaven National Laboratory and at Advanced Light Source, LBNL, respectively.

3. Fabrication of 2D crystal. Having demonstrated the initial feasibility of 2D single crystal on the surface of glass, we will continue with the optimization of the fabrication process, in particular the ‘stitching’ of single crystal lines that have rotating lattice. It will require an understanding of how lattice orientations are adjusted during laser growth process, such as seen in Fig. 3. The results obtained from the experiments described above will guide the fabrication of macroscopic 2D crystals.

Publications

Published papers:

1. D. Savytskii, M. Sanders, R. Golovchak, B. Knorr, V. Dierolf, H. Jain. Crystallization of stoichiometric SbSI glass, *J. Am. Ceram. Soc.*, **97** (2014) 198–205; DOI: 10.1111/jace.12734
2. D. Savytskii, K. Atwater, V. Dierolf and H. Jain. Formation of ferroelectric phases in Sb–S–I glasses, *J. Am. Ceram. Soc.*, **97** (2014) 3458–3462; DOI: 10.1111/jace.13152
3. R. Golovchak, P. Thapar, A. Ingram, D. Savytskii, H. Jain. Influence of phase separation on the devitrification of 45S5 bioglass, *Acta Biomater.* **10** (2014) 4878–4886; DOI: 10.1016/j.actbio.2014.07.024 (2014)

Publications in Press:

4. D. Savytskii, B. Knorr, V. Dierolf, H. Jain. Laser-induced growth of oriented Sb₂S₃ single crystal dots on the surface of 82SbSI–18Sb₂S₃ glasses, *J. Non-Cryst. Solids* (2015), <http://dx.doi.org/10.1016/j.jnoncrysol.2015.03.007>. Corrected Proof, Available online 16 March 2015.

Submitted Publications:

5. D. Savytskii, B. Knorr, V. Dierolf, H. Jain. Demonstration of single crystal growth via solid-solid transformation of a glass, Submitted to *Scientific Reports*.

Patent:

6. H. Jain, D. Savytskii, V. Dierolf. DEMONSTRATION OF SINGLE CRYSTAL GROWTH VIA SOLID-SOLID TRANSFORMATION OF A GLASS, *U.S. Provisional Patent*, Application No.: **62/221,888**, September 22, 2015

Presentations at conferences:

7. D. Savytskii, K. Atwater, B. Knorr, V. Dierolf, H. Jain, Laser-fabrication of ferroelectric Sb₂S₃ single crystal on the surface of Sb-S-I glasses. *Glass & Optical Materials Division Annual Meeting, Aachen, Germany 25-30 May 2014*.
8. D. Savytskii, M. Sanders, R. Golovchak, B. Knorr, V. Dierolf, H. Jain. Crystallization of stoichiometric SbSI glass. *Glass & Optical Materials Division Annual Meeting, Aachen, Germany 25-30 May 2014*.
9. (Invited) H. Jain. Laser-induced formation of single crystal architecture in glass: advantages and challenges. *10th Brazilian Symposium on Glass and Related Materials, São Carlos – SP, Brazil. 26-30 October, 2014*.
10. D. Savytskii, B. Knorr, V. Dierolf, H. Jain. Laser-fabrication of single crystal 1D and 2D patterns of Sb₂S₃ on Sb-S-I glasses. *International Symposium on Non-Oxide and New Optical Glasses (ISNOG 2014), Jeju, South Korea, 24-28 August, 2014*.

11. D. Savytskii, R. Golovchak, V. Dierolf, H. Jain. Unusual crystallization of SbSI phase in glasses of Sb-S-I system. *International Symposium on Non-Oxide and New Optical Glasses (ISNOG 2014), Jeju, South Korea, 24-28 August, 2014.*
12. D. Savytskyy, N. Tamura, V. Dierolf, H. Jain. Rotatory laser-induced single crystal growth of Sb₂S₃ on the surface of Sb-S-I glass. *Glass & Optical Materials Division American Ceramic Society, Annual Meeting, Miami, USA 17-21 May 2015.*
13. P. Thapar, D. Savytskyy, W.R. Heffner, H. Jain. Exceptional kinetic stability of vapor deposited As₂S₃ films. *Glass & Optical Materials Division American Ceramic Society, Annual Meeting, Miami, USA 17-21 May 2015.*
14. D. Savytskyy, V. Dierolf, H. Jain. Fabrication of laser-induced Sb₂S₃ single crystal architecture on Sb-S-I glass. *Annual Meeting and International Congress on Glass, Bangkok, Thailand. 20-23 September 2015.*
15. (Invited) H. Jain, V. Dierolf, D. Savytskii, A. Stone, M. Sakakura, Y. Shimotsuma, K. Miura, K. Hirao. Laser fabrication of single crystal architecture in glass: A new frontier of crystal growth. *Crystallization 2015, 11th International Symposium on Crystallization in Glasses and Liquids, Nagaoka, Japan, October 11-14, 2015.*

Synthesis and Processing Research in Group IV Nanomembranes

Max G. Lagally and Mark A Eriksson
University of Wisconsin-Madison, Madison, WI 53706
(with Feng Liu, Utah)

Program Scope

Single-crystal semiconductor sheets present a platform for entirely new science and technology. They may form the basis for devices relevant in energy harvesting, transformation, and conservation. The novelty of thin crystalline sheets lies in the following. 1) They are **thin**; a factor that brings many new phenomena. The very high interface-to-volume ratio makes surfaces or interfaces, and their chemical and structural properties, very important contributors to unique membrane electrical, thermal, photonic, and mechanical behavior. 2) Thin sheets can be **strained** to a high degree, effectively allowing lattice constant choice over a significant range. Most fundamental materials properties are influenced by the lattice and distortions of the lattice. 3) Thin sheets are easily **stackable** and **bondable**, introducing the potential for an entirely new set of composite materials that change their properties vertically on the scale of 10s to 100s of nm. Because of this property, **interface effects** can be significant. Additionally and importantly, sheets are compatible with all top-down processing that is conventional in the semiconductor device industry, and thus provide ready potential for technological application.

Our work has focused on the development and use of Group-IV-element and alloy nanomembranes, The platform is extendable to other materials and a range of structures and functions, using the materials processing approaches we have developed. The platform of single-crystal semiconductor sheets offers the true advantage of working at the nanoscale in one dimension, while the other two dimensions are at the mesoscale or macroscale. Our work provides excellent prospects for modifying and enhancing materials properties, and new areas of NM processing that can act as technology drivers.

The program scope is broad and includes:

- Investigations of
 - electronic transport in surfaces of crystalline sheets (primarily Si and Ge of different orientations), including graphene bonded to such NMs and two-dimensional electron gases
 - strain engineering of new structures, including local and global lattice strain, externally applied strain, and thermal mismatch strain
 - novel interfaces, including structure and thermal/electrical transport through NM stacks and periodically rippled NMs
 - surface or materials modification to affect the kinetic barriers for defect formation during stress application
- Fabrication of our own unique NMs, make novel materials via NM strain engineering
- Application of theory to quantify the outcomes of our synthesis and processing efforts
- Focus on structure and defects, electronic band structure, electronic and thermal transport, and mechanical behavior.

Recent Progress

We are actively investigating a number of research topics at the forefront of semiconductor (and to a slight degree oxide) NM science. Our core competencies are making NMs via thinning, release, etching and transfer, using MBE and CVD growth at very high purities; charge transport measurements in very thin sheets; structural and strain measurements; surface characterization, and investigation of fundamental mechanisms of growth. We have focused in the last two years on

- Use of strain engineering to make defect free Si-Ge crystals and their use for multiple-quantum well growth of Si/SiGe heterostructures and strained-Si 2DEGs
- Exploration of the properties of strained-Si quantum wells related to interface roughness, growth, impurities, and extended defects
- Mechanical strain of Ge for band engineering, including now the formation and straining of P/graphene/N junctions
- Charge transport in graphene grown on or transferred to semiconductors; influence of interface; measurements of lateral conduction
- Thermal transport through stacked-NM interfaces, so far SiNMs, but other variants in progress.
- Surface charge transport in Si(001) using a gated van der Pauw technique. Now attempting to do Si(111). NMs attached to oxide (as a gate dielectric) are required for this work
- Initial efforts on improving the quality of oxide NMs by annealing thin sheets
- Use of free-standing SiNM as a strain gauge to investigate thin-film stress evolution during growth

We describe here examples of the above bullets. Of considerable recent interest is the work on charge transport in graphene transferred to Ge(001).¹ The excellent conductivity and high charge carrier mobility of graphene suggests several applications in fast analog electronics, including transistors potentially operating in the THz regime, as well as graphene electrodes to replace indium tin oxide and graphene interconnects with low resistance and capacitance to replace copper. These applications do not require a band gap. The realization of any graphene-based device is dependent, however, on finding functional substrates on which the high carrier mobility observed for freestanding sheets of graphene is maintained. Transfer to the several materials that have been tested as hosts has always led to a degradation of this mobility. In contrast, when we transfer graphene to Ge(001), its conductivity is extremely high and remains high over time: the mobility is higher than for freestanding graphene and the carrier density is also very high. We have determined that the suboxide of Ge, which is very difficult to remove with conventional methods, provides the charges and thus effectively dopes the graphene. We explain the results with a metal-semiconductor junction model of this complex interface.

Corresponding measurements on graphene grown (rather than transferred) to Ge do not show the high conductivity. In such samples, the Ge oxide disappears because the growth process occurs at high temperatures. The removal of the oxide apparently eliminates the source of dopant charges for the graphene. On the other hand, graphene grown on Ge effectively passivates Ge from oxidation,² a fact that provides encouraging potential for future use of Ge in semiconductor devices. This research began as a serendipity result that is expanding rapidly, with potentially major consequences.

Free-standing SiNMs, tethered only at their perimeter to a host, represent a uniform canvas on which one can deposit materials and indirectly observe their growth and the resulting stress evolution and nanoparticle distribution on a highly localized (sub-micron) scale by mapping the imparted stress from the adsorbate to the NM using Raman spectroscopy. The thin single crystalline Si (or other semiconductor) nanomembrane serves as a strain gauge, where the film stress can be inferred from the required balance of forces in the film/NM system. The reliability of microelectronic and micro-electromechanical systems is limited by stress induced failure mechanisms. Most defects are caused by local stresses, requiring development of local probes that could dynamically measure film stress evolution during growth, or post processing. We performed preliminary measurements of this sort,³ that were not entirely successful because we did the experiment incorrectly, but we learned how to do them correctly. We have demonstrated the fabrication of tethered NMs for this purpose, and analyzed the average strain evolution of amorphous SiN films.

In a thin semiconductor sheet, the simple existence of surfaces can have significant impact on the “bulk” conductance of the sheet by providing states, via a mechanism called “surface transfer doping”. But the surface may itself conduct, independent of the bulk, through extended electronic states at the surface, an important function in many current nanostructure investigations that is quite difficult to measure. We use an electrode at the back of the wafer (“back gate”) to deplete the “bulk” of the thin Si layer, revealing the non-zero conductivity in the surface bands, caused by the 2x1 reconstruction of the clean surface. A change in NM thickness modifies the coupling strength between the front free surface and the back gate. Any changes in the front surface then act as an additional gate to counter or enhance the effect of the back gate. The NM “bulk” conductance is continuously tunable by the back gate voltage and hence can be made negligible relative to the surface contribution.

We are continuing conductance measurements in UHV on thin SiNMs, but now on Si(111). From the shape of conductance plots as a function of back gate voltage, we can determine electron transport through potential surface bands separately from the bulk conduction. The reason for investigating Si(111) is to resolve a controversy whether the surface is metallic or semiconducting. We have had difficulties because SOI(111) is not readily commercially available and is mostly of very poor quality, with leakage through the oxide. We hope to resolve this problem by careful selection and presorting of the material. We have similar problems with availability of GOI (for Ge NMs), and have begun to make our own, using III-V templates and Ge OMVPE. We use – and plan to use – GeNMs for a wide variety of applications, because we can make Ge direct-bandgap by applying biaxial tensile stress of sufficient magnitude.⁴

We have now been successful in measurements of thermal transport through interfaces created by NMs stacked on top of a substrate or each other.⁵ Thermal transport and management is a critical issue for semiconductors with structural interfaces. In applications in thermoelectrics, high thermal resistance is desired, while in other applications low thermal resistance is of benefit in dissipating heat from hotspots. We show that the thermal resistance across a Si/SiNM stack can be very low and is highly dependent on the nature of the surface preparation prior to assembly. Here, the inclusion of an oxide layer at the interface reduces the thermal resistivity beyond a simple clean H-terminated surface; a feature attributed to increased interfacial binding energy in

the former case. The development of electronics based on stacked systems of both identical and dissimilar materials renders the question of thermal transport across different interfaces increasingly important. We will therefore continue such experiments.

Future Plans

We are in the last half year of this grant. Rather than attempt to define here what we plan to propose in a renewal grant, we will simply say here that the most interesting parts of the above projects will be continued. Work on combining graphene and Ge will continue. Mechanically straining Ge to investigate optoelectronic and light emission effects will continue (e.g., possibly improved light emitting diodes). Thermal transport measurements will be expanded to multiple interfaces and different NMs and combinations, including graphene. For both the surface transport and the SiGe NM substrate and growth studies, we will continue to fabricate step-free mesas. For surface transport this is important because we can eliminate steps and thus dimer row orientation as causes for limited surface mobility. For the growth studies it is important because steps influence the behavior of a strained-Si 2DEG. Several other projects will continue.

The effort on hard/soft materials combinations will be ended or scaled back, not for lack of success, but because they were primarily the work of a postdoc, Francesca Cavallo, who now has a faculty position at the University of New Mexico, and is successfully continuing the work there. We do not want to compete with our own offspring.

References

1. “Exceptional Charge Transport Properties of Graphene on Germanium”, F. Cavallo, R. Rojas Delgado, M.M. Kelly, H. Xing, J.R. Sánchez Pérez, D.P. Schroeder, M. A. Eriksson, and M.G. Lagally, *ACS Nano* **8**, 10237-10245 (2014).
2. “Passivation of Germanium by Graphene”, R. Rojas Delgado, R. Jacobberger, F. Cavallo, S. S. Roy, M.S. Arnold, and M.G. Lagally, in preparation
3. “Silicon Nanomembranes as a Means to Evaluate Stress Evolution in Deposited Thin Films”, A.M. Clausen, D.M. Paskiewicz, A. Sadeghirad, J. Jakes, D.E. Savage, Feng Liu, D.S. Stone, M.G. Lagally, *Extreme Mechanics Letters* **1**, 9-14 (2014).
4. “Strained-Germanium Nanostructures for Infrared Photonics”, C. Boztug, J. R. Sánchez Pérez, M. G. Lagally, and R. Paiella, *ACS Nano* **8**, 3136 (2014). (invited review).
5. “Thermal Resistance of Transferred Silicon Nanomembrane Interfaces”, D. P. Schroeder, Z. Aksamija, A. Rath, P. M. Voyles, M. G. Lagally, and M. A. Eriksson, *Phys. Rev. Letters*, under review

Patents Issued (since September 2013)

1. “Semiconductor Nanowire Thermoelectric Materials And Devices, and Processes for Producing Same”, M.G. Lagally P.G. Evans, and C.S. Ritz, U.S. Patent #8,536,440, September 17, 2013
2. “Nanomembrane Structures Having Mixed Crystalline Orientations and Compositions”, M.G. Lagally, S.A. Scott, and D.E. Savage, U.S. Patent #8,803,195, August 12, 2014
3. ”Anisotropic Conducting Films for Electromagnetic Radiation Applications”, F. Cavallo, MG. Lagally, and R. Rojas Delgado, US Patent #9,059,335, Jun 16, 2015

4. “Semiconductor Nanowire Thermoelectric Materials And Devices, and Processes for Producing Same”, M.G. Lagally P.G. Evans, and C.S. Ritz, continuation of U.S. Patent #8,536,440, to issue October 2015

Publications (since September 2013)

1. “Semiconductor Quantum Dot Qubits”, M.A. Eriksson, S.N. Coppersmith, and M.G. Lagally, MRS Bulletin 38, 794 (2013).
2. “Long-Term Reduction in Poly(dimethylsiloxane) Surface Hydrophobicity via Cold-Plasma Treatments”, B.J. Larson, S.D. Gillmor, J.M. Braun, L.E. Cruz-Barba, D.E. Savage, F.S. Denes, and M.G. Lagally, Langmuir 29, 12990 (2013).
3. “Grating-Coupled Mid-Infrared Light Emission from Tensilely Strained Germanium Nanomembranes”, C. Boztug, J.R. Sánchez-Pérez, J. Yin, M.G. Lagally, and R. Paiella, Appl. Phys. Letters 103, 201114 (2013).
4. “Strain Engineered Surface Transport in Si(001): Complete Isolation of the Surface State via Tensile Strain”, Miao Zhou, Zheng Liu, Zhengfei Wang, Zhaoqiang Bai, Yuanping Feng, M.G. Lagally, and Feng Liu, Phys. Rev. Letters 111, 246801 (2013).
5. “Fast Coherent Manipulation of Three-Electron States in a Double Quantum Dot”, Zhan Shi, C.B. Simmons, D.R. Ward, J.R. Prance, Xian Wu, T.S. Koh, J.K. Gamble, D.E. Savage, M.G. Lagally, Mark Friesen, S.N. Coppersmith, and M.A. Eriksson, Nature Communications 5, 3020 (2014).
6. “Heteroepitaxial Growth on Thin Sheets and Bulk Material: Exploring Differences in Strain Relaxation via Low-Energy Electron Microscopy”, C. Euaruksakul, M.M. Kelly, B. Yang, D.E. Savage, G.K. Celler, and M.G. Lagally, J. Phys. D 47, 025305 (2014).
7. “Nanomembrane-based Materials for Group IV Semiconductor Quantum Electronics”, D. M. Paskiewicz, D.E. Savage, M.V. Hole, P.G. Evans, and M.G. Lagally, Nature Scientific Reports 4, 04218 (2014).
8. “Facile Fabrication of Ordered Crystalline-Semiconductor Microstructures on Compliant Substrates”, F. Cavallo, K.T. Turner, and M.G. Lagally, Adv. Functional Mats. 24, 1730 (2014).
9. “Strained-Germanium Nanostructures for Infrared Photonics”, C. Boztug, J.R. Sánchez-Pérez, M. G. Lagally, and R. Paiella, ACS Nano 8, 3136 (2014). (invited review).
10. “Integrating Classical Semiconductor Devices with Si/SiGe Quantum Dots”, D.R. Ward, R. Foote, J.K. Gamble, D.E. Savage, M.G. Lagally, S.N. Coppersmith, and M.A. Eriksson. ECS Transactions 64, 915 (2014).

11. “Measurement of Valley Kondo Effect in a Si/SiGe Quantum Dot”, M.Y. Yuan, R. Joynt, Z. Yang, C.Y. Tang, D. E. Savage, M. G. Lagally, M. A. Eriksson, and A. J. Rimberg, *Phys. Rev.* **B90**, 035302 (2014).
12. “Quantum Control and Process Tomography of a Semiconductor Quantum Dot Hybrid Qubit”, Dohun Kim, Zhan Shi, C.B. Simmons, D.R. Ward, J. R. Prance, Teck Seng Koh, John King Gamble, D.E. Savage, M.G. Lagally, Mark Friesen, S.N. Coppersmith, and M.A. Eriksson, *Nature* **511**, 70 (2014).
13. “Two-Axis Control of a Singlet-Triplet Qubit with an Integrated Micromagnet”, Xian Wu, D. R. Ward, J. R. Prance, Dohun Kim, John King Gamble, Robert Mohr, Zhan Shi, D. E. Savage, M. G. Lagally, Mark Friesen, S.N. Coppersmith, and M.A. Eriksson, *PNAS* **111**, 11938 (2014).
14. “Electrical Control of a Long-Lived Spin Qubit in a Si/SiGe Quantum Dot”, E. Kawakami, P. Scarlino, D.R. Ward, F. R. Braakman, D.E. Savage, M.G. Lagally, M. Friesen, S.N. Coppersmith, M.A. Eriksson, and L.M.K. Vandersypen, *Nature Nanotechnology* **9**, 666 (2014)
15. “Exceptional Charge Transport Properties of Graphene on Germanium”, F. Cavallo, R. Rojas Delgado, M.M. Kelly, H. Xing, J.R. Sánchez Pérez, D.P. Schroeder, M.A. Eriksson, and M.G. Lagally, *ACS Nano* **8**, 10237-10245 (2014).
16. “Neurite Guidance and Three-Dimensional Confinement via Compliant Semiconductor Scaffolds, F. Cavallo, Yu Huang, J.C. Williams, and M.G. Lagally, *ACS Nano* **8**, 12219-12227 (2014).
17. “Silicon Nanomembranes as a Means to Evaluate Stress Evolution in Deposited Thin Films”, A.M. Clausen, D.M. Paskiewicz, A. Sadeghirad, J. Jakes, D.E. Savage, Feng Liu, D.S. Stone, M.G. Lagally, *Extreme Mechanics Letters* **1**, 9-14 (2014).
18. “Fabrication of Flat SiGe Heterostructure Nanomembrane Windows via Strain-Relief Patterning”, K.M. McElhinny, G. Gopalakrishnan, D.E. Savage, J.C. Silva-Martínez, M.G. Lagally, M.V. Holt, and P.G. Evans, *J. Phys. D* **48**, 015306 (2015).
19. “Microwave-Driven Coherent Operation of a Semiconductor Quantum Dot Charge Qubit”, D.H. Kim, D.R. Ward, C.B. Simmons, J.K. Gamble, R. Blume-Kohout, E. Nielsen, D.E. Savage, M.G. Lagally, M. Friesen, S.N. Coppersmith, and M.A. Eriksson, *Nature Nanotechnology* **10**, 243-7 (2015).
20. “Direct Evidence of Strain Transfer for InAs Island Growth on Compliant Si Substrates”, L. A. B. Marçal, M.-I. Richard, R. Magalhães-Paniago, F. Cavallo, M.G. Lagally, O.G. Schmidt, T.U. Schüllli, Ch. Deneke, and A. Malachias, *Appl. Phys. Letters* **106**, 151905 (2015).

21. "Identifying Single Electron Charge Sensor Events using Wavelet Edge Detection", J. Prance, B. Van Bael, C. Simmons, D.E. Savage, M.G. Lagally, M. Friesen, S. Coppersmith, and M.A. Eriksson, *Nanotechnology* 26, 215201 (2015).
22. "Enhanced Electronic Transport Properties in Epitaxial Si/SiGe Heterostructures Grown on Single-Crystal SiGe Nanomembranes", Y. Stephanie Li, P. Sookchoo, X.R. Cui, R.T. Mohr, D.E. Savage, R. Foote, RB Jacobson, J.R. Sanchez-Perez, D.M. Paskiewicz, X. Wu, D.R. Ward, S.N. Coppersmith, M.A. Eriksson, and M.G. Lagally, *ACS Nano* 9, 4891 (2015).
23. "Oriented Bottom-Up Growth of Semiconducting Armchair Graphene Nanoribbons on Germanium", R.M. Jacobberger, B. Kiraly, M. Fortin-Deschenes, P.L. Levesque, K.M. McElhinny, R. Rojas Delgado, S.S. Roy, A. Mannix, M.G. Lagally, P.G. Evans, R. Martel, M.C. Hersam, N.P. Guisinger, and M.S. Arnold, *Nature Communications* 6, 8006 (2015).
24. "High-Fidelity Resonant Gating of a Silicon Based Quantum Dot Hybrid Qubit", D.H. Kim, D.R. Ward, C.B. Simmons, D.E. Savage, M.G. Lagally, M. Friesen, S.N. Coppersmith, and M.A. Eriksson, *npj Quantum Information*, in press
25. "Nano-Origami: Art and Function", F. Cavallo and M.G. Lagally, *Nano Today* 10 (4), October 2015
26. "Passivation of Germanium by Graphene", R. Rojas Delgado, R. Jacobberger, F. Cavallo, S. S. Roy, M.S. Arnold, and M.G. Lagally, in preparation
27. "Silicon Nanomembranes Incorporating Strain and Mixed Crystal Orientations", S.A. Scott, D.M. Paskiewicz, Ch. Deneke, H.J. Ryu, D.E. Savage, M.A. Eriksson, and M.G. Lagally, in progress
28. "Electronic Transport in Thin Crystalline Semiconductor Sheets", Y.Li and M.G. Lagally, *Advanced Materials*, invited review, in progress.

Quasiepitaxial Growth of Organic Crystalline Thin-Films

Richard R. Lunt
Department of Chemical Engineering and Materials Science,
Department of Physics
Michigan State University, East Lansing, MI

Program Scope:

The presence of excitons in organic semiconductors at room temperature distinguish them from traditional semiconductors, providing exceptional opportunities for manipulating energy in a range of structures from light emitting diodes, lasers, transparent photovoltaics, and optical switches, and have already shown superior performance in the light emitting diode (LED) field. However, control over crystalline order, orientation, and defect formation are crucial to the fabrication and optimization of these excitonic organic electronics. For organic growth, lattice matching is not strictly required as with inorganic epitaxy, and the modes of epitaxy are therefore uniquely distinct. For example, unmistakable azimuthal relationships have been observed for many organic molecules grown on inorganic crystals that are consistent with theoretical energetic minima, despite a lack of true commensurate “epitaxial” relationship (hence the term “quasi-epitaxy”). While there is a growing body of literature on organic quasiepitaxy (QE) on inorganic substrates, very little is known about organic-organic QE needed to push excitonic electronics to their full potential.¹ Indeed, very little is even known about homo-epitaxial vapor-phase growth. This is due, in large part, to 1) a lack of high quality starting crystalline organic layers, 2) limited implementation of real-time probing methods and 3) a lack of understanding governing organic-organic QE selection rules. Moreover, there have been few examples of preserved-ordering during multilayer crystalline organic growth despite the keen interest in the novel physics afforded by crystalline organic semiconductors. Accordingly, there is a wealth of opportunities for this unexplored regime of organic crystalline growth phenomena. The overarching goal of this project is to understand and explore bottom-up vapor-deposition routes to the growth of large-area organic crystalline films with controlled thickness, doping, and defect concentration.

Recent Progress

We have realized the growth of the first *set* of heteroquasiepitaxial multilayer organic thin film crystals with unprecedented ordering and demonstrated an entirely new growth mode in organic-organic quasiepitaxy. We have grown crystals composed of incommensurate organic semiconductors with sustained azimuthal ordering and controlled orientation grown from the bottom up. By probing a range of molecular pairings with *in-situ* and *real-time* diffraction, we are uncovering the key driving forces behind this underexplored growth regime that derives from interactions which are completely distinct from the requirements of lattice matching for inorganic epitaxial growth. We subsequently focus on the quasiepitaxial growth of a range of key organic molecules including diindenoperylene (important in thin film transistors and light emitting diodes), rubrene (high mobility transistors, light emitting diodes, and photovoltaics), perylenes, and phthalocyanines (important in photovoltaic applications), among others.

A) Uncovering a New Growth Mode: Edge-Driven Organic-on-Organic Quasiepitaxy

We have demonstrated an entirely new growth mode and unique ordering of alternating hetero-quasiepitaxy of 1,4,5,8-naphthalenetetracarboxylic-dianhydride (NTCDA) and diindenoperylene (DIP) crystalline films. Despite matching of the lowest energy surfaces (LES) between the two systems, DIP orients on NTCDA by exposing the β -DIP(020) surface, a non-lowest energy plane. Calculations of potential energy for the two-layer stacking model are performed to understand the quasiepitaxial relationship and highlight the complex dynamics of this new quasiepitaxial growth mode, driven not by surface energy landscape, but by organic-organic step-edge nucleation interactions. Understanding this new growth mode ultimately provides a novel mechanism to highly ordered organic quantum wells with tailored orientation and anisotropy that can enhance excitonic electronic devices, and provides an intriguing counterpoint to the understanding of organic multilayer epitaxy.

A typical series of reflection high energy electron diffraction (RHEED) patterns for the growth of NTCDA/DIP alternating layer structures grown at room temperature are shown in Fig. 1. Although there is no lattice matching between layers, RHEED patterns reveal that each layer is highly crystalline with its own well-defined surface lattice and registry. When NTCDA is grown on the KBr substrate, the RHEED patterns show continuous streak features, indicative of crystalline flat surface that is consistent with the two-dimensional growth. With the subsequent growth of the DIP layer at room temperature, long unbroken NTCDA diffraction streaks are replaced by spotty diffraction patterns of DIP which indicates a roughening of the crystalline surface. Nonetheless, clear azimuthal registry is still observed and the single-crystal-like rotational dependence of the RHEED patterns indicates that the DIP grains are all aligned in-plane on top of the NTCDA layer. Despite the fact that β -DIP(001) is the LES and has a close energy matching with NTCDA(100), the β -DIP(020) plane is formed on the NTCDA surface, which is confirmed by both RHEED and XRD data. This multilayer growth was repeated for a number of cycles and clearly demonstrates the ability to grow incommensurate organic

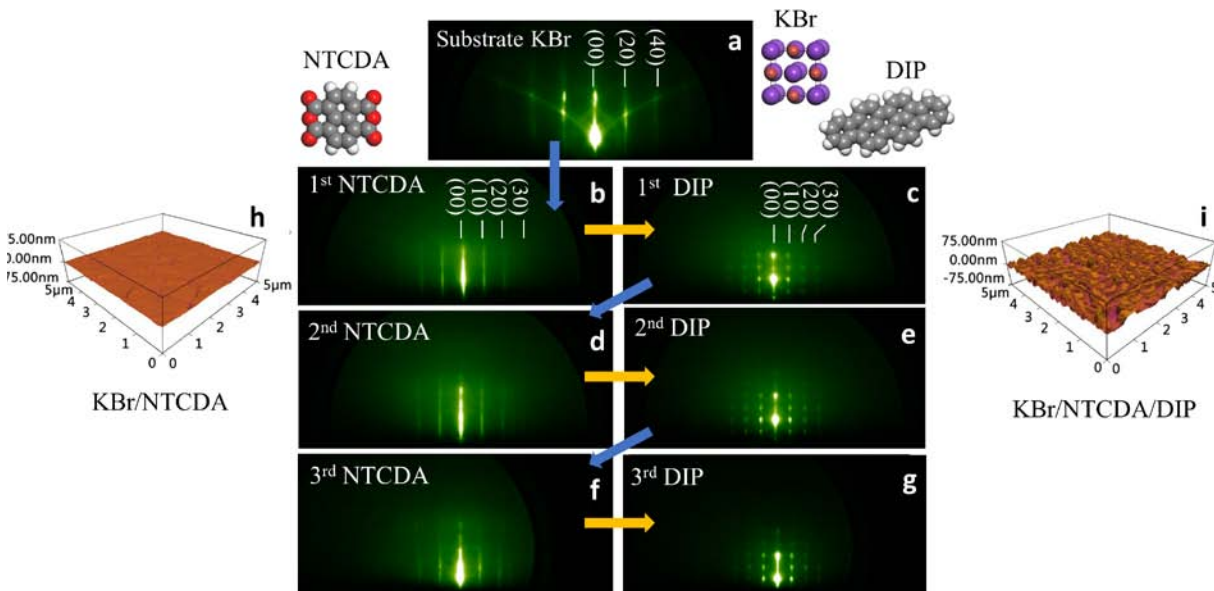


Figure 1. RHEED patterns of the (a) the initial substrate and (b-c) the first, (d-e) second, and (f-g) third pair growth of NTCDA(10nm)/DIP(10nm) multilayers. (h-m) with representative AFM image for each molecular film included. (inset) Structures of the KBr substrate and molecular structures of NTCDA and DIP.

films, layer after layer, with sustained azimuthal ordering and controlled orientation, reminiscent of molecular beam epitaxy of inorganic quantum wells.

This surprising growth configuration is shown to be driven by edge-nucleation driven quasiepitaxial dynamics confirmed by *in situ* diffraction, equilibrium energetic predictions, growth order reversal, and early growth studies. For example, growths were performed with reverse layer sequence, starting with the DIP layer first. Interestingly, the spotty RHEED patterns in Fig. 2 no longer align orthogonally to the surface plane, indicating the formation of DIP with an entirely different stacking orientation. AFM shows the formation of long nanowire features also distinct from the growth on NTCDA. Subsequent growth of NTCDA on DIP/KBr results in ring diffraction patterns which indicates the evolution of three dimensional crystalline disorder (i.e. crystalline powder) after just the first layer pair. Thus, the initial presence of the NTCDA is key to enable highly ordered multilayer growth. An important distinguishing factor in this pairing is that DIP has a perylene core capable of near covalent-like bonding to other aromatic rings, metals,^{2, 3} and can support hydrogen bonding interactions,⁴ which has been previously seen in perylene tetracarboxylic dianhydride (PTCDA) and exploited for molecular templating.⁵ This can create stronger interactions between the DIP molecule and the flat facing edge of the NTCDA step and indeed is consistent with the clear tendency of DIP to nucleate from the step edges of the NTCDA seen in early growth AFM (Fig. 3). In contrast with this picture, we have found that many common organic molecules, including tetracene, coronene, CuPc and C₆₀, grow without a preferential nucleation at edges (intra-terrace nucleation) on NTCDA. Additionally, despite growths with coverage of 1 ML (and a uniform deposition coverage observed concurrently for DIP on SiO₂) we do not find DIP nuclei uniformly distributed on every terrace, and find particularly few DIP nuclei on the largest terraces indicating that there is both a small Ehrlich–Schwöebel barrier⁶ for DIP molecules to reach different terraces and there is a high diffusivity for DIP on NTCDA. This high diffusivity also likely plays a role in the ability to observe this growth mode, similarly to the role diffusivity plays in the transition between layer-by-layer (intra terrace nucleation) and step flow (step edge nucleation) growth in homoepitaxial inorganic systems.

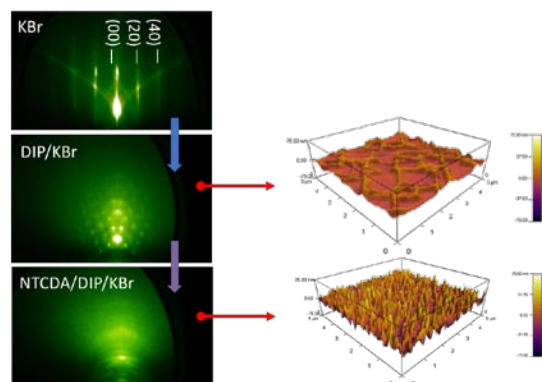


Figure 2. RHEED patterns of DIP/NTCDA starting with DIP first. (a) The pattern for DIP on KBr is distinct to the pattern for DIP grown on NTCDA indicating a significantly altered molecular stacking orientation. Subsequent growth of NTCDA leads to a 3D disordered powder.

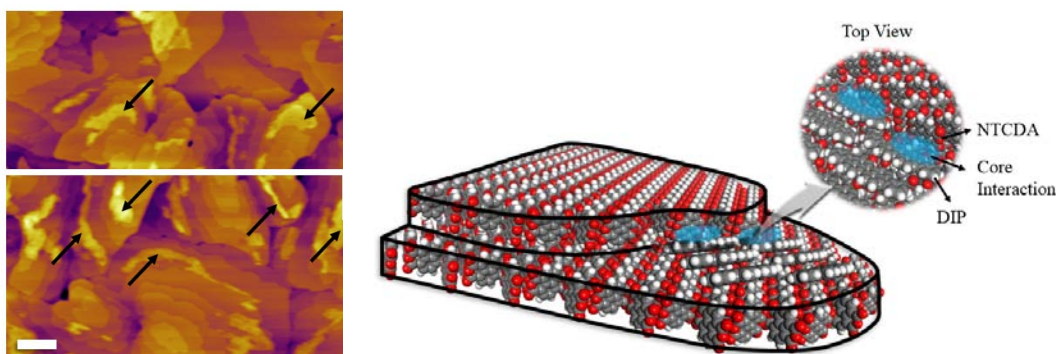


Figure 3. (left) AFM images of submonolayer growth of DIP (< 1nm) on NTCDA. The DIP nuclei are marked with the black arrows. The white scale bar corresponds 0.2 μ m. (right) Schematic structural model of the NTCDA terraces and edge nucleation of DIP, highlighting the molecular core interactions (shown in blue)

Ultimately, understanding this non-equilibrium quasiepitaxial growth of crystalline organic multilayers will provide new routes to controlling molecular orientation in organic quantum wells via control over nucleation dynamics through the rational design of step-edge molecule interactions, and therefore can enable pathways to enhanced excitonic devices and novel exciton confinement photophysics.

B) Matched Multilayer Growth: NTCDA and Rubrene

We have grown a full range of key molecules on NTCDA to explore the impact of surface energy matching, including metal phthalocyanines, tetracene, pentacene, rubrene, C₆₀, coronene, p-6p, and sexithiophene, and found well-defined ordering only in specific cases. Through close surface energy matching of the lowest energy planes, we demonstrate growth of rubrene that is not only crystalline, but also quasiepitaxial ordered. Rubrene is a particularly important organic molecule as mobilities ($> 10\text{cm}^2/\text{V-s}$) have been demonstrated in bulk single crystals. However, the ability to utilize thin films of rubrene with high performance has been long-standing challenge since the growth of crystalline films is notoriously difficult and commonly yields amorphous layers. As shown in Figure 3, rubrene grows in highly ordered films on the NTCDA layer forming clearly defined streaks with a distinct and incommensurate lattice, providing another platform to characterize carrier transport with tailored crystal structures for highly ordered organic electronic systems.

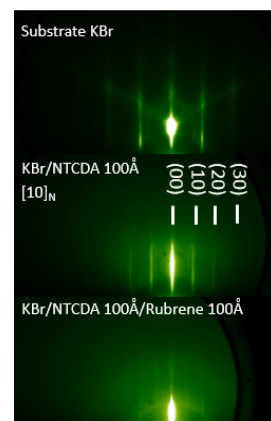


Figure 4. RHEED patterns of the substrate and the NTCDA/rubrene multilayer growth.

Future Plans

We plan to fully explore homoepitaxial and heteroquasiepitaxial growth modes for the complete representative range of key archetypal organic semiconductors, (2) correlate growth mode with dynamic parameters such as surface diffusivity and growth conditions; (3) correlate optical and electrical properties of highly ordered single- and multi-layer crystalline films via transistor, quantum well (optical), and exciton diffusion length measurements; (4) demonstrate phosphorescent doping during homo- and quasi-epitaxial growth; and (5) exploit this ability to grow highly ordered films to enhance the performance of excitonic devices.

References

1. R. R. Lunt, K. Sun, M. Kroger, J. B. Benziger, and S. R. Forrest, *Phys. Rev. B* **83**, 064114 (2011).
2. M. Eremtchenko, J. Schaefer, and F. Tautz, *Nature* **425**, 602 (2003).
3. D. G. Oteyza, E. Barrena, H. Dosch, and Y. Wakayama, *Phys. Chem. Chem. Phys.* **11**, 8741 (2009).
4. N. Koch, N. Ueno, and A. T. S. Wee, *The molecule-metal interface* (John Wiley & Sons, 2013).
5. B. E. Lassiter, R. R. Lunt, C. K. Renshaw, and S. R. Forrest, *Opt. Exp.* **18**, A444 (2010).
6. G. Ehrlich and F. G. Hudde, *J. Chem. Phys.* **44**, 1039 (1966).

DoE Sponsored Publications in the Last Two Years

1. P. Chen, R. Lunt, “Edge-Nucleation Driven Hetero-Quasiepitaxial Growth of Organic Multilayer Films”. *Submitted and In Review*, (PRL) 2015.
2. P. Kuttipillai, Y. Zhao, C. J. Traverse, B. G. Levine, **R. R. Lunt**, “Phosphorescent Nanocluster Light Emitting Diodes”, *Advanced Materials*, (In Print) 2015.
3. P. Chen, P. Kuttipillai, R. Lunt, “Growth of Phosphorescent-Doped Homepitaxial Films” *In Prep*, 2015
4. P. Chen, R. Lunt, “Molecular Dynamics of Organic-Organic Surface Diffusion”. *In Prep.*, 2015.

Non-equilibrium effects in the processing of materials using plasmas

Lorenzo Mangolini

Mechanical Engineering Department, Materials Science and Engineering Program

University of California Riverside

Program Scope

In the last few years, it has become obvious that non-thermal plasmas are an excellent route for the synthesis and processing of free-standing silicon nanoparticles. Silicon nanoparticles have many interesting properties and relevant applications [1], and have been successfully integrated in nanoelectronics [2], light emitting devices [3, 4] and photovoltaic devices [5]. Nanostructures based on silicon are potentially compatible with large-scale applications, since silicon is the second most abundant element on Earth. Silicon nanoparticles have successfully been produced using non-thermal plasma reactors deliberately optimized for the production of nanoparticles [6, 7]. Non-thermal plasma continuous flow reactors convert silane into silicon nanocrystals sufficiently small to show quantum confinement effects [8]. Despite the fact that plasma-based techniques are promising candidates for the large volume synthesis of silicon nanocrystals, a detailed understanding of the correlation between plasma properties and nanoparticle structure is missing. The question remains of how the continuous flow reactor introduced in [6] fully converts the silane precursor into particles with a crystalline structure within few milliseconds. The goal of this program is to address this open issue and to investigate the interaction between non-thermal plasmas and silicon nanoparticles dispersed within it, with the goal of understanding the influence of plasma parameters of nanoparticle properties such as surface passivation and structure.

Recent Progress

We have pursued two different approaches to establish a correlation between plasma and nanoparticle properties. In the first approach, we have used the kinetics of nucleation, growth and crystallization of nanoparticles in plasma to estimate the temperature to which nanoparticles are heated to when immersed in a non-thermal plasma. In the second approach, we have monitored the evolution of nanoparticle surface coverage during plasma exposure to obtain a nanoparticle temperature measurement.

The first approach [9] is based on the sampling of nanoparticles during different stages of the growth process. Figure 1a is a photograph of the reactor used for that purpose. Nanoparticles are aerodynamically extracted from the plasma volume and collected onto a substrate for *ex-situ* characterization (XRD, TEM, Raman). *In-situ* FTIR is also used to monitor the consumption of the precursor (silane) as the nanoparticles nucleate and grow. Figure 1b summarizes the findings: silane is consumed and converted into nanoparticles on a time scale of 50 milliseconds. This time scale is determined using the gas flow velocity through the reactor and the distance over which the silane signal is no longer detectable. At the end of the nucleation process the nanoparticles

have a size of 5-10 nm with an amorphous structure, as determined by TEM and Raman. At this point the nanoparticles are immersed into an argon-hydrogen plasma, with the hydrogen being the result of the silane decomposition process. The structure of the particles evolves from amorphous to crystalline on a time scale of 100-150 milliseconds, as determined by the distance over which the particles go from a fully amorphous structure to a crystalline one. This direct measurement of the time scale over which crystallization occurs allows determining the nanoparticle temperature during this process, under the assumption that the non-thermal plasma effectively behaves as an “annealing furnace”, and once the crystallization rate of the particles is known. Regarding this first point, there are several theoretical contributions predicting that reactions occurring at the nanoparticle surface (H-atom and argon ion recombination) lead to substantial heating [10, 11]. Regarding the second point, we have performed an independent measurement of the nanoparticle crystallization rate by producing amorphous silicon particles and by annealing them in-flight through a tube furnace [12]. By using this experimentally determined crystallization rate, and by using the 150 millisecond crystallization time measured using the approach described above, we have determined that the particles must be heated to a temperature of at least 1100K while in the non-thermal plasma.

The second approach is based on the monitoring of the nanoparticle surface while exposed to the non-thermal plasma [13]. We have used the reactor shown in figure 2 to (a) produce silicon particles in a first plasma and then (b) pass them through a second plasma where they are treated at different input powers. An IR beam is passed through the second plasma, and the Si-H surface coverage is monitored as a function of input power in the second plasma. In figure 3 we plot the integral absorption from the SiH_x stretching modes centered around 2100 cm⁻¹ vs. input power. We find that the surface coverage decreases as the plasma power is increased, and that the hydride moieties are effectively removed from the particle surface for an input power of 60W. We compare these results to simple theoretical calculation based on the kinetics of hydrogen desorption from flat silicon surfaces exposed to a hydrogen-containing

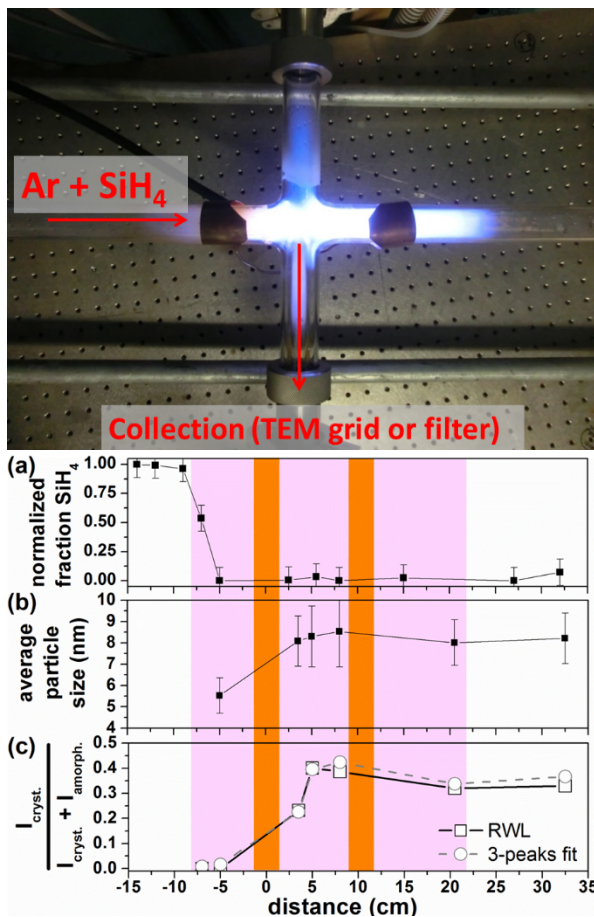


Figure 1. (a) Photograph of reactor for the aerodynamic extraction of nanoparticles at different stages of growth. (b) Summary of precursor consumption, particle diameter and particle structure along reactor length.

plasma. The flux of atomic hydrogen to the silicon surface maintains the coverage to near 100% up to 600-700K, when thermal desorption leads to a decrease in hydrogen surface coverage. We should stress that we have performed careful control experiments to account for the contribution from UV exposure and ion bombardment to the hydrogen desorption kinetics. We have collected nanoparticles onto a stainless steel mesh placed in the center of the second plasma, and exposed them to the discharge at different power levels while monitoring the signal from SiH_x species. We have found that even with a 1 second exposure to the plasma (compared to the ~ 100 millisecond residence time for the in-flight exposure case) there is only a minimal loss of surface hydride species. The difference between the supported case (particles onto a stainless steel mesh) and the in-flight case (particle free-standing in the gas stream) is that in the second case are effectively thermally insulated and become sufficiently hot to desorb the surface hydrogen.

The results from these two different techniques are consistent with each other. When using the crystallization rate to determine the nanoparticle temperature, we obtain a temperature excess compared to the gas temperature (which is safely assumed to be 300K for a non-thermal plasma) of 800K for a power density of 0.8 W/cm^3 , which is calculated using the electrical power input to the discharge and the plasma volume. When using desorption of hydrogen from the particle surface as a temperature probe, we obtain 400K for a density of 0.5 W/cm^3 , indicating that the two techniques are in reasonably good agreement.

Future Plans

The studies outline above confirm that non-thermal plasma induce significant nanoparticle heating despite the fact that the gas temperature is near to room temperature. This has important implications from the materials processing point of view. Our future efforts will focus on exploring the consequences of non-equilibrium processing conditions not only on nanoparticle structure but on the surface chemistry of the nanopowder as well. We will in

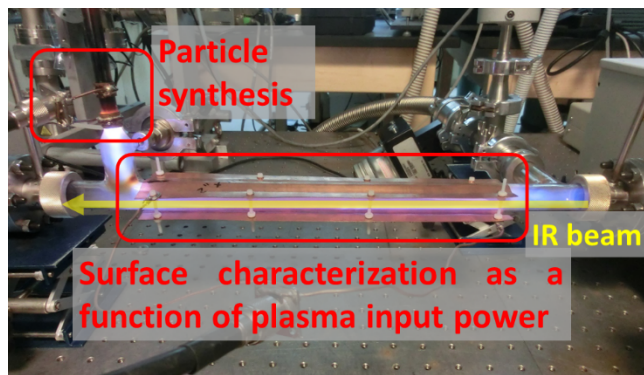


Figure 2. Photograph of reactor for the *in-situ* characterization of nanoparticle surface as a function of plasma input power.

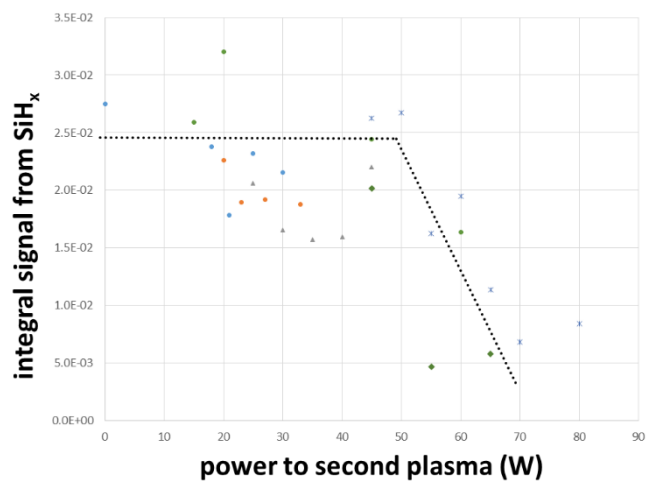


Figure 3. Nanoparticle surface coverage with SiH_x groups as a function of plasma power.

particular explore the mechanisms enabling the in-flight plasma-induced surface modification of particles.

References

1. Mangolini, L., Journal of Vacuum Science & Technology B: Microelectronics and Nanometer Structures, 2013. **31**(2): p. 020801.
2. Oda, S., Materials Science and Engineering, 2003. **B101**: p. 19-23.
3. Cho, K.-S., N.-M. Park, T.-Y. Kim, K.-H. Kim, G.-Y. Sung, and J.H. Shin, Applied Physics Letters, 2005. **86**: p. 071909.
4. Cheng, K.-Y., R. Anthony, U.R. Kortshagen, and R.J. Holmes, Nano Letters, 2011. **11**(5): p. 1952-1956.
5. Liu, C.-Y., Z.C. Holman, and U.R. Kortshagen, Nano letters, 2009. **9**(1): p. 449-452.
6. Mangolini, L., E. Thimsen, and U. Kortshagen, Nano Letters, 2005. **5**(4): p. 655-659.
7. Mariotti, D. and R.M. Sankaran, Journal of Physics D-Applied Physics, 2010. **43**(32): p. 323001.
8. Jurbergs, D., E. Rogojina, L. Mangolini, and U. Kortshagen, Applied Physics Letters, 2006. **88**: p. 233116 1-3.
9. Lopez, T. and L. Mangolini, Journal of Vacuum Science & Technology B, 2014. **32**(6): p. 061802.
10. Mangolini, L. and U. Kortshagen, Physical Review E, 2009. **79**(2): p. 026405.
11. Kramer, N.J., R.J. Anthony, M. Mamunuru, E.S. Aydil, and U.R. Kortshagen, Journal of Physics D: Applied Physics, 2014. **47**(7): p. 075202.
12. Lopez, T. and L. Mangolini, Nanoscale, 2014. **6**(3): p. 1286-1294.
13. Lopez, T. and L. Mangolini, submitted for publication, 2015.

Publications

1. Lopez, T. and L. Mangolini, *Thermal effects in the non-thermal plasma processing of nanoparticles*. Submitted for publication, 2015.
2. Yasar-Inceoglu, O., L. Zhong, and L. Mangolini, *Core/shell silicon/polyaniline particles via in-flight plasma-induced polymerization*. Journal of Physics D: Applied Physics, 2015. **48**(31): p. 314009.
3. Coleman, D., et al., *Hollow silicon carbide nanoparticles from a non-thermal plasma process*. Journal of Applied Physics, 2015. **117**(19): p. 193301.
4. Lopez, T. and L. Mangolini, *On the nucleation and crystallization of nanoparticles in continuous-flow nonthermal plasma reactors*. Journal of Vacuum Science & Technology B, 2014. **32**(6): p. 061802.
5. Lopez, T. and L. Mangolini, *Low activation energy for the crystallization of amorphous silicon nanoparticles*. Nanoscale, 2014. **6**(3): p. 1286-1294.

Novel exotic properties of two-dimensional atomic crystals of layered ternary transition metal chalcogenides

Zhiqiang Mao and Jiang Wei

Department of Physics and Engineering Physics, Tulane University,
New Orleans, LA 70118

Program Scope

Individual atomically-thin layer of transition metal dichalcogenides (TMDCs) such as MoS₂ and WS₂ has recently attracted enormous interest [1-3]. Their distinct properties, such as large direct band gaps and high photoresponsibility, have tremendous potential for applications in nanoelectronics and optoelectronics. Given the fascinating properties of 2D *binary* TMDCs, the PIs are particularly interested in studying whether 2D atomically-thin semiconductors can be realized in layered *ternary* transition metal chalcogenides (TTMCs). The distinct properties of 2D TMDCs are attributed to the combined effects of quantum confinement, localized *d*-bands, spin-orbital coupling (SOC), and inversion symmetry breaking. In layered TTMCs, some of these parameters can have greater tunability. Including a *3d*-element in a TTMC can enhance Van Hove singularities in the density of states, which likely results in a remarkable enhancement to the electric field effect and optical absorption. *3d* ions such as Fe and Mn can also carry magnetic moments and possibly lead to coexistence of semiconductivity and magnetism. Including a heavy element such as a *4d/5d*-element or Sb/Bi in a TTMC would bring in strong SOC, which, when combined with strong electron correlation, may create emergent properties. Moreover, many TTMCs have lower structural symmetry and inversion symmetry breaking often occurs in their single layer forms, which, combined with strong SOC, can result in spin splitting. Therefore, 2D atomic crystals of TTMCs can reasonably be expected to exhibit distinctive properties. There are many layered, semiconducting layered TTMCs which allow combinations of *3d* and *4d/5d/Sb/Bi*, such as Cu₂MX₄ (M=W/Mo; X=S/Se) [4-7], Mn(Sb/Bi)₂S₄ [8-10] and (Mn/Fe)Bi₄S₇ [11]. Many of these materials have optical bandgaps in the visible range and their layered structures may allow accessibility of 2D atomic crystals. One major objective of this research project is to discover novel 2D TTMC materials with distinct and useful properties as well as establish the synthesis science of for the proposed TTMCs. The research work of this project includes bulk single crystal growth and characterization of TTMCs, preparation of 2D atomic crystals of TTMCs, nanoscale transport measurements, and the search for exotic properties on 2D TTMCs using field effect in transistors device. The PIs have performed preliminary studies on some layered TTMCs such as Nb₃SiTe₆ and Ta₂Pd₃Se₈; few-layer 2D crystals were found to be accessible and stable for both systems. In addition, the PIs also plan to search for high temperature superconductivity on 2D nanocrystals of iron chalcogenides Fe_{1+y}(Te_{1-x}Se_x) using field effect in double gated transistor devices.

Recent Progress

Under the motivation that ternary 2D materials may exhibit exciting properties as discussed above, the PI have attempted synthesizing several layered, ternary materials, including MnPS₃, FeNbTe₂, Nb₃SiTe₆, Ta₂Pd₃Se₈ and Ta₂NiSe₅ using flux and chemical vapor transport methods. These efforts have been very successful; high-quality single crystals have been obtained for all of them. Figure 1a-e shows their crystal images. Crystals of MnPS₃, FeNbTe₂,

Nb_3SiTe_6 and Ta_2NiSe_5 show lamellar shapes, consistent with their layered structures. Crystals of $\text{Ta}_2\text{Pd}_3\text{Se}_8$ are needle-like, consistent with its quasi-one-dimensional structure.

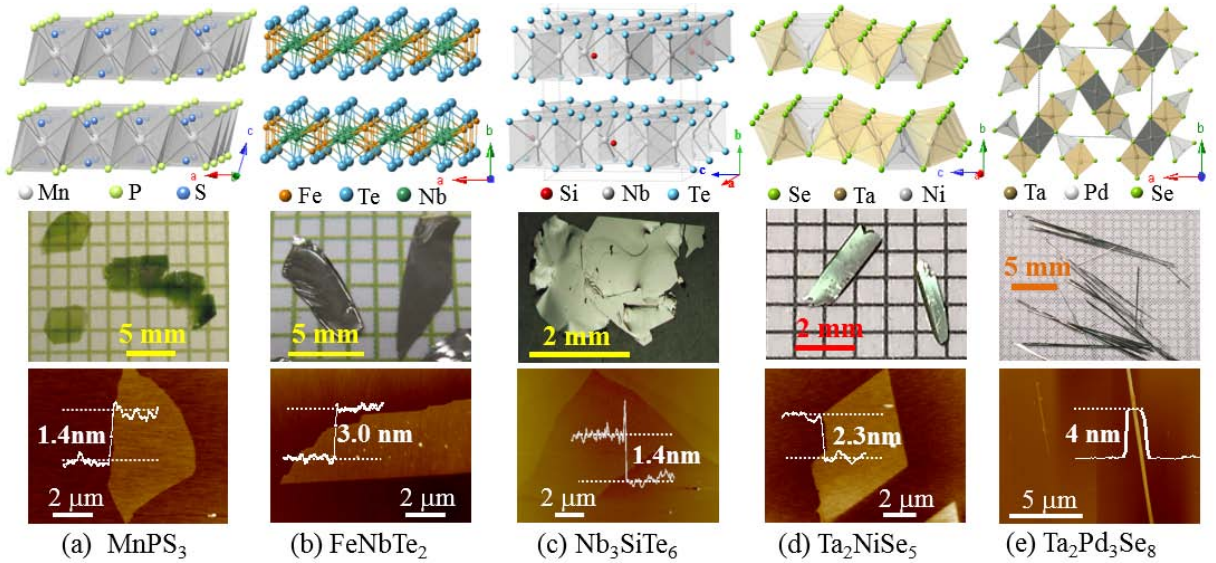


Figure 1: Crystal structures (top panel), optical crystal images (middle panel) and AFM image (bottom) of layered ternary transition metal chalcogenides MnPS_3 (a), FeNbTe_2 (b), Nb_3SiTe_6 (c), Ta_2NiSe_5 (d), and $\text{Ta}_2\text{Pd}_3\text{Se}_8$ (e).

The PIs have explored the accessibility of 2D thin layers of these materials and demonstrated 2D atomic thin layers are indeed accessible for MnPS_3 , FeNbTe_2 , Nb_3SiTe_6 and Ta_2NiSe_5 via microexfoliation. The bottom panels of Fig. 1 show micrographs of tri/bi-layer thin flakes of these materials. Given these materials show diverse bulk properties, their atomically thin layers offer fertile ground for exploring novel functional properties of 2D materials.

MnPS_3 is an antiferromagnetic (AFM) insulator with the Neel temperature of 78 K [12]. Theoretical studies have suggested that the entangle of antiferromagnetism and valley degree of freedom in the monolayer MnPS_3 may lead to lifted spin degeneracy [13]. 2D atomic crystals of MPX_3 are accessible, as shown in Fig. 1a. We also demonstrated bulk MnPS_3 single crystals display photoluminescence.

FeNbTe_2 and Ta_2NiSe_5 are also layered materials with Van der Waals (vdW) gaps (see Fig. 1b and 1c). FeNbTe_2 is a small gap semiconductor ($\Delta \sim 0.5$ eV) with an AFM order involving competing AFM and FM interactions [14], while Ta_2NiSe_5 is a candidate for excitonic insulator [15] and shows metal-to-semiconducting transition near 500K [16]. Atomic crystals are accessible for both materials.

$\text{Ta}_2\text{Pd}_3\text{Se}_8$ possesses a quasi-1D structure and its electronic properties of $\text{Ta}_2\text{Pd}_3\text{Se}_8$ have not been reported. The PIs have shown that the single crystals of this materials can be easily exfoliated to stable nano-wires with the smallest diameter reaching ~ 1.5 nm and such nano-wires exhibit semiconducting properties with the gap being ~ 1 eV. The accessibility of such stable 1D nano wires offers wonderful opportunities to explore transport properties in 1D limit. We have already observed impressive transistor performance in a nano-device based on a $\text{Ta}_2\text{Pd}_3\text{Se}_8$ nano wire (see Fig. 2).

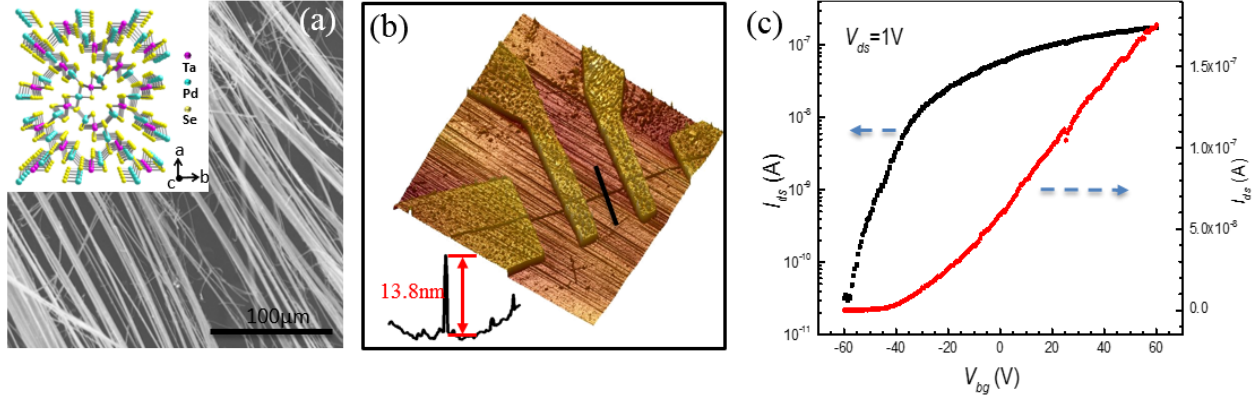


Figure 2: (a) SEM image of $\text{Ta}_2\text{Pd}_3\text{Se}_8$ fiber bundles. Upper insert shows the crystal structure projected along c axis. (b) AFM image of a $\text{Ta}_2\text{Pd}_3\text{Se}_8$ nanowire device. The wire is exfoliated from a bulk crystal. The insert at the bottom left shows the height profile. (c) Transconductance of a $\text{Ta}_2\text{Pd}_3\text{Se}_8$ nanowire device measured at room temperature.

In our previous work, we also found Nb_3SiTe_6 atomic crystals show unusual quantum transport properties, which provides strong evidence for a long-standing theoretical prediction--electron-phonon interaction is suppressed by dimensionality confinement on phonons [17-18]. This work has recently published in *Nature Physics*[19].

Our accomplishments obtained in the preliminary studies demonstrate that layered ternary materials would offer rich opportunities for exploring novel functional properties in the 2D world.

Future Plans

The research work of this project includes bulk single crystal growth and characterization of TTMCs, preparation of 2D atomic crystals of TTMCs, nanoscale transport measurements; and the search for exotic properties on 2D TTMCs using field effect in transistor devices.

Single crystal growth: The Mao (PI) group has a strong background in single crystal growth of various materials using the floating-zone, flux and chemical vapor transport (CVT) techniques. We have successively synthesized single crystals for MnPS_3 , FeNbTe_2 , Nb_3SiTe_6 , $\text{Ta}_2\text{Pd}_3\text{Se}_8$ and Ta_2NiSe_5 . Future efforts towards crystal growth will be extended to other interesting materials, including Cu_2MX_4 ($\text{M}=\text{W}/\text{Mo}$; $\text{X}=\text{S}/\text{Se}$)[4-7], $\text{Mn}(\text{Sb}/\text{Bi})_2\text{S}_4$ [8-10] and $(\text{Mn}/\text{Fe})\text{Bi}_4\text{S}_7$ [11], using various approaches mentioned above.

Structure and bulk properties characterization: We will use x-ray diffraction and an energy dispersive x-ray spectrometer to characterize the structures and compositions of the synthesized materials, respectively. Band gap and carrier mobility are two important parameters for semiconductor devices, since the former affects the on-off ratio and the off-state power consumption rate of a device, while the latter is crucial for high speed response. We will perform resistivity measurements on synthesized crystals and estimate their electronic band gap from the fits of temperature dependence of resistivity in high temperature ranges. Together with Hall effect measurements, we can also evaluate the mobility of these bulk samples. Additionally, we will also conduct specific heat and thermal conductivity measurements on synthesized single crystals to examine their thermodynamic properties.

For the proposed materials containing magnetic ions, such as $\text{Mn}(\text{Sb}/\text{Bi})_2\text{S}_4$, $(\text{Mn}/\text{Fe})\text{Bi}_4\text{S}_7$ and MPS_3 ($\text{M}=\text{Fe}$, Ni and Mn), we will also investigate their magnetic properties by magnetization and magneto-transport measurements.

Nanoscale transport measurements: Once these 2D TTMCs bulk single crystals with characterized properties become available, we will use microexfoliation [41, 141] to produce 2D atomic crystals for nanoscale transport measurements. We have made various technical improvements, such as the pretreatment of the substrate to enhance the surface adhesion for better exfoliation. Additionally, we have developed a new approach, i.e., using low energy ion milling to thin down crystals with atomic level precision.

The obtained 2D atomic crystals will be characterized by Atomic force microscopy (AFM), Raman spectrum, and transmission electron microscopy (TEM). In addition, we will also exam the stability of the obtained 2D atomic crystals using the above characterization techniques. Then we will study the electronic transport properties of atomically thin materials of TTMCs. Electronic transport measurements will be performed on multi-terminal electronic devices prepared on 2D TTMC crystals obtained by microexfoliation or ion milling combined with electron-beam or photo lithography.

We will fabricate the field effect transistor (FET) devices based on TTMCs semiconductors and study their potential electronic and optoelectronic applications (for example, we have recently demonstrated FET device based on new ternary material $\text{Ta}_2\text{Pd}_3\text{Se}_8$, see Fig. 2). We will also search for exotic emerging quantum properties of 2D TTMC and $\text{Fe}_{1.02}(\text{Te}_{1-x}\text{Se}_x)$ atomic crystals using field effect in double gated transistor devices.

References

- [1] Q. H. Wang, K. Kalantar-Zadeh, A. Kis, et al., *Nat Nano* **7**, (2012)
- [2] M. Chhowalla, H. S. Shin, G. Eda, et al., *Nat. Chem.* **5**, (2013)
- [3] S. Z. Butler, S. M. Hollen, L. Cao, et al., *ACS Nano* **7**, (2013)
- [4] P. D. Tran, M. Nguyen, S. S. Pramana, et al., *Energy Env. Sci.* **5**, (2012)
- [5] D. Jing, M. Liu, Q. Chen, et al., *Int. J. Hydrogen Energy* **35**, (2010)
- [6] C. J. Crossland, P. J. Hickey and J. S. O. Evans, *J. Mater. Chem.* **15**, (2005)
- [7] H. Liang and L. Guo, *International Journal of Hydrogen Energy* **35**, (2010)
- [8] S. Lee, E. Fischer, J. Czerniak, et al., *J. Alloys Compd.* **197**, (1993)
- [9] A. Pfitzner and D. Kurowski, *Z. Kristallogr. Cryst. Mater.* **215**, 373 (2000)
- [10] D. Kurowski. Mangan-Chalkogenometallate der 15. Gruppe und binäre Kupfertellurid - Synthese, Strukturen, Hochdruckchemie und physikalische Eigenschaften. Ph.D thesis, Universität Regensburg, 2003.
- [11] Z.-Z. Luo, C.-S. Lin, W.-D. Cheng, et al., *Cryst. Growth Des.* **13**, (2013)
- [12] G. Le Flem, R. Brec, G. Ouvard, et al., *J. Phys. Chem.* **43**, (1982)
- [13] X. Li, T. Cao, Q. Niu, et al., *Proc. Natl. Acad. Sci. USA* **110**, (2013)
- [14] J. Li, M. E. Badding and F. J. DiSalvo, *Inorg. Chem.* **31**, (1992)
- [15] T. Kaneko, T. Toriyama, T. Konishi, et al., *Journal of Physics: Conference Series* **400**, (2012)
- [16] F. J. Di Salvo, C. H. Chen, R. M. Fleming, et al., *J. Less Common. Met.* **116**, (1986)
- [17] B. A. Glavin, V. I. Pipa, V. V. Mitin, et al., *Phys. Rev.B* **65**, (2002)
- [18] I. M. Tienda-Luna, F. G. Ruiz, A. Godoy, et al., *Appl. Phys. Lett.* **103**, (2013)
- [19] J. Hu, X. Liu, C. L. Yue, et al., *Nat Phys* **11**, 471 (2015)

Publications

We just started this project from Sep, 2015 and have not had any publications yet.

Growth of InGaN Quantum Dots by Liquid Phase Epitaxy (LPE) in an MBE Reactor

T. D. Moustakas* and R. Paiella

Dept. of Electrical Engineering and Photonics Center, Boston University, Boston, MA 02215

* Phone: 617-353-5431, Fax: 617-353-1283, Email: tdm@bu.edu

Program Scope

This research program is focused on the investigation of surface-plasmon-enhanced light emission and absorption in semiconductor photonic materials coupled to metallic nanostructures. The specific efforts described below are aimed at the development of a materials platform that can optimally enable these investigations, i.e., InGaN quantum dots (QDs) with composition across the entire alloy range. These materials are ideally suited to the study of plasmon-matter interactions, because of their widely tunable bandgap energies across the visible spectrum (where the plasmonic resonances of typical metallic nanostructures occur) and favorable near-surface radiative properties (unlike other III-V semiconductors which are limited by Fermi-level pinning). InGaN QDs are also technologically significant for a wide range of applications that could benefit strongly from these plasmonic interactions, including all-solid-state lighting and photovoltaics based on the intermediate-band device concept. In addition, the use of highly localized QDs in low-density samples would allow for the direct probing of the giant optical-field enhancements produced by metallic nanoparticles in their near-field vicinity. Other recent activities in this program, focused on the directional control of light emission and photodetection with plasmonic metasurfaces, are summarized in a separate abstract.

Recent Progress

The traditional method of forming semiconductor QDs is the strain-driven Stranski-Krastanov (SK) method [1]. The SK growth mode relies upon

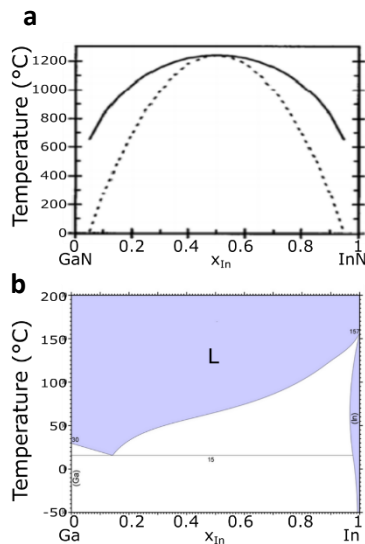


Figure 1: phase diagram for (a) InGaN [4] and (b) In-Ga [5]

accumulated in-plane compressive strain in order to induce a transition from 2D to 3D growth. This method by nature has a number of limitations, since there is an optimum amount of strain required for the formation of QDs and therefore it is impossible to decouple wetting layer thickness, QD composition, QD dimensions, and template material from one another. This method has also been used extensively for the development of GaN QDs and InGaN QDs [2, 3]. However, because InGaN alloys tend to undergo phase separation by spinodal decomposition as shown in Figure 1(a) [4], the aforementioned limitations of the SK growth method do not allow for the fabrication of InGaN QDs in the entire alloy composition. For high In-content InGaN QDs on GaN the resulting SK QDs are fully incoherent or defective.

In this project we are developing a novel method of forming InGaN QDs. This method relies upon our ability to form

an In-Ga liquid solution in the entire compositional range at relatively low temperatures. As seen in the phase diagram of Figure 1(b), a mixture of In and Ga has a single liquid phase above temperatures ranging from a minimum of 15 °C for 14% In (at the eutectic point) to a maximum of 157 °C for 100% In [5].

Upon simultaneous or sequential deposition in an MBE chamber of In and Ga on a substrate, the In and Ga adatoms form a liquid solution, whose composition is controlled by the ratio of the fluxes of the two constituents ($F_{\text{In}}/F_{\text{In}}+F_{\text{Ga}}$). Thus, the control of the composition by this method avoids the complex relationship between strain and chemical potentials that governs the SK growth mode. The nucleation of this liquid film on the substrate is governed by the interfacial free energy between the liquid deposit and substrate σ_{ds} , the liquid deposit and vapor σ_{dv} , and the vapor and substrate σ_{vs} . At equilibrium the liquid deposit forms a hemispherical cap on the top of the substrate and the contact angle θ is given by the expression $\cos \theta = (\sigma_{\text{vs}} - \sigma_{\text{sd}}) / \sigma_{\text{dv}}$ [6].

If $\sigma_{\text{vs}} - \sigma_{\text{sd}} = \sigma_{\text{dv}}$ then $\theta = 0$ and the deposit is said to wet the substrate and form a continuous liquid film. So far we have investigated the deposition of In-Ga solution on GaN and AlN templates. In both cases we found that the In-Ga liquid solution forms nano-droplets on the top of the substrate.

After the formation of the In-Ga liquid nano-droplets, active nitrogen (N , N^+ , N_2^*),

produced in an RF plasma source, is used to convert the In-Ga nano-droplets into InGaN QDs. These QDs are expected to have the same composition as the In-Ga nano-droplets. It should be pointed out that although the solubility of molecular N_2 in Ga at the growth temperature of InGaN alloys is very low, the solubility of active N is expected to be very high [7]. It should also be stressed that LPE, in general, is a thermodynamic process, and thus, one expects the produced InGaN QDs to be of higher crystalline quality, compared to the SK growth mode which is kinetically controlled.

Our LPE growth method has effectively produced InGaN QDs across a range of growth parameters. Figure 2 shows representative AFM and SEM images of LPE InGaN QDs on AlN. In-plane grazing incidence x-ray diffraction (IP-GID) showed the QDs to be coherent to the AlN template. Due to the thinness of the QD layers, conventional high resolution x-ray diffraction was found to be unsuitable for the compositional analysis. We have however observed a shift of the critical angle (α_c) in x-ray scattering experiments that is consistent with the relative electron densities. We are currently investigating x-ray reflectivity for compositional analysis, as it can probe α_c with high resolution.

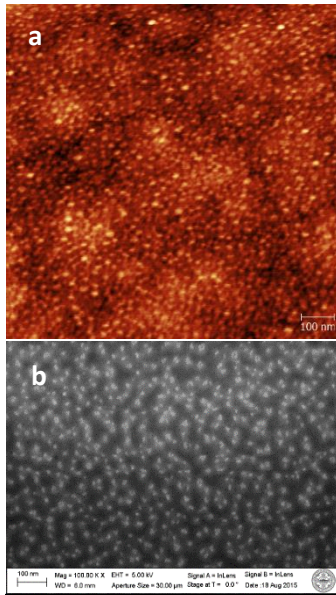


Figure 2: (a) AFM and (b) SEM images for LPE InGaN QDs on AlN

We have also developed the capability for in-house lab-scale grazing incidence small angle x-ray scattering (GISAXS) characterization of single- and multi-layer QD samples.

GISAXS traditionally relies upon access to synchrotron radiation at a beamline, which forces a significant delay between growing a sample and producing meaningful data. We have uniquely incorporated advanced GISAXS techniques into our standard characterization procedure for single- and multi-layer QD samples, enabling effective determination of parameters such as the dimensions, shape, lateral and vertical correlation, and areal density. The technique is non-destructive and integral, and as such perfectly complements the destructive and localized TEM technique that we also have access to.

The correlation length (L) and areal density (ρ_N) of several LPE grown samples were investigated as a function of flux ratio, approximate thicknesses D , and template material. All samples were grown with a substrate temperature of 300 °C during all stages of the growth. GISAXS was performed with incident angle $\alpha_i = .5$ degrees. This exceeds the critical angle of InN, GaN, and AlN, and thus yields quasi-kinematical scattering behavior [8]. Experiments were performed with the incident beam along the [10-10] and the [11-20] directions. The Table below shows the growth parameters and the values of L and ρ_N .

Sample	Substrate	$F_{In}/F_{In}+F_{Ga}$	Thickness D (nm)	Correlation length L (nm)	Areal density ρ_N (cm^{-2})
V3581	GaN	.61	6.03	36.86	7.36×10^{10}
V3584	GaN	.62	2.03	33.20	9.07×10^{10}
V3604	AlN	.62	2.03	30.44	1.08×10^{11}
V3605	AlN	.62	1.35	31.51	1.07×10^{11}
V3610	AlN	.40	2.02	42.76	5.47×10^{10}
V3611	AlN	.40	1.35	51.63	3.75×10^{10}
V3613	AlN	.21	2.04	48.87	4.19×10^{10}

L and ρ_N were determined from the analysis of horizontal slices of the GISAXS patterns along the Yoneda wing as shown in Figure 3. Figure 3 (a) shows the GISAXS pattern of sample V3613 with annotated descriptions of the various features and the extracted intensity vs q_y plot is shown in Figure 3 (b). L was calculated from the q_y positions of the correlation peaks, using $L = 2\pi/q_y$. ρ_N was approximated using $\rho_N = (1/L)^2$. For all samples, L was found to be almost identical for both azimuthal orientations and the tabulated values are the averages of the two [9].

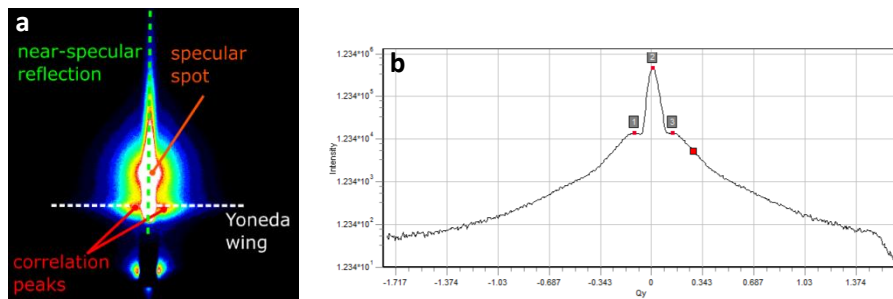


Figure 3: (a) GISAXS pattern; and (b) 1D intensity plot along the Yoneda wing

Future Plans

Future work will focus on the optoelectronic properties of the LPE InGaN QDs, including their use for intermediate-band photovoltaics. These samples will then be combined with the plasmonic nanostructures which are also under development in this program, for the further investigation of plasmon-enhanced light emission and absorption. The tunability of ρ_N will also be explored to make low areal density samples, for the study of highly localized plasmon-matter interactions.

References

- [1] A. Pimpinelli, and J. Villain, *Physics of Crystal Growth*. Cambridge University Press (1998)
- [2] T. Xu, et al., J. Appl. Phys. **102**, 073517 (2007)
- [3] T. D. Moustakas, et al., Physica Status Solidi A **205**, 2560 (2008).
- [4] I. H. Ho and G. B. Stringfellow, Appl. Phys. Lett. **69** (18), 28 October 1996.
- [5] T. J. Anderson and I. Ansara, Journal of Phase Equilibria, Vol. 12 (1991)
- [6] L. D. Landau and I. M. Lifshitz, Statistical Physics, 3rd ed. (Pergamon, Oxford, 1980).
- [7] T. D. Moustakas and A. Bhattacharyya Phys. Status Solidi C **9**, 580 (2012)
- [8] D. M. Smilgies. *GISAXS and GIWAXS*. Retrieved from <http://staff.chess.cornell.edu/>
- [9] J. Woodward, T.D. Moustakas (to be published)

Publications

J. DiMaria, E. Dimakis, T. D. Moustakas, and R. Paiella, “Plasmonic off-axis unidirectional beaming of quantum-well luminescence,” *Appl. Phys. Lett.* 103, 251108 (2013).

W. Pan, E. Dimakis, G. T. Wang, T. D. Moustakas, and D. C. Tsui, “Two-dimensional electron gas in monolayer InN quantum wells,” *Appl. Phys. Lett.* 105, 213503 (2014).

R. Paiella, “Plasmonic control of quantum-well luminescence for enhanced efficiency and beam shaping,” 35th Progress in Electromagnetics Research Symposium, Guangzhou (China), 2014 (**Invited Talk**).

T. D. Moustakas, “Fundamental differences between cubic III-V compounds and wurtzite nitride semiconductors produced by molecular beam epitaxy,” 18th International Conference on Molecular Beam Epitaxy, Flagstaff (Arizona), September 2014 (**Plenary Talk**).

J. DiMaria, E. Dimakis, T. D. Moustakas, and R. Paiella, “Plasmonic collimation and beaming from LED active materials,” IEEE Conference on Lasers and Electro-Optics, paper CF2E.2, San Jose (CA), 2013.

T. D. Moustakas, “Fundamental differences between traditional III-V compounds and Nitride Semiconductors” 11th Int. Conf. on Nitride Semiconductors, Beijing, China, Sept., 2015 (**Invited Talk**)

Project Title: Thermochemistry of Oxides with Electrochemical and Energy Applications

Grant number: DEFG0203ER46053

Principal Investigator:

Alexandra Navrotsky

NEAT-ORU & Peter A. Rock Thermochemistry Laboratory

University of California, Davis

Davis, CA 95616

Phone: (530) 752-3292, Fax: (530) 752-9307

anavrosky@ucdavis.edu

Program Scope

The focus of the current project is to emphasize the thermodynamic properties of materials relevant to energy conversion. The main objectives are: (a) to advance and use unique calorimetric capabilities to determine the energetics of oxide and other materials having possible energy applications, with an emphasis on new materials for batteries, fuel cells and solar energy conversion, (b) to understand, in terms of both macroscopic energetics and microscopic structure and bonding, the interplay of defect chemistry, oxidation-reduction, and size effects at the bulk and nanoscale in determining materials properties. This project emphasizes mixed ionic - electronic conducting materials containing transition metals (M) of variable valence, especially perovskites and lithium containing phases, with M = Mn, Fe, Co, Ni. The thermochemistry of new families of complex halide, chalcogenide, nitride, and hybrid (organic-inorganic) perovskite materials are being explored. The major and unique technique employed is high temperature oxide melt solution calorimetry, with careful attention given to materials synthesis and characterization.

The materials under study find important applications in solid oxide fuel cells, gas separation membranes, catalysts, batteries, and solar energy, as well as nuclear energy and aerospace technologies. Thus they are directly relevant to one of the Department of Energy's basic missions, namely the development of more efficient energy sources and energy utilization. Fundamental and systematic thermodynamic data are essential for predicting possible new materials, for determining materials compatibility and longevity as well as use-inspired fundamental questions. In addition, the project trains students and postdocs in careful measurements and rigorous data analysis and in working in a large multi-disciplinary group to

prepare them for careers in the materials science of energy. This project is leveraged by a number of international collaborations, which both extend the science and provide opportunities for students and postdocs to work in a global environment.

Recent Progress

Although the current renewal started this July, we have already made progress in several areas and here we highlight work related to hybrid perovskites, which have gained considerable interest for their applications in photovoltaics and multiferroics.

Dimethylammonium metal formates [DMA-M-F]: We have synthesized, characterized, and measured the heats of formation of a series of isostructural dimethylammonium metal formate perovskites, $[(\text{CH}_3)_2\text{NH}_2][\text{M}(\text{HCOO})_3]$ with $\text{M} = \text{Ni}, \text{Mn}, \text{Zn}$ and Co , which have shown promising multiferroic behavior. Their enthalpy of formation from components becomes less exothermic in the order $\text{Mn}, \text{Zn}, \text{Co}, \text{Ni}$ (Table 1). The stability of the hybrid perovskite decreases as the tolerance factor increases, unlike trends seen in inorganic perovskites.

[DMA-M-F]	Enthalpy of formation (kJ/mol)	Tolerance factor	Cation radius ^a □ (pm)
[DMA-Mn-F]	-47.95±1.12	0.941	83
[DMA-Co-F]	-34.89±0.68	0.968	74.5
[DMA-Ni-F]	-28.45±0.25	0.986	69
[DMA-Zn-F]	-41.66±0.66	0.970	74

Table 1. Calculated tolerance factors of [DMA-M-F] hybrid perovskites and their formation enthalpies

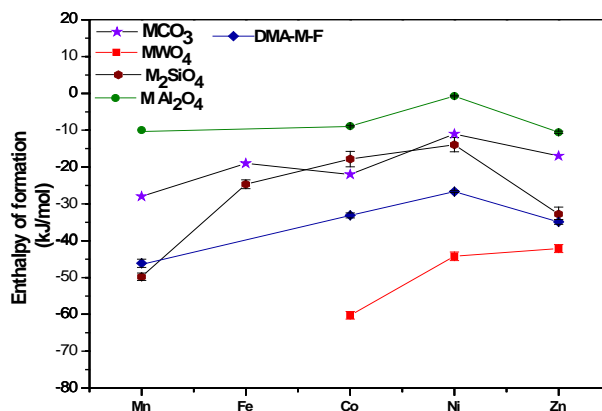


Fig 1. Enthalpy of formation of ternary oxides containing divalent transition metals [*J. Amer. Chem. Soc.*, **137**, 10351-10356 (2015)]

Our study shows that the stability of $[(\text{CH}_3)_2\text{NH}_2][\text{M}(\text{HCOO})_3]$ hybrid perovskites, is comparable to those of a number of inorganic ternary oxides (Fig 1). Among the four isostructural compounds we studied, the Mn analogue is most stable, followed by Zn, Co, and Ni. The energetics of these ternary transition metal materials seem to be governed more by the acid–base properties of the associated moiety and the transition metal oxide than by a bond length misfit as measured by the tolerance factor.

Metal formates: The simplest organic - inorganic hybrid materials are metal formate, with divalent cations connected by formate anions. They show great potential for applications in gas storage and Li-ion battery materials. We report synthesis, characterization, and enthalpies of formation of five isostructural metal formates, $M(\text{HCOO})_2 \cdot x\text{H}_2\text{O}$ with $M = \text{Mg, Mn, Co, Ni}$ and Zn . The enthalpies of formation of $\text{Mg}(\text{HCOO})_2 \cdot 2.12\text{H}_2\text{O}$, $\text{Mn}(\text{HCOO})_2 \cdot 2.02\text{H}_2\text{O}$, $\text{Co}(\text{HCOO})_2 \cdot 1.85\text{H}_2\text{O}$, $\text{Ni}(\text{HCOO})_2 \cdot 2.13\text{H}_2\text{O}$ and $\text{Zn}(\text{HCOO})_2 \cdot 2.08\text{H}_2\text{O}$ are -91.27 ± 1.86 , -64.26 ± 1.04 , -49.68 ± 0.90 , -38.30 ± 0.92 , -70.01 ± 0.88 kJ/mol, respectively. The stability of the metal formates follows the order: $\text{Mg} > \text{Zn} > \text{Mn} > \text{Co} > \text{Ni}$.

Methylamine lead halide perovskites: $\text{CH}_3\text{NH}_3\text{PbX}_3$ is a light-harvesting material proposed for organic-inorganic hybrid perovskite solar cells (PSC). Sensitivity towards moisture of these materials is a potential drawback in practical applications. We are currently working on the synthesis, characterization and calorimetry of methylamine lead halide perovskites, MAPbX_3 [$X = \text{I, Br}$]. Thermodynamic data will help establish the best compositions and conditions for synthesis, stability and applications.

Inorganic rare earth perovskites: We have completed work with our Romanian colleagues on rare earth cobaltite and ferrite - manganite perovskites applicable to solid oxide fuel cells and this work is now published or in press. Lanthanide cobalt perovskites $\text{LnCoO}_{3-\delta}$ ($\text{Ln} = \text{La, Nd, Sm, and Gd}$) are important materials for electroceramics, catalysts, and electrodes in solid oxide fuel cells. Formation enthalpies of $\text{LnCoO}_{3-\delta}$ compounds were measured using high temperature oxide melt solution calorimetry. The formation enthalpies of $\text{LaCoO}_{2.992}$, $\text{NdCoO}_{2.985}$, $\text{SmCoO}_{2.982}$ and $\text{GdCoO}_{2.968}$ from constituent binary oxides (Ln_2O_3 , CoO) and O_2 gas are 111.87 1.36, 98.49 1.33, 91.56 1.46 and 88.16 1.45 kJ/mol, respectively. Thus these perovskites become energetically less stable with decrease in ionic radius of the lanthanide (from La to Gd), which corresponds to a decreasing tolerance factor and increasing oxygen deficiency. The thermodynamic stability of $\text{LaCoO}_{2.992}$, $\text{NdCoO}_{2.985}$, $\text{SmCoO}_{2.982}$ and $\text{GdCoO}_{2.968}$ correlates well with that expected from their tolerance factors and oxygen partial pressures corresponding to their decomposition.

Future Plans

Antiperovskites: These are ternary halides with cubic structure with the general formula AXM_3 , where A is oxygen, X is halogen and M is Li –These are being considered as solid electrolytes in Li Ion batteries. The metastability of Li_3OX relative to Li_2O based on DFT calculation indicates that they are subject to decomposition under applied voltage. Hence directly measured formation enthalpies will help in understanding the phase stability of these electrolytes.

Tin halide perovskites: Tin halide perovskites have attracted attention a promising class of materials for optoelectronic applications. Their systematic thermochemistry is not known and we plan to study their heats of formation.

Rare earth hybrid perovskites: The rare earth elements are important components in materials used in sustainable energy and high technology applications. Several rare earth metal compounds containing formate with the composition $(FA)_2Ln(HCOO)_3 \cdot xH_2O$ (where $x = 0-2$, $FA = HCONH_2$ and $Ln = La-Lu, Y$) are considered as materials relevant for rare earth recovery from end-of-life products and also are important as phosphors. Understanding their thermodynamic properties is hence important and we will start a study of their heats of formation.

Mixed anion lithium ion battery materials: We are continuing thermochemical studies of transition metal compounds containing Li and sulfate, halide, and hydroxide groups prepared by J.-M. Tarascon in France

Publications supported by grant 2014-15

- (1) "High Temperature Materials and Mechanisms" S. K. Sahu and A. Navrotsky, Y. Bar-Cohen, Ed., CRC Press, Taylor & Francis Group, Boca Raton, Florida, 17-30 (2014).
- (2) "Possible Correlation Between Enthalpies of Formation and Redox Potentials in LiMSO_4OH ($M = \text{Co, Fe, Mn}$), Li-ion Polyanionic Battery Cathode Materials" A. V. Radha, C. V. Subban, M. L. Sun, J. M. Tarascon, and A. Navrotsky, *J. Mat. Chem. A*, 2, 6887-6894 (2014).
- (3) "Thermochemistry, Morphology, and Optical Characterization of Germanium Allotropes" J. V. Zaikina, E. Muthuswamy, K. I. Lilova, Z. M. Gibbs, M. Zeilinger, G. J. Snyder, T. F. Fassler, A. Navrotsky and S. M. Kauzlarich, *Chem. Mater.*, 26, 3263-3271 (2014).
- (4) "Defect Chemistry of Singly and Doubly Doped Ceria: Correlation between Ion Transport and Energetics" S. Buyukkilic, S. Kim, and A. Navrotsky, *Angew. Chem.*, 126, 9671-9675 (2014).
- (5) "Enthalpy of Formation and Thermodynamic Insights into Yttrium Doped BaZrO_3 " M. D. Goncalves, P. S. Maram, R. Muccillo, and A. Navrotsky, *J. Mater. Chem. A*, 2, 17840-17847 (2014).
- (6) "Energetics of Bismuth Vanadate" G. P. Nagabhushana, A. H. Tavakoli, and A. Navrotsky, *J. Solid State Chem.*, 225, 187-192 (2015).
- (7) "Thermodynamic Stability and Correlation with Synthesis Conditions, Structure and Phase Transformations in Orthorhombic and Monoclinic $\text{Li}_2\text{M}(\text{SO}_4)_2$ ($M = \text{Mn, Fe, Co, Ni}$) Polymorphs" A. V. Radha, L. Lander, G. Rousse, J.-M. Tarascon, and A. Navrotsky, *J. Mater. Chem. A*, 3, 2601-2608 (2015).
- (8) "Formation Enthalpies of $\text{LaLn}'\text{O}_3$ ($\text{Ln}' = \text{Ho, Er, Tm and Yb}$) Interlanthanide Perovskites" J. Qi, X. Guo, A. Mielewczyk-Gryn, and A. Navrotsky, *J. Solid State Chem.*, 227, 150-154 (2015).
- (9) "Thermal Conversion of Scheelite-Type ABO_4 into Perovskite-Type $\text{AB}(\text{O,N})_3$ " W. Li, D. Li, A. Gurlo, S. Zander, P. Jones, A. Navrotsky, Z. Shen, R. Riedel, and E. Ionescu, *Dalt. Trans.*, 44, 8238-8246 (2015).
- (10) "Thermochemistry of Multiferroic Organic-Inorganic Hybrid Perovskites $[(\text{CH}_3)_2\text{NH}_2][\text{M}(\text{HCOO})_3]$ ($M = \text{Mn, Co, Ni and Zn}$)" G. P. Nagabhushana, R. Shivaramaiah, and A. Navrotsky, *J. Amer. Chem. Soc.*, 137, 10351-10356 (2015).
- (11) "Thermochemistry of Perovskites in the Lanthanum-Strontium-Manganese-Iron Oxide System" C. Marinescu, L. Vradman, S. Tanasescu, and A. Navrotsky, *J. Solid State Chem.*, 230, 411-417 (2015).

- (12) “Energetics of Lanthanide Cobalt Perovskites: $\text{LnCoO}_{3-\delta}$ (Ln = La, Nd, Sm, Gd)” S. K. Sahu, S. Tanasescu, B. Scherrer, C. Marinescu, and A. Navrotsky, *J. Mater. Chem. A*, 3, 19490-19496 (2015).

Program Title: Exploring superconductivity at the edge of magnetic or structural instabilities

Principal Investigator: Ni, Ni

Mail: Department of Physics and Astronomy, 475 Portola Plaza, University of California, Los Angeles, 90024, CA

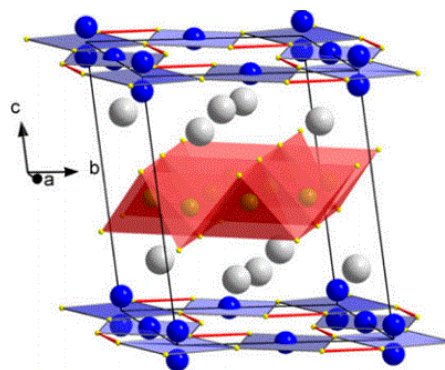
E-mail: nini@physics.ucla.edu

Project Scope:

Modern research of condensed matters devotes in understanding how properties of complex solids are determined by their structural and electronic degrees of freedom. Despite of the complicity in real materials where competing orders often exist, significant progress has been driven by the discovery of new materials with emergent ground states. The recent discovered Fe-based superconductors (FBS), together with the cuprates, are the only two high T_c superconducting families in the world. Although they differ in various ways, both of them are quasi two dimensional materials at the edge of structural/magnetic instabilities. The discovery and characterization of materials of this type can advance our understanding of high T_c superconductivity significantly. The objective of this research is to discover superconductors that lie at the edge of structural/magnetic instability using solid state reaction and crystal-growth methods, and to characterize them and examine their structure-property relations through thermodynamic, transport, X-ray, and neutron measurements.

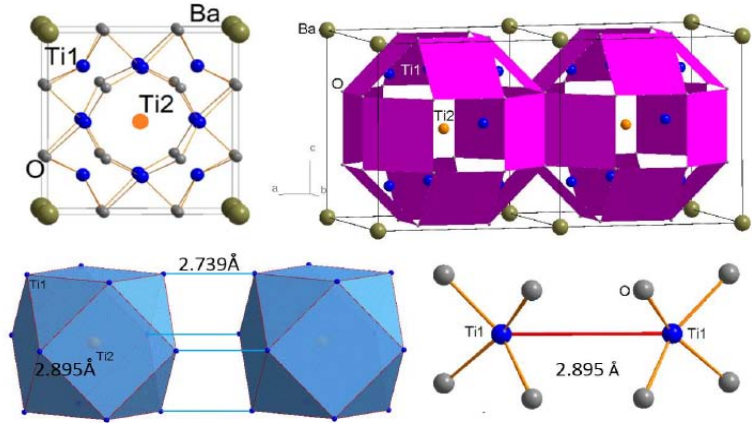
Recent Progress:

1. We have successfully grown and characterized two new series of Fe-based superconductors, the Co and Ni doped 10-3-8 superconducting family using the high temperature flux-growth method. The structural/magnetic phase transitions in the parent compound were suppressed to lower temperature and superconductivity up to 15 K occurs. Single crystal quality has been significantly increased, indicating by a clear specific jump at T_c . The comparison between the two families shows rigid band approximation is applicable here. T_c is relatively lower in Ni doped 10-3-8, may be due to the strong impurity scattering from Ni atoms comparing to Co dopants.
2. We have attempted to grow the $\text{BaTi}_2\text{Bi}_2\text{O}$ single crystals, which has CDW around 200 K and became SC at ~ 10 K when Na is doped. Although we failed in this trial, we discovered a new suboxide, $\text{Ba}_{1+\delta}\text{Ti}_{13-\delta}\text{O}_{12}$ ($\delta = 0.11$) [2]. It is a paramagnetic poor metal with hole carriers dominating the transport. Fermi liquid behavior appears at low temperature. The oxidization state of Ti obtained by the XAS is consistent with the



metallic Ti^{2+} state. Local density approximation band structure calculations reveal the material is near the Van Hove singularity.

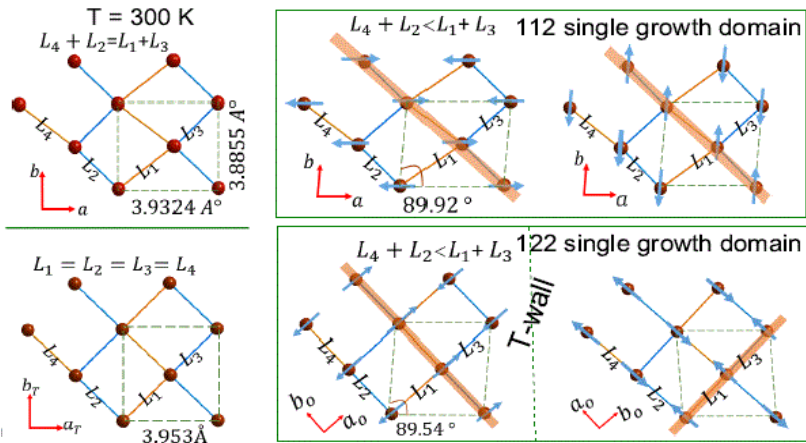
The pseudogap behavior in the Ti-d band and the strong hybridization between the Ti-d and O-p orbitals reflect the characteristics of the building blocks of the Ti_{13} semi-cluster and the TiO_4 quasi-squares, respectively.



- We have successfully grown and characterized high quality single crystals of $Ca_{0.73}La_{0.27}FeAs_2$, the "parent" compound of the 112 superconducting family for the first time using the high temperature flux growth method.

The $Ca_{1-x}La_xFeAs_2$ (CaLa112) Fe pnictide superconductors (FPS) shows the record bulk T_c up to 42 K in nonoxide FPS [1]. The breaking of C_4 rotational symmetry even at room temperature makes it unique among all FPS. The comparison of this CaLa112 with the other FPS will enable us to distill the important information on inducing high T_c . However, until now, no systematic study has been made on this system. Our comprehensive study of $Ca_{0.73}La_{0.27}FeAs_2$ single crystal established it is the parent compound of the CaLa112 FPS with structural/magnetic phase transitions. We unraveled the nature of both phase transitions and found a new stripe type magnetic structure. What's more, by studying $Ca_{0.73}La_{0.27}FeAs_2$, we established that this CaLa112 family is characterized by the

presence of metallic spacer layers and it is intrinsically structurally untwinned. Electronic nematicity has been argued to exist in both cuprate and FPS, which lowers the rotational symmetry but keeps the translational symmetry. It has been argued to be the origin of the



pseudogap in cuprate. In order to study the nematicity in FPS, uniaxial pressure/strain is usually used to detwin the sample. However, the external pressure itself already breaks the rotational symmetry, which has caused lots of debates on the origin of the observed in-plane anisotropy. The naturally detwinned 112 FPS provide a new avenue to examine the electronic nematicity in FPS. In addition, as the first tunable FPS with metallic layers,

this material can also serve as a great platform to study the effect of metallic spacer layers on superconductivity.

The comparison of this material with the prototype 122 FPS is fruitful and revolutionary. The consensus of the Fe based superconductor is that the parent compound of the FPS is a semimetal with equal hole and electron carriers. The fact that the “parent” compound of CaLa112 is the apparently electron overdoped $\text{Ca}_{0.73}\text{La}_{0.27}\text{FeAs}_2$ is intriguing. A closer look into the ARPES data suggests a reasonable Fermi surface nesting exists in this electron-over doped material while the DMFT calculations indicate the Fermi surface nesting is enhanced when it is hole doped. This sheds light on the important role of both Fermi surface nesting and the superexchange interaction in the magnetism in FPS.

4. We have made high quality Cd_3As_2 single crystals using the high temperature solution growth method for high pressure measurements [3]. Our collaboration with the high pressure group find that Cd_3As_2 undergoes a structural phase transition from a metallic tetragonal phase in space group I41/acd to a semiconducting monoclinic phase in space group P21/c at critical pressure 2.57 GPa, together with this structural phase transition, a metallic to semiconducting behavior is observed, indicating a breakdown of this 3D Dirac semimetal.
5. We have grown high quality $(\text{Ca}_{1-x}\text{La}_x)_{10}(\text{Pt}_3\text{As}_8)(\text{Fe}_2\text{As}_2)_5$ single crystals using the high temperature solution growth method to study the doping-dependent superconducting gap structure by measuring the in-plane London penetration depth [4]. The gap is isotropic close to the optimal doping,—a trend commonly found in charge-doped FeSCs. While there is no evidence for the static microscopic coexistence of superconductivity and magnetism in the underdoped regime in this compound, the gap anisotropy increases dramatically in the underdoped regime which may suggest a possibility of either dynamic or much finer scale coexisting superconductivity and short-range magnetic correlations.

Future Plans:

1. The double doping study of $\text{Ba}(\text{Fe}_{1-x}\text{Co}_x)_2(\text{As}_{1-y}\text{P}_y)_2$. We will use Ba_2As_3 flux to grow single crystals of this kind to explore the quantum criticality of in this system. Transport and thermodynamic measurements will be performed.
2. The recent discovery of increased T_c in KFe_2As_2 under high pressure up to 20 Gpa has been argued to be due to the enhanced superconducting pairing in collapsed tetragonal FeAs phase. On the other hand, the collapsed tetragonal phase has been believed and proved to be harmful for spin fluctuation and thus superconductivity in CaFe_2As_2 . Therefore, it is important to clarify the relation between superconductivity in collapsed tetragonal phase. The $\text{Na}_{1-x}\text{La}_x\text{Fe}_2\text{As}_2$ system has the potential to be a chemical-doping analog of the pressure-induced KFe_2As_2 . We will grew single crystals and do systematic study of this series.
3. It has been a long-time debate if the magnetism in FBS is localized or itinerant. Recent study on the $\text{Na}(\text{Fe}_{1-x}\text{Cu}_x)\text{As}$ shows a Mott insulator phase at $x=0.5$ doping, providing strong evidence that FBS is near to Mott phase. We would like to investigate if this is in general for all FBS or just specific for NaFeAs system. We plan to study Cu doped 1038 to and use elastic neutrons scattering to study the possible magnetism inside.

4. The interplay between SC and magnetism in collapsed tetragonal phase in double doped CaFe_2As_2 . CaFe_2As_2 is special in 122 because of the existence of collapsed tetragonal phase in it when chemical doping/pressure is applied, which is believed to be unfavorable for spin fluctuation and thus superconductivity. On the other hand, rare earth doped Ca122 shows trace superconductivity up to 45 K. We plan to use double doping trials to avoid the collapsed tetragonal phase and induced bulk superconductivity up to a record temperature.

References since 2014 which acknowledge DOE support:

1. Shan Jiang, Chang Liu, Huibo Cao, Turan Birol, Jared M. Allred, Wei Tian, Lian Liu, Kyuil Cho, Matthew M. Krogstad, Jie Ma, Keith Taddei, Makariy A. Tanatar, Ruslan Prozorov, Stephan Rosenkranz, Yasutomo J. Uemura, Gabriel Kotliar, Ni Ni, Naturally structurally detwinned Fe pnictide superconducting family with metallic spacer layers, in review (2015) arxiv 1505:05881
2. Costel R. Rotundu, Shan Jiang, Xiaoyu Deng, Yiting Qian, Saeed Khan, David G. Hawthorn, Gabriel Kotliar and Ni Ni Physical properties and electronic structure of a new barium titanate suboxide $\text{Ba}_{1+\delta}\text{Ti}_{13-\delta}\text{O}_{12}$ ($\delta = 0.11$), *APL Mat.* **3**, 041517 (2015)
3. Shan Zhang, Qi Wu, Leslie Schoop, Mazhar N. Ali, Youguo Shi, Ni Ni, Quinn Gibson, Vladimir Sidorov, Jing Guo, Yazhou Zhou, Peiwen Gao, Dachun Gu, Chao Zhang, Sheng Jiang, Ke Yang, Aiguo Li, Yanchun Li, Xiaodong Li, Jing Liu, Xi Dai, Zhong Fang, Robert J. Cava, Liling Sun, Zhongxian Zhao, Breakdown of Three-dimensional Dirac Semimetal State in pressurized Cd_3As_2 , *PHYSICAL REVIEW B* **91**, 165133 (2015)
4. K Cho, M A Tanatar, N Ni and R Prozorov, Doping-evolution of the superconducting gap in single crystals of $(\text{Ca}_{1-x}\text{La}_x)_{10}(\text{Pt}_3\text{As}_8)(\text{Fe}_2\text{As}_2)_5$ superconductor from London penetration depth measurements, *Supercond. Sci. Technol.* **27** 104006 (2014)

A Fundamental Study of Inorganic Clathrates and other Open-Framework Materials

George S. Nolas

Department of Physics, University of South Florida, Tampa, FL 33620

Program Scope

Inorganic clathrates exhibits a wide range of physical properties that can be tuned, or completely altered, with chemical composition. Relatively few compositions have however been investigated due to the formidable synthetic challenges in synthesizing most compositions. We have developed different synthetic techniques to overcome the serendipitous advances that traditional synthetic approaches allow and obtain targeted thermodynamically metastable compositions. Among the new synthetic approaches developed under this program spark plasma sintering (SPS) is unique in that a pulsed DC current is applied to the material directly while under uniaxial pressure. Our laboratory is one of only a few world-wide that is synthesizing materials, in microcrystalline as well as single-crystal form, by SPS. Together with our recently developed kinetically controlled thermal decomposition (KCTD) technique, we are able to synthesize new clathrate compositions, many for the first time. These techniques can also be employed for the synthesis and crystal growth of other intermetallic or metastable ternary and quaternary compounds.

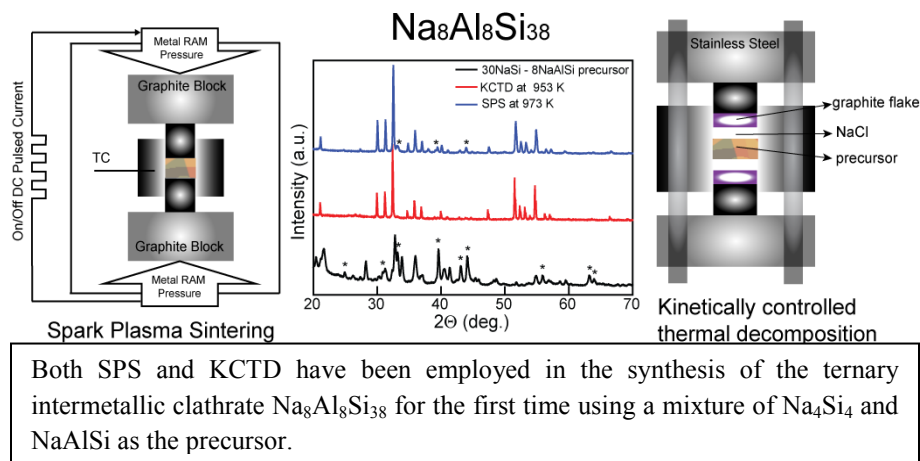
Recent Progress

Our novel synthetic techniques have been employed in processing new multinary clathrate compositions that have until now not been obtained, and allowed for the investigation of their physical properties. Examples of recent progress include:

- (i) Expanded the SPS and KCTD synthetic techniques to ternary and quaternary clathrate compounds as well as other open-framework materials.
- (ii) The development of a new processing approach whereby ternary clathrate-II $A_8Na_{16}Si_{136}$ ($A = K, Rb, Cs$) single crystals were obtained by SPS via ion-exchange and electrochemical redox reactions between $NaSi$ and $AlCl$.
- (iii) Expanding on (ii) in selectively synthesizing clathrate-I and -II compositions by changing the SPS reaction conditions. In addition, the synthesis of clathrate-I $K_{4.2}Na_{3.8}Si_{46}$ was achieved for the first time, and in single-crystal form, by this new multi-precursor approach.

Future Plans

We will expand on our KCTD and SPS techniques while continuing our investigation of new clathrate compounds. The new approach whereby more than one precursor is used, along with ion-exchange reactions during processing, will allow for the processing of new compositions. In



addition, Sn clathrate-II compositions that are of interest for thermoelectrics applications will be synthesized and their structural and transport properties investigated.

Publications (2014 & 2015)

1. Y. Dong and G. S. Nolas, 'Crystal Growth through Field-Assisted Electrochemical Redox and Ion-Exchange Reactions: A Case Study of $K_{4.2}Na_{3.8}Si_{46}$ Clathrate-I', *Cryst. Growth Des.* DOI: 10.1021/acs.cgd.5b00329 (2015).
2. Y. Dong, P. Chai, M. Beekman, X. Zeng, T.M. Tritt and G. S. Nolas, 'Precursor Routes to Complex Ternary Intermetallics: Single-Crystal and Microcrystalline Preparation of Clathrate-I $Na_8Al_8Si_{38}$ from $NaSi + NaAlSi$ ', *Inorg. Chem.* 54, 5316 (2015).
3. Y. Dong, A.R. Khabibullin, K. Wei, J.R. Salvador, G.S. Nolas, and L.M. Woods, Bournonite $PbCuSbS_3$: Stereochemically Active Lone-Pair Electrons that Induce Low Thermal Conductivity', *ChemPhysChem*, DOI: 10.1002/cphc.201500476 (2015).
4. L. Krishna, P. Chai, C. A. Koh, E. S. Toberer, and G. S. Nolas, 'Synthesis and structural properties of type I potassium SiGe alloy clathrates', *Mater. Lett.* 149, 123 (2015).
5. Y. Dong and G. S. Nolas, 'Rapid Crystal Growth of Type-II Clathrates $A_8Na_{16}Si_{136}$ ($A = K, Rb, Cs$) by Spark Plasma Sintering', *Cryst. Eng. Comm.* 17, 2242 (2015).
6. Z. Ge, K. Wei, H. Lewis, J. Martin, and G. S. Nolas, 'Bottom-up processing and low temperature transport properties of polycrystalline SnSe', *J. Solid State Chem.* 225, 354 (2015).
7. A. Biswas, S. Chandra, S. Stefanoski, J. S. Blazquez, J. J. Ipus, A. Conde, M. H. Phan, V. Franco, G. S. Nolas, and H. Srikanth, 'Enhanced cryogenic magnetocaloric effect in $Eu_8Ga_{16}Ge_{30}$ clathrate nanocrystals', *J. Appl. Phys.* 117, 033903 (2015).
8. G.S. Nolas, editor, *The Physics and Chemistry of Inorganic Clathrates*, Springer Series on Materials Volume 199, 2014.
9. H. J. Jakobsen, H. Bildsøe, M. Beekman, S. Stefanoski, G. S. Nolas, and C. R. Bowers, 'Low-Temperature ^{23}Na MAS NMR Reveals Dynamic Effects and Compositions for the Large and Small Channels in the Zeolite-Like Ge-Framework of $Na_{1-x}Ge_{3+z}$ Materials', *J. Phys. Chem.* 118, 28890 (2014).
10. K. Wei, J. Martin, and G. S. Nolas, 'Synthesis, SPS processing and low temperature transport properties of polycrystalline $FeSb_2$ with nano-scale grains', *Mater. Lett.* 122, 289 (2014).

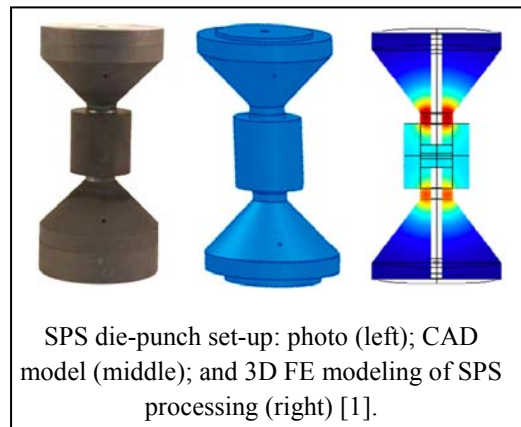
FUNDAMENTALS OF SPARK-PLASMA SINTERING: MATERIALS PROCESSING FOR ENERGY APPLICATIONS

PI: Eugene A. Olevsky, San Diego State University, Award No. DE-SC0008581

Program Scope

The fundamental aspects of this research program are focused on the development of the theory of spark-plasma sintering (SPS) of powder components. SPS is a rapidly emerging powder consolidation technique capable of producing highly dense materials with a significant potential for grain size retention. SPS is based on the conjoint application of fast heating rates, high axial pressure and field (electric current - based) assisted sintering. Potentially, SPS has many significant advantages over the conventional powder processing methods, including the lower process temperature, the shorter holding time, dramatically improved properties of sintered products, low manufacturing costs, and environmental friendliness. Practical implementations of the SPS' bright potential, however, are limited by the lack of theoretical concepts enabling the process predictiveness and optimization.

This project's fundamental research activities are aimed at the determination of the SPS dominant driving forces, contributing to the formulation of the general theory of spark-plasma sintering. Thereby the project specifically addresses the following issues: (i) modeling of the heat transfer during SPS of powder materials; influence of the heating rate on the consolidation and grain structure evolution; analysis of the impact of the thermal runaway effect on the "flash" sintering phenomenon; (ii) experimental de-convolution of the thermal and non-thermal phenomena occurring during SPS; (iii) coupled densification – grain growth – electromagnetic field – temperature distribution modeling at micro- and macroscopic levels; (iv) optimized (based on the developed model and experimental concepts) low-pressure SPS and free pressureless SPS processing and characterization of novel functionally structured porous nuclear fuel materials enabling the damage-free fission product escape.



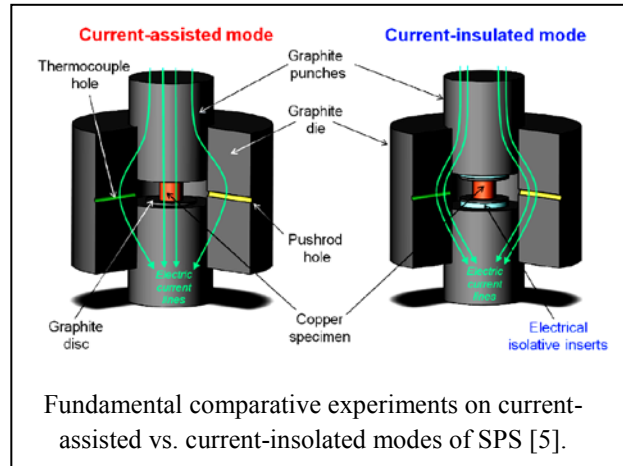
SPS die-punch set-up: photo (left); CAD model (middle); and 3D FE modeling of SPS processing (right) [1].

The collaborative component of the proposed program involves interactions between SDSU and General Atomics - one of the world's leading resources for the high-technology systems development. The developed concepts are implemented in a novel modeling framework describing spark-plasma sintering for the optimization of the fabrication of functional porous structures of nuclear fuel for modular multiplier reactors. The porous structure is an essential element of the design of novel nuclear fuel pellets enabling fission product evolution. Thereby, the main applied aspects of the project are concerned with exploring the previously non-

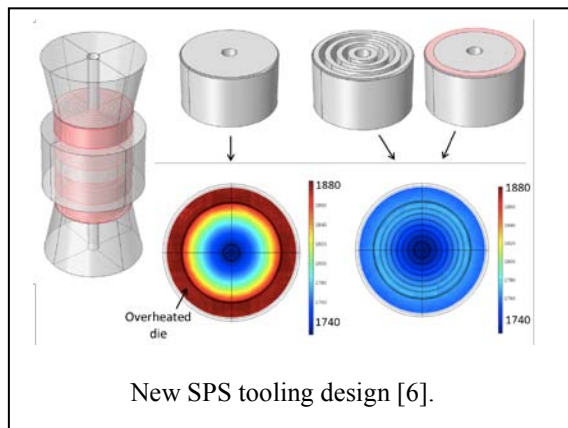
investigated applications of spark-plasma sintering to the fabrication of structurally strong porous materials, which are of great interest for nuclear fuel and other energy-related applications [2-4].

Recent Progress

The PI's recently conducted research indicates that the understanding of the material constitutive behavior during SPS is impossible without the analyses of mechanical consolidation, heat transfer and electric field-induced phenomena at multiple scale levels. The project introduces important mechanisms of both thermal and non-thermal nature in a novel generic micro-macro modeling framework for the description of spark-plasma sintering. The modeling activities are supported by unique experiments on the de-convolution of the heating rate - driven and electromagnetic field - imposed effects at various scale levels. The developed new constitutive models of SPS and the interconnected codes at different analysis scales should ultimately lead to the creation of the generic multi-scale framework for modeling of spark-plasma sintering.



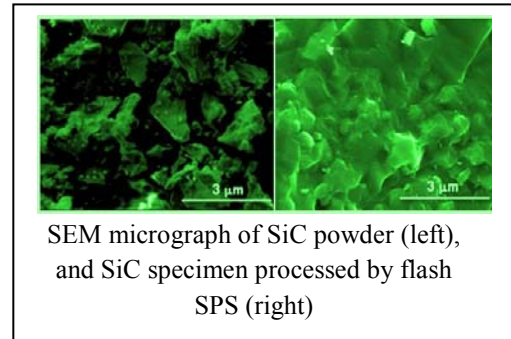
Based on the developed modeling framework, a novel tooling design, consisting in the



tailored drilling of axial cylindrical or ring-shaped holes within the punch, has been recently individuated and optimized through a campaign of fully coupled thermal, electrical and mechanical finite element simulations. The analysis of the numerical results, experimentally assessed, allows for a comprehensive understanding of the phenomena underlying radial temperature distributions in SPS and leads to the individuation of a technological solution for the uniformization of temperature distribution.

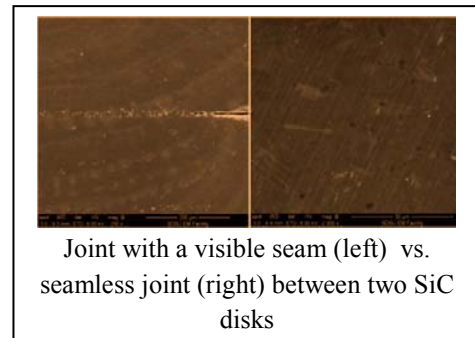
In addition, during the progress of the conducted project, new, exciting capabilities of SPS have been revealed, including the new potentially transformative Flash Hot Pressing (Flash SPS) approach, as well as the possibility of the SPS usage for seamless joining of ceramic and metallic materials.

Recent investigations conducted at SDSU showed that the consolidation efficiency can be dramatically further improved by enabling an ultra-rapid “flash” regime of processing, when super-hard powder materials can be consolidated in a matter of few seconds. The idea of the “flash SPS” is based upon the idea of recently explored “flash sintering, however, it does not require the usage of higher voltage ranges, employed by “flash sintering” setups (and, therefore, not achievable in the industrially produced SPS devices.) Hence, flash SPS can be conducted in regular SPS devices. Flash SPS utilizes the theoretical idea of the thermal-runaway-based origin of the flash sintering phenomenon. As opposed to flash sintering, which should generally render uncontrollable clustered area heating of the processed specimen and therefore lead to highly spatially non-uniform distribution of temperature, density and of microstructure parameters, Flash SPS explores the possibility of the pressure-controlled thermal runaway, under which the mass transport driven by externally applied pressure should equalize the distribution of temperature and stabilize the process of consolidation. In contrast to flash sintering, which should have drastic scalability problems, Flash SPS has a potential of being employed for large scale specimens, where the uniformity of relative density and grain size is of great importance.



SEM micrograph of SiC powder (left), and SiC specimen processed by flash SPS (right)

At SDSU, we have recently demonstrated the potential of SPS to produce practically seamless joints between SiC components without using any filler material. Both the localized and rapid heating contributed to the inherent energy saving of electric current assisted joining technique. Our preliminary results already showed that especially by rightly adjusting electric current, applied pressure and heating time, almost perfect joint within seconds can be obtained so that the heat-affected zone can be markedly reduced.



Joint with a visible seam (left) vs. seamless joint (right) between two SiC disks

Future Plans

The outcomes of the carried out work indicate the global nature of the targeted scientific problems. The achievement of the ultimate goal of the formulation of the general theory of spark plasma sintering requires the continuation of the initiated research in a systematic way identifying the contributions of all the thermal and non-thermal factors in the enhancement of mass transport under SPS processing conditions. Indeed, at the previous project stage, the emphasis has been made on the thermal factors acting during spark-plasma sintering and their de-convolution from the field-assisted phenomena. The impact of the electric current on the specifics of SPS, while being clearly confirmed by the fundamental comparative (“current-assisted” vs. “current-insolated”) experiments, has not been incorporated in the constitutive

model of SPS. The SPS-specific non-thermal factors are related to the direct impact of electromagnetic field on the diffusion mass transport through electromigration, electroplasticity mechanisms, and dielectric breakdown of oxide films at grain boundaries.

These new developments and the need for a physically consistent modeling framework lend impetus to the continuation of the research on the fundamentals of spark-plasma sintering.

During the next stage of the project, the modeling and fundamental experimental efforts will be essential at multiple scale levels including the detailed meso-scale description of the electric current-affected pore-grain structure evolution coupled with a macro-scale reliable assessment of the processing of real-world macroscopic components. The main fundamental issues that will be addressed in the proposed program are: what is the contribution of the “non-thermal field effect” involved during SPS? How is the microstructure developed during current-affected processing? What is the physical basis of the ultra-rapid consolidation/joining? The developed constitutive concepts will be implemented in a novel multi-scale modeling framework describing spark-plasma sintering. The main applied aspects of the renewal proposal will be concerned with exploring the novel technologies of Flash SPS and SPS joining.

Thus, the planned future activities include the analysis of the SPS physical basis at multiple scales specifically exploring the role of electric current in the acceleration of mass transport and with an emphasis on ultra-rapid materials consolidation and joining.

References

1. D. Giuntini, E. A. Olevsky, C. Garcia-Cardona, A. L. Maximenko, M. S. Yurlova, C.D. Haines, D. G. Martin, and D. Kapoor, Localized Overheating Phenomena and Optimization of Spark-Plasma Sintering Tooling Design, *Materials*, 6, 2612-2632 (2013)
2. W. Li, E.A. Olevsky, O.L. Khasanov, C.A. Back, O. Izhvanov, J. Opperman, H.E. Khalifa, Spark plasma sintering of agglomerated vanadium carbide powder, *Ceram. Int.*, 41, 3748-3759 (2015)
3. G. Lee, M.S. Yurlova, D. Giuntini, E.G. Grigoryev, O.L. Khasanov, O. Izhvanov, C. Back, J. McKittrick, E.A. Olevsky, Densification of zirconium nitride by spark plasma sintering and high voltage electric discharge consolidation: a comparative analysis, *Ceram. Int.*, 41, 14973-14987 (2015)
4. X. Wei, C. Back, O. Izhvanov, C. Haines, O.L. Khasanov, E. A. Olevsky, Spark plasma sintering of commercial zirconium carbide powder: Densification behavior and mechanical properties, *Materials*, 8, 6043-6061 (2015)
5. E.V. Aleksandrova, A.M. Ilyina, E.G. Grigoryev, E.A. Olevsky, Contribution of electric current into densification kinetics during spark-plasma sintering of conductive powder, *J. Amer. Ceram. Soc.*, DOI: 10.1111/jace.13816 (2015)
6. D. Giuntini, J. Raethel, M. Herrmann, A. Michaelis, E.A. Olevsky, Advancement of tooling for spark-plasma sintering, *J. Amer. Ceram. Soc.*, DOI: 10.1111/jace.13621 (2015)

Publications

Refereed Journal Papers

1. E.V. Aleksandrova, A.M. Ilyina, E.G. Grigoryev, E.A. Olevsky, Contribution of electric current into densification kinetics during spark-plasma sintering of conductive powder, *J. Amer. Ceram. Soc.*, DOI: 10.1111/jace.13816 (2015)
2. D. Giuntini, J. Raethel, M. Herrmann, A. Michaelis, E.A. Olevsky, Advancement of tooling for spark-plasma sintering, *J. Amer. Ceram. Soc.*, DOI: 10.1111/jace.13621 (2015)
3. W. Li, E.A. Olevsky, O.L. Khasanov, C.A. Back, O. Izhvanov, J. Opperman, H.E. Khalifa, Spark plasma sintering of agglomerated vanadium carbide powder, *Ceram. Int.*, 41, 3748-3759 (2015)
4. X. Wei, D. Giuntini, A.L. Maximenko, E.A. Olevsky, Electric Contact Resistance in Spark Plasma Sintering Tooling Setup, *J. Amer. Ceram. Soc.*, DOI: 10.1111/jace.13621 (2015)
5. G. Lee, M.S. Yurlova, D. Giuntini, E.G. Grigoryev, O.L. Khasanov, O. Izhvanov, C. Back, J. McKittrick, E.A. Olevsky, Densification of zirconium nitride by spark plasma sintering and high voltage electric discharge consolidation: a comparative analysis, *Ceram. Int.*, 41, 14973-14987 (2015)
6. X. Wei, C. Back, O. Izhvanov, C. Haines, O.L. Khasanov, E. A. Olevsky, Spark plasma sintering of commercial zirconium carbide powder: Densification behavior and mechanical properties, *Materials*, 8, 6043-6061 (2015)
7. J. Alvarado-Contreras, A.L. Maximenko, E.A. Olevsky, Multi-scale modeling of consolidation of agglomerated nano-powders, *Acta Mater.* (2015) – *submitted*
8. I. Bogachev, I. Chernov, E. Grigoryev, M. Staltsov, O.L. Khasanov, E. Olevsky, Effect of Y₂O₃ on densification kinetics of 13Cr-2Mo ferritic/martensitic steel during spark plasma sintering, *JOM* (2015) – *submitted*
9. D. Giuntini, Jan Raethel, M. Herrmann, A. Michaelis, C. Haines, E.A. Olevsky, spark plasma sintering novel tooling design: Temperature uniformization during consolidation of silicon nitride powder, *J. Ceram. Soc. Jap.* (2015) – *submitted*
10. I. Bogachev, A. Yudin, E. Grigoryev, I. Chernov, M. Staltsov, O.L. Khasanov, E. Olevsky, Microstructure investigation of 13Cr-2Mo ods steel components obtained by high voltage electric discharge compaction technique, *Materials* (2015) - *submitted*
11. I. Bogachev, E. Grigoryev, O.L. Khasanov, and E. Olevsky, Fabrication of 13Cr-2Mo Ferritic/Martensitic Oxide-Dispersion-Strengthened Steel Components by Mechanical Alloying and Spark-Plasma Sintering, *JOM*, 66, 1020-1026 (2014)
12. J. Milligan, P. Hendrickx, M.M. Tünçay, E.A. Olevsky, M. Brochu, Modeling residual porosity in thick components consolidated by spark plasma sintering, *Scripta Mater.*, 76, 53-56 (2014)
13. M.S. Yurlova, E.V. Krikun, A.N. Novoselov, Y-S. Lin, O.N. Sizonenko, E.G. Grigoryev, O.L. Khasanov, E.A. Olevsky, Field-assisted powder synthesis and consolidation of Fe-Ti metal matrix composites, *Adv. Eng. Mater.*, 16, 785-791 (2014)

14. E.G. Grigoryev, L.Y. Lebedeva, O.L. Khasanov, E.A. Olevsky, Structure of Zirconium alloy powder coatings processed by high voltage electric discharge consolidation, *Adv. Eng. Mater.*, 16 (6), 792-796 (2014)

Patent Application

- D. Giuntini, E. Olevsky, J. Raethel, M. Herrmann, Process stabilizing tooling for spark plasma sintering, U.S. Provisional Patent Application 62/086,694 (2015)

Conference Proceedings

1. X. Wei, E. Olevsky, O. Izhevskiy, C. Back, Spark plasma sintering of zirconium carbide powders: densification kinetics and mechanical properties, *Adv. Powder Partic. Mater.* (2015) - *accepted*
2. E. Olevsky, Flash spark-plasma sintering of powder carbides, *Adv. Powder Partic. Mater.* (2015) – *accepted*
3. G. Lee, M.S. Yurlova, E.G. Grigoryev, J. McKittrick, E.A. Olevsky, Comparative study of spark plasma sintering and high voltage electric discharge consolidation of zirconium nitride powder, *Adv. Powder Partic. Mater.* (2015) – *accepted*
4. D. Giuntini, J. Raethel, M. Herrmann, E. A. Olevsky, Optimization of spark plasma sintering tooling design, *Adv. Powder Partic. Mater.* (2015) – *accepted*
5. E. A. Olevsky, A. M. Ilyina, E. V. Aleksandrova, E. G. Grigoryev, Electric current effect on spark plasma sinter-forging of conductive materials, *Proc. PM2014 World Congress on Powder Met. Partic. Mater.*, Orlando, pp. 1526-1529, NJ, Princeton (2014)
6. Lee, G., Olevsky, E., & McKittrick, J., Field-assisted consolidation of zirconium nitride powder, *Proc. PM2014 World Congress on Powder Met. Partic. Mater.*, Orlando, pp. 1522-1525, NJ, Princeton (2014)

Plasmonic Metasurfaces for the Directional Control of Light Emission and Photodetection

R. Paiella* and T. D. Moustakas

Dept. of Electrical Engineering and Photonics Center, Boston University, Boston, MA 02215

** Phone: 617-353-8883, Fax: 617-353-1283, Email: rpaiella@bu.edu*

Program Scope

This program is focused on the development of novel plasmonic nanostructures designed to engineer the radiation and absorption properties of semiconductor photonic materials. Our key building blocks are metallic nanoparticles (NPs) fabricated by top-down lithographic techniques, acting as geometrically tunable optical antennas. These NPs can dramatically increase the spontaneous emission rate of an underlying active material, through the near-field excitation and subsequent radiative decay of their plasmonic resonances (i.e., collective oscillations of the NP electron gas). Under these conditions, the far-field radiation pattern of the emitted light can be tailored with remarkable flexibility by controlling the NP size, shape, and spatial distribution. By reciprocity, if the same nanostructures are fabricated on an absorbing material, they can be used to enhance the absorption strength and control it as a function of direction and polarization of the incident light. The study of these phenomena can shed new light on the unique optical properties of metallic nanostructures, while at the same time open the way to new device concepts and applications in optoelectronics.

Additional activities in this program are aimed at the development of a semiconductor materials platform that can optimally enable the investigation of such plasmonic interactions, i.e., InGaN quantum dots with composition across the entire alloy range. These materials are ideally suited to the proposed studies, because of their widely tunable bandgap energies across the visible spectrum (where the plasmonic resonances of typical metallic nanostructures occur) and favorable near-surface radiative properties. Furthermore, they are technologically significant for a wide range of applications, including solid-state lighting and photovoltaics, which could benefit strongly from the same plasmonic interactions. Our recent progress in this materials development effort is summarized in a separate abstract.

Recent Progress

Recent activities have focused on the design of complex NP arrays for the directional control of light emission and photodetection. Our main achievements, summarized in the following, include (1) the theoretical investigation of radiation processes in the near-field vicinity of gradient metasurfaces, and (2) the initial experimental demonstration of plasmon-assisted directional photodetection.

(1) LIGHT EMISSION NEAR A GRADIENT METASURFACE

Gradient metasurfaces (GMSs) have recently emerged from extensive research in nanophotonics as a powerful tool for the control of externally incident optical waveforms [1]. Their basic

geometry consists of a planar array of optical nanoantennas with sub-wavelength separation and spatially varying size, shape, and/or orientation, designed to introduce a linearly graded phase shift in the light reflected from and/or transmitted through the array. In recent years, GMSs have been used to demonstrate several remarkable functionalities, including anomalous reflection and refraction, light focusing in ultrathin lenses, and the generation of optical vortices [1].

In all of these prior efforts, the surface was illuminated with externally incident light having fixed wavevector and polarization. However, the unique properties of GMSs also appear to be ideally suited to the near-field control of radiation processes. In our recent work, this idea has been explored theoretically and then substantiated with rigorous full-wave simulations [2]. To describe the most general possible situation, we consider the homogenized continuum model shown in Fig. 1(a), which can be applied to any (reflective) GMS, regardless of the detailed implementation of the nanoantenna array. The light source is provided by a simple electric dipole, as appropriate to the description of spontaneous emission in typical luminescent media.

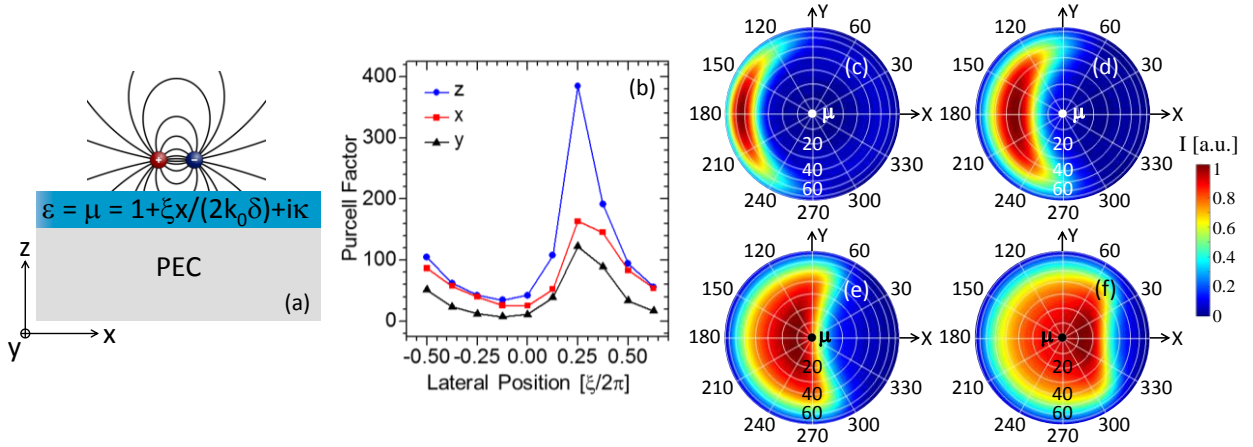


Fig. 1. (a) Schematic cross-sectional view of the system under study. The GMS is modeled with a perfect electric conductor (PEC) coated with an ultrathin metamaterial slab having position dependent permittivity ϵ and permeability μ , designed to produce a linear gradient $\xi \hat{\mathbf{x}}$ in the reflection phase shift. (b) Purcell enhancement factor of a dipole oriented along the x , y , and z directions [as defined in (a)] versus dipole lateral position along x . The Purcell factor is defined as $F_p = \Gamma_{sp}/\Gamma_{sp}^0$, where Γ_{sp} and Γ_{sp}^0 are the dipole spontaneous emission rates near the GMS and in free space, respectively. (c)-(f) Far-field radiation patterns (i.e., optical intensity I versus emission angles) produced by a z -oriented dipole for $\xi/k_0 = 0.2$ (c), 0.6 (d), 1.0 (e), and 1.4 (f). Here k_0 is the free-space wavenumber. In each plot, the radial distance from the origin corresponds to the polar angle, while the direction on the circle corresponds to the azimuthal angle. Each color map is normalized to its peak value.

Our results show that the dipole radiation output is dramatically affected by the nearby GMS, in several important and unusual ways. First, the spontaneous emission decay can be strongly accelerated, by an amount that depends on the dipole lateral position in an oscillatory fashion [Fig. 1(b)]. Second, highly asymmetric directional radiation patterns can be produced with broad geometrical tunability of the angle of peak emission [Figs. 1(c)-1(f)]. Furthermore, the total output radiation power can be increased in the case of low-efficiency emitters, or quenched in favor of asymmetric surface-wave excitation depending on the GMS phase gradient.

Importantly, these phenomena could not be explained simply in terms of anomalous reflection of externally incident dipole radiation by the GMS. Instead, they highlight a unique near-field behavior of GMSs, related to a strong coupling between evanescent and propagating waves enabled by the GMS phase gradient. In addition, these results suggest a novel approach to control the output of radiation processes directly at the source level, without the need for any external optics. This ability has significant technological potential for future applications involving, e.g., nanoscale and high-speed light emitting devices, photonic integrated circuits, and highly multiplexed fluorescence sensors.

(2) PLASMON-ASSISTED DIRECTIONAL PHOTODETECTION

During prior work in this project, we have demonstrated the use of plasmonic NP arrays to produce geometrically tunable unidirectional light emission [3]. As shown in Figs. 2(a) and 2(b), the basic device geometry developed in this work consists of a semiconductor active layer coated with an ultrathin metal film supporting a periodic array of metallic NPs. In this geometry, light emission occurs via a two-step process, where surface plasmon polaritons are first excited on the metal film by the active layer and then scattered into radiation by the NPs. The far-field pattern of the emitted light can then be engineered by controlling the NP size, shape, and periodicity. With this approach, we have demonstrated the generation of highly collimated optical beams, emerging from the sample surface along a single direction determined by the array design.

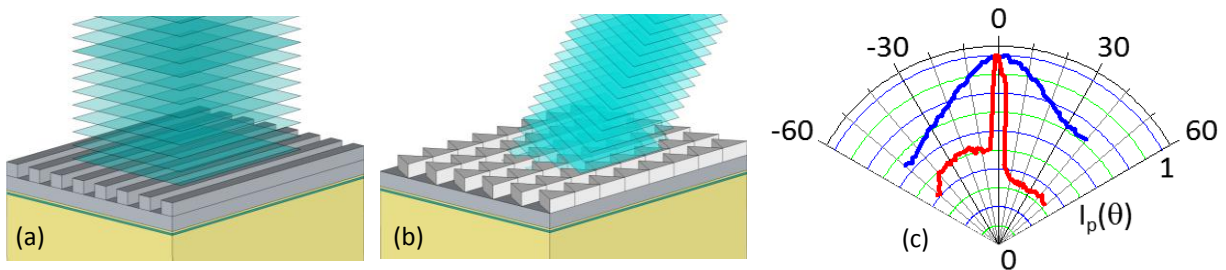


Fig. 1. Plasmonic nanostructures designed to produce unidirectional light emission/absorption (a) along the sample surface normal, and (b) along a single geometrically tunable oblique direction. (c) Red trace: photocurrent I_p of a device based on the design of (a) versus angle of incidence θ of the detected light. Blue trace: photocurrent pattern of a similar device without any NP array. Both photocurrent patterns have been normalized to unit peak value.

By reciprocity, if similar nanostructures are fabricated on an absorbing layer, only light incident along a single geometrically tunable direction would be absorbed. In order to investigate this novel phenomenon, recently we have developed suitable samples where the NP arrays are fabricated between the electrodes of standard photoconductive devices. The red trace in the polar plot of Fig. 2(c) is the photocurrent of such a sample based on the design of Fig. 2(a), measured as a function of the angle of incidence of the incoming light. Highly directional photodetection along the sample surface normal is clearly observed. By comparison, a much broader pattern is obtained if no NP arrays are employed, as shown by the blue trace in Fig. 2(c).

We are currently in the process of fabricating similar samples based on the triangular NPs

of Fig. 2(b), to demonstrate directional photodetection along arbitrary off-axis angles. It should be noted that these devices are functionally analogous to the individual elements (ommatidia) of compound eyes, which represent the most prevalent vision modality in nature. Therefore, this research may lead to development of image sensors with the unique attributes of compound-eye vision (including large fields of view, nearly infinite depth of focus, and high acuity to motion), but in a flat ultrathin package. The same nanostructures may also find important applications in the areas of solid-state smart lighting and photovoltaics.

Future Plans

Both research thrusts above will be continued going forward. Specifically, we are now setting up an experimental effort to investigate the unique properties of GMSs for the control of light emission in their near-field zone, as predicted by our recent simulations. Furthermore, we will continue our current work towards the full demonstration of the “plasmonic ommatidia” just described. Finally, these and similar nanostructures designed for the plasmonic control of radiation and absorption processes will be integrated with the InGaN quantum-dot samples that are also under development within this program.

References

- [1] For a review, see N. Yu and F. Capasso, “Flat optics with designer metasurfaces,” Nature Mater. 13, 139 (2014).
- [2] L. C. Kogos and R. Paiella, “Light emission near a gradient metasurface,” submitted.
- [3] J. DiMaria, E. Dimakis, T. D. Moustakas, and R. Paiella, “Plasmonic off-axis unidirectional beaming of quantum-well luminescence,” Appl. Phys. Lett. 103, 251108 (2013).

Publications

- J. DiMaria, E. Dimakis, T. D. Moustakas, and R. Paiella, “Plasmonic off-axis unidirectional beaming of quantum-well luminescence,” Appl. Phys. Lett. 103, 251108 (2013).
- W. Pan, E. Dimakis, G. T. Wang, T. D. Moustakas, and D. C. Tsui, “Two-dimensional electron gas in monolayer InN quantum wells,” Appl. Phys. Lett. 105, 213503 (2014).
- R. Paiella, “Plasmonic control of quantum-well luminescence for enhanced efficiency and beam shaping,” 35th Progress in Electromagnetics Research Symposium (PIERS), Guangzhou (China), 2014 (**Invited Talk**).
- T. D. Moustakas, “Fundamental differences between cubic III-V compounds and wurtzite nitride semiconductors produced by molecular beam epitaxy,” 18th International Conference on Molecular Beam Epitaxy, Flagstaff (Arizona), 2014 (**Plenary Talk**).
- J. DiMaria, E. Dimakis, T. D. Moustakas, and R. Paiella, “Plasmonic collimation and beaming from LED active materials,” IEEE Conference on Lasers and Electro-Optics, paper CF2E.2, San Jose (CA), 2013.

J.H. Perepezko
University of Wisconsin-Madison
Department of Materials Science and Engineering
1509 University Ave. Madison, WI 53706

Program Scope

The development of ceramics that provide a robust performance in an aggressive high temperature environment is a continuing challenge. Materials for high temperature environments must satisfy several stringent requirements that dictate a high melting temperature and stability in an oxidizing environment that often contains water vapor as well as other compatibility issues. The available ceramics such as zirconates, sialons, diborides or carbides satisfy some of the requirements such as high melting temperature, but they also exhibit limitations such as a high oxidation rate or surface decomposition especially in the presence of water vapor

What is needed for enhanced high temperature capability are new oxide materials. From the existing experience we are pursuing a new strategy that involves internal modification control of the outer surface to promote enhanced oxidation resistance. The internal modification focuses upon the development of a new oxide type based upon $\text{Hf}_6\text{Ta}_2\text{O}_{17}$ (HfTaO superstructure) and $\text{Zr}_6\text{Ta}_2\text{O}_{17}$ superstructures which lowers the oxidation rate. The oxide superstructures are metastable in the binary Hf-O and Zr-O systems, but experiments confirm that they can be stabilized by Ta additions.

The research focus is on a systematic fundamental study of the phase stability, defect structure and reaction kinetics of the oxide superstructures. The program also includes an investigation of the oxide superstructures constitution, the development of a microstructure based kinetics model for the oxidation behavior of multicomponent composites and an evaluation of the thermal barrier characteristics.

Recent Progress

1. Oxidation synthesis of HfTaO superstructure from Hf-Ta alloy.

The HfTaO superstructures can be synthesized via direct oxidation of Hf-Ta binary alloys with certain compositions (Fig. 1). The XRD investigation of the oxidation products shows that the direct oxidation of Hf-26.7Ta (atomic percent) and Hf-34.7Ta alloys can lead to the synthesis of HfTaO superstructures, while for Hf-Ta alloys with other compositions, the oxidation products are either HfO_2 excess (Hf-19.7Ta) or Ta_2O_5 excess (Hf-49.6Ta). The examination of the cross section microstructures of oxidized Hf-Ta alloys unveils a novel multistep oxidation process (Fig. 2), in which, a three layered microstructure is developed with the single phase oxide, a reaction layer composed of Hf-rich oxide phase and Ta-rich phase and a two phase of Hf-rich phase and Ta-rich phase region forming by a displacement reaction along the oxygen diffusion direction. The microstructure at the interface of substrate and reaction layer indicates that the substrate Hf-rich phase is preferentially oxidized while the Ta-rich phase is almost

unaffected. The interface between the reaction layer and the oxide indicates that the Ta-rich phase is gradually oxidized and forms a solid solution with Hf-rich oxide and finally yields the single phase oxide superstructure.

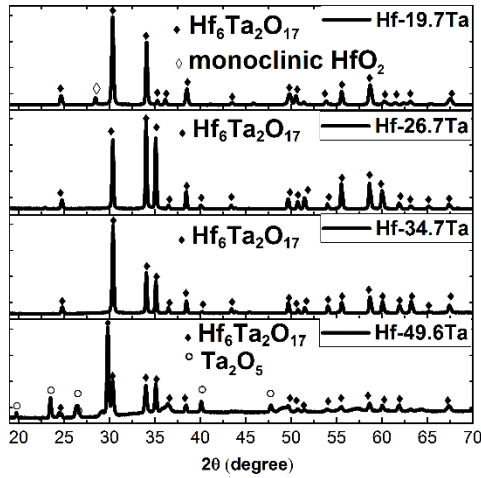


Fig. 1 XRD pattern of oxidized Hf-Ta alloy.

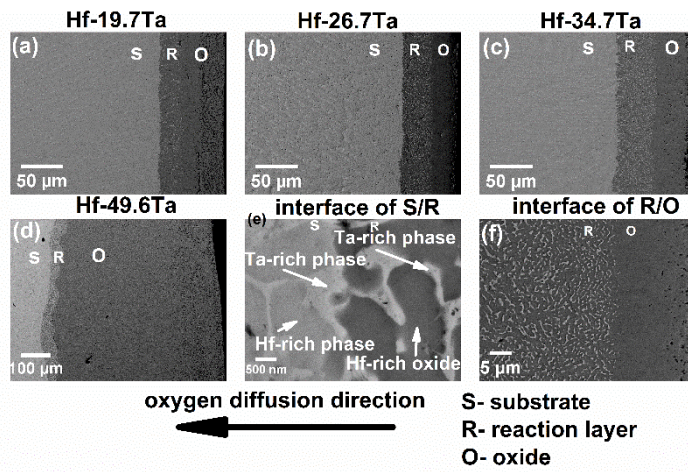


Fig. 2 Structural transitions of oxidized Hf-Ta

To elucidate the structural evolution during the oxidation synthesis of the HfTaO superstructures, a depth profile for the oxidized Hf-26.7Ta sample was constructed by carefully polishing the sample from the oxide surface to the substrate. At selected depths, XRD analysis was applied to identify the crystal structure of each phase (Fig. 3). It is evident that along the oxygen diffusion direction, the outer oxide layer is the HfTaO superstructure, the reaction layer is monoclinic HfO₂ and body-centered cubic (BCC) Hf-Ta solid solution, and the substrate is close-packed hexagonal (HCP) Hf-O solid solution and BCC Hf-Ta solid solution. Thus, the oxidation process is summarized as: Hf-Ta (solid solution, ss) → HCP Hf-O (ss) + BCC Hf-Ta → monoclinic HfO₂ + BCC Hf-Ta → HfTaO superstructure (orthorhombic).

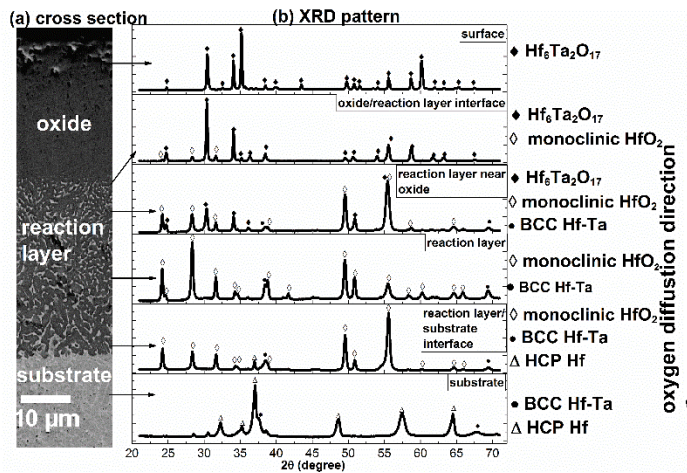


Fig. 3 Structural depth profile from oxide to substrate.

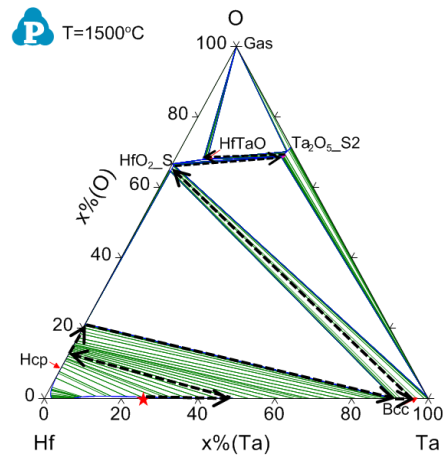


Fig. 4 Calculated Hf-Ta-O 1500°C isothermal section; arrows depict oxidation reaction path.

Moreover, this multistep oxidation process is not only observed in the Hf-26.7Ta alloy but also it is widely observed for other compositions in a wide temperature range (1200°C to 1650°C). It is also observed in the Zr-Nb system and leads to the formation of a ZrNbO superstructure.

2. Thermodynamic evaluation of Hf-Ta-O ternary system.

Based on the oxidation process of Hf-Ta alloy, a thermodynamic evaluation of Hf-Ta-O system was conducted (Fig. 4). The evaluation is based upon the reported thermodynamic data[1,2] and treats the superstructure as a line compound. The initial calculated isothermal section at 1500°C corresponds well with the experimentally observed reaction path (Fig. 4), as a thermodynamic favored process and supports the HfTaO superstructure as a thermodynamically stable phase.

3. Synthesis of HfTaO superstructure through sintering.

Another approach to form HfTaO superstructures has been conducted. Monoclinic HfO₂ powders and orthorhombic Ta₂O₅ powders were mixed with a mole ratio of 6:1. The mixed powders were cold pressed with a 300MPa pressure and then pressureless sintered at 1650°C for 24 hours. After sintering, the mixed powders were taken out as a bulk ceramic (Fig.5). The XRD investigation indicates that the ceramic is pure HfTaO superstructure.

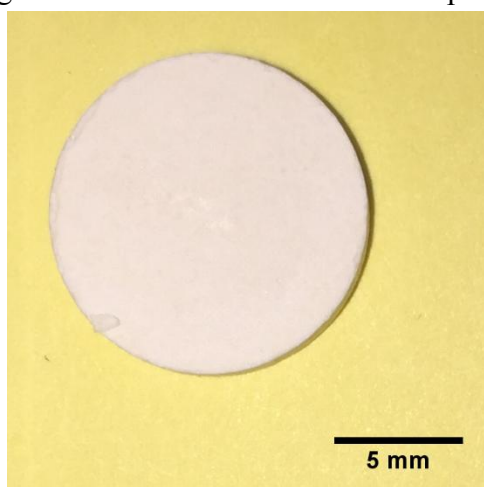


Fig. 5 sintered HfTaO ceramic sample.

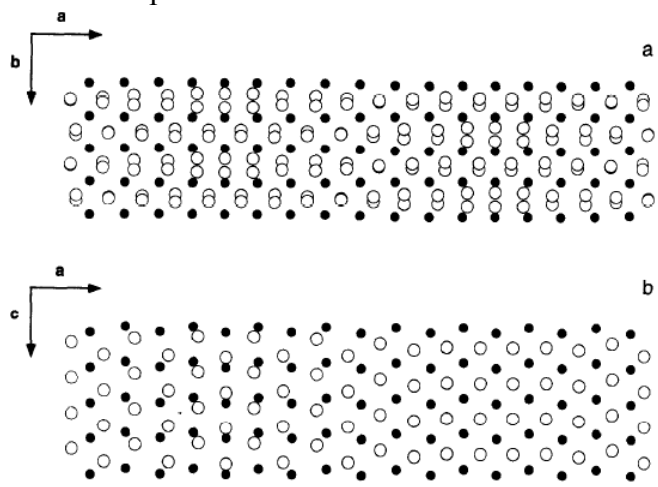


Fig. 6 Model for HfTaO superstructure, cation is large circle anion is small circle.a) projection along C axis; b) projection along B axis.

4. Crystallography of HfTaO superstructure formation.

As mentioned above, the synthesis of HfTaO superstructure through either oxidation of Hf-Ta alloy or through the sintering of mixed oxides, the initial HfO₂ is in monoclinic form, which is stable from room temperature through 1820°C [1]. However, in the crystal structure of the HfTaO superstructure, the HfO₂ is arranged in a cubic form after alloying with Ta oxide. The ready alloying of the Hf and Ta oxides indicates that the HfTaO superstructure can accommodate the excess cations and O²⁻ anions involved in the mixing. A model regarding the similar ZrNbO

crystal structure can shed some light on this mixing process. [3]. Since the cubic HfO₂ possesses a fluorite structure, the cations and anions can be represented by layered arrangements, where excess cations can substitute easily, which is true for Ta substituting for Hf; however, in the O layer, excess O²⁻ anions need to be arranged properly. This leads to the original square mesh arrangement of O²⁻ anions being transformed into in plane close packed arrangements, which can accommodate the excess O²⁻ (Fig. 6) and yields an overall incommensurate structure..

5. Refractory properties of HfTaO superstructures.

As a material intended to be used at high temperature, some refractory properties are of particular interest. The superstructure is observed to remain stable above 1810°C under torch exposure. The superstructure did not melt or transform after exposure. Moreover, the specific heat of HfTaO at 1650°C was measured as 0.6358 J/g⁻¹·K⁻¹, which is smaller than that of ZrO₂ (0.6675 J/g⁻¹·K⁻¹). The lower specific heat indicates a lower thermal conductivity. For the HfTaO superstructure, the incommensurate structure illustrated in figure 6 offers a lower thermal conductivity than the periodic ZrO₂ crystal. Since ZrO₂ is a widely used thermal barrier coating, the superstructure has a potential to be a new thermal barrier coating material.

Future Plans

- Determine the detailed crystal structure of HfTaO superstructure.
- Quantify the thermal conductivity and melting point of HfTaO superstructure.
- Relate the crystal structure to the low thermal conductivity of the HfTaO superstructure.
- Verify the oxidation-resistant properties of superstructures with TGA and construct an oxidation kinetics model for the Hf-Ta alloys.
- Explore the oxidation process in other systems composed with Group IV elements (Ti, Zr, Hf) and their β-stabilizer.

References

1. Shin D., Arroyave R., and Liu Z.K., "Thermodynamic modelling of the Hf-Si-O system", CALPHAD: Comput. Coupling Phase Diagrams Thermochem., Vol. 30, 2006, p 375-386
2. R. P. Turcotte, "Phase relations in high temperature ceramics." Naval Surface Weapons Center, April, 1987, NSWC 87-200.
3. Sellar, J. R. "A frustrated planar XY model for niobia–zirconia ceramic alloys." *Micron* 32.8 (2001): 871-877.

Publications

1. "Synthesis of HfTaO superstructures", Y. Yang and J.H. Perepezko, Materials Chemistry and Physics, submitted.
2. "Oxidation resistance of HfTaO superstructures", Y. Yang and J. H. Perepezko, in preparation.

Tailoring Charge Transport and Magnetism in Complex Half-Heusler/Full-Heusler Nanocomposites

- ❖ **Dr. Pierre Ferdinand Poudeu; Materials Science and Engineering, University of Michigan**
- ❖ **Dr. Ctirad Uher; Department of Physics, University of Michigan**
- ❖ **Dr. Anton Van der Ven; Materials Department, University of California Santa-Barbara**

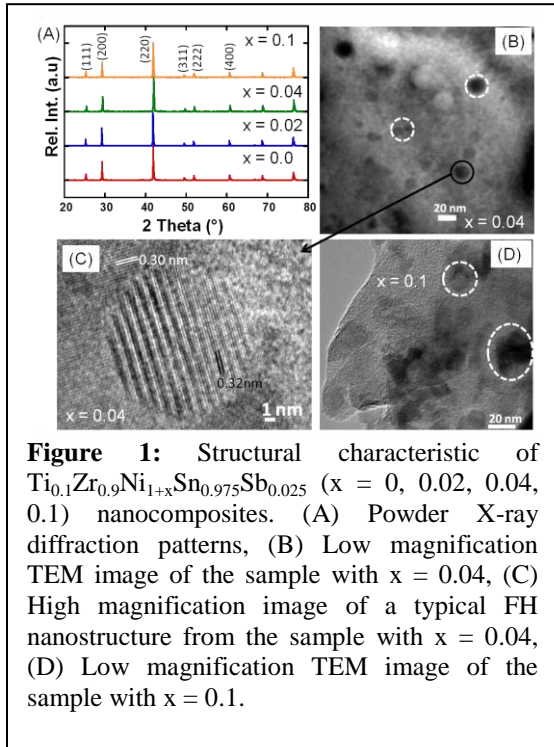
Program Scope

This project exploits (1) the facile co-crystallization of the half-Heusler (HH) and full-Heusler (FH) structures, (2) the high coherency and stability of the HH/FH interfaces, and (3) the solid-state inter-conversion between HH and FH structures through local atomic diffusion, to investigate, for selected compositions of the HH and FH phases, the effect of size, dimensionality, dispersion and volume fraction of FH nanostructures on the electronic, phonon and magnetic behavior of the resulting HH/FH nanocomposites. Our goal is to identify and control key material and growth parameters governing phase formation, microstructural evolution, and to understand the mechanism by which these changes of the internal structure modify the material's performance. To elucidate the mechanism by which the FH nanostructures regulate electronic charge transport and induce ferromagnetism within non-magnetic and magnetic semiconducting HH matrices, suitable series of HH/0D-FH and HH/2D-FH nanocomposites will be fabricated using synthesis conditions suggested by theoretical calculations of the formation energy and stability of various FH phases (varying M) in HH matrices with known chemical composition. The structure of the HH/FH interfaces (size, chemical composition, volume fraction and dispersion) will be investigated along with the evaluation of the electronic (carrier density, mobility, thermopower, electrical conductivity, effective mass), thermal and magnetic (susceptibility, magnetization etc.) properties of the resulting HH/FH nanocomposites.

Recent Progress

During the first three years of this research program, we successfully established that nanocomposites consisting of a HH TNi(Co)Sn(Sb) (T = Ti, Zr, Hf) matrix and coherent FH nanoinclusions can be fabricated by (1) co-nucleation of HH and FH phases during a solid-state reaction of the elements at high temperature or (2) solid-state diffusion of elemental Ni or Co into vacant atomic sites within the crystal lattice of the HH matrix [1-14]. The effect of synthesis and processing methods on the microstructure and electronic transport of bulk nanostructured half-Heusler phases was investigated along with the theoretical investigation of the formation of full-Heusler precipitates in (TiZrHf)NiSn half-Heusler matrix. Theoretical calculations of the HH – FH phase diagram indicate that both phases are very stable up to above 1400 K with minimal solubility between them [2]. In addition, we have also initiated a novel approach for fast design and energy efficient fabrication and characterization of a wide range of technologically important earth-abundant copper-metal-chalcogenide, $\text{Cu}(\text{M}^{\text{n}+})_{3/n}\text{Q}_2$ (Q = Se, Te) materials using a synergistic iterative combination of predictive theory and innovative synthesis strategies [3,5].

1) Electronic and Phonon Transports in Sb-doped $\text{Ti}_{0.1}\text{Zr}_{0.9}\text{Ni}_{1+x}\text{Sn}_{0.975}\text{Sb}_{0.025}$ Nanocomposites



The thermoelectric behavior of n-type Sb-doped half-Heusler (HH) – full-Heusler (FH) nanocomposites with general composition $\text{Ti}_{0.1}\text{Zr}_{0.9}\text{Ni}_{1+x}\text{Sn}_{0.975}\text{Sb}_{0.025}$ ($x = 0, 0.02, 0.04, 0.1$) was investigated in the temperature range from 300 to 775K. Samples used for structural characterization and transport measurements were obtained through solid-state reaction of high purity elements at 950 °C and densification of the resulting polycrystalline powders using a uniaxial hot press. X-ray diffraction study of the powder samples suggested the formation of single-phase HH alloys regardless of the Ni concentration (x value). However, high-resolution transmission electron microscopy investigation revealed the presence of spherical nanoprecipitates with a broad size distribution coherently embedded inside the HH matrix (Figure 1). The size range and dispersion

of the precipitates depend on the concentration of Ni in the starting mixture. Well-dispersed nanoprecipitates with size ranging from 5 nm to 50 nm are observed in the nanocomposite with $x = 0.04$, while severe agglomeration of large precipitates (>50 nm) is observed in samples with $x = 0.1$. Hall Effect measurements of various samples indicate the carrier concentration within the Sb-doped HH matrix remains nearly constant ($\sim 7 \times 10^{20} \text{ cm}^{-3}$) for samples with $x = 0.02$ and $x = 0.04$, whereas a significant increase of the carrier concentration to $\sim 9 \times 10^{20} \text{ cm}^{-3}$ is observed for the sample with $x = 0.1$. Interestingly, only a marginal change in thermopower value is observed for various samples despite the large difference in the carrier density. In addition, the carrier mobility remains constant up to $x = 0.04$ suggesting that the small nanoprecipitates in these samples do not disrupt electronic transport within the matrix. Results of this work are reported in a manuscript published in *Dalton Transactions* [1].

2) *Ab Initio* study of nano-structured Half-Heusler alloys

Experimental results have shown that FH nano-inclusions coherently integrated into the matrix HH material result in enhanced ZT . This effect is attributed to energy filtering effects that occur at the HH/FH grain boundaries as well as moderate reductions in thermal conductivity by nano-inclusion phonon scattering. Using *Ab Initio* calculations, in combination with a cluster expansion, we have investigated the stability of FH structures in the HH matrix and create a thermodynamic pseudo-binary phase diagram for $\text{MNiSn-MNi}_2\text{Sn}$ compositions. This was accomplished using the “Cluster Assisted Statistical Mechanics” or CASM, program developed

by Van der Ven group's. We were able to create using first principles calculations a temperature-composition thermodynamic phase diagram of the TiNiSn- TiNi₂Sn system (Figure 2).

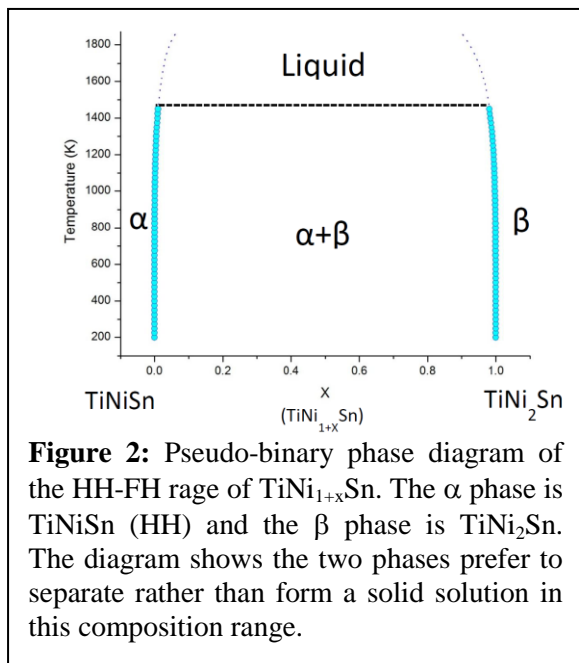


Figure 2: Pseudo-binary phase diagram of the HH-FH range of TiNi_{1+x}Sn. The α phase is TiNiSn (HH) and the β phase is TiNi₂Sn. The diagram shows the two phases prefer to separate rather than form a solid solution in this composition range.

The software creates symmetrically unique arrangements of atoms along the concentration range of HH to FH structure. Density functional theory as implemented in the Vienna Ab initio Simulation Package (VASP) is then used to calculate the formation energies of the configurations along the composition range. In this calculation of the TiNiSn-TiNi₂Sn system, forty configurations were considered. The formation energies are used in a cluster expansion that results in an effective Hamiltonian able to predict the formation energy of any configuration in the composition range. Using a Monte Carlo simulation the behavior of the system at non-zero temperatures is found and the resulting thermodynamic phase diagram is found (Figure 2). The results show a large miscibility gap between the HH and FH

compounds [2]. This is in agreement with experiments, which confirm that the formation of nano-inclusions is preferred over a solid solution mixture. Detailed calculations of the stability of HH/FH and coarsening of the FH phases at high temperatures are in progress.

3) Rapid Direct Conversion of Cu_{2-x}Se to CuAgSe Nanoplatelets via Ions Exchange

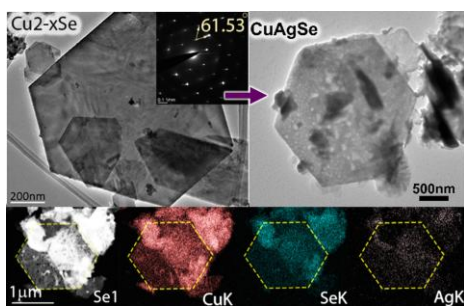


Figure 3: Above: HRTEM images of the Cu_{2-x}Se nanoplatelet template and the final CuAgSe nanoplatelets, Below: EDAX of NPs made with Ag:Se ratio of 0.67.

The use of template nanostructures for the creation of photovoltaic and thermoelectric semiconductors is becoming a quickly expanding synthesis strategy. In this work we report a simple two-step process enabling the formation of ternary CuAgSe nanoplatelets with a great degree of control over the composition and shape. Starting with hexagonal nanoplatelets of cubic Cu_{2-x}Se, ternary CuAgSe nanoplatelets were generated through a rapid ion exchange reaction at 300 K using AgNO₃ solution. The Cu_{2-x}Se nanoplatelet template and the final CuAgSe nanoplatelets were analyzed by

electron microscopy and X-ray diffraction (XRD). It was found that both the low temperature pseudotetragonal and the high temperature cubic forms of CuAgSe phase were created while maintaining the morphology of Cu_{2-x}Se nanoplatelet template. Thermal and electronic transport measurements of hot-pressed pellets of the synthesized CuAgSe nanoplatelets showed a drastic reduction in the thermal conductivity and a sharp transition

from n-type ($S = -45 \mu\text{V/K}$) to p-type ($S = +200 \mu\text{V/K}$) semiconducting behavior upon heating above the structural transition from the low temperature orthorhombic to the high temperature super-ionic cubic phase. This simple reaction process utilizing a template nanostructure matrix represents an energy efficient, cost-efficient, and versatile strategy to create interesting materials with lower defect density and superior thermoelectric performance [5].

4) Topochemical Solid-State Reactivity: Redox-Induced Direct Structural Transformation from CuSe_2 to CuInSe_2

CuInSe_2 and its solid solution with other trivalent metals (M) have emerged as technologically significant device materials with applications in photovoltaics, thermoelectric, nonlinear optics, etc. However, the complex chemical composition and large tolerance of the CuMSe_2 structure to a wide range of off-stoichiometry generally lead to the formation of undesirable impurity binary phases and electronic defects during fabrication starting from elements. In this work, we demonstrate a simple and elegant strategy for the synthesis of CuInSe_2 with improved control over the chemical composition. The reaction proceeds via a redox induced phase transformation of the line compound copper diselenide (CuSe_2) upon incremental addition of elemental indium. Taking into consideration the chemical and structural similarity between CuSe_2 and CuInSe_2 , we demonstrate the stepwise direct conversion of the structural template CuSe_2 into $(1-x)\text{CuSe}_2/x\text{CuInSe}_2$ nanocomposites without the formation of undesirable binary or ternary indium phases. Through X-ray diffraction and transmission electron microscopy it is observed that the structural template provided by CuSe_2 serves as pathway for the formation of CuInSe_2 particles in the size range of 5 to 50 nm [3].

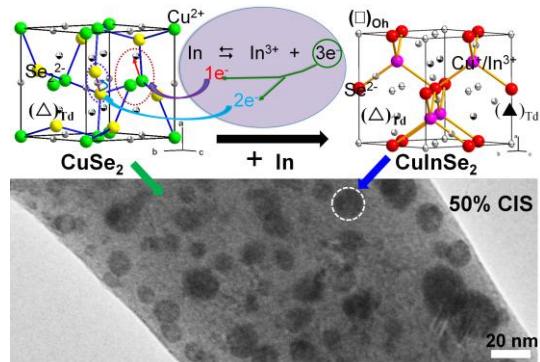


Figure 4: Schematic illustration of the proposed mechanism of the redox-induced direct solid-state transformation of CuSe_2 pyrite structure into CuInSe_2 sphalerite structure and TEM image of the 50% CuSe_2 /50% CuInSe_2 nanocomposite.

Future Plans

(1) Synthesis, structural characterization and electronic and magnetic properties of $\text{TNi}(\text{Co})\text{Sn}/\text{T}(\text{NiM})\text{Sn}(\text{Sb})$ [HH(1-x)/OD-FH(x)] nanocomposites; (2) Theoretical predictions of temperature-composition phase diagram of $\text{TNiSn}/\text{T}(\text{NiM})\text{Sn}$ (HH/FH) systems; (3) Investigation of the mechanism and kinetics of phase transformations in $\text{TNiSn}/\text{T}(\text{NiM})\text{Sn}$ HH(1-x)/FH(x) nanocomposites using temperature dependent X-ray diffraction of $\text{TNiSn}/\text{T}(\text{NiM})\text{Sn}$ HH(1-x)/FH(x) nanocomposites annealed at various temperatures and quenching, (4) Investigation of the dependence of bulk free energies and M (Cr-Zn) diffusion coefficients on HH(1-x)/FH(x) composition, and (5) Continuum simulations of precipitation kinetics and precipitate coarsening in HH(1-x)/OD-FH(x) composites.

Publications 2014-2015

- 1) Yuanfeng Liu, Julien P.A. Makongo, Alexander Page, Pranati Sahoo, Ctirad Uher, Kevin Stokes, Pierre F.P. Poudeu; Distribution of impurity states and charge transport in $Zr_{0.25}Hf_{0.75}Ni_{1+x}Sn_{1-y}Sb_y$ nanocomposites; *J. Solid State Chem.* **2015**, submitted.
- 2) Alexander Page; Ctirad Uher; Pierre Ferdinand Poudeu; Anton Van der Ven, Phase separation of full-Heusler nano-structures in half-Heusler thermoelectrics and vibrational properties from first principle calculations; *Phys. Rev. B*, **2015**, accepted.
- 3) Alan Olvera, Pranati Sahoo, Stephanie Tarczynski and Pierre F.P. Poudeu; Topochemical Solid-State Reactivity: Redox-Induced Direct Structural Transformation from $CuSe_2$ to $CuInSe_2$; *Chem. Mater.* **2015**; accepted.
- 4) Pierre F.P. Poudeu, Julien P. A. Makongo, Yuanfeng Liu, Dinesh K. Misra, Pranati Sahoo¹, Kevin L. Stokes; Thermoelectric behavior of nanostructured $Zr_{0.25}Hf_{0.75}NiCo_xSn$ half-Heusler alloys, *Sci. Lett. J.* **2015**, accepted.
- 5) N. A. Moroz, A. Olvera, G. M. Willis and P. F. P. Poudeu; Rapid Direct Conversion of $Cu_{2-x}Se$ to $CuAgSe$ Nanoplatelets via Ions Exchange Reactions at Room Temperature; *Nanoscale*; **2015**; 7; 9452–9456.
- 6) Yuanfeng Liu, Pierre F.P. Poudeu; Thermoelectric properties of Ge doped n-type $Ti_xZr_{1-x}NiSn_{0.975}Ge_{0.025}$ half-Heusler alloys *J. Mater. Chem. A*; **2015**; 3; 12507–12514.
- 7) Alan Olvera, Guangsha Shi, Honore Djieutedjeu, Alexander Page, Ctirad Uher, Emmanouil Kioupakis, and Pierre F. P. Poudeu*, $Pb_7Bi_4Se_{13}$: A Lillianite (^{4,5}L) Homologue with Promising Thermoelectric Properties, *Inorganic Chemistry* **2015**, 54, 746–755.
- 8) Yuanfeng Liu, Alexander Page, Pranati Sahoo, Hang Chi, Ctirad Uher and Pierre F. P. Poudeu; Electronic and Phonon Transports in Sb-doped $Ti_{0.1}Zr_{0.9}Ni_{1+x}Sn_{0.975}Sb_{0.025}$ Nanocomposites, *Dalton Trans.* **2014**; 43; 8094–8101.
- 9) Pranati Sahoo, Yuanfeng Liu and Pierre F. P. Poudeu; Nanometer scale interface engineering boosts the thermoelectric performance of n-type $Ti_{0.4}Hf_{0.6}Ni_{1+z}Sn_{0.975}Sb_{0.025}$ alloys; *J. Mater. Chem. A*, **2014**, 2, 9298–9305.
- 10) Honore Djieutedjeu, Xiaoyuan Zhou, Hang Chi, Neel Haldolaarachchige, Kulugamma G. S. Ranmohotti, Ctirad Uher, David Young, Pierre F. P. Poudeu*, Donor and Acceptor Impurities-Driven Switching of Magnetic Ordering in $MnSb_{2-x}Sn_xSe_4$, *Journal of Materials Chemistry C* **2014**, 2, 6199 – 6210.

2013

- 11) Yuanfeng Liu, Pranati Sahoo, Julien P. A. Makongo, Xiaoyuan Zhou, Sung-Joo Kim, Hang Chi, Ctirad Uher, Xiaoqing Pan and Pierre F. P. Poudeu; Large Enhancements of Thermopower and Carrier Mobility in Quantum Dots Engineered Bulk Semiconductors; *J. Am. Chem. Soc.* **2013**, 135, 7486–7495.
- 12) Pranati Sahoo, Julien P. A. Makongo, Xian-Li Su, Sung Joo Kim, Yuanfeng Liu, Nathan Takas, Hang Chi, Ctirad Uher, Xiaoqing Pan, Pierre F. P. Poudeu, Full-Heusler

Nanostructures Boost Thermopower and Hole Mobility in Bulk *p*-type Half-Heuslers, *Nanoscale* **2013**, DOI: 10.1039/c3nr03145d.

- 13) J.P.A. Makongo, X. Zhou, D. K. Misra, C. Uher, and P.F.P. Poudeu, Correlation between processing conditions, microstructure and charge transport in half-Heusler alloys, *J. Solid State Chemistry* **2013**, 201, 280–287.
- 14) P. Maji, J.P.A. Makongo, X. Zhou, H. Chi, C. Uher, and P.F.P. Poudeu, Thermoelectric performance of nanostructured *p*-type $\text{Zr}_{0.5}\text{Hf}_{0.5}\text{Co}_{0.4}\text{Rh}_{0.6}\text{Sb}_{1-x}\text{Sn}_x$ half-Heusler alloys, *J. Solid State Chemistry* **2013**, 202, 70–76.

New optoplasmonic materials for next generation energy systems

Bjoern Reinhard, Department of Chemistry and the Photonics Center, Boston University

Program Scope

Optoplasmonic materials are metallo-dielectric hybrid structures that combine metallic and dielectric components into defined geometries in which plasmonic and photonic modes synergistically interact. These beneficial interactions can be harnessed by integrating plasmonic nanoantennas into photonic environments generated, for instance, by discrete optical resonators or extended systems of diffractively coupled nanoparticles (**Figure 1**). Optoplasmonic structures facilitate photonic-plasmonic mode coupling and offer degrees of freedom for creating optical fields with predefined amplitude and phase in space and time that are absent in conventional photonic or plasmonic structures. Synergistic electromagnetic interactions between plasmonic nanostructures localized in the near-field of photonic resonators offers tremendous potential to address long standing limitations of both metallic plasmonic and dielectric photonic resonators.¹ Potential applications include efficient waveguides that transfer energy between nanoscale hot-spots efficiently, all-optical frequency multiplexers and demultiplexers,² and the next generation of metasurfaces with higher compositional complexity. The realization of hybrid materials and structures that contain metallic nanoantennas and photonic resonators in sufficiently well defined geometries to utilize the synergistic electromagnetic interactions remains, however, challenging from a fabrication perspective as it requires the integration of two components (metallic and dielectric structures) of very different size into intricate geometries. The scope of this project is to develop scalable fabrication strategies that allow the experimental realization of optoplasmonic materials of well defined geometry that can utilize synergistic interactions between photonic and plasmonic resonators in a rational way and to elucidate the underlying electromagnetic working principles of these new materials by systematic experimental and theoretical characterization.

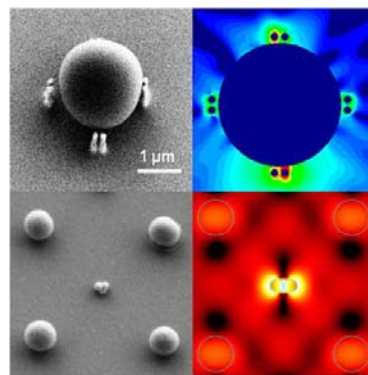


Figure 1: Examples of optoplasmonic structures. SEM images (left) and electromagnetic simulations of the field distribution (right) are shown. Top: Discrete optoplasmonic structure containing a whispering gallery mode resonator surrounded by pillars carrying gold antennas. Bottom: Section of an extended array containing 300 nm TiO₂ nanoparticles and clusters of 60 nm gold nanoparticles at pre-defined locations.

Recent Progress

To address the fabrication challenges associated with optoplasmonic materials we have developed template guided self-assembly approaches that allow the fabrication of two optoplasmonic structures: Optoplasmonic hybrid nanoparticle arrays and discrete optoplasmonic resonators that contain both whispering gallery mode resonators and plasmonic antennas.

We have demonstrated that template guided self-assembly approaches facilitate the integration of electromagnetically strongly coupled metallic nanoparticles and dielectric (or semiconductor) nanoparticles at separate, pre-defined locations. In the first step of the assembly procedure nanoparticle assembly sites are created through a lithographic fabrication technique (*e.g.* electron beam lithography). In the second step these sites are charged positively through incubation with poly-lysine, and in the last step negatively charged colloidal nanoparticles are immobilized and assembled into clusters on positively charged assembly sites through a charge-mediated assembly process. While electron beam lithography makes it possible to define the separation, Λ , between individual assembly sites on the tens to hundreds of nanometer length scale, the number of nanoparticles on the sites, their separation and the morphology of the assembly are determined by the size and shape of the binding site and the assembly conditions. We have shown that the interparticle separation in the nanoparticle clusters on the assembly sites can be systematically varied on lengths scales of a few nanometers and below through choice of the nanoparticle ligands and buffer conditions. Through combination of top-down and chemical assembly driven bottom-up fabrication, template guided assembly strategies achieve control over interparticle separations ranging from truly nanoscale separation to photonic length scales. The advantages of template guided assembly strategies for generating multiscale E -field enhancements in noble metal nanoparticle cluster arrays (NCAs) are well documented.³ What is relevant from an optoplasmonic perspective is that the template guided self-assembly also facilitates the selective binding of particles of different compositions at pre-defined lattice sites, provided these particles also differ in their sizes. Of course, the same strategy can also be applied to arrange particles of identical chemical composition but different sizes (and thus resonance conditions) in pre-defined morphologies.

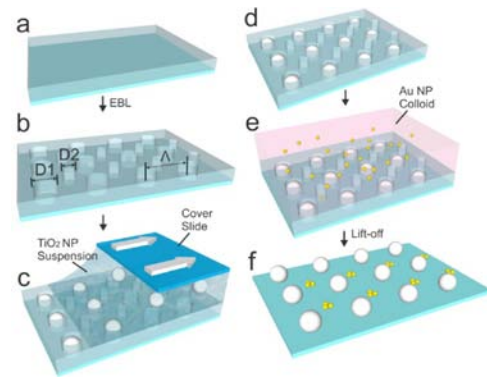


Figure 2: Scheme of template-guided self-assembly of extended optoplasmonic arrays. (a) Regular pattern of wells with diameters $D1$ and $D2$ ($D1 > D2$) is created through EBL in a PMMA layer to generate (b) a regular mask of assembly sites with two different diameters. The center-to-center separation in the $D1$ and $D2$ subarrays is Λ . (c) Dragging of a suspension of TiO_2 nanoparticles with diameters too large to bind to $D2$ across the surface results in (d) an immobilization of TiO_2 nanoparticles onto $D1$ sites. (e) Smaller Au nanoparticles are assembled onto vacant $D2$ binding sites from a colloidal solution. (f) After PMMA lift-off, the final optoplasmonic array is released.

The underlying strategy is schematically outlined in **Figure 2** for an example in which (large) TiO_2 nanoparticles are combined with clusters of (small) Au nanoparticles. First, two different binding sites are patterned in the electron beam resist. Then, the larger TiO_2 nanoparticles are immobilized on the large diameter binding sites, leaving the small-diameter binding sites vacant for the binding of Au nanoparticles in a subsequent binding step. **Figure 3** contains exemplary SEM images of different arrays obtained from 60 nm Au nanoparticles and 250 nm diameter TiO_2 nanoparticles with binding sites containing diameters of $D_2 = 140$ nm and $D_1 = 270$ nm, respectively. The resulting arrays show a successful localization of TiO_2 nanoparticles and Au nanoparticle cluster to distinct lattice sites. The optical resonances of these hybrid arrays were investigated in detail and showed clear evidence for synergistic electromagnetic coupling.

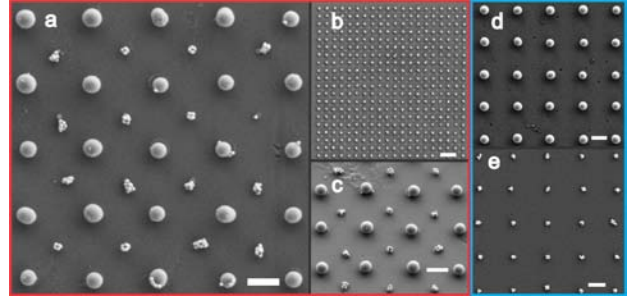


Figure 3. SEM images of 2D arrays generated through template guided self-assembly of 250 nm TiO_2 nanoparticles and 60 nm Au nanoparticles. (a) Section of optoplasmonic array. (b) Complete optoplasmonic array with 20×20 TiO_2 nanoparticles. (c) Side-view (30° tilt angle) of optoplasmonic array section. (d) Section of TiO_2 nanoparticle array. (e) Section of Au nanoparticle cluster array. Λ is 1000 nm in (a) – (e). Scale bars are 500 nm in (a) and (c) – (e), and 2 μm in (b).

An alternative strategy to position metallic antennas into a well defined photonic environment relies on placing metal nanostructures in direct vicinity of whispering gallery mode resonators that provide a rich spectrum of sharp spectral features. The particular challenge for the experimental realization of these structures with defined optical responses is the requirement to position one or multiple plasmonic antennas at defined locations in the evanescent field of an individual microsphere resonator or network of microsphere resonators. A chemical or charge mediated direct attachment of nanoparticles to the resonator is limited in scope for this purpose, as these strategies do not provide control over the location and, in the case of anisotropic nanoparticles and assemblies, orientation of the plasmonic components. Furthermore, it is difficult to create gap antennas in a controlled fashion

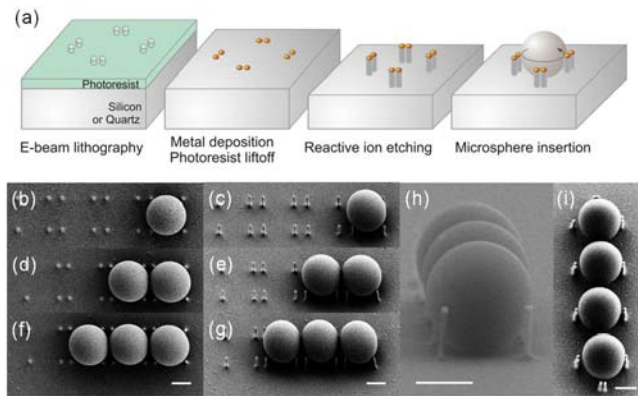


Figure 4. (a) Schematic illustration of the fabrication process for optoplasmonic structures. Noble metal nanoparticle tipped pillars were fabricated through electron beam lithography followed by reactive ion etching. The generated cavities were filled with microspheres by convective self-assembly of an aqueous solution of PS microspheres. (b-i) SEM images of diverse optoplasmonic structures generated through template-guided self-assembly. Scale bars in all images are 1 μm .

by nanoparticle attachment, and the separation between the antenna and the dielectric resonator can also not be systematically varied. Instead, we developed the template guided self-assembly process outlined in **Figure 4**, which positions plasmonic antennas supported by dielectric posts into the equatorial plane of the whispering gallery mode resonator for maximum coupling efficiency. We are currently investigating the ability of these structures to guide light over long distances and subsequently relocalize it into plasmonic hot-spots. As shown in **Figure 5**, the preliminary results are encouraging and show emission of reporter dyes from antennas localized along the optoplasmonic chain. This is an important accomplishment as it proves that optical functionalities such as long range energy transfer, multiplexing and demultiplexing based on optoplasmonic geometries are feasible.

We are currently expanding this design approach to silicon resonators with metal nanoparticles at defined locations. So far, we were able to demonstrate a strong enhancement of both near-field and radiative rates when compared with the isolated building blocks.

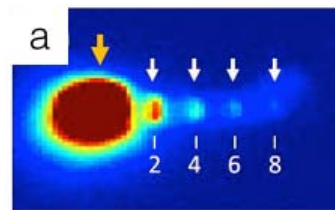


Figure 5: Fluorescence images of an optoplasmonic chain whose gold antennas are functionalized with Cy5. The detected fluorescence intensity 2, 4, 6 and 8 μm away from the quantum dot covered bead that acts as excitation source confirms long distance energy transfer and relocalization at the nanoantennas.

Future Plans

There is an increasing interest in the materials science community in non-metallic materials for plasmonic applications.⁴ Conducting oxides, germanides, nitrides, silicides, to name only a few, have all shown great potentials as plasmonic materials and are – different than metals – completely CMOS compatible and much cheaper. In metal plasmonics we have learned that the ability to pattern nanoparticles in discrete arrays provides a significant gain in functionality due to collective resonances. In the future we intend to develop a new class of optoplasmonic materials that incorporates non-metallic plasmonic materials. This research builds immediately on our recent accomplishments of patterning metallic and dielectric nanoparticles and will result in a completely new class of metasurfaces that can provide exquisite control over light fields in ultra-thin materials.

References

- (1) Hong, Y.; Ahn, W.; Boriskina, S. V.; Zhao, X.; Reinhard, B. M. *J. Phys. Chem. Lett.* **2015**, *6*, 2056.
- (2) Boriskina, S. V.; Reinhard, B. M. *Proceedings of the National Academy of Sciences of the U.S.A* **2011**, *108*, 3147.
- (3) Yan, B.; Thubagere, A.; Premasiri, R.; Ziegler, L.; Dal Negro, L.; Reinhard, B. M. *ACS Nano* **2009**, *3*, 1190
- (4) Naik, G. V.; Shalaev, V. M.; Boltasseva, A. *Adv. Mater.* **2013**, *25*, 3264.

Publications

Published:

W. Ahn, Y. Hong, S.V. Boriskina, X. Zhao, B.M. Reinhard, Template Guided Self-Assembly of Discrete Optoplasmonic Array, *Nanophotonics* DOI 10.1515/nanoph-2015-0019 (in press).

J. Burgmeier, A. Feizpour, W. Schade, B.M. Reinhard, Plasmonic nanoshell functionalized etched fiber Bragg gratings for highly sensitive refractive index measurements, *Opt. Lett.* **40**, 546-549 (2015).

Y. Hong, W. Ahn, S.V. Boriskina, X. Zhao, B.M. Reinhard, Directed Assembly of Optoplasmonic Hybrid Materials with Tunable Photonic Plasmonic Properties, *J. Phys. Chem. Lett.* **6**, 2056-2064 (2015).

Y. Hong, B.M. Reinhard, Collective photonic-plasmonic resonances in noble metal – dielectric nanoparticle hybrid arrays. *Opt. Mater. Express* **4**, 2409-2422 (2014).

M. H. Alizadeh, B.M. Reinhard, Plasmonically Enhanced Chiral Optical Fields and Forces in Achiral Split Ring Resonators, *ACS Photonics* **2**, 361-368 (2015).

M. H. Alizadeh, B.M. Reinhard, Enhanced Optical Chirality through Locally Excited Surface Plasmon Polaritons, *ACS Photonics*, *ACS Photonics* **2**, 942-949 (2015).

H. Sugimoto, T. Chen, R. Wang, M. Fujii, B.M. Reinhard, L. Dal Negro, Plasmon Enhanced Emission Rate in Gold Nanorod Composites Decorated with Silicon Nanocrystals, *ACS Photonics* **2**, 1298 – 1305 (2015).

Under review:

W. Ahn, X. Zhao, Y. Hong, B.M. Reinhard, “Optoplasmonic Networks with Morphology-Dependent Near- and Far-Field Responses”, *MRS Communications* under review.

W. Ahn, X. Zhao, Y. Hong, B.M. Reinhard, “Low Power Guiding and Localization in Optoplasmonic Chains Obtained by Directed Self-Assembly”, *Adv. Opt. Mater.* under review

R. Orghici, W. Schade, B.M. Reinhard, “Trace Detection of Alkanes in Water by Pairs of Hydrophobic and Hydrophilic Microring Resonators” *Anal. Chem.* under review.

M. H. Alizadeh, B.M. Reinhard, “Transverse Chiral Optical Forces by Locally Excited Surface Plasmon Polaritons”, *ACS Photonics* under review.

Using Interfaces to Create Strongly-Coupled Magnetic-Ferroelectrics

Darrell G. Schlom¹, Craig J. Fennie¹, David A. Muller¹, Peter Schiffer²

¹Cornell University, Ithaca, NY 14853

²University of Illinois at Urbana-Champaign, Urbana, IL 61801, USA

I. PROGRAMSCOPE

Our objective is to create a ferromagnetic ferroelectric that can be deterministically switched between symmetry equivalent states using an electric field. Until recently, the electric-field switching of a magnetization between 180° symmetry equivalent states had not been demonstrated in any material.¹ The required coupling between ferroelectric and ferromagnetic domains allowing such switching is a missing feature in most multiferroics and is key to advancing the field both scientifically and technologically. Starting at the level of electrons and atoms our goal is to rationally design complex oxide heterostructures and interface-materials with this targeted emergent behavior. Using a combination of symmetry arguments and first-principles calculations to explore the connection between structural distortions and ferroelectricity in the perovskite family of materials, we have predicted electrical control of magnetism in the hexagonal rare earth ferrites². These realizations are created with atomic-layer precision, microscopically interrogated to see if there are competing mechanisms to the intended realization, and finally their macroscopic properties are measured. Here we will develop the scientific ideas and experimental tools necessary to apply this design paradigm to the creation of multiferroics with unprecedented coupling between ferroelectric and magnetic order parameters.

II. RECENT PROGRESS

Over the last 3 years our team has been able to investigate strongly coupled magnetic ferroelectrics in a comprehensive way—from materials-by-design theory to state-of-the-art synthesis and characterization. Our work has overcome and pushed the multiferroic field beyond the limiting notion that it is best to start with a material that displays ferromagnetism, and devise a way to induce ferroelectricity or vice-versa. While highly successful at creating new multiferroics (materials that are both ferromagnetic and ferroelectric), generally speaking this approach has not led to a widespread solution to the central problem of *strong coupling* between the polarization and the magnetism. The reason is believed to be due to the common origin of the ferroelectricity in these materials (small cation displacements such as those in the prototypical perovskite ferroelectric BaTiO₃).

Our team has invented new mechanisms for multiferroics, which provide strong coupling between polarization and magnetism. Specifically, multiferroics based on spin-phonon coupling,³ rotation-driven multiferroicity,^{4,5} and novel geometric multiferroics.⁶ Importantly, the latter two of these mechanisms enable the deterministic switching of magnetism by an applied electric field,^{12,7} which is key to the application of multiferroics to future device technologies. In addition to coming up with these strongly coupled magnetic ferroelectric ideas in this program,^{3-6,8-10} we have also made and studied these materials to compare them to expectations from theory.¹¹⁻¹⁹

Overall, our team has discovered new frontiers for strongly coupled multiferroics in thin film form. Our DOE-supported work has led to 22 publications in peer-reviewed journals.^{3-6,8-18,20-26} Below we highlight our most recent breakthrough in the field of multiferroics that builds upon our understanding of related phases.^{6,11,15,17-19}

LuFe₂O₄ was reported to be simultaneously ferrimagnetic and ferroelectric at 250 K, the highest temperature of any known material.²⁷ Although its ferrimagnetic ordering is widely affirmed,²⁸ recent studies from multiple groups find that LuFe₂O₄ is *not* ferroelectric.²⁹⁻³² Interestingly, a robust high-temperature ferroelectric with a closely related structure and chemistry exists: hexagonal LuFeO₃. Although metastable, hexagonal LuFeO₃ has been grown in thin film form by epitaxial stabilization.³³⁻³⁵ Isostructural to YMnO₃, it is an improper ferroelectric,^{6,36} where the rumpling of the Lu-O planes and corresponding tilt of the Fe-O trigonal bipyramids lead to geometric ferroelectricity that persists well above room temperature.^{18,35} At low temperature hexagonal LuFeO₃ orders antiferromagnetically (T_N); slight canting of the spins gives rise to weak ferromagnetism.^{6,18,35}

We created a new multiferroic through the atomic-layer integration of LuFe₂O₄ and LuFeO₃ and identify (LuFeO₃)₉(LuFe₂O₄)₁ as a strongly magnetically ordered ferroelectric up to 281 K. The claim of a phase that is simultaneously ferroelectric and ferromagnetic (or ferrimagnetic) at room temperature has been made before.³⁷⁻⁴⁰ In contrast to prior reports, however, we corroborated this result using methods that are insensitive to magnetic impurity phases (e.g., neutron diffraction) or electrical leakage (e.g., high-resolution electron microscopy) and also showed how our results are consistent with first-principles calculations.

Figure 1(a) shows the high-angle annular dark field scanning transmission electron microscopy (HAADF-STEM) of the LuFeO₃ and LuFe₂O₄ end-members and Fig. 1(b) the (LuFeO₃)_m(LuFe₂O₄)₁ superlattices for $m=1$ to $m=10$. The characteristic “up-up-down” pattern of the lutetium atoms in LuFeO₃, which is also observed in LuFeO₃^{35,41} and the hexagonal

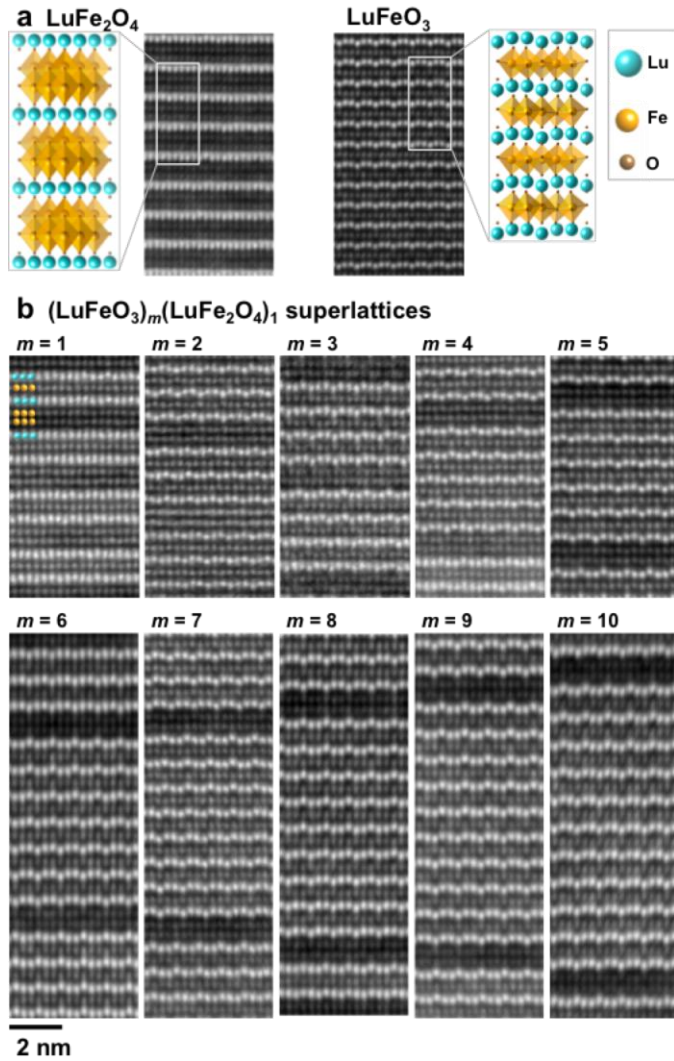


Fig. 1. HAADF-STEM images of the (a) end members LuFe₂O₄ and LuFeO₃ and (b) (LuFeO₃)_m(LuFe₂O₄)₁ superlattice series for $1 \leq m \leq 10$. Samples are imaged along the LuFeO₃ $P6_3cm$ [100] zone axis. LuFe₂O₄ is imaged down the equivalent zone axis, which due to the primitive unit cell of LuFe₂O₄ is the [120] zone axis. Cartoons are shown of the LuFe₂O₄ and LuFeO₃ crystal structures with lutetium, iron, and oxygen in turquoise, yellow, and brown, respectively.

manganites⁴²⁻⁴⁴ is evident and reflects the polar nature of these superlattices. The polarization monotonically tracks the magnitude of this lutetium trimer distortion,⁶ rendering HAADF-STEM a local probe of ferroelectricity. Inspecting the images in Fig. 1, we note that distortions are present in the $(\text{LuFeO}_3)_m(\text{LuFe}_2\text{O}_4)_1$ series for $m \geq 2$.

The measured magnetic properties of the $(\text{LuFeO}_3)_m(\text{LuFe}_2\text{O}_4)_n$ superlattices are displayed in Fig. 2. The shapes of the M - T curves for the superlattices are the same as that of the LuFe_2O_4 M - T curve, suggesting that the magnetization observed in the superlattices most likely is ferrimagnetic of the same kind as LuFe_2O_4 . In Fig. 2(c), T_C is plotted as a function of the fraction of the iron layers that sit in LuFeO_3 layers, $m/(m+2n)$. Strikingly, the superlattice transitions are higher than thin films of both of the constituent layers, LuFeO_3 ($T_N=147$ K)¹⁵ and LuFe_2O_4 ($T_C=219$ K).¹¹ For the $(\text{LuFeO}_3)_m(\text{LuFe}_2\text{O}_4)_1$ series, the ferromagnetic Curie temperature increases to $T_C=281$ K for $m=9$. The magnetization vs. applied magnetic field (M - H) loops of $(\text{LuFeO}_3)_9(\text{LuFe}_2\text{O}_4)_1$ show that the saturation magnetization remains to ~ 350 K, suggesting that short-range ferromagnetic fluctuations persist well above room temperature.

The observed enhancement of the magnetic transition temperature and moment shown in Figs. 2(c) and 2(d) could arise from the LuFe_2O_4 matrix incurring structural, stoichiometric or spin-lattice changes when epitaxially integrated with the LuFeO_3 layers. Figure 2 suggests two distinct regions with a separate interplay of these effects: Region I for $0 < m/(m+2n) < 0.5$ where the T_C saturates at ~ 250 K and the LuFe_2O_4 moment is constant and Region II for $0.5 \leq m/(m+2n) < 1$ where a further increase of T_C to 281 K is

coupled with an enhanced magnetic moment and the observation of lutetium atomic distortions.

First-principles density functional theory (DFT) calculations were used to probe the

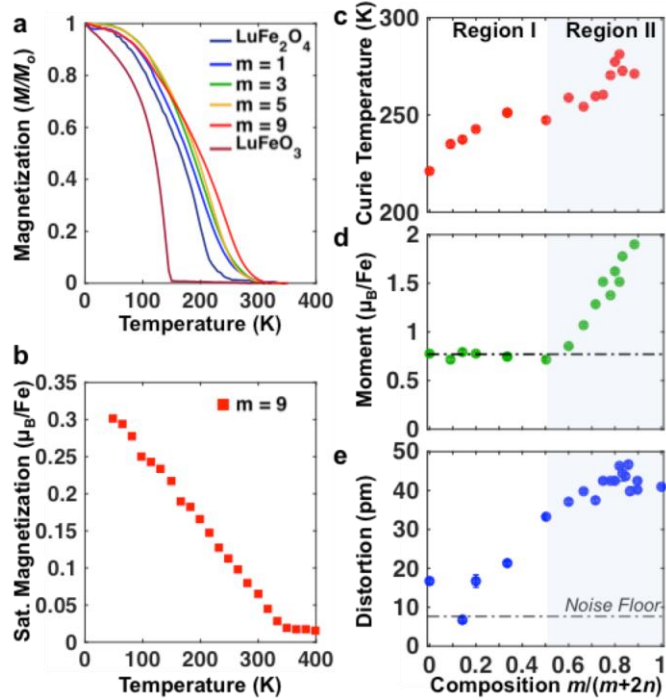


Fig. 2. Magnetic characterization of the $(\text{LuFeO}_3)_m(\text{LuFe}_2\text{O}_4)_n$ superlattices. (a) M - T curves for a series of $(\text{LuFeO}_3)_m(\text{LuFe}_2\text{O}_4)_1$ superlattices cooled in a 1 kOe field. (b) Saturation magnetization of the $(\text{LuFeO}_3)_9(\text{LuFe}_2\text{O}_4)_1$ superlattice. (c) The ferromagnetic Curie temperature extracted from the curves in (a). The ferromagnetic Curie temperature reaches a maximum of 281 K for the $(\text{LuFeO}_3)_9(\text{LuFe}_2\text{O}_4)_1$ compound. The total moment per LuFe_2O_4 iron atom at 50 K is plotted in (d) assuming the moment of LuFeO_3 remains constant. (e) Average lutetium displacement from HAADF STEM for superlattice layering plotted as a function of the composition for the $(\text{LuFeO}_3)_m(\text{LuFe}_2\text{O}_4)_1$ and $(\text{LuFeO}_3)_1(\text{LuFe}_2\text{O}_4)_n$ series. Ferroelectric distortions are observed in the samples in Region II where $m/(2n+m) \geq 0.5$, corresponding to $(\text{LuFeO}_3)_m(\text{LuFe}_2\text{O}_4)_1$ superlattices with $m \geq 2$.

enhanced moment and T_C observed in Region II. The ground state of LuFe_2O_4 is an antiferroelectric charge-ordered state, “COI,” as shown in Fig. 3(a). The ferroelectric charge-ordered state “COII” as well as non-polar charge-ordered “COIII” configurations shown in Figs. 3(b) and 3(c) have energies higher than the COI ground state. The magnetization as a function of temperature for the COI ground state calculated from the Heisenberg spin model is shown in Fig. 3(d). The low-energy state COII was found to be susceptible to the tri-fold lutetium distortions characteristic of LuFeO_3 (but not observed in the LuFe_2O_4 state in bulk). Artificially increasing the distortion vector, Q , in the COII state monotonically increased the in-plane super-exchange interaction and in turn the magnetic transition T_C as shown in Fig. 3(d). While this already suggests that the enhancement of the magnetic transition temperature in the $(\text{LuFeO}_3)_m(\text{LuFe}_2\text{O}_4)_1$ compounds with $m \geq 2$ is attributable to the lutetium distortions borrowed from the LuFeO_3 layers, we also calculated the structure of the $m=1$ and $m=3$ superlattices directly.

In contrast to LuFe_2O_4 , DFT calculations of the $m=1$ superlattice found the most stable configuration corresponds to a “ Fe^{3+} -doped” COII-type configuration with a 2:1 ratio between Fe^{3+} and Fe^{2+} in each layer. In the Fe^{3+} -doped superlattices, the net magnetization is due to ferromagnetically aligned Fe^{2+} ions

located at the centre of Fe^{3+} hexagons and the magnetization observed is higher than in the COII structure. The $m=3$ superlattice in the “ Fe^{3+} -doped” state also displays charged-ferroelectric domain walls: the polarization aligns “tail-to-tail” at the LuFe_2O_4 bilayers and has a corresponding “head-to-head” domain wall in the LuFeO_3 block. Plotting the density of states at each layer, we observe that electrons migrate from the Fe^{3+} -doped LuFe_2O_4 layers to screen the excess of bound charges at these domain walls resulting in a further increase in the

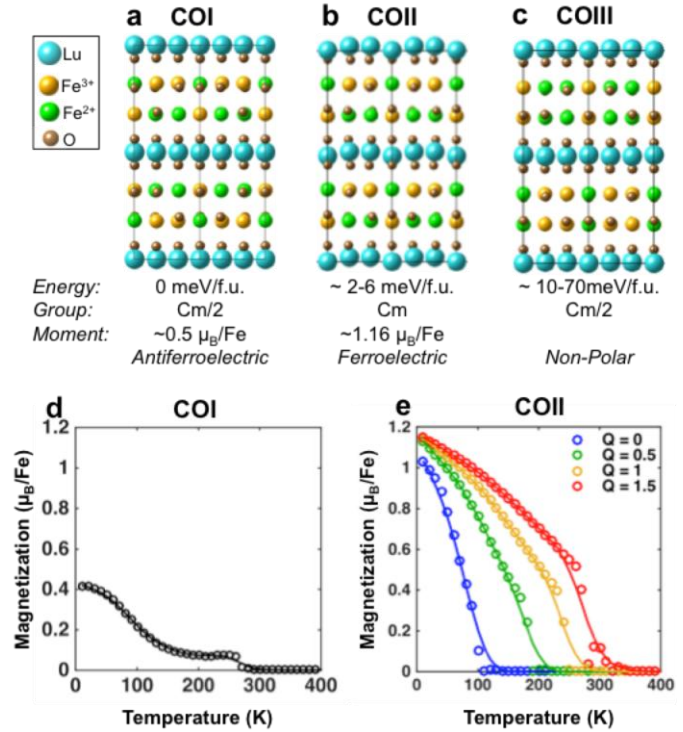


Fig. 3. First-principles calculations of the LuFe_2O_4 spin configuration. Monoclinic structures of LuFe_2O_4 for $\text{Fe}^{2+}/\text{Fe}^{3+}$ (a) antiferroelectric charge-ordered (CO) state (COI), (b) ferroelectric CO state (COII), (c) non-polar CO state (COIII), respectively. The energy of the structure is given in meV per formula unit for a range of Hubbard U values. (d) Calculated saturation magnetization per iron as a function of temperature for the ground state antiferroelectric COI state shown in (a). The magnetization saturates at $\sim 0.4 \mu_B/\text{Fe}$. (e) Calculated saturation magnetization per iron as a function of temperature for the ferroelectric COII state shown in (b). Q represents the amplitude of the atomic distortions from the high symmetry $R\bar{3}m$ structure. The magnetic transition temperature increases with the magnitude of the structural distortion associated with the ferroelectric state.

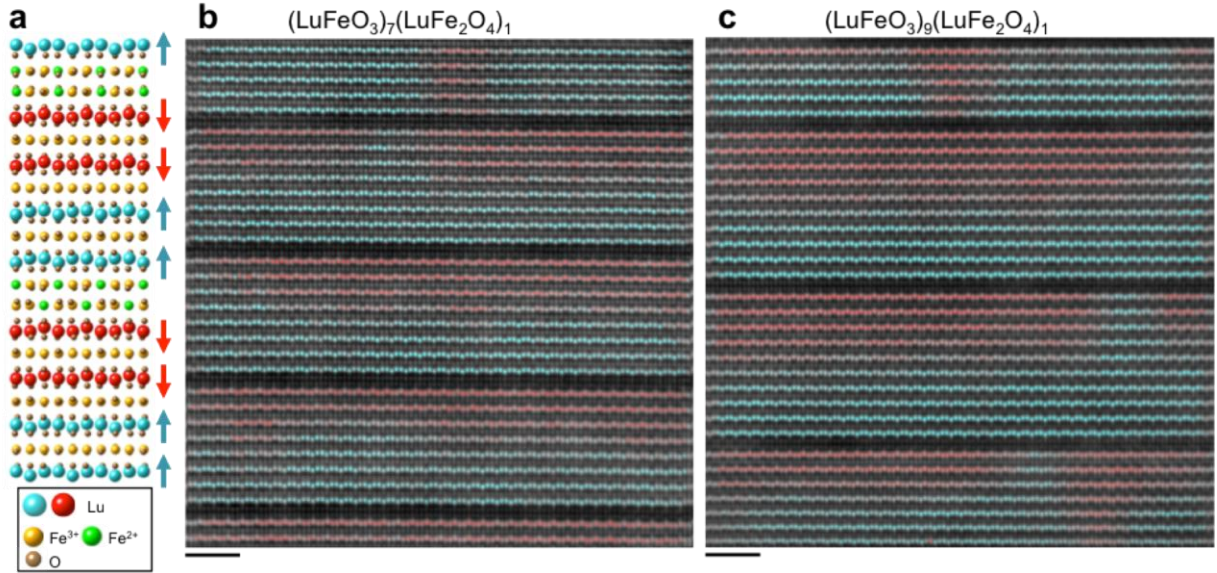


Fig. 4. Ferroelectric domain structure of $(\text{LuFeO}_3)_m(\text{LuFe}_2\text{O}_4)_1$ superlattices. ³⁺(a) First-principles calculations of the $(\text{LuFeO}_3)_3(\text{LuFe}_2\text{O}_4)_1$ superlattice found that the “Fe³⁺ doped” structure is the lowest in energy, where the LuFe_2O_4 layers are composed of a 2:1 ratio of Fe to Fe^{2+} cations as pictured in yellow and green, respectively. This structure aligns tail-to-tail domain walls at the LuFe_2O_4 layer positions. Lutetium atoms contributing to “up” polarization are plotted in turquoise and lutetium atoms contributing to “down” polarization are plotted in red. (b) and (c) show the experimental HAADF-STEM images of the $(\text{LuFeO}_3)_7(\text{LuFe}_2\text{O}_4)_1$ and $(\text{LuFeO}_3)_9(\text{LuFe}_2\text{O}_4)_1$, respectively. The images are colored according to the measured polarity. Tail-to-tail domain walls are observed at the LuFe_2O_4 layer positions.

magnetization.

HAADF-STEM images of the $m=7$ and $m=9$ superlattices are shown in Figs. 4(b) and 4(c). We observe a clear repetition of the tail-to-tail domain walls at the LuFe_2O_4 bilayers and meandering head-to-head walls in the LuFeO_3 blocks corresponding to the predicted structure for higher m . This domain architecture is not observed in the lower m superlattices, perhaps due to the stability of the COII structure for these layerings.

In summary, we have synthesized a series of compounds, $(\text{LuFeO}_3)_m(\text{LuFe}_2\text{O}_4)_1$ with $m \geq 2$, in which ferroelectricity enhances magnetism at all relevant length scales. The room-temperature ferroelectric polar distortions of the Lu-O planes enhance the ferromagnetic (or ferrimagnetic) transition temperature in the LuFe_2O_4 layers. This results in a structure that is strongly magnetically ordered with a T_C near room temperature that retains ferromagnetic fluctuations above room temperature. Moreover, precise atomic-layer engineering of the tail-to-tail domain walls to the LuFe_2O_4 further increases the magnetic moment.

III. FUTURE PLANS

Our renewal project has two research objectives, both of which relate to the better understanding of a new class of $A_{n+1}B_nO_{3n+1}$ Ruddlesden-Popper phases possessing a ferroic instability. Our first-principles calculations indicate that the ferroelectric vs. antiferroelectric alignment of neighboring polar slabs in $\text{Sr}_{n+1}\text{Ti}_n\text{O}_{3n+1}$ is nearly energetically degenerate,⁴⁵ The

first research objective of our project is to manipulate control parameters to create novel functionalities in a new family of ferroics. The near degeneracy between ferroelectric vs. antiferroelectric alignment of neighboring polar slabs in $\text{Sr}_{n+1}\text{Ti}_n\text{O}_{3n+1}$ ⁴⁵ begs the question of whether relaxor ferroelectricity can be created and systematically studied in this system without the chemical disorder^{46,47} or free surfaces⁴⁸ that are present in all known relaxor ferroelectrics. Our studies will go beyond strained $\text{Sr}_{n+1}\text{Ti}_n\text{O}_{3n+1}$ by considering the site-specific incorporation of species that lead to ferroelectric instabilities without strain, e.g., the introduction of calcium, barium, and lead into this general family to form ordered $(\text{Ca,Sr,Ba,Pb})_{n+1}\text{Ti}_n\text{O}_{3n+1}$ phases. These hypothetical phases containing calcium, barium, and lead are metastable. Nonetheless, we have already demonstrated that one such phase, $\text{BaSr}_2\text{Ti}_2\text{O}_7$, can be grown by MBE,⁴⁹ making it likely that we will be able to synthesize these novel phases. Intriguingly, our first-principles calculations reveal a nearly isotropic in-plane polarization of Pb_2TiO_4 under appropriate biaxial strain (about 0.7%).⁵⁰ This unusual energetic landscape is tantalizing in that it might give rise to an electrical analog of ferromagnetic resonance. Guided by theory, we will explore this and other unusual physical properties of these ordered $(\text{Ca,Sr,Ba,Pb})_{n+1}\text{Ti}_n\text{O}_{3n+1}$ phases. Our second research objective is to better understand the role of defects in these structures. The extremely low dielectric losses exhibited by the strained $\text{Sr}_{n+1}\text{Ti}_n\text{O}_{3n+1}$ phases that we have studied to date lead us to *hypothesize* that these Ruddlesden-Popper structures contain fewer point defects than their perovskite analogs.⁵¹ But is this true? We will assess this through experiments on ordered $(\text{Ca,Sr,Ba,Pb})_{n+1}\text{Ti}_n\text{O}_{3n+1}$ films vs. their perovskite analogs, SrTiO_3 , BaTiO_3 , and PbTiO_3 analyzed by scanning transmission electron microscopy (STEM) utilizing a new mixed-mode pixel array detector capable of imaging polarity, strain fields, and contrast and dechanneling from vacancies and interstitials. We will also study the defects by positron annihilation spectroscopy, phonon spectroscopy, and the frequency dependence of dielectric loss (especially in the GHz frequency regime). Theory is an integral part of interpreting these experiments.

IV. REFERENCES

- ¹ J.T. Heron, J.L. Bosse, Q. He, Y. Gao, M. Trassin, L. Ye, J.D. Clarkson, C. Wang, J. Liu, S. Salahuddin, D.C. Ralph, D.G. Schlom, J. Íñiguez, B.D. Huey, and R. Ramesh, “Deterministic Switching of Ferromagnetism at Room Temperature using an Electric Field,” *Nature* **516** (2014) 370–373.
- ² H. Das, A.L. Wysocki, Y. Geng, W. Wu, and C.J. Fennie, “Bulk Magnetoelectricity in the Hexagonal Manganites and Ferrites,” *Nature Communications* **5** (2013) 1–11.
- ³ T. Birol and C.J. Fennie, “Origin of Giant Spin-Lattice Coupling and the Suppression of Ferroelectricity in EuTiO_3 from First Principles,” *Phys. Rev. B* **88** (2013) 094103.
- ⁴ N.A. Benedek, A.T. Mulder, and C.J. Fennie, “Polar Octahedral Rotations: A Path to New Multifunctional Materials,” *J. Solid State Chem.* **195** (2012) 11–20.
- ⁵ A.T. Mulder, N.A. Benedek, J.M. Rondinelli, and C.J. Fennie, “Turning ABO_3 Antiferroelectrics into Ferroelectrics: Design Rules for Practical Rotation-Driven Ferroelectricity in Double Perovskites and $\text{A}_3\text{B}_2\text{O}_7$ Ruddlesden-Popper Compounds,” *Adv. Funct. Mater.* **23** (2013) 4810–4820.
- ⁶ H. Das, A.L. Wysocki, Y. Geng, W. Wu, and C.J. Fennie, “Bulk Magnetoelectricity in the Hexagonal Manganites and Ferrites,” *Nature Commun.* **5** (2014) 2998.
- ⁷ N.A. Benedek and C.J. Fennie, “Hybrid Improper Ferroelectricity: A Mechanism for Controllable Polarization-Magnetization Coupling,” *Phys. Rev. Lett.* **106** (2011) 107204.
- ⁸ M. Stengel, C.J. Fennie, and P. Ghosez, “Electrical Properties of Improper Ferroelectrics from First Principles,” *Physical Review B* **86** (2012) 094112.

- ⁹ T. Birol, N.A. Benedek, H. Das, A.L. Wysocki, A.T. Mulder, B.M. Abbett, E.H. Smith, S. Ghosh, and C.J. Fennie, “The magnetoelectric effect in transition metal oxides: Insights and the rational design of new materials from first principles,” *Current Opinion in Solid State & Materials Science* **16** (2012) 199-215.
- ¹⁰ N.A. Benedek and C.J. Fennie, “Why Are There So Few Perovskite Ferroelectrics?,” *The Journal Physical Chemistry C* **117** (2013) 13339–13349.
- ¹¹ C.M. Brooks, R. Misra, J.A. Mundy, L.A. Zhang, B.S. Holinsworth, K.R. O’Neal, T. Heeg, W. Zander, J. Schubert, J.L. Musfeldt, Z.K. Liu, D.A. Muller, P. Schiffer, and D.G. Schlom, “The Adsorption-Controlled Growth of LuFe₂O₄ by Molecular-Beam Epitaxy,” *Applied Physics Letters* **101** (2012) 132907.
- ¹² L.W. Martin and D.G. Schlom, “Advanced Synthesis Techniques and Routes to New Single-Phase Multiferroics,” *Current Opinion in Solid State and Materials Science* **16** (2012) 199–215.
- ¹³ P.J. Ryan, J.-W. Kim, T. Birol, P. Thompson, J.-H. Lee, X. Ke, P.S. Normile, E. Karapetrova, P. Schiffer, S.D. Brown, C.J. Fennie, and D.G. Schlom “Reversible Control of Magnetic Interactions by Electric Field in a Single-Phase Material,” *Nature Communications* **4** (2013) 1334.
- ¹⁴ X. Ke, T. Birol, R. Misra, J.-H. Lee, B.J. Kirby, D.G. Schlom, C.J. Fennie, and J.W. Freeland, “Structural Control of Magnetic Anisotropy in a Strain-Driven Multiferroic EuTiO₃ Thin Film,” *Physical Review B* **88** (2013) 094434.
- ¹⁵ J.A. Moyer, R. Misra, J.A. Mundy, C.M. Brooks, J.T. Heron, D.A. Muller, D.G. Schlom, and P. Schiffer, “Intrinsic Magnetic Properties of Hexagonal LuFeO₃ and the Effects of Nonstoichiometry,” *APL Materials* **2** (2014) 012106.
- ¹⁶ Y. Geng, H. Das, A.L. Wysocki, X. Wang, S.W. Cheong, M. Mostovoy, C.J. Fennie, and W. Wu, “Direct Visualization of Magnetoelectric Domains,” *Nature Materials* **13** (2014) 163–167.
- ¹⁷ B.S. Holinsworth, D. Mazumdar, C.M. Brooks, J.A. Mundy, H. Das, J.G. Cherian, S.A. McGill, C.J. Fennie, D.G. Schlom, and J.L. Musfeldt, “Direct Band Gaps in Multiferroic *h*-LuFeO₃,” *Applied Physics Letters* **106** (2015) 082902.
- ¹⁸ S.M. Disseler, J.A. Borchers, C.M. Brooks, J.A. Mundy, J.A. Moyer, D.A. Hillsberry, E.L. Thies, D.A. Tenne, J. Heron, M.E. Holtz, J.D. Clarkson, G.M. Stiehl, P. Schiffer, D.A. Muller, D.G. Schlom, and W.D. Ratcliff, “Magnetic Structure and Ordering of Multiferroic Hexagonal LuFeO₃,” *Physical Review Letters* **114** (2015) 217602.
- ¹⁹ J.A. Mundy, Y. Kumagai, M. Stengel, I.P. Krug, J. Schaab, D.M. Gottlob, H. Doganay, M. E. Holtz, R. Held, Z. Yan, E. Bourret, C.M. Schneider, D.G. Schlom, D.A. Muller, R. Ramesh, N.A. Spaldin, and D. Meier, “Local Electronic Reconstruction at Charged Domain Walls,” submitted to *Nature Nanotechnology*.
- ²⁰ A. Melville, T. Mairoser, A. Schmehl, T. Birol, T. Heeg, B. Holländer, J. Schubert, C.J. Fennie, and D.G. Schlom, “Effect of Film Thickness and Biaxial Strain on the Curie Temperature of EuO,” *Applied Physics Letters* **102** (2013) 062404.
- ²¹ Y. Zhu, A. Soukiassian, D.G. Schlom, D.A. Muller, and C. Dwyer, “Towards Artifact-Free Atomic-Resolution Elemental Mapping with Electron Energy-Loss Spectroscopy,” *Applied Physics Letters* **103** (2013) 141908.
- ²² R. Jany, C. Richter, C. Woltmann, G. Pfanzelt, B. Förg, M. Rommel, T. Reindl, U. Waizmann, J. Weis, J.A. Mundy, D.A. Muller, H. Boschker, and J. Mannhart, “Oxide Microelectronics: Monolithically Integrated Circuits from Functional Oxides,” *Advanced Materials Interfaces* **1** (2014) 1300031.
- ²³ J.A. Mundy, Y. Hikita, T. Hidaka, T. Yajima, T. Higuchi, H.Y. Hwang, D.A. Muller, and L.F. Kourkoutis, “Visualizing the Interfacial Evolution from Charge Compensation to Metallic Screening Across the Manganite Metal–Insulator Transition,” *Nature Communications* **5** (2014) 3464.
- ²⁴ T. Yajima, Y. Hikita, M. Minohara, C. Bell, J.A. Mundy, L.F. Kourkoutis, D.A. Muller, H. Kumigashira, M. Oshima, and H.Y. Hwang, “Controlling Band Alignments by Artificial Interface Dipoles at Perovskite Heterointerfaces,” *Nature Communications* **6** (2015) 6759.

- ²⁵ T. Mairoser, J.A. Mundy, A. Melville, D. Hodash, P. Cueva, R. Held, A. Glavic, J. Schubert, D.A. Muller, D.G. Schlom, and A. Schmehl, “High-Quality EuO Thin Films the Easy Way via Topotactic Transformation,” *Nature Communications* **6** (2015) 7716.
- ²⁶ C.M. Brooks, R.B. Wilson, A. Schäfer, J.A. Mundy, M.E. Holtz, D.A. Muller, J. Schubert, D.G. Cahill, and D.G. Schlom, “Tuning Thermal Conductivity in Homoepitaxial SrTiO₃ Films via Defects,” *Applied Physics Letters* **107** (2015) 051902.
- ²⁷ N. Ikeda, H. Ohsumi, K. Ohwada, K. Ishii, T. Inami, K. Kakurai, Y. Murakami, K. Yoshii, S. Mori, Y. Horibe, and H. Kito, “Ferroelectricity from Iron Valence Ordering in the Charge-Frustrated System LuFe₂O₄,” *Nature* **436** (2005) 1136–1138.
- ²⁸ A. Christianson, M. Lumsden, M. Angst, Z. Yamani, W. Tian, R. Jin, E. Payzant, S. Nagler, B. Sales, and D. Mandrus, “Three-Dimensional Magnetic Correlations in Multiferroic LuFe₂O₄,” *Phys. Rev. Lett.* **100** (2008) 107601.
- ²⁹ A. Ruff, S. Krohns, F. Schrettle, V. Tsurkan, P. Lunkenheimer, and A. Loidl, “Absence of Polar Order in LuFe₂O₄,” *Eur. Phys. J. B* **85** (2012) 290–296.
- ³⁰ D. Niermann, F. Waschkowski, J. de Groot, M. Angst, and J. Hemberger, “Dielectric Properties of Charge-Ordered LuFe₂O₄ Revisited: The Apparent Influence of Contacts,” *Phys. Rev. Lett.* **109**, (2012) 016405.
- ³¹ S. Lafuerza, J. García, G. Subías, J. Blasco, K. Conder, and E. Pomjakushina, “Intrinsic Electrical Properties of LuFe₂O₄,” *Phys. Rev. B* **88** (2013) 085130.
- ³² J. de Groot, K. Marty, M. Lumsden, A. Christianson, S. Nagler, S. Adiga, W. Borghols, K. Schmalzl, Z. Yamani, S. Bland, R. de Souza, U. Staub, W. Schweika, Y. Su, and M. Angst, “Competing Ferri- and Antiferromagnetic Phases in Geometrically Frustrated LuFe₂O₄,” *Phys. Rev. Lett.* **108** (2012) 037206.
- ³³ A.A. Bossak, I.E. Graboy, O.Y. Gorbenko, A.R. Kaul, M.S. Kartavtseva, V.L. Svetchnikov, and H.W. Zandbergen, “XRD and HREM Studies of Epitaxially Stabilized Hexagonal Orthoferrites RFeO₃ (R = Eu-Lu),” *Chem. Mater.* **16** (2004) 1751-1755.
- ³⁴ A.R. Akbashev, A.S. Semisalova, N.S. Perov, and A.R. Kaul, “Weak Ferromagnetism in Hexagonal Orthoferrites RFeO₃ (R=Lu, Er-Tb),” *Appl. Phys. Lett.* **99** (2011) 122502.
- ³⁵ W. Wang, J. Zhao, W. Wang, Z. Gai, N. Balke, M. Chi, H. N. Lee, W. Tian, L. Zhu, X. Cheng, D. J. Keavney, J. Yi, T. Z. Ward, P. C. Snijders, H. M. Christen, W. Wu, J. Shen, and X. Xu, “Room-Temperature Multiferroic Hexagonal LuFeO₃ Films,” *Phys. Rev. Lett.* **110** (2013) 237601.
- ³⁶ E. Magome, C. Moriyoshi, Y. Kuroiwa, A. Masuno, and H. Inoue, “Noncentrosymmetric Structure of LuFeO₃ in Metastable State,” *Jpn. J. Appl. Phys.* **49** (2010) 09ME06.
- ³⁷ L. Keeney, T. Maity, M. Schmidt, A. Amann, N. Deepak, N. Petkov, S. Roy, M.E. Pemble, and R.W. Whatmore, “Magnetic Field-Induced Ferroelectric Switching in Multiferroic Aurivillius Phase Thin Films at Room Temperature,” *J. Am. Ceram. Soc.* **96** (2013) 2339–2357.
- ³⁸ D.M. Evans, A. Schilling, A. Kumar, D. Sanchez, N. Ortega, M. Arredondo, R.S. Katiyar, J.M. Gregg, and J.F. Scott, “Magnetic Switching of Ferroelectric Domains at Room Temperature in Multiferroic PZTFT,” *Nature Communications* **4** (2013) 1534–1537.
- ³⁹ E.-M. Choi, T. Fix, A. Kursumovic, C.J. Kinane, D. Arena, S.-L. Sahonta, Z. Bi, J. Xiong, L. Yan, J.-S. Lee, H. Wang, S. Langridge, Y.-M. Kim, A.Y. Borisevich, I. MacLaren, Q.M. Ramasse, M.G. Blamire, Q. Jia, and J.L. MacManus-Driscoll, “Room Temperature Ferrimagnetism and Ferroelectricity in Strained, Thin Films of BiFe_{0.5}Mn_{0.5}O₃,” *Adv. Funct. Mater.* **24** (2014) 7478–7487.
- ⁴⁰ K.I. Doig, J.J.P. Peters, S. Nawaz, D. Walker, M. Walker, M.R. Lees, R. Beanland, A.M. Sanchez, C.F. McConville, V.R. Palkar, and J. Lloyd-Hughes, “Structural, Optical and Vibrational Properties of Self-Assembled Pb_{n+1}(Ti_{1-x}Fe_x)_nO_{3n+1-δ} Ruddlesden-Popper Superstructures,” *Sci. Rep.* **5** (2015) 7719.
- ⁴¹ V.V. Roddatis, A.R. Akbashev, S. Lopatin, and A.R. Kaul, “Complex Structural-Ferroelectric Domain Walls in Thin Films of Hexagonal Orthoferrites RFeO₃ (R = Lu, Er),” *Appl. Phys. Lett.* **103** (2013) 112907.

- ⁴² Q.H. Zhang, L.J. Wang, X.K. Wei, R.C. Yu, L. Gu, A. Hirata, M.W. Chen, C.Q. Jin, Y. Yao, Y.G. Wang, and X.F. Duan, “Direct Observation of Interlocked Domain Walls in Hexagonal $RMnO_3$ ($R=Ti, Lu$),” *Phys. Rev. B* **85** (2012) 020102.
- ⁴³ M.-G. Han, Y. Zhu, L. Wu, T. Aoki, V. Volkov, X. Wang, S.C. Chae, Y.S. Oh, and S.-W. Cheong, “Ferroelectric Switching Dynamics of Topological Vortex Domains in a Hexagonal Manganite,” *Adv. Mater.* **25** (2013) 2415–2421.
- ⁴⁴ T. Matsumoto, R. Ishikawa, T. Tohei, H. Kimura, Q. Yao, H. Zhao, X. Wang, D. Chen, Z. Cheng, N. Shibata, and Y. Ikuhara, “Multivariate Statistical Characterization of Charged and Uncharged Domain Walls in Multiferroic Hexagonal $YMnO_3$ Single Crystal Visualized by a Spherical Aberration-Corrected STEM,” *Nano Lett.* **13** (2013) 4594–4601.
- ⁴⁵ T. Birol, N.A. Benedek, and C.J. Fennie, “Interface Control of Emergent Ferroic Order in Ruddlesden-Popper $Sr_{n+1}Ti_nO_{3n+1}$,” *Phys. Rev. Lett.* **107** (2011) 257602.
- ⁴⁶ L.E. Cross, “Relaxor Ferroelectrics,” *Ferroelectrics* **76** (1987) 241–267.
- ⁴⁷ A.A. Bokov and Z.G. Ye, “Recent Progress in Relaxor Ferroelectrics with Perovskite Structure,” *J. Mater. Sci.* **41** (2006) 31–52.
- ⁴⁸ B. Meyer and D. Vanderbilt, “*Ab Initio* Study of $BaTiO_3$ and $PbTiO_3$ Surfaces in External Electric Fields,” *Phys. Rev. B* **63** (2001) 205426.
- ⁴⁹ D.G. Schlom, J.H. Haeni, C.D. Theis, W. Tian, X.Q. Pan, G.W. Brown, and M.E. Hawley, “The Importance of *in situ* Monitors in the Preparation of Layered Oxide Heterostructures by Reactive MBE,” *Recent Developments in Oxide and Metal Epitaxy—Theory and Experiment* edited by M. Yeadon, S. Chiang, R.F.C. Farrow, J.W. Evans, and O. Auciello, Vol. 619 (Materials Research Society, Warrendale, 2000), pp. 105–114.
- ⁵⁰ C. Fennie and K. Rabe, “First-Principles Investigation of Ferroelectricity in Epitaxially Strained Pb_2TiO_4 ,” *Phys. Rev. B* **71** (2005) 100102.
- ⁵¹ C.H. Lee, N.D. Orloff, T. Birol, Y. Zhu, V. Goian, E. Rocas, R. Haislmaier, E. Vlahos, J.A. Mundy, L.F. Kourkoutis, Y. Nie, M.D. Biegalski, J. Zhang, M. Bernhagen, N.A. Benedek, Y. Kim, J.D. Brock, R. Uecker, X.X. Xi, V. Gopalan, D. Nuzhnyy, S. Kamba, D.A. Muller, I. Takeuchi, J.C. Booth, C.J. Fennie, and D.G. Schlom, “Exploiting Dimensionality and Defect Mitigation to Create Tunable Microwave Dielectrics,” *Nature* **502** (2013) 532–536.

V. PUBLICATIONS RESULTING FROM THIS WORK

1. M. Stengel, **C.J. Fennie**, and P. Ghosez, “Electrical Properties of Improper Ferroelectrics from First Principles,” *Physical Review B* **86** (2012) 094112.
2. C.M. Brooks, R. Misra, J.A. Mundy, L.A. Zhang, B.S. Holinsworth, K.R. O’Neal, T. Heeg, W. Zander, J. Schubert, J.L. Musfeldt, Z.K. Liu, **D.A. Muller**, **P. Schiffer**, and **D.G. Schlom**, “The Adsorption-Controlled Growth of $LuFe_2O_4$ by Molecular-Beam Epitaxy,” *Applied Physics Letters* **101** (2012) 132907.
3. T. Birol, N.A. Benedek, H. Das, A.L. Wysocki, A.T. Mulder, B.M. Abbett, E.H. Smith, S. Ghosh, and **C.J. Fennie**, “The magnetoelectric effect in transition metal oxides: Insights and the rational design of new materials from first principles,” *Current Opinion in Solid State & Materials Science* **16** (2012) 227–242.
4. L.W. Martin and **D.G. Schlom**, “Advanced Synthesis Techniques and Routes to New Single-Phase Multiferroics,” *Current Opinion in Solid State and Materials Science* **16** (2012) 199–215.
5. N.A. Benedek, A.T. Mulder, and **C.J. Fennie**, “Polar Octahedral Rotations: A Path to New Multifunctional Materials,” *Journal of Solid State Chemistry* **195** (2012) 11–20.
6. P.J. Ryan, J.-W. Kim, T. Birol, P. Thompson, J.-H. Lee, X. Ke, P.S. Normile, E. Karapetrova, **P. Schiffer**, S.D. Brown, **C.J. Fennie**, and **D.G. Schlom**, “Reversible Control of Magnetic Interactions by Electric Field in a Single-Phase Material,” *Nature Communications* **4** (2013) 1334.

7. A. Melville, T. Mairoser, A. Schmehl, T. Birol, T. Heeg, B. Holländer, J. Schubert, **C.J. Fennie**, and **D.G. Schlom**, “Effect of Film Thickness and Biaxial Strain on the Curie Temperature of EuO,” *Applied Physics Letters* **102** (2013) 062404.
8. N.A. Benedek and **C.J. Fennie**, “Why Are There So Few Perovskite Ferroelectrics?,” *The Journal Physical Chemistry C* **117** (2013) 13339–13349. Featured on the Cover of the July 4, 2013 issue.
9. T. Birol and **C.J. Fennie**, “Origin of Giant Spin-Lattice Coupling and the Suppression of Ferroelectricity in EuTiO₃ from First Principles,” *Physical Review B* **88** (2013) 094103.
10. X. Ke, T. Birol, R. Misra, J.-H. Lee, B.J. Kirby, **D.G. Schlom**, **C.J. Fennie**, and J.W. Freeland, “Structural Control of Magnetic Anisotropy in a Strain-Driven Multiferroic EuTiO₃ Thin Film,” *Physical Review B* **88** (2013) 094434.
11. Y. Zhu, A. Soukiassian, **D.G. Schlom**, **D.A. Muller**, and C. Dwyer, “Towards Artifact-Free Atomic-Resolution Elemental Mapping with Electron Energy-Loss Spectroscopy,” *Applied Physics Letters* **103** (2013) 141908.
12. A.T. Mulder, N.A. Benedek, J.M. Rondinelli, and **C.J. Fennie**, “Turning ABO₃ Antiferroelectrics into Ferroelectrics: Design Rules for Practical Rotation-Driven Ferroelectricity in Double Perovskites and A₃B₂O₇ Ruddlesden-Popper Compounds,” *Advanced Functional Materials* **23** (2013) 4810–4820.
13. H. Das, A.L. Wysocki, Y. Geng, W. Wu, and **C.J. Fennie**, “Bulk Magnetoelectricity in the Hexagonal Manganites and Ferrites,” *Nature Communications* **5** (2014) 2998.
14. J.A. Moyer, R. Misra, J.A. Mundy, C.M. Brooks, J.T. Heron, **D.A. Muller**, **D.G. Schlom**, and **P. Schiffer**, “Intrinsic Magnetic Properties of Hexagonal LuFeO₃ and the Effects of Nonstoichiometry,” *APL Materials* **2** (2014) 012106.
15. Y. Geng, H. Das, A.L. Wysocki, X. Wang, S.W. Cheong, M. Mostovoy, **C.J. Fennie**, and W. Wu, “Direct Visualization of Magnetoelectric Domains,” *Nature Materials* **13** (2014) 163–167.
16. R. Jany, C. Richter, C. Woltmann, G. Pfanzelt, B. Förg, M. Rommel, T. Reindl, U. Waizmann, J. Weis, J.A. Mundy, **D.A. Muller**, H. Boschker, and J. Mannhart, “Oxide Microelectronics: Monolithically Integrated Circuits from Functional Oxides,” *Advanced Materials Interfaces* **1** (2014) 1300031. Featured on inside cover of the February 13, 2014 issue.
17. J.A. Mundy, Y. Hikita, T. Hidaka, T. Yajima, T. Higuchi, H.Y. Hwang, **D.A. Muller**, and L.F. Kourkoutis, “Visualizing the Interfacial Evolution from Charge Compensation to Metallic Screening Across the Manganite Metal–Insulator Transition,” *Nature Communications* **5** (2014) 3464.
18. B.S. Holinsworth, D. Mazumdar, C.M. Brooks, J.A. Mundy, H. Das, J.G. Cherian, S.A. McGill, **C.J. Fennie**, **D.G. Schlom**, and J.L. Musfeldt, “Direct Band Gaps in Multiferroic *h*-LuFeO₃,” *Applied Physics Letters* **106** (2015) 082902.
19. T. Yajima, Y. Hikita, M. Minohara, C. Bell, J.A. Mundy, L.F. Kourkoutis, **D.A. Muller**, H. Kumigashira, M. Oshima, and H.Y. Hwang, “Controlling Band Alignments by Artificial Interface Dipoles at Perovskite Heterointerfaces,” *Nature Communications* **6** (2015) 6759.
20. S.M. Disseler, J.A. Borchers, C.M. Brooks, J.A. Mundy, J.A. Moyer, D.A. Hillsberry, E.L. Thies, D.A. Tenne, J. Heron, M.E. Holtz, J.D. Clarkson, G.M. Stiehl, **P. Schiffer**, **D.A. Muller**, **D.G. Schlom**, and W.D. Ratcliff, “Magnetic Structure and Ordering of Multiferroic Hexagonal LuFeO₃,” *Physical Review Letters* **114** (2015) 217602.
21. T. Mairoser, J.A. Mundy, A. Melville, D. Hodash, P. Cueva, R. Held, A. Glavic, J. Schubert, **D.A. Muller**, **D.G. Schlom**, and A. Schmehl, “High-Quality EuO Thin Films the Easy Way via Topotactic Transformation,” *Nature Communications* **6** (2015) 7716.
22. C.M. Brooks, R.B. Wilson, A. Schäfer, J.A. Mundy, M.E. Holtz, **D.A. Muller**, J. Schubert, D.G. Cahill, and **D.G. Schlom**, “Tuning Thermal Conductivity in Homoepitaxial SrTiO₃ Films via Defects,” *Applied Physics Letters* **107** (2015) 051902.

In Situ Thermodynamics and Kinetics of Mixed-Valence Inorganic Crystal Formation

Daniel P. Shoemaker
Materials Science and Engineering Department
University of Illinois at Urbana-Champaign, Urbana, IL 61801

Program Scope

We are developing efficient routes to discover inorganic materials that straddle the semiconducting regime while we map their energy landscape experimentally and computationally. Our ability to move through chemical and thermal space in situ is accomplished by our in-house capillary diffraction setup, shown schematically in Figure 1. We are free to run reactions of any duration, which is a distinct departure from user facilities. Gas flow capability will allow us to conduct synthesis and metathesis reactions that move this beyond an observational study and into the realm of control. Concurrently, we will establish sets of best practices for utilizing computational genome-based tools for high-throughput prediction of enthalpies to guide synthesis.

As representative systems we will test hypotheses of phase formation in light-absorbing semiconductors in the Fe–Si–S and Ba–Fe–S systems. First, we seek to verify whether new non-magnetic phases exist in this phase space that contain FeS_6 octahedra. Second, we believe that valence stability in these phases, which is known to be a serious problem in pyrite FeS_2 , [1] is highly dependent on the crystal structure of each individual phase, and not mandatory for the Fe^{2+} ion. We will test this hypothesis by strong reduction and sulfidization in situ. This route to investigate valence stability has applications in many systems, notably chalcogenide semiconductors and transparent conducting oxides. We will conduct gas flow reactions to probe the thermodynamics and kinetics of valence stability. Current theory is outmatched by this problem and will be informed by our experiments.

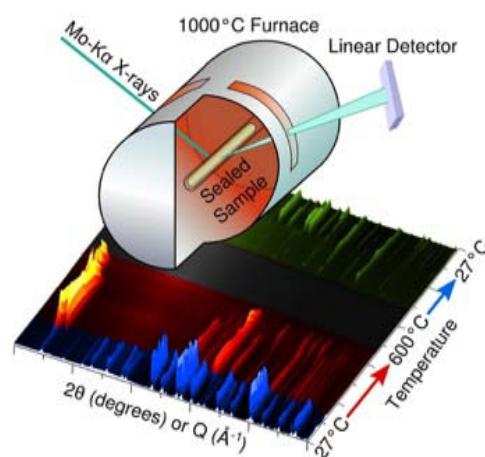


Figure 1. Schematic of our in-house setup for encapsulated materials synthesis with transmission X-ray diffraction.

Our experimental efforts interface with computation on two fronts. First, exploratory synthesis parallels the genetic-algorithm searches by programs such as USPEX, [2] which offloads enthalpy calculations to DFT. Our preliminary work has shown us that this approach, while valuable in some systems, has notable drawbacks for transition metal compounds and those with relatively flat energy landscapes. Our attention now turns to prediction of *which systems* will benefit from this approach, rather than individual phases.. Second, big-data genomic

approaches such as the Materials Project [3] provide a new and convenient framework to track and compare enthalpy values during reactions and find routes to new compounds. The scope of this work is to understand how to efficiently leverage the vast amount of thermodynamic data that is available. In this sense, finding the proper reagents for a synthesis is a genomic task, and so is uncovering fertile ground for the genetic algorithm approach.

Recent Progress

Two in situ furnaces are necessary for this work. A uniform “oven” type furnace that slides over a capillary, and a fast-heating furnace that permits gas flow through the capillary. First, we optimized the geometry of our existing oven furnace to remove scattering contributions from the thermal insulation and the Soller slits, by trimming and masking the insulation and machining a custom anti-scatter slit. The resulting “empty” run is shown in Figure 2, with multiple steps in the process shown. We now have a clean background, with substantially improved signal-to-noise and clear resolution of even very minor phases that nucleate in our in situ reactions. Second, we have begun machining a Chupas-style flow furnace for our in-house diffractometer. [4] This is not a straightforward task since the gap between the goniometer mount and the sample is quite short in our instrument, which necessitated a redesign of the gas inlet block.

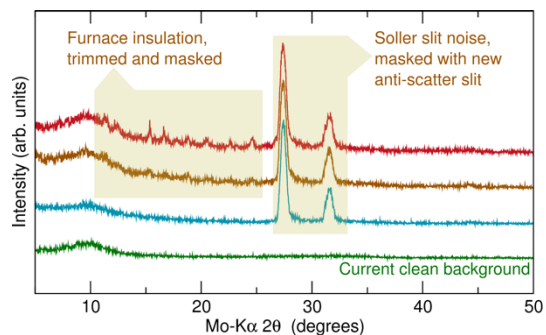


Figure 2. Our commercial in situ furnace produced noise from spurious Bragg peaks from insulation and the Soller slits, which we have trimmed and masked to give the clean background in the bottom pattern.

In our previous work doing in situ characterization at beamlines, [5] the inability to efficiently program and log the in situ reaction temperature impaired our ability to monitor long experiments, or those with complex or fast heating and cooling steps. We have designed an experimental suite to program the furnace setpoint, log temperature, and collect diffraction data simultaneously on the fly on our in-house system. We expect that these capabilities will be extended to any beamlines (e.g. APS 17-BM) where a similar furnace is used but not yet interfaced with an automatic logging system.

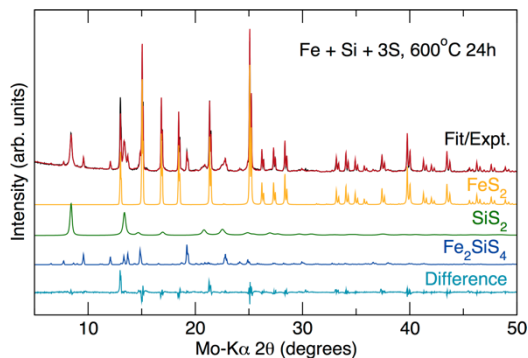


Figure 3. Preliminary ex situ synthesis in the Fe—Si—S system shows strong kinetic tendency to form binary phases, which we will engineer in subsequent in situ reactions.

Our first synthetic work on the Fe—Si—S system has shown very strong kinetic effects, which is an encouraging signature of multiple synthetic routes to new phases in this and related systems. For the target phase Fe_2SiS_4 , it may be expected that heating

to relatively high temperatures, such as 600°C, would lead to formation of the thermodynamic ground state. Instead, we found that SiS_2 forms quickly and is so kinetically sluggish that it prevents formation of a stoichiometric amount of Fe_2SiS_4 , resulting in the diffraction pattern in Figure 3. Instead, the prereaction of $\text{Fe} + 2\text{S}$ to form FeS_2 , followed by subsequent reaction by Si , should be an effective route to pure Fe_2SiS_4 . [6]

Future Plans

To search for new phases and verify the predicted ternary phase diagram from calculated enthalpies, we will conduct two investigations of the Fe–Si–S system, with the ternary phase diagram shown in Figure 4. First, a “classical” equilibrium study with long annealing times and slow cooling will be performed in situ. Second, a kinetic phase diagram starting from FeS_2 , $\text{FeS}_{1-\delta}$, and elemental Si will show how these phases respond without the fast initial formation of the parasitic phase SiS_2 . This technique of selectively flattening the energy landscape will be examined starting from other points on the edges of the ternary space (e.g. FeSi , FeSi_2 , etc.). Probing for new phases will occur in at least 8 composition points, shown as (+) marks in Figure 4. Our method of in situ synthesis is also vastly more informative than experiments that search for metastable compounds by quenching reactions for post-mortem characterization.

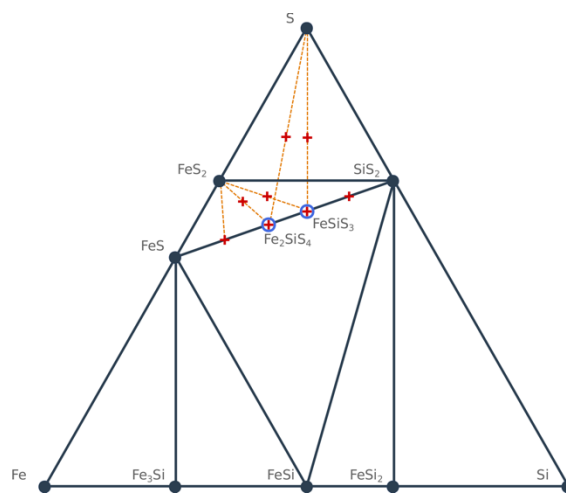


Figure 4. Only the filled, solid points in the Fe–Si–S phase diagram appear in the thermodynamic literature. Open-circled phases are calculated to be unstable by the Materials Project. Note that, despite being experimentally accessible, the olivine phase Fe_2SiS_4 is calculated to be $\Delta H = +0.27$ eV/atom above the hull (unstable).

Our preliminary computational work began with the intent to predict new target compounds with genetic algorithms. We have since found that the computation is actually significantly *slower* than experiment in the current implementation. This is an opportunity for our group to use our synthetic expertise to identify model synthetic systems where the predictive approach can be validated, before extending it to unknown systems. While the potential for USPEX searches to contribute to synthesis remains, there is no consensus on how accurate the enthalpy calculations must be to return value to the process, or even if ΔH alone constrains the process. Fe_2SiS_4 and Fe_7S_8 , among others, are calculated to be as much as 0.5 eV above the hull (unstable), but these phases are in fact easily synthesized. This may be due to entropic or kinetic contributions or errors in the DFT-calculated enthalpy. In any case, our experimental calorimetric and isothermal in situ kinetic data will answer these questions and define the next steps in computationally-assisted synthesis.

References

1. D. S. Tannhauser. Conductivity in iron oxides. *J. Phys. Chem. Solids*, 23(12):25–34, 1962.
2. C. W. Glass, A. R. Oganov, and N. Hansen. USPEX—evolutionary crystal structure prediction. *Comput. Phys. Commun.*, 175(1112):713–720, 2006.
3. A. Jain, S. P. Ong, G. Hautier, W. Chen, W. D. Richards, S. Dacek, S. Cholia, D. Gunter, D. Skinner, G. Ceder, and K. A. Persson. The Materials Project: A materials genome approach to accelerating materials innovation. *APL Mater.*, 1(1):011002, 2013.
4. P. J. Chupas, K. W. Chapman, C. Kurtz, J. C. Hanson, P. L. Lee, and C. P. Grey. A versatile sample-environment cell for non-ambient x-ray scattering experiments. *J. Appl. Cryst.*, 41(4):822–824, 2008.
5. D. P. Shoemaker, Y.-J. Hu, D. Y. Chung, G. J. Halder, P. J. Chupas, L. Soderholm, J. F. Mitchell, and M. G. Kanatzidis. In situ studies of a platform for metastable inorganic crystal growth and materials discovery. *Proc. Nat. Acad. Sci.*, 111(30):10922–10927, 2014.
6. T. Ericsson, K. Holényi, Ö. Amcoff. A Mössbauer study of Fe_2SiS_4 , having the olivine structure: comparison with fayalite and related minerals. *J. Phys. Condens. Matter*, 9: 3943, 1997)

Discovery and Crystal Growth of New Oxide Phases from Metal Fluxes

T. Siegrist

Department of Chemical and Biomedical Engineering

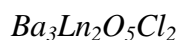
Florida State University, Tallahassee, FL 32310

Program Scope

Discovery and growth of crystalline materials is one of the key areas in materials research. New materials, and engineering of their properties, have produced tremendous progress; and the search for new materials with novel properties remains an ongoing activity. Of the many oxide single crystal growth methods, flux growth has proven to be an excellent method for exploratory synthesis work that also will yield crystals large enough for structural and physical characterization. Using metal fluxes to grow oxide phases produces a unique crystal growth environment, where oxygen is now a minority constituent. The low melting point of certain metal fluxes in use allows low temperature synthesis, and gives access to potentially metastable and hard to crystallize phases. We are investigating single crystal oxide growth from alkaline earth metal fluxes, where the sizable oxygen solubility as well as good solubility of lanthanides is used to discover new phases. The reactivity of the flux can be tailored to provide reducing conditions for oxide growth by using alkaline earth mixtures, or the flux material can also be incorporated into the oxide. Especially the low temperature eutectic mixtures of magnesium with calcium, strontium and barium provide control not only over crystal growth temperatures, but also the reactivity of the flux and its power to reduce lanthanide oxides. Furthermore, alkaline earth metal fluxes have simultaneous solubility for oxides, halides, and chalcogenides, and new multi-anion phases have been synthesized.

Recent Progress

Our research activities resulted in the discovery of new phases in the $Ba_3Ln_2O_5Cl_2$ system, with Ln a lanthanide ion from Sm to Lu. The ferromagnetic semiconductor EuO was investigated further to optimize the crystal growth and control the inclusion of barium into the Eu sublattice. The magnetic properties of a series of crystals were measured.



The alkaline earth metal fluxes are found to have sufficient solubility for halides, allowing the crystallization of new oxyhalide phases. Similar to the recently discovered

oxytelluride, $\text{Ba}_3\text{Yb}_2\text{O}_5\text{Te}$, both systems contain perovskite-like $\text{Ba}_2\text{Ln}_2\text{O}_5$ double-pyramidal layers.¹ In contrast to $\text{Ba}_3\text{Yb}_2\text{O}_5\text{Te}$, where so far, only the Yb and Lu phases could be synthesized, the $\text{Ba}_3\text{Ln}_2\text{O}_5\text{Cl}_2$ system accommodates a larger range of lanthanides, from Sm to Lu. Here, the lanthanide is on the perovskite B-site, and structurally, it is a highly strained configuration. These layers are separated by BaCl_2 layers, which help to stabilize the perovskite-type layers. The presence of the BaCl_2 layers separates the magnetic lanthanides, so that their magnetic behavior is that of a square lattice. $\text{Ba}_3\text{Gd}_2\text{O}_5\text{Cl}_2$ has an antiferromagnetic phase transition at low temperatures, at $T_N=2\text{K}$, which is expected to be the highest transition temperature in the series. The structural study is almost complete, and the magnetic susceptibility measurements are in progress.

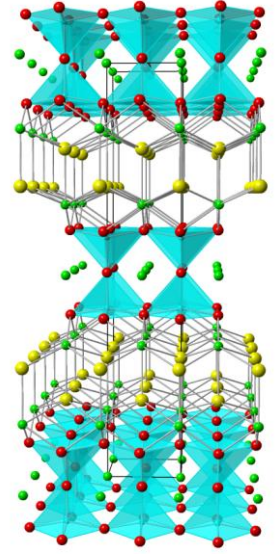


Figure 1: $\text{Ba}_3\text{Ln}_2\text{O}_5\text{Cl}_2$ structure

Europium Oxide, EuO

Among ferromagnetic semiconductors, EuO is one of the first compounds that were discovered, and investigated in detail.² The simple rock-salt structure of EuO makes this material a model compound to study magnetic interactions. In addition, the highly coupled electronic and magnetic interactions give rise to properties that reflect this coupling. For instance, the ferromagnetic order changes the electronic band structure, splitting into spin up and spin down bands.

Crystal growth of EuO is usually performed at high temperatures ($>2000\text{C}$) using excess Eu in sealed tungsten crucibles.³ Here, we demonstrate a low temperature growth method for EuO , using a barium/magnesium flux and Eu_2O_3 . The reactivity of the flux is tailored via its Mg content, to reduce Eu_2O_3 to EuO . Single crystal growth is achieved at temperatures below 1000C , with some inclusion of Ba

into the EuO , forming $(\text{Eu},\text{Ba})\text{O}$. The Ba inclusion depends on the Mg content of the flux, with increasing Mg lowering the Ba inclusion.

The system $(\text{Eu},\text{Ba})\text{O}$ was investigated for its magnetic properties: susceptibility and M-H loops were measured for all crystals along the $[100]$ direction. The magnetic properties depend linearly on the Ba content, with the ferromagnetic Curie temperature T_c decreasing with increasing Ba content (Figure 2). All crystals showed universal behavior when scaled to a reduced temperature T/T_c and reduced magnetic susceptibility, demonstrating that the magnetic interactions scale linearly with the Ba content. However, the ferromagnetic T_c as determined by

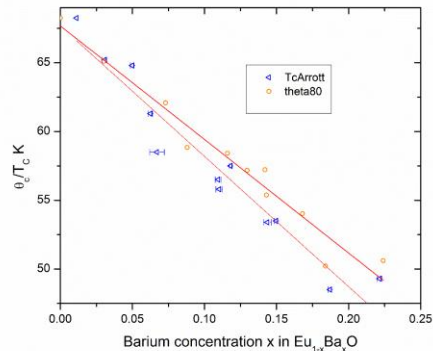


Figure 2: $\text{Eu}_{1-x}\text{Ba}_x\text{O}$ ferromagnetic ordering temperature vs Ba concentration.

Arrott-plots and the high temperature exchange determined from the Weiss constant show that the fluctuations differ at high Ba concentrations. Doping of (Eu,Ba)O was attempted, but so far, all crystals are highly insulating.

Ba₂TeO

A new oxytelluride was synthesized using molten Ba metal flux, with a simple structure closely related to PbFCl.⁴ Ba₂TeO is comprised of alternating inverse PbO-type BaO layers and slightly puckered NaCl-type BaTe layers. The Ba₂O₂-type layer can also be considered as a strongly puckered NaCl-layer, and the structure is a combination of a Ba₂O₂ layer and two BaTe layers (Figure 3). Insulating behavior is observed: an optical band gap of 3eV is found.

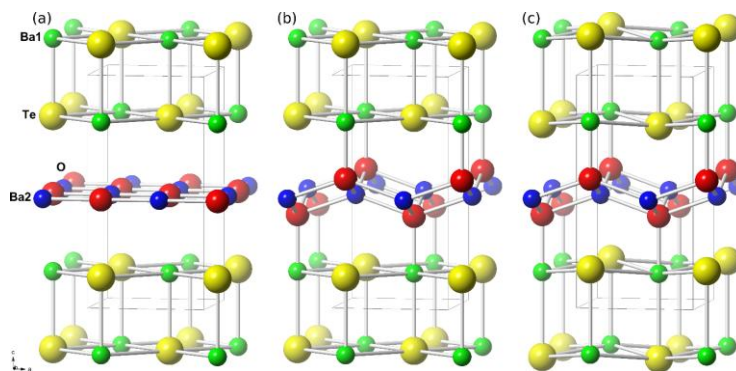


Figure 3: (a) Ideal structure of layered BaO and BaTe, (b) structure where the oxygen atoms have moved, and finally (c) the actual structure of Ba₂TeO with puckered BaTe layers.

SmMg₂Bi₂ and SmMg₂Sb₂

We have grown the new compounds SmMg₂Sb₂ and SmMg₂Bi₂ as single crystals from a molten flux.⁵ The two crystals contain samarium in the divalent Sm²⁺ state; as determined from magnetic measurements. The electronic properties of these materials show that they are p-type materials with a low electron density, making them potential thermoelectric materials. The synthesis of the materials is performed in a magnesium-rich flux to engineer the reducing conditions needed for stabilization of Sm²⁺. Magnetic, electronic and thermal properties have been measured to determine the electronic ground state of the material and to confirm that the valence of Sm is indeed 2+, since the stabilization of divalent samarium in a molten metal flux is unprecedented. The flux was engineered to provide the reducing conditions by adjusting the magnesium content. Understanding how to access Sm²⁺ broadens the availability of chemical constituents in various materials.

Future Plans

Ba₃Ln₂O₅Cl₂

The series of lanthanide phases of Ba₃Ln₂O₅Cl₂ will be characterized for their magnetic properties. Potentially, magnetic 2-dimensional behavior will be looked for, since the structure

separates Ba₂Ln₂O₅ double-pyramidal perovskite-type layers by BaCl₂ layers. These phases are reasonably stable in the ambient.

LnOCl, LnOBr

The oxychlorides of lanthanides are used as host materials for optical down conversion and luminescent materials in solid state lighting applications.⁶ However, of the lanthanide series, only a few oxychlorides have been prepared as single crystals. Using alkaline earth fluxes, BaO as oxygen source and FeCl₃ as chlorine source, it was possible to grow, for the first time, single crystals for most of the LnOCl. We plan to investigate DyOCl for its low temperature magnetic properties since crystal field effects may provide an anisotropic g-factor resulting in Ising behavior. Oxybromide growth will be pursued to investigate the phase stability and crystal growth of LnOBr. Optical characterization of these systems is planned.

New flux compositions

New flux compositions with transition elements added are investigated. Recent experiments using Ba/Cu fluxes look promising, where the oxygen solubility is maintained. In addition, a Mg rich flux shows good solubility for phosphorus concurrent with oxygen. In this way, a different route to phosphides is possible that does not use the transitional tin flux. We plan to explore lanthanide oxyphosphide phases, and study their magnetic properties. Extension to arsenic is considered.

References

1. Whalen, J.B., Besara, T., Vasquez, R., Herrera, E., Sun, J., Ramirez, D., Stillwell, R.L., Tozer, S.W., Tokumoto, T.D., McGill, S.A., Allen, J., Davidson, M., and Siegrist, T., *A new oxytelluride: Perovskite and CsCl intergrowth in Ba₃Yb₂O₅Te*. Journal of Solid State Chemistry, **203**, 204-211 (2013).
2. Matthias, B.T., Bozorth, R.M., and Van Vleck, J.H., *Ferromagnetic Interaction in EuO*. Physical Review Letters, **7**(5), 160-161 (1961).
3. Reed, T.B. and Fahey, R.E., *Growth of EuO, EuS, EuSe and EuTe Single Crystals*. Journal of Crystal Growth, **8**(4), 337-341 (1971).
4. Besara, T., Ramirez, D., Sun, J., Whalen, J.B., Tokumoto, T.D., McGill, S.A., Singh, D.J., and Siegrist, T., *Ba₂TeO: A new layered oxytelluride*. Journal of Solid State Chemistry, **222**, 60-65 (2015).
5. Ramirez, D., Gallagher, A., Baumbach, R., and Siegrist, T., *Synthesis and characterization of the divalent samarium Zintl-phases SmMg₂Bi₂ and SmMg₂Sb₂*. Journal of Solid State Chemistry, **231**, 217-222 (2015).
6. Brixner, L.H., Ackerman, J.F., and Foris, C.M., *Rare-Earth Fluorescence In Some LnOCl Type Hosts*. Journal of Luminescence, **26**(1-2), 1-19 (1981).

Publications

1. Whalen, J.B., Besara, T., Vasquez, R., Herrera, E., Sun, J., Ramirez, D., Stillwell, R.L., Tozer, S.W., Tokumoto, T.D., McGill, S.A., Allen, J., Davidson, M., and Siegrist, T., *A new oxytelluride: Perovskite and CsCl intergrowth in $Ba_3Yb_2O_5Te$* . Journal of Solid State Chemistry, **203**, 204-211 (2013).
2. Besara, T., Lundberg, M.S., Sun, J., Ramirez, D., Dong, L., Whalen, J.B., Vasquez, R., Herrera, F., Allen, J.R., Davidson, M.W., and Siegrist, T., *Single crystal synthesis and magnetism of the $BaLn_2O_4$ family ($Ln = \text{lanthanide}$)*. Progress in Solid State Chemistry, **42**(3), 23-36 (2014).
3. Besara, T., Ramirez, D., Sun, J., Whalen, J.B., Tokumoto, T.D., McGill, S.A., Singh, D.J., and Siegrist, T., *Ba_2TeO : A new layered oxytelluride*. Journal of Solid State Chemistry, **222**, 60-65 (2015).
4. Ramirez, D., Gallagher, A., Baumbach, R., and Siegrist, T., *Synthesis and characterization of the divalent samarium Zintl-phases $SmMg_2Bi_2$ and $SmMg_2Sb_2$* . Journal of Solid State Chemistry, **231**, 217-222 (2015).
5. Baumbach, R.E., Gallagher, A., Besara, T., Sun, J., Siegrist, T., Singh, D.J., Thompson, J.D., Ronning, F., and Bauer, E.D., *Complex magnetism and strong electronic correlations in Ce_2PdGe_3* . Physical Review B, **91**(3), 035102 (2015).
6. Svanidze, E., Liu, L., Frandsen, B., White, B.D., Besara, T., Goko, T., Medina, T., Munsie, T.J.S., Luke, G.M., Zheng, D., Jin, C.Q., Siegrist, T., Maple, M.B., Uemura, Y.J., and Morosan, E., *Non-Fermi Liquid Behavior Close to a Quantum Critical Point in a Ferromagnetic State without Local Moments*. Physical Review X, **5**(1), 011026 (2015).
7. Svanidze, E., Wang, J.K., Besara, T., Liu, L., Huang, Q., Siegrist, T., Frandsen, B., Lynn, J.W., Nevidomskyy, A.H., Gamza, M.B., Aronson, M.C., Uemura, Y.J., and Morosan, E., *An itinerant antiferromagnetic metal without magnetic constituents*. Nature Communications, **6**, 7701 (2015).
8. Turkiewicz, A., Paley, D.W., Besara, T., Elbaz, G., Pinkard, A., Siegrist, T., and Roy, X., *Assembling Hierarchical Cluster Solids with Atomic Precision*. Journal of the American Chemical Society, **136**(45), 15873-15876 (2014).
9. Schneemeyer, L.F., Siegrist, T., Besara, T., Lundberg, M., Sun, J., and Singh, D.J., *A family of rare earth molybdenum bronzes: Oxides consisting of periodic arrays of interacting magnetic units*. Journal of Solid State Chemistry, **227**, 178-185 (2015).

10. Roy, X., Lee, C.-H., Crowther, A.C., Schenck, C.L., Besara, T., Lalancette, R.A., Siegrist, T., Stephens, P.W., Brus, L.E., Kim, P., Steigerwald, M.L., and Nuckolls, C., *Nanoscale Atoms in Solid-State Chemistry*. *Science*, **341**(6142), 157-160 (2013).
11. Scheuerlein, C., Arnau, G., Alknes, P., Jimenez, N., Bordini, B., Ballarino, A., Di Michiel, M., Thilly, L., Besara, T., and Siegrist, T., *Texture in state-of-the-art Nb₃Sn multifilamentary superconducting wires*. *Superconductor Science & Technology*, **27**(2), 025013 (2014).
12. Scheuerlein, C., Di Michiel, M., Buta, F., Seeber, B., Senatore, C., Flukiger, R., Siegrist, T., Besara, T., Kadar, J., Bordini, B., Ballarino, A., and Bottura, L., *Stress distribution and lattice distortions in Nb₃Sn multifilament wires under uniaxial tensile loading at 4.2 K*. *Superconductor Science & Technology*, **27**(4), 044021 (2014).
13. Choi, B., Paley, D.W., Siegrist, T., Steigerwald, M.L., and Roy, X., *Ligand Control of Manganese Telluride Molecular Cluster Core Nuclearity*. *Inorganic Chemistry*, **54**(17), 8348-8355 (2015).
14. Lee, C.-H., Liu, L., Bejger, C., Turkiewicz, A., Goko, T., Arguello, C.J., Frandsen, B.A., Cheung, S.C., Medina, T., Munsie, T.J.S., D'Ortenzio, R., Luke, G.M., Besara, T., Lalancette, R.A., Siegrist, T., Stephens, P.W., Crowther, A.C., Brus, L.E., Matsuo, Y., Nakamura, E., Uemura, Y.J., Kim, P., Nuckolls, C., Steigerwald, M.L., and Roy, X., *Ferromagnetic Ordering in Superatomic Solids*. *Journal of the American Chemical Society*, **136**(48), 16926-16931 (2014).

Electrodeposition of Water-Splitting Catalysts and Epitaxial Perovskite Films for Solar Energy Conversion

Jay A. Switzer
Department of Chemistry & Materials Research Center
Missouri University of Science and Technology
Rolla, MO 65409-1170
jswitzer@mst.edu

Program Scope

In our lab, we have studied the epitaxial electrodeposition of metal oxide thin films onto single-crystal substrates for several years. We recently applied these methods to the production of materials for solar energy conversion. In this presentation we present work on two topics: i) the electrodeposition of water-splitting catalysts for photoelectrochemical cells, and ii) the electrodeposition of epitaxial methylammonium lead iodide perovskite thin films for solid-state photovoltaic cells.

The kinetic bottleneck of electrochemical and photoelectrochemical water splitting is the four-electron oxygen evolution reaction (OER).¹ OER catalysts include transition metal oxides such as RuO₂, IrO₂, PtO₂, MnO₂, and Co₃O₄. Although the most active of these catalysts are the expensive noble metal oxides RuO₂, IrO₂, and PtO₂, there is interest in developing OER catalysts based on earth-abundant metals such as Co.^{2,3} We are interested in understanding the effect that these catalysts have on the interfacial energetics (e.g., barrier height) in photoelectrochemical solar cells.⁴ That is, do they serve simply as innocent catalysts, or do they produce solid-state Schottky barriers?

Methylammonium lead iodide (MAPbI₃) perovskites are efficient light harvesters in photovoltaic solar cells. Since their introduction as a light absorber in TiO₂-based solar cells in 2009, the conversion efficiency of perovskite-based photovoltaic cells increased from 3.8 to 20.1% in only four years. Although most research on perovskites has focused on producing polycrystalline films by simple and inexpensive solution processing methods, recent results have shown that large-grained materials and single crystals have lower trap densities, longer diffusion lengths, enhanced photoluminescence, and higher photovoltaic conversion efficiency. In addition to producing higher efficiencies, highly ordered samples provide the opportunity to measure the intrinsic electronic and optical properties of the perovskites. An important next step in perovskite research is to grow the material as epitaxial films, in which the out-of-plane and in-plane orientation of the material is controlled by the substrate.

Recent Progress

Water Splitting Catalysts:

Photoelectrochemical water splitting is an intriguing way to convert solar energy into a storable fuel. Electron-hole pairs are generated and separated in the depletion region in a semiconductor electrode, and the carriers are then driven to the electrode surface to oxidize (for n-type semiconductors) or reduce (for p-type semiconductors) water. A thin catalyst layer applied to the semiconductor surface improves the kinetics of electron transfer from the semiconductor to the solution, and protects the semiconductor from photocorrosion and

passivation. A fundamental question in these modified semiconductor electrodes is how this catalyst affects the band bending (and, therefore, the photovoltage) in the semiconductor. We have recently introduced a simple and inexpensive electrodeposition method to produce an efficient n-Si/SiO_x/Co/CoOOH photoanode for the photoelectrochemical oxidation of water to oxygen gas. We also quantitatively analyze the interfacial energetics. We find that the photovoltage is determined by the catalyst, but that the barrier height for thin, inhomogeneous catalyst layers is 0.30 eV larger than the 0.61 eV that has been observed for a solid-state Schottky barrier produced in vacuum.

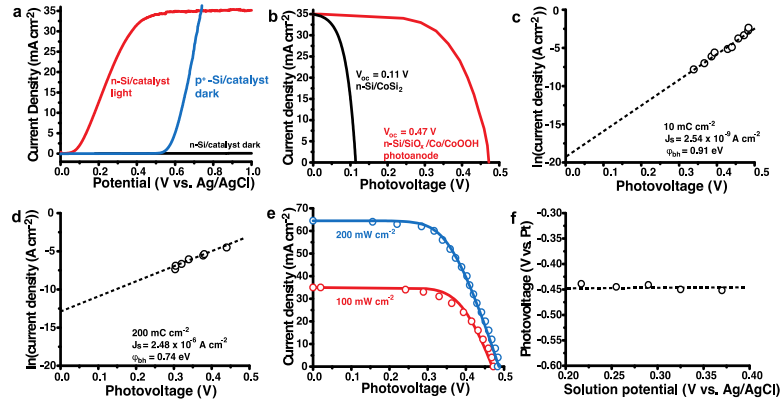


Figure 1 | Photoelectrochemical performance of the n-Si/SiO_x/Co/CoOOH photoanode. **a**, Linear sweep voltammetry comparing n-Si in the dark (black), p⁺-Si/SiO_x/Co/CoOOH in the dark (blue), and n-Si/SiO_x/Co/CoOOH under 100 mW cm⁻² AM 1.5 irradiation (red) in 1 M KOH at a 10 mV s⁻¹ scan rate. **b**, Calculated photoresponse of an n-Si/Co Schottky cell with a barrier height of 0.61 eV (black), and measured photoresponse of the n-Si/SiO_x/Co/CoOOH photoanode under 100 mW cm⁻² AM 1.5 irradiation (red). **c,d**, ln(J)-V plots collected by measuring the limiting photocurrent and photovoltage of photoanodes at different light intensities for the photoanodes with 10 mC cm⁻² (**c**) and 200 mC cm⁻² (**d**) cobalt. **e**, Measured (o) and simulated (solid line) photoresponse of the photoanode under 100 mW cm⁻² (red) and 200 mW cm⁻² (blue) AM 1.5 irradiation in 1 M KOH using Eq. 1 and values of J_s and n measured in (**c**) for the photoanode with 10 mC cm⁻² Co. **f**, Measured photovoltage for 10 mC cm⁻² photoanode in a 1 M KOH electrolyte with a series of potassium hexacyanoferrate(II) and potassium hexacyanoferrate(III) concentrations under 100 mW cm⁻² AM 1.5 irradiation. The open-circuit photovoltage is independent of the solution potential. (From reference 4).

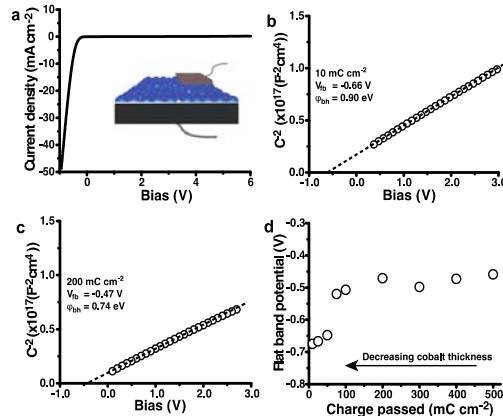


Figure 2 | Solid-state characterization of the electrodeposited n-Si/SiO_x/Co junction. **a**, Current-voltage response of n-Si/SiO_x/Co solid-state cell with an In front contact at a 10 mV s⁻¹ scan rate showing diode behavior. Inset shows schematic of the solid-state cell. **b,c** Solid-state Mott-Schottky plots collected at reverse bias with a frequency of 100 kHz and scan rate of 10 mV s⁻¹ showing barrier heights (ϕ_{bh}) of 0.90 eV (**b**) and 0.74 eV (**c**) for n-Si coated with 10 mC cm⁻² (**b**) and 200 mC cm⁻² (**c**). **d**, Flat band potentials of solid state cells as a function of cobalt

coverage determined by Mott-Schottky plots collected at a 10 mV s^{-1} scan rate and 100 kHz frequency. The flat band potential increases as the Co layer thickness decreases. At the lower Co coverages the Co has not coalesced into a dense film. (From reference 4).

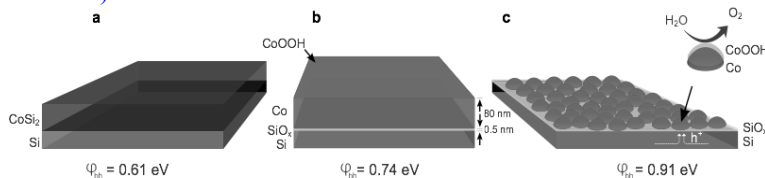


Figure 3 | Schematic of solid-state Schottky barrier and electrodeposited n-Si/SiO_x/Co/CoOOH junctions. a, Solid-state, epitaxial n-Si/CoSi₂ Schottky barrier produced in vacuum with 0.61 eV barrier height (ϕ_{bh}). **b,** Electrodeposited n-Si/SiO_x/Co/CoOOH junction of thick Co layer (200 mC cm^{-2}) with barrier height of 0.74 eV. **c,** Electrodeposited n-Si/SiO_x/Co/CoOOH junction of thin, inhomogeneous Co layer (10 mC cm^{-2}) with barrier height of 0.91 eV. The photogenerated holes are collected at the Co/CoOOH islands where they oxidize water to oxygen gas. (From reference 4).

Electrodeposition of Epitaxial Perovskite Thin Films:

An electrochemical/chemical route is introduced to deposit both textured and epitaxial films of methylammonium lead iodide (MAPbI₃) perovskites. The perovskite films are produced by chemical conversion of lead dioxide films that have been electrodeposited as either textured or epitaxial films onto [111]-textured Au and [100] and [111] single-crystal Au substrates. The epitaxial relationships for the MAPbI₃ films are MAPbI₃(001)[010]||PbO₂(100)<001> and MAPbI₃(110)[111]||PbO₂(100)<001> regardless of the Au substrate orientation, because the in-plane order of the converted film is controlled by the epitaxial PbO₂ precursor film. The textured and epitaxial MAPbI₃ films both have lower trap densities and higher photoluminescence intensities than polycrystalline films produced by spin coating.

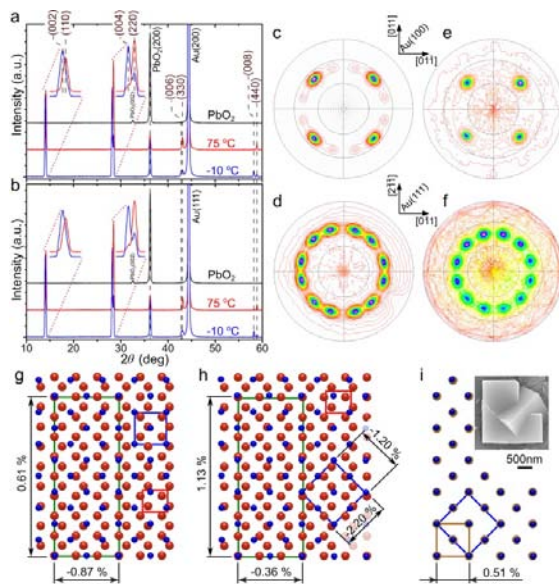


Figure 4 | XRD patterns of as-deposited PbO₂ (black), MAPbI₃ film converted at 75 °C (red) and at -10 °C (blue) deposited on Au(100) (a), and Au(111) (b) substrates. (c) (111) pole of electrodeposited PbO₂ on Au(100). (d) (111) pole of electrodeposited PbO₂ on Au(111). (e) (224) pole of MAPbI₃ film converted at 75 °C on Au(100). (f) (224) pole of MAPbI₃ film converted at 75 °C on Au(111). (g) Interface model of MAPbI₃(001) (blue) on PbO₂(200) (red). (h) Interface model of MAPbI₃(110) (blue) on PbO₂(200) (red). (i) Interface model of MAPbI₃(110) (blue) on MAPbI₃(001) (orange) showing a lattice mismatch of only 0.51%. The inset in (i) is an SEM image showing the intergrowth of two [110]- and [001]-oriented MAPbI₃ crystals obtained at 50 °C. (Unpublished).

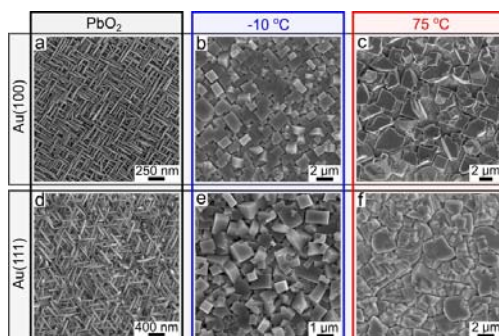


Figure 5 | Plan-view SEM images of as-deposited PbO_2 (a,d), MAPbI_3 films converted at -10°C (b,e) and at 75°C (c,f) on Au(100) and Au(111) substrates. (Unpublished).

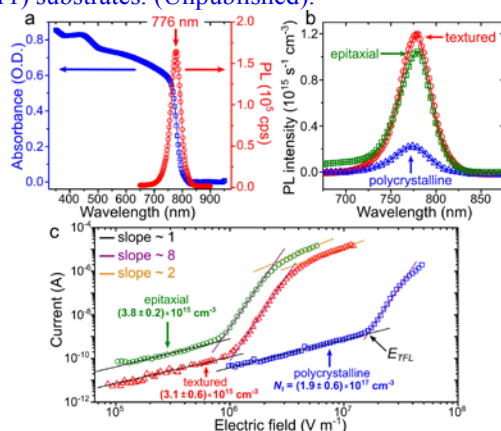


Figure 6 | (a) Absorption (blue squares) and photoluminescence (PL) spectra (right circles), measured for the [110]-textured MAPbI_3 film converted at 75°C on a gold-coated glass substrate. (b) Comparison of PL spectra of the epitaxial (green squares) and [110]-textured (red circles) MAPbI_3 films converted from PbO_2 at 75°C and polycrystalline film converted at room temperature from spin-coated PbI_2 (blue triangles). The PL intensity was normalized to the material volume. (c) Trap density measurements for the epitaxial MAPbI_3 film converted from PbO_2 at 75°C on Au(100) (green circles), a [110]-textured film converted from PbO_2 at 75°C on Au-coated glass (red triangles) substrates, and the polycrystalline film converted at the room temperature from spin coated PbI_2 on Au-coated glass substrate (blue squares). (Unpublished).

Future Plans

1. Study the interfacial energetics of other nanocrystalline, inhomogeneous catalyst contacts to semiconductors.
2. Explore the use of a nanometer-thick Au epitaxial layer on Si(111) as an inexpensive proxy for bulk Au single crystals, as a protecting layer for photoelectrodes, and as a way to integrate electrodeposited epitaxial structures with traditional Si devices.
2. Produce a working cell based on the epitaxial perovskites.

References

1. M. G. Walter, E. L. Warren, J. R. McKone, S. W. Boettcher, Q. Mi, E. A. Santori, and N. S. Lewis, *Chem. Rev.* **110**, 6446 (2010).
2. J. A. Koza, Z. He, A. S. Miller, and J. A. Switzer, *Chem. Mater.* **24**, 3567 (2012).
3. J. A. Koza, C. M. Hull, Y.-C. Liu, and J. A. Switzer, *Chem. Mater.* **25**, 1922 (2013).
4. J. C. Hill, A. T. Landers, and J. A. Switzer, *Nature Mater.*, published online, September 14, 2015, DOI: 10.1038/nmat4408.

Publications over the past two years resulting from work supported by the DOE project

1. Z. He, J. A. Koza, G. Mu, A. S. Miller, E. W. Bohannon, and J. A. Switzer, "Electrodeposition of $\text{Co}_x\text{Fe}_{3-x}\text{O}_4$ Epitaxial Films and Superlattices," *Chem. Mater.* **25**, 223-232 (2013).
2. J. A. Koza, C. M. Hull, Y.-C. Liu, and J. A. Switzer, "Deposition of $\beta\text{-Co(OH)}_2$ films by electrochemical reduction of tris(ethylenediamine)cobalt(III) in alkaline solution," *Chem. Mater.* **25**, 1922-1926 (2013).
3. J. A. Koza, E. W. Bohannon, and J. A. Switzer, "Superconducting filaments formed during nonvolatile resistance switching in electrodeposited $\delta\text{-Bi}_2\text{O}_3$," *ACS Nano* **7**, 9940-9946 (2013).
4. Y.-C. Liu, J. A. Koza, and J. A. Switzer, "Comparison of the catalytic activity of Co_3O_4 , Co(OH)_2 , and CoOOH for the oxygen evolution reaction," *Electrochim. Acta*, **140**, 359-365 (2014).
5. J. A. Koza, I. P. Schroen, M. M. Willmering, and J. A. Switzer, "Electrochemical synthesis and nonvolatile resistance switching of Mn_3O_4 thin films," *Chem. Mater.*, **26**, 4425-4432 (2014).
6. N. K. Mahenderkar, Y.-C. Liu, J. A. Koza, and J. A. Switzer, "Electrodeposited germanium nanowires," *ACS Nano* **8**, 9524-9530 (2014).
7. J. A. Switzer, "Electrodeposition on the Nanoscale," Chapter 17, *Nanoelectrochemistry*, M. V. Mirkin and S. Amemiya, Eds., CRC Press, Taylor and Francis Group, Boca Raton, FL, pp. 601-620 (2015). Book Chapter.
8. J. C. Hill, A. T. Landers, and J. A. Switzer, "An electrodeposited inhomogeneous metal-insulator-semiconductor junction for efficient photoelectrochemical water oxidation," *Nature Materials*, published online, September 14, 2015, DOI: 10.1038/nmat4408. Featured in Editors' Highlights in *Science*, **350**, 54 (2015).
9. J. C. Hill, J. A. Koza, and J. A. Switzer, "Electrodeposition of epitaxial lead iodide and conversion to textured methylammonium lead iodide perovskite," *ACS Applied Materials and Interfaces*, submitted, manuscript am-2015-07222v.R1 (2015).
10. J. A. Koza, J. C. Hill, A. C. Demster, and J. A. Switzer, "Epitaxial electrodeposition of methylammonium lead iodide perovskites," *J. Am. Chem. Soc.*, submitted, manuscript ja-2015-07776x.R1 (2015).

Enhanced Materials Based on Submonolayer Type-II Quantum Dots

M. C. Tamargo, I. K. Kuskovsky, C. A. Meriles and I. C. Noyan
Department of Chemistry, The City College of New York, NY, NY 10031
Department of Physics, Queens College of CUNY, Queens, NY 11367
Department of Physics, The City College of New York, NY, NY 10031

Department of Applied Physics and Applied Mathematics, Columbia University, NY, NY 10027

Program Scope

During the past several years we have investigated a class of nanostructured materials that we refer to as submonolayer (SML) type-II quantum dots (QDs) made from wide bandgap II-VI semiconductors. Our goal is to understand and exploit their tunable optical and electrical properties, by taking advantage of the type-II band alignment and quantum confinement effects.¹ Type-II ZnTe QDs in a ZnSe host are particularly interesting because of their relatively large valence band and conduction band offsets. Exploring the potential for designing new materials with enhanced properties was the primary motivation of our previous award. During that time we advanced our understanding of these novel nanostructures and our ability to control and manipulate their structural properties and we obtained materials with new and enhanced properties. We also developed experimental approaches to characterize the structures with high precision and insight. We have also shown that a variation of this material system, ZnTeSe QDs in a ZnCdSe host material, has nearly ideal properties for the fabrication of intermediate band solar cells (IBSC),^{2,3} a novel high performance photovoltaic device that has yet to be realized with real materials.

Over the last two years we have greatly advanced our understanding of these materials and their growth habits. We have developed a methodology to correlate the dot size and density with growth parameters. We have developed a new approach for the structural characterization of these materials using high resolution X-ray diffraction (HR-XRD), from which the size and distribution as well as the shape of the dots can be extracted, and we have investigated the effects of this shape anisotropy on the optical and magneto-optical properties of the dots. It should be noted that previous modeling efforts have used quantum well based analysis. This is the first direct account of quantum dot shape and distribution in the analysis of XRD from multilayer QDs. Finally, we have continued to make progress in demonstration of the IBSC made from these materials.

Recent Progress and New Results:

1. Measurement and control of size and density of type-II ZnTe/ZnSe submonolayer quantum dots grown by migration enhanced epitaxy

Combining a variety of characterization tools, including XRD and SIMS to establish the Te content and the structural parameters, and photoluminescence (PL) and magneto-PL to estimate the QD thickness, QD radial sizes and weighted QD volume, the dependence of the QD size (thickness and radius) as well as the QD areal density on the Te content in the samples were extracted.

First, to examine the effect of varying growth conditions on the formation of the type-II QD structures, a new parameter ' τ ' (the product of the Te flux times the number of MEE cycles used during growth) was introduced, as a measure of actual Te content in the samples. The optical characterization was done by performing PL as well as magneto-PL experiments at 10 K.

As previously reported, ‘green band’ (<2.7 eV) originates from the QD.⁴ This part of spectra were fitted with Gaussian lineshapes, and the corresponding peak positions were used to estimate the average QD size, specifically the thickness, by solving the 1-D Schrödinger equation. Magneto-PL was used to obtain an accurate estimation of the radial sizes of these SML QDs, through the observation of excitonic Aharonov-Bohm (AB) effect.^{5, 6} The average QD radii for the samples in this study are estimated to be about 13 to 20 nm, justifying the claim that most of the confinement in these disc-shaped QDs is along the growth direction i.e. due to the QD thicknesses. The combined result of the calculated QD thicknesses and radii overlaid on the complete PL spectrum for the set of samples investigated is shown in Fig. 1.

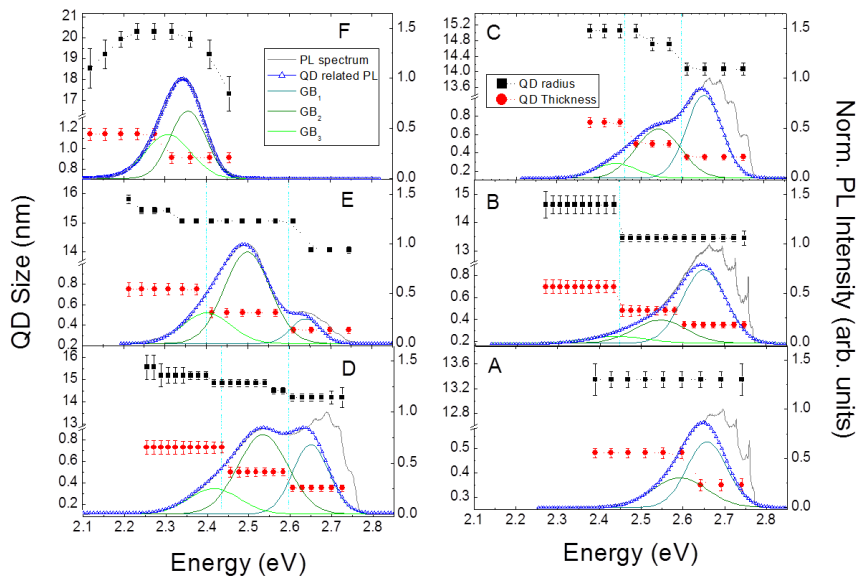


Figure 1. Combined diagram of the spectral dependence of QD radii and thicknesses overlaid on the corresponding PL spectra. The green bands are specifically highlighted as they correspond to QD-related emissions.

Upon obtaining the spectral distribution of QD radii and thicknesses, the intensities of the green bands were used to estimate weighted QD volume over the full PL spectrum for each of the samples, and with this, the density of QDs was then estimated from the calculated QD volume. We then plot the average QD radii and thicknesses as well as areal QD density vs. the corresponding values of τ for a set of samples A through F in Figs. 2 (a) and (b).

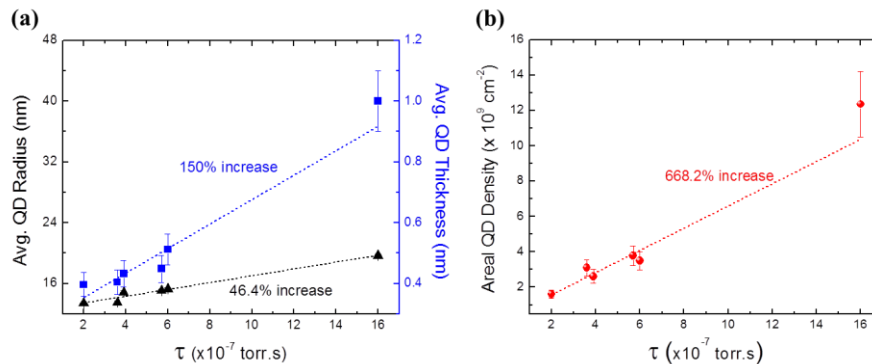


Figure 2. (a) Plot showing average QD radii and thicknesses as a function of τ . (b) Plot showing the dependence of areal QD density on τ ; dashed lines are for eye guidance only.

Two important conclusions were reached from this study. First, we noted that concentrations at least one order of magnitude higher would be required to form a full ZnTe-rich monolayer (i.e. for the QDs to physically coalesce into a continuous layer). Secondly, the

observed dependence of average QD size and density as a function of Te flux as well as number of Te MEE cycles shows that these are the key parameters to control QD dimensions and distribution.

2. Determination of shape anisotropy in embedded low contrast submonolayer quantum dot structures:

We have developed and implemented a powerful characterization formalism which utilizes experimental and simulated high resolution in-plane reciprocal space maps (RSM) to investigate the morphology of embedded type-II ZnTe/ZnSe SML QDs with required precision and detail. Our results clearly demonstrate that this combination of characterization techniques is uniquely suited to elucidate the morphology of these hard-to-image SML QD structures. Our approach provides a fast, accurate and precise way of characterizing embedded ultra-small QD arrays.

The QD morphology was deduced from diffuse scattering data obtained by measuring in-plane RSM. Specific trajectories in reciprocal space have been recorded to measure the in-plane map around the (004) SL(-1) peak. A set of rocking curves along 360° has been merged to obtain proper $q_x - q_y$ map as shown in Fig. 3(a). The width Δq_x shows periodic oscillations as a function of azimuthal angle ϕ ; hence in-plane RSM presents a strong anisotropy in the diffuse scattering signal.

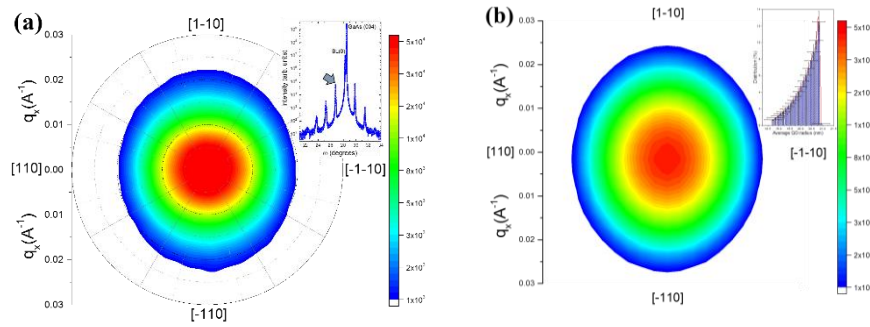


Figure 3. (a) In-plane reciprocal space map around satellite SL(-1) of (004) Bragg peak (inset) depicting clear anisotropic shape. (b) Simulated rocking curves as a function of azimuthal angle for a known size dispersion of elongated QDs.

To explain the experimental observation, in-plane diffuse scattering has been computed using kinematic sum and *realistic* QD shape and size distribution, with the aid of magneto-PL derived QD size dispersion estimates (Fig. 3 (b), inset). A set of different QD configurations has been computed to reproduce the experimental results (Fig. 4). It was observed that QD size distribution presenting centro-symmetric shapes leads to centro-symmetric diffuse scattering pattern, and that ellipsoid dots with random orientation leads also to a similar centro-symmetric feature. Only an assembly of elongated ellipsoidal QDs with definite orientation explains the experimental signal. Thus, ellipsoidal QDs elongated along [110] axis with varied in-plane aspect ratios (i.e. b/a , as

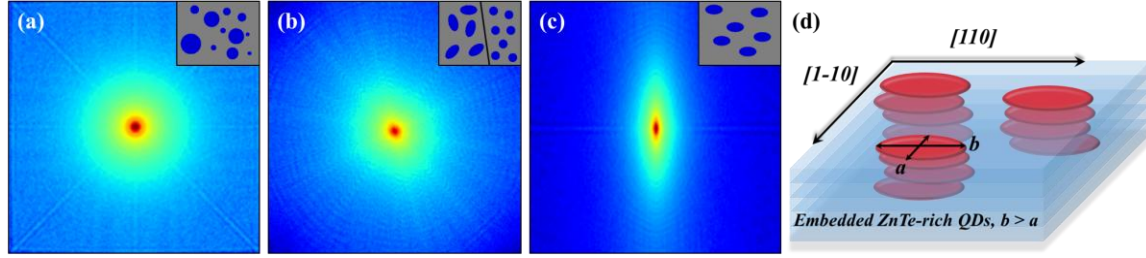


Figure 4. (a) - (c) Simulated RSMs of QDs with various shapes and orientations, the insets show the corresponding QD configuration. (d) Schematic of the disc-shaped embedded SML QDs elongated along [110] orientation.

shown in Fig. 4.) were used for the purpose of the simulations. The simulations, as shown in Fig. 3(b), present clear evidence of the anisotropically shaped QDs elongated along [110] orientation. The best match with the experimental data was obtained for the QD aspect ratio of 1.17.

Anisotropically shaped SK grown QDs have been reported to show optical anisotropy as observed in their PL emission.^{7,8} In order to study the effect of the asymmetric shape of these ultra-small QDs, we investigated the linear polarization of the PL at 8 K. The contour map showing PL spectra as a function of the angle between axis of the linear polarizer and the [110] axis of the sample is shown in Fig. 5(a). Moreover, the axis of polarization and the asymmetric shape of the $\omega - \phi$ scan show excellent correlation (Fig. 5(b)) further confirming the presence of the elongated QDs, preferentially orientated along [110] direction.

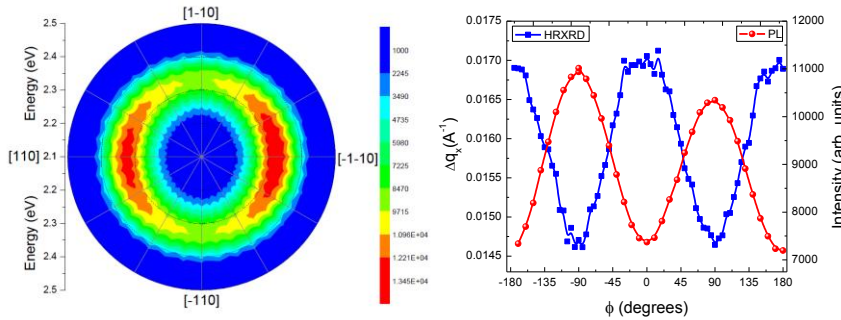


Figure 5. (a) Linearly polarized photoluminescence spectra plotted as a function of azimuthal angle revealing in-plane anisotropy; (b) correlation between the width of rocking curve and the intensity of linearly polarized PL emission as a function of azimuthal angle ϕ .

considerations is 1.27 for the sample studied by XRD.

Future Plans:

We have begun to investigate other materials, namely CdSe/CdTe heterostructures and QDs, to identify other systems in which similar phenomena may be observed. We are also pursuing doping of the ZnTe/ZnCdSe QD structures for demonstration of IBSC behavior.

References:

1. Y. Gong, W. MacDonald, G. F. Neumark, M. C. Tamargo and I. L. Kuskovsky, *Phys. Rev. B* **77**, 155314-155316 (2008)
2. A. Luque and A. Martí, *Phys. Rev. Lett.* **78**, 5014 (1997)
3. Luque, A. Martí, and C. Stanley, *Nat. Photonics* **6**, 146 (2012)
4. Y. Gu, I.L. Kuskovsky, M. van der Voort, G.F. Neumark, X. Zhou, M.C. Tamargo, *Phys. Rev. B.* **71**, 045340 (2005).
5. H. Ji, S. Dhomkar, B. Roy, V. Shuvayev, V. Deligiannakis, M.C. Tamargo, J. Ludwig, D. Smirnov, A. Wang, and I. L. Kuskovsky, *J. Appl. Phys.* **116**, 164308 (2014).
6. B. Roy, H. Ji, S. Dhomkar, F.J. Cadieu, L. Peng, R. Moug, M. C. Tamargo, and I. L. Kuskovsky, *Appl. Phys. Lett.* **100**, 213114 (2012).
7. M. Schmidbauer, F. Hatami, M. Hanke, P. Schäfer, K. Braune, W. Masselink, R. Köhler, and M. Ramsteiner, *Phys. Rev. B* **65**, 125320 (2002).
8. W. Sheng, *Appl. Phys. Lett.* **89**, 173129 (2006)
9. W. Sheng and S. J. Xu, *Phys. Rev. B* **77**, 113305 (2008).

Publications Related to This Project in the Last Two Years

1. S. Dhomkar, N. Vaxelaire, H. Ji, V. Shuvayev, I. C. Noyan, M. C. Tamargo, and I. L. Kuskovsky, Determination of shape anisotropy in embedded low contrast submonolayer quantum dot structures, submitted to *Applied Physics Letters*.
2. S. Dhomkar, H. Ji, B. Roy, V. Deligiannakis, A. Wang, M. C. Tamargo and I. L. Kuskovsky, Measurement and control of size and density of type-II ZnTe/ZnSe submonolayer quantum dots grown by migration enhanced epitaxy, *J. Cryst. Growth* **422**, 8-14 (2015).
3. H. Ji, S. Dhomkar, B. Roy, V. Shuvayev, V. Deligiannakis, M. C. Tamargo, J. Ludwig, D. Smirnov, A. Wang, and I. L. Kuskovsky, Determination of lateral size distribution of type-II ZnTe/ZnSe stacked submonolayer quantum dots via spectral analysis of optical signature of the Aharanov-Bohm excitons, *J. Appl. Phys.* **116** (2014) 164308. (Partial funding from DOE)
4. S. Dhomkar, U. Manna, I. C. Noyan, M. C. Tamargo, I. L. Kuskovsky, Vertical correlation and miniband formation in submonolayer Zn(Cd)Te/ZnCdSe type-II quantum dots for intermediate band solar cell application, *Appl. Phys. Lett.* **103** (2013) 181905.
5. H. Ji, B. Roy, S. Dhomkar, R. T. Moug, M. C. Tamargo, A. Wang, and I. L. Kuskovsky, Tuning Between Quantum-Dot- and Quantum-Well-Like Behaviors in Type II ZnTe Submonolayer Quantum Dots by Controlling Tellurium Flux During MBE Growth, *J. Electron. Mater.* **42** (2013) 3297–3302. (Partial funding from DOE)

Manuscripts in preparation

1. H. Ji, S. Dhomkar, V. Shuvayev, V. Deligiannakis, M. C. Tamargo, J. Ludwig, D. Smirnov, A. Wang, and I. L. Kuskovsky, Optical Anisotropy in Type-II ZnTe/ZnSe Submonolayer Quantum Dots.
2. N. Vaxelaire, S. Dhomkar, V. Deligiannakis, H. Ji, M. C. Tamargo, I. L. Kuskovsky, and I. C. Noyan, Multilayered Structures of Ultra-small (Submonolayer) Quantum Dots as Probed by High Resolution X-Ray Diffraction.
3. V. Deligiannakis, S. Dhomkar, H. Ji, D. Pagliero, I. L. Kuskovsky, M. C. Tamargo, and C. A. Meriles, Investigation of spin dynamics of Te-related defect centers in type-II ZnTe/ZnSe multilayer nanostructures using Non-linear Optical Techniques.
4. S. Dhomkar, H. Ji, R. Wu, Z. Lu, J. Ludwig, D. Smirnov, M. C. Tamargo, and I. L. Kuskovsky Magneto-photoluminescence of Tellurium Isoelectronic Bound Excitons in Zn-Se-Te in the Presence of Type-II Submonolayer Quantum Dots.

The Dynamics of Complex Two-Phase Mixtures During Coarsening: From Dendritic to Bicontinuous Mixtures

Peter W. Voorhees*, Katsuyo Thornton**

Department of Materials Science and Engineering,

*Northwestern University, Evanston IL

**University of Michigan, Ann Arbor MI

Program Scope

Dendrites frequently form during solidification into an undercooled melt. In systems with nearly isotropic interfacial energy, these dendrites possess secondary and sometimes even tertiary arms. In systems with anisotropic interfacial energy, the growth shapes can be highly crystallographic and thus of very different morphology from those in systems with isotropic interfacial energy. The resulting two-phase mixtures are topologically and morphologically complex with spatially varying mean and Gaussian curvatures. These solid-liquid mixtures are one example from a large class of morphologically and topologically complex structures found in nature that undergo coarsening. Included in this class are the bicontinuous two-phase mixtures produced following spinodal decomposition and ordering in crystals. Understanding the coarsening process in all of these systems requires theory, simulation, and experiments that capture their three-dimensional topology and morphology. Given the complicated morphology and topology of these systems it is not surprising that our understanding of this process is in its infancy.

Recent Progress

Shown in Figure 1(a) and (c), are results from coarsening of Si particles in an Al-Si eutectic liquid. These data were obtained using 4D phase contrast tomography. Phase contrast tomography is employed because of the small atomic number difference between Si and Al. There is a striking change in the morphology of the particles during coarsening from those with slow-moving and low-interfacial-energy $\{111\}$ interfaces to a much more isotropic structure. The degree of isotropy is quantified by measurements of the probability of finding a patch of interface with a given shape factor S and curvature C (1). Using this representation, interfacial patches that are solid cylinders have $S = 0.5$, liquid cylinders $S = -0.5$, solid spheres $S = 1.0$ liquid spheres $S = -1.0$ and saddle shaped surfaces have $-0.5 < S < 0.5$. The curvature C is zero for flat interfaces, and nonzero for interfaces with any curvature. In Fig. 1 the curvature is normalized by the surface area per volume, S_v . Here the interface shape distribution is the probability of finding a patch of interface with a given C and S . In the early stage of coarsening, a significant fraction of the interfacial area is nearly flat, which is evident by the large, broad peak with $C/S_v < 0.5$. There is a strong peak at $S = 0.5$ that has a large range of curvatures up to nearly 4. These large curvatures are the patches that make up the edges of the plates. By contrast, at later time most of the flat interfaces and patches on edges of the plates with large C have disappeared. The surprising result is that, as the coarsening process proceeds, the particles are

not evolving towards the Wulff shape, which is the equilibrium shape based on the interfacial energy and is a shape consisting of $\{111\}$ and/or $\{100\}$ facets for this system. Electron Backscatter Diffraction (EBSD) analysis shows that certain Si plates are defective with twin boundaries running parallel to the $\{111\}$ solid-liquid interfaces. These twins can provide sources of the steps at the solid-liquid interfaces that allow the interfaces to grow and dissolve in a non-crystallographic fashion. The high density of twins within the structure leads to the development of a nearly morphologically isotropic structure during coarsening. This illustrates the qualitatively different evolution process in systems with anisotropic interfacial energy and mobility compared with two-phase mixtures with nearly isotropic interfacial energy and constant mobility.

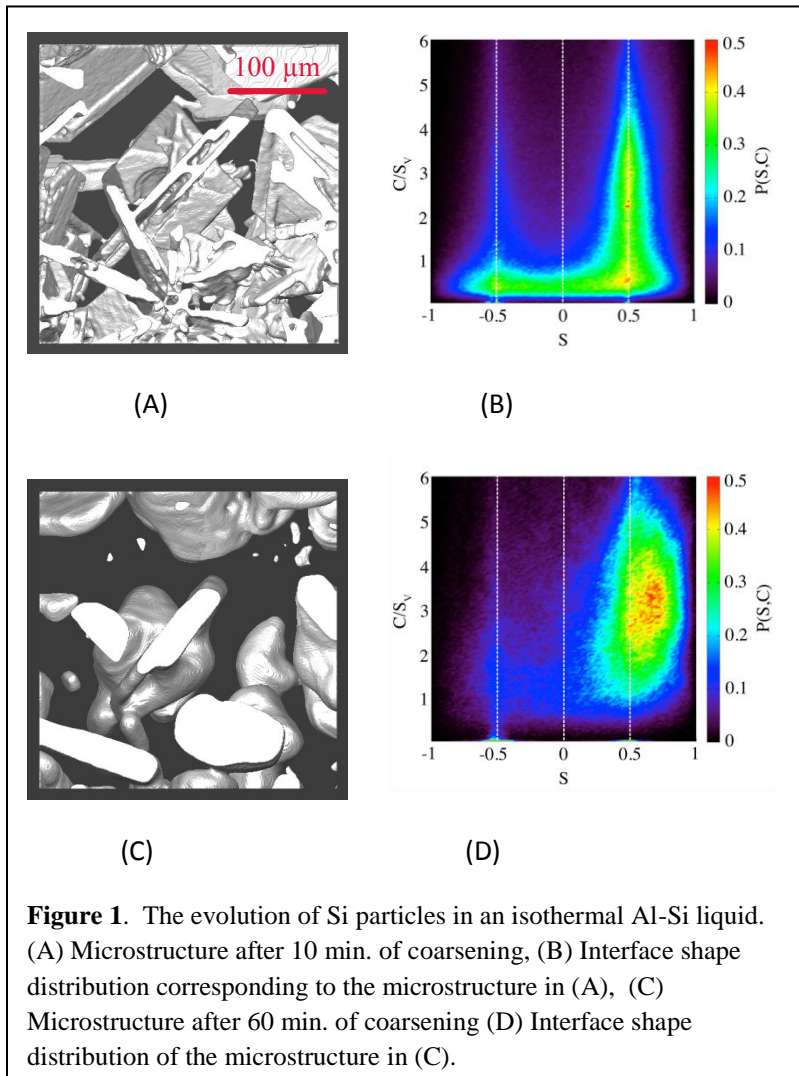
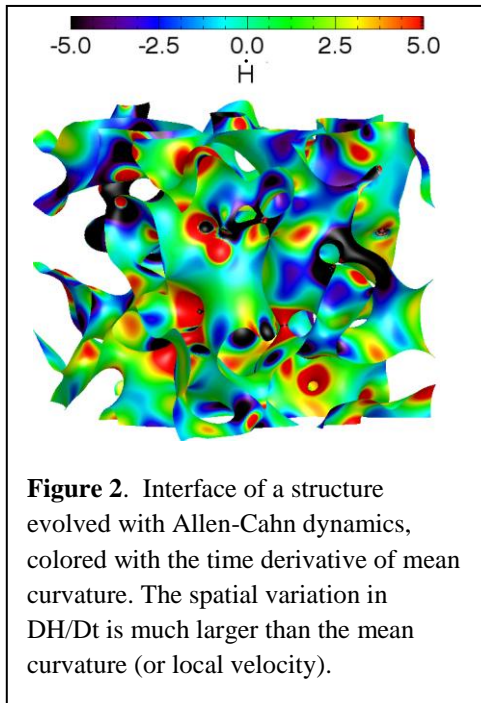


Figure 1. The evolution of Si particles in an isothermal Al-Si liquid. (A) Microstructure after 10 min. of coarsening, (B) Interface shape distribution corresponding to the microstructure in (A), (C) Microstructure after 60 min. of coarsening (D) Interface shape distribution of the microstructure in (C).

The mathematical description of the evolution of the mean and Gaussian curvatures, which together define the interfacial morphology, can be derived from differential geometry for a given interfacial normal velocity (2). Due to their relative simplicity, as compared to structures that involve multiple feature sizes (such as dendritic structures), we have chosen to examine the implication of these questions for the bicontinuous structures that form from phase decomposition (in the case of conserved dynamics) or ordering (in the case of nonconserved dynamics). In spite of their relative simplicity, a theoretical study of the dynamics of coarsening is still challenging because bicontinuous structures inherently possess multiple length scales, as the interfaces

have two independent curvatures. Thus, we must develop a framework for theoretical development. To this end, we considered two cases: (1) interfacial evolution due to nonlocal bulk diffusion and (2) interfacial evolution due solely to the interfacial curvature.



We first focused on the evolution of interfacial curvature by examining the evolution of the Allen-Cahn structure (3). Under the Allen-Cahn dynamics, the interfacial velocity is directly proportional to the mean curvature (i.e., the structure evolves by “motion by mean curvature”), and therefore it provides an ideal test bed with which to investigate the evolution of a bicontinuous structure. The results show that the evolution proceeds with some interfaces evolving toward topological singularities (pinching) while the majority of interfaces flatten. Most notably, we find that, while the normal velocity is solely a function of the mean curvature H , its evolution as quantified by DH/Dt is not simple at all, as shown in Fig. 2. We find that the terms involving the second derivatives of the velocity are very important. Consequently, the evolution of H at a point depends on the values of H in its neighborhood and, despite the local

nature of the motion-by-mean-curvature equation for the normal velocity, the evolution of H is nonlocal. What are the implications of these findings to conserved systems, the systems in which we are ultimately interested? To answer this question, we began performing preliminary simulations with Cahn-Hilliard structures. In particular, we have studied cases where diffusivities are equal between the two phases, as well as cases where diffusivities are not equal (as in solid-liquid mixtures).

Future Plans

Building upon these results, we plan to examine, both theoretically and experimentally, the distribution of interfacial velocities for a given pair of principal interfacial curvatures, the effects of a difference in diffusion coefficients on the morphology of solid-liquid mixtures during coarsening, the role of the Gaussian curvature in setting the interfacial velocities, and the coarsening process in systems with highly anisotropic interfacial energy such as that of Al-Si. The goal is to produce a theory for coarsening of these complex structures.

References

1. A. J. Shahani, E. B. Gulsoy, V. J. Rousochatzakis, J. W. Gibbs, J. L. Fife, P. W. Voorhees, *The Dynamics of Coarsening in Highly Anisotropic Systems: Si Particles in Al-Si Liquids*, *Acta Mater.* **97** 325-337 (2015).
2. Drew DA. 1990. Evolution of Geometric Statistics. *Siam Journal on Applied Mathematics* 50:649-66

3. C.-L. Park, P.W. Voorhees and K. Thornton, *Evolution of Interfacial Curvatures of a Bicontinuous Structure Generated via Nonconserved Dynamics*, *Acta Materialia*, **90**, 182-193 (2015).

Publications

1. J.W. Gibbs and P.W. Voorhees, *Segmentation of Four-Dimensional, X-ray Computed Tomography Data*, *Integrated Materials and Manufacturing Innovation*, 3, 6 (2014).
2. J.L. Fife, J.W. Gibbs, E.B. Gulsoy, C.-L. Park, K. Thornton and P.W. Voorhees, *The Dynamics of Interfaces During Coarsening in Solid-Liquid Systems*, *Acta Mater.* 70 66-78 (2014).
3. C.-L. Park, P.W. Voorhees and K. Thornton, *Application of the Level Set Method to the Analysis of an Evolving Microstructure*, *Comp. Mater. Sci.*, 85 46-58 (2014).
4. E.B. Gulsoy, A.J. Shahani, J.W. Gibbs, J.L. Fife and P.W. Voorhees, *Four-Dimensional Morphological Evolution of an Aluminum Silicon Alloy Using Propagation-Based Phase Contrast X-ray Tomographic Microscopy*, *Mater. Trans.*, 55, 161-164 (2014).
5. A.J. Shahani, E.B. Gulsoy, J.W. Gibbs, J.L. Fife and P.W. Voorhees, *Integrated approach to the data processing of four-dimensional datasets from phase-contrast x-ray tomography*, *Optics Express* 24606 (2014).
6. C.-L. Park, P.W. Voorhees and K. Thornton, *Evolution of Interfacial Curvatures of a Bicontinuous Structure Generated via Nonconserved Dynamics*, , **90**, 182-193 (2015).
7. A. J. Shahani, E. B. Gulsoy, V. J. Roussochatzakis, J. W. Gibbs, J. L. Fife, P. W. Voorhees, *The Dynamics of Coarsening in Highly Anisotropic Systems: Si Particles in Al-Si Liquids*, *Acta Mater.* **97** 325-337 (2015).

Synthesis of Three-Dimensional Nanowire Architecture with Enhanced Performance in Solar Energy Harvesting

Xudong Wang, Department of Materials Science and Engineering, University of Wisconsin-Madison

Program Scope

The objective of this project is to obtain in-depth understanding of the nanoscale crystal growth behavior in a surface-reaction-limited pulsed chemical vapor deposition (SPCVD) process, and thereby achieve well-controlled syntheses of three-dimensional (3D) nanowire (NW) arrays inside highly-confined spaces. An experiment-based project is proposed to study the nucleation and anisotropic crystal growth mechanisms of titanium dioxide (TiO_2). This understanding will then be applied to controlling the composition and dimensionality of TiO_2 NWs and eventually to the growth of other functional materials. The outcome of this project will be a powerful NW synthesis technique that can uniformly grow NW arrays of controlled composition and morphology inside 3D-confined and submicron-sized spaces, thus enabling the creation of a variety of new functional nanomaterial architectures.

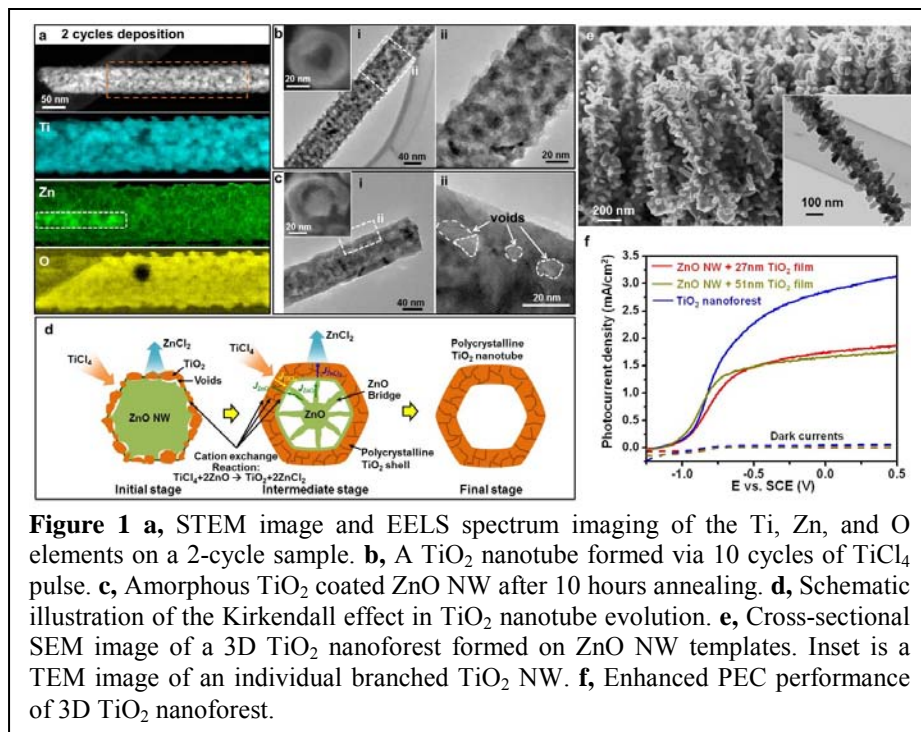
Recent Progress

SPCVD technique has been developed in our lab to create high-density uniform 3D branched NW architectures, which offers favorable surface area and charge transport properties for developing high performance photoelectrodes.^[1] By performing atomic-scale elemental analysis and high resolution scanning transmission electron microscopy (HR-STEM) study on the surface of a Si NW coated with a 10-cycle TiO_2 by 600 °C SPCVD, we discovered that the high-temperature SPCVD of TiO_2 nucleation followed the Ostwald-Lussac (OL) Law and the 1D TiO_2 anisotropic crystal growth was governed by the oriented attachment (OA) mechanism.^[2]

Following this research, we applied SPCVD of TiO_2 NRs to ZnO NW backbones.^[3] By introducing TiCl_4 vapor pulses to ZnO NW templates, we obtained TiO_2 nanotubes with well-preserved dimensions and morphology. This process involved the cation exchange reaction between TiCl_4 vapor and ZnO solid and the diffusion of reactants and products in their vapor or solid phases, which was found to be a manifestation of the Kirkendall effect.

We discovered that 2 cycles of TiO_2 SPCVD on ZnO NWs roughened the NW's surface (Fig. 1a). To understand this process, EELS mapping was conducted. Ti distribution clearly matched the grain morphology along the polycrystalline shell. The Zn map revealed a universal distribution of Zn in the entire structure with strong Zn signals located at the center region representing the remaining ZnO core. The homogeneous Zn distribution along the entire shell region suggests that the Zn elements from the core were diffused into and traveling through the TiO_2 shells during the growth. When only TiCl_4 vapor was present, 10-cycle deposition also

completely removed the ZnO core and same anatase TiO₂ polycrystalline nanotubes were obtained (Fig. 1b). When H₂O vapor precursor was used exclusively, only small pores were created on the ZnO NW surface. This comparison reveals that H₂O was an insignificant component in the ZnO to TiO₂ conversion, and the O in TiO₂ can be completely



provided by ZnO following the cation exchange reaction. The ZnCl₂ by-products would most likely exist in its vapor phase, which was favorable for rapid diffusion and complete removal of the Zn species from the core. We also found that simply annealing amorphous TiO₂-coated ZnO only formed a core-shell structure with yielded multiple voids were observed at the core/shell interface (Fig. 1c). This experiment revealed that solid-state diffusion of ZnO species cannot explain the vanishing of ZnO in the heterostructure and formation of pure TiO₂ phase.

Figure 1d schematically shows the Kirkendall effect in responsible for the formation of hollow TiO₂ nanostructures. When TiCl₄ vapor is first introduced, the exterior surface of the ZnO NW quickly converts to TiO₂ and generates ZnCl₂ by-product. Meanwhile, initial voids were created at the defective core/shell interface. Once the surface is fully covered by the TiO₂ shell, further removal of ZnO required the ZnCl₂ species to diffuse outward. The cation exchange reaction between TiCl₄ and ZnO occurs at the TiO₂/ZnO interface and TiO₂ outer surface, resulting inward and outward growth of the shell, respectively. Upon the consumption of ZnO at the TiO₂/ZnO interface, the void size increases leaving a typical Kirkendall bridge morphology. Eventually, the entire ZnO core is consumed yielding a hollow TiO₂ nanotube.

The TiO₂ nanotube arrays could serve as an excellent scaffold to support dense TiO₂ NR branch growth *via* our SPCVD technique, yielding a pure TiO₂-phased 3D NW architecture (Fig. 1e). TEM characterization on a single hierarchical NW structure revealed the dense single-crystalline TiO₂ NR coverage and the polycrystalline hollow trunk (Inset of Fig. 1e). PEC water splitting experiments were conducted to explore the application potential of the 3D TiO₂ nanoforest in comparison to TiO₂ film-coated ZnO NWs. Figure 1f shows the photocurrent

density (J_{sc}) versus applied bias acquired from the 3D TiO₂ nanoforest and the two reference samples under the illumination of a 150 W Xe lamp. The three samples exhibited similar open circuit voltage (V_{oc}) and followed the same trend; whereas, their J_{sc} were dramatically different. Owing to the enlarged surface area, the 3D TiO₂ nanoforest achieved a J_{sc} of ~ 3.14 mA/cm², which was remarkably higher than other reported TiO₂ NW-based PEC electrodes. This discovery offers a new route for hierarchical functional nanomaterial assembly and application.

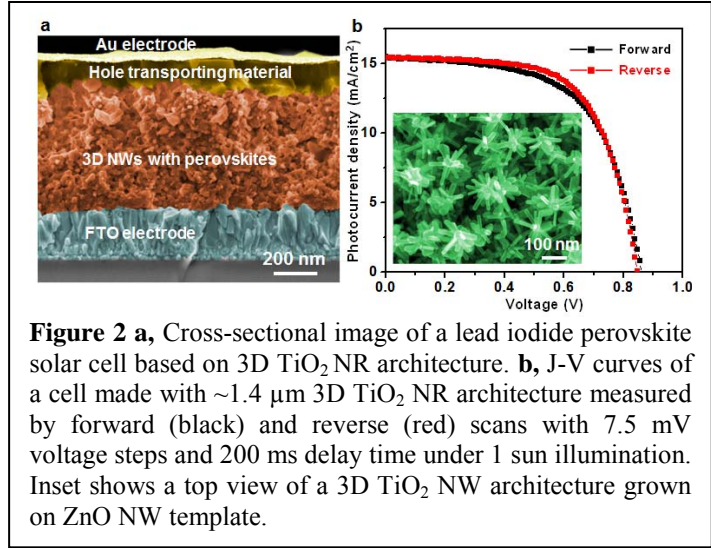


Figure 2 a, Cross-sectional image of a lead iodide perovskite solar cell based on 3D TiO₂ NR architecture. **b**, J-V curves of a cell made with ~ 1.4 μ m 3D TiO₂ NR architecture measured by forward (black) and reverse (red) scans with 7.5 mV voltage steps and 200 ms delay time under 1 sun illumination. Inset shows a top view of a 3D TiO₂ NW architecture grown on ZnO NW template.

Likewise, the 3D TiO₂ NW architecture is a superior electrode design for photovoltaic (PV) devices compared to NWs or nanoparticle systems in terms of improved large surface area and charge transport properties. CH₃NH₃PbI₃ perovskite solar cells were fabricated based on such 3D TiO₂ NW architectures with a length variation from ~ 600 nm to ~ 1.4 μ m (Fig. 2a).^[4] By increasing the length of the 3D TiO₂ scaffolds, J_{sc} was increased accordingly, while V_{oc} , fill factor (FF) of cells were decreased. The enlarged J_{sc} is attributed to the enhanced hole injection efficiency and increased light absorption from longer TiO₂ nanostructures. The length-related reduction of V_{oc} and FF is believed to be a result of decreased charge generation efficiency, increased charge recombination and higher electron transport resistance. The best PCE was offered by the ~ 600 nm 3D TiO₂ scaffold with a value of 9.0%, which was 1.5 times higher than 1D TiO₂ nanostructures made through the same process. The high-density 3D TiO₂ architecture

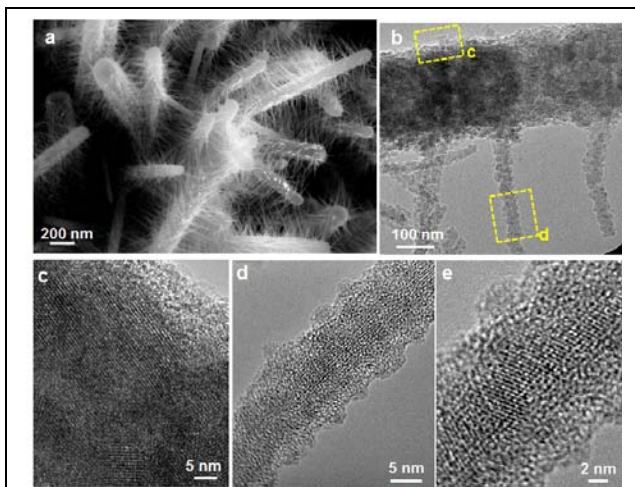


Figure 3 (a) SEM and **(b)** TEM of SPCVD V₂O₅ NRs on ZnO NWs. **(c)** HRTEM of the NW backbone showing polycrystalline V₂O₅ lattices. **(d, e)** HRTEM images of a V₂O₅ NR.

allowed higher perovskite loading and enhanced light harvesting compared with simple 1D nanostructure arrays. In addition, PV cells comprising 3D TiO₂ are found to be favorable in suppressing the hysteresis effect that is often observed from planar perovskite SCs (Fig. 2b). The 3D hierarchical NWs morphology offers a promising candidate for understanding the property-performance relationship in perovskite solar cells and developing high performance solar energy harvesting devices.

Through SPCVD, VO_x NRs were also synthesized on ZnO NW cores using

VOCl_3 and H_2O as the precursors.^[5] Dense VO_x NRs uniformly distributed on the ZnO NW templates (Fig. 3a). The VO_x NRs exhibited a necklace-like morphology (Fig. 3b) and the surface was covered with an amorphous layer (Fig. 3d,e). In addition, no ZnO phase was found from the polycrystalline backbone of hierarchical structure (Fig. 3c). These observations are consistent with the vapor-phase OA and Kirkendall effect in SPCVD process, suggesting our understandings on SPCVD mechanisms and kinetics could be generally applied to different material systems. This development demonstrated the versatility of the SPCVD technique in creating 3D NR branches from different material systems.

Future Plans

This is toward the end of our current DOE award. The understandings obtained through this award opened many new opportunities in designing 3D NW architectures with improved properties or new functionalities. Our future research plan is to follow these research achievements, and address three further key aspects of SPCVD. (1) Study the operation of the OL law of TiO_2 phase transition on heterogeneous, homogeneous, and carbon surfaces, and thus understand and eventually control the nucleation of TiO_2 NRs on desired material surfaces to create multilevel branching architectures and carbon-based heterostructures. (2) Understand the diffusion and aggregation kinetics of crystallites embedded in amorphous layers and reveal how the amorphous layer controls the OA process. (3) Understand the kinetics of ionic diffusion and surface etching reaction operated by the Kirkendall effect during SPCVD, and thereby achieve rational control of the morphology and phase of TiO_2 and perovskites NR branches.

References

- [1] J. Shi, Y. Hara, C. Sun, M. A. Anderson, X. Wang, Three-Dimensional High-Density Hierarchical Nanowire Architecture for High-Performance Photoelectrochemical Electrodes. *Nano Lett.* 11, 3413-3419 (2011).
- [2] J. Shi, Z. Li, A. Kvit, S. Krylyuk, A. V. Davydov, X. Wang, Electron Microscopy Observation of TiO_2 Nanocrystal Evolution in High-Temperature Atomic Layer Deposition. *Nano Lett.* 13, 5727-5734 (2013).
- [3] Y. Yu, X. Yin, A. Kvit, X. Wang, Evolution of Hollow TiO_2 Nanostructures via the Kirkendall Effect Driven by Cation Exchange with Enhanced Photoelectrochemical Performance. *Nano Lett.* 14, 2528-2535 (2014).
- [4] Y. Yu, J. Li, D. Geng, J. Wang, L. Zhang, T. L. Andrew, M. S. Arnold, X. Wang, Development of Lead Iodide Perovskite Solar Cells Using Three-Dimensional Titanium Dioxide Nanowire Architectures. *ACS Nano* 9, 564-572 (2015).
- [5] Z. Li, Y. Yu, X. Wang, High Density Three-Dimensional V_2O_5 Nanowire Architecture with Enhanced Supercapacitor Performance *In preparation* (2015).

Publications

- (1) J. Shi, Z. Li, A. Kvit, S. Krylyuk, A.V. Davydov, X.D. Wang “Electron Microscopy Observation of TiO₂ Nanocrystal Evolution in High-Temperature Atomic Layer Deposition”, *Nano Lett.*, 13 5727-5734 (2013).
- (2) Z. Li, C. Yao, Y. Yu, Z. Cai, X.D. Wang “Highly-Efficient Capillary Photoelectrochemical Water Splitting Using Cellulose Nanofiber-Templated TiO₂ Photoanodes”, *Adv. Mater.*, 26, 2262-2267 (2014).
- (3) Y. Yu, X. Yin, A. Kvit, X.D. Wang “Evolution of Hollow TiO₂ Nanostructures via the Kirkendall Effect Driven by Cation Exchange with Enhanced Photoelectrochemical Performance” *Nano Lett.*, 14, 2528–2535 (2014).
- (4) X.D. Wang, Z. Li, J. Shi, Y. Yu “One-Dimensional Titanium Dioxide Nanomaterials: Nanowires, Nanorods, and Nanobelts” *Chem. Rev.*, 114, 9346–9384 (2014).
- (5) Z. Li, C. Yao, F. Wang, Z. Cai, X.D. Wang “Cellulose Nanofiber-Templated Three-Dimension TiO₂ Hierarchical Nanowire Network for Photoelectrochemical Photoanode” *Nanotechnology*, 25, 504005 (2014).
- (6) Y. Yu, J. Li, D. Geng, J. Wang, L. Zhang, T.L. Andrew, M.S. Arnold, X.D. Wang “Development of Lead Iodide Perovskite Solar Cells Using Three-Dimensional TiO₂ Nanowire Architectures” *ACS Nano*, 9, 564–572 (2015).
- (7) Z. Li, F. Wang, A. Kvit, X.D. Wang “Nitrogen Doped 3D Titanium Dioxide Nanorods Architecture with Significantly Enhanced Visible Light Photoactivity” *J. Phys. Chem. C*, 119, 4397–4405 (2015).
- (8) Y. Yu, Z. Li, Y. Wang, S. Gong, X.D. Wang “Sequential Infiltration Synthesis of Doped Polymer Films with Tunable Electrical Properties for Efficient Triboelectric Nanogenerator Development” *Adv. Mater.*, 27, 4938–4944 (2015).
- (9) Z. Li, C. Yao, Y. Wang, Z. Cai, X.D. Wang “Highly-Efficient Capillary Photocatalytic Water Splitting Using Cellulose Nanofiber-templated Pt-TiO₂ 3D architectures” submitted.

Boron-based nanostructures, stability, functionality and synthetic routes

Boris I. Yakobson

Department of Materials Science and Nano-Engineering, Rice University, biy@rice.edu

Program Scope

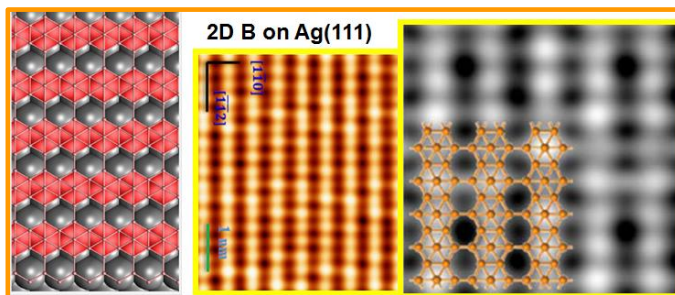
We focus on theoretical and computational modeling line of work, with general direction towards investigation of boron (B) clusters-fullerenes and of planar 2D (two dimensional) B-based materials. Specific sub-tasks, chosen based on priority or continuity criteria, include the following. We perform a theoretical assessment of the stability and the ways of confinement of the recently discovered pure boron buckyballs [1], as a spectacular confirmation of our early predictions [2, 3]. We explore the ways of (conceptual) unfolding of the B₄₀ cluster, to see if this can lead to unanticipated novel planar material. We further undertake a theory-guided approach to 2D-materials synthesis, to assist experimentalists with not only “final target” but also the ways to possibly reach this target. We expand this novel direction, already demonstrated on pure-B layers towards other important example, including h-BN.

2D pure boron is polymorphic, and we will verify the shape of the formation energy hull with higher precision (which take larger cell to be considered in the CE (cluster expansion [4]) calculations. This is important not to miss, due to technicality, any of real sharp preferred forms. Important physics aspect that must be explored is the possibility of very high thermal conductivity of B-sheets and also hypothetical possibility of superconductivity of these metallic phases with potentially large electron-phonon coupling. Within pure-boron 2D family, we investigate 2D cluster-assembled B₁₂-boron sheets, as a legitimate alternative to the monoatomic layers.

Monolayer h-BN is isomorphic to graphene and its alloying with C can yield ver useful band gap tenability, as demonstrated in our recent collaboration with Jilin University, China (Zhang et al. *Nanoscale*, 2015).

Recent Progress

Density functional theory is accepted as an accurate way to determine the ground electronic state of a material and its stable structure, not necessarily the most stable. Augmenting it by further search-algorithms like cluster expansion and more recently, grid-free evolutionary methods, makes it possible to find unknown materials structures as global minima. Moreover, if the search is



Predicted (left, our published work) versus STM-observed + simulated (right) monolayer B on Ag(111) [5].

performed in presence of a templating or even catalytic substrate, this further enables predicting the conditions and likely synthetic routes. Boron layers highlight the success of these developments, as detailed below.

While the experimental realization of 2D boron sheets remains a challenge, it is important to theoretically investigate the possible fabrication methods. Recently we have explored the formation of B sheets on metal (Cu, Ag, Au) and metal boride (MgB₂, TiB₂) substrates via first-principles calculations. Our results suggest that B sheets can be grown on the Ag(111) or Au(111) surfaces by deposition. B atoms decomposed from precursor, and driven by the gradient of chemical potential, will assemble into 2D clusters and further grow to a larger sheet, while formation of three-dimensional B structures is impeded due to high nucleation barrier (Liu et al. *Angew. Chemie*, 2013).

Further, after revealing the polymorphisms of 2D B, we find how this can be altered in presence of substrates. Indeed, typical two-dimensional (2D) materials—such as graphene and boron nitride—have specific lattice structure independent of external conditions. In contrast, the structure of 2D boron sensitively depends on metal substrate, as we have shown (Zhang et al. *Angew. Chemie*, 2015) using cluster expansion method and a newly developed surface structure-search method, both based on first-principles calculations. The preferred 2D boron on weaker interacting Au is nonplanar with significant buckling and numerous polymorphs as in vacuum, whereas on more reactive Ag, Cu and Ni, the polymorphic energy degeneracy is lifted and a particular planar structure is found to be most stable. We further show that a layer composed of icosahedral B₁₂ is unfavorable on Cu and Ni but unexpectedly becomes a possible minimum on Au and Ag. The substrate-dependent 2D boron choices originate from a competition between the strain energy of buckling and chemical energy of electronic hybridization between boron and metal. As a result we have not only identified Ag(111) as promising substrate but also which specific 2D B configuration should form (Zhang et al. *Angew. Chemie*, 2015). Recent experimental evidence [5] appears to be in remarkable accord with this prediction.

Future Plans

Future plans include to move forward from theoretical determination of possible 2D B structures to more detailed analysis of their properties: stability (cautiously) with possibly necessary confinement, thermal transport, and especially superconductivity assessment. The latter includes detailed band structure and Fermi surface analysis, electron-phonon interaction and estimated of the T_c values [6].

References

[1] Zhai, H. J.; Zhao, Y. F.; Li, W. L.; Chen, Q.; Bai, H.; Hu, H. S.; Piazza, Z. A.; Tian, W. J.; Lu, H. G.; Wu, Y. B.; Mu, Y. W.; Wei, G. F.; Liu, Z. P.; Li, J.; Li, S. D.; Wang, L. S. *Nature Chem* **2014**, 6, (8), 727-31.

[2] “The boron buckyball”, N. Gonzalez Szwacki, A. Sadrzadeh, and B.I. Yakobson, *Phys. Rev. Lett.*, **98**, 166804 (2007). -- **Editors’ Suggestion**.

[3] Research highlight: *Nature* 447, 4-5 (3 May 2007) | doi:10.1038/447004a.

[4] "Polymorphism of the two-dimensional boron", E.S. Penev, S. Bhowmick, A. Sadrzadeh, and B.I. Yakobson, *Nano Lett.*, **12**, 2441–2445 (2012).

[5] Kehui Wu, CAS, private communication.

[6] E.S. Penev, A. Kutana, and B.I. Yakobson, manuscript in preparation.

Publications (recent, selected)

"Two-dimensional boron monolayers mediated by metal substrates", Z. Zhang, Y. Yang, G. Gao, and B.I. Yakobson, *Angewandte Chemie*, DOI: 10.1002/anie.201505425 (2015). – **Cover article**.

“Probing the synthesis of two-dimensional boron by first-principles computations”, Y. Liu, E.S. Penev, and B.I. Yakobson, *Angewandte Chemie*, **52**, 3156-3159 (2013).

“Two-dimensional boron–nitrogen–carbon monolayers with tunable direct band gaps”, M. Zhang, G. Gao, A. Kutana, Y. Wang, X. Zou, J.S. Tse, B.I. Yakobson, H. Li, H. Liu, and Y. Ma, *Nanoscale*, **7**, 12023–12029 (2015).

Mapping the synthetic routes for 2-dimensional materials

Boris I. Yakobson

Department of Materials Science and Nano-Engineering, Rice University, biy@rice.edu

Program Scope

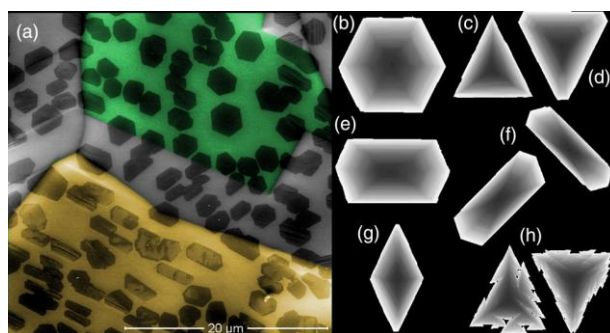
This project is motivated by three concurrent factors: (i) an intensified worldwide interest and research in two-dimensional materials, which emphasized the need for a deeper understanding and control of their synthesis; (ii) success in our laboratory in developing a general approach to modeling the growth of graphene, with basic ideas transferable to the broader 2D-materials family; (iii) emergent findings—including some in our own work—of specific functionalities among 2D materials, relevant to DOE interests, such as potential battery electrodes [1], catalytic activity, tunable energy band gaps for electronics, interfaces in heterogeneous systems for photovoltaics, etc. These very factors (i-iii) make the effort timely, as the rapid development of basic science of 2D materials synthesis facilitates their availability, improve quality, and diversify keenly sought functionalities for important practical applications. Indeed, the discovery of novel physics in graphene, combined with the hurdle of “opening” its electronic gap, has ignited the interest and expanded the scope of research worldwide, to the extended family of 2D-materials “beyond graphene”. This raised a number of broader compelling questions about the ways of making such monoatomic layers. The exfoliation from natural bulk precursors (3D bulk to 2D layer) is not scalable. On the other hand, their synthesis—often called “growth” due to visible change in size and shape—through chemical vapor deposition (CVD) involves complex gas-solid chemistry, which often works empirically, but its theoretical understanding and sentient design remain in infancy. This is the direction in which we embark to explore: developing state of the art multiscale models of 2D-layers on substrates and of atomistic mechanisms of their nucleation (when the 2D island may or may not be preferred over the 3D cluster) and subsequent growth. Our unique combination of methods, from the first principles density functional theory (for underlying forces and interface dynamics) to the nucleation and growth theories, organized together in the *nanoreactor* mass-flow diagram [2], is being connected to phenomenological larger-scale models (Monte Carlo simulations, phase field, level sets). This enables predicting the growth rates and morphology evolution on different substrates and at different conditions. We explore how a sentient choice of a substrate, interacting at just the right level with the commencing nucleus, can facilitate growth of planar materials forms, even for compositions currently unavailable. Our project materials focus is at two levels. The primary set includes those of already established great interest: graphene (C), planar hexagonal boron nitrogen (h-BN, “white graphene”), and transition metal disulfides like MoS₂. However, we also investigate nucleation and growth of emergent or even hypothetical 2D materials: phosphorene (P), stanene (Sn), silicene (Si), borene (B), and possibly others. Success of this project, even if limited to a subset of material examples, could be enormous, by leading to efficient synthesis and availability of materials with novel desired properties. It should impact

fundamental studies in this field, as well as permit various applications in devices, energy utility and production, of commercial and defense significance.

Recent Progress

One line of research was in exploring role of defects emerging in the course of synthesis or other fabrication (e. g. exfoliation, remaining almost exclusive way in case of phosphorene). The deep gap states created by defects in semiconductors typically deteriorate the performance of (opto-) electronic devices. This has limited the applications of two-dimensional (2D) metal dichalcogenides (MX_2), and underscored the need for a new 2D semiconductor without defect-induced deep gap states. In this work [Liu et al. *Nano Lett.* 2014, Wang et al. *Nanoscale* 2015] we demonstrate that a 2D mono-elemental semiconductor is a promising candidate. This is exemplified by first-principles study of 2D phosphorus (P) a.k.a. phosphorene, a recently fabricated high-mobility semiconductor. Most of the defects, including intrinsic point defects and grain boundaries, are electronically inactive, thanks to the homo-elemental bonding, which is not preferred in hetero-elemental system such as MX_2 . Unlike MX_2 , the edges of which create deep gap states and cannot be eliminated by passivation, the edge states of 2D P can be removed from the band gap by hydrogen termination. We further find that both the type and the concentration of charge carriers in 2D P can be tuned by doping with foreign atoms. Our work sheds light on the role of defects in the electronic structure of materials.

Another important line of progress is shaping as we study how graphene (and more generally 2D-material) morphology is affected by lower-symmetry metal surfaces supporting it during synthesis. For the Ni(111) triangular surface we find different ground-state structures (hexagonal and Klein) of zigzag edges in different directions and predict from first principles the equilibrium and growth shapes of graphene islands to explain the diversity of experimentally observed shapes. Then we



Observed and MC simulated variety of shapes of graphene on Ni(111) [Artyukhov et al. PRL 2015]

present experimental observations of shapes of graphene islands grown simultaneously on different crystallographic surfaces of Cu, and explain the origin of these shapes in the symmetry of respective Cu surfaces—(111), (110), (100)—using Monte Carlo simulations of growth. The insight straightforwardly generalizes to other substrates and 2D materials. We note that for equilibrium shape, edge energy variations δE manifest in just slightly distorted hexagons with different ground-state edge structures. In growth or nucleation, energy variation enters exponentially as $\sim e^{\delta E/k_B T}$, strongly amplifying the symmetry breaking, up to completely changing the shapes to triangular, ribbonlike, or rhombic (see Figure).

Future Plans

Future plans include the completion of extensive work, including the code development, on the phase field and multi-phase field modeling of 2-dimensional growth and especially fusion of multi-nuclei in determining the shapes of growing crystal. This already allows us to explain a number of puzzling shapes in numerous reported microscopy data (among them, notably, so called bowties and David Stars), which includes explanation of dominating inversion twins and grain boundaries [3]. Another line of work is to expand the application of nanoreactor approach [2] to growth model of h-BN, with borazine or ammonia borane as precursors.

References

[1] “Assessing carbon-based anodes for lithium-ion batteries: A universal description of charge-transfer binding”, Y. Liu, Y.M. Wang, B.I. Yakobson, and B.C. Wood, *Phys. Rev. Lett.*, **113**, 028304 (2014).

[2] “Equilibrium at the edge and atomistic mechanisms of graphene growth”, V.I. Artyukhov, Y. Liu, and B.I. Yakobson, *Proc. Natl. Acad. Sci.*, **109**, 15136-15140 (2012).

[3] “Formation of bowtie- and star-shaped MX₂ nanoislands via oriented attachments” V.I. Artyukhov, Z. Hu, Z. Zhang, and B.I. Yakobson (manuscript to be submitted for publication).

Publications (recent, selected)

“Electro-mechanical anisotropy of phosphorene”, L. Wang, A. Kutana, X. Zou, and B.I. Yakobson, *Nanoscale*, **7**, 9746-9751, DOI: 10.1039/C5NR00355E (2015).

“Two-dimensional mono-elemental semiconductor with electronically inactive defects: The case of phosphorus”, Y. Liu, F. Xu, Z. Zhang, E.S. Penev, and B.I. Yakobson, *Nano Lett.*, **14**, 6782–6786, DOI: 10.1021/nl5021393 (2014). – **Cover article.**

“Breaking of symmetry in graphene growth on metal substrates”, V.I. Artyukhov, Y. Hao, R.S. Ruoff, and B.I. Yakobson, *Phys. Rev. Lett.*, **114**, 115502 (2015).•

“Metallic high-angle grain boundaries in monolayer polycrystalline WS₂”, X. Zou and B.I. Yakobson, *Small*, DOI: 10.1002/sml.201500811 (2015).

Atomic Layer Deposition (ALD) of Metal and Metal Oxide Films: A Surface Science Study

Francisco Zaera

Department of Chemistry, University of California, Riverside, CA 92521, zaera@ucr.edu

i) Program Scope

The general objective of our project is to develop a molecular-level understanding of the thermal reactions that organometallic compounds used for atomic layer deposition (ALD) follow on surfaces. ALD is poised to become one of the dominant technologies for the growth of nanometer-sized conformal films in many industrial applications. In microelectronics in particular, the growth of diffusion, adhesion, and protection barriers and of metal interconnects is central to the buildup of diodes, transistors, and other elements within integrated circuits. All these processes require the deposition of isotropic films on complex topographies under mild conditions and with monolayer control. ALD is particularly suited to satisfy all those conditions, but many questions concerning the underlying surface chemistry need to be answer before it can find widespread use.

Our mechanistic studies of the ALD-related reactions is being pursued with the aid of a number of surface-sensitive techniques, including X-ray photoelectron (XPS), temperature programmed desorption (TPD), and infrared (IR) spectroscopies. One present focus is the study of processes for the deposition of copper metal interconnects and of diffusion barriers for those, a central need in the microelectronics industry. Specific questions are being addressed in terms of the kinetics and mechanisms of the reactions involved, and also in connection with the composition and morphology of the resulting films. This knowledge will be directed to the design of ALD processes that operate under the mildest conditions possible and deposit stoichiometric and pure films with good density, low resistance, and smooth surfaces.

ii) Recent Progress

In the initial stages of this project, we have characterized the thermal chemistry of copper(I)-*N,N'*-di-*sec*-butylacetamidinate on Ni(110) single-crystal and cobalt polycrystalline surfaces under ultrahigh vacuum (UHV) conditions by XPS and TPD [1; 2]. This chemistry was later tested on a Cu(110) surface in order to probe the chemistry associated with the build up of the metal film once the first copper layer has been grown [3]. A series of thermal stepwise conversions were identified, starting with the partial dissociative adsorption of the copper acetamidinate dimers into a mixture of monomers and dimers on the surface. On copper, an early dissociation of a C–N bond leads to the production of *N-sec*-butylacetamide, which is detected in TPD experiments in three temperature regimes, the last one centered around 480 K. Butene, and a small amount of butane, is also detected above approximately 500 K, and hydrogen production, an indication of dehydrogenation of surface fragments, is observed at 460, 550 and 670 K. In total, only about 10% of the initial copper(I)-*N,N'*-di-*sec*-butylacetamidinate adsorbed monolayer decomposes, and only about ~3% of carbon is left behind on the surface

after heating to high temperatures. It is interesting to note that deposition of copper films with this precursor is dirtier on Cu(110) than on Ni(110).

Using the lessons learned from those initial studies, we have continued to tailor the structure of the precursors to minimize their side reactions. With the assistance of the research group of Sean Barry, a synthetic inorganic chemist, we have expanded our surface-science studies to Cu(I)-iminopyrrolidinate and Cu(I)-guanidinate metalorganic compounds [4]. Specifically, the thermal chemistry of tetrakis[Cu(I)-*N-sec-butyl-iminopyrrolidinate*] and bis[Cu(I)-*N,N*-dimethyl-*N',N''*-di-*iso*-propyl-guanidinate] was investigated on a Ni(110) single-crystal. Both precursors, which exist as tetramers and dimers in the solid phase, respectively, undergo dissociative adsorption at temperatures below 200 K to produce adsorbed monomers on the surface. A β -hydride elimination step is then operative near 300 K that leads to the release of some of the ligands in dehydrogenated form. The remaining adsorbates obtained from either precursor undergo similar further decomposition between 350 K and 600 K as the copper atoms are reduced from a Cu(I) oxidation state to metallic Cu(0). Hydrocarbons resulting from the elimination of the terminal moieties include ethene and acetonitrile from the Cu(I)-iminopyrrolidinate and propene from the Cu(I)-guanidinate, which are ejected around 420 - 490 K, and HCN in both cases at approximately 570 - 580 K. These results show several similarities with the surface chemistry previously reported for bis[Cu(I)-*N,N'*-di-*sec*-butyl-acetamidinate], and suggest a common behavior in the surface reactions of these families of Cu(I)-amidinate, Cu(I)-iminopyrrolidinate, and Cu(I)-guanidinate ALD precursors. A schematic summary of these mechanisms is shown in Figure 1. This work has been extended to other surfaces (silicon oxide) [5] and to other types of precursors [6].

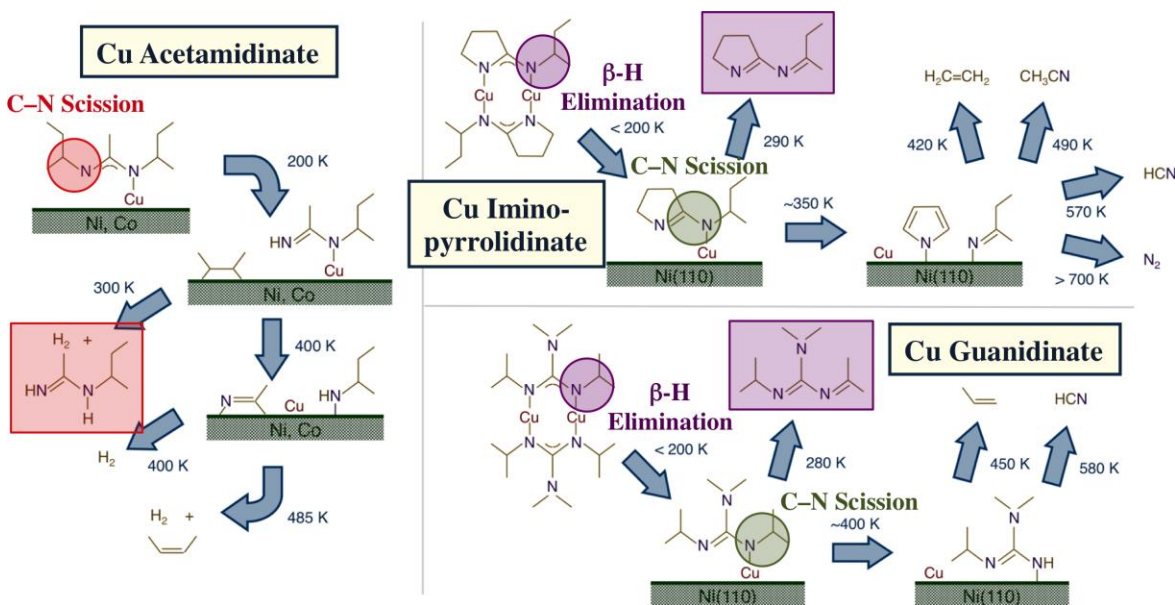


Figure 1. Mechanism for the thermal decomposition of the Cu(I) acetamidinate, iminopyrrolidinate, and guanidinate ALD precursors studied so far in this project. Highlighted are the weak bonds, those that are activated thermally to lead to the dissociation of the organic ligands and to the production of undesirable products. In the future, our goal is to stabilize the C–N bonds and to block the beta position to avoid β -hydride elimination steps.

Another area of research we have been pursuing is related to the deposition of manganese films as diffusion barriers in microelectronics. For this, the thermal chemistry of methylcyclopentadienyl manganese tricarbonyl ($\text{MeCpMn}(\text{CO})_3$) on silicon oxide surfaces was characterized by a combination of analytical techniques, including gas chromatography-mass spectrometry (GC-MS) and infrared absorption spectroscopy in addition to TPD and XPS [7]. The compound was found to be fairly stable, but to be able to dissociatively chemisorb on the surface via the loss of one or more carbonyl ligands followed by the oxidative addition of a surface silanol group. Further activation leads to the loss of the aromatic ligand, at temperatures above approximately 575 K. GC-MS data indicates that this takes place primarily via the addition of a hydrogen atom to the MeCp ligand to form methylcyclopentadiene, which is released to the gas phase, but a small competing channel starts at slightly lower temperatures that yields fulvene, and/or possibly benzene, after molecular rearrangement (Figure 2). The clean nature of the chemistry seen here for the methylcyclopentadienyl Mn complex makes it a good candidate as a precursor in the chemical deposition of metal thin films. However, the high stability and the high temperatures required for its decomposition do introduce some limitations.

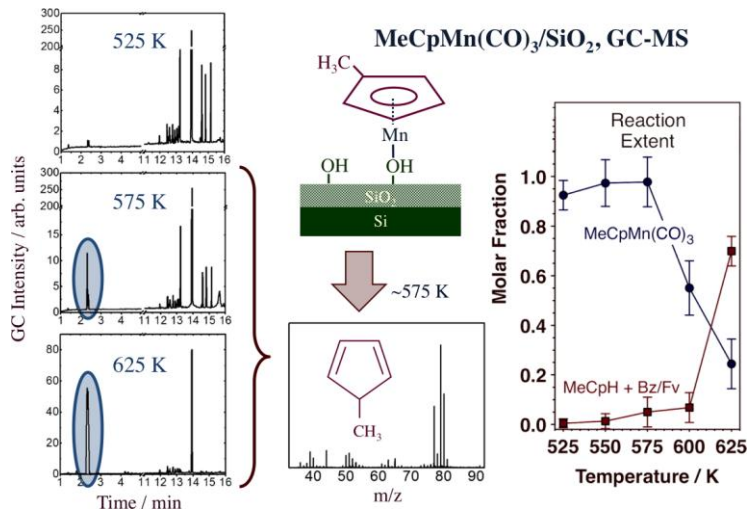


Figure 2. GC-MS data indicating that the main decomposition pathway for $\text{MeCpMn}(\text{CO})_3$ is a protonation step to produce methylcyclopentadiene. This makes the precursor promising for the deposition of clean films, but also difficult to activate.

Additional studies were carried out to test the further conversion of the Mn precursor on the surface using an oxidizing (N_2O) versus a reducing (H_2) co-reactant [8]. It was found that N_2O removes the majority of the MeCp adsorbed species, oxidizes the Mn silicide, and leads to the conversion of the $\text{MnO}_x + \text{SiO}_2$ oxide mixture into a Mn silicate top layer, whereas with H_2 only about half of the MeCp adsorbates can be removed in each cycle and only a small amount of additional Mn silicide is added in the second and third ALD cycles, but the original $\text{MnO}_x + \text{SiO}_2$ mixture is preserved and no significant increase in film thickness is detected.

Finally, a new process was developed to render surfaces selective toward ALD reactivity [9]. Specifically, a combination of silylation and UV/ozonolysis was tested as a way to control the concentration of the surface hydroxo groups required for subsequent atomic layer deposition (ALD) of metals or oxides. Water contact angle measurements were used to evaluate the hydrophilicity/hydrophobicity of the surface, a proxy for OH surface coverage, and to optimize the UV/ozonolysis treatment. Silylation with hexamethyldisilazane (HMDS), trichloro(octadecyl)silane (ODTS), or trimethylchlorosilane (TMCS) was found to be an efficient way to block the hydroxo sites and to passivate the underlying surface, and UV/ O_3 treatments were shown to effectively remove the silylation layer and to regain the surface reactivity. Both

O₃ and 185 nm UV radiation were determined necessary for the removal of the silylation layer, and additional 254 nm radiation was found to enhance the process. ATR-infrared absorption spectroscopy was employed to assess the success of the silylation and UV/O₃ removal steps, and AFM data provided evidence for the retention of the original smoothness of the surface. Selective growth of HfO₂ films via TDMAHf + H₂O ALD was seen only the UV/O₃ treated surfaces; total inhibition of the deposition was observed on the untreated silylated surfaces (as determined by XPS and ellipsometry). Residual film growth was still detected on the latter if the ALD was carried out at high temperatures (250 °C), because the silylation layer deteriorates under such harsh conditions and forms surface defects that act as nucleation sites for the growth of oxide grains (as identified by to electron microscopy, SEM). We believe that the silylation-UV/O₃ procedure advanced here could be easily implemented for the patterning of surfaces in many microelectronic applications.

iii) **Future Plans**

In the next year, we plan to continue along the research directions already ongoing in this project. Specifically, we intend to extend our initial studies to:

- Design and test new copper acetamidinate precursors without beta hydrogens in order to minimize their side decomposition.
- Look into the surface chemistry of the recently reported copper ALD using a combination of hydrazine and formic acid as co-reactants. This project has already been initiated, but requires further work.
- Study the use of oxidation reactions as a way to reduce the metal precursors in ALD. This may sound counterintuitive, but is an approach that has already been successfully tested with late transition metals.
- Incorporation of reflection-absorption infrared absorption spectroscopy (RAIRS) to our tools of surface sensitive techniques.

iv) **References**

- [1] Q. Ma, H. Guo, R. G. Gordon, F. Zaera, *Chem. Mater.* 22 (2010) 352-359.
- [2] Q. Ma, H. Guo, R. G. Gordon, F. Zaera, *Chem. Mater.* 23 (2011) 3325-3334.
- [3] Q. Ma, F. Zaera, R. G. Gordon, *J. Vac. Sci. Technol. A* 30 (2012) 01A114.
- [4] T. Kim, Y. Yao, J. P. Coyle, S. T. Barry, F. Zaera, *Chem. Mater.* 25 (2013) 3630-3639.
- [5] Y. Yao, F. Zaera, *J. Vacuum Sci. Technol. A* 34 (2016) 01A101.
- [6] Q. Ma, F. Zaera, *J. Vacuum Sci. Technol. A* 33 (2015) 01A108.
- [7] M. Bouman, X. Qin, V. Doan, B. L. D. Groven, F. Zaera, *Organometallics* 33 (2014) 5308-5315.
- [8] X. Qin, F. Zaera, *ECS J. Solid State Sci. Technol.* 3 (2014) Q89-Q94.
- [9] L. Guo, F. Zaera, *Nanotechnol.* 25 (2014) 504006.

v) **Publications Sponsored by This DOE Grant, 2014-2015**

1. Taeseung Kim, Yunxi Yao, Jason P. Coyle, Seán T. Barry, and Francisco Zaera, Thermal Chemistry of Cu(I)-Iminopyrrolidinate and Cu(I)-Guanidinate Atomic Layer Deposition (ALD) Precursors on Ni(110) Single-Crystal Surfaces, *Chem. Mater.*, **25(18)**, 3630-3639 (2013).
2. Xiangdong Qin and Francisco Zaera, Oxidizing versus Reducing Co-reactants in Manganese Atomic Layer Deposition (ALD) on Silicon Oxide Surfaces, *ECS J. Solid State Sci. Technol.*, **3(5)** Q89-Q94 (2014).
3. Menno Bouman, Xiangdong Qin, Vananh Doan, Benjamin L. D. Groven, and Francisco Zaera, Reaction of Methylcyclopentadienyl Manganese Tricarbonyl on Silicon Oxide Surfaces: Implications for Thin Film Atomic Layer Depositions, *Organometallics*, **33(19)**, 5308–5315 (2014).
4. Lei Guo, Francisco Zaera, Spatial Resolution in Thin Film Deposition on Silicon Surfaces by Combining Silylation and UV/Ozonolysis, *Nanotechnol.*, **25**, 504006/1-504006/10 (2014). INVITED, Special Issue: ‘Atomic Layer Deposition (ALD) in Energy, Environment, and Sustainability’
5. Qiang Ma and Francisco Zaera, Thermal Chemistry of the Cu-KI5 ALD Precursor on a Copper Surface, *J. Vac. Sci. Technol. A*, **33(1)**, 01A108/1-01A108/9 (2015). SPECIAL ISSUE: Atomic Layer Deposition.
6. Yunxi Yao and Francisco Zaera, Chemistry of Copper Acetamidinate ALD Precursors on Silicon Oxide, *J. Vac. Sci. Technol. A*, **34**, 01A101/1-01A101/8 (2016). ALD SPECIAL ISSUE
7. Yunxi Yao and Francisco Zaera, Adsorption and Thermal Chemistry of Formic Acid on Clean and Oxygen Predosed Cu(110) Single-Crystal Surfaces Revisited, *Surf. Sci.*, doi:10.1016/j.susc.2015.06.007 (2015). INVITED, Special Issue honoring Richard Lambert.
8. Yunxi Yao and Francisco Zaera, Thermal Chemistry of Hydrazine on Clean and Oxygen- and Water-Predosed Cu(110) Single-Crystal Surfaces, *Surf. Sci.*, doi:10.1016/j.susc.2015.08.034 (2015). INVITED, Special Issue in honor of Robert J. Madix.

Utilizing Molecular Self-Assembly to Tailor Electrical Properties of Si Nanomembranes

Pengpeng Zhang

Zhang@pa.msu.edu

Department of Physics and Astronomy
Michigan State University, East Lansing, MI 48824

Program Scope

The program is focused on understanding the various interfacial phenomena, including self-assembly of organic molecules, charge injection, distribution, and separation at the organic-inorganic hetero-interface that control electronic behavior. Interfacing organic molecules with semiconductors, in particular, with semiconducting nanostructures where materials transport properties are sensitive to surface and interface conditions offers a great opportunity to unravel the mechanistic basis of electronic interactions at hetero-interfaces. It can also potentially provide a nondestructive method for doping nanoscale semiconductors with molecular-scale precision. Technologically, the hetero-interfaces are crucial in the development of organic electronics, molecular electronics, molecular and biological sensors, and energy converting devices.

Recent Progress

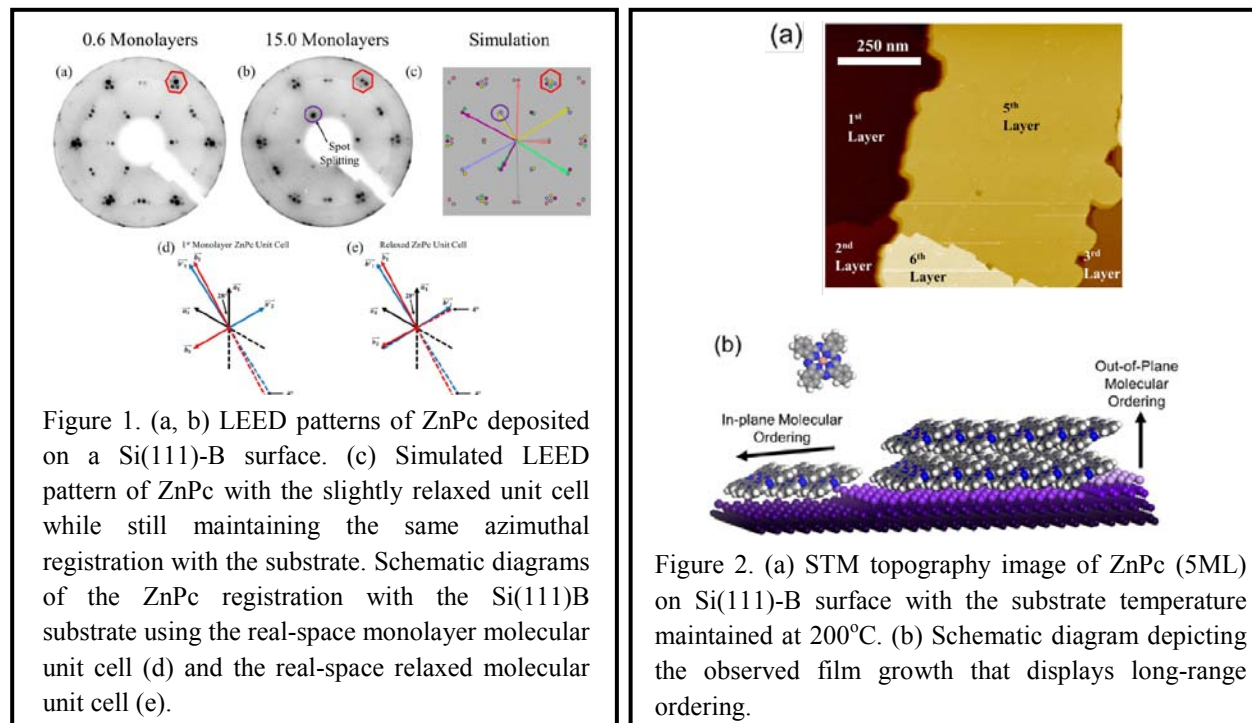
Organic π -conjugated molecules have become emerging materials for applications including light-emitting diodes, field effect transistors, and solar cell devices, in the current electronics market.¹ In these device platforms, molecules are often deposited onto or placed in contact with inorganic surfaces. Thus the resultant device performances are highly correlated with the electronic structure, molecular orientation, and molecular ordering at the hetero-interface. This has stimulated intense interest in understanding and further tuning the interfacial electronic structure and the molecule-substrate interaction, particularly, searching for routes towards controlled well-ordered organic molecular growth.

Previously, we reported the discovery of an anisotropic crystalline organic step-flow growth on the deactivated Si surfaces. Access to the step-flow growth mode provides a means to achieve long-range in-plane molecular ordering. However, a deep understanding of the out-of-plane molecular ordering for growth beyond the first layer remains unexplored. Furthermore, there is still a lack of understanding of the underlying molecule-substrate binding mechanism and the origin of this long-ranged ordered growth at the molecular level. Also, to what extent the molecule-substrate coupling strength can be rationally tuned and how it impacts the potential landscape, which is critical for controlling the growth kinetics and the thin film morphology, need to be addressed.

Recently, we have explored the out-of-plane molecular ordering of multilayered zinc phthalocyanine (ZnPc) thin films on the deactivated Si(111)-B surface by scanning tunneling microscopy (STM) and low energy electron diffraction (LEED). A change in the in-plane crystallization corresponds to a change in the molecular configuration, which will likely result in a change in the interlayer spacing. As shown in Fig. 1 (a) and (b), LEED patterns at the coverage of 0.6 monolayers and 15 monolayers only display subtle differences as marked by the red hexagon and purple circle, suggesting only a minor variation in the in-plane molecular ordering with increasing coverage. This minor variation is associated with a slightly relaxed unit cell in the multilayered ZnPc films, as illustrated in Fig. 1 (d) and (e), but the azimuthal registration between the molecular layer and the substrate is maintained. LEED simulation (Fig. 1(c)) carried

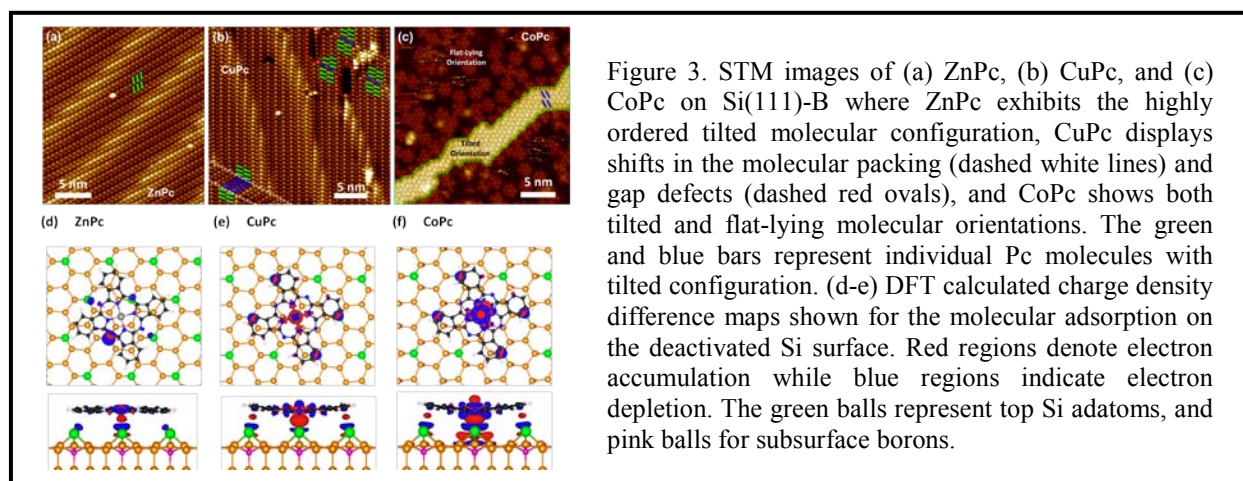
out using the relaxed ZnPc unit cell agrees well with the experimental observation. In fact, depositing up to a coverage of 40 monolayers results in the same LEED pattern as observed in Fig. 1(b), indicating that a highly ordered molecular structure is maintained in multilayered ZnPc films. Since the molecules starting from the initial monolayer are tilted above the Si(111)-B surface by $\sim 30^\circ$ (see schematics in Fig. 2(b)), it offers a large π - π interaction between adjacent layers. We speculate that it is this strong interlayer molecular interaction that drives the high degree of out-of-plane ordering in the molecular thin films, which is able to be maintained without relaxing to the bulk-like structure despite the gradually decreased molecule-substrate interaction.

Fig. 2(a) shows a STM image of multilayered ZnPc film. Layer-by-layer growth is established within each Si terrace. However, a variation of layer thickness exists across the terraces due to the Ehrlich-Schwöebel barrier associated with the Si step edges which prevents the downward mass transport of molecules. By decreasing the miscut of the Si substrate, the macroscopic roughness across the Si terraces will be reduced. This study contributes significant advances toward the formation of highly ordered molecular thin films both in-plane and out-of-plane which can be easily integrated into Si-based electronics or transferred to other substrates for organic device applications.



Next, we aim to establish a comprehensive understanding of the mechanisms of organic molecular growth on the deactivated Si(111)-B surface and the origin of this long-ranged ordered growth at the molecular level. Fig. 3 presents the surface topography of various MPc molecules deposited on the deactivated Si(111)-B surface with M=Zn, Cu, and Co respectively, where distinct molecular assembly and growth behaviors are identified. As shown in Fig. 3(a), ZnPc molecules adopt a tilted molecular configuration and crystallize to form densely packed structures. For CuPc, although it preserves the identical molecular orientation and packing motif as ZnPc, a notable degradation of the film quality is observed where a significant amount of gap defects and shifts in the molecular packing occur within the molecular domains (Fig. 3(b)).

Intriguingly, for the CoPc growth, we find that the molecules predominantly lie flat on the surface while the molecular patches with tilted configuration only emerge and are sparsely dispersed among the flat-lying molecules when the coverage is increased above a certain



threshold, as illustrated in Fig. 3(c).

This distinction is further corroborated by the difference observed in the initial molecular adsorption on the Si(111)-B surface. In contrast to CuPc where molecules display non-specific site registration with the deactivated Si surface, for the case of CoPc, both the Co ions and the 4 benzene rings preferentially register with the ad-Si atoms, as illustrated in Fig. 4(b) and (c). Due to the high degree of registration with the underlying surface, only 3 stable flat-lying CoPc orientations are allowed by the substrate symmetry, as highlighted by the red, blue and green rectangles. Such a drastically different molecular assembly and growth behavior observed for various MPc deposited on the Si(111)-B surface is in sharp contrast to the growth of these molecules on metallic surfaces where close-packed flat-lying molecular structures are formed regardless of the choice of the central transition-metal ion.²

Collaborating with Dr. Mina Yoon's group at ORNL, we have performed density functional theory calculations to account for the contrasting molecular adsorption and growth behavior of MPc on the deactivated Si(111)-B surface. By changing the metal ion from Zn to Co, the charge distribution within each orbital is altered and a depopulated d_{z^2} orbital is formed in CoPc. The d_{z^2} orbital, which is strongly localized on the central metal ion (over 90% of the molecular orbital), is the only symmetry-allowed orbital having nonzero overlap with the p_z state of ad-Si. Thus, a strong bond is anticipated to form between the singly-occupied d_{z^2} orbital of CoPc and the Si adatom, leading to a significantly higher energy gain as compared to the case of ZnPc and CuPc. Figure 4(a) presents the key mechanism of selective orbital hybridization between the singly-occupied d_{z^2} orbital of CoPc and the empty p_z orbital of ad-Si. This hybridization effect is also manifested in the charge density difference plot upon the adsorption of MPc on the substrate. As presented in Fig. 3(d)-(f), the strong orbital hybridization introduces

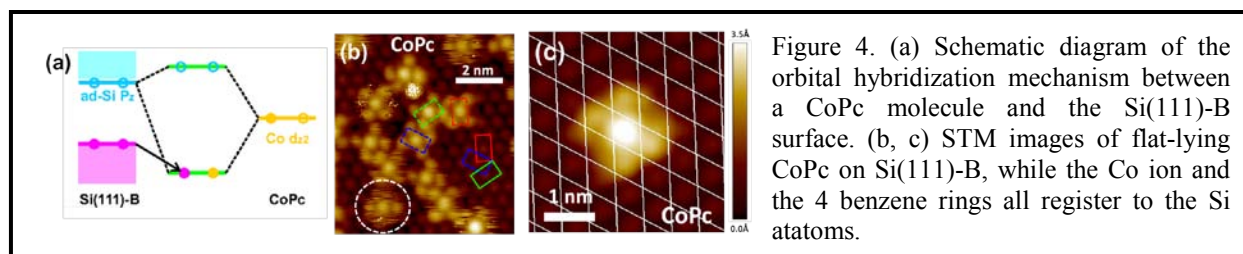
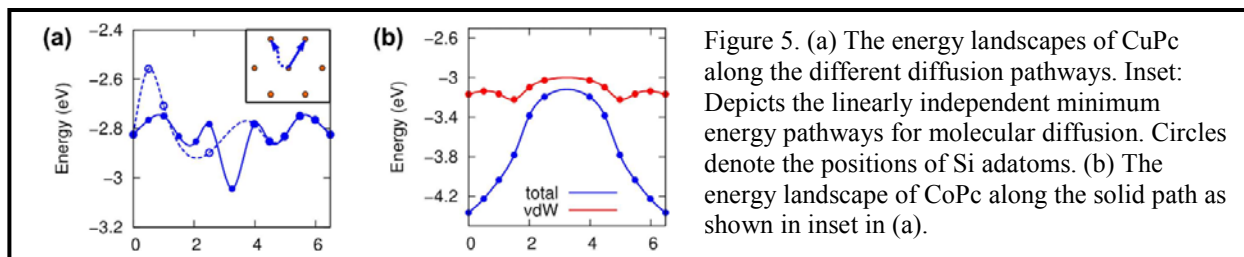


Figure 4. (a) Schematic diagram of the orbital hybridization mechanism between a CoPc molecule and the Si(111)-B surface. (b, c) STM images of flat-lying CoPc on Si(111)-B, while the Co ion and the 4 benzene rings all register to the Si adatoms.

a significant charge accumulation on the p_z orbitals of ad-Si for CoPc (red regions in Fig. 3(f)), while a negligible or minute charge accumulation is observed for ZnPc and CuPc, respectively (Fig. 3(d) and (e)).

Thus far, we have identified a distinct mechanism of molecular binding to the substrate mediated by the central transition-metal ions. To further investigate the interplay between molecule-substrate interaction and molecular growth, the potential energy landscape of the surface is examined along selective directions where the internal molecular coordination (including rotation) is fully optimized at each point. For CuPc (similar trends are expected for ZnPc), along the two linearly independent diffusion pathways there are many local minima separated by low potential barriers that are mainly due to the vdW energy corrugation (Fig. 6(a)). Nevertheless, these small diffusion energy barriers can be easily overcome by intermolecular attraction, resulting in unhindered molecular diffusion of CuPc on the deactivated Si(111) surface. In contrast, in the case of CoPc, the potential energy landscape exhibits a deep potential well associated with a significant energy barrier that is over 1.2 eV (Fig. 6(b)). The small vdW potential energy corrugation (solid red line) indicates that this large energy barrier originates from the breaking of the chemical bond between the Co and the ad-Si atom as discussed previously. This chemical bond dominates the potential energy landscape and results in a strong localization of molecules on the surface.



In summary, we have shown that the localized p_z orbitals on the Si(111)-B surface allow for highly selective orbital coupling with the d -orbitals of MPc molecules. By appropriately choosing the coordinated transition-metal ion in MPc to control the strength of the p - d orbital hybridization, the molecule-substrate interaction can be tuned accordingly. This leads to distinct molecular growth behavior ranging from a localized flat-lying molecular configuration to the formation of a highly ordered molecular thin film in a tilted configuration. The range of molecular ordering and orientation accessible with varying degree of molecular hybridization allows for the possibility of selecting a system exhibiting ideally balanced molecule-substrate and intermolecular interactions for forming well-ordered organic molecular growth that can be incorporated into modern electronics.

Future Plans

Beyond the topological control, it is also crucial to characterize electronic interactions at hetero-interfaces in order to utilize molecular adlayer as a nondestructive method for doping nanoscale semiconductors. To this end, we have utilized kelvin probe force microscopy to investigate interfacial charge transfer between various types of MPc molecules of differing electronegativity on ultrathin (15 nm) Si nanomembrane. We are currently concentrating on conducting transport measurements to evaluate the effects of surface chemical functionalization and interfacial charge transfer on electronic properties of Si nanomembranes.

References

1. G. Witte and C. Wöll, *J. Mater. Res.* **19**, 1889 (2004).
2. S. C. Bobaru, E. Salomon, J. -M. Layet, and T. Angot, *J. Phys. Chem. C* **115**, 5875 (2011).

DoE Sponsored Publications in the Last Two Years

1. S. R. Wagner, R. R. Lunt, and P. P. Zhang, *Anisotropic Crystalline Organic Step-Flow Growth on Deactivated Si Surfaces*, Phys. Rev. Lett. **110**, 086107 (2013).
2. S. R. Wagner and P. P. Zhang, *Surfaces and Interfaces of Nanoscale Silicon Materials*, Mater. Res. Soc. Symp. Proc. **1550**, 609 (2013).
3. S. R. Wagner and P. P. Zhang, *Formation of Highly Ordered Organic Molecular Thin Films on Deactivated Si Surfaces Studied by Scanning Tunneling Microscopy and Low Energy Electron Diffraction*, J. Phys. Chem. C. **118**, 2194 (2014).
4. J. Sun, K. Pimcharoen, S. R. Wagner, P. M. Duxbury, and P. P. Zhang, *Nanoscale Imaging of Dense Fiber Morphology and Local Electrical Response in Conductive Regioregular Poly(3-hexylthiophene)*, Org. Electron. **15**, 441 (2014).
5. S. R. Wagner and P. P. Zhang, *Nucleation and Evolution of Zinc Phthalocyanine Thin Films on the Deactivated Si(111)-B $\sqrt{3} \times \sqrt{3}$ R30° Surface*, Surf. Sci. **630**, 22 (2014).
6. J. Feng, S. R. Wagner, and P. P. Zhang, *Interfacial Coupling and Electronic Structure of Two-Dimensional Silicon Grown on the Ag(111) Surface at High Temperature*, Sci. Rep. **5**, 10310 (2015).
7. S. R. Wagner, B. Huang, C. Park, J. Feng, M. Yoon, and P. P. Zhang, *Growth of Metal Phthalocyanine on Deactivated Semiconducting Surfaces Steered by Selective Orbital Coupling*, Phys. Rev. Lett. **115**, 096101 (2015).

***In Situ* Visualization and Theoretical Modeling of Early-Stage Oxidation of Metals and Alloys**

Guangwen Zhou

Department of Mechanical Engineering, State University of New York, Binghamton, NY 13902

Program Scope

Oxidation processes occurring at metal surfaces have tremendous importance in the environmental, chemical, energy, pharmaceutical, and microelectronics industries. A precise knowledge of the oxidation process and the atomic structure of the oxide layer is essential to improving existing processes and designing new functional materials. While several theories (e.g. Wagner-type diffusion theories, Cabrera-Mott model of electric-field driven oxide growth) have been formulated which explain and predict the oxidation behavior of many metals and alloys, they are satisfactory only over limited oxide thickness regions and often are not transferable to the initial stages of surface oxidation. The objective of this program is to bridge this information gap by developing an atomistic understanding of the microscopic processes governing the initial stages of oxidation ranging from oxygen surface chemisorption to the subsequent stages of oxide nucleation and growth. To this end, *in situ* microscopy and spectroscopy techniques are utilized to monitor, in real time and at the atomic and nanometer scales, the surface oxidation of a number of model systems of metals and alloys. Such *in situ* experimental data feed into the density-functional theory (DFT) modeling for identifying the critical kinetic and thermodynamic factors controlling the surface oxidation process including adsorption sites, diffusion path, reaction barrier, and surface/interface effects.

Recent Progress

A detailed understanding of the initial oxidation processes of surfaces has always been complicated by overwhelming inhomogeneities due to high density of defects. Atomic steps are present on virtually any crystalline material in any environment and serve as natural sources and sinks of substrate atoms owing to the reduced coordination of atoms at step sites. Through the use of a combination of *in situ* microscopy tools (low-energy electron microscopy (LEEM), aberration-corrected environmental transmission electron microscopy (TEM), and scanning tunneling microscopy (STM)) and theoretical modeling, we addressed oxidation induced surface dynamics as a result of mass transfer from and to steps. This is a critical issue since it influences both the mechanism and kinetics of many surface physical and chemical processes.

There has been intensive interest in understanding oxidation behaviors of NiAl alloys since NiAl is an attractive material for high-temperature applications for its a high melting point, low density, good oxidation and corrosion resistance. Understanding the initial oxidation of NiAl alloys is important to gain better insight into the oxide film growth and alloy degradation. Using LEEM that spatially and temporally resolves oxide film growth during the oxidation of NiAl(100), we demonstrated that surface steps are impermeable to oxide film growth. The advancement of the oxide occurs exclusively on the same terrace and requires the coordinated migration of surface steps. The resulting piling up of surface steps ahead of the oxide growth front progressively impedes the oxide growth [1]. This process is reversed during oxide decomposition. Fig. 1 exemplifies a sequence of *in situ* LEEM images of the oxidation of NiAl(100). The surface has a step-terrace morphology, where dark lines show the locations of atomic steps on the NiAl substrate and the center area has well separated steps. The oxidation

results in the growth of Al_2O_3 stripes with the supply of Al atoms from surface steps. A remarkable growth feature revealed from the *in situ* LEEM observation is that the oxide stripes do not cross over substrate steps, instead, surface steps migrate in tandem with the advancement of the oxide stripes. Therefore, the oxide stripe pushes each substrate step that it encounters to advance jointly with the step edge in its path, which results in the bunching of a growing number of steps in front of the oxide stripe. These experiments demonstrated that an oxide stripe stays on the same terrace as it encounters either ascendant or descendant steps during the oxide growth or decomposition. By comparing with the oxidation of NiAl(110) that exhibits unimpeded oxide film growth over substrate steps [2-4], we suggest that whenever steps are the source of atoms used for oxide growth, they limit the oxidation process; when atoms are supplied from the bulk, the oxidation rate is not limited by surface steps. The difference in the oxidation of NiAl(100) and (110) can be attributed to the effect of the crystallographic orientation. NiAl(110) has a less compact surface structure than NiAl(100), which may facilitate surface-bulk mass transport. For NiAl(100), the more compact surface structure makes surface steps kinetically more favorable as the source of Al atoms for oxide growth. This is further confirmed by our DFT calculations, which indicate that the energy barriers for the step-edge detachment on NiAl(100) are much smaller than those for NiAl(110).

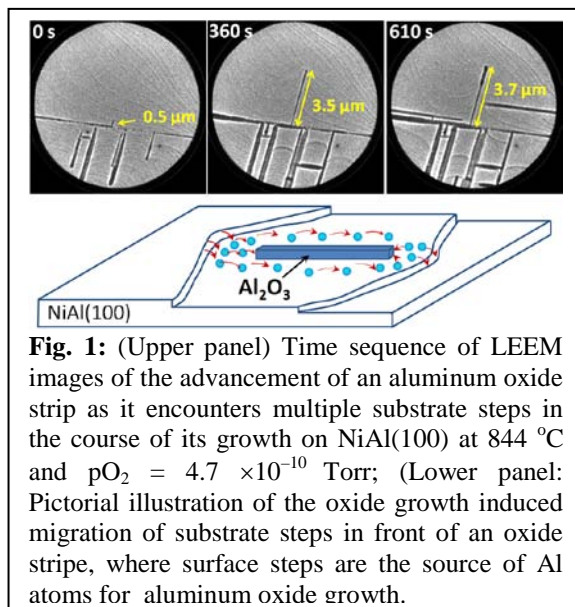


Fig. 1: (Upper panel) Time sequence of LEEM images of the advancement of an aluminum oxide strip as it encounters multiple substrate steps in the course of its growth on NiAl(100) at 844 °C and $p\text{O}_2 = 4.7 \times 10^{-10}$ Torr; (Lower panel: Pictorial illustration of the oxide growth induced migration of substrate steps in front of an oxide stripe, where surface steps are the source of Al atoms for aluminum oxide growth.

Using *in situ* environmental TEM, we also visualized oxide film growth at atomic resolution during the oxidation of stepped Cu surfaces. We observed that the presence of surface steps leads to the decomposition of the oxide overlayer at the growth front, thereby resulting in oscillatory oxide film growth that proceeds in tandem with the propagation of the surface step. DFT calculations and *ab initio* molecular dynamics (AIMD) were employed to address the experimental observations. Fig. 2(a) shows *in situ* high-resolution

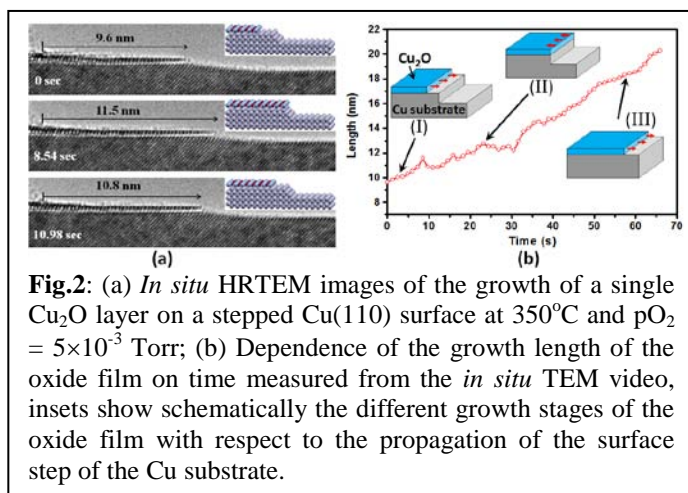


Fig.2: (a) *In situ* HRTEM images of the growth of a single Cu_2O layer on a stepped Cu(110) surface at 350°C and $p\text{O}_2 = 5 \times 10^{-3}$ Torr; (b) Dependence of the growth length of the oxide film on time measured from the *in situ* TEM video, insets show schematically the different growth stages of the oxide film with respect to the propagation of the surface step of the Cu substrate.

TEM images of the oxidation of a Cu(110) surface. The oxidation proceeds through the growth of a single Cu oxide layer on the Cu(110) surface. The Cu surface consists of two wide terraces separated by a $\sim 5\text{-\AA}$ height step-bunched region. The *in situ* TEM observation shows that the oxide layer does not sweep across the stepped region unimpeded. Instead, the stepped region moves synchronously with the oxide growth. Such in-step propagation is interrupted when the substrate step flow does not keep up with the oxide growth, and the growth front of the oxide layer reaches the downward edge of the Cu terrace. The oxide layer is seen to retract from the

terrace edge and then resumes its growth. Once the oxide growth front catches up with the step edge again, it undergoes another cycle of retraction/re-growth. Fig. 2(b) shows the evolution in the length of the oxide layer measured from the *in situ* TEM video. Insets in Fig. 2 show schematically several key stages of the observed oscillation (TEM electron-beam irradiation has a negligible effect on the observed oscillation as evidenced by the lack of oscillatory growth on flattened surface under the imaging condition). Our *in situ* TEM observations also demonstrated that the oscillatory oxide growth is not tied to a particular step-edge configuration [7], implying the broader applicability of the results to other systems. Indeed, similar oscillation in the growth of Al₂O₃ films in step-bunched regions was also observed from our *in situ* LEEM observations of the oxidation of NiAl(100).

Using *in situ* STM, we provided direct evidence that surface steps are the source of Cu adatoms for the Cu(110)-(2×1)-O restructuring [8]. As shown in Fig. 3, a screw dislocation intersects the Cu(110) surface, which results in the presence of a monoatomic-height surface. With increasing O coverage, -Cu-O- rows form stripe-shaped domains of the (2×1)-O reconstruction with coordinated retraction of the surface step from its original position, which demonstrates rather nicely that Cu atoms are

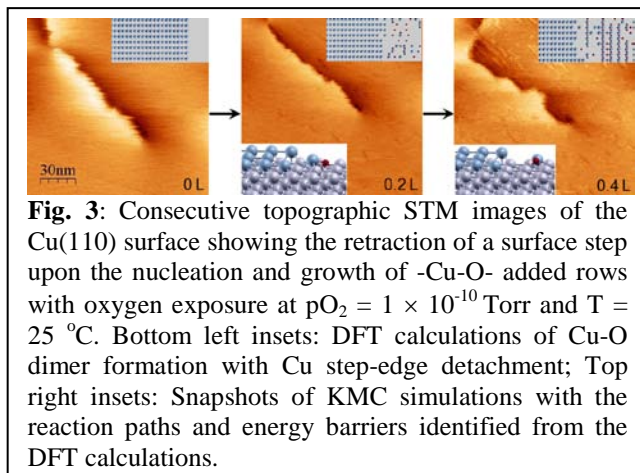


Fig. 3: Consecutive topographic STM images of the Cu(110) surface showing the retraction of a surface step upon the nucleation and growth of -Cu-O- added rows with oxygen exposure at $p\text{O}_2 = 1 \times 10^{-10}$ Torr and $T = 25$ °C. Bottom left insets: DFT calculations of Cu-O dimer formation with Cu step-edge detachment; Top right insets: Snapshots of KMC simulations with the reaction paths and energy barriers identified from the DFT calculations.

removed from the step edge to supply the growth of -Cu-O- added rows. Using STM, we also demonstrated that the Cu(110) surface restructuring proceeds via a sequential pathway of (2×1) → *c*(6×2) through a mechanism that consumes the existing (2×1) phase and depletes the underlying Cu terrace atoms. We employed DFT, AIMD, and NEB techniques to study the (2×1) → *c*(6×2) transition. We found that the transition from a configuration containing four Cu-O-Cu-O chains to the *c*(6×2) structure requires the concerted movement of three Cu atoms with an associated energy barrier of 1.41 eV [9], which is suggested as the origin of the kinetic hindrance that causes discrepancy between experimental observations and the theoretical O/Cu(110) equilibrium phase diagram obtained by the first-principle thermodynamics [10].

Future Plans

Sub-surface O incorporation represents a crucial step for initiating oxide formation. Developing a deep understanding of O penetration below metal and alloy surfaces is of importance not only for controlling the initial stages of metal and alloy oxidation but also for harnessing many other technologically important processes involving sub-surface O penetration, such as catalysis, oxygen storage at a metal/oxide interface, and metal passivation. We will elucidate the energetics and kinetics of O sub-surface adsorption and determine how they depend on the surface structure, morphology and composition with the research goal of controlling sub-surface oxidation via tuning O sub-surface incorporation. Two different experimental systems, i.e., surface orientation and surface alloying, along with the effect of temperature and oxygen pressure, will be investigated for establishing the principles capable of predicting the trend and controlling the process of sub-surface O adsorption. We will also study the atomic process governing the transformation of the crystal lattice of the parent metal into its oxide upon further subsurface O adsorption. Gaining a deeper knowledge of the oxide formation pathway is

essential not only for understanding the oxidation mechanism but has also practical importance because the likely lively dynamics between the metastable and stable configurations will affect the surface chemical properties under realistic conditions, and, for instance, any catalytic reactions taking place over them.

References

- [1] H. L. Qin, X. D. Chen, L. Li, P. Sutter, and G. W. Zhou, *Proc. Natl. Acad. Sci.* 112 (2015) E103.
- [2] J. P. Pierce and K. F. McCarty, *Phys. Rev. B* 71 (2005) 125428.
- [3] J. P. Pierce, N. C. Bartelt, R. Stumpf, and K. F. McCarty, *Phys. Rev. B* 77 (2008) 195438.
- [4] K. F. McCarty, J. P. Pierce, and C. B. Carter, *Appl. Phys. Lett.* 88 (2006) 141902.
- [5] K. F. McCarty, J. A. Nobel, and N. C. Bartelt, *Nature* 412 (2001) 622.
- [6] K. F. McCarty, J. A. Nobel, and N. C. Bartelt, *Phys. Rev. B* 71 (2005) 085421.
- [7] L. Li, L. L. Luo, J. Ciston, W. A. Saidi, E. A. Stach, J. C. Yang, and G. W. Zhou, *Phys. Rev. Lett.* 113 (2014) 136104.
- [8] L. Li, N. Cai, W. A. Saidi, and G. W. Zhou, *Chem. Phys. Lett.* 613 (2014) 64.
- [9] L. Li, Q. Q. Liu, J. Li, W. A. Saidi, and G. W. Zhou, *J. Phys. Chem. C* 118 (2014) 20858.
- [10] Q. Q. Liu, L. Li, N. Cai, W. A. Saidi, and G. W. Zhou, *Surf. Sci.* 627 (2014) 75.

Publications in the Last Two Years

1. J. Li, G.F. Wang, G.W. Zhou, "Surface segregation phenomena in extended and nanoparticle surfaces of Cu-Au alloys", *Surf. Sci.* (in press)
2. L. Yuan, X.M. Chen, S. Maganty, J. Cho, C.H. Ke, G.W. Zhou, "Enhancing the oxidation resistance of copper by using sandblasted copper surfaces", *Appl. Surf. Sci.* (in press)
3. J. Li, L. Li, G.W. Zhou, "The onset of sub-surface oxidation induced by defects in an oxygen chemisorbed layer", *J. Chem. Phys.* **142**, 084701 (2015)
4. L.L. Luo, Y.H. Kang, J.C. Yang, G.W. Zhou, "Nucleation and growth of oxide islands during the initial-stage oxidation of (100)Cu-Pt alloys", *J. Appl. Phys.* **117**, 065305 (2015)
5. H.L. Qin, X.D. Chen, L. Li, P. Sutter, G.W. Zhou, "Oxidation-driven surface dynamics on NiAl(100)", *Proc. Natl. Acad. Sci.* **112**(2), E103-109 (2015)
6. L. Li, L.L. Luo, J. Ciston, W.A. Saidi, E.A. Stach, J.C. Yang, G.W. Zhou, "Surface-step-induced oscillatory oxide growth", *Phys. Rev. Lett.* **113**, 136104 (2014)
7. L. Li, N. Cai, W.A. Saidi, G.W. Zhou, "Role of oxygen in Cu(110) surface restructuring in the vicinity of step edges", *Chem. Phys. Lett.* **613**, 64-69 (2014)
8. L. Li, Q.Q. Liu, J. Li, W.A. Saidi, G.W. Zhou, "Kinetic barriers of the phase transition in the oxygen chemisorbed Cu(110)-(2x1)-O as a function of oxygen coverage", *J. Phys. Chem. C* **118**, 20858-20866 (2014)
9. H.L. Qin, P. Sutter, and G.W. Zhou, "The crystallization of amorphous aluminum oxide thin films grown on NiAl(100)", *J. Am. Ceram. Soc.* **97**, 2762-2769 (2014)
10. Q.Q. Liu, L.Li, N. Cai, W.A. Saidi and G.W. Zhou, "Oxygen chemisorption-induced surface phase transitions on Cu(110)", *Surf. Sci.* **627**, 75-84 (2014)
11. L.L. Luo, Y.H. Kang, J.C. Yang, D. Su, Eric A. Stach and G.W. Zhou, "Comparative study of the alloying effect on the initial oxidation of Cu-Au(100) and Cu-Pt(100)", *Appl. Phys. Lett.* **104**, 121601 (2014)

Growth And Properties Of New Epitaxial Metal/Semiconductor Nanocomposites

Joshua M. O. Zide, Materials Science and Engineering, University of Delaware

Program Scope

Nanocomposites consisting of nanoparticles (such as ErAs) within III-V semiconductors represent a useful alternative to conventional materials for a variety of applications. The incorporation of nanoparticles into semiconductors can pin the Fermi level, drastically altering the electronic properties in ways that are fundamentally different from conventional doping. Carrier concentrations and dynamics can be altered, and phonon scattering of medium wavelength phonons can be observed. These effects allow applications such as terahertz source and detectors, thermoelectrics, enhanced tunnel junctions for multijunction solar cells, and others. These materials have been studied using molecular beam epitaxy (MBE)-grown materials, and the epitaxial relationship between the rocksalt crystal structure of the nanoparticles and the zincblende structure of the matrix allows high quality interfaces, allowing the study of the fundamental charge transfer mechanisms in nanostructured electronic composites.

Although the prior work by MBE has enabled significant advances in the understanding of a subset of this class of composite materials, the hallmarks of MBE-grown material are a lack of flexibility in composition, a slow growth rate, and very high cost. *To these ends, this project is focused on creating epitaxial nanocomposites via a hybrid approach in which nanoparticles are produced using inert gas condensation (IGC) and incorporated epitaxially into semiconductor films using liquid phase epitaxy (LPE).* This approach allows a wider cross-section of these materials to be studied by providing independent control over nanoparticle production and film growth. Additionally, from a technological point of view, the hybrid approach should allow growth rates of micrometers per minute rather than micrometers per hour, thus allowing thicker films and scaling of materials. The fundamental goal of this program is to develop this new growth approach and apply it to the study of this class of materials. Because this is a fundamentally new approach to nanocomposite synthesis, it presents many new challenges and also many new opportunities. As described below, many obstacles have been addressed, but as we overcome these obstacles, we can expand this approach beyond this particular class of materials in the hopes of establishing a new paradigm in nanocomposite synthesis for electronic materials.

Recent Progress

IGC Growth of ErAs

Because this program centers is based on a fundamentally new synthesis approach, we have encountered many challenges over the past two years. The first requirement of the program was the ability to generate controlled ErAs nanoparticles via inert gas condensation (IGC). Several changes have been made to the initial design of the IGC approach for this material system to improve performance. Due to relatively high operating pressure (5-100 torr of He gas), the arsenic source was changed from a valved arsenic cracker to the simultaneous ablation of both erbium and arsenic by a pulsed Nd:YAG laser. This allows for a more spatially confined

interaction region for the two vapors, leading to higher purity nanoparticles. Source powders are compressed into pellets, which are then placed into glass beakers; the walls of which serve as the collection substrate. The large collection area allows for hundreds of milligrams of powder to be collected at a time, resulting in a much higher yield than typical magnetron sputtering techniques for nanoparticles. Particles that are collected on the beaker are then scraped into a vial using a stainless steel scraper inside a glove bag attached to the chamber.

Through systematic experimentation, we have determined conditions appropriate for creating ErAs nanoparticles with sizes of 5 ± 1 nm diameters. This is the first demonstration of the growth of ErAs nanoparticles without a host matrix. A transmission electron microscopic (TEM) image of the ErAs particles is shown in Figure 1 along with the selected area electron diffraction (SAED) pattern obtained from the area. Powder x-ray diffraction (PXRD) and energy dispersive spectroscopy (EDS) are used to confirm the presence of ErAs as well as characterize other compounds in the resultant nanoparticle powders. From XRD analysis, we are able to confirm that the powders contain as much as 76% ErAs. Other phases present in the powders include (as expected) erbium, erbium oxide, arsenic, and arsenic oxide. These byproducts do not represent a problem; erbium itself acts as a gettering agent in the LPE growth of GaAs films, improving the overall film quality, and arsenic is already added to the LPE melt before it can be used for growth.

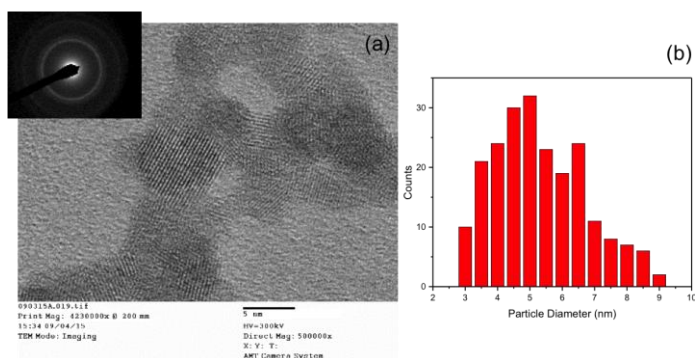


Figure 1: (a) TEM image (with corresponding SAED pattern, inset) for ErAs nanoparticles grown by IGC, (b) particle size distribution

Discovery and Characterization of new Er-As Phase

One of the opportunities presented by a new synthesis approach is the possibility of unexpected discoveries. Previously, only one phase of ErAs (specifically, the rocksalt monpnictide) was known to exist. While theoretical predictions of other phases have been made recently [1], we were excited to discover a phase that does not exist on any phase diagrams.

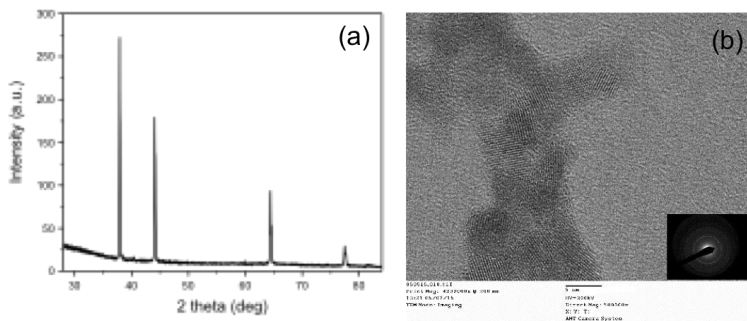


Figure 2: (a) XRD pattern of new phase observed (b) TEM image of particles and corresponding SAED pattern. Lattice fringes show crystalline nanoparticles.

Produced under erbium-rich growth conditions, this phase appears (from PXRD) to have a cubic $Pm\bar{3}m$ [221] structure with a lattice constant of approximately $a = 4.08 \text{ \AA} \pm 0.01 \text{ \AA}$. EDS and SAED patterns obtained from TEM analysis of this sample agree with the XRD results and suggest that the compound is Er-rich. (Figure 2) We have begun collaborations with Dr. James LeBeau and Dr.

Anderson Janotti to determine the crystal structure of this compound using scanning transmission electron microscopy (STEM) and density functional theory (DFT), respectively, to more accurately identify this phase and any important properties which it may possess.

LPE Growth of GaAs and ErAs:GaAs

The first objective of the work on thin film growth by liquid phase epitaxy (LPE) was to demonstrate the uniform growth of GaAs on a GaAs substrate. As growth conditions described in literature vary widely, optimization of these seemingly-simple growth conditions led to some initial delays. At the same time, proper control over growth conditions is a prerequisite for high-quality growth of nanocomposites. Recently, we have attempted to incorporate nanoparticles into the thin film by adding these nanoparticles obtained from IGC into the melt for LPE growth. The thin films that were grown with these melts were first characterized with spectrophotometry and Fourier Transform Infrared (FTIR) spectroscopy, as these are rapid characterization tools commonly used to study films grown with MBE. [2] While absorption features were observed in these first samples, the absorption intensity is reduced compared to MBE grown films. TEM study does appear to show the incorporation of particles (Figure 3), but quantification has not been possible. We attributed these observations to a relatively low concentration of ErAs nanoparticles in the melt, and have since increased the concentration from ~0.1% to ~5%. This change in the melt composition has changed the growth window somewhat for GaAs thin films, and we are now working to optimize growth conditions to control the incorporation of nanoparticles into the films.

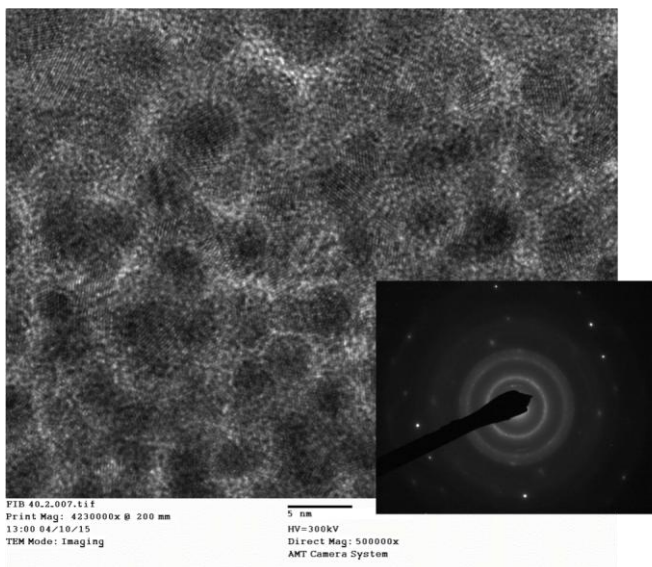


Fig. 3: TEM micrograph of ErAs:GaAs film. Inset: SAED of this region; the apparent polycrystallinity of the inclusion phase is not yet understood.

Future Plans

IGC Growth of Nanoparticles

We are currently working on controlling the size of particles that we are able to produce via the IGC method. Ideally, we would like to have particles that are ~1-2 nm in diameter in order to directly compare to MBE grown films. However, wider particle size distributions is actually beneficial for thermoelectric materials, as different size particles are able to scatter phonons of different wavelengths. Most fundamentally, control of particle size, while elusive in MBE, gives the ability to study surface vs. volume effects in nanoparticle-containing systems.

Other avenues of research in the near future include investigating the recently-discovered new phase further to try to identify any useful properties it may contain and the growth of other rare-earth arsenides, (namely Tb and Nd), which will begin in the next few months. Another topic of interest that merits further investigation is the oxidation of ErAs nanoparticles. Previous

work on ErAs thin films has shown that they oxidize rapidly, requiring a capping layer in order to be studied[3]. Initially, the IGC chamber was designed so that particles could be incorporated into a Ga melt without any exposure to air. However, it appears that the particles are able to remain stable in air or ethanol for moderate amounts of time (weeks). We are currently collaborating with Dr. Robert Opila to complete x-ray photoelectron spectroscopic analysis of the oxidation of these particles. An understanding of the oxidation of these particles allows the study of electronic band structure, which is a critical complement to existing studies performed in embedded-nanoparticles.

LPE Growth of Nanocomposites

As we complete our systematic study of the effects of growth conditions on film morphology and nanoparticle incorporation, we hope to expand our study of film morphology using STEM. As this growth approach becomes mature, we plan to study thermal and electrical properties of these materials. More specifically, Hall effect will be used to measure carrier concentration and mobility, while Seebeck measurements and thermal conductivity measurements (using time-domain thermoreflectance) will be employed to study thermoelectric properties. Through a long-standing collaboration with researchers at Los Alamos National Laboratory (through the CINT program), we intend to study the carrier dynamics in these materials. More importantly, as new nanoparticles are produced, we can use the ErAs:GaAs results as a benchmark for the study of this otherwise-underexplored class of materials.

Additionally, the LPE growth of InGaAs thin films on InP is an established technology [4], and we intend to study nanocomposites with this alternate matrix material for applications in thermoelectrics and terahertz devices.

References

- [1] P. Pandit, V. Sricastava, M. Rajagopalan, and S. Sanyal, "Structural and Electronic properties of Er-Monopnictides Under High Pressure", *Physica B*, vol. 405, pgs 2245-2250, (2010).
- [2] E. R. Brown, A. Bacher, M. H. D. Driscoll, C. Kadow, and A. C. Gossard, "Evidence for a Strong Surface-Plasmon Resonance on ErAs Nanoparticles in GaAs," *Phys. Rev. Lett.* vol. 90, no. 077403, February 2003.
- [3] H. Jeong, T. Komesu, C. Yang, P. Dowben, D. Schultz, and C. Palmstron, "Photoemission and Forward Scattering from ErAs(100)/GaAs(100)", *Materials Letters*, vol. 58, pgs. 2993-2996, (2004).
- [4] W. Gao, P. R. Berger, M. H. Ervin, J. Pamulapati, R. T. Lareau, and S. Schauer. "Liquid phase epitaxial growth of InGaAs on InP using rare earth treated melts," *Journal of Applied Physics*, vol. 80, no. 7094, 1996.

Publications

M. Lewis, K. Bichoupan, J. LeBeau, J. Zide. “Growth and Characterization of ErAs Nanoparticles Grown by Pulsed Laser Ablation in an Inert Environment” (In preparation).

B. E. Tew, M. R. Lewis, C. C. Bomberger, J. M. LeBeau, J. M. O. Zide. “Demonstration of a new hybrid synthesis approach for epitaxial metal/semiconductor nanocomposites” (In preparation).

B. E. Tew et al. “Thermoelectric Transport in GaAs with Varying Concentration of Rare-Earth ErAs Embedded Nanoparticles by Liquid Phase Epitaxy” (In preparation).

Participant List

<u>Name</u>	<u>Organization</u>	<u>E-mail Address</u>
Arnold, Michael	University of Wisconsin	michael.arnold@wisc.edu
Bent, Stacey	Stanford University	sbent@stanford.edu
Bhattacharya, Anand	Argonne National Laboratory	anand@anl.gov
Božović, Ivan	Brookhaven National Laboratory	bozovic@bnl.gov
Chabal, Yves	University of Texas at Dallas	chabal@utdallas.edu
Chambers, Scott	Pacific Northwest National Laboratory	sa.chambers@pnnl.gov
Chason, Eric	Brown University	Eric_chason_phd@brown.edu
Chen, I-Wei	University of Pennsylvania	iweichen@seas.upenn.edu
Clarke, Amy	Los Alamos National Laboratory	aclarke@lanl.gov
Csathy, Gabor	Purdue University	gcsathy@purdue.edu
Cui, Jun	Ames Laboratory	cuijun@iastate.edu
Davenport, James	U.S. Department of Energy	james.davenport@science.doe.gov
De Yoreo, Jim	Pacific Northwest National Laboratory	james.deyoreo@pnnl.gov
Dee, Nicholas	Massachusetts Institute of Technology	nicktdee@mit.edu
DiTusa, John	Louisiana State University	ditusa@www.phys.lsu.edu
Dudney, Nancy	Oak Ridge National Laboratory	dudneynj@ornl.gov
Ediger, Mark	University of Wisconsin-Madison	ediger@chem.wisc.edu
Eom, Chang-Beom	University of Wisconsin-Madison	eom@engr.wisc.edu
Fedorov, Andrei	Georgia Institute of Technology	AGF@gatech.edu
Fichthorn, Kristen	Pennsylvania State University	fichthorn@psu.edu
Geohegan, David	Oak Ridge National Laboratory	geohegandb@ornl.gov
Gersten, Bonnie	U.S. Department of Energy	bonnie.gersten@science.doe.gov
Gupta, Malancha	University of Southern California	malanchg@usc.edu
Han, Jung	Yale University	jung.han@yale.edu
Hart, Anastasios John	Massachusetts Institute of Technology	ajhart@mit.edu
Huang, Hanchen	Northeastern University	h.huang@neu.edu
Jain, Himanshu	Lehigh University	h.jain@lehigh.edu
Jalan, Bharat	University of Minnesota	bjalan@umn.edu
Jin, Rongying	Louisiana State University	rjin@lsu.edu
Johnson, Duane	Ames Laboratory	ddj@ameslab.gov
Kaganovich, Igor	Princeton Plasma Physics Laboratory	ikaganov@pppl.gov
Kramer, Matthew	Ames Laboratory	mjkramer@ameslab.gov
Kuskovsky, Igor	Queens College, The City Univ. of New York	Igor.Kuskovsky@qc.cuny.edu
Lagally, Max G.	University of Wisconsin-Madison	lagally@engr.wisc.edu
Levin, Evgenii	Ames Laboratory	levin@iastate.edu
Li, Dongsheng	Pacific Northwest National Laboratory	dongsheng.li2@pnnl.gov
Li, Jing	Rutgers University	jingli@rutgers.edu
Liu, Feng	University of Utah	fliu@eng.utah.edu
Liu, Jun	Pacific Northwest National Laboratory	jun.liu@pnnl.gov
Lograsso, Thomas	Ames Laboratory	lograsso@ameslab.gov
Lunt, Richard	Michigan State University	rlunt@msu.edu
Manfra, Michael	Purdue University	mmanfra@purdue.edu
Mangolini, Lorenzo	University of California, Riverside	lmangolini@engr.ucr.edu
Mao, Zhiqiang	Tulane University	zmao@tulane.edu
Napolitano, Ralph	Ames Laboratory	ren1@iastate.edu
Ni, Ni	University of California, Los Angeles	nini@physics.ucla.edu
Nolas, George	University of South Florida	gnolas@usf.edu
Olevsky, Eugene	San Diego State University	eolevsky@mail.sdsu.edu
Paiella, Roberto	Boston University	rpaiella@bu.edu
Perepezko, John	University of Wisconsin-Madison	perepezk@engr.wisc.edu

Perry, Kelly	U.S. Department of Energy	kelly.perry@science.doe.gov
Petrovic, Cedimir	Brookhaven National Laboratory	petrovic@bnl.gov
Poudeu, Pierre Ferdinand	University of Michigan	ppoudeup@umich.edu
Puttaiah, Nagabhushana GP	University of California	ngp@ucdavis.edu
Raitses, Yevgeny	Princeton Univ. Plasma Physics Laboratory	yraitses@pppl.gov
Reinhard, Bjoern	Boston University	bmr@bu.edu
Rioux, Robert	Pennsylvania State University	rioux@enr.psu.edu
Schlom, Darrell	Cornell University	schlom@cornell.edu
Shoemaker, Daniel	University of Illinois	dpshoema@illinois.edu
Siegrist, Theo	Florida State University	tsiegrist@fsu.edu
Sushko, Petr	Pacific Northwest National Laboratory	peter.sushko@pnl.gov
Switzer, Jay	Missouri Univ. of Science and Technology	jswitzer@mst.edu
Tamargo, Maria	The City College of New York	tamar@sci.ccnycun.edu
Thonhauser, Timo	Wake Forest University	thonhauser@wfu.edu
Thornton, Katsuyo	University of Michigan	kthorn@umich.edu
Tringides, Michael	Ames Laboratory Iowa State University	tringides@ameslab.gov
Voorhees, Peter	Northwestern University	p-voorhees@northwestern.edu
Wang, Xudong	University of Wisconsin-Madison	xudong@enr.wisc.edu
Xiao, Kai	Oak Ridge National Laboratory	xiaok@ornl.gov
Yakobson, Boris	Rice University	biy@rice.edu
Yoon, Mina	Oak Ridge National Laboratory	myoon@ornl.gov
Young, David	Louisiana State University	dyoung@phys.lsu.edu
Zaera, Francisco	University of California	zaera@ucr.edu
Zhang, Pengpeng	Michigan State University	zhang@pa.msu.edu
Zhou, Guangwen	SUNY at Binghamton	gzhou@binghamton.edu
Zide, Joshua	University of Delaware	zide@udel.edu

Author Index

An, Ke.....	25	Jain, Himanshu	168
Arnold, Michael S.	101	Jin, R.....	129
Banerjee, Debasis	112	Kaganovich, Igor	75
Bent, Stacey F.....	107	Kaspar, T. C.	13
Bhattacharya, Anand	3	Keidar, Michael	75
Bollinger, Anthony T.....	8	Koel, Bruce.....	75
Božović, Ivan.....	8	Kramer, M. J.....	55, 60, 65
Canepa, Pieremanuele	112	Krstic, Predrag	75
Car, Roberto	75	Kuskovsky, I. K.....	259
Chabal, Yves J.....	112	Lagally, Max G.....	174
Chambers, Scott A.....	13	Levin, Evgenii M.....	38
Chason, Eric	118	Li, Dongsheng	42
Chen, I-Wei	123	Li, Jing.....	112
Chen, Yan	25	Li, Juchuan	25
Chi, Miaofang.....	25	Li, Xufan.....	31, 85, 92
Clarke, Amy J.....	19	Liang, Chengdu	25
Coughlin, D. R.....	19	Liu, Jun	45
Csathy, Gabor	125	Liu, Yong.....	51
Dalal, S. S.....	133	Lograsso, Thomas A.....	38, 51
De Yoreo, James J.	45	Lunt, Richard R.	181
Deibert, Benjamin J.....	112	Ma, Cheng	25
Dierolf, Volkmar	168	Mahjouri-Samani, Masoud	31, 85, 92
DiTusa, John F.....	129	Manfra, Michael	125
Droubay, T. C.....	13	Mangolini, Lorenzo	185
Du, Y.	13	Mao, Zhiqiang	129, 189
Dudney, Nancy J.	25	Mendelev, M. I.	60, 65
Duscher, Gerd.....	31, 85, 92	Meriles, C. A.	259
Ediger, Mark D.....	133	Mertens, J. C. E.	19
Eom, Chang-Beom	137	Moustakas, T. D.	193, 215
Eres, Gyula	31, 85, 92	Muller, David A.....	234
Eriksson, Mark A.....	174	Napolitano, R. E.	55, 60, 65
Fedorov, Andrei G.....	141	Navrotsky, Alexandra.....	197
Fennie, Craig J.....	234	Ni, Ni	203
Fichthorn, Kristen A.....	146	Nolas, George S.....	207
Fuentes, Erika	112	Noyan, I. C.	259
Geohegan, David B.	31, 85, 92	Olevsky, Eugene A.....	209
Gibbs, J. W.	19	Ott, R. T.....	55, 60, 65
Gujral, A.	133	Paiella, Roberto	193, 215
Gupta, Malancha.....	150	Patterson, B. M.	19
Han, Jung.....	153	Perepezko, John H.....	219
Hart, A. John.....	159	Petrovic, Cedomir	70
Ho, K. M.....	55, 60, 65, 79	Plummer, E. W.	129
Huang, Bing.....	31, 85, 92	Poudeu, Pierre Ferdinand	223
Huang, Hanchen	164	Puretzky, Alex	31, 85, 92
Hupaló, M.....	79	Raitses, Yevgeny	75
Imhoff, S. D.....	19	Reinhard, Bjoern.....	229

Rioux, R. M.	146	Zhou, Guangwen	290
Rouleau, Christopher M.	31, 85, 92	Zide, Joshua M. O.	294
Ryu, Hyejin.....	70	Zuluaga, Sebastian.....	112
Sankaran, Mohan.....	75		
Schiffer, Peter	234		
Schlom, Darrell G.....	234		
Shelton, W. A.	129		
Shneider, Mikhail	75		
Shoemaker, Daniel P.	244		
Siegrist, Theo.....	248		
Song, Jie	153		
Song, X. Y.	65		
Spurgeon, S. R.....	13		
Stratton, Brent.....	75		
Sushko, Maria.....	45		
Sushko, P. V.	13		
Switzer, Jay A.....	254		
Tamargo, Maria C.	259		
Tan, Kui.....	112		
Thallapally, Praveen	45		
Thiel, P. A.....	79		
Thonhauser, Timo.....	112		
Thornton, Katsuyo.....	265		
Tian, Mengkun	31, 85, 92		
Touret, D.	19		
Tringides, Michael C.	79		
Uher, Ctirad	223		
Van der Ven, Anton.....	223		
Voorhees, Peter W.....	265		
Walters, D. M.	133		
Wang, C. Z.	55, 60, 65, 79		
Wang, Hao.....	112		
Wang, Kai.....	31, 85, 92		
Wang, Xudong.....	269		
Wei, Jiang	189		
Wu, Jie	8		
Xiao, Kai.....	31, 85, 92		
Xing, Qingfeng	38, 51		
Yablinsky, C. A.	19		
Yakobson, Boris I.....	274, 277		
Yoon, Mina.....	31, 85, 92		
Young, D. P.	129		
Yuan, Ge.....	153		
Zaera, Francisco	280		
Zhang, J. D.	129		
Zhang, Pengpeng	285		